Proceedings of Second Specialists' Meeting on

SHIELDING ASPECTS OF ACCELERATORS, TARGETS AND IRRADIATION FACILITIES

CERN
Geneva, Switzerland
12-13 October 1995

organised by the

OECD Nuclear Energy Agency

the Shielding Working Group of the Reactor Physics Committee – Japan

the Radiation Shielding Information Center – U.S.A.

NUCLEAR ENERGY AGENCY
ORGANISATION FOR ECONOMIC CO-PERATION AND DEVELOPMENT

ORGANISATION FOR ECONOMIC CO-OPERATION AND DEVELOPMENT

Pursuant to Article 1 of the Convention signed in Paris on 14th December 1960, and which came into force on 30th September 1961, the Organisation for Economic Co-operation and Development (OECD) shall promote policies designed:

- to achieve the highest sustainable economic growth and employment and a rising standard of living in Member countries, while maintaining financial stability, and thus to contribute to the development of the world economy;
- to contribute to sound economic expansion in Member as well as non-member countries in the process of economic development; and
- to contribute to the expansion of world trade on a multilateral, non-discriminatory basis in accordance with international obligations.

The original Member countries of the OECD are Austria, Belgium, Canada, Denmark, France, Germany, Greece, Iceland, Ireland, Italy, Luxembourg, the Netherlands, Norway, Portugal, Spain, Sweden, Switzerland, Turkey, the United Kingdom and the United States. The following countries became Members subsequently through accession at the dates indicated hereafter: Japan (28th April 1964), Finland (28th January 1969), Australia (7th June 1971), New Zealand (29th May 1973), Mexico (18th May 1994), the Czech Republic (21st December 1995) and Hungary (7th May 1996). The Commission of the European Communities takes part in the work of the OECD (Article 13 of the OECD Convention).

NUCLEAR ENERGY AGENCY

The OECD Nuclear Energy Agency (NEA) was established on 1st February 1958 under the name of the OEEC European Nuclear Energy Agency. It received its present designation on 20th April 1972, when Japan became its first non-European full Member. NEA membership today consists of all European Member countries of OECD as well as Australia, Canada, Japan, Republic of Korea, Mexico and the United States. The Commission of the European Communities takes part in the work of the Agency.

The primary objective of NEA is to promote co-operation among the governments of its participating countries in furthering the development of nuclear power as a safe, environmentally acceptable and economic energy source.

This is achieved by:

- *encouraging harmonization of national regulatory policies and practices, with particular reference to the safety of nuclear installations, protection of man against ionising radiation and preservation of the environment, radioactive waste management, and nuclear third party liability and insurance;*
- *assessing the contribution of nuclear power to the overall energy supply by keeping under review the technical and economic aspects of nuclear power growth and forecasting demand and supply for the different phases of the nuclear fuel cycle;*
- *developing exchanges of scientific and technical information particularly through participation in common services;*
- *setting up international research and development programmes and joint undertakings.*

In these and related tasks, NEA works in close collaboration with the International Atomic Energy Agency in Vienna, with which it has concluded a Co-operation Agreement, as well as with other international organisations in the nuclear field.

Figure caption of cover page: ***Rem counter LINUS – Longitudinal cross-section.***
Credit: INFN Milan and Frascati – Italy.

FOREWORD

While accelerators were used in the past essentially for basic research, they are now playing an increasingly important role in technological and medical applications. Several new facilities will be started up in the near future and others are being built or planned. These will be of a greater variety, not only in terms of energy but also of intensity, size and application, giving thus rise to new and interesting shielding issues.

It is for this reason that specialists' meetings on Shielding Aspects of Accelerators, Targets and Irradiation Facilities (SATIF) are held: two already took place on 28-29 April 1994, in Arlington, Texas-U.S.A., and on 12-13 October 1995 at the Centre européen de recherche nucléaire (CERN) in Geneva, Switzerland. A third meeting is scheduled for 12-13 May 1997 at CYRIC, University of Tsukuba in Japan. These meetings are jointly organised by the OECD Nuclear Energy Agency, the Shielding Working Group of the Reactor Physics Committee of Japan, and the Radiation Shielding Information Center, U.S.A.

The objectives of the first meeting were to promote the exchange of information among scientists in this particular field, to identify areas where international co-operation would be fruitful, and to initiate a programme of work in order to achieve progress in specific priority areas. Proceedings were published in **Shielding Aspects of Accelerators and Irradiation Facilities**, in 1995.

About 50 experts from 11 countries and two international organisations attended the second meeting, the objective of which was first to review the progress achieved since the first meeting. It was then to monitor the status of actions relating to basic data, methods, codes and experiments required for shielding calculations and identify new co-operation incentives in view of meeting the requirements and improving common understanding in the field of technical and safety issues.

As a whole, considerable progress and work have been achieved since the first meeting. These proceedings give a thorough insight of the work accomplished and draw up the state of shielding aspects related to accelerators, targets and irradiation facilities in Member countries, as a follow-up to the ones published after the first meeting.

The opinions expressed in these proceedings are those of the authors only and do not necessarily represent the position of any Member country or international organisation. These proceedings are published on the responsibility of the Secretary-General of the OECD.

CONTENTS

EXECUTIVE SUMMARY

1. Introduction

Two specialists' meetings on Shielding Aspects of Accelerators, Targets and Irradiation Facilities (SATIF) were held so far:

- SATIF-1 at Arlington, Texas, 28-29 April 1994,
- SATIF-2 at CERN, Geneva, 12-13 October 1995.

Both meetings were jointly organised by the OECD/NEA, the Shielding Working Group of the Reactor Physics Committee of Japan and the RSIC (U.S.A.).

The objective of the first meeting was to exchange information in this field among scientists, to identify areas that would benefit from international co-operation and to propose a programme of work and initiatives in order to achieve progress in priority areas. The results of the meeting were published at the beginning of 1995 and were widely distributed ("Shielding Aspects of Accelerators, Targets and Irradiation Facilities", OECD, 1995, ISBN 92-64-14327-0)

The objectives of the second meeting were to review the progress made since the first meeting in the topics discussed, monitor the status of the agreed actions concerning basic data, methods, codes and experiments required for shielding calculations, identify and initiate new concrete co-operative actions to meet the requirements of this discipline and improve the common understanding of the different problems that have technical and safety significance.

A considerable amount of work has been achieved since the first meeting and which is reported in these proceedings covering the second meeting. This second meeting was held in conjunction with another meeting, the second one on Simulating Accelerator Radiation Environments (SARE-2). The specific objectives of the two meetings are different but in order to avoid potential overlap they were reviewed again and it was agreed that they should continue to be held in conjunction with each other because of their complementarity but should aim at separate objectives.

The programme of the meeting is enclosed as Appendix A and the list of about 50 participants is given in Appendix B.

2. Second meeting (SATIF-2)

The meeting was opened by T. Nakamura from the Tohoku University, Chairman of the Shielding Working Group of the Reactor Physics Committee of Japan.

It was attended by 47 experts from 11 countries and 2 international organisations.

The programme of the meeting is enclosed as Appendix A and the list of participants as Appendix B.

3. Technical summary of presentations and discussions

Most technical issues identified at SATIF-1 are still relevant. They are recalled here on the left half of the page, while specific actions are listed on the right half of the page.

3.1 Electron accelerators

a) Photons

Narrow beams present special dosimetry problems because the detector size is larger than the beam size (e.g., gas bremsstrahlung); with such small beams it is difficult to carry out dosimetry measurements. Gas brems-strahlung has to be considered in the shielding of synchrotron radiation facilities, and calculations agree with measurements if proper care is taken in the modelling.	A report describing the issue has been published as CERN/TIS/RP/JM 95-06 by G. Stevenson. It is suggested that a subgroup is formed to prepare an update at SATIF-3. (N. Ipe - Chair, T. Gabriel, G. Stevenson, S. Ban, M. Pelliccioni).

b) Neutrons

For mid- and high-energy neutrons, the dependence of source term on electron energy, target properties and emission angles, and the dependence of attenuation length on electron energy, shield material and angle is not well known.	P. Degtyarenko and G. Stapleton (CEBAF) will collaborate with SLAC and provide an update at SATIF-3.
Improved instruments are needed for measuring neutrons in mixed fields with high photon dose rates.	M. Hoepfert and G. Stevenson (CERN), N. Ipe (SLAC), S. Ban (KEK) P. Degtyarenko (CEBAF) will co-operate in this.
In general, basic photoneutron data files are needed.	Work is in progress in Japan, Fasso` has collected cross-sections.

3.2 Proton accelerators

Various transport computer codes produce reasonable agreement but experimental verification at all shielding depths is needed for the intermediate energy region. Better methods for measuring high-energy dose equivalents are needed. Simple methods for	

Experiments carried out at ISIS (Japan).

dose equivalent calculations have been developed based on state of the art simulation (i.e., FLUKA, LAHET, etc.), but the resulting attenuation lengths need to be checked for consistency against the ones determined in the 1960's.

This is difficult, but attempts have been made below 400 MeV (P. Tabarelli).

3.3 All accelerators

It was recognized that criteria such as maximum credible accident, possible beam loss scenarios, credit for active protection systems, reasonable dose equivalent limits for accidents, etc., are issues that will need increased attention in the future.

"The Control of Prompt Radiation Hazards at Accelerator Facilities" in draft form has been prepared by G. Stapleton (CEBAF). There exists also a CERN internal report (G. Stevenson, M. Hoepfert).

3.4 Spallation target stations and medium energy accelerators

a) Neutrons

Neutron cross sections can be calculated using HETC for energies above 800 MeV by extending the DLC-119/HILO86 multigroup library above 400 MeV. Coupling Monte Carlo with one-dimensional discrete ordinates calculations works well as long as the coupling surface is far enough from the target, so neutrons are the dominant particle.

Coupling with two-dimensional discrete ordinates codes should be considered for studying streaming problems.

Work in progress for low-energy transport by R. Lillie and J. Johnson (ORNL) S. Lee and R. Alcouffe (LANL).

b) Intermediate energy heavy ions

Measured differential neutron and proton data are reproduced fairly well by Intranuclear Cascade Evaporation (INCE) codes (100-800 MeV), but the resulting attenuation length and the geometry under which they were determined need to be compared with those determined in the 1960's.

Proposal made at LANL.
Update at SATIF-3.

The QMD code is an alternative still being developed.	The first stage has been developed (H. Nakashima). Update will be provided at SATIF-3.
Systematic measurements, including neutron production cross sections, are needed for a range of ions.	Work is in progress in Japan: 3 accelerators: – 70 MeV/nucleon, – 100 MeV/nucleon, – 800 MeV/nucleon. Update at SATIF-3.
Theoretical models for neutron yields calculations need to be benchmarked.	QMD code can be used. R. Donahue will provide data and T. Gabriel will carry out the work and report at SATIF-3.
Takasaki Ion Accelerators for Advanced Radiation Application (TIARA) The quasi-monoenergetic neutron source facility in Japan has been developed for shielding experiments and cross-section measurements (20-90 MeV) and Monte Carlo and discrete ordinates codes using HILO86 have been used to compare with measurements.	
Interest was expressed in exploring the possibility of the international community making proposals to JAERI for use of the neutron beam line.	T. Nakamura should be contacted. It is open for universities.

c) Computer codes and data

Reports on the various major shielding code systems were made. It is felt that the NEADB and RSIC can provide beneficial services to the accelerator shielding specialists by packaging and disseminating modern frozen versions of the transport and auxiliary codes and data libraries in common use. That is not the current situation. It is recommended that the Centers obtain state-of-the-art codes.	Codes have reached a certain maturity today. Further progress is being made. Several new codes were released to the information centers as reported in the last paper of the proceedings. Several other codes have been discussed at SATIF-2 which have not yet been released yet. These are:

FLUKA95, LAHET2.8, MARS13(95), CINDER95, GEANT3.21, DPMJET-II, STRUCT, DTUNUC, GCALOR, SENSIBL, DTUJET, HILO86R, MUCARLO, MCPHOTO, PHOJET, QMD, DINREG, NMTC-3STEP, HETC-3STEP, NMTC-ISOBAR, HERMES, PKN-H, HETC95, SINBAD, PEREGRINE, QKERMA.

RSIC and the NEADB recommend that this codes are released and shared among the international experts.

Extensive work is being carried out in code development for relativistic heavy ion physics, however this aspect has not been covered by participants.

4. Data needs and suggestions expressed by the participants

4.1 Basic atomic and nuclear data

Shielding of modern high -intensity accelerators in the intermediate energy range (< 5 GeV) requires double differential cross-sections for neutrons, pions, light and heavy ions (at least up to A=18), for energies between 20 MeV and 5 GeV. At the present time these data are scarce and scattered among internal reports and journal articles.

Efforts should be made on two fronts:
first, to compile existing data in a computer-readable form;

Some data has been collected by A. Ferrari, by LANL and by the NEA Data Bank (Intermediate Energy EXFOR data base).

and second, to carry out experiments to fill the main gaps.

Experimental Facilities capable of carrying out these experiments are located at LANL and SATURNE in France.

A search of available nuclear models which could be used to complement experimental data would also be useful.

A lot of work is in progress by many facilities. E. Menapace agreed to co-ordinate efforts within Subgroups 12+13 of WPEC.

Other data of interest include isotope production data, total and elastic cross sections, and thick target yields and angular distributions for the particles and energies listed above.

The NEADB has collected some data in a data base. Experts from Japan, LANL and Fasso` have also some data available.

In some cases, new experimental data are required to resolve conflicts between different experiments, or to confirm data which are in apparent conflict with the most widely used models. As an example there are inconsistencies in the available data for pion absorption cross-sections in the resonance region, and trends such as pi-charge exchange versus A should be confirmed by further experiments.

Concerning electron accelerators, there is a lack of knowledge about forward brems-strahlung yields from thick targets at energies higher than 100 MeV.	Work being carried out at SLAC.
The existing compilations of photonuclear cross sections (Dietrich and Berman) are useful but insufficient: They cover only a limited number of nuclei and some of the most common ones (e.g., iron) are missing. In addition, only the giant resonance energy range is considered, and only photoneutron production is reported. There is a need for total photonuclear cross-sections, photo-neutron yields from thin and thick targets, photoneutron angular distributions for all most common elements at all energies.	A. Fasso` has collected some data.
In the highest energy range (E > 200 MeV), photopion yields and angular distributions are necessary. More generally, there is a lack of available data for double differential cross sections of pion emission in nuclear interactions by any kind of projectile (proton, neutron, pion, photon) at energies larger than 300 MeV.	
Other data needs concern albedo of neutrons with energies higher than 20 MeV (useful for streaming calculations),	
Isotope production data (possibly for thin targets), and (n, gamma) cross sections above 20 MeV.	
The lack of (n, gamma) data for barium isotopes below 20 MeV was also mentioned.	Work in progress at ENEA Bologna (G. Maino, G.C. Panini). Updates will be provided at SATIF-3.

4.2 Shielding experiments

Forward and lateral attenuation should be measured up to at least 5 or 6 m of concrete for proton and ion accelerators with energies lower than 5 GeV. There is a particular need for data in the 100-800 MeV/m energy range. The dependence on energy of attenuation length and apparent source term should be established with	better accuracy than

at present. It was stressed that the results should be expressed also in terms of fluence or other basic physical quantity in order to allow a re-evaluation of the data in case new dose conversion coefficients should apply. At electron accelerators, forward and lateral attenuation curves should be measured in order to check the semi-empirical formulae in general use. This information is needed for both thin and thick targets, and should include thin shielding layers.

4.3 Other experimental information

There is a need for better measurements of many activation detector excitation functions, in particular 11-C production by neutrons and pions in the energy range above 100 MeV.

Work being carried out at CYRIC (T. Nakamura).

Determining the response function above 20 MeV of other detectors (instruments based on moderation, scintillators) with mono-chromatic neutron beams would also be useful. A measurement of target heating with targets of low atomic number was suggested in order to resolve existing conflicting calculated data.

LINUS at INFN Milan and Frascati. Similar REMmeter by S. Ban.

4.4 Improvements in modelling and computer codes

Light and heavy ions are not treated by existing Monte Carlo transport codes, or are with an accuracy not yet comparable with that of reactions induced by protons and neutrons. Models are needed to implement satisfactory event generators.

The intranuclear cascade model for hadron interactions in the intermediate energy range has been used successfully for over 20 years. However some deficiencies are well known, in particular, the backward particle emission and the emission at very small angles is not satisfactory. Improvements based on modern physical concepts which have already shown promising results in some recent code developments can help solving most known problems.

Work in progress.

Also fragmentation models are necessary to improve residual nuclei predictions.

A special issue was raised about the quality control of computer programs. It was suggested that a theoretical analysis be made about models and experimental data, aiming at identifying common features and differences among various codes, so that the cause of discrepancies in the results could be traced.

5. Recommendations and agreed actions

This section compares the recommendations made at SATIF-1 and describes the achievements reported at SATIF-2. (In parenthesis the names of the persons or organisations involved in specific work are given).

Action	*Achievements/Further Action*
1. Collect and make available anthropo morphic phantom geometries including material compositions as used in Monte Carlo radiation transport codes (RSIC, NEADB, PTB, GSF);	Work in progress as reported in "Anthropomorphic Computational Models" (Sartori, NEA). Put on World Wide Web before the next meeting (L. Waters, LANL). Differences in models will be stated.
2. Collect and make available existing data on:	
– Thin target measurements (p, n, pi, HI) (A. Ferrari, L. Waters, E. Sartori);	Some data has been collected (A. Ferrari) Provide data to E. Sartori (NEADB) for open distribution by SATIF-3. (A. Fasso`, A. Ferrari).
– Thick target measurements (T. Nakamura);	Neutron targets work is in progress (K. Hayashi). Send data to T. Nakamura who will send it later to NEA (G. Stevenson, A. Ferrari). They will be included in the SINBAD.
– Deep penetration measurements (T. Nakamura);	• Collection started (T. Nakamura); • KEK reported on this; • Data will be available at SATIF-3; • Experiments at ISIS in progress. L. Waters and G. Stevenson will send data to T. Nakamura which will be sent later to E. Sartori for inclusion into the Shielding Experiment Data Base SINBAD; (RSIC, NEADB)

– Photonuclear data
(A. Fasso`, W.R. Nelson, R.W. Roussin, Y. Kikuchi);

For E < 140 MeV data is provided by Japanese Nuclear Data Center (JAERI) File will be released in 1996.
Available data should be summarised at SATIF-3 by information centres.

The following has been added to the wishlist at SATIF-2:
New experiments should be carried out to get giant resonance photonuclear cross section in the GDR range, as existing data is scarce.

3. Contact ICRP and ICRU about dosimetry issues (R. Thomas);

A report on this is needed for SATIF-3.
(N. Ipe, R. Thomas).

4. Agree on definitions of attenuation length and source term parameters (aH, H0) (H. Dinter, G. Stevenson, T. Nakamura);

A subgroup should be formed to discuss this: (H. Hirayama, Chair, A. Ferrari, L. Waters, T. Gabriel, K.Tesch, N. Mokhov, G. Stevenson).
- Attenuation length in iron + concrete was calculated using the HILO86 library and PIC-N codes. Neutron buildup factors were studied by Y. Sakamoto and K. Shin;
- Calculations for protons (100-400 MeV) from 0-180 degrees done by P. Tabarelli.

5. Establish regular exchanges of relevant publications among participants;

Participants from Japan have sent out publications. Other groups are encouraged to do so too.

6. Set up an electronic network listserver for exchange of communications.
(W. R. Nelson, R. Donahue);

Done by R. Donahue at SLAC. Circulate list of subscribers with their e-mail addresses.

Other actions were agreed upon that require larger efforts and coordination:

7. Courses on intermediate energy transport codes to ensure correct understanding of their models and their correct use;

channel;

8. Experiments-measurements:

a) at LANL, U.S.A.:

– pi+ and pi- projectiles
double differential pion cross-sections in the exit channel double differential proton/neutron cross sections in the exit

- Tutorial on FLUKA at ANS, April'96.
- EGS4 Course in Montpellier, June'96.
- For tutorial on LAHET contact L. Waters.
- For scheduling sign up on RSIC or NEADB.

A thesis is being prepared on this.

– proton/neutron projectiles double differential proton cross sections in the exit channel high resolution measurements in the forward direction double differential pion production;	Proposal has been submitted. C(n.2n) data measured at LANL needs to be analysed. An update should be provided at SATIF-3.
b) at TIARA and other facilities in Japan:	
– excitation functions of activation detectors (C-11, Bi);	Carried out by T. Nakamura. Work in progress. An update will be provided at SATIF-3
– monoenergetic calibration of active instruments;	Carried out by S. Ban for REMmeter. Collaboration L. Waters, S. Ban, G. Stevenson, M. Pelliccioni. Update will be provided by S. Ban at SATIF-3
c) follow-up meeting in 18 months to monitor progress on the different actions, to discuss and exchange ideas in code development and validation, decide further actions to speed-up progress.	2nd meeting held at CERN in conjunction with SARE-2. SATIF-3 and SARE-3 scheduled for May 1997 in Japan. Further meetings possibly in conjunction with ANS Topical, Nashville'98.

Further, the following recommendations were retained from the SATIF-1:

All the data mentioned do not need to be available for all nuclei but should span the whole range of atomic masses in order to allow complete benchmarking of nuclear reaction models

All details of the shielding layout should be reported especially concerning density and composition of the materials. The adopted definition of attenuation length should always be stated clearly.

Evaluated data versus nuclear models

This issue was debated at length and transport code developers, who essentially would be the clients of an evaluated data library encompassing the full energy range, came to the following conclusions:

- Rather coarse evaluated data sets would demand about 4 megabytes of computer storage per nuclide and in view of the many nuclides involved in realistic cases such a library would make large demands on computer resources.
- Evaluated data libraries are updated rather infrequently and therefore improved modelling and data will reach the user only very late

- New experimental data can be used for improving the nuclear model performance included in the code and thus the improved data are immediately available for the transport calculation. All codes contain now pre-equilibrium models.

- The upper energy limit for data evaluations in the intermediate energy range is still debated. Some say that they feel comfortable only with libraries up to 100 MeV. HILO-86 goes up to 400 MeV not without problems. All agree that beyond 350 MeV evaluated data libraries are not useful.

Recommendations to NEA/NSC Working Party on International Evaluation Co-operation – WPEC – Subgroup 13 on Intermediate Energy Data

Being a major concern of the SATIF experts' group that of shielding, particular emphasis is placed on shielding experiments and modelling codes for radiation/particle transport and their benchmarking.

As the transport codes generate cross-sections through nuclear models in the higher energy part of the particle spectrum, a specific need exists to verify the cross-section generation modules of such systems against basic data as measured from "thin target" experiments.

A score of such measurements have been carried out over the years and many have been compiled into the EXFOR data base. Several, newer experiments have been compiled recently and the experts' group has expressed their high interest in this activity and recommends that it is continued.

The specialists' encourage Subgroup 13 to continue their work in improving data and to ensure that experimental data for thin and thick targets continue to be included into the international EXFOR data base.

Benchmark session at the SATIF-3 meeting

A specific session on the benchmark experiment analysis should be organised in which results relative to several selected shielding experiments calculated with various computer codes and cross section data sets should be compared. The objective is to identify problems and clarify limitations in computer codes, cross section data and experimental data by analysing the same experiments at different organisations.

Future meetings, their scope and objectives, recommendation to NEANSC

The objectives of both SARE and SATIF were reviewed and are described in the following:

- SARE:
  - Presentation of developments, new work and experience in simulating radiation environments,
  - Exchange of information.

- SATIF:
  - Identification of needs and carrying out experiments to improve the knowledge of thin and thick target neutron yields, neutron penetration, streaming, skyshine etc.;
  - Proposals, discussion and execution of shielding experiments in support of improved shield modelling;
  - Exchange of information on the present status of computer codes and nuclear data files in use;
  - Selection of shielding benchmark experiments and international collaboration of benchmark calculations;
  - High energy dosimetry aspects including anthropomorphic computing models;
  - Draw conclusions about work carried out and report to NEA NSC.

It is recommended that the specialists' meetings of SATIF be transformed into regular meetings under the responsibility of a specific Task Force on Shielding Aspects of Accelerators, Targets and Irradiation Facilities [1].

Organisers and participants have proposed that future meetings be held about every 18 months and each time in a different geographical area with the aim of arranging through this rotation larger participation of hosting country's scientists in connection with visits to National Accelerator Facilities. This approach has proven so far to be effective and to allow improved international contacts.

One of the recommendations issued at the last meeting is to hold the next meeting in Japan in 1997, after having held the first two in USA and Europe respectively.

The suggestions for the next meetings are as follows:

- SARE-3 at KEK, Tsukuba from 7-9 May 1997;
- SATIF-3 at CYRIC, Tohoku University from 12-13 May 1997.

The organising committee would be set up by the the Shielding Working Group of the Reactor Physics Committee of Japan.

A preliminary membership for the scientific committee has been proposed from:

- Europe: F. Clapier (CNRS), A. Ferrari (INFN),
- Japan: T. Nakamura (U-Tohoku), H. Hirayama (KEK),
- U.S.A.: A. Fasso` (SLAC), T. Gabriel (ORNL), N. Mokhov (Fermilab), R. Roussin (RSIC), L. Waters (LANL),
- International organisations: G. Stevenson (CERN), E. Sartori (NEA)

[1] The NEA Nuclear Science Committee has approved the setting-up of such a Task Force at its 7th meeting held on 29-30 May 1996.

Session I

BASIC PHYSICS DATA – DOUBLE-DIFFERENTIAL CROSS-SECTIONS, YIELDS

CHAIR

Takashi NAKAMURA

CO-CHAIR

Alfredo FERRARI

REVIEW OF EXISTING OR PLANNED PROTON ACCELERATORS AND NEUTRON BEAMS IN THE INTERMEDIATE ENERGY RANGE

Pedro Vaz
OECD/NEA

Abstract

Different fields and disciplines in Science and Technology are imposing more stringent and accurate measurements of the proton and neutron total and differential cross-sections in the intermediate-energy range, from a few dozens of MeV up to a few GeV.

Such measurements could be performed in facilities disposing of proton or light ion beams (namely facilities to produce Radioactive Nuclear Beams) or of neutron beams (spallation source facilities). In order to assess the availability of these facilities and the feasibility of experiments leading to the measurements previously mentioned, a survey and compilation study was performed in the framework of the Intermediate Energy Nuclear Data (IEND) project of the Nuclear Science Committee (NSC) of the OECD Nuclear Energy Agency (NEA). The results of this study are compiled in this paper. Five tables summarise the main parameters (the accelerator systems, the characteristics of the primary and secondary beams, of the targets, etc.) of existing facilities as well as of facilities currently being designed, commissioned, under construction, or still being approved.

Introduction

Data and measurements of total and differential cross-sections concerning proton and neutron reactions in the Intermediate Energy Range, from several tens of MeV up to a few GeV, acquire an increasing interest in applications like Nuclear Waste Transmutation, Nuclear Medicine and Nuclear Astrophysics, among others.

Facilities providing proton (or light ion) beams accelerated to these energies and hitting a target (like the ones designed for the production of Radioactive Nuclear Beams), or neutron beams (available from Spallation Sources) could play an important role for performing the measurements of the proton and neutron reactions in such energy range. The availability of proton and neutron beams facilities to perform such experiments and measurements becomes a key item when assessing the existing nuclear data and measurements, as well as the prospects and needs for additional data and measurements in the future.

In this report, the inventory of the existing or planned accelerator facilities in the major Nuclear and Particle Physics Laboratories around the world is presented. The existing particle beams in the energy range from several tens of MeV up to a few (2-3) GeV are listed. Such facilities can be grouped in three main categories, according to the intended usage of the particle beams:

- **Radioactive Nuclear Beams,**
- **Spallation Sources,**
- **Particle Factories.**

Over the past few years a host of scientific questions has been raised which can only be addressed with the use of Radioactive Nuclear Beams (**RNB**). Even more important, several crucial technological advances occurred in the preceding years, that opened the way to the generation of intense RNBs. Also, an increasing number of projects have been proposed, which involve the use of high intensity proton (or ion) accelerators in Spallation Sources or in Radioactive Nuclear Beam facilities.

Most of these projects were born and designed near existing facilities and major laboratories. The accelerator infrastructures in some cases already exists and needs to be upgraded to accommodate the raise in energy and intensity of the beams, while some others imply the construction of new accelerators to achieve the high intensity desired.

Radioactive nuclear beams (RNB)

Over the last years there has been growing interest in nuclear physics experiments with unstable nuclear beams[1]. Indeed, a number of questions has been raised in fields and disciplines like nuclear, astrophysical, atomic and material sciences and applications, which could be addressed in facilities with experimental programs involving the manipulation of Radioactive Nuclear Beams.

[1] Exhaustive descriptions of the physics case(s) to perform experiments at RNB facilities can be found at references [1] to [3].

The two methods for producing high-intensity and high-quality unstable Radioactive Nuclear Beams (**RNB**) involve the interplay of different issues like particle acceleration, nuclear reactions, targets, ion sources, A (atomic mass) and Z (charge) separation and post -acceleration.

The first method, called ***Projectile Fragmentation*** (**PF**) is based on the fragmentation of high energy heavy ion projectiles on a heavy target while the second method, called ***On-Line Isotope Separation*** (**ISOL**) consists on the fragmentation, spallation or fission of heavy targets by energetic light-ion beams (p, Be, Deuterium, etc.), followed by the post-acceleration of the radioactive species produced. The two methods are the kinematics inverse of each other.

The PF method has been successfully implemented and used in several existing facilities, whereas the ISOL approach is still in a development phase in some of the operating facilities or in the design phase in the majority of the proposed facilities. In the sequence, a description of both methods is performed.

The Projectile Fragmentation (PF) method

The Projectile Fragmentation process[2] is obtained in a reaction consisting on a heavy ion projectile (beam energies typically in the range from a few dozens of MeV up to a few GeV), colliding peripherally with a target nucleus. As a result, the projectile fragments are left with much of the initial momentum and are scattered at forward angles in the laboratory system . These fragments are characterised by a wide distribution in A (atomic mass) and Z(electric charge) and need to be purified in magnetic spectrometers before being used for physics experiments. Due to their overlapping charge-to-mass ratios, a purely electromagnetic separation is often inadequate and a Z-dependent ion-optical element in the form of a degrader has to be added to the system. In the past, many RNBs produced using the PF method have been used at the full projectile energy. For other experiments however, lower energies are needed and the RNBs have to be decelerated by passage through an absorber or, after injection into a storage ring, by an RF (radiofrequency) system.

The On-Line Isotope Separator (ISOL) method

In the ISOL method, a "high energy" beam of light ions (typically protons) impinges on a thick target and creates radioactive species through target fragmentation, spallation and fission reactions. These species are produced with low kinetic energies and go through a diffusion process inside the target. To facilitate the removal of the activity from the target and the transport to an ion source, all parts with which the radioactive elements come into contact are kept at elevated temperatures (typically 2500º C). Chemical and physical methods are used with an inherent delay, to separate the various species and transfer them in gaseous form into an ion source where they are transformed into singly or multiply charged ions which are then accelerated to energies of a few tens of keV and mass-analysed by an isotope separator.. The function of this separator is to provide beams for post-acceleration that are free of unwanted isotopes, isobars, ionic charges and molecular ions. Post-acceleration of the beams can be achieved either by LINACs, cyclotrons, synchrotrons and different

[2] The cross-section for PF represents a significant fraction of the total reaction cross-section for heavy ion beam energies in the range from 50 MeV/A up to several GeV/A.

storage rings operating individually, or by combination of these components. A typical On-Line Isotope Separator facility therefore consists essentially of:

- A primary beam accelerator,
- A target,
- An ion source,
- An isotope/isobar separator,
- A post-acceleration system.

Almost all available bombarding particles have been tested or used for the production of radioactive beams, They range from light particles like p, d, ^{3}He, ^{12}C in the interval 30-1000 MeV/A, over thermal neutrons to heavy ions. The production rate (**R**) is governed by the expression:

$$\mathbf{R} = s\ F\ \mathbf{t}$$

where s is the cross-section [cm^2], F is the beam intensity [particles/s] and **t** is the target "thickness" [atoms/cm^2]. High available intensities and the long range in matter strongly favours light particles where thick targets can be used. The yield (**Y**) of radioactive ions is obtained from the production rate, taking into account the efficiencies for the different processes intervening at each of the different steps (diffusion in the target, transfer to the ion source, ionisation, isotope separation and post-acceleration). Defining ε_1 as the transfer efficiency, ε_2 as efficiency of the ion source and ε_3 as the efficiency associated to the acceleration processes following the ion source, one obtains:

$$\mathbf{Y} = s\ F\ \mathbf{t}\ e_1\ e_2\ e_3$$

Comparison between the two production methods

The advantages of the PF method can be summarised as:

- Fast (separation times ~ μs),
- No losses due to radioactive decay,
- General (no Z or A selectivity, no chemical selectivity),
- Simple production targets,
- High collection efficiency,
- Reliable operation.

while its disadvantages (compared to the ISOL method) are:

- Lower intensities of the primary beams available,
- Target thicknesses are limited by the acceptable momentum spread of the secondary beams,
- "High" projectile energies (~ 50-500 MeV/A) necessary for fully stripped ions in the separator,
- Poorer quality of the secondary beams, namely:
  - Lower intensities,
  - Moderated purities (higher level of contaminants from other A, Z species),
  - Wider energy spreads,
  - Larger emittances,
- Difficult deceleration without intensity loss and degradation of the quality of the beams.

On the other hand, the ISOL method exhibits as advantages:

- Higher intensities of the primary beam (e.g. protons) available,
- Thicker targets,
- Higher luminosities [3]. (maximum luminosities in the range 10^{38} - 10^{39} are projected with the ISOL method, while luminosities of 10^{35} can be achieved with PF method),
- Superior quality of the secondary beams, namely:
  - Higher beam purities,
  - Wider range for the choice of the beam energies,
  - Smaller emittances.

and the following disadvantages:

- RNB yields are strongly dependent on the target "chemistry", through the element-dependent diffusion and ionisation processes,
- High Z-selectivity,
- Losses due to radioactive decay can be significant,
- Generation of considerable amounts of radioactivity,
- The need for a post-acceleration system.

Status of the RNB projects

The ISOL-based projects have different approaches to the choice of the three accelerators which constitute the facility, e.g. the primary beam accelerator, the isotope separator and the post-accelerator. Some of them combine in an ingenious way, accelerator systems and infrastructures already in operation in existing laboratories, with upgrades, extensions and developments to achieve the design beam specifications (energies, intensities, mass separation, etc.). The choice of the particle accelerators puts some of the planned projects in the class of a national or international laboratory which ideally could be implemented at one of the world operating 0.5-1 GeV high intensity proton accelerators like **ISIS**, **LAMPF**, **PSI** or **TRIUMF** .

The existing or planned Radioactive Nuclear Beam facilities world-wide are displayed in Tables 1 and 2, together with the main characteristics of the corresponding accelerator systems.

Spallation sources

The use of high intensity linear proton accelerators in pulsed spallation sources is at present intensively studied for applications in the fields of condensed matter research [4], materials science, biology, chemistry and nuclear waste transmutation, among others.

For many years, nuclear reactors were the main source of neutrons producing a continuous flow of particles. However, during the last years, pulsed neutron sources with high peak intensities and very short pulses (∝sec) have found a growing interest.

---

[3] L, the luminosity in units of [cm^{-2} s^{-1}], is the product of the beam intensity and effective target thickness.

[4] A detailed listing of the applications in the field of condensed matter research can be found in references [7] to [9].

Principles of neutron spallation sources

When high energy (e.g. 800 MeV) protons impinge on a heavy metal target, they do not interact with the nucleus as a whole, but -due to their short Broglie wavelength- with the individual nucleons, creating an intranuclear cascade inside the nucleus. Some high energy (secondary) neutrons and protons escape from the nucleus producing similar cascades in neighbouring nuclei. The nucleus is left in a highly excited state and relaxes mainly by evaporating low energy neutrons. The high energy neutrons are of no use, but the others, produced either by evaporation or directly by the incident protons, can be slowed down to thermal (epithermal for time of flight measurements) velocities by optimised moderators. This optimisation is not possible with reactors, since a special moderator layout is needed to sustain the chain reaction. For primary protons of energies of the order of 800 MeV, the energy dissipated in the target per produced neutron is much smaller by spallation ($\approx$ 30 MeV) than by fission ($\approx$200 MeV). This leads to a lower power load in spallation sources compared to fission reactors.

The number of neutrons produced by protons depends on the proton energy, target geometry and target material. As an example, for a cylindrical Pb-target, 10 cm in diameter and 60 cm length, the yield **Y** [neutrons/s], is given by (ref.[11]):

$$\mathbf{Y} = 14.2\ 10^{16}\ (\mathbf{E} - 0.12)\ \mathbf{I}$$

with E = proton energy [GeV], I = proton current [mA] and 0.12 GeV is the threshold energy. At 800 MeV about 15 neutrons are obtained per incident proton; whereas in the case of a target of depleted U^{238} the fission process considerably contributes to achieve higher neutron yields [5] per incident proton ($\approx$25 instead of 15). As explained in ref. [11], the neutron production rate normalised to the beam power is essentially independent of the proton energy, for energies above 1.3 GeV. From the target side, energies ranging between 0.8 GeV and 3 GeV are more suitable. For accelerators, high energies are in principle not a problem, whereas limitations exist on the maximum beam currents that can be achieved for a given energy. As a general rule, the most "pragmatic" solution consists in a design favouring high values of the beam current, which then set the choice of the beam energy values in the lower part of the interval previously mentioned.

Over the last ten years, a number of pulsed spallation sources have been designed, as displayed in Tables 4 and 5. The basic "architecture" common to most of these facilities consists in the combined use of a linear proton injector accelerating the particles to an energy of a few tens of MeV, and a cycling synchrotron further accelerating the particles to the hundreds of MeV (or GeV) range. Two main schemes are used for the accelerator part [13]:

i) short linear accelerator (**Linac**) plus rapid cycling synchrotron (**RCS**)
ii) long linear accelerator (**Linac**) plus **compressor** rings,

both solutions delivering the required short pulses of the order of 1 μs on the target. The RCS demands for high energies and low current whilst for the pulsed Linac with accumulator rings it is just the inverse. Example: proposals for a 5 MW solution look for 3.6 GeV and 1.35 mA (RCS type of solution) or 1.4 GeV and 3.8 mA (for Linac with compressor rings).

[5] But also results in more heat per neutron and hence enhanced cooling requirements.

Neutron detection and measurements using spallation sources

Neutrons are produced by protons of energies of the order of 1 GeV hitting a heavy material target and exciting nuclei to energies at which neutron evaporation becomes significant. Typical production rates for 1 GeV protons are of the order of 20 neutrons per incident proton.

Neutrons are produced in a wide range of energies reaching up to the energies of the incident protons and have to be slowed down in a hydrogen rich moderator, to energies adequate for the study of condensed matter or any other purposes. For a suitably chosen moderator, the emerging neutrons exhibit a Maxwellian velocity distribution, covering a wide range of wavelengths (or equivalently momenta).

By compressing the neutron pulses in a short time interval, one does not increase the peak intensity but time of flight measurements can be used for the determination of the incident neutron energies. This allows, in principle, to use a wide band of wavelengths since each neutron will arrive with a specific time-tag at the detector. It avoids the neutron mono-chromatisation used in CW sources, which decreases considerably the neutron intensity at the detector, making possible a more efficient use of the neutrons produced. CW linear proton accelerators in the GeV range, operated with beam intensities of several hundreds mA and beam power of many hundred MW, present another big step with respect to existing accelerators or to H^- accelerators currently used or considered for spallation sources

Neutron spallation sources world-wide

In Tables 4 and 5, the list of existing and planned Spallation Source facilities world-wide is displayed, together with the main characteristics of the corresponding accelerator systems. In Table 5, mention is made to the two planned spallation sources **AUSTRON** and **ESS** (European Spallation Source), the last one making use of a "high-energy" Linac and an accumulator ring that can handle up to a few times 10^{14} circulating protons accumulated in about 1000 turns before being injected into the target.

The factories and meson utilities

Examples of meson facilities in operation in the past are TRIUMF, LAMPF, IUCF, and SIN/PSI. A good example of a particle factory under construction at TRIUMF is **KAON**[6], a high intensity Kaon factory using the present TRIUMF machine as an injector, consisting in a multipurpose facility for producing beams of Kaons, pions, muons, protons, anti-protons, neutrinos and possibly other hadrons at intensities typically a factor of 100 greater than existing beams. The KAON proposal envisions a couple of accelerators which could produce a primary proton beam of 30 GeV and 100 μA current.

The present machine at TRIUMF runs routinely at 500 MeV and 100-140 μA and is a H^- cyclotron[7]. In the KAON proposal, this machine is used as an injector to an accumulator that would then inject it into a Booster accelerating the beam to 3 GeV before being send to the main accelerating stage, a synchrotron that accelerates the proton beam to 30 GeV.

---

[6] **KAON** stands for **K**aons, **A**ntiprotons, **O**ther Hadrons and **N**eutrinos.

[7] The H^- beam is later converted to a proton beam by charge exchange.

Another example of a particle factory is the Moscow Meson Factory (**MMF**) currently being projected, and to operate as a RNB utility.

Linear accelerators for nuclear waste transmutation

At present, about 400 GWe, corresponding to 17% of the world electricity consumption, is produced by nuclear reactors and considerable amounts of burned fuel has been accumulated. The safe disposal of resulting radioactive materials poses a number of technical problems but also political concern. Geological and sea-bed disposal of long-lived and highly concentrated wastes is under study in a number of countries and many experts consider that geological storage will be an inescapable issue but the task could be alleviated by nuclear transmutation e.g. the transformation in an intense neutron flux of long-lived radioactive species to isotopes with shorter half-live.

The idea of using high-intensity accelerators to produce fissionable material by transmutation, was already advanced around 1950 by E.O. Lawrence and others at Berkeley and it seems a natural idea to extend transmutation to unwanted radioactive species.

Today's accelerator technology has been developed to a level of sophistication and reliability where a new approach to its role for waste transmutation seems justified.

Recently a new proposal has been advanced at Los Alamos by Bowman et. al.. It is based on the production of extremely high fluxes of thermal neutrons (of the order of 10^{16} n/cm^2, about two orders of magnitude higher than standard reactor fluxes) by high power proton accelerator. Neutrons are produced by a high current proton beam of energies typically in the range 1-1.6 GeV, impinging on a liquid (flowing) Pb-B target, and generating about 35 spallation neutrons per interacting proton. The primary target is surrounded by a D_2O blanket moderating neutrons to thermal energies. Waste material is carried continuously in pipes through the moderator and transmuted in the high thermal neutron flux.

As the cross-sections for thermal neutron capture are large and the neutron fluxes are high enough, the probability of absorbing two neutrons in succession in one target nucleus is high. The higher actinides (e.g. Np-237) are converted by a fast neutron capture to daughter products that are then fissioned by a second neutron interaction before they can decay to "non-fissionable" isotopes. The average neutron yield is about 2.7 and actinides act as net neutron producers of fuel.

In this approach, waste must be separated chemically or electro-chemically "on-line", and a continuous flow of material through the target is necessary.

Acknowledgements

The author wishes to thank Tony Gabriel (ORNL) for the technical information and feedback provided on the parameters of the ORSNS Spallation Source facility, Eberhard Lehmann (PSI) for the information on the SINQ target, and François Clapier (IPN) for the technical reports and documentation on the SPIRAL project.

References

[1] "European Radioactive Beam Facilities", report from the Study Group of the Nuclear Physics European Collaboration Committee - NuPECC, an Associated Committee of the European Science Foundation (1993).

[2] "The IsoSpin Laboratory (ISL) - Research Opportunities with Radioactive Nuclear Beams", report prepared by the North American Steering Committee for the IsoSpin Laboratory, LALP 91-51 (1991).

[3] "Prospective Radioactive Beam Facilities", by R.H.Siemssen, contributed to the Proceedings of the Third International Conference on Radioactive Nuclear Beams, East Lansing, Michigan, 24-27 May 1993 (Editions. Frontieres).

[4] "Radioactive Nuclear Beam Facilities Based on ISOL-Postaccelerator Schemes", by H.L.Ravn, CERN-PPE 91-173 (1991).

[5] "Accelerator Radioactive Nuclear Beams: Existing or Planned Facilities", by J.M. Nitschke, LBL-33072 (1992).

[6] "ISOL based radioactive nuclear beam facilities", by T.Nomura, INS-Rep-883, (1989)".

[7] "ISIS 1994 Annual Report", LAL 94-050 (1994).

[8] "The Spallation Neutron Source SINQ - A New Large Facility for Research at PSI", PSI report (1994).

[9] "The AUSTRON Feasibility Study", editors P.Bryant, M.Regler and M.Schuster, (1994).

[10] "Superconducting Cavities for Neutron Spallation Sources and other High Intensity Proton Accelerators", by H.Lengeler, CERN-PRE 93-078 (1993).

[11] "Spallation Neutron Sources", by H.Klein, paper presented at the 1994 Linear Accelerator Conference, Tsukuba, Japan, 21-26 August 1994.

[12] "A Pulsed Spallation Source in Central Europe", by K.Schindl and H.Schonauer, CERN-PS 92-26 (HI) (1992).

[13] "Proposals for Spallation Sources in Europe", by H.Lengeler, invited talk at the European Particle Accelerator Conference (EPAC), London (1994).

[14] "Present and Future Radioactive Beam Studies at GANIL: From SISSI to SPIRAL", by D.Guerreau, GANIL P-96-04 (1996).

[15] "The SPIRAL Radioactive Ion Beam Facility", Technical Report and Feasibility Study of the SPIRAL project, GANIL R-94-02 (1994).

[16] "Radioactive Ion Beams at SPIRAL", by A.C.C. Villari et. al., in Nuclear Physics A588 (1995).

Table 1 ***Radioactive nuclear beam facilities worlwide, using the PF method*** *[2], [5] and [14].*

FACILITY / LOCATION	PRIMARY ACCELERATOR	MASS RANGE (u)	ENERGY RANGE (MeV/u)	INTENSITY RANGE (part./s)	STATUS
B1/B42/B44 **LBL**, Berkeley, U.S.A.	Bevelac 8-2100 MeV/u $\leq 10^9$ part./s	≤ 238	≤ 800	$\leq 10^8$	Bevelac shutdown in 1994
LISE-3/SPEG **GANIL**, Caen, France	Two K=400 coupled cyclotrons 25-95 MeV/u $\leq 10^{12}$ part./s	≤ 136	≤ 80	$\leq 10^9$	Intensity upgrade n progress (**SISSI** completed, **THI** in progress)
RIPS **RIKEN**, Wako, Japan	K=540 ring cyclotron 30-135 MeV/u $\leq 10^{11}$ part./s	≤ 136	≤ 110	$\leq 10^8$	In operation
A1200 **NSCL**, East Lansing, U.S.A.	K=1200 superconduct. cyclotron 30-200 MeV/u $\leq 10^{11}$ part./s	≤ 136	≤ 150	$\leq 10^8$	In operation
K4-K10 Complex Dubna, Russia	3 cyclotrons coupled to 2 storage rings 85-170 MeV/u $\leq 3x10^9$ part./s	≤ 238	≤ 600	$\leq 2x10^8$	Proposed
FRS ESR **GSI** Darmstadt, Germany	SIS18 Synchrotron 100-2000 MeV/u $\leq 10^8$ part./s ($\leq 10^{11}$ part./s)	≤ 238	≤ 1000	$\leq 10^5$ ($\leq 10^8$)	Being commissioned (foreseen upgrade)

Table 2 ***Existing or Planned Radioactive Nuclear Beams facilities worlwide using the ISOL method*** *(compiled from references. [1] to [5] , [15])*

PROJECT	PRODUCTION BEAM				TARGET		RADIOACTIVE BEAMS				STATUS
	Driver Accelerator	Particle	Energy (MeV)/A	Intensity (μA)	Element Z	Thickness (g/cm^2)	Post Accelerator	Beam A	Energy (MeV)/A	Intensity (s^{-1})	
Louvain la Neuve (Belgium)	K=30 Cyclotron	p	30	500	6	1	K=110 Cyclotron	6-19	0.6-4.5	10^6 - 10^9	Operating facility
ARENAS (Louvain, Belgium)	K=110 Cyclotron	p,d,He H.I. < Kr	80	20	13	5	45 MV SC Linac	< 100	3-30	$5x10^7$ -$7x10^{10}$	Project
CERN ISOLDE PRIMA (Geneva, Switzerland)	1.0 GeV Cyclotron	p	1000	2.1	4-92	3-300	SC Linac	< 91	4-9	10^4 - 10^{10}	Project
GANIL PLUS/SPIRAL (Caen, France)	K=30+380+380 Cyclotrons	He-U	25-95	8	6-92	3	K=262 Cyclotron	< 220	1.7-25	$2x10^4$ - $6x10^9$	Project
EXCYT (Catania, Italy)	K=800 Cyclotron	p-U	20-100	1	?	?	15 MV tandem	< 40	3-9	$2x10^3$ - 10^9	Project
PIAFE (Grenoble, France)	ILL reactor	n	thermal	10^{15} n/cm^2s (max. flux)	Graphite -U	-	K=88 +160 Cyclotrons	75-150	3.8-20	10^3 - $8x10^9$	Project
ORNL HHIRF (Oak Ridge, USA)	K=100 Cyclotron	p.d.He,Li,B	55-86	10-130	6-32	5	25 MV tandem	80	5	$1x10^6$ -$1x10^{11}$	Project
TRIUMF-TISOL-ISAC (Vancouver, Canada)	K=500 Cyclotron	p	500	10	4-92	3-100	Linac	< 60	10	$1x10^7$-$1x10^{12}$	Project
KEK-JHP (Japan)	1.0 GeV Linac	p	1000	10-100	4-92	3-300	Linac	< 60	6.5	$1x10^7$-$1x10^{12}$	Project
INS E-ARENA (Tokyo, Japan)	K=68 Cyclotron	p	40	10	6	1	Linac	11-19	0.8		Project
Rutherford Appleton Laboratory (RAL) (United Kingdom)	800 MeV synchrotron	p	800	100	4-92	3-200	Linac or Synchrotron	< 80	6.5	$1x10^7$-$1x10^{12}$	Project
Moscow Meson Factory (Russian Federation)	Linac	p	600	500	4-92	3-200	Linac	< 80	6.5	$1x10^{12}$	Operating
ISOLAB Thin Target **ISOLAB** Thick Target (North America)	Under discussion	p d,He	800 500-1000	1000 100-300	92 4-92	0.02-0.1 100-300	Under discussion	< 220	10	$1x10^9$ $5x10^9$-$1x10^{12}$	Project

Table 3 ***Existing or planned facilities (not falling in the category of RNB's) worlwide***

FACILITY	**AVAILABLE BEAMS & CHARACTERISTICS**							**STATUS**
	Accelerator system	Particle	Energy (MeV/A)	Intensity (per pulse)	Pulse Length (∝ sec)	Repetition rate (Hz)	Special features	
SATURNE (LNS)	Two Synchotrons	p d,He C,N,O Ne Ar,Kr	2950 1150 1150 1150 < 820	$8x10^{11}$ $<5x10^{11}$ $<10^{9}$ $2x10^{8}$ 10^{6}-10^{8}			Polarized p,d,He, Li beams available	Operational
FERMILAB Linac	Pulsed Linac	p (H^-)	100-400	$< 10^{13}$ per pulse	min < 1 max < 30	15	-	Under study

Table 4 ***Existing spallation sources facilities worldwide*** *(compiled from references.[8], [10] and [11])*

FACILITY	ACCELERATORS	AVERAGE P-CURRENTAT TARGET (μA)	REPETITION RATE (Hz)	PULSE LENGTHON TARGET (μs)	AVERAGEBEAM POWERAT TARGET (kW)	AVERAGEENERGY OF ONEPULSE AT TARGET (kJ)	NUMBER OF PROTONS PER PULSE AT TARGET	TARGET MATERIAL	TIME AVERAGED THERMAL FLUX ($n/cm^2/s$)
IPNS, Argonne	50 MeV Linac 500 MeV RCS	15	30	0.1	7.5	0.25	$3x10^{12}$	^{238}**U** ^{235}**U**	$1.4x10^{11}$ $3.5x10^{11}$
KENS-I KEK, Japan	40 MeV Linac 500 MeV Synchr.	10	20	0.05	5	0.25	$3.1x10^{12}$	^{238}**U**	$7x10^{11}$
ISIS, Rutherford Lab. (RAL)	70 MeV Linac 800 MeV Synchr.	200	50	0.45	160	3.2	$2.5x10^{13}$	**Ta** ^{238}**U**	$1.5x10^{12}$ $3x10^{12}$
LANCSE, Los Alamos	800 MeV Linac + storage ring	60(100)	12(20)	0.27	50(80)	3.9	$3x10^{13}$	**W**	$(0.85\text{-}1.1)x10^{12}$
SINQ PSI (operation.1996)	590 MeV Cyclotr.	1000	CW	CW	900	CW	CW	**Pb** **Pb-Bi** [1]**Liquid metal**	$2x10^{14}$

[1] A liquid metal target is envisaged for the operation of SINQ. However, for safety reasons, a “First Day Target” consisting of a rod bundle of Zircalloy pins cooled with heavy water will most likely be used at the start of operation of SINQ, foreseen for October 1996.

Table 5 ***Planned spallation sources facilities worldwide*** *(compiled from refs.[9], [10], [11], [12] and [13])*

FACILITY	ACCELERATORS	AVERAGE P-CURRENT AT TARGET (μA)	REPETITION RATE (HZ)	PULSE LENGTH ON TARGET (μS)	AVERAGE BEAM POWER AT TARGET (KW)	AVERAGE ENERGY OF ONE PULSE AT TARGET (KJ)	NUMBER OF PROTONS PER PULSE AT TARGET
NCNR Los Alamos	800 MeV Linac accumulator ring	1250	20(40)	0.5	1000	16.6	$1.3x10^{14}$
IPNS (upgrade) Argonne	400 MeV Linac 2 GeV RCS	500	10/30	0.3	1000	32	$1x10^{14}$
PSNS Brookhaven	600 MeV Linac 2x3.6 GeV RCS	1350	2x30	1.3	5000	160	$2.8x10^{14}$
ANS, Moscow Russia	1 GeV Linac 10 GeV Synchr.	400(100)	40/10	1	4000(1000)	-	-
KENS-II KEK, Japan	1 GeV Linac+ compressor	200	50	0.2	200	4	$2.5x10^{13}$
ETA Based SNS, Japan	1.5 GeV Linac+ compressor	10000(1300)	100(50)	1000	15000(2000)	150(40)	$6.3x10^{14}$ ($1.6x10^{14}$)
AUSTRON I Austria	70 MeV Linac 1.6 GeV RCS	63	25	1	102.5	4	$1.6x10^{13}$
AUSTRON II Austria	130 MeV Linac 1.6 GeV RCS	128	25	1	205	8	$3.2x10^{13}$
AUSTRON III (2 targets)	130 MeV Linac 1.6 GeV RCS	256	50	1	410 (2x205)	8	$3.2x10^{13}$
ESS, European Spallation Source (2 rings)	1.334 GeV Linac 2xcompressor	3800	50(10)	1	5000(1000)	100	$4.7x10^{14}$
ORSNS Oak Ridge	not specified	not specified	10 (50)	1 - 3	1000 (5000)	100	not specified

REVIEW OF ACTIONS IN JAPAN AFTER SATIF-1

Hideo Hirayama
National Laboratory for High Energy Physics, Japan

Abstract

This article reviews actions performed in Japan after SATIF-1. The details of these actions will be reported by each participant during this meeting. The data collection of photonuclear data performed by the Japanese Nuclear Data Committee and the Nuclear Data Center at JAERI is presented in this article.

1. Introduction

At SATIF-1, it was agreed that the following actions would be performed in Japan:

- Collect and make available existing data on:
  - Thick target measurements,
  - Deep penetration measurements,
  - photonuclear data;
- Agree on definitions of attenuation length and source-term parameters;
- Perform experimental measurements at TIARA and other facilities in Japan:
  - Excitation functions of activation detector (C-11, Bi),
  - Monoenergetic calibration of active instruments.

Two working groups are organised under the *Accelerator Shielding Working Group* of the Sub-Committee of Shielding of the Research Committee on Reactor Physics. Co-operations are also undertaken with the Research Committee on Radiation Behavior in the Atomic Energy Society of Japan.

The research group concerning the radiation shielding experiments for high energy neutrons at TIARA and other facilities continues its programmes related to the actions listed above.

The actions carried out in Japan including the above-mentioned are briefly developed in this article. Details of these actions will be reported by each participant during this meeting.

The photonuclear data collection performed by the Japanese Nuclear Data Committee and the Nuclear Data Center at JAERI is also addressed within this article.

Organisations related to these actions are shown in Figure 1.

2. Collection and making available of existing data

The collection and making available of existing data on thick target measurements were performed in co-operation with the Accelerator Shielding Working Group of the Research Committee on Radiation Behavior of the Atomic Energy Society of Japan. Thick target neutron data and accelerator shielding experiments were surveyed from 14 journals published from 1990 to 1995. This survey was the third in a row after two reports published by the similar working group [1,2].

The current situation of this work will be reported by K. Hayashi.

3. Accelerator shielding benchmark experiment analyses

Analyses on benchmark experiments on thick target yields and benchmark shielding experiments [3] were carried out by the *Benchmark Problem Analysis Sub-Working Group* in order to estimate the validity of the computer code and nuclear data.

This work will be reported by H. Nakashima and N. Yoshizawa.

4. Definitions of attenuation length and source-term parameters

The *Attenuation Length Sub-Working Group* of the Sub-Committee worked in order to better understand the attenuation phenomena of main medium-energy neutrons. The dose attenuation inside iron and concrete was calculated by using the HILO86R library [4] and the PKN-H code [5]. Neutron buildup factors were also studied as another approach.

These works will be reported by Y. Sakamoto and K. Shin.

5. Quasi-monoenergetic neutron calibration facilities

The new quasi-monoenergetic neutron source was developed at Ring Cyclotron of Riken to extend the energy range of neutrons up to 150 MeV. T. Nakamura at Tohoku University and Y. Uwamino at Riken received the award from the Atomic Energy Society of Japan for their achievements while constructing monoenergetic neutron fields at INS, CYRIC, TIARA, and Riken.

Measurements of neutron activation cross-sections for C and Bi were continued at these facilities. The calibrations of modified rem-counter were also done at these facilities.

These works will be reported by T. Nakamura and S. Ban.

6. Fluence to dose equivalent conversion coefficients for high-energy neutrons

Effective dose equivalent or effective dose for high-energy neutrons were studied systematically as a joint work between JAERI and the Mitsubishi group.

This work will be reported by S. Iwai.

7. Evaluation of photonuclear data

For γ-ray induced reaction data up to 140 MeV, the photonuclear data file is provided both by the Japanese Nuclear Data Committee and the Nuclear Data Center at JAERI [6] for applications suc h as electron accelerator shielding and radiation therapy.

The photon absorption cross-section is evaluated both with the giant dipole resonance model and the quasideuteron model; furthermore, the cross-sections of decaying process are calculated with the statistical model with preequilibrium correction. For this last purpose, MCPHOTO [7] and ALICE [8] codes are mainly used. The isotopes evaluated are shown in Table 1. The (γ, xn) cross-section of Mn-98 is illustrated in Figure 2 as an example.

The evaluation work has been almost finished, and the file will be released in 1996.

References

[1] T. Nakamura et al., "Annotated References on Neutron and Photon Production from Thick Targets Bombarbed by Charged Particles", Atomic Data and Nuclear Tables, 32, 471-501 (1985).

[2] H. Hirayama et al., "Annotated References of Shielding Experiment and Calculation of High Energy Particles", KEK Report 90-18 (1990).

[3] H. Nakashima et al., "Benchmark Problems for Intermediate and High Energy Accelerator Shielding", JAERI-DATA/Code 94-012 (1994).

[4] H. Kotegawa et al., "Neutron-Photon Multigroup Cross Sections for Neutron Energies up to 400 MeV: HILO80R – Revision HILO86 Library –", JAERI-M-93-020 (1193).

[5] H. Kotegawa, Y. Sakamoto and S. Tanaka, "A Point Kernel Shielding Code for Neutron Source up to 400 MeV", JAERI-DATA/Code 95-004 (1995).

[6] T. Fukahori and S. Chiba: "Status of Nuclear Data Evaluation for JENDL High Energy File", Proc. Second Specialists' Meeting on High Energy Nuclear Data, JAERI-CONF-96-016, 46-56 (1995).

[7] N. Kishida, "MCPHOTO Code", private communication (1991).

[8] T. Fukahori, "ALICE-F Calculation of Nuclear Data up to 1 GeV", Proc. Specialists' Meeting on High Energy Nuclear Data, Oct. 3-4, 1991, JAERI-M-92-039, 114 (1992).

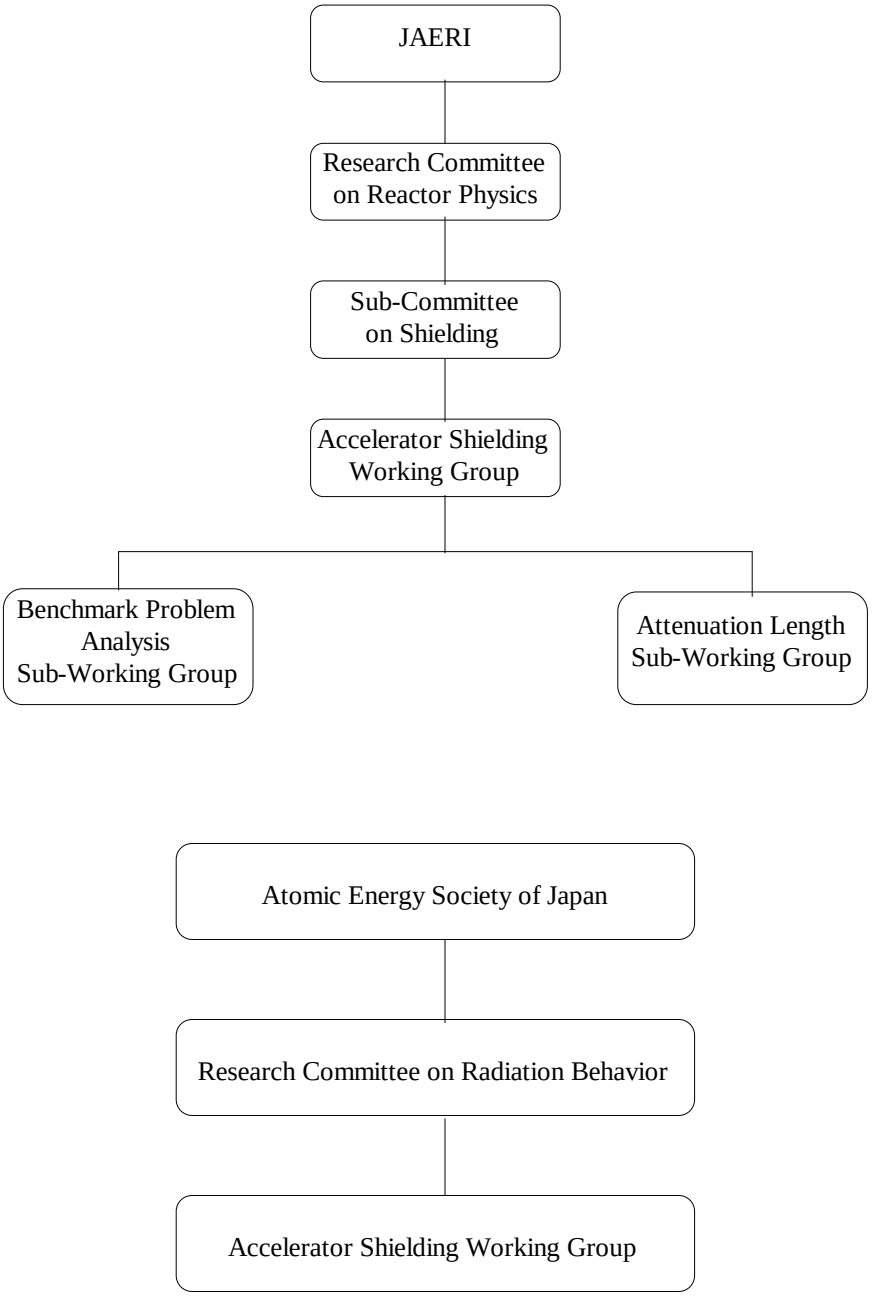

Figure 1 ***Organisations related to the actions in Japan***

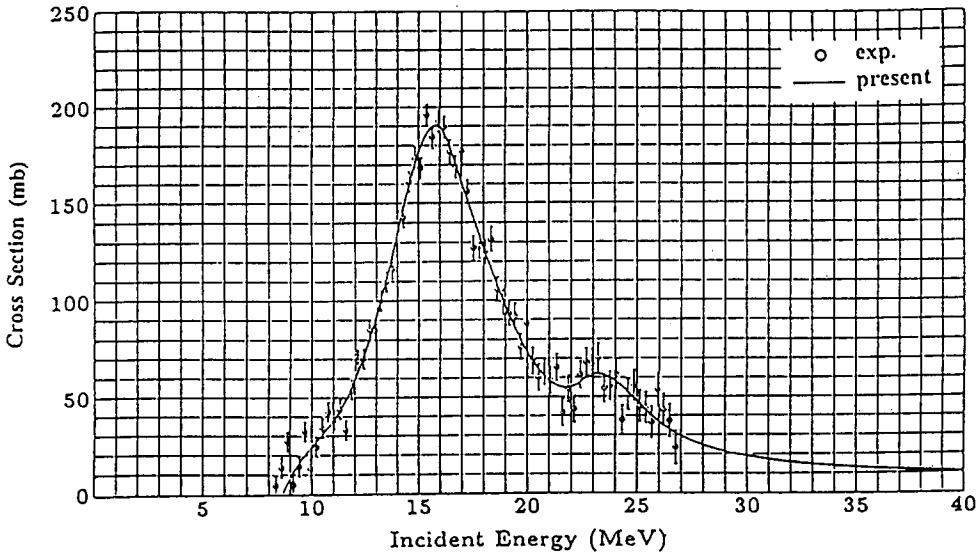

Figure 2 (γ, xn) cross-section of Mo-98

Table 1 ***Nuclei to be included in the Photonuclear Data File***

24 elements, 42 isotopes
^{2}H, ^{12}C, ^{14}N, ^{16}O, ^{24}Na, $^{24,25,26}Mg$, ^{27}Al, $^{28,29,30}Si$,
$^{40,48}Ca$, $^{46,48}Ti$, ^{52}Cr, ^{55}Mn, $^{54,56}Fe$, ^{59}Co,
$^{58,60}Ni$, $^{63,65}Cu$, ^{90}Zr, $^{92,94,96,98,100}Mo$, ^{181}Ta,
$^{181,184,186}W$, ^{197}Au, $^{206,207,208}Pb$, ^{209}Bi, $^{235,238}U$

SURVEY OF THICK TARGET NEUTRON YIELD DATA AND ACCELERATOR SHIELDING EXPERIMENTS

K. Hayashi
Hitachi Engineering Company, Japan

Y. Sakamoto
Japan Atomic Energy Research Institute, Japan

Working Group of Accelerator Shielding *
of the Research Committee on Radiation Behavior in the Atomic Energy Society of Japan

1. Introduction

In accelerator shielding design, certain calculations on neutron and photon emission energy spectra from the target and their behavior in shield materials are necessary.

Although we nowadays can use several computer codes to calculate these quantities, the quantity and the quality of the codes are still not enough to solve all the encountered problems in accelerator shielding design compared to the reactor shielding design.

Benchmark experiments have been performed in several laboratories, and the results of these experiments and calculations using above mentioned codes have been compared and discussed by several investigators.

Many of these papers were compiled in two reports [1] [2] as annoted references in 1985 and in 1990, in aim to find out appropriate paper with ease. Benchmark experiments are summarized and compiled in two reports [3] [4] in 1993 and in 1994, in aim to evaluate the calculational algorithm, the accuracy of computer codes and the nuclear model and data used in the codes. Simultaneously, five benchmark experiments are uploaded as electric media to SINBAD [5] database which is developed and maintained by the Radiation Shielding Information Center in Oak Ridge National Laboratory. These compilation work was done by Working Group of Accelerator Shielding in the Research Committee on Radiation Behavior in the Atomic Energy Society of Japan.

---

* Members of Accelerator Shielding Working Group :
T. Nakamura (Tohoku Uni.), Sh. Tanaka, Su. Tanaka, N. Sasamoto, Y. Sakamoto, H. Nakashima, Y. Asano, Y. Nakane (JAERI), K. Kawachi (National Institute of Radiological Science), Y. Uwamino (RIKEN), H. Hirayama, S. Ban, Y.Namito (KEK), N. Otani (PNC), K. Shin (Kyoto-Uni.), K. Hayashi (Hitachi Engineering Company), N. Yamano (Sumitomo Atomic Energy Industries), M. Kawai, Y. Hayashida, M. Uematsu (Toshiba Corp.) Y. Suzuoki, S. Iwai, T. Kubota (Mitsubishi Heavy Industries), O. Sato, S. Takagi (Mitsubishi Research Institute), K. Mio (Ishikawajima-Harima Heavy Industries), H. Ida, M. Shimizu (NKK), A. Oishi (Shimizu Corp.), A. Hara (Hazama Corp.), M. Kinno, T. Ishikawa (Fujita Corp.), K. Kanai, N. Odano (Ship Research Institute), Y. Harima (CRC Research Institute), T. Ichimiya (Japan Radioisotope Association).

Since many papers on thick target neutron emission data and accelerator shielding experiments are published without interruption in many kinds of journals and conference proceedings, this kind of survey work should be done as a continuous work. Five years has passed since the last compilation, the working group started the survey work again. In this report, we summarize the surveyed results.

2. Survey work

2.1 Literature coverage

The papers referenced are from the following journals published from 1989 through 1995.

(1) Phys. Rev.,
(2) Nucl. Phys.,
(3) Nucl. Instrum. Methods,
(4) Nucl. Sci. Eng.,
(5) Phys. Med. Biol.,
(6) Med. Phys.,
(7) Particle Accelerators,
(8) Health Phys.,
(9) Rad. Prot. Dosimetry,
(10) IEEE Trans. Nucl. Phys.,
(11) Int. J. Appl. Radiat. Isotopes,
(12) Proc. ICANS Mtg.,
(13) 8th Int. Conf. on Radiation Shielding,
(14) Proc. SATIF-1.

2.2 Selection criteria

Neutron production data from thick targets bombard by charged particles are selected. The projectile energy is typically restricted to above 20 MeV. Shielding experiments and calculations of high energy particles are selected with the same projectile energy.

3. Surveyed results

3.1 Thick target neutron yield

1

Table 1 compiles the references arranged in alphabetical order of the abbreviated labels. Each entry block lists the full title of the paper, authors' names, and the literature source followed by information on the accelerator (facility), type and energy of the projectile, composition and thickness of the target, experimental and calculational method, and measured and calculated quantities.

Table 2 compiles the references surveyed by Japanese Nuclear Data Committee[6]. Each entry block lists the full title of the paper, author's' names, and the literature source. The neutron yield data given in these references are compiled in EXFOR format database. Figure 1 and 2 summarize the (p, xn) and (a, xn) data points which has compiled in this database. In this figure, horizontal axis shows the incident particle energy and vertical axis shows the target material. Numerical data typed in the figure shows the incident particle energy. The data point shown in Åú means that this data has the neutron yield data with neutron spectrum information and Åõ means that this data point that this data has only neutron total yield data. Numbers in bracket means the literature number shown in Table 2. By this figure, one can find the necessary data easily. Also we can find out the energy band and target material which we do not have.

3.2 Accelerator shielding experiment

Table 3 compiles references arranged in alphabetical order of the abbreviated labels. Each entry block lists the full title of the paper, author's' names, and the literature source followed by information on the accelerator (facility), type and energy of the projectile. Each entry block lists the same ones as in Table 1 with composition and thickness of the shielding materials and the geometry.

4. Proposal for future work

i. This type of collected references on accelerator shielding and thick target neutron yield should be reached within easy access. Therefore it is better to store these as database in server machine at proper site such as RSIC. Through the Internet, we can access this database using WWW browser.

ii. Although the maintenance of this database is still necessary, we can maintain with less power by registering papers by the author oneself or other person who is using this database. Still nicer thing we get by this idea is that we can have more perfect database because many specialists fill the missing data or correct the mistake.

iii. Furthermore, SINBAD[5] type of database on "Accelerator Shielding Benchmark Problems" should be reached within easy access. Drawings on shielding geometry should be supplied in GIF or other condensed format along with other text data. This idea may have a copyright problem which we should find the solution.

References

[1] T. Nakamura et al. "Annoted References on Neutron and Photon Production from Thick Targets Bombarded by Charged Particles", Atomic Data and Nuclear Data Tables, 32, 471-501 (1985).

[2] H. Hirayama et al. "Annoted References of Shielding Experiment and Calculation of High Energy Particles", KEK report 90-18 (1990).

[3] H. Hirayama et al. "Accelerator Shielding Benchmark Problems", KEK report 92-17 (1993).

[4] H. Nakashima et al. "Benchmark Problems for Intermediate and High Energy Accelerator Shielding", JAERI-Data/Code 94-012, Japan Atomic Energy Research Institute (1994).

[5] H. T. Hunter et al. "SINBAD-A Shielding Integral Benchmark Archive and Database for PC's", 8th International Conference on Radiation Shielding, Arlington, USA, (1994).

[6] Working Group on High Energy Nuclear Data Evaluation of Japanese Nuclear Data Committee, Japan Atomic Energy Research Institute, Private communication.

Table 1 ***Reference on neutron production data***

ALSMILLER-91
"Low Energy Particle Production and Transport for 200 GeV/C Protons in Iron and Comparisons with Experimental Data"
R.G. ALSMILLER Jr. and F.S. ALSMILLER
Nucl. Instr. and Meth., A306, 500-503 (1991)

1) Accelerator:
2) Projectiles: p (200 GeV)
3) Target: Fe
4) Experimental method:
5) Calculation: HETC88
6) Calculated quantities: Particle production

BRADY-90
"Summary of Monoenergetic Neutron Beam Sources for Energies > 14 MeV"
F.P. BRADY and J.L. ROMERO
Nucl.Sci.Eng., 106, 318-331(1990)

1) Accelerator:
2) Projectile: p (20-200 MeV)
   d (20-90 MeV)
3) Target: p : H-2, H-3, Li-6, Li-7
   d : H-2, H-3
4) Shielding Material:
5) Geometry:
   Cylindrical bottle (H-2, H3)
6) Experimental Method:
   TOF, associated particle method
7) Calculation:
8) Measured Quantities:
   Neutron production cross section, neutron spectra and neutron yield

BREDE-89
"Neutron Yields from Thick Be Targets Bombarded with Deuterons or Protons"
H.J. BREDE, G. DIETZE, K. KUDO, U.J. SCHREWE, F. TANCU and C. WEN
Nucl. Instr. and Meth., A274, 332-344 (1989)

1) Accelerator:
   Energy-variable compact cyclotron, PTB
2) Projectiles: p (17.2- 22 MeV)
   d (9.4 - 13.6 MeV)
3) Target: Be
4) Experimental method: Time of flight method
5) Calculation:
6) Calculated quantities:
   Angular differential spectral neutron yield (Yield /unit charge)

MEIER-89
"Differential Neutron Production Cross Sections and Neutron Yields from Stopping-Length Targets for 113-MeV Protons"
M.M. MEIER, D.A. CLARK, C.A. GOULDING, J.B. McCLELLAND, G.L. MORGAN and C.E. MOSS
Nucl.Sci.Eng., 102, 310-321 (1989)

1) Accelerator (Organization):
   LAMPF Linear Accelerator (LANL)
2) Projectile (Energy):
   p (113 MeV)
3) Target (thickness):
   Be, C, O, Al, Fe, W, Pb, U-238
   (thin for cross section and thick for neutron yield)
4) Experimental method:
   TOF of 28.7 to 58.5 m flight path with BC-418 plastic scintillator
5) Calculation:
   HETC calculation
6) Measured or calculated quantities:
   Differential (p,xn) cross sections of Be, C, O, Al, Fe, Pb and U-238 at angles of 7.5, 30, 60 and 150 degree Absolute (p,xn) neutron yields of Be, C, Al, Fe and U-238 at angles of 7.5, 30, 60 and 150 degree

MEIER-90
"Neutron Yields from Stopping- and Near Stopping-Length Targets for 256-MeV Protons"
M.M. MEIER, C.A. GOULDING, G.L. MORGAN and J.L. ULLMANN
Nucl.Sci.Eng., 104, 339-363 (1990)

1) Accelerator (Organization):
   LAMPF Linear Accelerator (LANL)
2) Projectile (Energy): p (256 MeV)
3) Target (thickness): C (30.00 cm and 17.45 cm)
   Al (20.00 cm and 12.15 cm)
   Fe (8.00 cm and 4.70 cm)
   U-238 (5.00 cm and 3.00 cm)
4) Experimental method:
   TOF of 28.7 to 66.8m flight path with BC-418 plastic scintillator
5) Calculation: HETC and ISABEL calculation
6) Measured and calculated quantities:
   Absolute (p,xn) neutron energy spectra and yields at angles of 30, 60, 120 and 150 degree

MEIER-92
"Neutron Yields from Stopping-Length Targets for 256-MeV Protons"
M.M. MEIER, W.B. AMIAN, C.A. GOULDING, G.L. MORGAN and C.E. MOSS
Nucl.Sci.Eng., 110, 299-301 (1992)

1) Accelerator:
   Clinton P.Anderson Meson Physics Facility (LAMPF)
2) Projectile: p(256MeV)
3) Target(thickness):
   Be (27.86cm), Be (17.86cm), C (30cm), Al (20cm), Fe (8cm)
4) Shielding Material:
5) Geometry:
   Cylinder Be:(13.2 cm ϕ), C, Al, Fe: (16cm ϕ)
6) Experimental Method: TOF
7) Calculation: HETC
8) Measured Quantities: Neutron yield

NIKOLAEV-90
"Neutron Production in Thick Lead Target by 13.7 GeV Protons and Deuterons"
V.A.NIKOLAEV ET AL.
ICANS 11 Report

1) Accelerator: Dubna (JINR) Synchrophasotron
2) Projectile: p (1-3.7 GeV)
   d (1-3.7 GeV)
3) Target: Pb
4) Shield:
5) Geometry:
6) Experimental method: SSNTD, TOF
7) Measured quantities:
   Neutron Spectra (1keV – 1 GeV)

SARKAR-91
"Neutron Production from Thick Targets Bombarded by Alpha Particles: Experiment and Theoretical Analysis of Neutron Energy Spectra"
P.K. SARKAR, T. BANDYOPADHYAY, G. MUTHUKRISHNAN, and S. GHOSH.
Phys.Rev. C43, 1855 (1991).

1) Accelerator(Organization):
   Variable Energy Cyclotron Centre,
   Bhabha Atomic Research Centre,
   Calcutta, India.
2) Projectile (Energy):
   alpha particle: 40 MeV for 197-Au, 50 MeV for 9-Be and 181-Ta, 60 MeV for 181-Ta.
3) Target (thickness):
   9-Be (3.0±05mm), 181-Ta (4.0±05mm), 197-Au (0.8±05mm)
4) Experimental method:
   TOF of 1.4 m flight path with NE213 liquid scintillator. n-gamma pulse discrimination.
5) Calculation:
   Excition model and evaporation model. PRECO-D2 code was modified to calculate the thick target yield.
6) Measured quantities:
   Neutron energy spectra from Be, Ta, and Au targets at angles of 0°, 30°, 60° and 90°.
7) Calculated quantities:
   Neutron energy spectra from Be, Ta, and Au targets at angles of 0°, 30°, 60°and 90°. Neutron energy spectra from Cu with 65 MeV incident alpha at emission angles of 0°, 15°, 45°, 75°and 135°. Angle integrated neutron energy spectra from Ta at 50 and 60 MeV, Au at 40 MeV, and Cu at 65 MeV.

SHIN-94
"Systematics in Differential Thick Target Neutron Yields Parametrized by Moving Source Model"
K.SHIN, K.MIYAHARA, E.TANABE and Y.UWAMINO
8th International Conference on Radiation Shielding, 666-673, April 24-28, 1994, Arlington, Texas, USA.

1) Accelerator:
   SF-cyclotron of University of Tokyo
2) Projectile:
   Proton (30, 52 MeV), alpha (40, 65MeV), C (75, 120 MeV), O (153 MeV)
3) Target: C, Al, Fe, Cu, Pb
4) Experimental method: NE-213
5) Calculation:
6) Calculation quantities:

VASSIL'KOV-90
"Neutron Emission from an Extended Lead Target under the Action of Light Ions in the GeV Region"
R.G.VASSIL'KOV and V.I.YUREVICH
ICANS 11 Report

1) Accelerator: Dubna (JINR) Synchrophasotron
2) Projectile: p (2GeV)
   d (2 GeV)
   He-3
   He-4
   C-12
3) Target: Pb
4) Shield:
5) Geometry:
6) Experimental method: SSNTD, TOF
7) Measured quantities:
   Neutron Spectra (0.1MeV - 1 GeV)

ZAZULA-91

"Study of the Neutron Field from a Hadronic Cascade in Iron: Verification of a Monte Carlo Calculational Model by Comparison with Measured Data"

J.M.ZAZULA and K.TESCH

Nucl. Instr. and Meth., A300, 164-178 (1991)

1) Accelerator:
2) Projectiles: p (25 - 800 GeV)
3) Target: Fe, Ag, C, Al, Pb
4) Experimental method:
5) Calculation: FLUNEV, HETC88
6) Calculated quantities:
   Mass distribution, neutron yield and energy distribution of secondary neutron

Table 2 ***Surveyed database on neutron production in Nuclear Data Committee of JAERI*** *— 35 Articles*

Thick target neutron yield data in EXFOR format for projectile proton and alpha

1. **COLEMAN-68**
   W.A. COLEMAN and R. G.ALSMILLER, JR.
   NSE, 34, PP.104-113 (1968).

2. **ALSMILLER-69**
   R.G. ALSMILLER, JR., J.W. WACHTER,
   H.S. MORAN
   NSE, 36, PP.291-294 (1969).

3. **BAIR-79**
   J.K.BAIR and J.G.D.CAMPO
   NSE, 71, PP.18-28 (1979).

5. **NAKAMURA-83**
   T. NAKAMURA, M. FUJII and K. SHIN
   NSE, 83, PP.444-458 (1983).

6. **MEIER-89**
   M.M. MEIER, D.A. CLARK,
   C.A. GOULDING, J.B. MCCLELLAND,
   G.L. MORGAN and C.E. MOSS
   NSE, 102, PP.310-321 (1989).

7. **VEESER-74**
   L.R. VEESER, R.R. FULLWOOD,
   A.A. ROBRA and E.R. SHUNK
   NIM, 117, PP.509-512 (1974).

8. **FASSO-76**
   A. FASSO and M. HOFERT
   NIM, 133, PP.213-218 (1976).

11. **NIEMIMEN-81**
    M. NIEMIMEN and J.J. TORSTI
    NIM, 179, PP.85-93 (1981).

15. **NAKAMURA-85**
    T. NAKAMURA
    NIM, A240, PP.207-215 (1985).

16. **LONE-87**
    M.A. LONE, R.T. JONES, B.M. TOWNES
    and L. NIKKINEN, R.B. MOORE
    NIM, A256, PP.135-142 (1887).

17. **CONDE-87**
    H. CONDE, E. GRUSELL, B. LARSSON,
    C.B. PETTERSSON, L. THURESSON,
    J. CRAWFORD, H. REIST, B. DAHL
    and H.G. SJOSTRAND
    NIM, A261, PP.587-590 (1987).

18. **GOODELL-53**
    W.F. GOODELL, JR., H.H. LOAR,
    R.P. DURBIN and W.W. HAVENS, JR.
    PR, 89, PP.724-727 (1953).

19. **WACHTER-67**
    J.W. WACHTER, W.R. BURRUS
    and W.A. GIBSON
    PR, 161, PP.971-981 (1967).

20. **STELSON-64**
    P.H. STELSON and F.K. MCGOWAN
    PR, B133, PP.911-919 (1964).

21. **WATCHER-72**
    J.W. WATCHER, W.A. GIBSON
    and W.R. BURRUS
    PR, C6, PP.1496-1508 (1972).

22. **MADEY-73**
    R. MADEY and F.M. WATERMAN
    PR, C8, PP.2412-2418 (1973).

23. **BONNER-78**
    B.E. BONNER, J.E. SIMMONS,
    C.R. NEWSOM, P.J. RILEY, G. GLASS,
    J.C. HIEBERT, M. JAIN
    and L.C. NORTHCLIFFE
    PR, C18, PP.1418-1425 (1978).

24. **CECIL-80**
    R.A. CECIL, B.D. ANDERSON,
    A.R. BALDWIN, R. MADEY,
    A. GALONSKY, P. MILLER, L. YOUNG
    and F.M. WATERMAN
    PR, C2l, PP.2471-2484 (1980).

25. **SHIN-84**
    K. SHIN, K. HIBI and T. NAKAMURA
    PR, C29, PP.1307-1316 (1984).

27. **SKYRME-62**
    D.M. SKYRME
    NP, 35, PP.177-193 (1962).

28. **LEVINE-72**
    G.S. LEVINE, D.M. SQUIER,
    G.B. STAPLETON, G. STEVENSON,
    K. GOEBEL and J. RANFT
    PARTICLE ACCELERATORS, 3, PP.91-101
    (1972).

29. **RANFT-72**
J.RANFT and J.T.ROUTTI
PARTICLE ACCELERATORS, 4, PP.101-110 (1972).

30. **BIRATTARI-85**
C. BIRATTARI and A. SALOMONE
HEALTH PHYS., 49, PP.919-936 (1985).

31. **BROOME-83**
T.A. BROOME, D.R. PERRY,
G.B. STAPLETON and D. DUC
HEALTH PHYS., 44, PP.487-499 (1983).

32. **TAKAHASHI-80**
H. TAKAHASHI, H.J.C. KOUTS,
P. GRANDO, J.R. POWELL
and M. STEINBERG
ATOMKERNENERGIE, 36, PP.195-199 (1980).

35. **BARASHENKOV-74**
B.C. BARASHENKOV et al.
ATOMNAYA ENERGIA, 37(6), PP.475-479 (1974).

36. **BAKHMUTKIN-87**
S.V. BAKHMUTKIN, A.I. BOGDANOV,
V.G. BODGANOV, N.P. KOCHEROV,
V.I. KUCHERYUK, A.A. NOSOV,
and A.A. RIMSKI-KORSAKOV
SOV.AT.ENERGY, 62, PP.81 (1987).

38. **HOLMQVIST-86**
B. HOLMQVIST and E. RAMSTROM
PHYS.SCR., 33, PP.107 (1986).

39. **BAIR-81**
J.K.BAIR, P.D.MILLER and
B.W.WIELAND)
INT.J.OF APPL.RADIAT.ISOTOPES, 32,
PP.389-395 (1981).

41. **FULLWOOD-72**
R.R. FULLWOOD, J.D. CRAMER,
R.A. HEARMAN, R.P. FORREST, JR.
and R.G. SCHRANDT
LA-4789, PP.1-27 (1972).

45. **SUGIMOTO-79**
K. SUGIMOTO
TOKYO U. ANNUAL REPORT, PP.58 (1979).

46. **GREENWOOD-80**
L.R. GREENWOOD
SYMP. ON NEUTRON CROSS SECTIONS
FROM 10 TO 50 MEV, BNL, MAY 12-14,
BNL-NCS-51245, 1, PP.75 (1980).

47. **FRASER-80**
J.S. FRASER, P.M. GARVEY,
J.C.D. MILTON, F.M. KIELY,
I.M. THORSON and B.D. PATE
SYMP. ON NEUTRON CROSS SECTIONS
FROM 10 TO 50 MEV, BNL, MAY 12-14,
BNL-NCS-51245, 1, PP.155 (1980).

48. **RUSSELL-80**
G.J. RUSSELL, J.S. GILMORE, R.E. PRAEL,
H. ROBINSON and S.D. HOWA
SYMP. ON NEUTRON CROSS SECTIONS
FROM 10 TO 50 MeV, BNL, MAY 12-14,
BNL-NCS-51245, 1, PP.169 (1980).

50. **CIERJACKS-80**
S. CIERJACKS, M.T. RAINBOW,
M.T. SWINHOE and L. BUTH
PROC. 4th ICANS MEETING. at KEK,
OCT.20-24 (1980).

Table 3 ***References on shielding experiments***

AGOSTEO-93
"Photoneutron Dose in Soft Tissue Phantoms Irradiated by 25 MV X-Rays"
S. AGOSTEO, A.F. PARA, F. GERARDI,
M. SILARI, A. TORRESIN and G. TOSI
Phys.Med.Biol. 38, 1509-1528 (1993)

DINTER-94a
"Fluence Spectra and Dose Equivalents of Neutrons Behind Shielding of High Energy Proton Accelerators"
H. DINTER and K. TESCH
DESY D3-77 (Internal Report) (1994)

DINTER-94b
"Studies on the Neutron Field Behind Side Shielding of a Target Bombarded with High Energy Protons"
H. DINTER and K. TESCH
DESY D3-78 (Internal Report) (1994)

DINTER-95
"Studies on the Neutron Field Behind Side Shielding of Proton Accelerators. Part II: Iron Shielding"
H. DINTER and K. TESCH
DESY D3-81 (Internal Report) (1995)

DRAKE-91
"Experimental Simulation of Martian Neutron Leakage Spectra"
D.M. DRAKE, S.A. WENDER, R.O. NELSON,
D.A. CLARK, M. DROSG, W. AMIAN,
J. BRUCKNER and P.A.J. ENGLERT
Nucl. Instr. and Meth., A309, 575-580 (1991)

1) Accelerator: LAMPF
2) Projectiles: p (800 MeV)
3) Target: Martian sand
4) Experimental method: Time of flight method
5) Calculation: LAHET
6) Calculated quantities: Neutron leakage spectrum

EBELING-88
"Simulation of Hadronic Showers with Monte Carlo Codes at 40, 86, 300 and 1000 GeV: Comparison with Published Measurements and First Application to the Design of HERA Beam Dump"
F. EBELING, R. FOHRMANN, U. OTTERPOHL and H.J. MOHRING
Particle Accelerators, 23, 103-120 (1988)

HOFERT-94
"The CERN-CEC High-Energy Reference Field Facility"
M. HOFERT and G.R. STEVENSON
8th International Conference on Radiation Shielding, 635-642, April 24-28, 1994, Arlington, Texas, USA.

1) Accelerator: CERN-CEC
2) Projectile: Proton(120GeV/c), Pion(205GeV/c)
3) Target: Cu
4) Experimental method:
5) TEPC, Rem counter, Plastic scintillator, Au activation (10 inch pseudo sphere), CR39
6) Calculation: FLUKA, EGS4
7) Calculation quantities:
   Neutron fluence spectra, outside the iron and concrete shield, detector response

NAKAMURA-94
Development of p-Li Quasi-Monoenergetic Neutrons Field Between 20 and 90 MeV for Cross Section and Shielding Experiments
T. NAKAMURA, T.S. SOEWARSONO, Y. UNO,
N. NAKAO, Y. UWAMINO, M. IMAMURA,
T. ISHIKAWA, S. TANAKA, H. NAKASHIMA,
S. TANAKA, M. BABA and T. IWASAKI
8th International Conference on Radiation Shielding, 264-271, April 24-28, 1994, Arlington, Texas, USA.

1) Accelerator:
   AVF cyclotron (INS, CYRIC, TIARA)
2) Projectile: Proton (20-90 MeV)
3) Target: Li, Li+C
4) Experimental method: TOF
5) Calculation:
6) Calculation quantities:

NAKAO-94
Spectrometry of Several Tens MeV Neutrons Penetrating Shields Using Organic Liquid Scintillator at 90 MeV AVF Cyclotron Facility, TIARA
N. NAKAO, T. NAKAMURA, M. TAKADA, S. TANAKA, H. NAKASHIMA, Y. SAKAMOTO, Y. NAKANE, S. TANAKA, K. SHIN, E. TANABE, T. SHIBATA, Y. UWAMINO and M. BABA
8th International Conference on Radiation Shielding, 272-279, April 24-28, 1994, Arlington, Texas, USA.

1) Accelerator: TIARA
2) Projectile: Proton (40.5, 64.5 MeV)
3) Target: Li
4) Experimental method:
BC501A organic liquid scintillator, Bonner ball
5) Calculation: MORSE-CG
6) Calculation quantities: neutron spectra

SAKAMOTO-94
"Shielding Experiments with Quasi-Monoenergetic Neutrons Between 15 and 90 MeV at 90 MeV AVF Facility TIARA"
Y. SAKAMOTO, H. NAKASHIMA, T. NAKAMURA, M. BABA, N. NAKAO, S. TANAKA and K. SHIN
8th International Conference on Radiation Shielding, 809-815, April 24-28, 1994, Arlington, Texas, USA.

1) Accelerator:
TIARA
(Japan Atomic Energy Research Institute)
2) Projectile: Proton (15-90MeV)
3) Target: Li-7
4) Experimental method:
fission counter, rem counter, solid state nuclear track detector, LiF TLD
5) Calculation: DOT3.5
Calculation quantities: reaction rate
dose equivalent

TANAKA-94
"Shielding Experiments and Analysis at 90MV AVF Cyclotron Facility TIARA"
S. TANAKA, T. NAKAMURA, JAERI-UNIVERSITIES Collaboration Group

1) Accelerator: TIARA AVF cyclotron
2) Projectile: proton (43, 67MeV)
3) Target: 7Li
4) Source Neutrons: quasi-monoenergetic
5) Shields: iron(10-130cm)
concrete(25-200cm)
6) Geometry: source: collimated beam
detector points: on axis, 20cm of axis
7) Experimental Method:
Fission counters: U-238, Th-232 Solid state track detector, TLD: 6LiF/7LiF
spectrometer: BC501A
8) Measured Neutron Energy Range:
Thermal to source energy

UWAMINO-94A
"Shielding Experiment at Spallation Neutron Source Facility
Y. UWAMINO, T. SHIBATA, T. OHKUBO and S. SATO
8th International Conference on Radiation Shielding, 288-293, April 24-28, 1994, Arlington, Texas, USA.

1) Accelerator:
ISIS spallation neutron source facility (Rutheford Appleton Laboratory)
2) Projectile: Proton (800MeV)
3) Target: Ta
4) Experimental method:
SSTD, TLD (LiF), Activation Detector (In, C, Al, Bi)
5) Calculation:
6) Calculation quantities:

UWAMINO-94B
"Study on Bulk Shielding of an 800-MeV Proton Accelerator"
Y. UWAMINO, T. SHIBATA, T. OHKUBO, S. SATO and D. PERRY

1) Accelerator: ISIS proton synchrotron
2) Projectile: proton (800MeV)
3) Target: Ta
4) Shields:
iron(291cm)+concrete(96cm) Geometry:
5) Geometry: point isotropic
6) Experimental Method:
Activation method: Bi(n,xn), C(n,2n), I(n,3na)
TLD: 5LiF/7LiF, In activation multi-moderator spectrometer
7) Measured Neutron Energy Range:
Thermal to -90MeV

Fig.1-1 (p,xn) thick target yield data

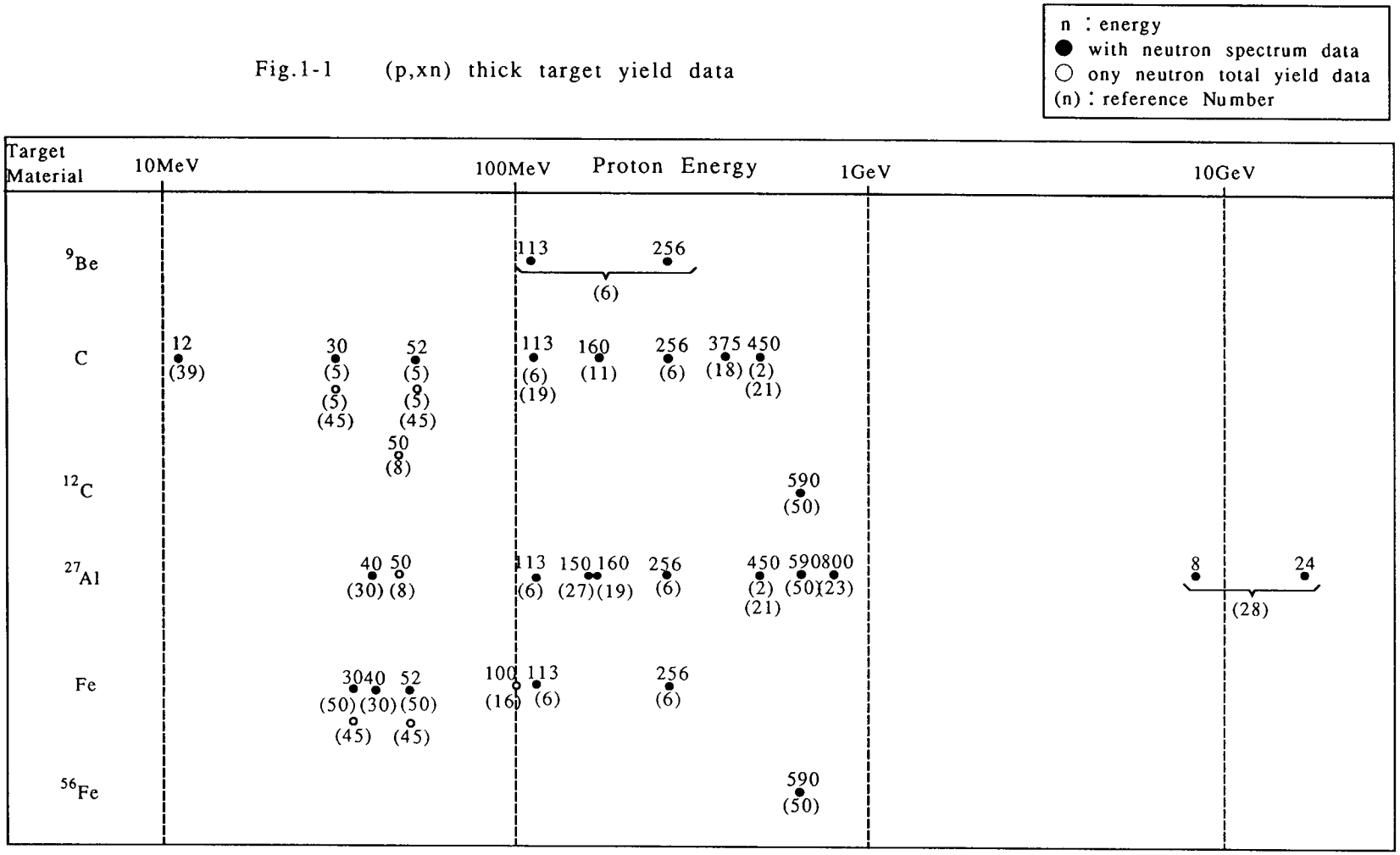

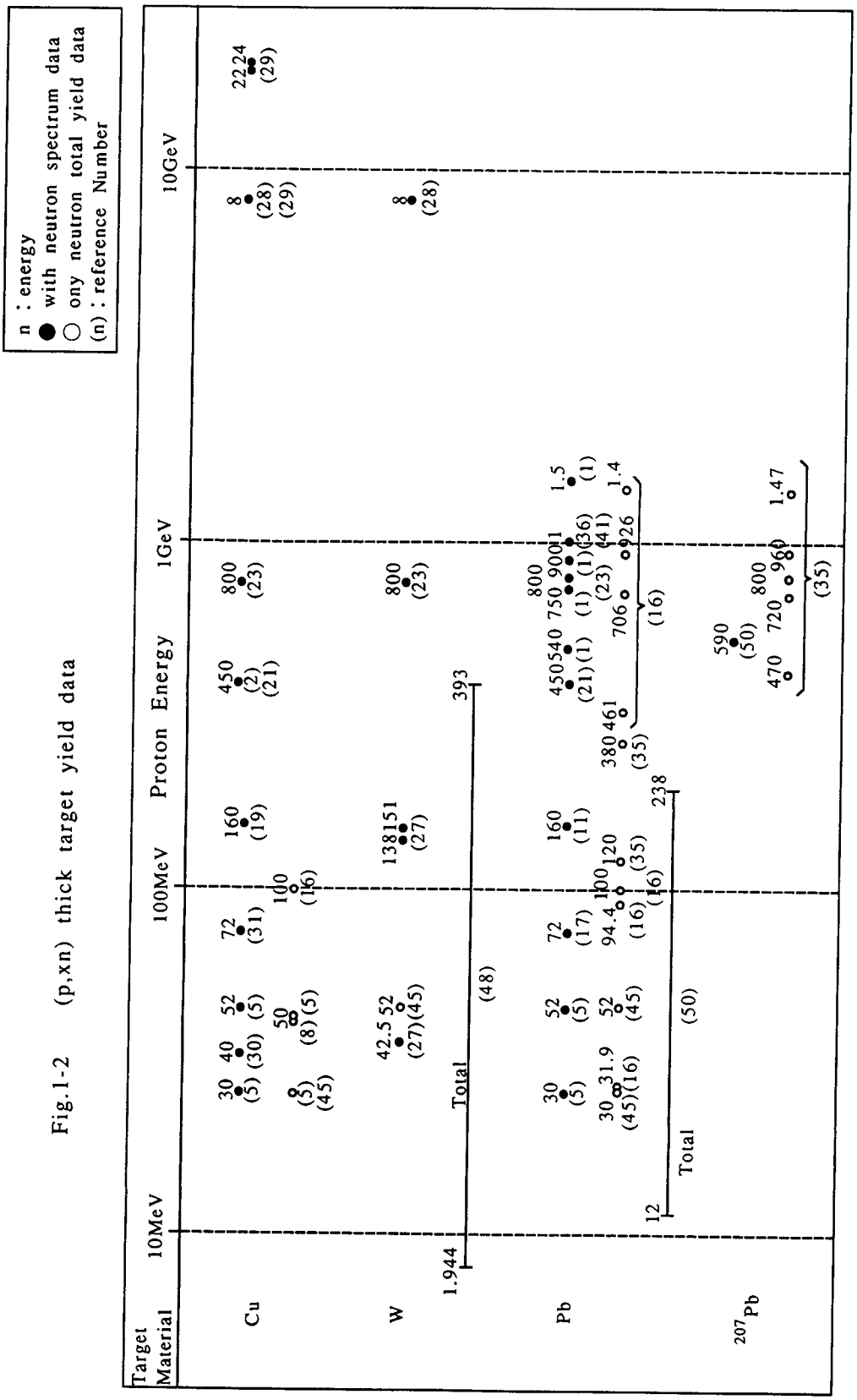

Fig.1-2 (p,xn) thick target yield data

Fig.1-3 (p,xn) thick target yield data

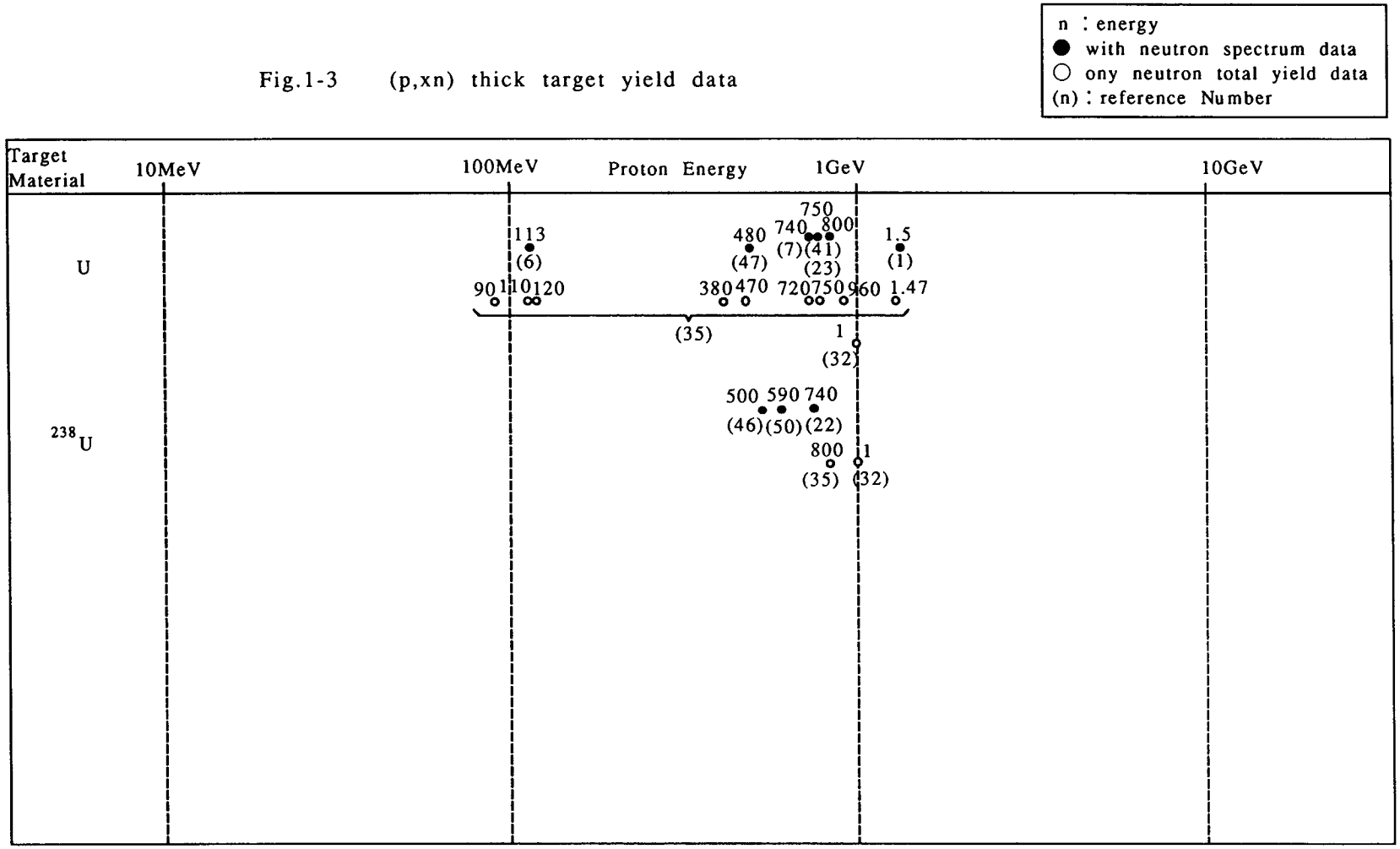

Fig.2 (α ,xn) thick target yield data

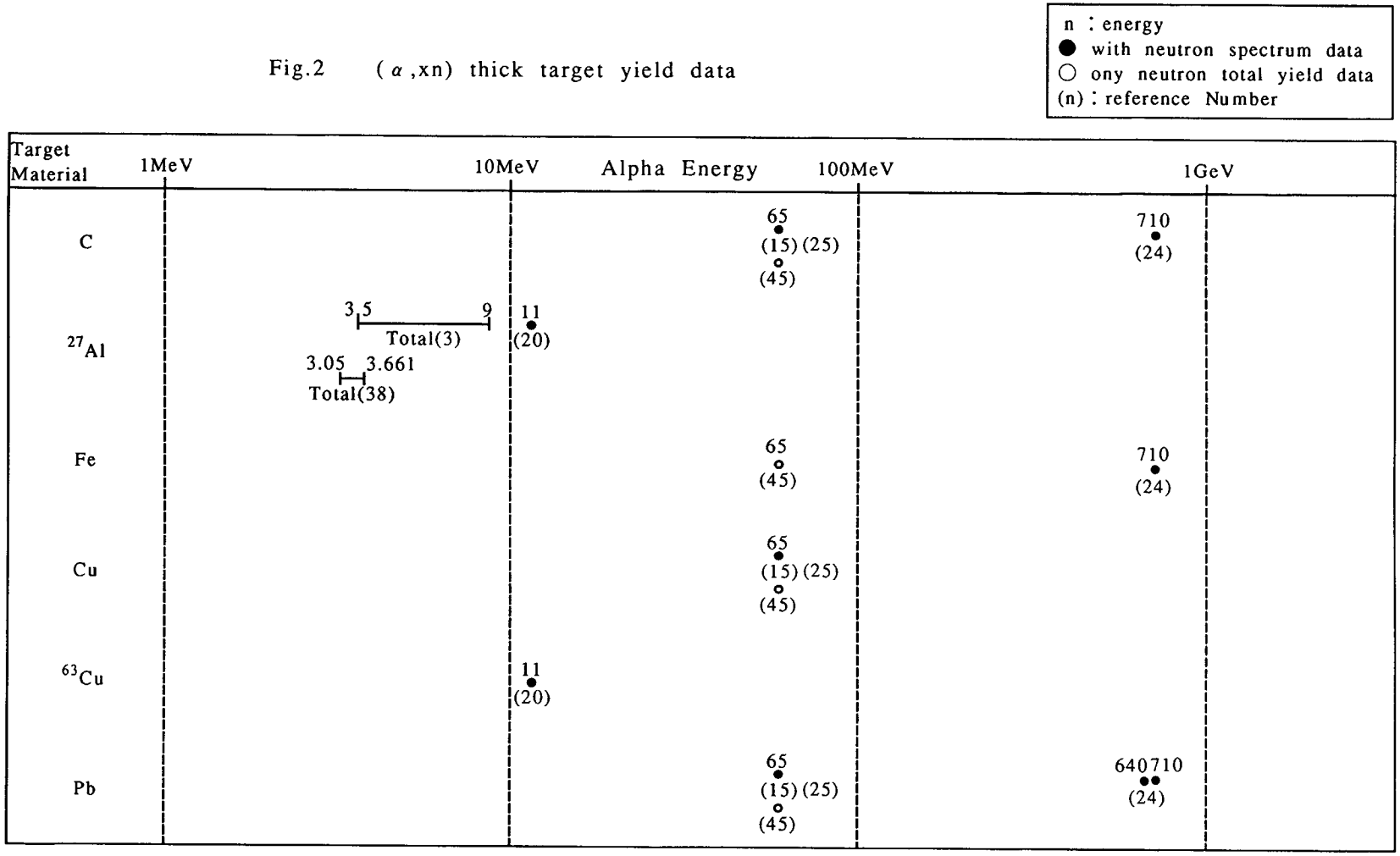

HADRONIC PHOTON-HADRON AND PHOTON-PHOTON INTERACTIONS AT HIGH ENERGIES

R. Engel
Institut für Theoretische Physik, Universität Leipzig
Fachbereich Physik, Universität Siegen
Germany

J. Ranft
Laboratoire de Physique Théorique LAPP, Groupe d'Annecy, France

Abstract

Photon-photon collisions are investigated in the framework of the two-component Dual Parton Model. The model contains contributions from direct, resolved soft and resolved hard interactions. All free parameters of the model are determined in fits to hadron-hadron and photon-hadron cross-section data. The model is shown to agree well to hadron production data from hadron-hadron and photon-hadron collisions. The multiparticle production in hadron-hadron, photon-hadron and photon-photon collisions as predicted by the model is compared. Strong differences are only found as function of the transverse momentum variable.

1. Introduction

In its high-energy interactions with hadrons, the photon behaves very much like a hadron, with cross-sections reduced strongly though against pure hadronic cross-sections. Besides this hadronic interaction, usually described using the Vector Dominance Model, the photon has a direct pointlike interaction with hadronic constituents. At moderate energies the hard interactions of the photons do not change significantly the general picture of photon-hadron and photon-photon interactions. Even at high energies, hadronic interactions of photons are characterised by soft multiparticle production. Since the soft component of hadron production cannot be understood purely on the basis of perturbative QCD one has to rely on models like the Dual Parton Model [1] or the model by Schuler and Sjöstrand [2,3] to calculate multiparticle final states. Assuming an universal behaviour of soft hadronic interactions, the Dual Parton Model (DPM) can be extended to hadronic interactions involving photons [4,5]. here we apply the model described in [4,5,6] to the study of hadronic photon-photon interactions.

2. The event generator PHOJET

The realisation of the DPM with a hard and a soft component in PHOJET is similar to the event generator DTUJET-93 [7,8]. In the model, the dual nature of the photon is taken into account by considering the physical photon state as a superposition of a "bare photon" and virtual hadronic states having the same quantum numbers as the photon. Two generic hadronic states $\left|q\bar{q}\right\rangle$ and $\left|q\bar{q}^{*}\right\rangle$ have been introduced to describe the hadronic piece of the photon. The low-mass state $\left|q\bar{q}\right\rangle$ corresponds to the superposition of the vector mesons ρ, ω and ϕ and a $\pi^{+}\pi^{-}$ background. The state $\left|q\bar{q}^{*}\right\rangle$ is used as an approximation for hadronic states with higher masses. The physical photon reads

$$\left|\gamma\right\rangle = \sqrt{Z_3}\left|\gamma_{\text{bare}}\right\rangle + \left|\gamma_{\text{had}}\right\rangle \tag{1}$$

with

$$Z_3 = 1 - \frac{e^2}{f^2_{q\bar{q}}} - \frac{e^2}{f^2_{q\bar{q}^*}} \tag{2}$$

and

$$\left|\gamma_{\text{had}}\right\rangle = \frac{e}{f_{q\bar{q}}}\left|q\bar{q}\right\rangle + \frac{e}{f_{q\bar{q}^*}}\left|q\bar{q}^{*}\right\rangle \tag{3}$$

where *e* denotes the elementary charge.

The interactions of the hadronic fluctuations are described within the Dual Parton Model in terms of reggeon and pomeron exchanges. For soft processes, photon-hadron duality is used. The energy-dependence of the reggeon and pomeron amplitudes is assumed to be the same for all hadronic processes. Therefore, data on hadron-hadron and photon-hadron cross(sections can be used to determine the parameters necessary to describe soft photon-photon interactions. The pomeron exchange is subdivided into processes involving only *soft* processes and all the other processes with at least one

least one large momentum transfer (*hard* processes) by applying a transverse momentum cut-off $p_{\perp}^{cut-off}$ to the partons. On Born-graph level, for example, the photon-photon cross-sections is built up by:

i. reggeon and pomeron exchange (soft processes only),
ii. hard resolved photon-photon interaction,
iii. single direct interactions, and
iv. double direct interactions.

If not explicitly stated, all the Parton Model calculations of the hard processes have been done using the leading order GRV parton distribution functions for the proton [9] and the photon [10].

The amplitudes corresponding to the one-pomeron exchange between the hadronic fluctuations are unitarized applying a two-channel eikonal formalism similar to [7]. In impact parameter representation, the eikonalized scattering amplitude for resolved photon interactions has the following structure:

$$a_{res}(s,B) = \frac{i}{2}\left(\frac{e^2}{f_{qq}^2}\right)^2 \left(1 - e^{-\chi(s,B)}\right) \tag{4}$$

with the eikonal function $$\chi(s,B) = \chi_S(s,B) + \chi_H(s,B) + \chi_D(s,B) + \chi_C(s,B) \tag{5}$$

Here, χ_i (s,B) denotes the contributions from the different Born graphs:

(S) *soft* part of the pomeron and reggeon,
(H) *hard* part of the pomeron,
(D) *triple-* and *loop*-pomeron, and
(C) *double*-pomeron graphs.

The probabilities to find a photon in one of the generic hadronic states, the coupling constants to the reggeon and pomeron, and the effective reggeon and pomeron intercepts cannot be determined by basic principles. These quantities are treated as free parameters and determined by cross-section fits [4]. For example, in Figures 1 and 2 we show the model predictions for the inelastic photon-photon cross-section (including quasi-elastic vector meson production).

The probabilities for the different final state configurations are calculated from the discontinuity of the scattering amplitude (optical theorem) which can be expressed as a sum of graphs with k_c soft pomeron cuts, l_c hard pomeron cuts, m_c triple- or loop-pomeron cuts, and n_c double pomeron cuts by applying the Abramovski-Gribov-Kancheli cutting rules [12,13].

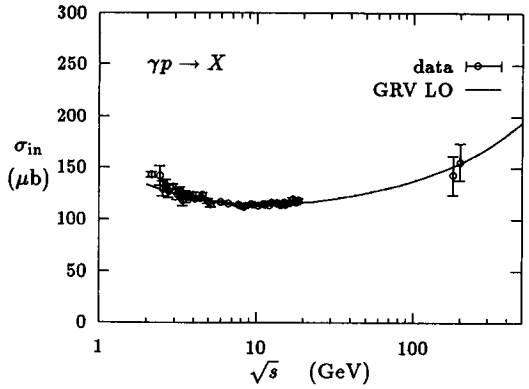

Figure 1
Inelastic photon-photon cross-section calculated with the model and compared with data [4].
The two curves from the model were calculated using the GRV LO photon structure function [10] and the SaS 2M photon structure function [11].

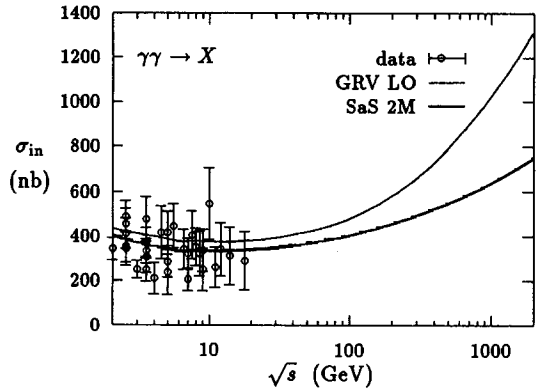

Figure 2
Inelastic photon-photon cross-section calculated with the model and compared with data [4].
The two curves from the model were calculated using the GRV LO photon structure function [10] and the SaS 2M photon structure function [11].

In impact parameter space one gets for the inelastic cross-sections

$$\sigma(k_c, l_c, m_c, n_c, s, B) = \frac{(2\chi_S)^{k_c}}{k_c!}\frac{(2\chi_H)^{l_c}}{l_c!}\frac{(2\chi_D)^{m_c}}{m_c!}\frac{(2\chi_C)^{n_c}}{n_c!}\exp[-2\chi(s,B)] \qquad (6)$$

Since the triple-, loop-, and double-pomeron graphs are objects involving several pomerons, a further resummation is done [7,6] to allow for the probability interpretation of Equation (6).

For pomeron cuts involving a hard scattering, the complete parton kinematics and flavours/colours are sampled according to the Parton Model using a method similar to [14], extended to direct processes. For pomeron cuts without hard large momentum transfer, the partonic interpretation of the Dual Parton Model is used: photons or mesons are split into a quark-antiquark

pair whereas baryons are approximated by a quark-diquark pair. The longitudinal momentum fractions of the soft partons are given by Regge asymptotics [15,16]. The transverse momenta of the soft partons are sampled from an exponential distribution in order to get a smooth transition between the transverse momentum distributions of the soft constituents and the hard scattered partons. In diffraction dissociation or double-pomeron scattering, the parton configurations are generated using the same ideas described above applied to pomeron- photon/pomeron scattering processes. Finally, the fragmentation of the sampled partonic final states is done by forming colour neutral strings between the partons according to the colour flow. In the limit of many colours in QCD, this leads to the two-chain configuration characterising a cut pomeron and a one-chain system for a cut reggeon. The chains are fragmented using the Lund fragmentation code JETSET 7.3 [17].

3. Comparison of PHOJET calculations with data

We present a few comparisons of PHOJET results with hadron-hadron and photon-hadron data in order to illustrate that the model as formulated in PHOJET is very well able to describe these channels. For photon-photon collisions we have to rely on the predictive power of the model.

In Figures 3 and 4 we compare the pseudo-rapidity distributions of π^- and charged particles calculated with PHOJET to the results from experiments [18,19].

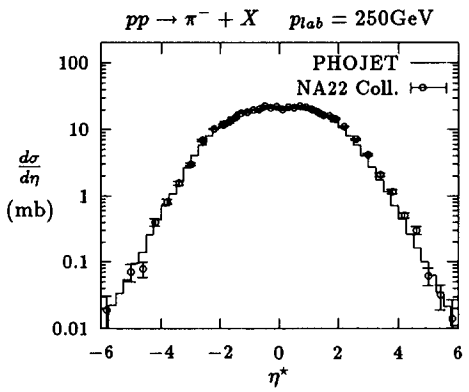

Figure 3 ***Pseudo-rapidity distributions calculated with the model and compared to data*** [18]

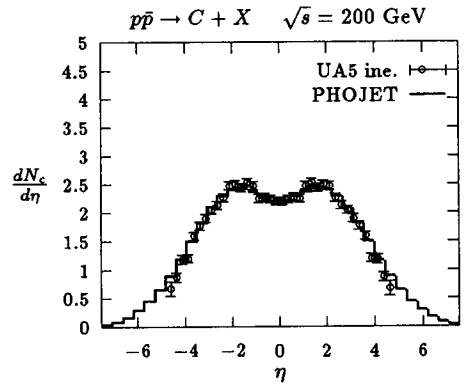

Figure 4 ***Pseudo-rapidity distributions calculated with the model and compared to data*** [19]

The rise of the pseudo-rapidity plateau with the collision energy is understood with the model by one of its most important ingredients: the production of multiple soft interactions and multiple hard interactions (minijets) rises with energy.

In Figures 5 and 6 PHOJET calculations are compared to data of the OMEGA photon Collab. [20] $\left(\langle\sqrt{s}\rangle = 15\ GeV\right)$ and H1 Collab. [21] $\left(\langle\sqrt{s}\rangle = 200\ GeV\right)$

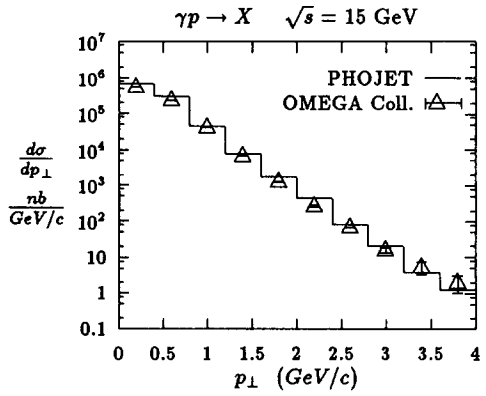

Figure 5
Transverse momentum distributions of charged particles calculated with PHOJET and compared to data [20]

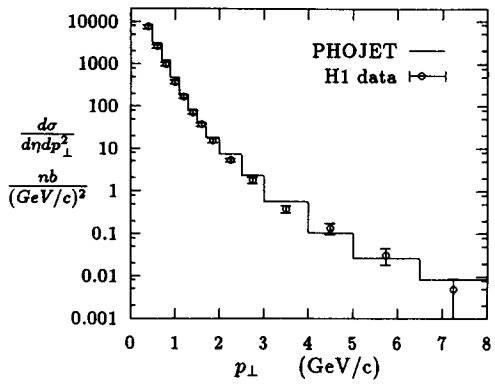

Figure 6
Transverse momentum distributions of charged particles calculated with PHOJET and compared to data [21]

4. Comparison of minimum-bias hadron production in hadron-hadron, photon-hadron and photon-photon collisions

In this section we compare the model predictions for inelastic hadron production in proton-proton, photon-proton and photon-photon collisions at fixed centre-of-mass (CMS) energies $\sqrt{s}$. Since elastic hadron-hadron collisions usually are excluded studying inclusive secondary distributions, we also exclude in the reactions with protons and photons the corresponding quasi-elastic diffractive channel i.e., $\gamma + \gamma/p \rightarrow V + V/p$, $(V = \rho, \omega, \phi)$.

In Figures 7 and 8 we show the transverse momentum distribution at 20 and 200 GeV and the transverse energy flow of proton-proton, photon-proton and photon-photon interactions at $\sqrt{s} = 200\,\mathrm{GeV}$.

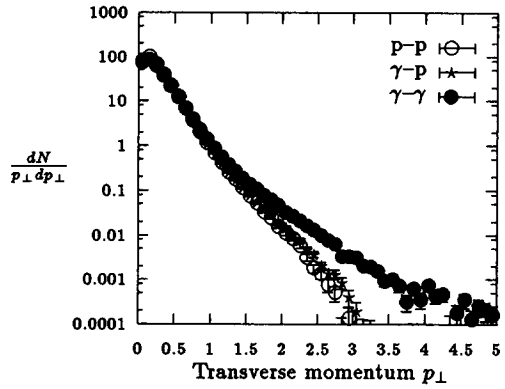

Figure 7

We compare at the collision energy $\sqrt{s} = 20\,\mathrm{GeV}$ the transverse momentum distribution in invariant form for all charged hadrons produced in p-p, γ-p and γ-γ collisions. The calculation was done with PHOJET for inelastic collisions.

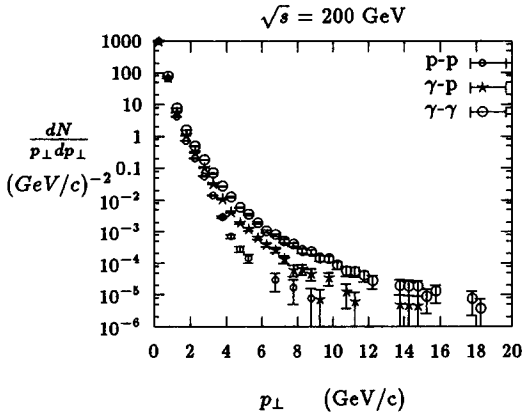

Figure 8

Transverse momentum distributions of charged particles calculated with PHOJET for proton-proton, photon-proton, and photon-photon interactions

The differences in the $p_\perp$ distributions come from the direct photon interaction and the fact that the photon structure function is considerably harder than the proton structure function. However, these differences in the hard scattering do not strongly influence such properties of the collision as average multiplicities or the transverse energy flow. Minimum bias hadron production in hadron-hadron, photon-hadron, and photon-photon collisions of the same CMS energy is remarkably similar. The only striking differences appear in the transverse momentum distribution or distributions where the transverse momentum behaviour is essential.

However, these differences in the hard scattering do not strongly influence such average properties of the collision as average multiplicities or even average transverse momenta. This can be seen from Table 1 where we collect some average quantities characterising non-diffractive proton-proton, proton-photon, and photon-photon collisions at CMS energies at 10 and 200 GeV. The total and charged multiplicities at all energies are rather near to each other in all channels. probably the differences in the multiplicities of newly produced hadrons like π^- and $\bar{p}$ are more significant, we find them at all energies rising from *p-p* over *γ-p* to *γ-γ* collisions. Also the average transverse momenta rise as expected from *p-p* over *γ-p* to *γ-γ*. In Table 1 we give also the number of soft

pomerons to be the same in all three channels. The number of cut hard pomerons rises at all energies from *p-p* over γ-*p* to γ-γ.

In Figure 9 we compare the longitudinal momentum distributions in the form of $x_r dN/dx_r$ for the three channels. $x_r = \left(p_\parallel / |p_\parallel|\right) 2E/\sqrt{s}$ is the so-called radial scaling variable, very similar to the Feynman variable $x_r = 2p_\parallel / \sqrt{s}$. Significant differences between the three channels are only found in the region near $x_r = 1$ or -1. The reason is the single diffractive component, which in the *p-p* and γ-*p* case leads to the diffractive protons, which are obviously missing in γ-γ collisions.

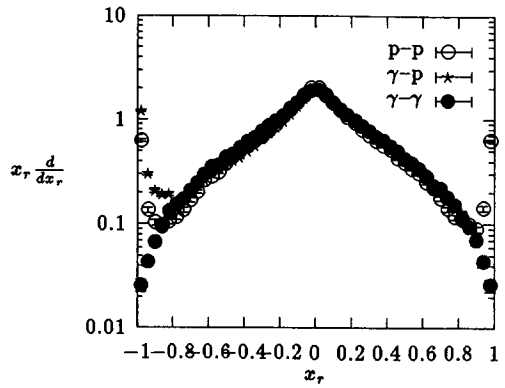

Figure 9

We compare at the collision energy $\sqrt{s} = 20\,GeV$ the radial $x_r = 2E/\sqrt{s}$ distribution in invariant form for all charged hadrons produced in *p-p*, γ-*p and* γ-γ collisions. The calculation was done with PHOJET for inelastic collisions.

In Figure 10 we compare the seagull effect in the three channels. We find due to the direct processes in photon-photon collisions that the rise of $\langle p_\perp \rangle$ with rising Feynman x_F is more prominent in photon-photon collisions than in proton-proton collisions. In photon-proton interactions we find backwards in the proton fragmentation region, agreement with the *p-p* collision and in the forward direction, in the photon fragmentation region, agreement with photon-photon collisions.

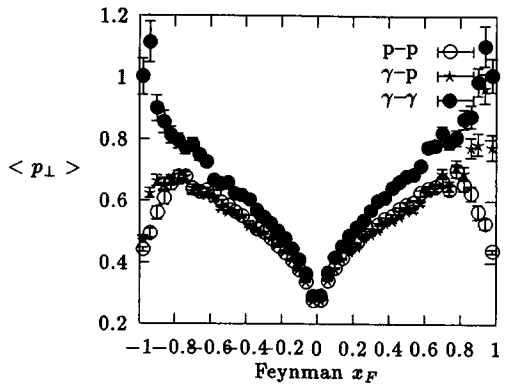

Figure 10

We compare at the collision energy $\sqrt{s} = 20\,\mathrm{GeV}$ the average transverse momentum of charged hadrons produced in *p-p*, γ-*p and* γ-γ collisions as function of the Feynman x_F variable (seagull effect). The calculation was done with PHOJET for inelastic collisions.

In Figure 11 the transverse energy flow of proton-proton, photon-proton and photon-photon interactions at $\sqrt{s} = 200\,GeV$ on a logarithmic scale. In Figure 12 we plot linearly the transverse

In Figure 11 the transverse energy flow of proton-proton, photon-proton and photon-photon interactions at $\sqrt{s = 200\,GeV}$ on a logarithmic scale. In Figure 12 we plot linearly the transverse energy distribution $dE_{\perp}/d\eta$. Roughly, these distributions should be equivalent to the pseudo-rapidity distribution $dN/d\eta$ multiplied with the average transverse energy per particle. We observe characteristic differences, which can be understood from the features already discussed. The transverse energy distribution is wider in photon-photon collisions than in proton-proton collisions. The transverse energy distribution rises at all η from p-p over γ-p to γ-γ. For γ-p the distribution agrees backwards with p-p and forwards with γ-γ.

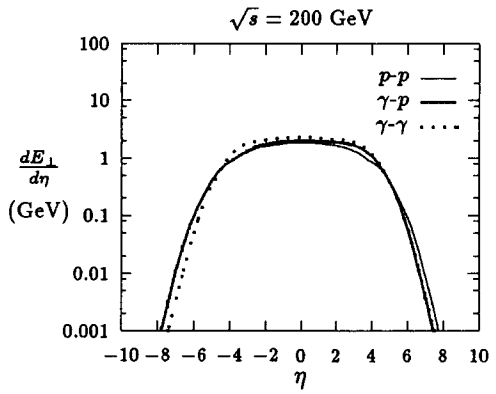

Figure 11
Transverse energy flow calculated with PHOJET for proton-proton, photon-proton and photon-photon interactions.

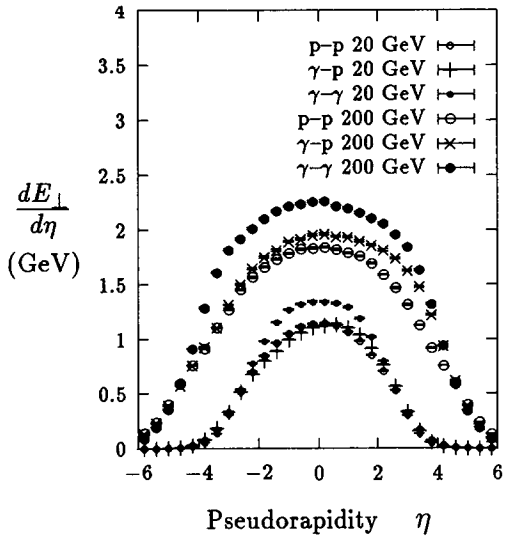

Figure 12

We compare at the collision energies $\sqrt{s} = 20\,GeV$ *and* $200\,GeV$ in a linear plot distribution of the transverse energy $E_{\perp}$ as function of the pseudo-rapidity η for p-p, γ-p, γ-γ collisions. The calculation was done with PHOJET for inelastic collisions.

For $p - p$ *or* $\bar{p} - p$ collisions the transverse energy distribution at $\eta = 0$ is known from ISR experiments and experiments at the CERN collider. The values calculated with PHOJET agree well with these measurements. At HERA is was found that practically the same transverse energy at $\eta = 0$ is found like in p-p interactions and in collisions of real or virtual photons with protons. This observation agrees well with our results in Figures 11 and 12.

The PHOJET model can be used to calculate hadronic events in hadron-hadron, photon-hadron and photon-photon collisions. The model is found to agree well with data in hadron-hadron, photon-hadron collisions, the predictions for photon-photon collisions do not need any new parameters.

The authors are grateful to P. Aurenche for his many helpful discussions and suggestions. They acknowledge the hospitality by LAPP, Annecy-le-Vieux. One of the authors (R.E.) was supported by the Deutsche Forschungsgemeinschaft under contract No. Schi 422/1-2.

Table 1

Comparison of average quantities characterising hadron production in non-diffractive p-p, γ-p, γ-γ collisions at cm energies between 10 and 200 GeV. All average transverse momenta are given in GeV/c

$\sqrt{s}$	Quantity	p–p	γ–p	γ–γ
10	n_{tot}	11.2	11.1	11.7
10	n_{ch}	6.65	6.53	6.86
10	n_{π^-}	2.17	2.44	2.88
10	$n_{\bar{p}}$	0.027	0.063	0.11
10	$< p_{\perp ch} >_{centr.\eta}$	0.39	0.38	0.42
10	$< p_{\perp} >_{\pi^-}$	0.32	0.33	0.36
10	$< p_{\perp} >_{\bar{p}}$	0.41	0.43	0.47
10	$< n >_{softch.}$	1.16	1.19	1.22
10	$< n >_{minijets}$	0.	0.00004	0.0020
20	n_{tot}	16.4	16.6	17.1
20	n_{ch}	9.64	9.71	10.00
20	n_{π^-}	3.44	3.78	4.18
20	$n_{\bar{p}}$	0.086	0.14	0.20
20	$< p_{\perp ch} >_{centr.\eta}$	0.37	0.38	0.44
20	$< p_{\perp} >_{\pi^-}$	0.32	0.34	0.38
20	$< p_{\perp} >_{\bar{p}}$	0.42	0.45	0.52
20	$< n >_{softch.}$	1.26	1.33	1.31
20	$< n >_{minijets}$	0.0003	0.0025	0.028
50	n_{tot}	24.8	26.5	26.9
50	n_{ch}	14.5	15.5	15.6
50	n_{π^-}	5.49	6.19	6.53
50	$n_{\bar{p}}$	0.21	0.27	0.34
50	$< p_{\perp ch} >_{centr.\eta}$	0.38	0.40	0.46
50	$< p_{\perp} >_{\pi^-}$	0.33	0.35	0.40
50	$< p_{\perp} >_{\bar{p}}$	0.44	0.47	0.57
50	$< n >_{softch.}$	1.50	1.68	1.44
50	$< n >_{minijets}$	0.0096	0.035	0.17

References

[1] A. Capella, U. Sukhatme, C. I. Ta, and J. Tran Thanh Van, Phys. Rep. 236 (1994) 227.

[2] G. A. Schuler and T. Sjöstrand, Nucl. Phys. B B407 (1993) 539.

[3] G. A. Schuler and T. Sjöstrand, CERN-TH.7193/94, presented at the Workshop on Two-Photon Physics, Paris (1994).

[4] R. Engel, Z. Phys. C C66 (1995) 203.

[5] R. Engel and J. Ranft, 'Hadronic Photon-Photon Collisions at High Energies", ENSLAPP-A540/95 (hep-ph/9509373) (1995).

[6] R. Engel, "Multiparticle Photoproduction within the Two-Component Dual Parton Model, in preparation (1995).

[7] P. Aurenche, F. W. Bopp, A. Capella, J. Kwiecinski, M. Maire, J. Ranft and J. Tran Thanh Van, Phys. Rev. D45 (1992) 92.

[8] P. Aurenche, F. W. Bopp, R. Engel, D. Pertermann, J. Ranft and S. Roesler, Comp. Phys. Commun. 83 (1994) 107.

[9] M. Glück, E. Reya and A. Vogt, Phys. Rev. D45 (1992) 3986.

[10] M. Glück, E. Reya and A. Vogt, Phys. Rev. D46 (1992) 1973.

[11] G. A. Schuler, 'Low- and high-mass components of the photon distribution functions", CERN-TH/95-62 (1994).

[12] V. A. Abramovski, V. N. Gribov and O. V. Kancheli, Yad. Fis. C 18 (1973) 595.

[13] K. A. Ter-Martirosyan, Phys. Lett. B44 (1973) 377.

[14] K. Hahn and J. Ranft, Phys. Rev. D41 (1990) 1463.

[15] A. Capella, U. Sukhatmen C. I. Tan and J. Tran Thanh Van, Z. Phys. C C10 (1980) 249.

[16] A. B. Kaidalov, Phys. Lett. B116 (1982) 459.

[17] H. U. Bengtsson and T. Sjöstrand, Comp. Phys. Commun. 46 (1987) 43.

[18] NA22 Collab., M. Adamus et al., Z. Phys. C C39 (1988) 311.

[19] UA5 Collab., G. J. Alner et al., Z. Phys. C C33 (1986) 1.

[20] OMEGA Photon Collab., R. J. Apsimon et al., Z. Phys. C C43 (1989) 63.

[21] H1 Collab., I. Abt et al., Phys. Lett. B328 (1994) 177.

APPLICATIONS OF THE PHOTONUCLEAR FRAGMENTATION MODEL TO RADIATION PROTECTION PROBLEMS

P. Degtyarenko [1]
Department of Physics and Astronomy, University of Massachusetts, MA
Continuous Electron Beam Accelerator Facility, Newport News, VA
United States of America

Introduction

In order to provide radiation protection systems for high energy electron accelerators it is necessary to define the yields of hadrons produced when the electron beam interacts with a fixed target. In practical terms this will occur when any beam or fraction of the beam is lost from the accelerator orbit or when any fraction of the beam is intercepted by a target inserted in the path of the beam or when the beam is totally absorbed by a beam dump. The electron and gamma yields from these interactions are well characterised and amenable to calculation utilising Monte Carlo shower codes. However, the yield of hadrons has been less well defined. Neutron production has received most attention because of its importance to radiation shielding. Production mechanisms such as the giant dipole and the quasi-deuteron resonances have provided valuable information for total neutron yields for electron beams at energies less than about 400 MeV. For electron beams at energies extending to 10 GeV it is necessary to include the higher energy resonance structures and the various intranuclear production channels that are available for the production of higher energy neutrons. The production model described in this paper permits the calculation of laboratory angle and energy of all hadrons produced when an electron beam of energy between 100 MeV and 10 GeV interacts with a fixed target. This model can be used as an event generator for Monte Carlo codes used for many radiation protection purposes including calculation of radiation shielding.

Hadron production in electro-nuclear interactions

Calculation methods available

At the low end of the photon energy spectrum, characterised by the giant dipole resonance region, cross-sections are reasonably well known for given production channels but there appears to be limited quantitative information on the energy spectra of the hadrons produced in the reaction. At intermediate energies (< 0.5 GeV), there are few event generators. The code PICA has been available since the early 70's; this code, written by Gabriel, utilises the quasi deuteron model including single pion production, and reproduces the angular energy doubly differential cross-sections reasonably well when compared with limited existing experimental data [1,2]. For electro - production the Lightbody code is currently available but its utility is limited to thin experimental type targets [3]. At high energies (> 10 GeV) well

[1] On leave from Institute of Theoretical and Experimental Physics, Moscow, Russia 117259.

above the pion production region, groups at SLAC and CERN have implemented the vector meson dominance model for the nuclear reaction to provide an event generator which couples with the e/ γ shower code EGS and the hadronic cascade code FLUKA [4].

Another alternative is to provide an event generator, where each interaction is simulated so that individual hadrons for the event are scored for energy and direction. This technique is generally used as input for other transport codes. However, such an event generator can also be used to produce spectra or tabulated data if so required.

This paper is a presentation of an event generator which simulates hadron production from electron and photon interactions from very low energies to 10 GeV. The examples of its use for a number of practical applications will be given.

Deep inelastic nuclear reaction exclusive generator

Historically, this model begins with the original work by M. Kossov (ITEP, Moscow), where experimentally observed regularities of nuclear multi-fragmentation at high energies (for a review, see [5]) were understood within the concept of a thermodynamic quark source in the excited nucleus and the rules of hadronization [6]. The first simple and non-exclusive event generator using this model is known as GENGAS [7]. The model then was implemented in the form of a computer program DINREG - an exclusive event generator of nuclear multi-fragmentation which generates secondary neutrons, protons, pions and nuclear fragments fully conserving energy, momentum, and charge in the reaction [8]. The DINREG event generator was used in the data analysis of electro-nuclear interactions measured by the ARGUS detector at DESY [9]. The present version of the program (unpublished) was re-written by M. Kossov in 1992 [10] and developed, debugged and applied to photonuclear reactions by P. Degtyarenko in 1993-1995. It was used in the analysis of electro-nuclear data measured by the TPC/Twogamma detector at SLAC [11]. The phenomenological basis for the model was discussed in some detail in [11], where the model concepts were used to derive a parametrization formula well describing the spectra and angular distribu tions of secondary protons and charged pions in the electron-induced nuclear reactions with final states.

The event generator reproduces particle multiplicities and spectra in the reactions with multi-hadron production at nuclear excitations 0.2 GeV and more. Empirically, it was found possible to extend its applicability to the region of lower nuclear excitations, and for single hadron production in γA interactions.

DINREG in GEANT

Why GEANT

- Professionally maintained detector simulation package developed at CERN [12]
- Detailed MC-simulation of all major physics processes
- Good implementation of electromagnetic interactions
- Reasonably good implementation of hadron interactions
  - GHEISHA, FLUKA- packages included

- Neutron transport code GCALOR [13]
- Flexible geometry package with powerful graphics
- Powerful data analysis package PAW embedded
- Detailed write-up available
- User-open

Why DINREG

- Exclusive Monte Carlo event generator
- Charge, energy and momentum conservation
- Reproduces multiplicities and spectra in reactions with multi-hadron production
- Empirically found possible to be extended to the region of lower nuclear excitations
- Use of experimental values of total cross-sections

DINREG - GEANT interface: **GDINR**

The implementation of the nuclear fragmentation package DINREG in GEANT replaces the photoabsorption part of the 'PFIS' mechanism in GEANT.

For the newly implemented mechanism the total photonuclear cross-sections are stored for all nuclei, and the interface to DINREG (GGDINR) is called to generate exclusively an event of gamma-nucleus inelastic interaction with the production of protons, neutrons, nuclear fragments, and pions. The map of the photonuclear hadron production cross-sections for the nuclei currently implemented in GDINR is shown in Figure 1. The cross-sections for other nuclei are obtained by interpolation.

Electron (positron) - nuclear interactions are modelled using equivalent photon representation of an electron. At each step of electron propagating through a material, an equivalent photon is virtually generated in accordance with the standard flux formula, and the probability of its interaction with the nuclei of the material is estimated using the tables of photoabsorption cross-sections. When an interaction occurs the remaining energy is given back to the electron, and GGDINR is called to generate the products of the interaction.

As the photoabsorption cross-sections are in general much smaller than pure electro magnetic electron and gamma interaction cross-sections, a mechanism of amplification of the nuclear cross-sections is provided. The cross-sections can be multiplied by the user-given factor to make the interactions 'visible'. All hadronic yields should then be divided by this factor to get correct values.

High energy hadrons in photonuclear reactions are generally strongly suppressed. The equivalent photons and real photons in the electromagnetic shower are peaked at low energies, the photonuclear cross-section has its sharp maximum at $E_g \leq 25$ MeV (giant dipole resonance), and the spectrum of hadrons exponentially decreases with increasing kinetic energy of the hadrons. To enhance production of

the energetic hadrons in the event generator it is possible to set up a threshold on the energy of a photon. If the photon energy is below the threshold, the value of the cross-section is not multiplied by the amplification factor. Amplification is open for energetic photons. One should be careful in choosing of the amplification and cut -off parameters to keep the structure of electromagnetic shower unchanged. To achieve that, the mean number of the 'amplified' photonuclear interactions must be smaller than one per shower.

For amplification one can also use the following mechanism. When the number of hadronic interactions per shower is not large, the shower may be considered to be a pure undisturbed electromagnetic cascade. In such cases it is possible to turn off the energy transfer from electrons and photons in the hadronic interactions. Hadrons are produced in accordance with the amplified cross-section, but photons are kept in cascade, and electrons do not lose energy in hadronic interactions. Thus the shower structure is preserved, and hadronic output could be generated, in principle, with any amplification. This approach could be useful in modelling of complicated detector structures, where developing of the electromagnetic cascade takes a lot of CPU power. In any case, using of this approach would give slightly overestimated hadron production. The switch turning this mechanism on and off is given in the control cards.

Another user-specified parameter cuts off tracking in GEANT of low energy hadrons produced in photonuclear reactions. It can be used when the propagation of higher energy hadrons produced in an electromagnetic shower is being studied.

The mechanism of 'Secondary Cascade' in the amplification is also provided. In the tasks of radiation shielding there might be problems encountered, which require very large number of generated hadrons to calculate very small leakages through the shielding. In such cases there is a possibility to use generated hadronic events many times ('multiplicate' them) to investigate hadron propagation through the shielding. However, the statistical reliability of the chosen parameters should be investigated carefully in each case.

As DINREG is an exclusive event generator and produces nuclear fragments along with pions and nucleons, it may be used in simulations of material ageing, etc. where local energy depositions from heavy fragments might be essential. To make the simulation faster in other applications user can switch off the tracking of the heavy fragments in GEANT and assign their kinetic energy to the stopped photon as DESTEP parameter, or add it to electron DESTEP. The user parameter given in the data card DRFR specifies the atomic number of the heaviest nuclear fragment allowed for tracking.

The DINR mechanism is turned on by the 'PFIS 1' directive.

The user-specified parameters are given in special user -defined GEANT input data cards:

- DRAM 'amplification factor'
- DRGT 'amplification threshold'
- DRHT 'low kin.energy threshold for hadron tracking'
- DRMU 'multiplication factor', 'parameters of the multiplication'
- DRFR 'atomic number of heaviest nuclear fragment allowed'
- DRET '1 - energy transfer is ON, 0 - energy transfer is OFF'

By default: no thresholds, no multiplication, no amplification; the heaviest fragment allowed is alpha-particle; the energy transfer from electromagnetic s hower particles to hadrons is ON. The default state will reproduce physics processes 'as they are'. For example, developed electromagnetic cascade at 4 GeV on a thick heavy nuclear target will produce nuclear interactions almost in every event, so it may not require any kind of amplification. Whereas to observe and measure hadrons produced at low energy and thin light nuclear targets may require amplification and/or cut -offs. In any case, the default parameters are good to start with first.

Comparison with experimental data

To check and to tune up the parameters of the generator, we performed a series of comparisons with the experimental data on hadron production in photon - and electron nucleus interactions available in the energy scale from ~ 10 MeV to ~ 10 GeV.

Low energies

Figures 2 and 3 show the comparison of DINREG + GEANT calculation with the results of experiment by W.C. Barber and W.D. George [14] for determining of neutron yield out of the copper and lead targets of different thicknesses bombarded by electrons with energies 10 - 35 MeV. Good agreement is seen which indicates that both the development of electromagnetic shower is fairly well modelled within GEANT, and the cross-section for neutron production is well modelled by GDINR + DINREG at low excitation energies.

Medium energies

At medium energy we have the opportunity to compare the spectra of neutrons produced in electron interactions with thick nuclear targets. The experiment by H. J. von Eyss and G. Luhrs [15] was performed at electron energies from 150 to 266 MeV. In Figure 4 we present the comparison of DINREG + GEANT calculation with the data. Strong increase of the high energy component of the neutron spectra with the increasing energy of incident electron is well reproduced.

High energies

In the high energy region we have made a comparison with the results of the experiment performed by G. Bathow et al. [16]. Neutron yields from the interactions of bremsstrahlung photons with thick aluminium, copper, and lead targets were measured at electron energy 6.3 GeV. The comparison with DINREG + GEANT calculation is shown in Figure 5 and is reasonably good.

The angular dependence of the neutron and proton flux density measured in the interactions of the bremsstrahlung photons with thick (10 cm) copper target at electron energy 6.3 GeV is shown in Figure 6.

Exercise in shielding problem

We may conclude, therefore, that the newly developed software tool, GDINR, is capable to reproduce photonuclear neutron production cross-sections, at least with the accuracy of the order of 50% in the wide range of initial electron and photon energies.

So we may try to utilise the powerful capabilities of GEANT as a transport code. Figures 7 and 8 illustrate the exercise in solving of a standard shielding problem. Electron interacts in a thick copper target inside infinite concrete tube. The secondary neutrons produced with the cross-section amplification in the target, are traced through the wall by CALOR neutron transport code embedded in GEANT.

The neutron yield outside the concrete tube is calculated as the neutron flux at the outer surface of the concrete tube, at 90 degrees, in *(neutrons* cm^{-2}*)*, multiplied by $4\pi R^2$. The yield dependence of the wall thickness is shown by the solid lines in the Figure 8, for two initial electron energies, E_o = 200 MeV (open squares), and E_o = 4 GeV (open triangles). The data set shown by the dotted lines refers to the problem of calculating the yield of energetic (E_n > 20 MeV) neutrons and their attenuation in the shielding. Using the thresholds in the generation procedure, only the energetic neutrons were produced in the target. The figure illustrates that (1) lower energy neutrons have smaller absorption length and, (2) the portion of higher energy neutrons in the secondary neutron spectrum is much larger at higher beam energy.

Examples of calculations using DINREG in GEANT

Model of CEBAF Hall A End Station

The next step is application of the developed technique to the realistic geometries and materials. Figure 9 illustrates GEANT model of the CEBAF Hall A End Station. The Hall is a cylindrical volume inside the ground, with a ground wall surrounding it, and covered by a dome roof of 1.22 m thickness made of concrete and earth. An event is shown of 4 GeV electron interaction in a thick (20 cm) copper target situated in the middle of the hall. The lines indicate particles going out of the target: solid lines for charged particles, dotted lines for photons, dash - dotted lines for neutrons. The photonuclear hadron production cross-section is amplified by factor 200 to make the shielding calculations more effective.

Neutron flux at the roof and around

Sometimes, as we may see in Figure 9, the neutrons produced in the target escape the roof of the End Station into the air, and thus produce radiation field outside the End Station. Figure 10 shows the positions of the neutrons exiting the roof projected onto horizontal plane as dots. The squares superimposed onto this plot show the relative neutron flux intensity at the roof. Linear size of the squares is proportional to the neutron flux.

The Z-co-ordinate-dependence of the neutron flux at the roof of the Hall A End Station is shown in Figure 11 in three intervals in X -co-ordinate: 0 - 8 m, the closest to the beam, 8 - 16 m, and 16 - 24 m, the farthest interval. The neutron flux is in *(neutrons* cm^{-2} s^{-1}*)*, assuming 40 Watt, 4 GeV beam hitting thick copper target in the middle of the Hall.

The neutron flux can be transformed into the dose map on the roof, shown in Figure 13, utilising the angular and energy spectra of neutrons exiting the roof, shown in Figure 12.

And finally, the dependence of the dose from the skyshine neutrons on the distance from the End Station can be calculated (Figure 14). The neutron importance functions calculated by R. G. Alsmiller et al. [17] were used to convert the neutron flux and angular energy distribution of the neutrons exiting the roof, calculated by DINREG + GEANT, into the surface dose. The data shown are

previous analytical calculations based on neutron spectra from 400 MeV electrons bombarding thick copper target, and DINREG + GEANT calculations at 400 MeV and 4 GeV electron beams.

Examples of detailed neutron skyshine calculations for an experiment set -up at the Hall C at CEBAF are discussed elsewhere [18].

Model of beam dump

Another example of the realistic geometry implemented in GDINR is shown in Figure 15. The CEBAF Hall A End Station Beam Dump has a complicated geometry of many aluminium layers of different thickness, and cooling water between them. GEANT produces electromagnetic cascade from 4 GeV electron in the beam dump, and DINREG is called to produce 200 times amplified hadron component of the shower.

Neutron flux from the beam dump

Figure 16 shows the angular - momentum distribution of neutrons entering Hall A backward from the Beam Dump as calculated by DINREG + GEANT. This calculation is one of the most CPU -time consuming, as one has to generate electromagnetic shower and trace neutrons in a very complicated geometrical structure of the beam dump device, and then trace neutrons through the long ($\approx$ 25 m) tunnel of the beam dump. However the result shows that the problem may be solved successfully.

Conclusions

DINREG - GEANT interface has been developed which provides generation of hadron yield in e/γ-A interactions within GEANT simulation framework.

The newly developed software tool, GDINR, is capable to reproduce photonuclear neutron production cross-sections, at least with the accuracy of the order of 50% in the wide range of initial electron and photon energies.

The GDINR facility provides tools for calculations of background conditions, neutron fluxes, and solving shielding problems at (several GeV) electron accelerators using realistic geometries.

Future work that needs to be done is to study and optimise performance of the program, to provide better cross-section database, including all data and all nuclei available, to produce versions running on different computer platforms.

More details of GDINR and its implementation will be provided in a CEBAF Technical Note currently in preparation.

In order to make detailed description of DINREG, ruggedizing and freezing the code, performing benchmark tests and producing a formal release of the generator for the community would require additional work from the two authors, P.Degtyarenko and M.Kossov.

Acknowledgements

The author would like to thank Gerald Peterson and Geoffrey Stapleton for their kind hospitality and support and the CEBAF Radiation Control Group for help. The work was supported by the U.S. Department of Energy under contract number DE-AC05-84ER4015 and grant number DE-FG02-88ER40415.

References

[1] T. A. Gabriel and R. G. Alsmiller Jr., "Photonuclear Disintegration at High Energies (< 350 MeV)n, Phys. Rev. 181, 1035, (1969).

[2] PICA - Monte Carlo Medium-Energy Photon-Induced Intranuclear Cascade Analysis Code System, RSIC Computer Code Collection, Documentation for CCC-160/PICA Code Package, Oak Ridge National Laboratory, Oak Ridge, Tennessee, 1994.

[3] J. W. Lightbody, Jr. and J. S. O'Connell, "Modeling Single Arm Electron Scattering and Nucleon Production from Nuclei by GeV Electrons", Computers in Physics, May-June 1988, p.57.

[4] J.Ranft and W.R.Nelson, "Hadron Cascades Induced by Electron and Photon Beams in the GeV Range", Nucl.Instrum. and Methods, A257, 177 (1987).

[5] V. B. Gavrilov, G. A. Leksin, S. M. Shuvalov and K. Sh. Egiyan, Nucl. Phys. **A532,** 321 (1991).

[6] M. V. Kossov, L. M. Voronina, "Thermodynamic Quark-Parton Model of Multiple Hadron Production on Nuclei", Preprint ITEP-165, Moscow (1984).

[7] P. V. Degtyarenko, CLAS-NOTE 89-020, (1989).

[8] P. V. Degtyarenko, M. V. Kossov, "Monte - Carlo Program for Nuclear Fragmentation", Preprint ITEP-11-92, Moscow (1992).

[9] P. V. Degtyarenko, Yu. V. Efremenko, V. B. Gavrilov, G. A. Leksin and N. L. Semenova, Z.Phys.A - Atomic Nuclei 335, 231 (1990).

[10] M. V. Kossov, "Monte Carlo Generator for Nuclear Fragmentation Induced by Pion Capture", MC93 International Conference on Monte Carlo Simulation in High Energy and Nuclear Physics, Tallahassee, Florida, USA, 22-26 February 1993, p. 190.

[11] P. V. Degtyarenko et al., Phys. Rev. C50, R541-R545 (1994).

[12] GEANT User's Guide, CERN Program Library, Geneva, Switzerland (1994).

[13] C. Zeitnitz and T. A. Gabriel, "The GEANT - CALOR Interface User's Guide", (1995).

[14] W. C. Barber and W. D. George, Phys.Rev. 116, 1551 (1959).

[15] H. J. von Eyss and G. Luhrs, Z.Physik 262, 393 (1973).

[16] G. Bathow, E. Freytag and K. Tesch, Nuclear Physics B2, 669 (1967).

[17] R. G. Alsmiller, Jr., J. Barish, and R. L. Childs, "Skyshine at neutron energies S 400 MeV", Particle Accelerators, 11, 131 (1981).

[18] P. Degtyarenko and G.Stapleton, "Radiation Shielding for High Energy Electron Accelerators - Past and Future", presentation at the second workshop on Simulating Accelerator Radiation Environment (SARE2), 9-11 October 1995, CERN, Geneva, Switzerland.

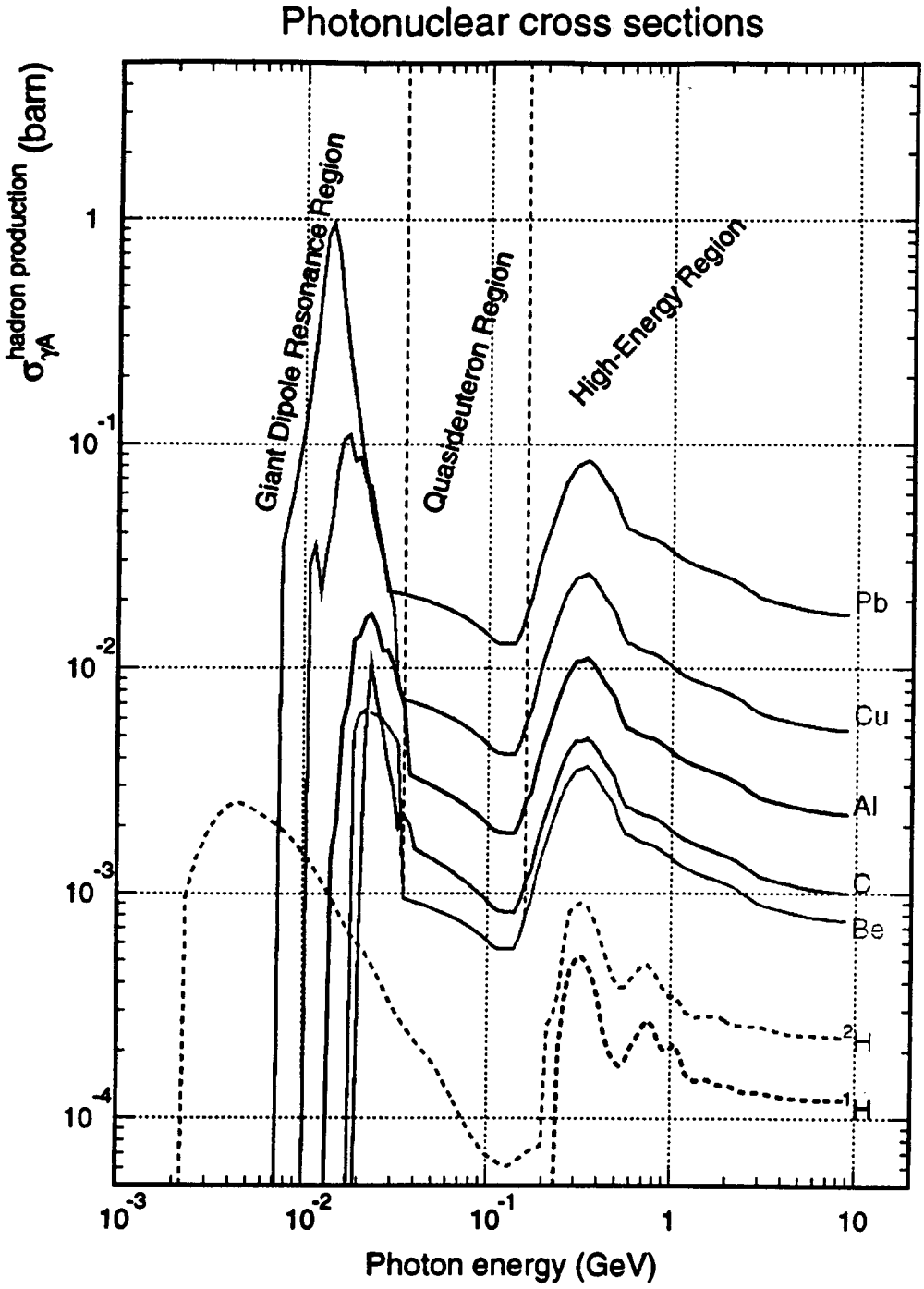

Figure 1

The γ-nucleus hadron production cross-section as a function of photon energy for the set of nuclei currently implemented in GDINR. The dashed lines show the approximate limits of low, medium, and high energy regions.

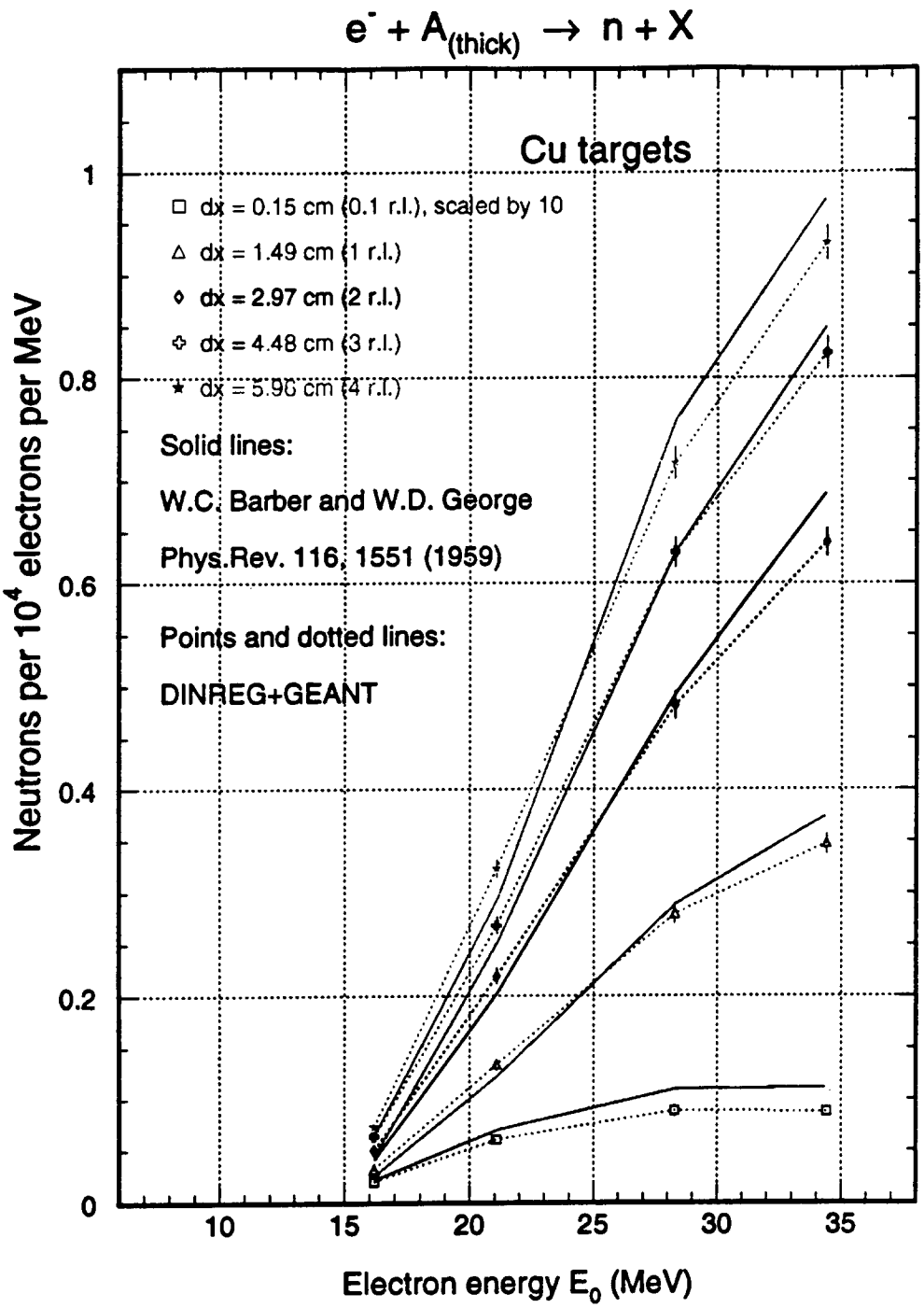

Figure 2

The comparison of DINREG + GEANT calculation (symbols and dotted lines) with the results of experiment by W. C. Barber and W. D. George [14] (solid lines) for determining of neutron yield out of the copper targets of different thicknesses (≈ 0.1, ≈ 1, ≈ 2, ≈ 3, ≈ 4 rad. lengths) bombarded by electrons with energies of 10 - 35 MeV. The errors shown are statistical from the Monte Carlo calculation. The experimental errors (~ 15%) are not shown.

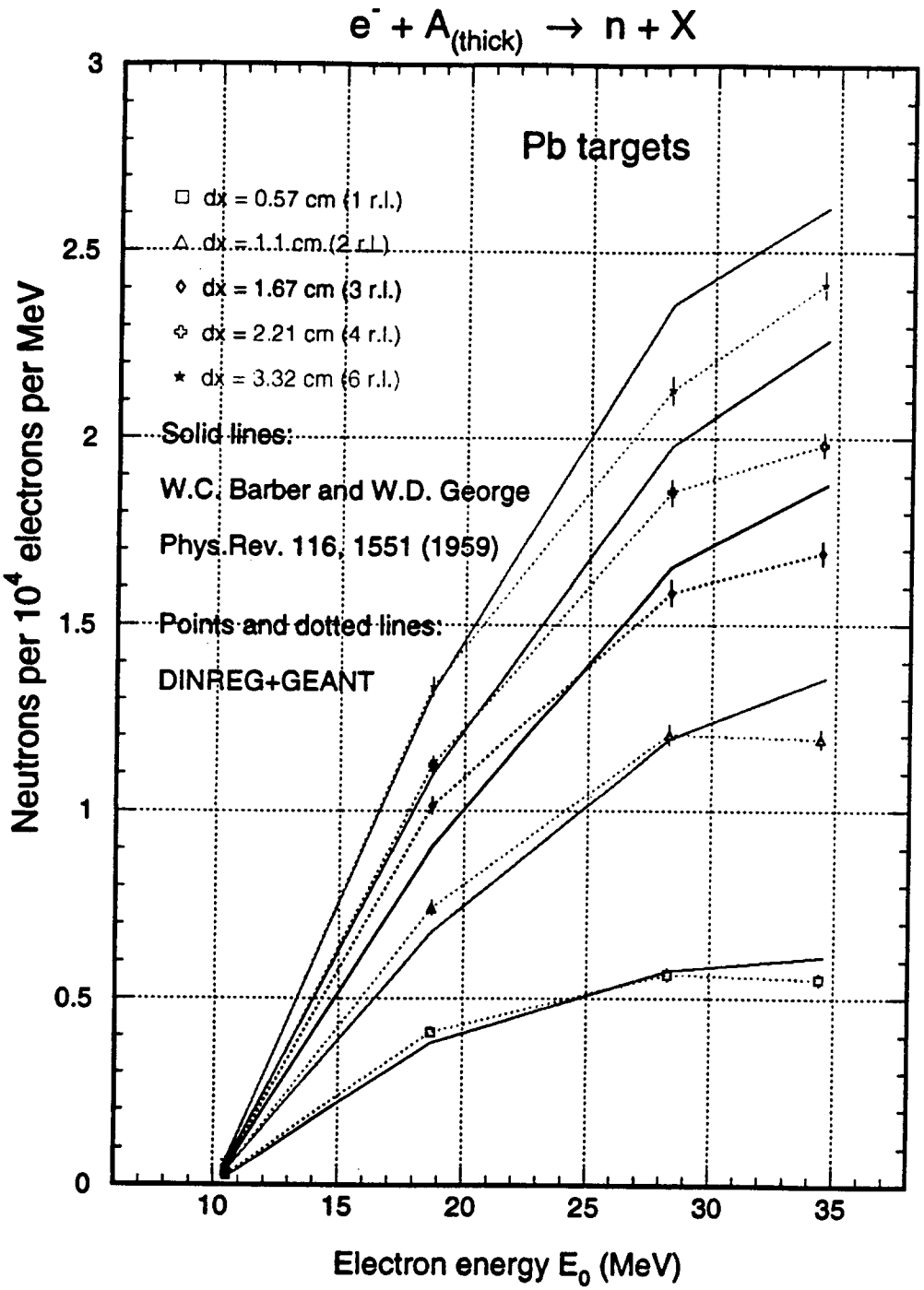

Figure 3

Same as Figure 2, but for the lead targets of different thicknesses.
($\approx 1, \approx 2, \approx 3, \approx 4, \approx 6$ rad. lengths).

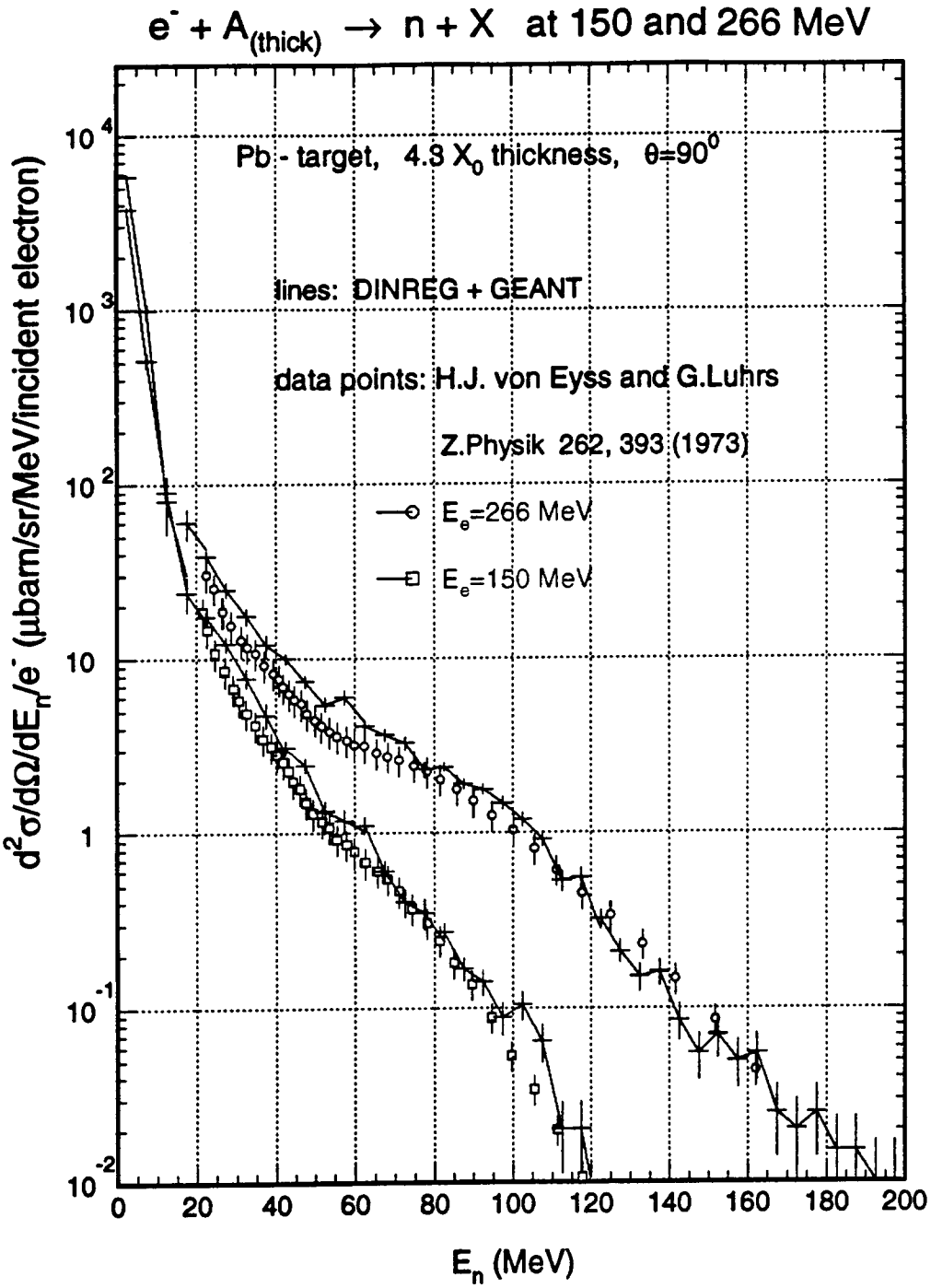

Figure 4

The comparison of DINREG + GEANT calculation (points with statistical errors shown connected by solid lines) with the results of experiment by H. J. von Eyss and G. Luhrs [15] (open dots with the estimated systematical errors shown). The neutron production cross-section at 90 degrees from thick (4.3 r.l.) lead target, normalised per electron incident, is shown as a function of the kinetic energy of the neutron. The two data sets correspond to initial electron energies 150 and 266 MeV.

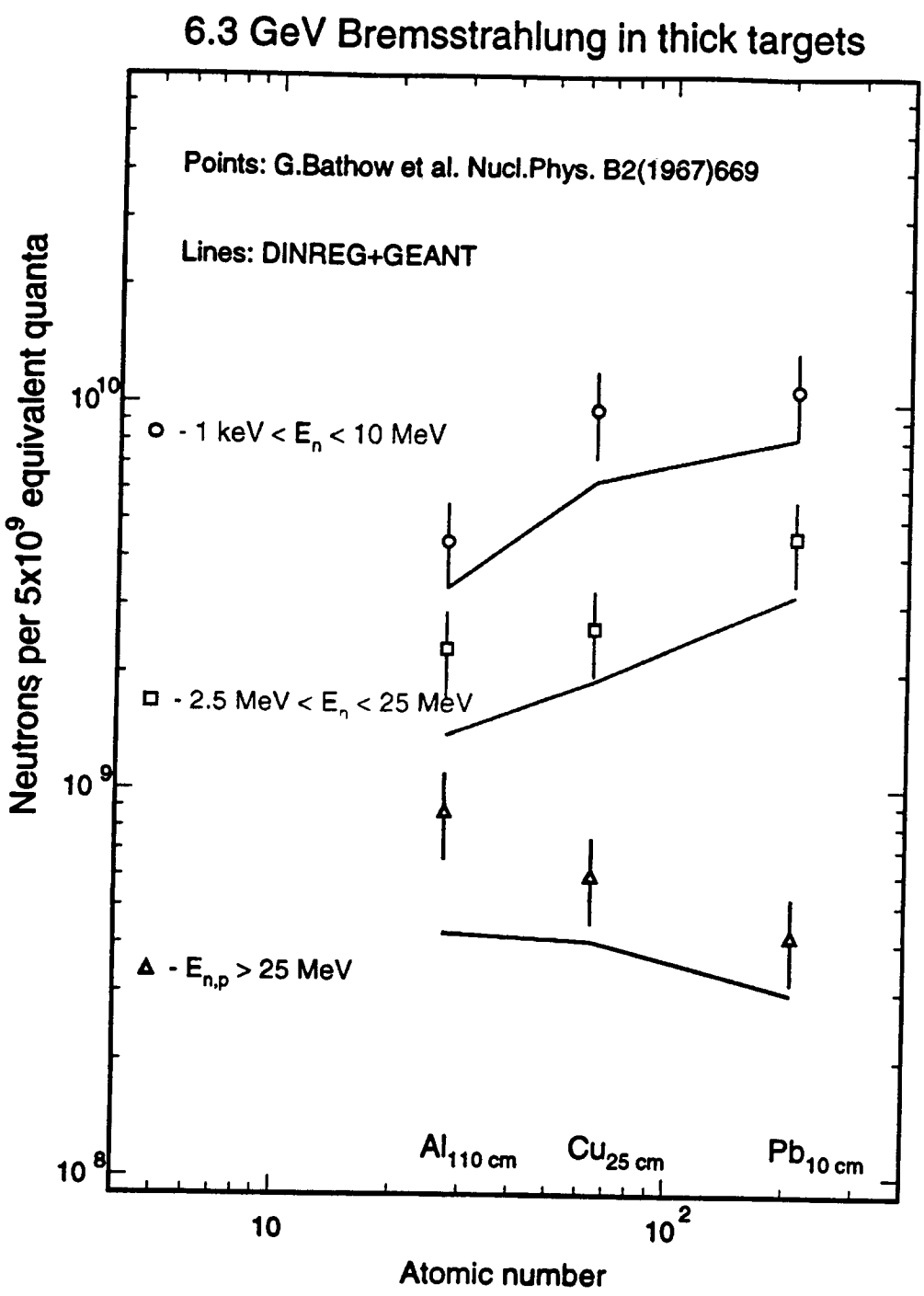

Figure 5

Neutron yields from the interactions of bremsstrahlung photons with thick aluminium (110 cm), copper (25 cm), and lead (10 cm) targets measured by G. Bathow et al. [16] at electron energy 6.3 GeV. Points with errors show the experimental data with estimated systematic error in the three regions of neutron kinetic energy: 1 keV - 10 MeV, 2.5 MeV - 25 MeV, and greater than 25 MeV (proton yields included for the last interval). The solid lines connect the points representing the results of DINREG + GEANT calculation performed for the same conditions.

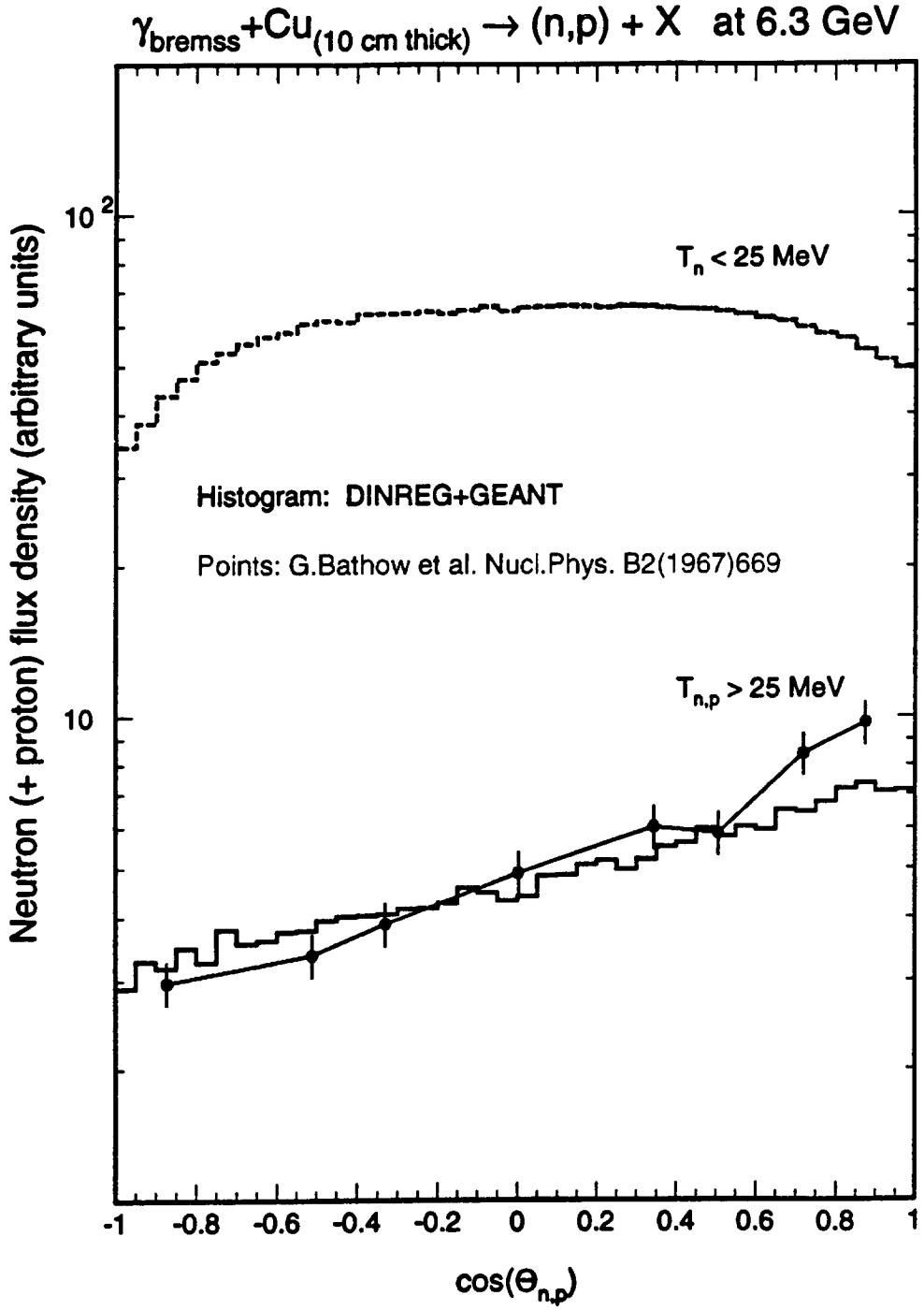

Figure 6

The angular dependence of the neutron and proton flux density measured in the interactions of bremsstrahlung photons with thick (10 cm) copper target at electron energy 6.3 GeV. Solid histogram shows neutrons and protons with kin. energy > 25 MeV generated by DINREG + GEANT, to be compared with the experimental points connected by solid line measured by G. Bathow et al. [16]. The dashed histogram shows the angular dependence of low energy neutrons generated in the same sample. The experimental and the generated angular dependencies are normalised arbitrarily.

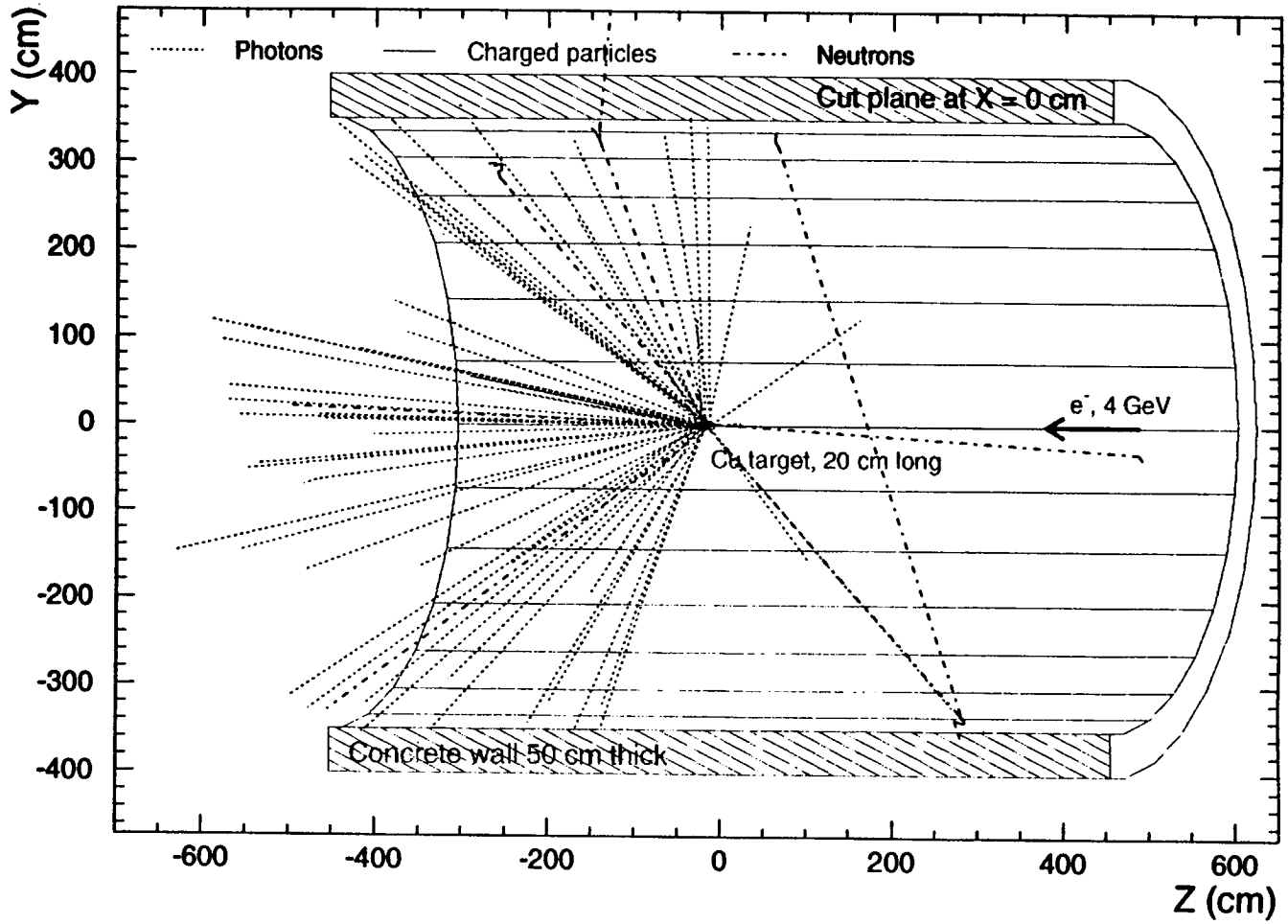

Figure 7

The illustration to the exercise in a shielding problem. An event of electron interaction in a thick (20 cm) copper target is shown, in a concrete tube of outer radius R = 4 m and thickness 50 cm. The lines indicate particles going out of the target: solid lines for charged particles, dotted lines for photons, dash-dotted lines for neutrons.

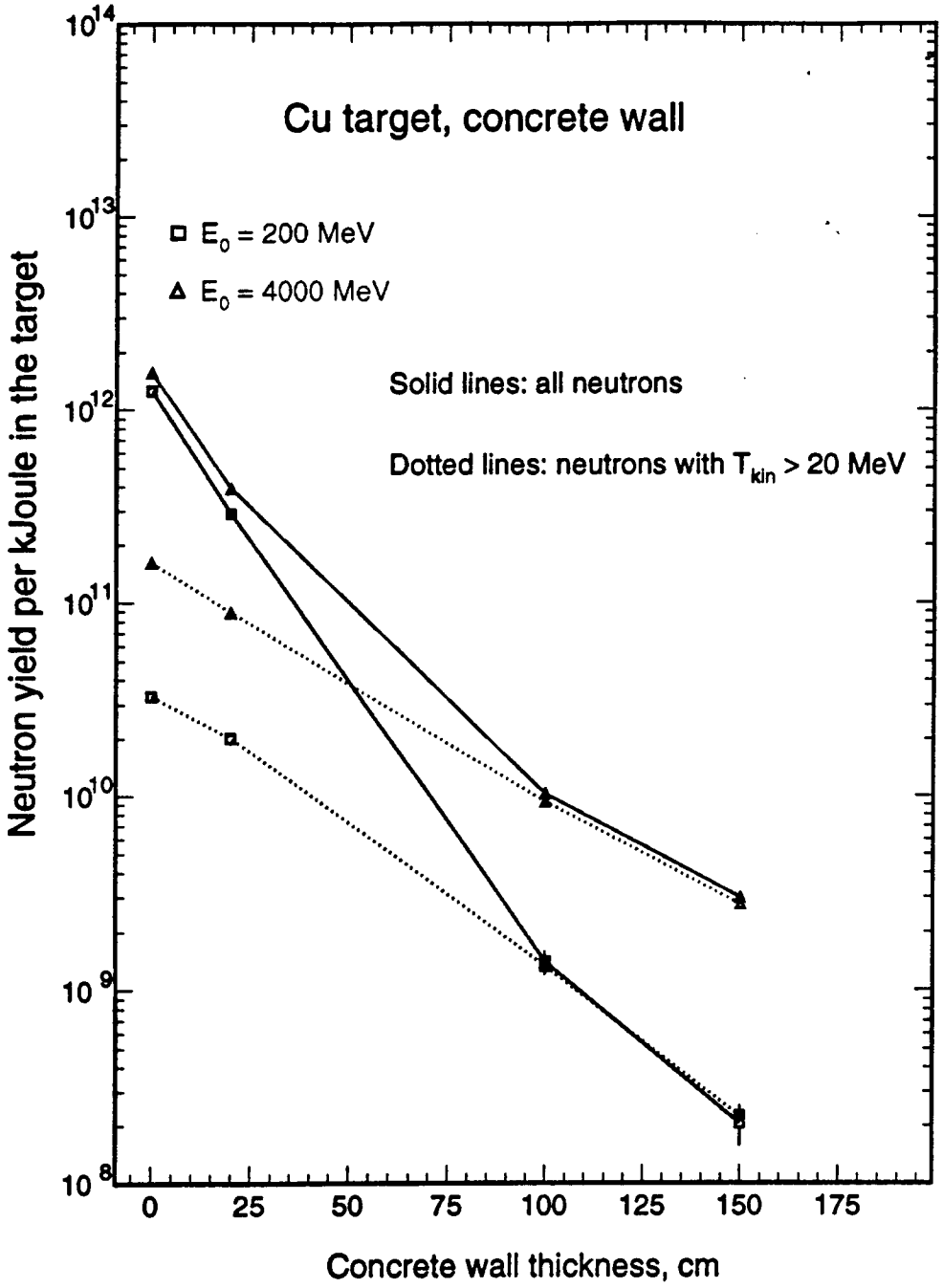

Figure 8

The neutron yield for the set-up shown in the Figure 7 calculated as the neutron flux at the outer surface of the concrete tube, at 90 degrees, in *(neutrons cm^{-2})*, multiplied by $4\pi R^2$. The yield dependence on the wall thickness is shown by the solid lines, for two initial electron energies, E_o = 200 MeV (open squares), and E_o = 4 GeV (open triangles). The data set shown by the dotted lines refers to the problem of calculating the yield of energetic (En > 20 MeV) neutrons and their attenuation in the shielding.

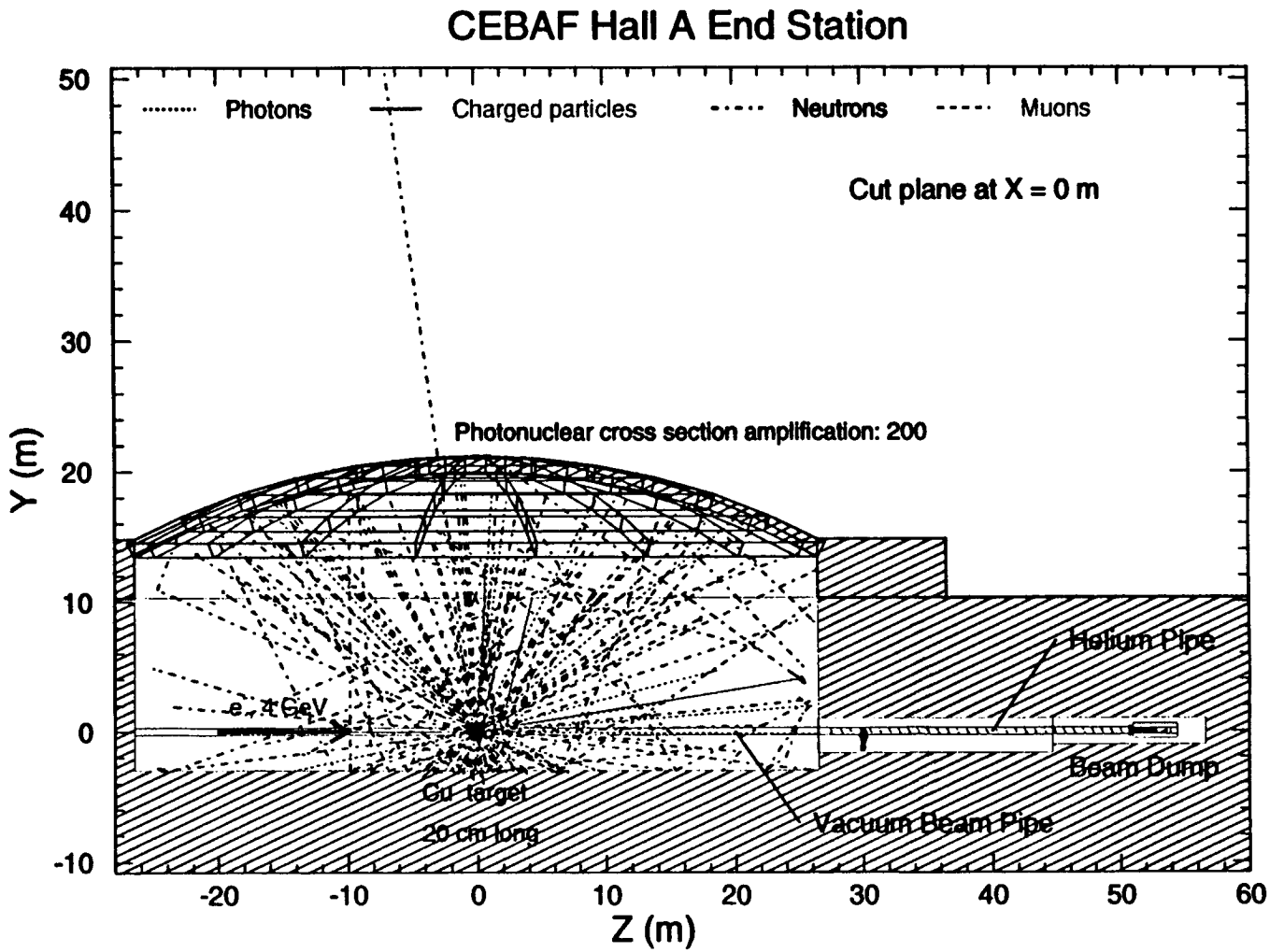

Figure 9

The illustration to the GEANT model of the CEBAF Hall A End Station. The Hall is a cylindrical volume inside the ground, with a ground ring surrounding it, and covered by a dome roof of 1.22 m thickness made of concrete. An event is shown of 4 GeV electron interaction in a thick (20 cm) copper target situated in the middle of the hall. The lines indicate particles going out of the target: solid lines for charged particles, dotted lines for photons, black dash–dotted lines for neutrons. The photonuclear hadron production cross-section is amplified by factor 200 to make the shielding calculations more effective.

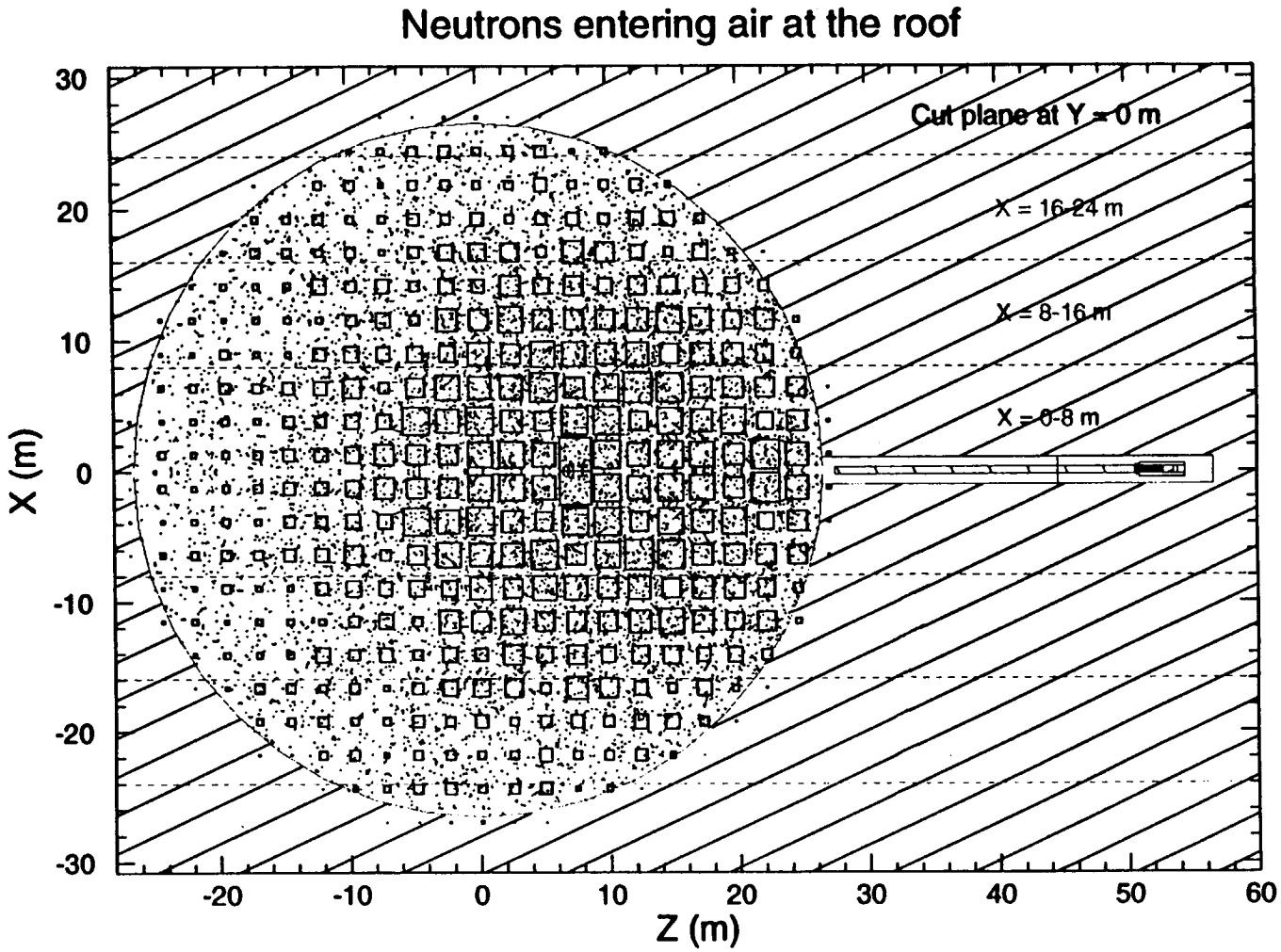

Figure 10

The figure shows the cut of the Hall A End Station at the Y=0 plane (horizontal plane, the beam axis being Z-co-ordinate). The positions of the neutrons exiting the roof are projected onto this plane and shown as dots. The squares superimposed onto this plot show the relative neutron flux intensity at the roof. Linear size of the squares is proportional to the neutron flux. The dashed lines indicate the regions on X-co-ordinate in which the Z-dependence of the neutron flux was studied.

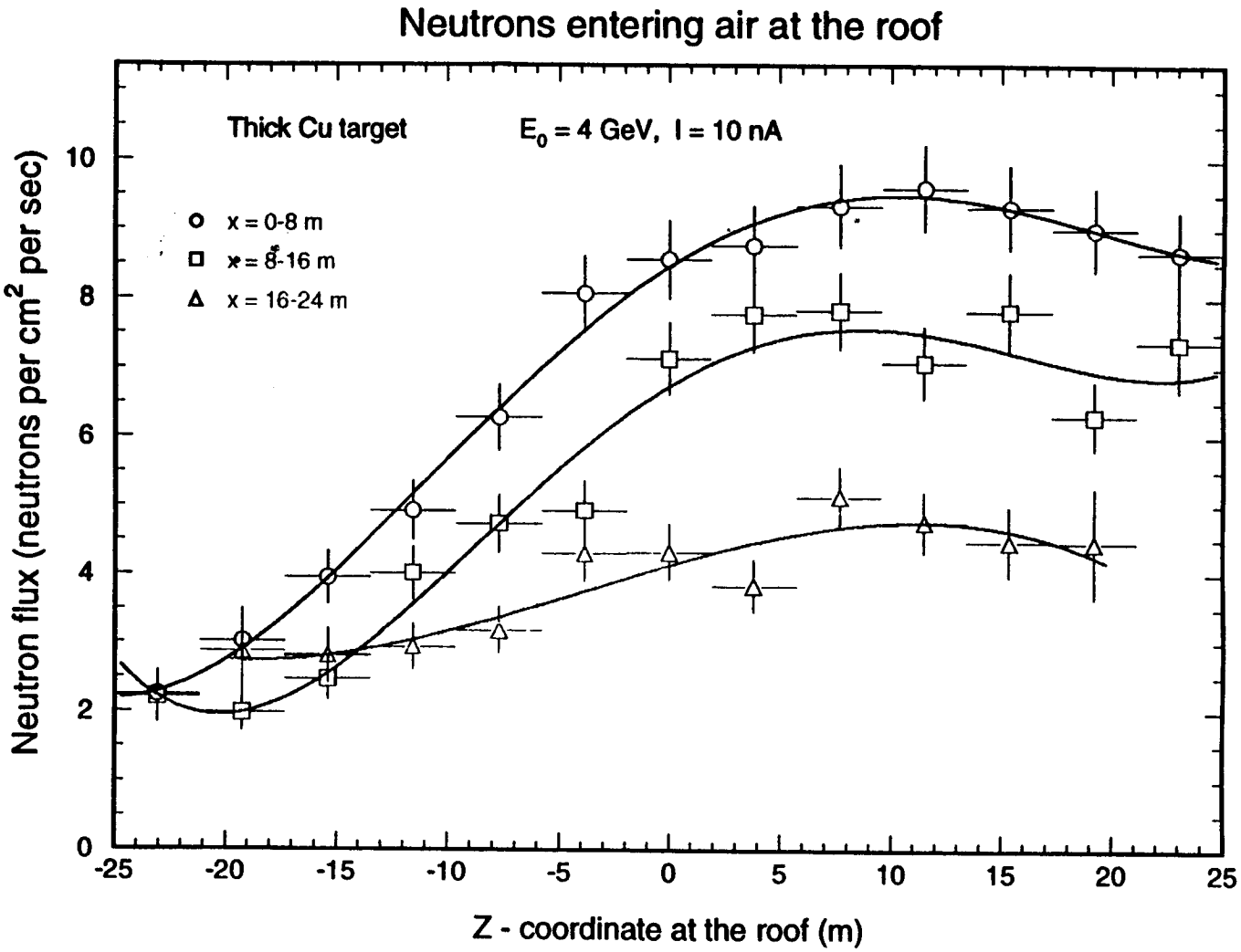

Figure 11

The Z-dependence of the neutron flux at the roof of the Hall A End Station shown in three intervals in X-co-ordinate: 0 - 8 m, the closest to the beam, 8 - 16 m, and 16 - 24 m, the farthest interval. The neutron flux is in *(neutrons cm^{-2} s^{-1})*, assuming 40 Watt, 4 GeV beam hitting thick copper target in the middle of the Hall.

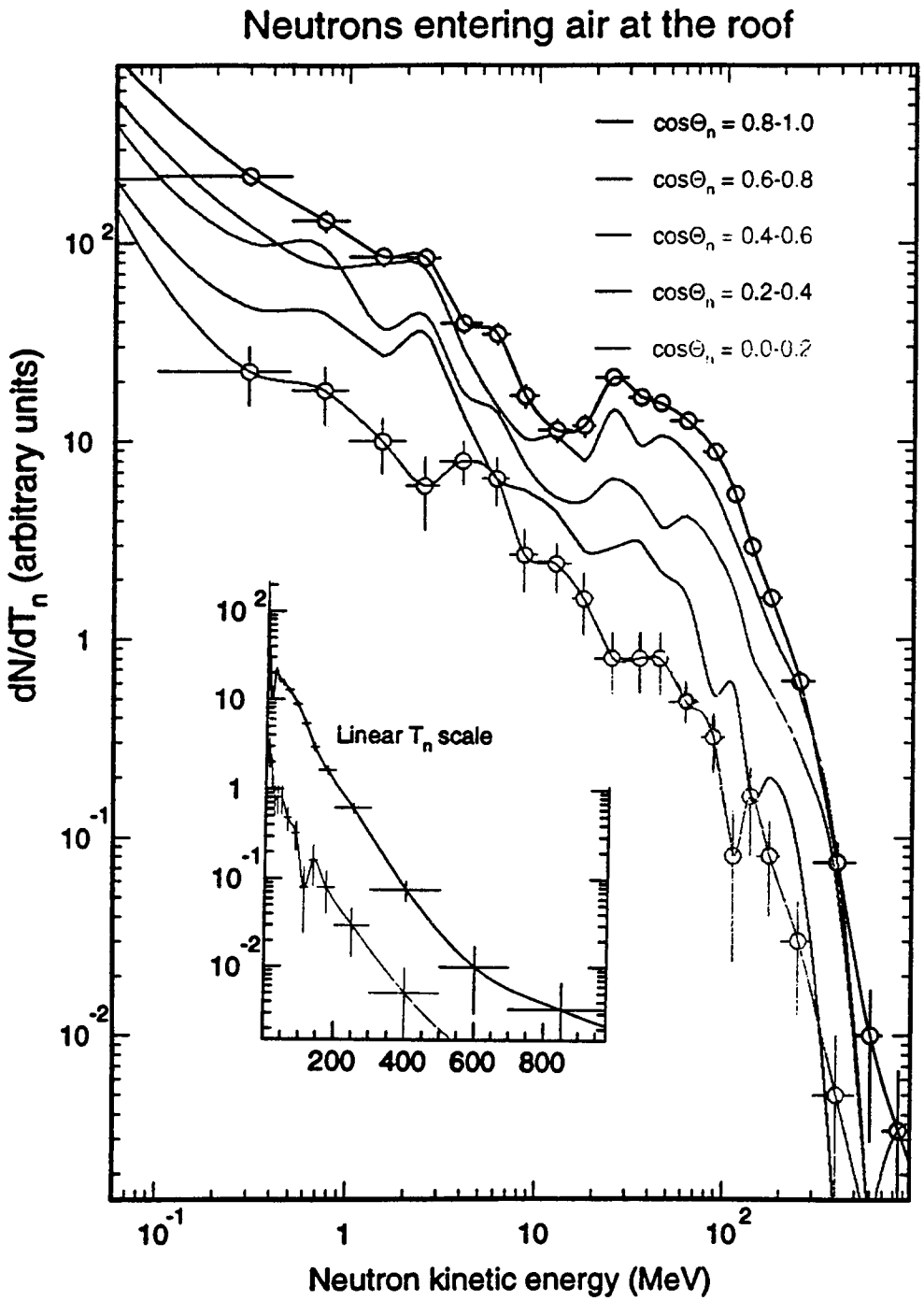

Figure 12

The neutron kinetic energy spectra are shown in 5 angular intervals from $O < cos.\theta < 0.2$ (neutrons exiting roof almost horizontally), to $0.8 < cos.\theta < 1$ (vertical interval). The double-logarithmic scale gives the opportunity to present the whole spectrum, while the insert with the linear energy scale shows the abundance of the very slow neutrons.

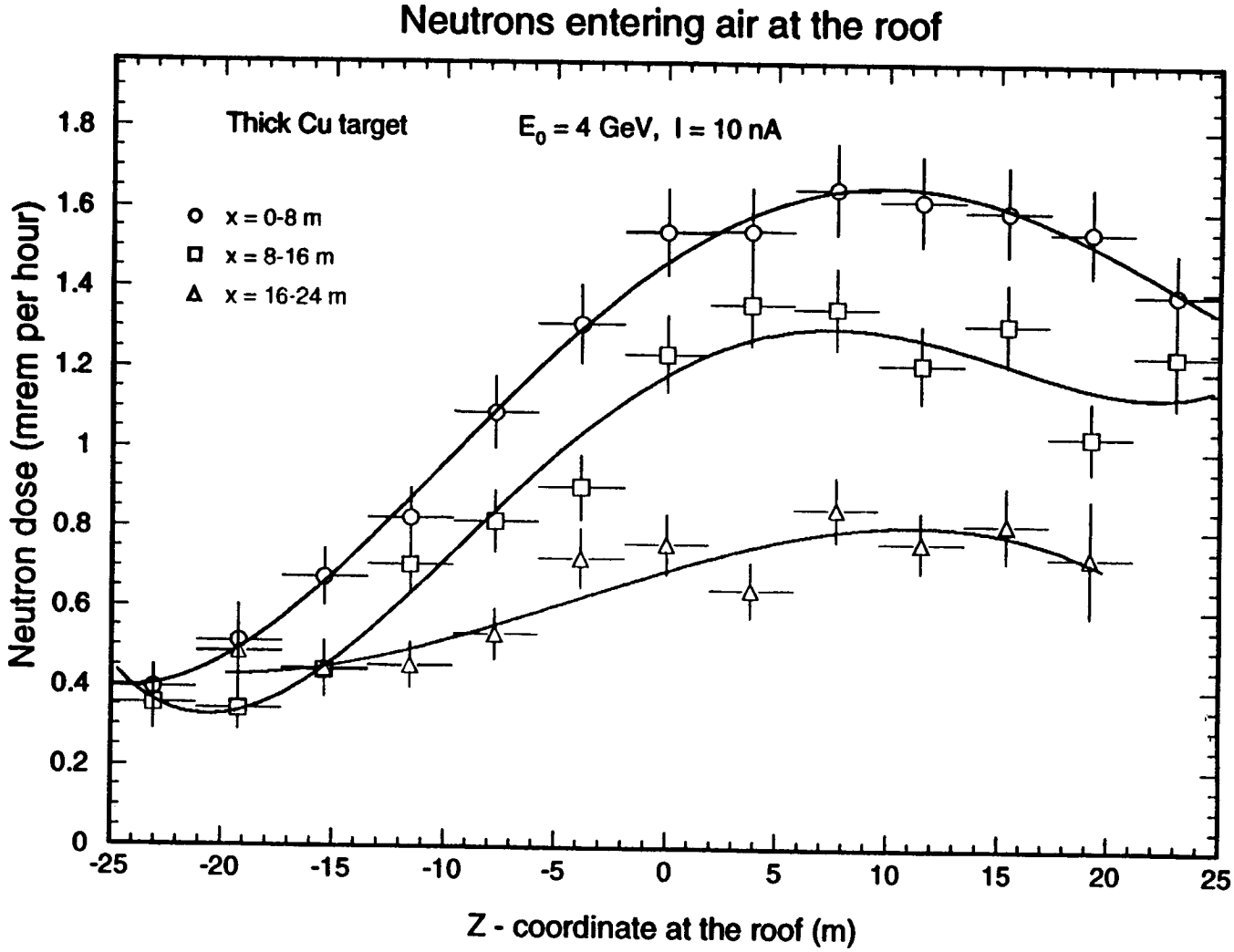

Figure 13

The same as 11, but shown is the Z-dependence of the equivalent dose at the roof of the Hall A End Station.

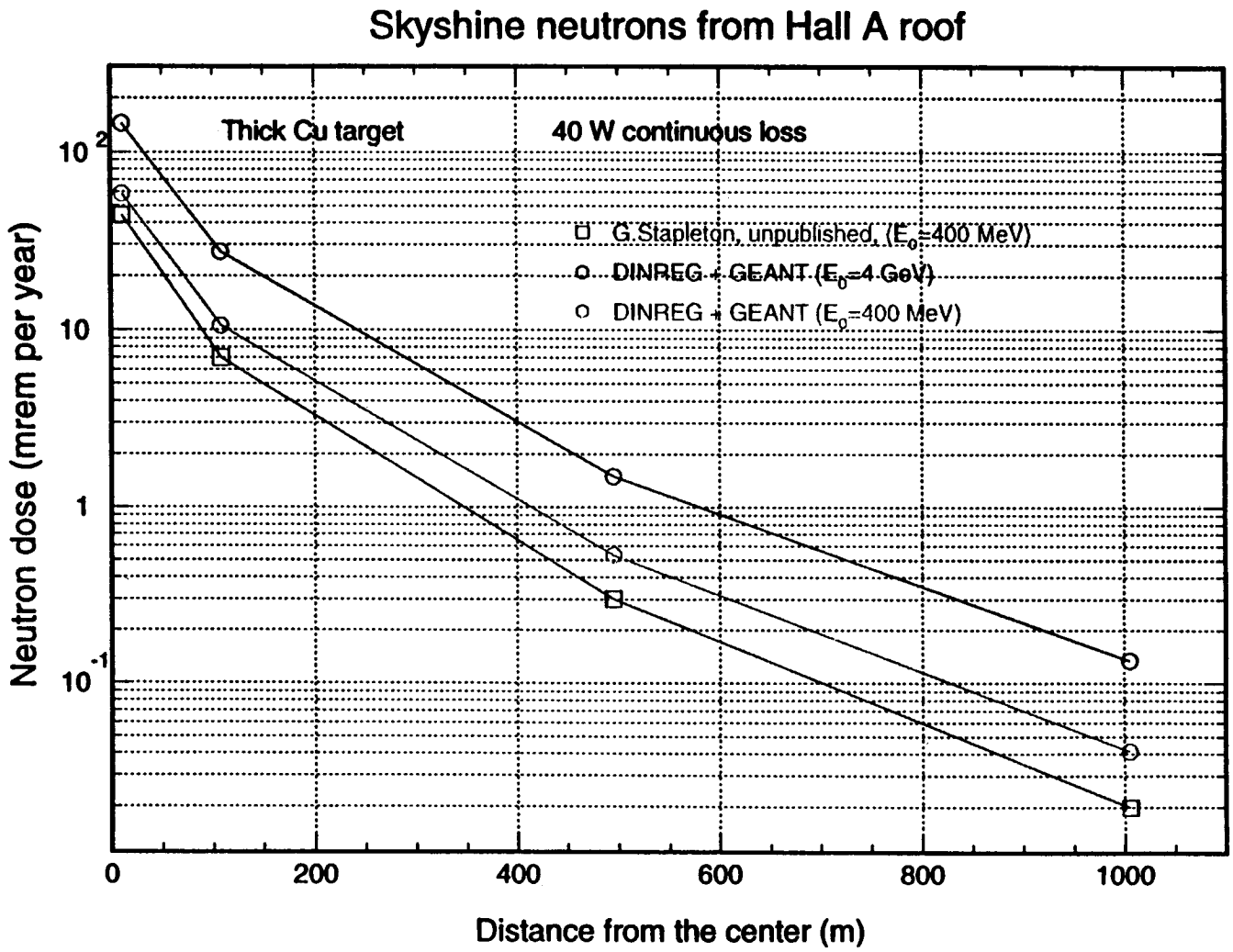

Figure 14

The dependence of the dose from the skyshine neutrons on the distance from the End Station is shown. 40 Watt of continuous beam loss is assumed. The neutron importance functions calculated by R. G. Alsmiller et al. [17] were used to convert the neutron flux and angular energy distribution of the neutrons exiting the roof, calculated by DINREG + GEANT, into the surface dose. The data shown are previous analytical calculations based on neutron spectra from 400 MeV electrons bombarding thick copper target (squares), and DINREG + GEANT calculations at 400 MeV and 4 GeV electron beams.

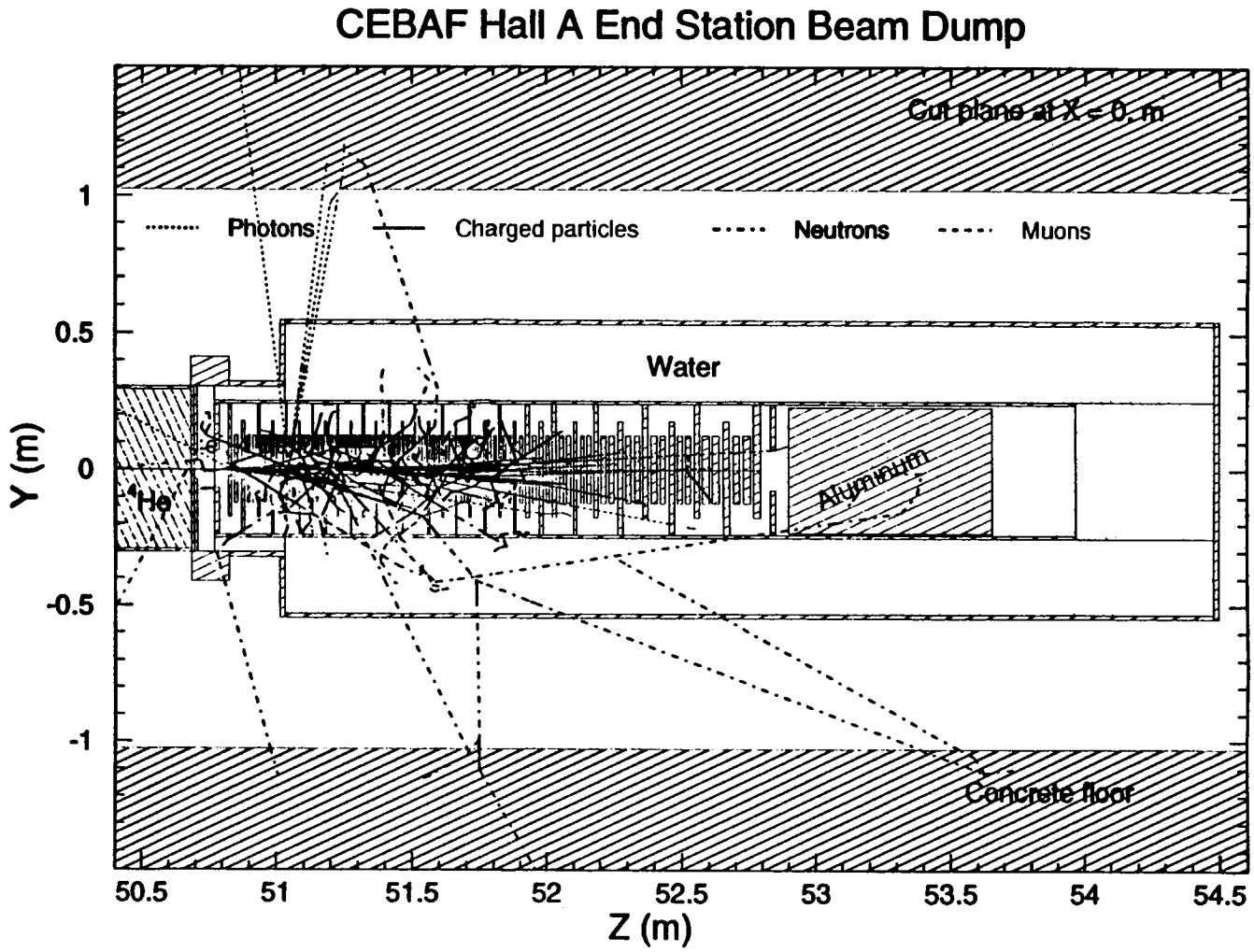

Figure 15

The illustration to the GEANT model of the CEBAF Hall A End Station Beam Dump. The notation is the same as in Figure 9. The beam dump has a complicated geometry of many aluminium layers of different thickness, and cooling water between them. GEANT produces electromagnetic cascade from 4 GeV electron in the beam dump, and DINREG is called to produce 200 times amplified hadron component of the shower.

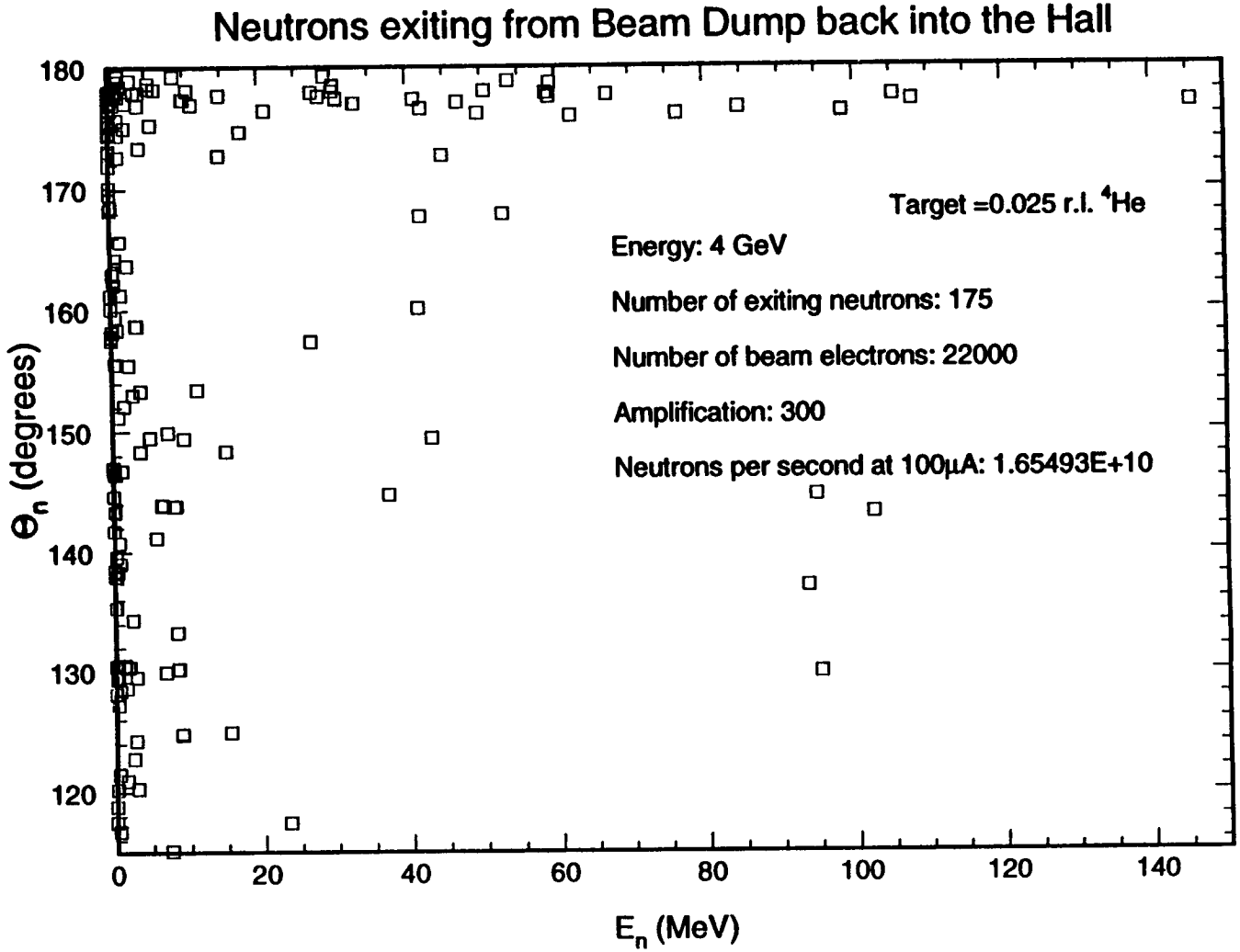

Figure 16

The angular - momentum distribution of neutrons entering Hall A backward from the Beam Dump as calculated by DINREG + GEANT.

THE PHOTONEUTRON YIELD PREDICTIONS BY PICA AND COMPARISON WITH THE MEASUREMENTS [1]

P. K. Job
Argonne National Laboratory, U.S.A.

T. A. Gabriel
Oak Ridge National Laboratory, U.S.A.

Introduction

The photoneutron yields at higher photon energies have become very important since the advent of high energy electron accelerators [1,2]. Bremsstrahlung is produced when the particle beam interacts with the storage-ring components or residual-gas molecules in the storage-ring vacuum. Bremsstrahlung thus produced interacts with the high-Z materials in the beamline like the beam dumps and collimators to produce photoneutrons. There are three modes of neutron production by bremsstrahlung. At low energies (<25 MeV), photons are absorbed by the dipole interaction and the compound nucleus thus formed decays emitting protons and neutrons and other heavier particles. At higher energies (225 MeV), photon interacts with the nucleus through absorption on a quasi-deuteron, which subsequently decays producing a neutron and proton pair which can interact with the rest of the nucleus. At still higher energies the photopion production becomes possible and competes with the quasi-deuteron process. In this paper we have calculated the photoneutron yield from a thick copper target using the photonuclear interaction code PICA [3]. Using this as the neutron source, we have calculated the dose rates through heavy concrete and compared it with the measurements [4] made at the Advanced Photon Source at Argonne National Laboratory.

PICA photonuclear interaction code

PICA calculates the results of nuclear reaction caused by the collision of the photons with the nuclei [5]. PICA can do these calculations for incident monoenergetic photons as well as for bremsstrahlung spectra. For the dipole interaction the available cross-sections are used [6]. The higher energy interaction cross-sections are derived from the quasi-deuteron model of Levinger [7]. This is the photoabsorption by a neutron- proton pair. For photons above the pion threshold photon -pion production on nucleons is allowed to compete with the quasi-deuteron absorption process. The effect of the secondary nucleon- nucleus and pion-nucleus interactions following the photon absorption is calculated by the intranuclear cascade concept [8]. Each particle involved in the collision is traced through the nucleus using the appropriate particle-particle cross-sections until the particle escapes or is captured by the nucleus. In all parts of the calculation, the fermi momentum of the struck particle,

[1] Work supported in part by U.S. Department of Energy, Contracts W-31-109-ENG-38 (Argonne National Laboratory), and DE-AC05-840R21400 (Oak Ridge National Laboratory).

the exclusion principle and the non-uniform density distribution of the nucleus are taken into account. After the cascade process is complete, the nucleus is in an excited state and the excitation energy is dissipated through particle emission. The de -excitation of the nucleus is handled by the evaporation model [8].

Geometry used for the simulation

Figures 1 and 2 give the schematic and the simulated geometry for the PICA calculations. The particle beam during injection at the Advanced Photon Source can be partially or fully lost in one of the transition regions between the storage ring vacuum chamber and the insertion device straight section. The transition piece is a copper interface between the two vacuum chambers. The 56-cm thick high density concrete ratchet wall is located 164 cm from the transition piece. The photon track lengths from the electromagnetic shower, when the injected particle beam is fully lost on the transition piece, were calculated by EGS4 [9]. The neutron yield from these photon track lengths was then calculated by PICA. These neutrons were transported by the one dimensional ANISN code using the 400 MeV HILO86 cross-section library to estimate the photon and neutron dose rates outside the ratchet wall. The results are given in Table 1.

Table 1
Dose rates due to beam loss at the insertion device transition region during injection into the storage ring.

	CHARGE [a] / pulse	NO. OF e^- / sec	DOSE RATES (mrem/h)	
			NEUTRON	GAMMA
Expt. 1	1.1 nC	6.87x 109	26.4	1.5
Expt. 2	1.1 nC	6.87x 109	39.6	1.1
PICA/ANISN	1.1 nC	6.87x 109	55.0	1.0

[a] Injection rate is 1 Hz.

Measurements

Radiation survey measurements were conducted outside the ratchet wall, while injected beam was being lost at one of the transition pieces. The primary objective of this was to study two potential beam loss scenarios, although some other measurements were also accomplished. First of all one of the corrector magnets adjacent to the transition piece was used at full strength to deflect the particle beam into the transition piece. Secondly, the beam was directed onto the closed gate valve which is just upstream of the transition piece. In both cases data was collected for 10 minutes while the charge entering the storage ring through the beamline transfer section was integrated. Prior to taking the data, the injection was tuned by the operating personnel to insure minimum loss between the booster transport system current monitor and the intended loss point.

The radiation survey instruments used for these measurements were a Victoreen 450P ionisation chamber for gamma radiation and an Eberline ASP -1 electronics package with a HP 2080 (Albatross)

placed at that location and at three other locations along the ratchet wall and a 5 minute count was taken in the integral mode. The gamma dose rate at the maximum dose location and the neutron dose rate at 90° from the transition piece are given in Table I, along with the PICA predictions.

Results and discussion

The PICA simulation shows reasonable agreement with the measurements. The possible errors in this study are the beam loss scenario and the response of the neutron detectors to the high energy neutron radiation. The photoneutron yield from the transition piece depends on the shower development in the transition piece. Depending on the shower containment, this quantity and the resultant dose may vary at the most by a factor of three. For the present calculations we have assumed that only one-third of the electromagnetic shower is contained in the transition piece. The gamma dose rates outside the ratchet wall are negligible. This is attributed to the incomplete development of the electromagnetic shower in the copper transition piece (which is a maximum of 4 cm thick) so that much of the radiation is forward peaked and contributes to a resultant shower downstream. This also explains slightly elevated readings of the gamma dose rates at approximately 450 cm downstream of the transition piece on the ratchet wall. When incident on the ratchet wall, the shower encounters a much larger effective concrete thickness because of the shallow incidence angle. It can be seen from figure 1 that the slant thickness of concrete, downstream of the transition piece, is much large compared to the real thickness of 56 cm. The increased gamma attenuation through the slant thickness of concrete accounts for low gamma radiation levels outside the ratchet wall.

References

[1] W. P. Swanson, "Radiological Safety Aspects of the Operation of Electron Linear Accelerators", IAEA Technical Series No. 188 (1979).

[2] H. J. Moe, "Advanced Photon Source: Radiological Design Considerations" ANL- APS-LS-141 (1991).

[3] T. A. Gabriel et al., "PICA, An Intranuclear Cascade Calculation for High Energy Photon-Induced Nuclear Reactions", ORNL- 4687 (1971).

[4] P.K. Job and H. J. Moe, ANL- APS- LS 243 (1995).

[5] T. A. Gabriel and R. G. Alsmiller, "Photoneutron Disintegration at High Energies", ORNL-TM-2481 (1969).

[6] B. L. Berman, "Atlas of Photoneutron Cross Sections", UCRL 78482 (1976).

[7] J. S. Levinger, Phy. Rev., 84 (1951) 43.

[8] H. W. Bertini, "Intranuclear Cascade Calculations of the Secondary Nucleon Spectra from Nucleon-Nucleus Interactions", Phy. Rev. 188 (1969).

[9] W.R. Nelson et al., "EGS4 Code System", SLAC 265 (1985).

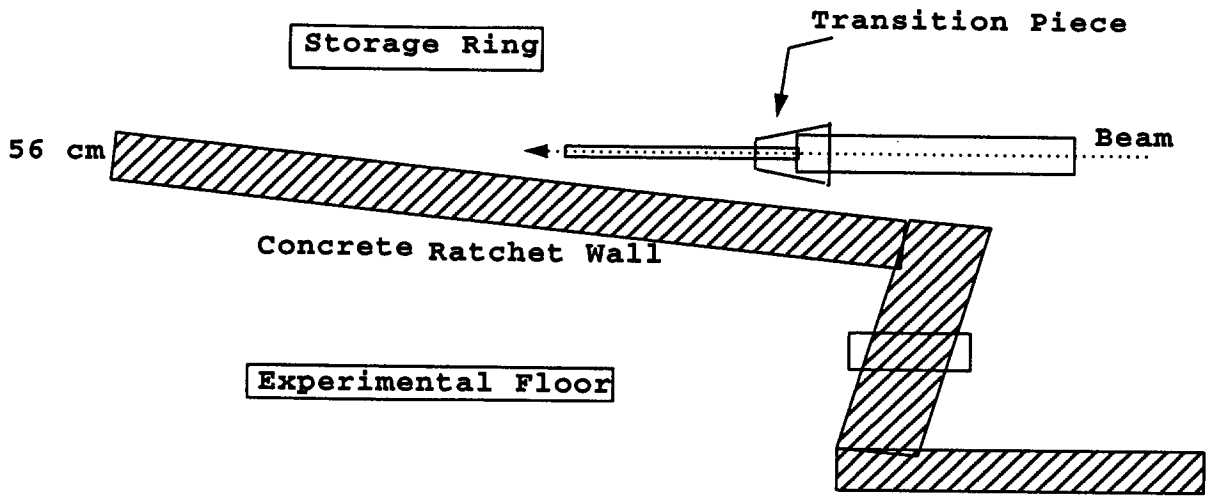

Figure 1 ***Beam loss configuration***

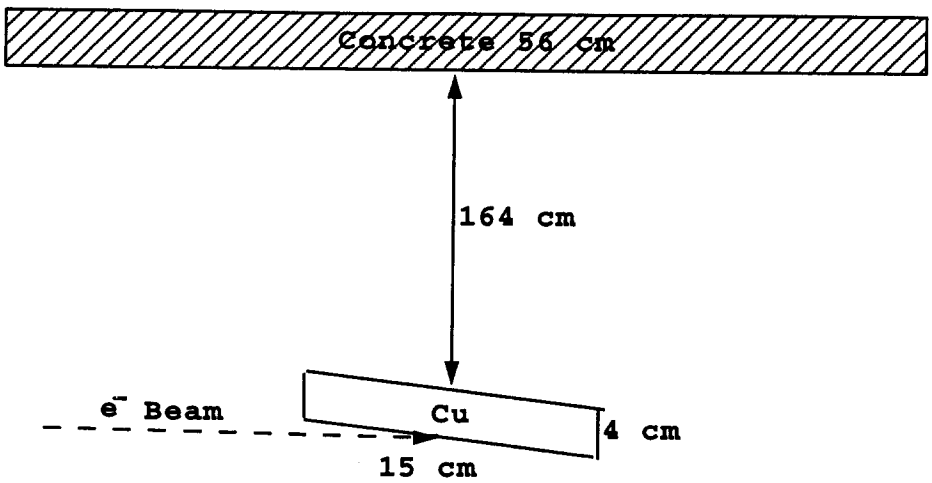

Figure 2 ***Geometry used for PICA simulation***

Session II

SHIELDING – EXPERIMENTAL BENCHMARKS, SOURCE TERMS AND ATTENUATION LENGTHS, EMPIRICAL METHODS, SHIELDING POLICY

CHAIR

Herbert DINTER

CO-CHAIR

Laurie WATERS

DOUBLE DIFFERENTIAL DISTRIBUTIONS, ATTENUATION LENGTHS AND SOURCE TERMS FOR PROTON ACCELERATOR SHIELDING

S. Agosteo[1], A. Fassò[2], A. Ferrari[3], P.R. Sala[3], M. Silari[4] and P. Tabarelli de Fatis[5]

(1) Politecnico di Milano, Dipartimento di Ingegneria Nucleare, Via Ponzio 34/3, 20133 Milano, Italy
(2) CERN, 1211 Geneve 23, Switzerland
(3) Istituto Nazionale di Fisica Nucleare, Sezione di Milano, Via Celoria 16, 20133 Milano, Italy
(4) Consiglio Nazionale delle Ricerche, Istituto Tecnologie Biomediche Avanzate, Via Ampère 56, 20131 Milano, Italy
(5) Fondazione TERA, Via Puccini 11, 28100 Novara, Italy

Abstract

Double differential distributions of neutrons produced by 100, 150, 200, 250 and 400 MeV protons stopped in thick iron and soft tissue targets were calculated by two Monte Carlo codes, FLUKA and LCS, from 0° (forward shielding) to 180°. The results are compared with calculated and experimental data available in the literature. The attenuation in ordinary concrete of the dose equivalent due to neutrons and other particles was calculated. The contribution due to photons and protons was found to range from a few percent up to 50 % of the total dose equivalent. Source terms and attenuation lengths are given as a function of energy and emission angle.

Introduction

Proton accelerators in the intermediate energy range (a few hundred MeV), mainly used in nuclear physics until a few years ago, are now finding an increasing number of applications in radiation therapy of cancer, in industry and in various domains of research. A number of facilities are being built or planned worldwide [1-4]. Machines in this energy range are also employed as injectors to accelerators of energy in the GeV region and above.

Shielding of these accelerators requires particular attention, either due to the high intensities required for industrial or research applications or, in the case of radiation therapy, because they need to be installed in a hospital environment, often located in a highly populated area. The radiation field dictating the shielding requirements is mainly due to the secondary neutrons produced by the interaction of the proton beam with the structures of the accelerator, of the beam transfer lines and - in the case of medical machines - of the beam delivery system used to irradiate the patient (such as collimators), and with the patient himself (where the remaining beam is ultimately lost).

Shielding data in this energy range are not abundant in the literature and are usually limited to specific conditions, geometries and energy values [5]. To overcome this lack of information, the attenuation through ordinary concrete of the dose equivalent produced by 100, 150, 200, 250 and 400 MeV protons stopped in thick iron and soft tissue targets were calculated by two Monte Carlo codes, FLUKA and LCS, from 0° (forward shielding) to 180°. Backward angles were included to account for special conditions found in modern radiation therapy facilities, where the beam extracted from the accelerator can be rotated 360° around the patient by means of a large mechanical structure (isocentric gantry). The iron target reproduces the structural materials of the accelerator and beam transfer lines (mainly the magnets), while tissue represents the patient. The results of the calculations were fitted by the classical two-parameter formula. The source terms and attenuation lengths derived as a function of proton energy and emission angle can be used to design shielding of proton accelerators in any realistic geometry. The results are compared with calculated and experimental data available in the literature. The calculated dose equivalent behind the shield includes contribution from both neutrons and their secondaries produced in the concrete. The complete numerical data can be found in ref. [6].

Neutron source: energy and angular distributions

The energy and angular distributions of neutrons produced by a monoenergetic and monodirectional proton beam ("pencil beam") impinging on an iron or soft tissue target, were calculated by the LCS [7] and FLUKA [8] Monte Carlo codes. The target is cylindrical, with the axis coincident with the incoming beam direction, and is slightly thicker than the proton range in the material at the given energy. For soft tissue, the elemental composition of ICRU 33 [9] has been adopted. A comparison of double differential distributions predicted by FLUKA at a proton energy of 256 MeV with experimental data [10] is shown in Fig. 1. A comparison of the same experimental data with LCS results has already been published by Prael et al. [11]. The two codes agree better in the forward direction [6] than at large angles. This is probably due to the lack of the pre-equilibrium module in the LCS version used.

A preliminary set of simulations was also carried out to assess the target radius which would ensure the most conservative combination between neutron yield and spectrum hardness. As a general rule, the larger is the transverse dimension of the target, the higher is the yield and the lower is the average energy of the distribution [6]. Differences at low energy are of no relevance for shielding. As the high energy neutron yield varies little with target size, the radius of the target was chosen

according to practical considerations (e.g., typical dimensions of machine components).

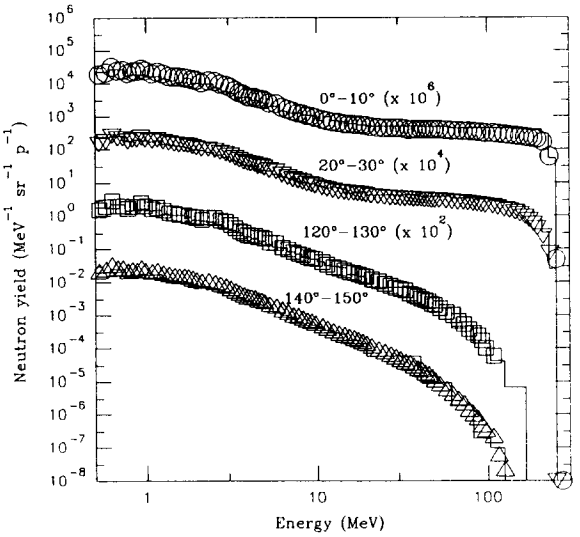

Fig. 1 Comparison between FLUKA double differential neutron distributions and experimental data for 256 MeV protons striking a thick iron target. O 7.5°, ∇ 30°, □ 130°, Δ 150°.

Figs. 2-11 show the double differential distributions produced by 100-400 MeV protons on iron and soft tissue, calculated with FLUKA. The statistical errors associated to the distributions are below 15 % in the angular interval 0°-90° and below 40 % in the interval 90°-180°. Table 1 lists the integrated neutron yields as calculated with FLUKA (100-400 MeV).

Neutron attenuation in concrete

The neutron production and attenuation in ordinary concrete (type TSF 5.5) were computed with FLUKA for slab thicknesses from 0 to 600 cm and with LCS for thicknesses from 0 to 180 cm. Variance reduction techniques are not available in the LCS code above 20 MeV; calculations for larger shield thicknesses could therefore not be performed because of insufficient statistics. The results obtained with the two codes for slab thicknesses up to 180 cm and 90° are in agreement, in spite of the differences in the emission at large angles [6].

Monte Carlo calculations were made from 0° to 180° with FLUKA and from 0° to 90° with LCS, both in spherical and slab geometries. The inner radius of the sphere was sufficiently large to ensure that effects related to curvature are negligible. Results obtained in the two geometries agree within the statistical errors. The origin was in the centre of the target. The dose equivalent due to the neutrons transmitted through the shield was calculated by folding the fluence with appropriate fluence to ambient dose equivalent conversion factors. Since up-to-date conversion factors for neutrons up to 400 MeV, "officially" recommended, are not yet available, three sets of coefficients in common use were employed [13-15]. Conversion factors for photons were taken from ref. [16].

Amongst the variance reduction techniques available in FLUKA, use was made of "geometry splitting" and "russian roulette", adjusting the importances so as to maintain the number of particles approximately constant with increasing concrete thickness. Each data point is the average of the

results of a number of independent simulations. The total number of protons per data point was at least 500'000 with FLUKA and 200'000 with LCS.

The simulations with FLUKA were made separately for several slab thicknesses from 10 cm to 600 cm. The LCS simulations were carried out for slab thicknesses from 2 cm to 180 cm for the iron target. No calculations were made with LCS for the tissue target. The transmission curves at four angles (forward, intermediate, lateral and backward) are shown in Figs. 12-17 for 100, 200 and 400 MeV protons on iron and tissue.

Shielding parameters

The contributions to the total dose equivalent come mainly from neutrons, but photons are also not negligible and can give a substantial contribution at backward angles at the lowest energies. The proton component has some relevance only at the highest energy (see Table 2 for both contributions). The values of the calculated total dose equivalent were fitted with an exponential function:

$$H(E_p,\theta,d/\lambda_\theta) = \frac{H_0(E_p,\theta)}{r^2}\exp\left[-\frac{d}{\lambda_\theta\cos\theta}\right]$$

in which H is the dose equivalent beyond the shield, H_0 is the source term along the direction θ with respect to the beam, r is the distance between the radiation source (the target stopping the protons) and the point where the dose equivalent is scored, d is the shielding thickness and λ_θ is the attenuation length in the material in the direction θ.

The source terms H_0 (Sv m^2 proton^{-1}) and the attenuation lengths λ (g cm^{-2}) are given in ref. [6] for the various energies and targets. The deviations of the Monte Carlo data from the best fit are within 15 % in all cases. Here λ has been obtained by fitting the data for concrete thicknesses above a certain value (0.5 m at 100 MeV to larger than 2 m at 400 MeV), where the attenuation is roughly exponential. For lower shielding thickness the transmission curve is no longer strictly exponential. This is because the neutron spectrum has not reached equilibrium in the material. Including data at lower thicknesses in the fit, results in an overestimate of λ and an underestimate of H_0. The estimated attenuation length decreases with increasing the minimum shielding thickness included in the fit and reaches a value approximately constant only at a depth in the material which depends on the incoming proton energy. This behaviour for the iron target is shown in Fig. 18 two proton energies (200 and 400 MeV), where the present results are also compared with those from ref. [17]. Fig. 19 shows the same for the tissue target. Figs. 20 and 21 show, for three energies and the iron target, the behaviour of H_0 and λ as a function of angle θ. The "jump" observed in the source term at 100 MeV and 200 MeV (Fig. 20) is related to the variation in the attenuation length at the corresponding angles. Figs. 22 and 23 show H_0 and λ versus proton energy at forward, lateral and backward angles θ, for the iron target.

The values of H_0 and λ for the iron target were compared with calculated and experimental data available in the literature [18-24] and listed in Table 3. No literature data are available for a comparison for the tissue target. Data from ref. [18] are results of Monte Carlo calculations with the FLUKA code, for a slightly different type of concrete. The source terms agree within 10% with the values calculated in the present work, while the attenuation lengths are within 6%. Data from ref. [19] are Monte Carlo calculations performed with the High Energy Transport Code (HETC-DO) [25]. The

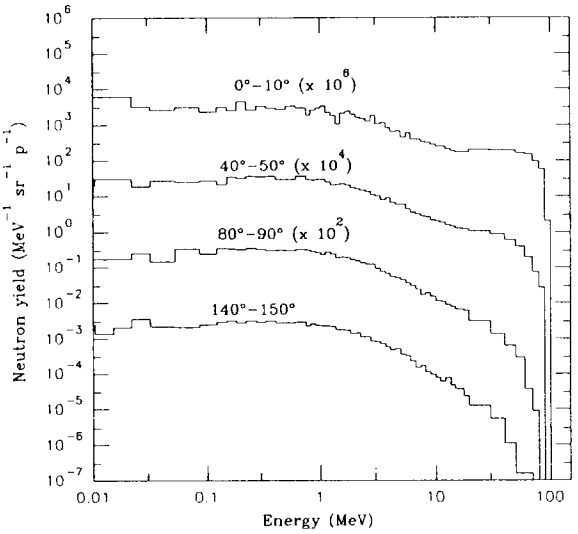

Fig. 2 Double differential neutron distributions for 100 MeV protons striking a thick iron target.

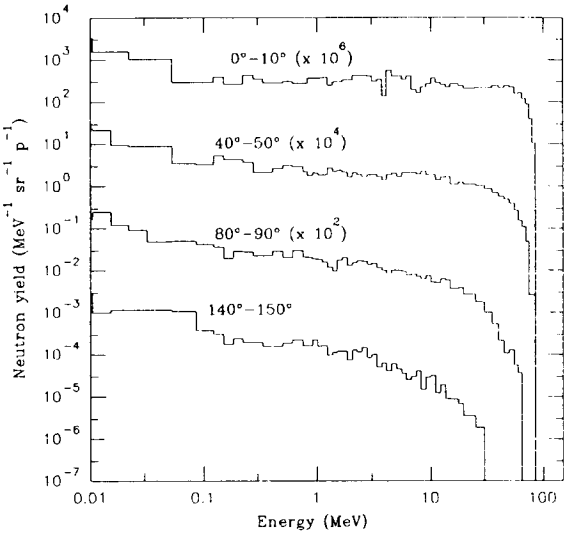

Fig. 3 Double differential neutron distributions for 100 MeV protons striking a thick tissue target.

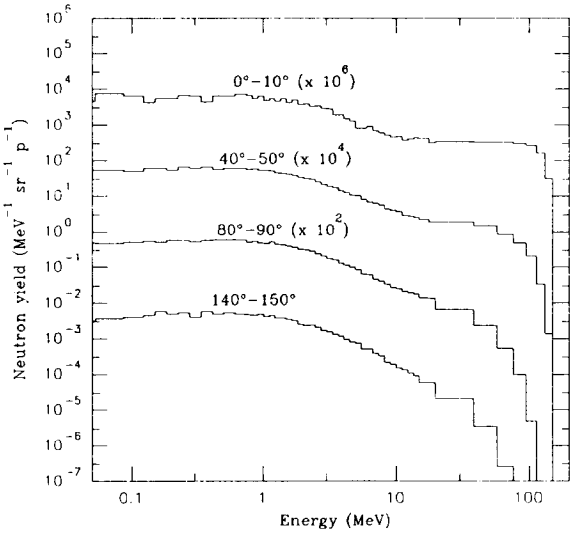

Fig. 4 Double differential neutron distributions for 150 MeV protons striking a thick iron target.

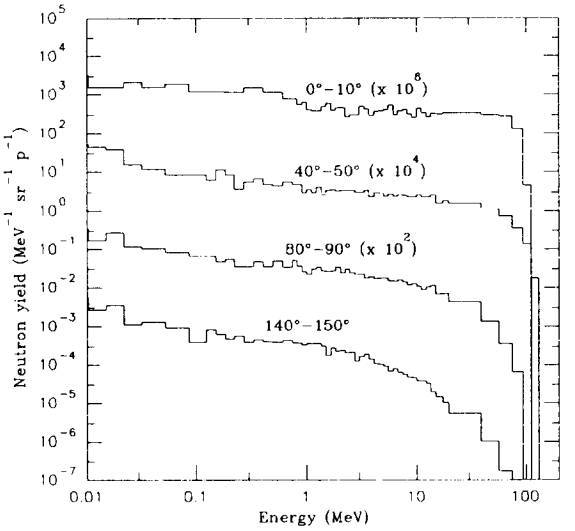

Fig. 5 Double differential neutron distributions for 150 MeV protons striking a thick tissue target.

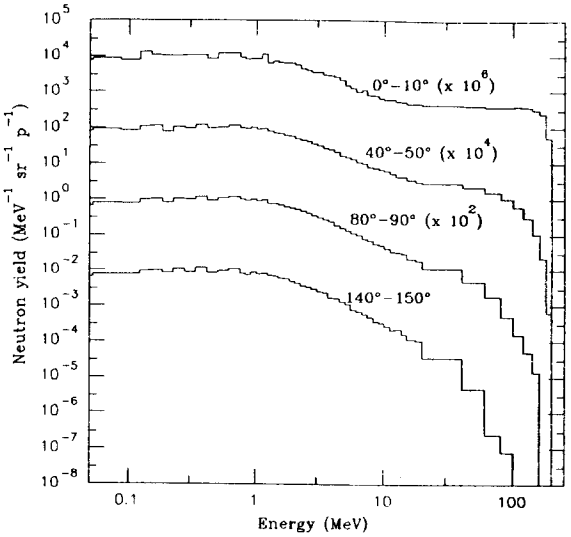

Fig. 6 Double differential neutron distributions for 200 MeV protons striking a thick iron target.

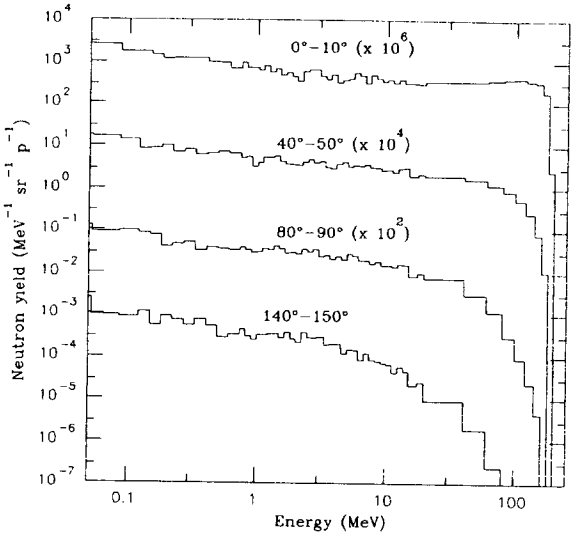

Fig. 7 Double differential neutron distributions for 200 MeV protons striking a thick tissue target.

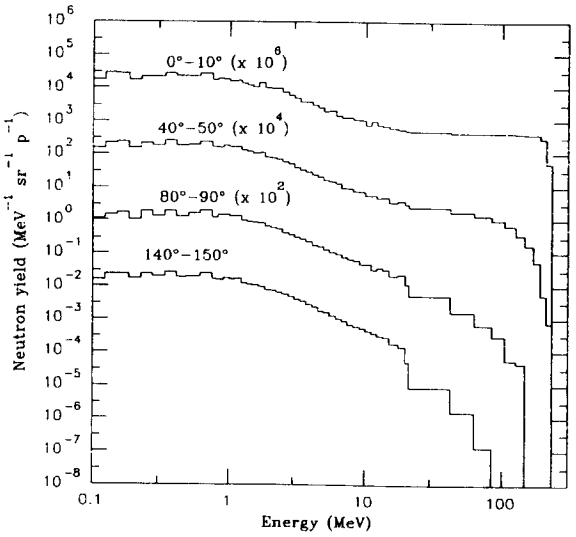

Fig. 8 Double differential neutron distributions for 250 MeV protons striking a thick iron target.

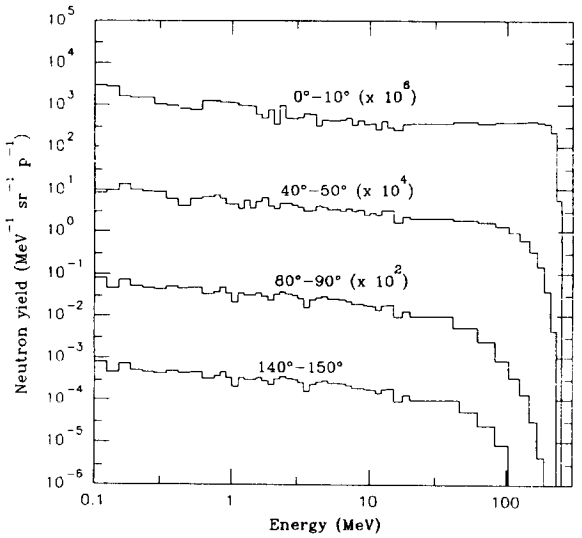

Fig. 9 Double differential neutron distributions for 250 MeV protons striking a thick tissue target.

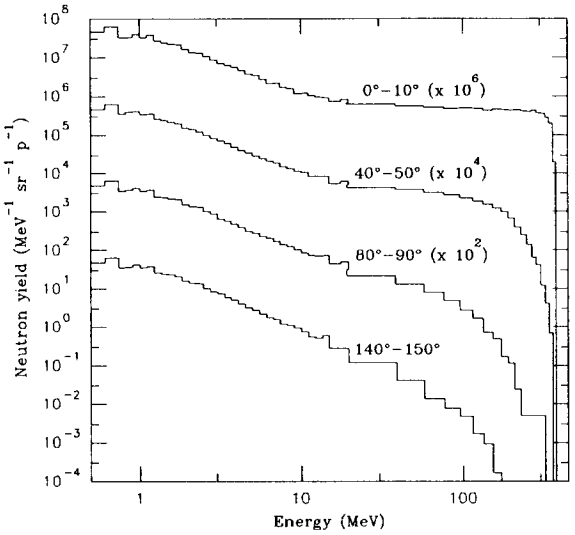

Fig. 10 Double differential neutron distributions for 400 MeV protons striking a thick iron target.

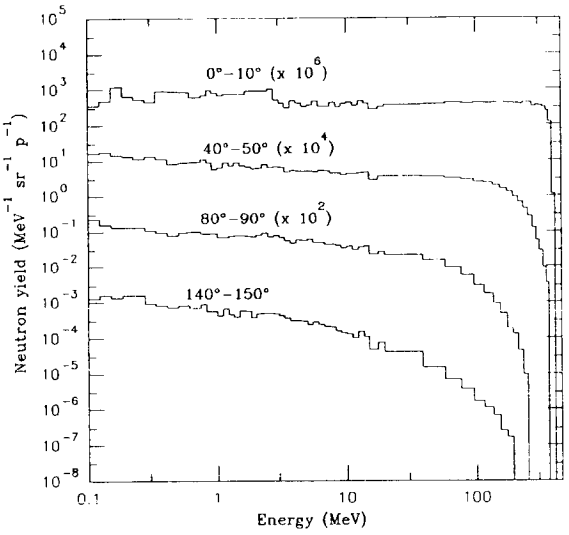

Fig. 11 Double differential neutron distributions for 400 MeV protons striking a thick tissue target.

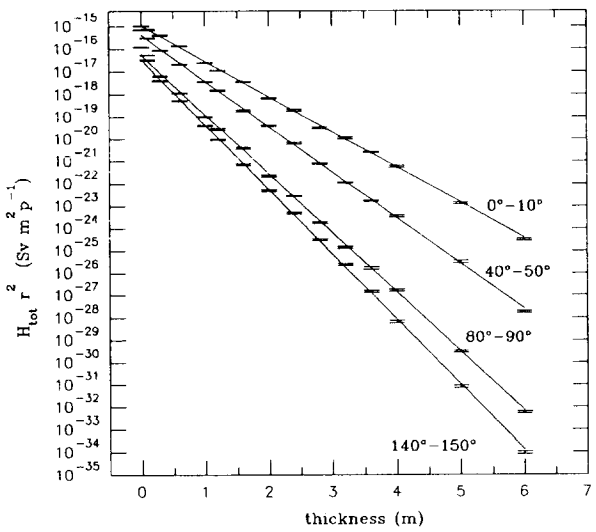

Fig. 12 Total dose equivalent attenuation in ordinary concrete for 100 MeV protons striking a thick iron target.

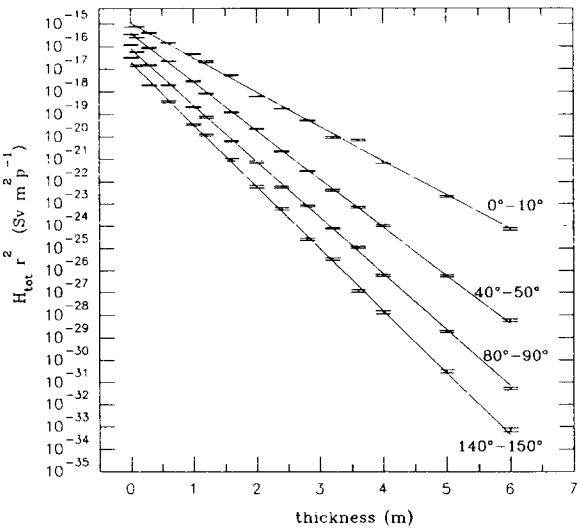

Fig. 13 Total dose equivalent attenuation in ordinary concrete for 100 MeV protons striking a thick tissue target.

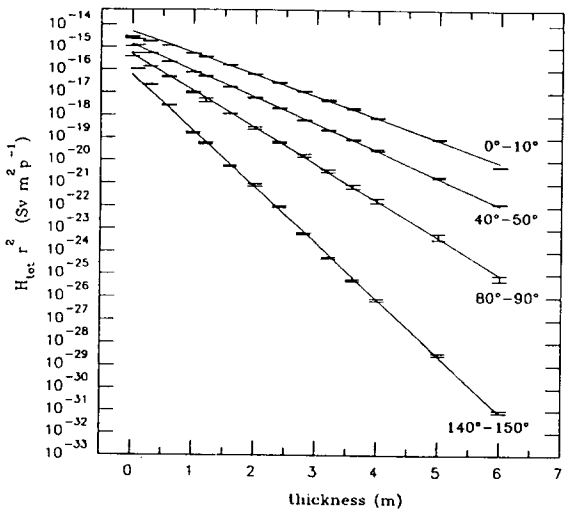

Fig. 14 Total dose equivalent attenuation in ordinary concrete for 200 MeV protons striking a thick iron target.

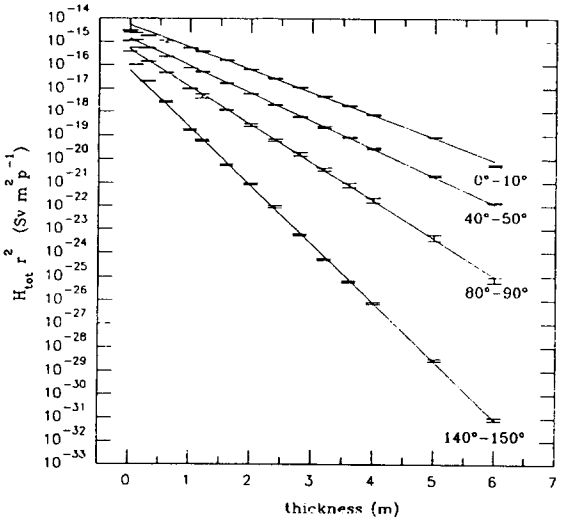

Fig. 15 Total dose equivalent attenuation in ordinary concrete for 200 MeV protons striking a thick tissue target.

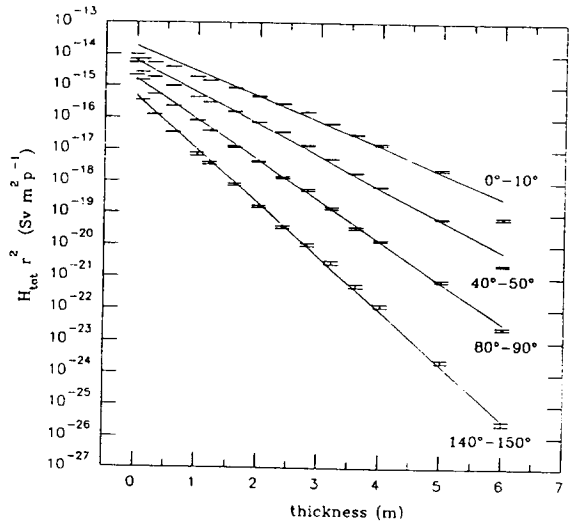

Fig. 16 Total dose equivalent attenuation in ordinary concrete for 400 MeV protons striking a thick iron target.

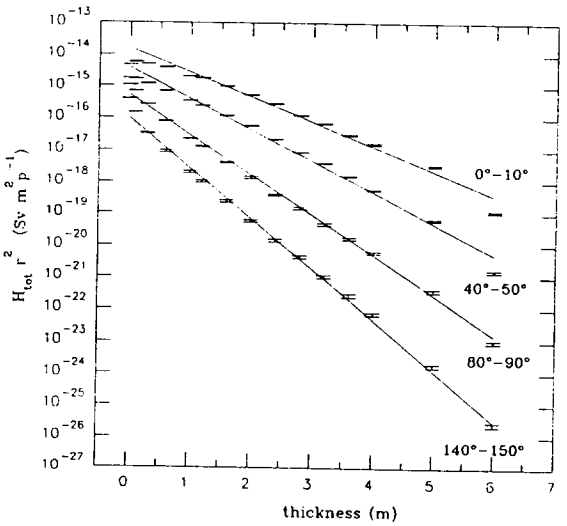

Fig. 17 Total dose equivalent attenuation in ordinary concrete for 400 MeV protons striking a thick tissue target.

source was placed at the centre of a concrete sphere and scoring was done inside the material. No results are given for the source term. The simulations were done with angular bins larger than those used in the present work (see Table 3). Differences are within 30%. Ref. [20] reports experimental results from measurements with 230 MeV protons, performed at Fermi National Accelerator Laboratory (Batavia, IL) with the proton synchrotron now installed at Loma Linda University Medical Center (California). The concrete composition is substantially different from that employed in the present calculations, which may explain the 20% difference between the attenuation lengths determined experimentally and calculated here. The concrete density is also lower than usual, but this should not affect the comparison. The measurements were carried out inside cavities in the shield and the measured quantity (lineal energy spectrum) differed considerably from the ambient dose equivalent used in the present paper. The agreement between the source terms is good. H_0 and λ for copper were calculated in ref. [21] by applying empirical correction factors to the values obtained for an aluminum target. The data are given in angular bins larger than those used in the present work. Differences for both source terms and attenuation lengths are within 15%. Data from ref. [22] are LCS results. Differences in the attenuation lengths are within 15%, while the source term calculated in the present work is higher by 17% at 0° and lower by 38% at 90°. Data from ref. [23] are analytical calculations for forward emission only. A comparison with the present results shows a discrepancy for source terms within 30% and within 20% for the attenuation lengths. Finally, ref. [24] reports data for lateral shielding obtained by fitting data from the literature. According to the energy, the agreement with the present results is within 25% for the attenuation length. For the source term there is a discrepancy of a factor 2 at 400 MeV, while the agreement at the other energies is good. From the above discussion it can be concluded that the agreement between the present calculations and the literature data summarised in Table 3 is in general satisfactory.

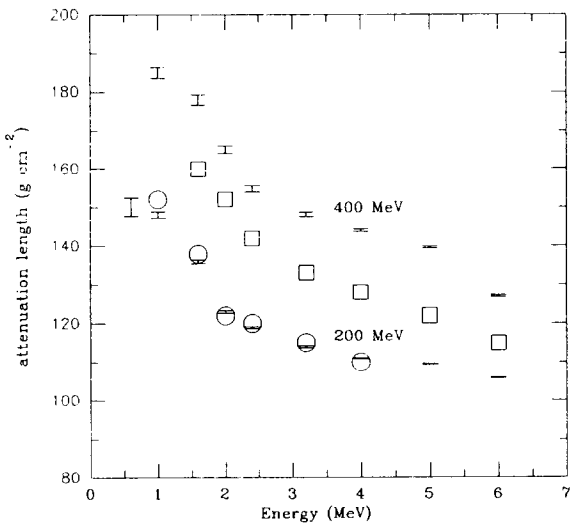

Fig. 18 Attenuation length versus concrete thickness for 200 and 400 MeV protons striking a thick iron target at 0°-10°. Circles and squares are data from ref. [17] at 200 and 400 MeV respectively.

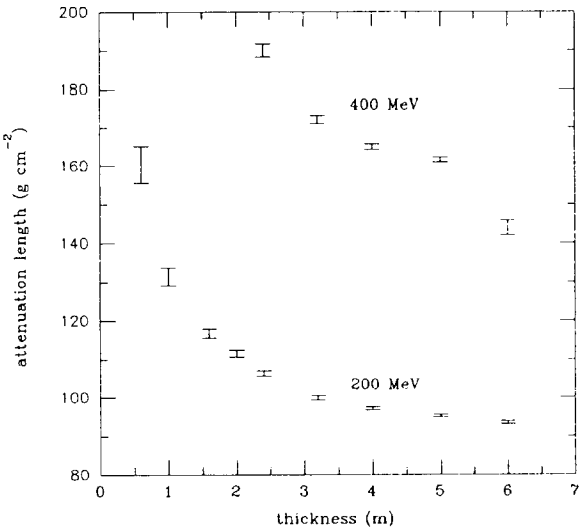

Fig. 19 Attenuation length versus concrete thickness for 200 and 400 MeV protons striking a thick tissue target at 0°-10°.

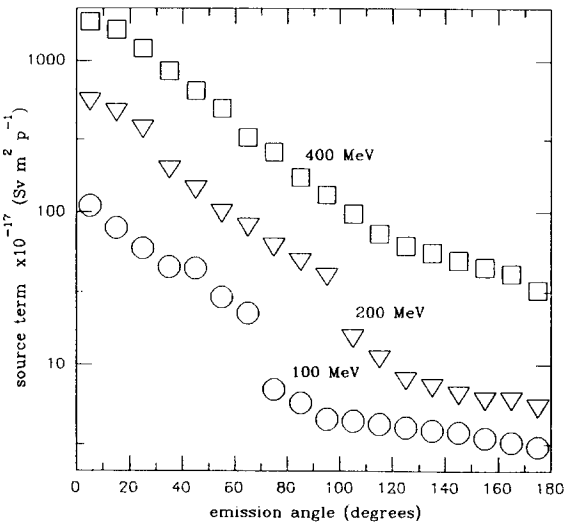

Fig. 20 Source term versus emission angle for 100, 200 and 400 MeV protons striking a thick iron target.

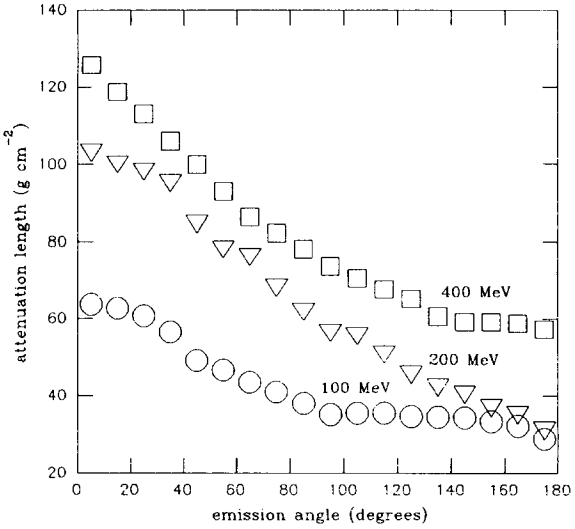

Fig. 21 Attenuation length versus emission angle for 100, 200 and 400 MeV protons striking a thick iron target.

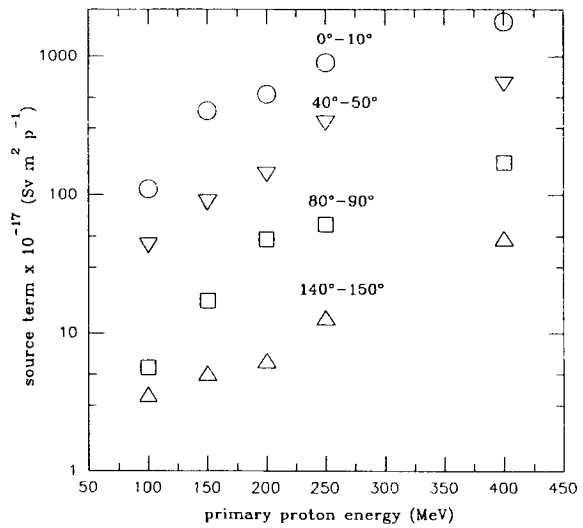

Fig. 22 Source term versus primary proton energy at 0°-10°, 40°-50°, 80°-90° and 140°-150° for a thick iron target.

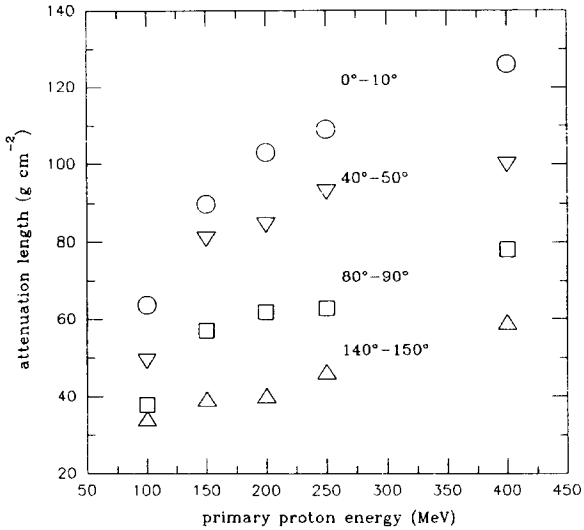

Fig. 23 Attenuation length versus primary proton energy at 0°-10°, 40°-50°, 80°-90° and 140°-150° for a thick iron target.

Conclusions

This paper, along with ref. [6], provides complete information for shielding calculations of proton accelerators in the energy range 100-400 MeV and compares the energy and angular distributions generated by the Monte Carlo codes FLUKA and LCS. The two codes give similar results concerning the neutron emission from the target, although LCS gives lower yields at large angles because of the lack of the pre-equilibrium model in the version used. For the shielding calculations, the results of the two codes agree at small attenuation depths. At large depths - required in most actual situations - the use of LCS becomes impractical due to the very long computing time required to achieve a sufficient statistics. At the lower end of the energy range considered here, the photon component appears to contribute up to 50 % (for the backward angles) of the total dose equivalent and cannot be completely neglected in shielding assessments. Secondary protons only give a substantial contribution at the highest energy.

An extensive comparison of source terms and attenuation lengths obtained in the present work with published data shows an acceptable agreement, despite the large differences in the configurations and techniques used. However, literature data are sparse and specific to given beam conditions and geometries. In the present paper an effort has been made to obtain a complete set of parameters which can be used in shielding design of proton facilities of widely different characteristics. These shielding data should to a large extent limit to a minimum the need for long and complex Monte Carlo calculations. The smooth behaviour of λ and H_0 versus proton energy and polar angle allows to interpolate the present data for application at any energy in the range considered.

Table 1 Thick target neutron yield.

	Yield (neutron per incident proton)			
E_p	Iron		Tissue	
(MeV)	n <20 MeV	n_{tot}	n <20 MeV	n_{tot}
100	0.0337	0.1094	0.0104	0.1024
150	0.0602	0.2079	0.0154	0.1383
200	0.0980	0.4400	0.0181	0.3011
250	0.1590	0.7687	0.0202	0.5154
400	0.3360	2.5061	0.0279	1.7409

Table 2 Percentage contributions to total dose equivalent due to proton and photon for iron and tissue targets bombarded by 100, 150, 200, 250, 400 MeV protons.

Fe								
E_p (MeV)	0°-10°		40°-50°		80°-90°		140°-150°	
	H_γ/H_{tot}	H_p/H_{tot}	H_γ/H_{tot}	H_p/H_{tot}	H_γ/H_{tot}	H_p/H_{tot}	H_γ/H_{tot}	H_p/H_{tot}
100	3.0	—	6.0	—	20.0	—	48.0	—
150	1.9	—	2.5	—	6.8	—	30.0	—
200	1.8	—	1.9	—	5.0	—	36.0	—
250	1.9	—	1.9	—	3.7	—	19.0	—
400	1.6	10.7	1.6	7.0	1.8	4.3	2.3	3.1
Tissue								
E_p (MeV)	0°-10°		40°-50°		80°-90°		140°-150°	
	H_γ/H_{tot}	H_p/H_{tot}	H_γ/H_{tot}	H_p/H_{tot}	H_γ/H_{tot}	H_p/H_{tot}	H_γ/H_{tot}	H_p/H_{tot}
100	5.6	—	13.6	—	33.3	—	50.0	—
150	2.1	—	2.5	—	3.5	—	40.0	—
200	1.8	—	2.4	—	6.9	—	20.0	—
250	1.6	—	2.0	—	4.7	—	10.0	—
400	1.6	9.9	1.7	7.5	1.8	4.5	6.0	3.5

Table 3 Literature data for source term and attenuation length in concrete for forward and lateral shielding for neutrons produced by 100 - 400 MeV protons on copper and iron targets.

Author	E_p (MeV)		Target		Emission angle		λ (g cm^{-2})		H_0 (Sv m^2 p^{-1})	
	lit. data	pres. work	lit. data	pres. work	literature data	present work	literature data	present work	literature data	present work
Fassò et al. [18]	100	100	Cu	Fe	0°-5°	0°-10°	60	63.6	9.1E-16	1.1E-15
	250	250	Cu	Fe	0°-5°	0°-10°	111	109	9.6E-15	9.0E-15
					20°-30°	20°-30°	114	110	4.5E-15	6.8E-15
Hagan et al. [19]	250	250	Fe	Fe	0°-15°	0°-10°	109	109		
					15°-30°	20°-30°	105	110		
					30°-45°	40°-50°	93	92.9		
					45°-60°	50°-60°	99	89		
					60°-90°	80°-90°	88	62.8		
Siebers et al. [20]	230	250	Fe	Fe	0°	0°-10°	90	109	7.9E-15	9.0E-15
					22°	20°-30°	88	110	4.7E-15	6.8E-15
					45°	40°-50°	75	92.9	2.7E-15	3.3E-15
					90°	80°-90°	51.9	62.8	7.6E-16	6.2E-16
Awschalom [21]	250	250	Cu	Fe	0°-30°	0°-10°	104	109	5.6E-15	9.0E-15
					30°-60°	50°-60°	93	89	2.2E-15	2.5E-15
					60°-90°	80°-90°	73	62.8	4.1E-16	6.2E-16
Knowles et al. [22]	230	250	Fe	Fe	0°-10°	0°-10°	99	109	6.6E-15	9.0E-15
					10°-30°	20°-30°	104	110	5.0E-15	7.5E-15
					40°-50°	40°-50°	89.4	92.9	2.3E-15	3.3E-15
					85°-95°	80°-90°	53.4	62.8	1.0E-15	6.2E-16
Braid et al. [23]	100	100	Cu	Fe	0°	0°-10°	77	63.6	1.8E-15	1.1E-15
	200	200	Cu	Fe	0°	0°-10°	90	103	7.4E-15	5.3E-15
	400	400	Cu	Fe	0°	0°-10°	127	126	1.3E-14	1.8E-14
Tesch et al. [24]	100	100	Fe	Fe	90°	80°-90°	50	38	4.0E-17	5.6E-17
	250	250	Fe	Fe	90°	80°-90°	78	62.8	6.0E-16	6.2E-16
	400	400	Fe	Fe	90°	80°-90°	89	78.1	3.2E-15	1.7E-15

References

1. T. Nakamura, Proc. of the AEN/NEA Specialists' Meeting on Shielding Aspects of Accelerators, Targets and Irradiation Facilities, Arlington (Texas), 28-29 April 1994, NEA/OECD (1995) p. 21
2. T.A. Gabriel, Proc. of the AEN/NEA Specialists' Meeting on Shielding Aspects of Accelerators, Targets and Irradiation Facilities, Arlington (Texas), 28-29 April 1994, NEA/OECD (1995), p. 41
3. M. Silari, Proc. of the AEN/NEA Specialists' Meeting on Shielding Aspects of Accelerators, Targets and Irradiation Facilities, Arlington (Texas), 28-29 April 1994, NEA/OECD (1995), p. 61
4. S. Serezhnikov, I. Azhgirey, A. Uzunian and V. Bamblesky, Proc. of the AEN/NEA Specialists' Meeting on Shielding Aspects of Accelerators, Targets and Irradiation Facilities, Arlington (Texas), 28-29 April 1994, NEA/OECD (1995), p. 81
5. R.H. Thomas and G.R. Stevenson, "Radiological safety aspects of the operation of proton accelerators", Technical report series No. 283, IAEA, Vienna (1988)
6. S. Agosteo, A. Fassò, A. Ferrari, P.R. Sala, M. Silari and P. Tabarelli de Fatis, "Double differential distributions and attenuation in concrete for neutrons produced by 100-400 MeV protons on iron and tissue targets", submitted to Nucl. Instr and Meth B.
7. R.E. Prael and H. Lichtenstein, Radiation Transport Group, Los Alamos National Laboratory (1989)
8. A. Fassò, A. Ferrari, J. Ranft and P.R. Sala, Proc. of the AEN/NEA Specialists' Meeting on Shielding Aspects of Accelerators, Targets and Irradiation Facilities, Arlington (Texas), 28-29 April 1994, NEA/OECD (1995), p. 287
9. International Commission on Radiation Units and Measurements, Report No. 33 Bethesda, Maryland, U.S.A. (1980) p. 20
10. M.M. Meier, C.A. Goulding, G.L. Morgan and J.L. Ullmann, Nucl. Sci. Eng. 104 (1990) 339
11. R.E. Prael, LA-UR-90-1620, Los Alamos National Laboratory, Los Alamos (1990)
12. International Commission on Radiation Units and Measurements, Report No. 49, Bethesda, Maryland, U.S.A. (1993)
13. E.A. Belogorlov et al., Nucl. Instr. and Meth. 199 (1982) 563
14. A.V. Sannikov and E.N. Savitskaya, CERN /TIS-RP/93-14 (1993)
15. International Commission on Radiological Protection, ICRP Publication 21, Pergamon Press (1971)
16. A. Ferrari and M. Pelliccioni, Rad. Prot. Dosim. 51 (1994) 251
17. K. Shin, Comments on "Neutron Attenuation Length and Build-up Factors in Energy Range < 500 MeV", presented at the AEN/NEA Specialists Meeting on Shielding Aspects of Accelerators, Arlington, Texas, USA, April 28-29, 1994
18. A. Fassò, A. Ferrari and G.R. Stevenson, Proc. of the AEN/NEA Specialists' Meeting on Shielding Aspects of Accelerators, Targets and Irradiation Facilities, Arlington (Texas), 28-29 April 1994, NEA/OECD (1995), p. 155

19. N.K. Hagan, B.L. Colborn and T.W. Armstrong Allen, Nucl. Sci. Eng. 98 (1988) 272
20. J.V. Siebers, P.M. DeLuca, D.W. Pearson and G. Coutrakon, Nucl. Sci. Eng. 115 (1993) 13
21. M. Awschalom, FNAL-TM-1354 (1987)
22. H.B. Knowles, J.L. Orthel and B.W. Hill, Proc. of the 1993 Particle Accelerator Conference, Washington D. C., May 17-20, 1993, IEEE (1993), p. 1762
23. T.H. Braid, R.F. Rapids, R.H. Siemssen, J.W. Tippie and K. O'Brien, IEEE Trans. Nucl. Sci. NS-18 (1971) 821
24. K. Tesch, Radiat. Prot. Dosim. 11 (1985) 165
25. T.W. Armstrong and C. Chandler, Nucl. Sci. Eng. 49 (1972) 110

ACCELERATOR SHIELDING BENCHMARK EXPERIMENT ANALYSES

Hiroshi Nakashima, Hiroshi Takada, Shinichio Meigo, Fujio Maekawa, Tokio Fukahori, Satoshi Chiba, Yukio Sakamoto, Nobuo Sasamoto and *Shun-ichi Tanaka*
Japan Atomic Energy Research Institute, Japan

Katsumi Hayashi
Hitachi Engineering Company, Ltd., Japan

Naoteru Odano
Ship Research Institute, Japan

Nobuaki Yoshizawa and *Osamu Sato*
Mitsubishi Research Institute Inc., Japan

Yoshiro Suzuoki, Satoshi Iwai and *Takashi Uehara*
Mitsubishi Heavy Industrial Co. Ltd., Japan

Hiroshi Takahashi
CRC Research Institute, Inc., Japan

Yoshitomo Uwamino
The Institute of Physical and Chemical Research, Japan

Yoshihito Namito, Syuichi Ban and *Hideo Hirayama*
National Laboratory for High Energy Physics, Japan

Kazuo Shin
Kyoto University, Japan

Takashi Nakamura
Tohoku University, Japan

Abstract

Analyses of benchmark experiments of the thick target neutron yields for protons, electrons and alpha particles and shielding experiments of neutrons and protons were carried out in order to investigate the validity of the existing computer codes and nuclear data, and to make clear what we have to proceed to in the future research. The results of the analyses and the related future items to be solved are summarized.

1. Introduction

In accelerator shielding design, it is necessary to calculate energy spectra of neutrons and photons emitted from the target and their behavior in shield materials. Recently, several computer codes have been developed and progressively modified in order to calculate the neutron and photon energy spectra. Besides, benchmark experiments have been performed in several laboratories, and the calculated values are compared with the measurements to validate the accuracy of the codes. These comparisons have provided good information for modifying the codes and estimating errors and safety margins in design.

Several benchmark experiments on thick target neutron yield for protons, electrons and alpha particles and on bulk shields were picked up and discussed by Hayashi et al. to sort out the items to be solved in the future. [1] Numerical data of the benchmark experiments were compiled in a report for analysis using the up-dated codes and nuclear data. [2]

In this report, the results calculated using the up-dated codes and nuclear data are summarized on the benchmark experiments, and the data and method to be improved and experiments to be further needed are discussed.

2. Benchmark calculations of thick target yields

2.1 Thick target neutron yields for 256 MeV protons

2.1.1 Experiment

The experiment was carried out at the Weapon Neutron Research Facility (WNR) of Los Alamos National Laboratory. The 256 MeV protons extracted from Los Alamos Clinton P. Anderson Meson Physics Facility (LAMPF) were injected into the stopping-length targets of C, Al, Fe and U-238. The physical characteristics of the targets are summarized in Table. 2.1.1. The absolute intensity of the proton beam was measured with a calibrated secondary electron monitor. The neutron energy spectra were measured at the emission angles of 30°, 60°, 120° and 150° using the time-of-flight technique with flight paths of 28.7 to 66.8 m. The BC-418 plastic scintillators of 5.08 cm in both diameter and length were employed for the neutron measurements with the long flight path, while those of 5.08 cm in diameter and 2.54 cm in length were used in the measurements with the short flight path. The details on the experimental procedure are described in Ref. 3.

2.1.2 Calculation

In the calculation, a revised version of the nucleon-meson transport code NMTC/JAERI [4] and the neutron transport code MCNP-4A [5] were employed. NMTC/JAERI simulates the nuclear reactions with the intranuclear cascade [6] and evaporation [7] models including high energy fission process [8] and calculates the transport of protons, neutrons and pions in the energy region above 20 MeV. The transport of neutrons with energies below 20 MeV was calculated with MCNP-4A using a continuous energy cross-section library: FSXLIB-J3R2 [9], which was processed from the nuclear data file JENDL-3.2 [10]. In the revised version of NMTC/JAERI, the following two modifications have been made in the intranuclear cascade (INC) calculation part. One is the inclusion of the preequilibrium process. The other is the inclusion of the nuclear medium effects in terms of the

reflection and refraction with the in-medium nucleon-nucleon (NN) cross-sections. In the transport calculation part, moreover, the code has been modified so that the total, elastic, and non-elastic cross-sections of the nucleon-nucleus reactions are given by the systematics of Pearlstein [11].

As for the preequilibrium calculation, the following procedure [12] has been adopted. The INC process is terminated at the cut-off value, E_c. The E_c value is randomly chosen in the region from 0 to E_0 MeV. The E_0 value has been determined as 40 MeV through a detailed study [13] of the double differential neutron spectra. For protons, if the sampled value is below the Coulomb barrier height, the value is substituted by the barrier height. In the INC calculation, the number of collisions is counted and used to determine the initial exciton number for the preequilibrium reaction analysis. The preequilibrium process is analyzed with a closed form exciton model proposed by Gudima el al. [14]. In the model, the transition probabilities of the exciton states, which are the increase (l_+), the unchange (l_0) and the decrease (l_-) of the exciton number, are multiplied by an adjustable parameter F:

$$F = \max\left(0.2,\ 3.5 - \frac{13}{\sqrt{A}}\right) \tag{2.1.1}$$

where A is the mass number of a target nucleus. If the emission rate of the particle j is denoted as G_j, the reaction rate L in the preequilibrium process is represented as

$$\Lambda = F\,(l_+ + l_0 + l_-) \sum_{j=1}^{6} \Gamma_j \tag{2.1.2}$$

In this calculation, the 6 kinds of particles: p, n, d, t, He-3 and He-4, are considered as the ejectile from the preequilibrium process. The angular distribution of the emitted particles is assumed to be isotropic. The details of the calculation procedure are described in Ref. 12.

For the INC calculation including the nuclear medium effects, the code ISOBAR [15] [16], which originally treats the reflection and refraction, has been substituted for the INC calculation part of NMTC/JAERI. The in-medium NN cross-sections parametrized similarly to those of Cugnon [17] [18] are employed instead of the free NN cross-sections in the code. The parametrization [19] is represented as follows,

$$s = \frac{C_1}{1 + 100\sqrt{s'}} + C_2 \quad (mb) \tag{2.1.3}$$

$$\sqrt{s'} = \max\left(0,\ \sqrt{s} - M_i - M_j - cutoff\right) \quad (GeV) \tag{2.1.4}$$

where $\sqrt{s}$ 0 is the total energy of a nucleon in the c.m. system, M_i the mass of an injectile and M_j the mass of a struck nucleon. Here, the *cut-off* energy is chosen as 0.02 GeV. C_1 and C_2 are the elastic cross-section parameters, and are set to be 35.0 and 20.0 mb for pp and nn collisions, while they are 28.0 and 27.0 mb for pn collision. This parametrization is applicable from 40 MeV to 1 GeV in the laboratory frame. For the energy region below 40 MeV, the elastic cross-sections extrapolated with the following parametrization [20] are used for all NN collisions.

$$s = 23.5 + 1000 \times (0.7 - p_{lab})^4 \qquad (2.1.4)$$

where p_{lab} stands for the momentum of the nucleon in the laboratory frame.

Moreover, the threshold energies for (p,n) and (n,p) reactions have been taken into account in the ISOBAR code to treat the quasi-elastic collision properly. In this work, the threshold energy is added to the cut-off energy, which is the sum of the Fermi energy, the binding energy and the Coulomb barrier, and is used to check the possibility of the escape of a travelling nucleon from a nucleus. The check with the threshold energy is applied to the nucleons which make only a single collision in the target.

For convenience, the calculation with NMTC/JAERI including the preequilibrium process and that including the nuclear medium effects are hereafter denoted as "NMTC -3STEP" and "NMTC-ISOBAR", respectively. In both calculations, the level density parameter derived by Baba [21] was employed in the statistical decay calculation with the evaporation model. The neutron yield was obtained by counting the neutrons which crossed a part of the spherical surface around the target having the width corresponding to ±5°. The calculations was carried out with the number of incident protons of 0.5 to 5 millions.

2.1.3 Comparisons between calculated and experimental results

In Figs. 2.1.1 through 2.1.4, the calculated neutron yields with NMTC -3STEP are shown with the experimental ones for the targets of C, Al, Fe and U-238, respectively. For comparison, the calculated results with the original NMTC/JAERI code are also exhibited in these figures. For the C target, the calculated results with NMTC -3STEP are in excellent agreement with the experimental ones in the energy region above 20 MeV except for the emission angle of 60°. It is observed at 60° that the calculated neutron yields are higher than the experimental ones about 30%. In the energy region below 10 MeV, good agreement is obtained between the calculated and the experimental results. The calculated results on the Al target with NMTC -3STEP are also in good agreement with the experimental ones in all energy regions at emission angles of 30°, 120° and 150°, respectively. The calculation, however, gives higher neutron yield than the experiment in the energy region above 20 MeV at 60° as well as in the case of the C target. For the Fe target, excellent agreement is obtained between the calculated results with NMTC -3STEP and the experimental ones in all energy regions at every emission angles although slight discrepancies are observed in the energy region below 15 MeV. For the U-238 target, moreover, NMTC-3STEP achieves excellent agreement with the experimental ones in all energy regions at 30° and 60°. It is observed that NMTC -3STEP gives

a little lower values in the energy region above 20 MeV at backward angles of 120° and 150°. The overall agreement, however, is quite reasonable.

In comparison with the calculated results of the original NMTC/JAERI code, NMTC -3STEP gives much better agreement with the backward neutron yields in the energy region above 20 MeV for all targets due to the inclusion of the preequilibrium process. The increase of the high energy neutron emission decreases the excitation energy of residual nucleus so that the numbers of evaporation neutrons with energies below 15 MeV are suppressed. It is confirmed through this calculation that the inclusion of the preequilibrium process improved the accuracy of NMTC/JAERI on the estimation of the neutron yields for the 256-MeV proton incidence.

In Figs. 2.1.5 through 2.1.8, the calculated neutron yields with NMTC -ISOBAR are compared with the experimental ones for the targets of C, Al, Fe and U-238, respectively. For comparison, the calculated results with the NMTC -ISOBAR using the free NN cross-sections are also exhibited in these figures. For the C target, NMTC-ISOBAR gives good agreement with the experimental results in the energy region above 10 MeV at emission angles from 30° to 120°. The code, however, largely overestimates the neutrons with the energies above 80 MeV at 150°. In addition, the code gives lower neutron yields about a half of the experimental ones. The reason of this discrepancy seems that the calculation with the in -medium NN cross-sections diminished the collision probability of a nucleon in a nucleus so that many nucleons could go out of the nucleus easily without losing its own kinetic energy by the collision. This leads to the decrease of low energy neutron yields. For the Al target, the agreement between the calculated and the experimental results is quite well. In particular, the neutron emission to the backward angles is reproduced successfully by NMTC-ISOBAR without taking into account the preequilibrium process. NMTC -ISOBAR also gives successful agreement with the experimental neutron yields of the Fe target. It is observed, however, that the calculated results are lower than the experimental ones by about a factor of 2 below 10 MeV at the emission angle of 60°. For the U-238 target, remarkable agreement is obtained between the calculated and the experimental results in all energy regions at every emission angles. It is confirmed from these results that NMTC-ISOBAR can predict the neutron yields in the targets of Al to U-238 quite well. At backward angles, in particular, excellent agreement is obtained between the calculated and the experimental results.

In comparison with the calculated results with NMTC -ISOBAR using the free NN cross-sections, NMTC-ISOBAR gives lower neutron yields to the evaporation component below 10 MeV for the C target. Since the in-medium NN cross-sections are lower than the free NN ones, the collision probability is estimated smaller in NMTC -ISOBAR. Hence, a nucleon after a collision can escape from a nuclei rather than make another collision. This leads to the increase of the high energy component of neutron spectra and the suppression of evaporation component. Judging from the results of the C target, it seems that the present NMTC-ISOBAR code may overestimate the number of nucleon emission.

2.1.4 Concluding remarks

Two kinds of calculations were carried out using the nucleon -meson transport code NMTC/JAERI by modifying the INC calculation part for 256-MeV proton incidence on the stopping -length targets of C, Al, Fe and U-238. One is the inclusion of the preequilibrium process (NMTC -3STEP) and the other is the inclusion of the nuclear medium effects in terms of the reflection and refraction and the in -medium NN cross-sections (NMTC-ISOBAR).

It was found through the calculation with NMTC-3STEP that the code gives excellent agreement with the experimental results at emission angles between 30° and 150° for all the targets. As for the calculation with NMTC-ISOBAR, the code has also achieved successful agreement with the experimental results of the targets of Al and U-238 without including the preequilibrium process. For the C target, however, remarkable underestimation was observed in the neutron yields below 10 MeV.

In conclusion, both codes are available with good accuracy to estimate the neutron yields of stopping-length targets of Al to U-238 at the emission angles beyond 30°. As for the tre atment of the nuclear reactions in the light nuclei such as C, the calculation with the preequilibrium process seems to be superior than that with the nuclear medium effects for the time being. The one of reasons of this discrepancy may be ascribed to the lack of an energy dependent potential depth in the INC calculation.

2.1.5 Further benchmark calculation

In other calculations [22] with NMTC-ISOBAR, it was found that the code gives better results than the NMTC-3STEP in the predictions of the neutron e mission to the very forward angles at incident energies lower than 160 MeV. In the energy regions, the code has also reproduced the experimental results, while the agreement of NMTC-ISOBAR using free NN cross-sections with the experiment gradually becomes worse. Therefore, further benchmark calculations are required to understand the accuracy of those codes for a variety of combinations of targets and incident energies. It is also of interest to study the applicability of the codes to the neutronics analysis of more massive targets.

2.2 Photoproduction of high-energy neutrons in thick targets by electrons in the energy range 150 to 270 MeV

2.2.1 Experiment

Figure 2.2.1 gives the schematic arrangement of the experiment [23] carried out with the undeflected beam of Mainz Electron Linac. The electron beams from the accelerator were focused on the target to a diameter of about 1 cm.

For the measurements relating to various primary electron energies, a thick target was composed of 8 lead sheets with a thickness of 0.3 cm and a diameter of 6.8 cm, placed one behind the other with a spacing of 0.2 cm for water cooling (Figure 2.2.2). The focused electron beams with energies of 150, 170, 182, 202, 234 and 266 MeV were incident to the thick lead target. Photoneutron spectra in the energy regions from 12 MeV up to around 160 MeV were measured at a fixed angle of 90° to the beam axis. The spectra were obtained with three independent neutron detection systems: two proton recoil counter telescope methods and one time-of-flight set-up.

2.2.2 Calculation

We calculated electro-magnetic shower development in a cylinder-slab geometry using the EGS4/PRESTA code [24] [25]. The geometry for the calculation is shown in Figure 2.2.3. Photon

flux due to the bremsstrahlung process of the incident electrons was scored by summing up track length of photon in the lead region. The energy bins for scoring photon track length are shown in Table 2.2.1. Transport calculation of neutrons produced by a photoneutron production process was ignored in the EGS4 calculation, because the neutron hardly affects the results. An example of photon track length in the Pb target at the electron beam energy of 266 MeV is shown in Figure 2.2.4. The number of histories was 10^5.

Photonuclear cross-sections below 30 MeV were prepared with the MCPHOTO code [26] which was a modified version of the MCEXCITON code [27] based on the exciton and evaporation models. A code based on the internuclear cascade model, PICA [28], was used to prepare photonuclear cross-sections above 30 MeV. In the PICA calculation, Levinger's phenomenological exponential factor was set to be 6.5 from the Chadwick's study [29]. Photoneutron production cross-sections were calculated for the photons with the midpoint energy of each bin. Because the MCPHOTO and the PICA codes assume isotropic angular distribution of the (g,n) cross-sections, the neutrons produced by (g,n) reaction are divided by 4p to obtain differential neutron production at the angle of 90°.

The double differential neutron production cross-section per electron is obtained by;

$$\frac{d^2 s}{d\Omega\, dE_n} = \frac{1}{4p}\frac{1}{c_t}\int_{10}^{E_e} dk\, s_{g,n}(k)\, f_g(k) \qquad (2.2.1)$$

where E_e is the incident electron energy, $s_{g,n}$ the (g,n) cross-section, $f_g(k)$ the photon flux obtained by the EGS4 calculation and c_t target thickness :2.4 cm for Pb in the arrangement a) of Figure 2.2.2, and 0.5 cm for C, 0.6 cm for Al, 0.3 cm for Cu and Pb in the arrangement b) of Figure 2.2.2.

2.2.3 Comparison between experiment and calculation

Figure 2.2.5 shows the comparison between the experiment and the calculation for the photoneutron spectra produced by the electrons with the primary energies of 150, 170, 182, 202, 234 and 266 MeV. In the figure the EGS4 calculations are multiplied by a factor of 3.3. The EGS4 calculations underestimate the measurements by a factor of 3.3 for all the primary electron energies. The calculated results reproduce the shape of the measurements.

Comparisons between the experiment and the calculation of the photoneutron production cross-sections from various target materials by the electrons with the primary energy of 234 MeV are shown in Figure 2.2.6. The EGS4 calculations underestimate the measurements by a factor of 3.3. The calculated results reproduce the shape of the measured spectra except for the calculation for the C target.

2.2.4 Necessary benchmark experiment to be done

The measurement and calculation apparently differ in absolute values. It, however, is difficult to find the reasons of the discrepancy in the EGS4 and cross-section calculations from these analyses. We require the measurements of photoneutrons produced by electron beams of several hundred MeV, because there are a few experimental data.

The discrepancy for the C target seems to be caused by the inadequacy of the mass dependence in the cross-section calculation. Cross-section measurements are also required to validate the cross-sections used in the present calculations.

2.3 Thick target neutron yield for 710-MeV alpha particles

2.3.1 Experiment

The experiments were carried out by Cecil et al. [30] at the Cyclotron of Space Radiation Effect Laboratory in Newport News, Virginia. Thick targets of carbon, water, iron and lead were irradiated by 710-MeV alpha particles, and differential thick target neutron yields above 10 MeV were measured at the directions of 0°, 6°, 15°, 30°, 45°, 60°, 90°, 120° and 150° with NE-102 counters using the time of flight method. The thickness of the targets used is listed in Table 2.3.1.

2.3.2 Calculation

The neutron production cross-section was calculated by the Quantum Molecular Dynamics (QMD) model [31] including the statistical decay process [32]. The QMD code deals with the time-evolution of the nucleon many-body system in the phase-space based on a self-consistent mean field and a stochastic collision taking account of the Pauli-blocking, in which the NN collision is treated quite similarly with the INC model. In the calculation, an impact parameter was set as the sum of the nuclear radius of the incident particle and the target nucle us. The double differential cross-sections (DDXs) were calculated at the incident energies of 20, 40, 60, 90, 120, 140, 160 and 177 MeV/u.

Double differential neutron yields were calculated with the following equation,

$$\frac{d^2N}{d\Omega\, dE_n} = \int_0^{E_a} n \frac{ds}{d\Omega\, dE_n}\left|\frac{dE}{dx}\right|^{-1} \exp\left(-\int_E^{E_a} \Sigma_{non}(E')\left|\frac{d'E}{dx}\right|^{-1} d'E\right)dE \qquad (2.2.1)$$

where *dN/dW/dEn* is the double differential neutron yields, *n* the atomic density of the target material (cm^{-3}), *ds /dW/dEn* (mb/sr/MeV) the double differential neutron production cross-section calculated by the QMD code, *dE/dx* (MeV/cm) the stopping power [33] and *Snon(E')* the non-elastic cross-section for alpha particles with energy *E'*. The exponential term of the equation (2.3.1) indicates the attenuation of the incident alpha particles by the nuclear reaction in the target. The non-elastic cross-sections of the alpha particles were calculated by the code ECIS-79 [34] based on the optical model. The elastic scattering process of the alpha particles was ignored in the present calculation, because the energy loss and cross-sections of the alpha particles due to the Rutherford scattering reaction are quite small.

In order to consider the scattering and the absorption reactions of the neutrons produced by the (a,n) reaction in the target, a Monte-Carlo code has been developed, which simulates the neutron transport using the evaluated nuclear data library ENDF/B-VI high energy file [35]. The neutron yields of the carbon target with and without including the calculation of neutron transport effects are compared in Figure 2.3.1. By considering the neutron transport effects, the neutron yields increase at the emission angle of 90°,120° and 150°in the energy region above 30 MeV, while slightly decrease at the other angles.

2.3.3 Comparison between calculation and experiment

Carbon Target

The calculated neutron yields for the carbon target are compared with the experimental results in Figure 2.3.2. The results calculated by the QMD code excellently reproduce the experimental ones, except for the underestimation of the calculated results at the angle of 0° in the energy region above 50 MeV.

For comparison, the calculated results by the intra-nuclear cascade-evaporation code HETC-KFA-1 [36] are also shown in Figure 2.3.2. The results calculated by the QMD code present better agreement with the measurements at the angle smaller than 15°and larger than 90° than the ones by HETC-KFA1. Better agreement of the QMD calculation is ascribed to that the QMD takes into account of the nuclear in-medium effects such as reflection and refraction.

Moreover, the maximum energy of the calculated spectra by HETC-KFA1 is 177 MeV, because the energy of the incident particle is equally divided into each nucleon in the incident particle and each nucleon is incident to the target nucleus in the HETC calculation.

Iron Target

In Fig 2.3.3, the calculated results for the iron target are compared with the experimental ones. The calculated results are in reasonable agreement with the experimental ones on the whole. In the energy above 40 MeV, the calculated results, however, considerably underestimate the experimental ones at the angle smaller than 6°. The results of HETC-KFA1 is also shown in Fig 2.3.3. The calculated results by HETC-KFA1 underestimate the experimental ones at 6°, 15° and 150°. The results calculated by the QMD are in better agreement with the experimental ones than the ones by HETC-KFA1 in the same reason as that for the carbon target.

2.3.4 Necessary improvement in the calculation

In the energy region above 40 MeV, the calculated results at 0° and 6° underestimate the experimental ones. This discrepancy might come from the underestimation of the DDX by the QMD calculation at the forward angle. In order to improve the result, in the QMD code for the (a,n) reaction further study is required.

2.3.5 Required experiments and data

Since the dominant reaction mechanism varies depending on the ion energy, the mea surements covering the wide energy range are desirable. The yield data for different incident ions covering from light to heavy mass are needed. Yield data for different target materials should be given., i.e., for low Z materials like carbon, intermediate Z materials of copper and iron, and high Z materials such as lead, tungsten and uranium. Inclusive thin target neutron yield data are also very useful for the check of calculation methods. In order to acquire the neutron yield data of the incident energies below 70 MeV/u, we have started to measure the data of the carbon, gold, iron and zirconium target irradiated by

the heavy ion at the facility of TIARA (Takasaki Ion Accelerators for Advanced Radiation Application).

3. Benchmark calculations of shielding experiment

3.1 Transmission through shielding materials of neutrons generated by 52- and 65-MeV protons

3.1.1 Experiment

The experiments with 52-MeV protons were performed at the FM cyclotron of Institute for Nuclear Study in University of Tokyo, and with 65-MeV protons at the AVF cyclotron of Research Center for Nuclear Physics in Osaka University. [37] [38] [39]

For the 52-MeV proton experiment, a thick graphite target was settled at the front face of the bulk shields, which generated source neutrons as shown in Figure 3.1.1. An NE213 scintillation detector was placed in contact with the rear face of the shields. The pulse height distributions were converted to neutron energy spectra by using the revised FERDO unfolding code [40] and a calculated response matrix. Angle-dependent source neutron spectra from the graphite target were measured with the same detection system.

A copper target of stopping range was used for the 65-MeV proton experiment. The source neutrons which were collimated with a 7.5-cm-diam. and 50-cm-long iron-lined hole, were incident to the bulk shields placed at the exit of the collimator as shown in Figure 3.1.2. The pulse height distributions were measured by an NE213 detector set just behind the shields, and were unfolded to energy spectra by the revised FERDO code and the calculated response matrix. The collimated source neutron spectrum was also measured with the same detection system.

3.1.2 Calculation

The MORSE-CG code [41] was used with the DLC119/HILO86 cross-sections [42] for the calculation of neutrons transmitted through shields as well as with the DLC87/HILO cross-sections [43] for comparison. The MCNP-4A code [5] was also used with the cross-sections of carbon, iron and lead which were based on the ENDF/B-VI high energy file [35] and processed by the NJOY-91.108 code [44]. Neutron production cross-sections with their energy-angle distributions in ENDF/B-VI was substituted as fission cross-sections in order to obtain the neutron multiplicity of neutron production cross-sections as the n-value of fission reactions.

As the source term, for 52-MeV proton experiment the measured angle-dependent source neutron energy spectra were used . While, for 62-MeV proton experiment a point source having a solid angle of 3.14×10^{-4} sr with the measured source neutron energy spectrum was assumed instead of including the collimator in the geometry. The splitting and R ussian roulette methods for both calculations were applied as the variance reduction techniques. The track length estimators, which have the same volume as that of the NE213 detectors, were utilized for neutron flux estimation behind the shields. In the case of the water shield, the point estimator put at the center of the detector was used.

3.1.3 Comparison between experiments and calculations

The measured neutron spectra behind shields are compared with the calculations in Figure 3.1.3 and 3.1.4 for the 52- and 65-MeV proton experiments, respectively.

In the case of carbon, the MORSE/HILO86 calculations well represent the measurements as shown in Figure 3.1.3. The dip around 16 MeV, however, appears in the calculation, because of the overestimation of non-elastic cross-section in HILO86. On the other hand, the MCNP calculation underestimates the measurement in the energy region around 10 MeV and above 22 MeV. The reasons are thought that (1)the secondary neutron energy distribution in ENDF/B-VI is inadequate in the energy region above 20 MeV, (2) the energy points of the 20 MeV intervals for the secondary neutron energy distributions are too coarse and (3)the cross-sections up to 20 MeV in the high energy file are too rough to reproduce the energy spectra. In Figure 3.1.4 all calculations underestimate the measurements in the energy region around 20 MeV. It is thought that the secondary neutron energy distributions are inadequate in the energy region above 40 MeV.

The calculations for the water shields almost agree with the measurements as shown in Figure 3.1.3.

Though the MORSE/HILO calculation for the concrete shields overestimates the measurements in the energy region between 10 and 25 MeV, the overestimation was improved by using HILO86 as shown in Figure 3.1.3. Both calculations, however, slightly overestimate the measurements between 30 and 40 MeV in Figure 3.1.4, but the reason of this discrepancy can not be clarified.

In Figure 3.1.3 the MCNP calculation for the iron shields well reproduces the measurements compared to the MORSE calculations, although it underestimates the measurements up to 8 MeV. The underestimation may be reduced to the same reason as that of the carbon. In Figure 3.1.4 the MORSE calculations with HILO86 and HILO agree with the measurements except for the overestimation of the MORSE/HILO calculation around 20 MeV. On the other hand, the MCNP calculation overestimates the measurement in the energy region above 30 MeV. The reason of this discrepancy can not be clarified from the comparison of the cross-sections in these libraries, because there is small difference of the cross-sections between HILO86 and ENDF/B-VI as shown in Figure 3.1.5.

In Figure 3.1.4 the MCNP calculation for the lead shields is in good agreement with the measurements, while the MORSE calculations overestimate the measurements, because elastic cross-sections are excluded in HILO and HILO86.

3.1.4 Necessary improvements in the calculation

Since some cross-sections in HILO were adjusted with experimental data of elastic scattering and revised in HILO86, the MORSE/HILO86 calculations are in better agreement with the measurements than the MORSE/HILO calculations. Other cross-sections should also be modified by using the experimental data and the cross-section calculations with revised global parameters in order to obtain better agreement for concrete. Moreover, elastic scattering cross-section of lead should be added in HILO86 for shielding calculation.

Improvement on the secondary neutron energy spectra of HILO86 and ENDF/B-VI could make good agreement with the experiments in the case of carbon and iron. More numerical data points in ENDF/B-VI high energy file should also be required in this energy region.

Since the cross-sections in ENDF/B-VI high energy file are given to the limited nuclei of carbon, iron, lead and bismuth, we would like to require the evaluated pointwise nuclear data for other nuclei.

3.1.5 Benchmark experiment to be done

The cross-section measurements are required to evaluate the nuclear data and the global parameters for cross-section calculations. From the view point of integral test of cross-section and acquisition of shielding data, experiments using mono-energetic source neutrons provides information on elastic and non-elastic scattering cross-sections. It is also required experiments using the collimated source neutrons to determine the angular distribution of scattering. We have measured neutron spectra transmitted through iron and concrete shields using quasi-monoenergetic neutron beam at TIARA.

In order to evaluate lateral spread of high energy neutrons in the design of a beam dump and a beam line, benchmark experiment at lateral direction of a collimated neutrons is expected. This kind of benchmark experiment is also expected to be done with high-energy neutrons.

3.2 Benchmark calculation of saturated activities in iron beam stop bombarded by 500MeV proton beam

3.2.1 Experiment

The experiment was carried out at the booster synchrotron of National Laboratory of High Energy Physics. [45] An iron beam stop was bombarded by 500-MeV protons. The cross-sectional plane view of the beam stop is shown in Figure 3.2.1. Activation detectors of Fe, Cu, Al and Au were inserted in the iron beam stop to measure lateral and longitudinal distributions of saturated activities: V-48, Mn -52, Mn-54, Co-56 in Fe-nat, Na-24 in Al-27, Co-58 in Cu-nat and Au-198 in Au-197.

3.2.2 Calculation

The calculated reaction cross-sections of Fe-nat(n,x) V-48, Fe-nat(n,x) Mn-52, Cu-nat(n,x) Co-58 and Al-27(n,a) Na-24 [2] are shown in Figure 3.2.2. Above 20 MeV cross-sections of Fe were calculated by ALICE-P [11]. ALICE-F [46] was used for cross-section calculations of Cu and Al over 20 MeV. Fe-56 and Fe-54 reaction cross-sections up to 20 MeV were referred from ENDF/B-VI [35], while Al-27 from JENDL-3 [9].

The HETC-3STEP [12] code was used in the neutron and proton energy range above 20 MeV. The HETC-3STEP code is a modified version of HETC [47] in the HERMES [48] code system, in which the exciton model is included between the cascade and evaporation models. In the HETC-3STEP calculation, neutron cut off energies were 19.6 MeV and elastic scattering was taken into account for protons and neutrons. Because Al-27(n,a) Na-24 reaction is dominant in the energy region below 20 MeV, MORSE-CG [41] in the HERMES code system was used for the neutron flux calculation up to 19.6 MeV with neutron group cross-section library HILO86R [49]. The HILO86R library is a modified version of HILO86 [42], in which neutron cross-sections below 19.6 MeV are based on JENDL-3 with self-shielding factors. Track length estimator was applied for neutron flux calculations.

A geometry used in the calculation is shown in Figure 3.2.3. There is an air gap between the beam catcher and the shielding box. 500-MeV proton beams parallel to the z-axis are incident to the origin in Figure 3.2.3, having the profile of 6.0 cm (FWHM) in horizontal and 3.0 cm (FWHM) in vertical direction. The saturated activities of samples inserted in the beam catcher were calculated in regions

given in Table 3.2.1. The densities of iron, aluminum and copper were 7.80, 8.96 and 2.70 g/cm ^{3}, respectively.

In the beam catcher (0 cm < r < 20 cm, -20 cm < z < 35 cm), high energy protons mainly contribute to nuclide production, and high energy neutrons produced by protons have also some contribution to it. Therefore, saturated activities in the beam catcher were estimated from yields of residual nuclide calculated with HETC-3STEP. For the Al-27(n,a) Na-24 reaction, saturated activities were calculated with neutron flux in the detector region given in Table 3.2.1 and the neutron reaction cross-section shown in Figure 3.2.2. All the saturated activities in the shielding box were also calculated with neutron flux in the detector region and the neutron reaction cross-section. Neutron flux in copper and aluminum samples was assumed to be equal to that in the iron sample.

3.2.3 Comparison between Calculation and Measurement

The calculated results of the Fe-nat(n,x) V-48 reaction are compared with the measurements in Figure3.2.4(a). In the beam catcher, the calculated saturated activities are about a half of the experimental data. On the contrary, the calculated results at r=0 cm and z=12.5 cm are about 10 times larger than the experimental data. In the shielding box, the calculated results are about 2 to 3 times larger than the experimental results.

Figure 3.2.4(b) shows the calculated and the measured results of the Fe-nat(n,x) Mn-52 reaction. The calculations of the saturated activities in the beam catcher are up to about 3 times larger than the experimental data. Similarly as the Fe-nat(n,x) V-48 reaction, the calculated results at r = 0 cm and z = 12.5 cm are large by a factor of about 20 of the experimental data. The calculated results in the shielding box are also about 5 times larger than the measured ones.

Figure 3.2.4(c) shows the calculated and the measured results for the Cu-nat(n,x) Co-58 reaction. For this reaction, the calculated results underestimate the measurements both in the beam catcher and the shielding box.

Figure 3.2.4(d) shows the calculated and the measured results for the Al-27(n,a) Na-24 reaction. The calculated results at 2.5 cm < z < 40 cm well reproduce the experimental results. At the region (z > 40 cm), the calculated results are about 2 to 4 times larger than the experimental data.

For almost all the reactions, the calculations of the saturated activities are large by a factor of about 2 to 5 of the experimental results. As an exception, the calculated results of the Cu-nat(n,x) Co-58 reaction are smaller than the experimental results.

3.2.4 Required data and methods

It is difficult to estimate the accuracy of the cross-section data calculated by the HETC-3STEP and ALICE codes, because there are only a few experimental data for these reactions. Thus, it is necessary to measure neutron induced activation cross-sections in the intermediate energy region. In the intermediate energy region, proton induced activation cross-sections are also important.

Measurements of neutron energy spectra are required to separately investigate the accuracy of calculation methods of particle transport and nuclear reaction. Most of the experiments with a beam dump have been carried out with proton energy greater than 1 GeV. The same type experiments are also expected to be done at the energy of 100 to 1000 MeV.

Benchmark calculations for various energies and targets are needed for the validation of simulation codes. We have a plan to do benchmark calculation for neutron transmission through concrete around the beam stop for 500 MeV protons [50].

4. Summary

The thick target neutron yields for 256-MeV protons were excellently reproduced by modified versions of NMTC: NMTC-3STEP and NMTC-ISOBAR. In other calculations at the incident energy below 160 MeV, however, NMTC-ISOBAR has given better results than NMTC-3STEP for the calculation of the neutron emitted to very forward direction. The QMD code reproduced the thick target neutron yields for alpha particles better than the HETC-KFA1 code. The underestimation of the QMD code , however, was observed in the energy region above 40 MeV at the forward angles less than 6°. Systematic measurements of thick target neutron yields covering the wide energies, various incident particles and target nuclei are highly required in order to investigate the causes of the discrepancies and to obtain a precise estimation of a source term of the shielding design.

On the other hand, the HETC-3STEP calculations overestimated the saturated activities in the analysis of the beam dump experiment for 500-MeV protons, in spite of excellent reproducibility of thick target neutron yields for protons. We, therefore, require measurements of neutron activation cross-sections in the intermediate energy region for validation of residual nucleus production calculation by the HETC-3STEP and ALICE codes, and measurements of neutron energy spectra around a beam dump to validate the particle transport calculation by the HETC-3STEP code.

In the analysis of photoneutron production, the EGS4 calculations with the photonuclear cross-sections calculated by the MCPHOTO and PICA codes underestimated the measurements by a factor of 3.3, although the calculations remarkably reproduced the shape of the measured neutron spectra. It, however, is difficult to investigate the causes of the discrepancies from this analysis. We require the spectrum measurements of photoneutrons produced by electron beams of several hundred MeV and photonuclear cross-section measurements for validation of the MCPHOTO and PICA codes.

The HILO86 data improved the reproducibility of the neutron spectra transmitted through thick shields except for the lead shield, compared to the HILO data. On the other hand, the ENDF/B-VI high energy file were inadequate because of the rough cross-section data. The ENDF/B-VI high energy file, therefore, should be modified. For the modification the cross-section measurements, especially of secondary neutron energy distribution, are highly required in this energy region. We think shielding experiments along the lateral direction are also useful to obtain information on angular distributions of scattering as well as on design calculations of a beam dump and a beam line. Similar experiments are expected for higher-energy neutrons.

Table 2.1.1. ***Physical characteristics of the stopping-length targets***

Element	Radius (cm)	Thickness (cm)	Density (g/cm^3)
C	8.00	30.00	1.646
Al	8.00	20.00	2.715
Fe	8.00	8.00	7.86
^{238}U	4.00	5.00	18.98

Table 2.2.1 ***Photon energy bin in MeV for Pb calculation***

No.	1	2	3	4	5	6	7	8	
Upper energy	270	260	250	240	230	220	210	200	
No.	9	10	11	12	13	14	15	16	
Upper energy	190	180	170	160	150	140	130	120	
No.	17	18	19	20	21	22	23	24	
Upper energy	110	100	90	80	70	60	50	40	
No.	25	26	27	28	29	30	31	32	-
Upper energy	30	25	20	18	16	14	12	10	5

Table 2.3.1 ***Target dimensions***

Element	Carbon	Iron	Lead
Geometry	Rectangular block		
Width(cm)	15.2	15.4	10.2
Height(cm)	12.7	10.2	10.2
Thickness (g/cm^2)	25.13	34.43	44.65
(cm)	14.73	4.445	3.937

Table 3.2.1. ***Calculated region of saturated activities***

z-direction				r-direction			
experiment	calculation(cm)			experiment	calculation(cm)		
-2.5 cm	-4.0	<z<	-1.0	0.0cm	0	<r<	1
12.5cm	11.0	<z<	14.0	7.0cm	6.25	<r<	7.75
27.5cm	26.0	<z<	29.0	14.0cm	12.5	<r<	15.5
40.0cm	38.5	<z<	41.5	28.0cm	26.5	<r<	29.5
52.5cm	51.0	<z<	54.0	44.0cm	42.5	<r<	45.5
67.5cm	66.0	<z<	69.0	56.0cm	54.5	<r<	57.5
82.5cm	81.0	<z<	84.0				

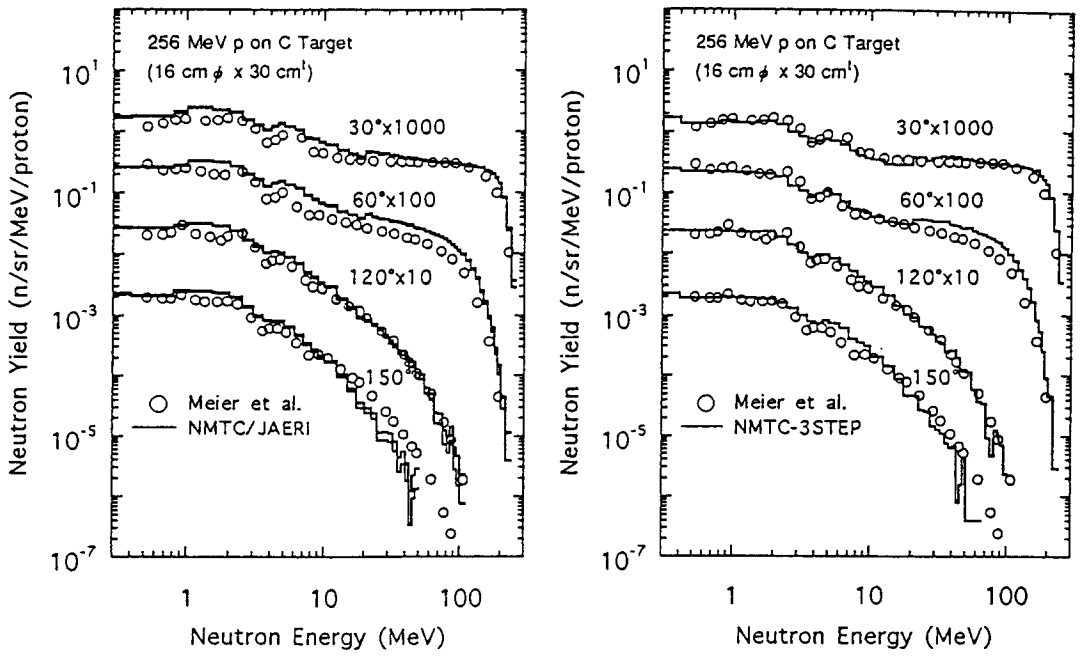

Figure 2.1.1

Neutron energy spectra for 256-MeV proton incident on a stopping-length target of C. The calculated results of original NMTC/JAERI-MCNP-4A code system are shown in the left-hand side, while those of NMTC/JAERI including the preequilibrium process are displayed in the right-hand side. The open circles denote the experimental data taken from [1] and [2]. The solid lines indicate the statistical uncertainties of the calculated results.

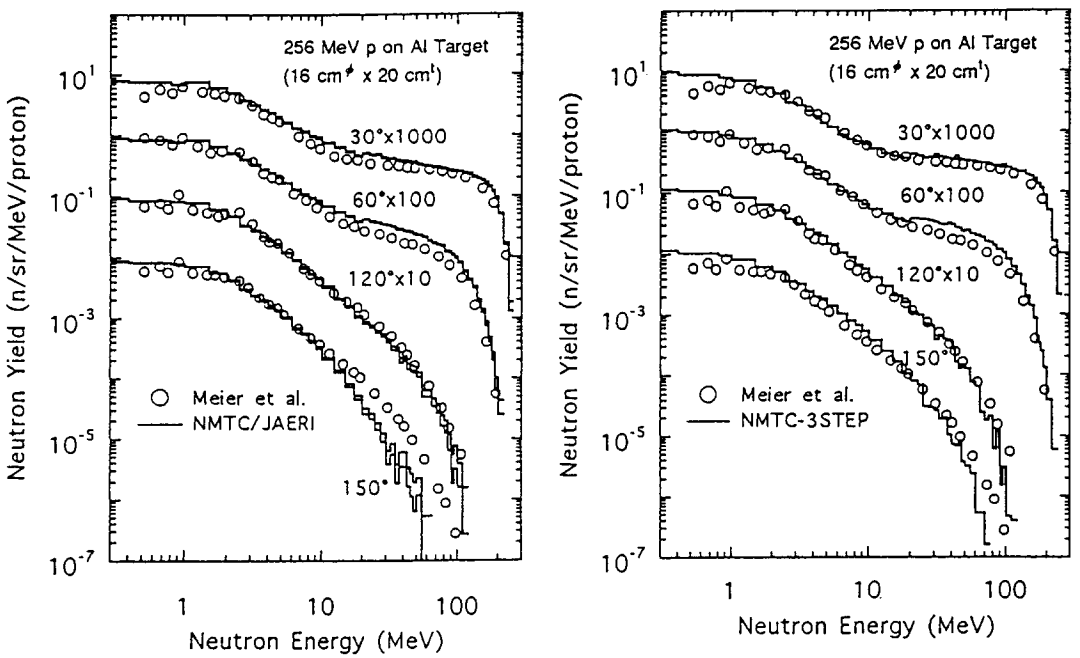

Figure 2.1.2

Neutron energy spectra for 256-MeV proton incident on a stopping-length target of Al. The notes to the marks and the lines are the same as for Figure 2.1.1.

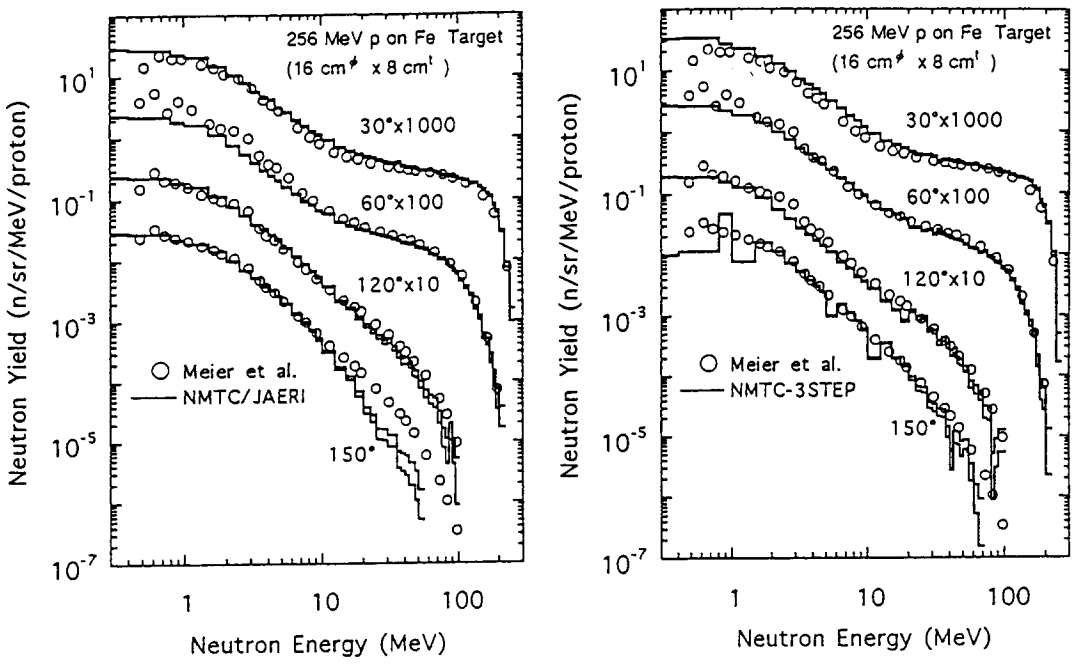

Figure 2.1.3

Neutron energy spectra for 256-MeV proton incident on a stopping-length target of Fe. The notes to the marks and the lines are the same as for Figure 2.1.1.

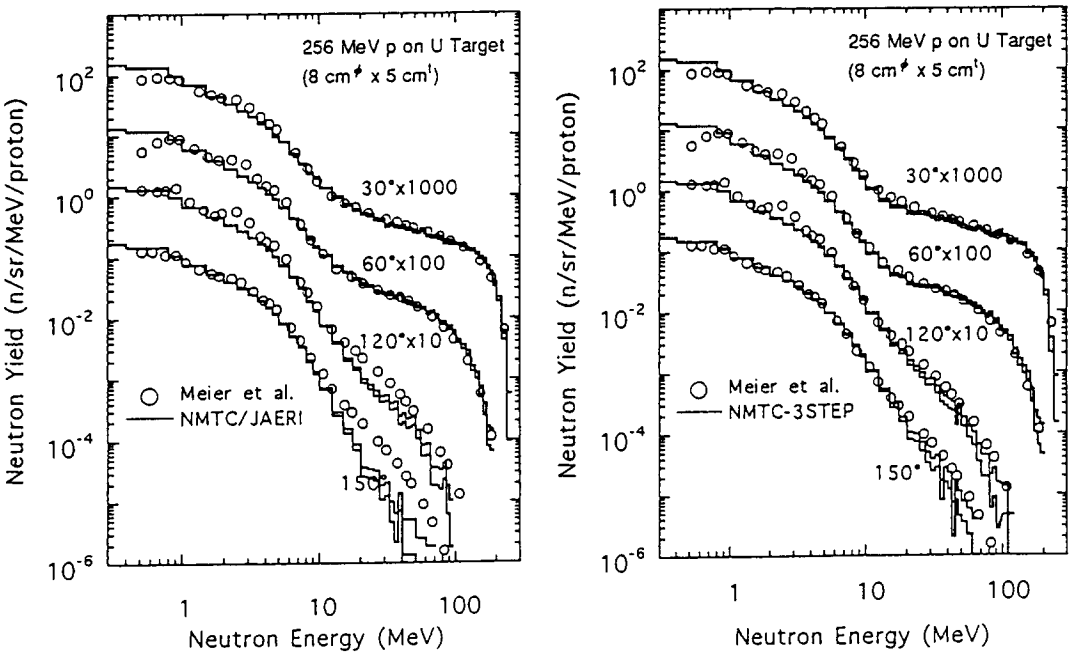

Figure 2.1.4

Neutron energy spectra for 256-MeV proton incident on a stopping-length target of U-238. The notes to the marks and the lines are the same as for Figure 2.1.1.

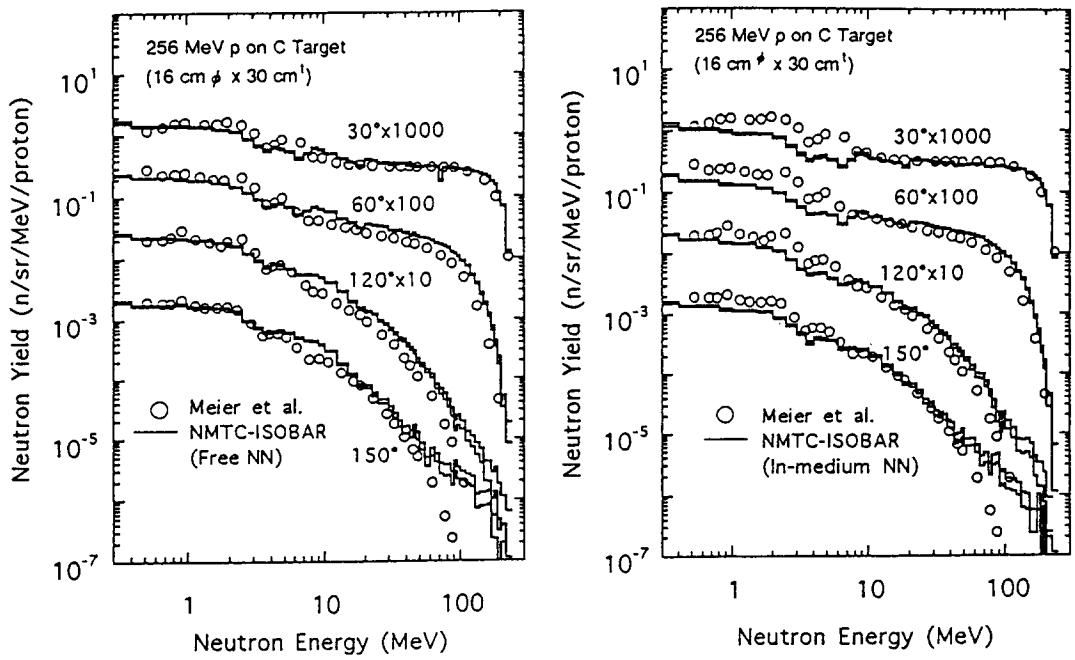

Figure 2.1.5

Neutron energy spectra for 256-MeV proton incident on a stopping-length target of C. The calculated results of NMTC/JAERI-MCNP-4A with ISOBAR code system are shown in the left-hand side, while those including the in-medium NN cross-sections are displayed in the right-hand side. The open circles denote the experimental data taken from [1] and [2]. The solid lines indicate the statistical uncertainties of the calculated results.

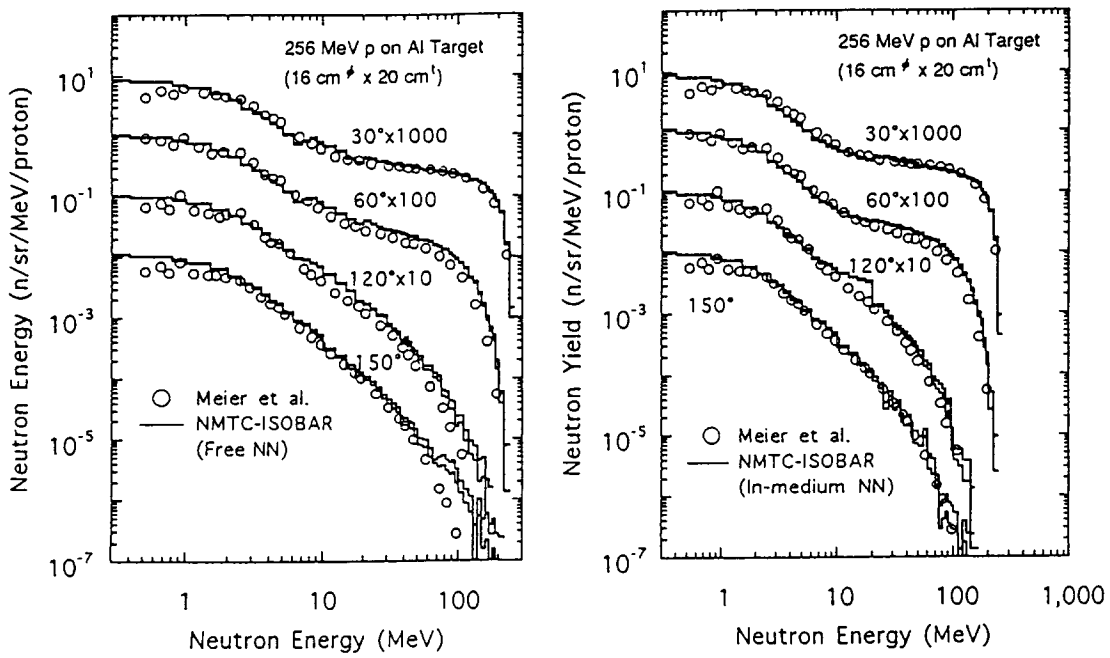

Figure 2.1.6

Neutron energy spectra for 256-MeV proton incident on a stopping-length target of Al. The notes to the marks and the lines are the same as for Figure 2.1.5.

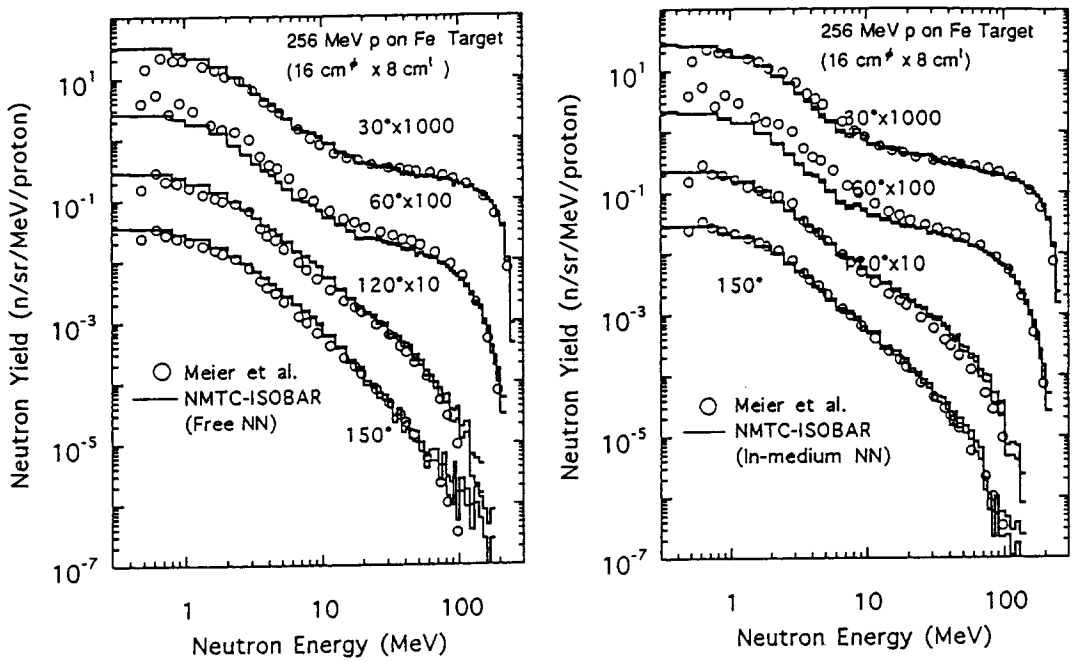

Figure 2.1.7

Neutron energy spectra for 256-MeV proton incident on a stopping-length target of Fe. The notes to the marks and the lines are the same as for Figure 2.1.5.

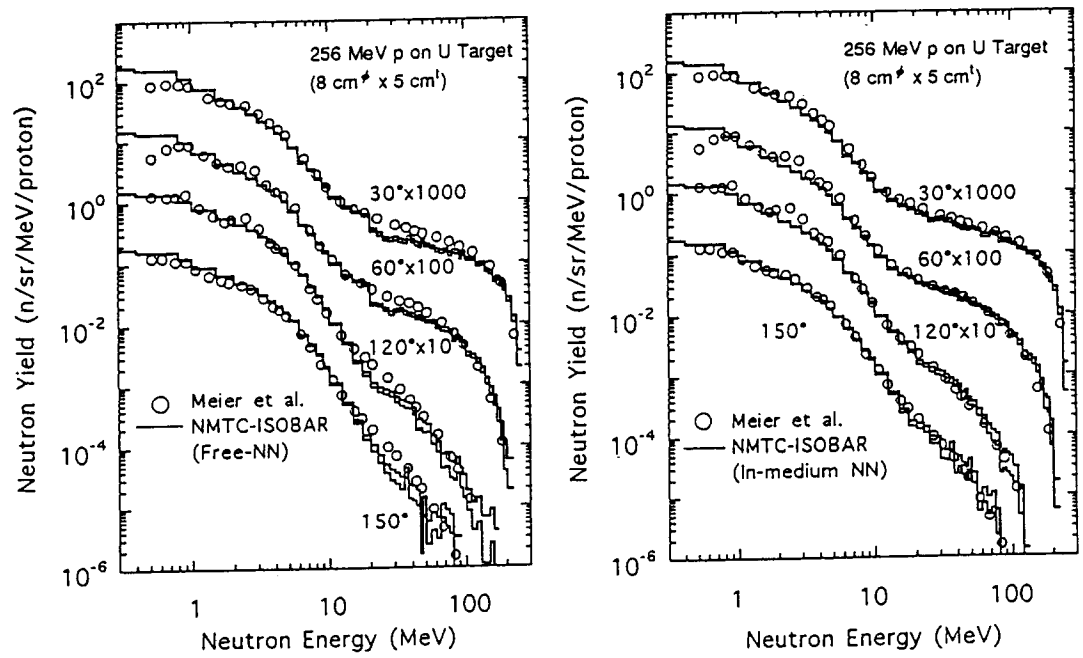

Figure 2.1.8

Neutron energy spectra for 256-MeV proton incident on a stopping-length target of U-238. The notes to the marks and the lines are the same as for Figure 2.1.5.

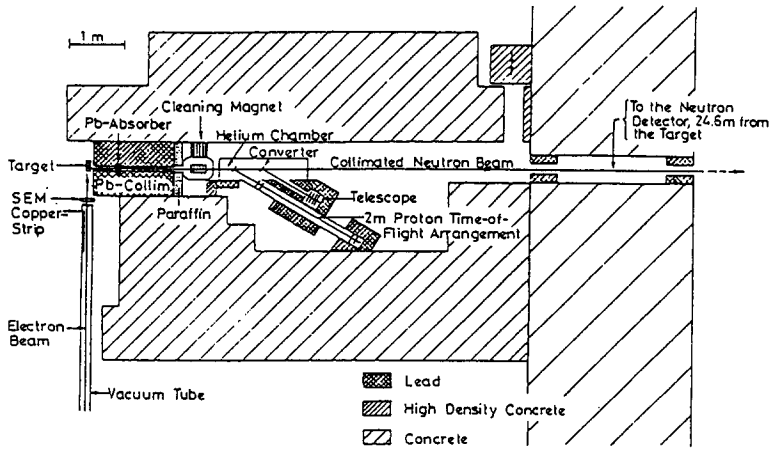

Figure 2.2.1 ***Experiment arrangement***

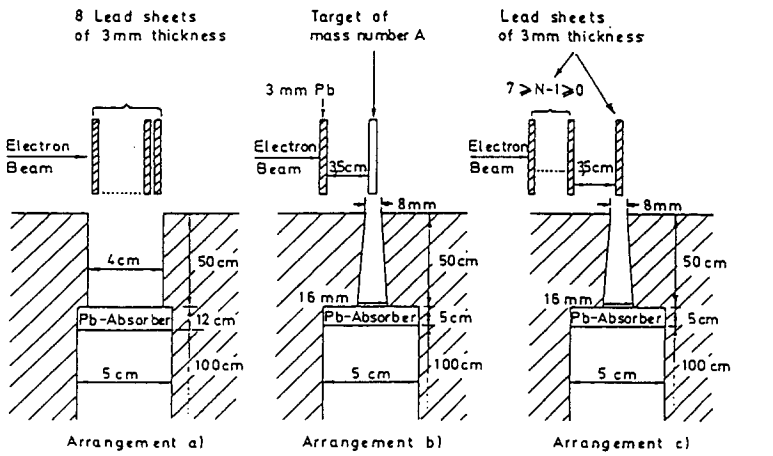

Figure 2.2.2 ***Diagrammatic view of the target and collimator setup***

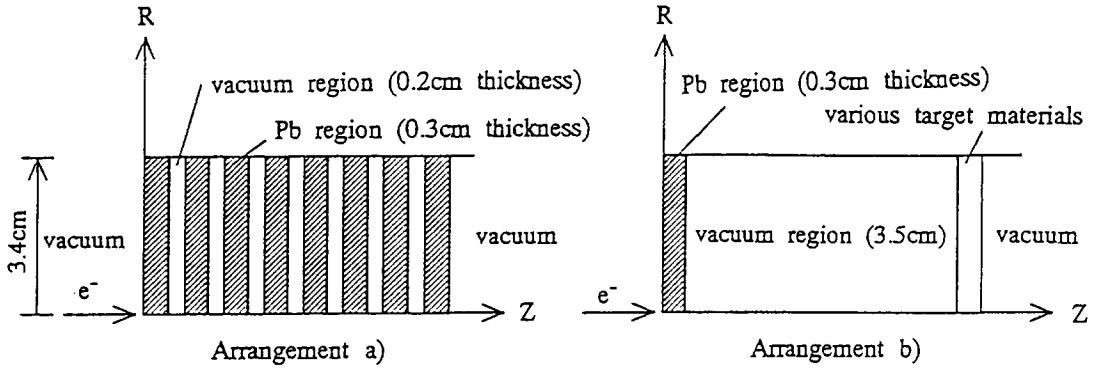

Figure 2.2.3 ***Cylinder-slab geometry for the EGS4 calculation***

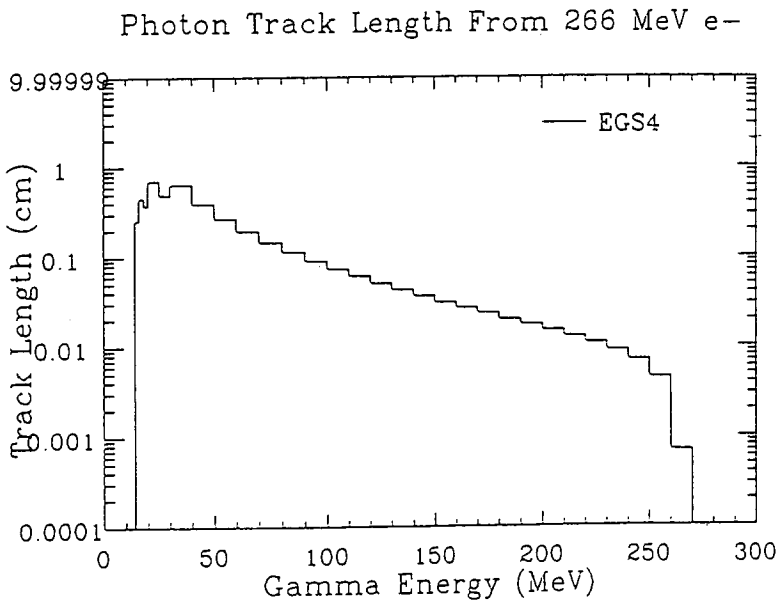

Figure 2.2.4 ***Photon track length on Pb target by 234-MeV electron beam***

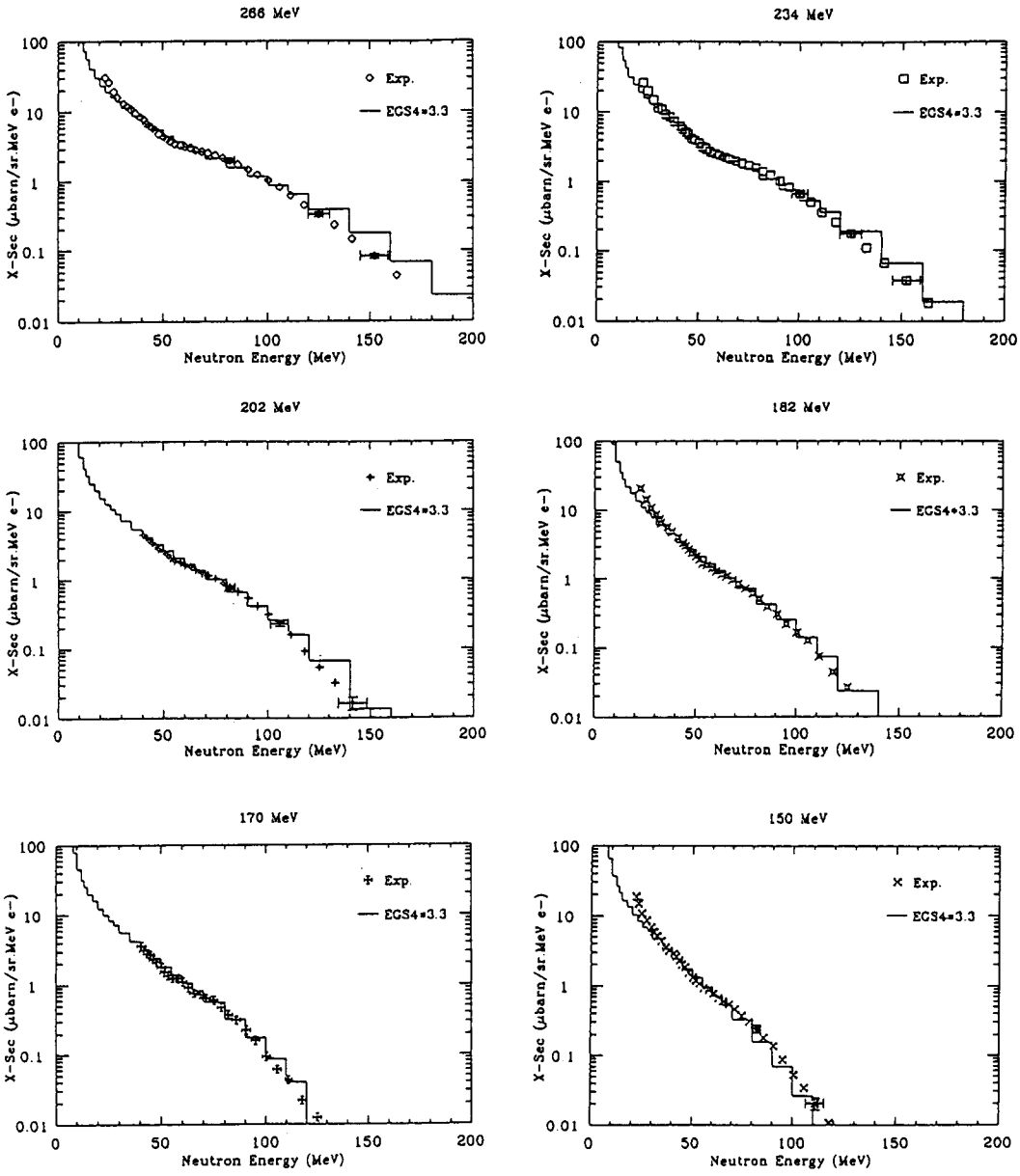

Figure 2.2.5
Comparison of calculation with experiment.
Photoneutron spectra produced by electron beam (150-266 MeV) on lead target

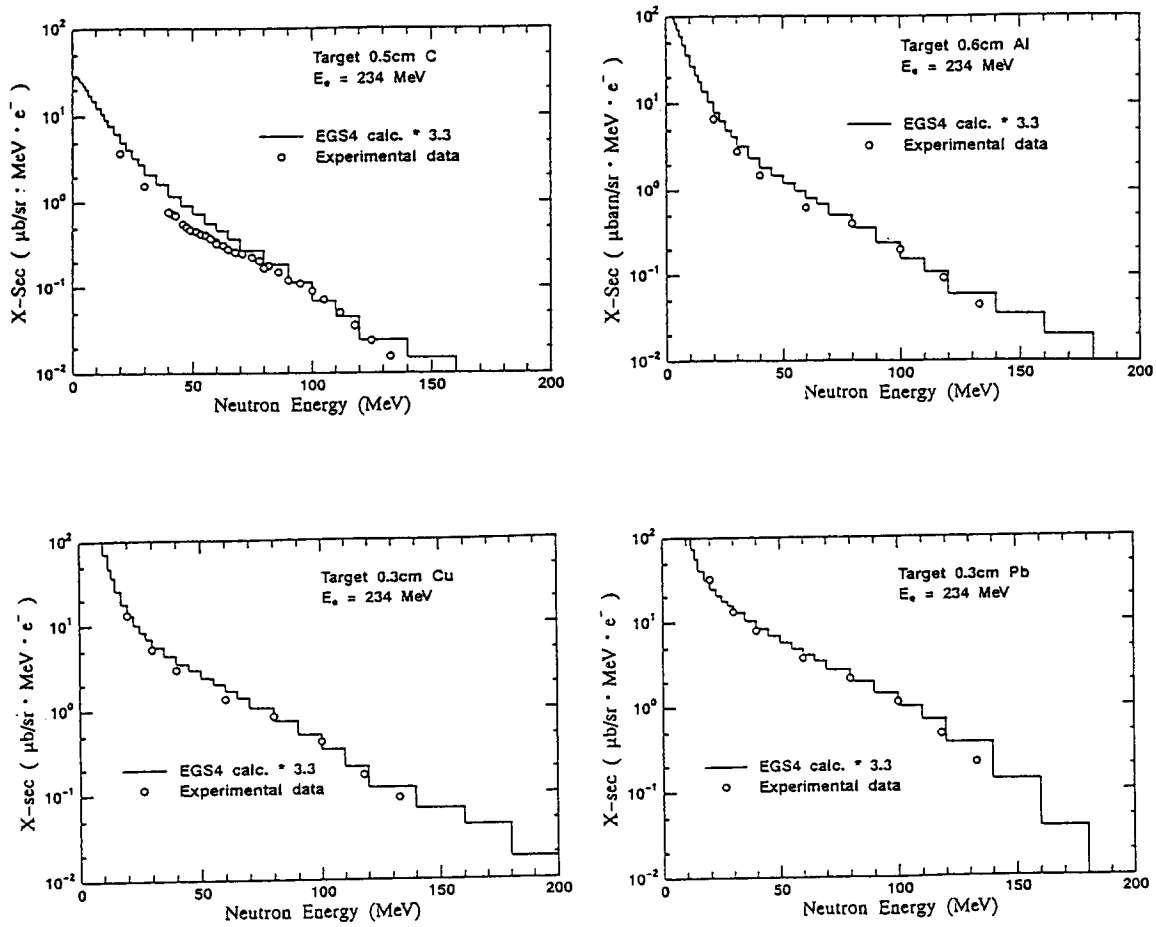

Figure 2.2.6
Comparison of calculation with experiment.
Photoneutron spectra produced by electron beam (234 MeV) on various target

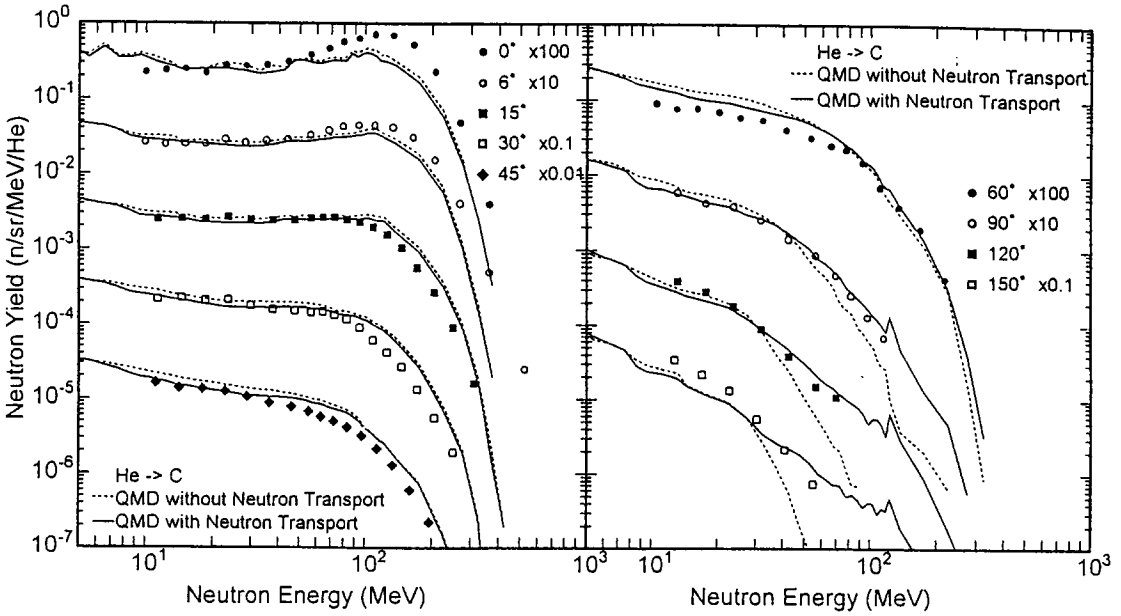

Figure 2.3.1 ***Double differential neutron yields of the carbon target calculated by QMD with and without the calculation of neutron transport in the target***

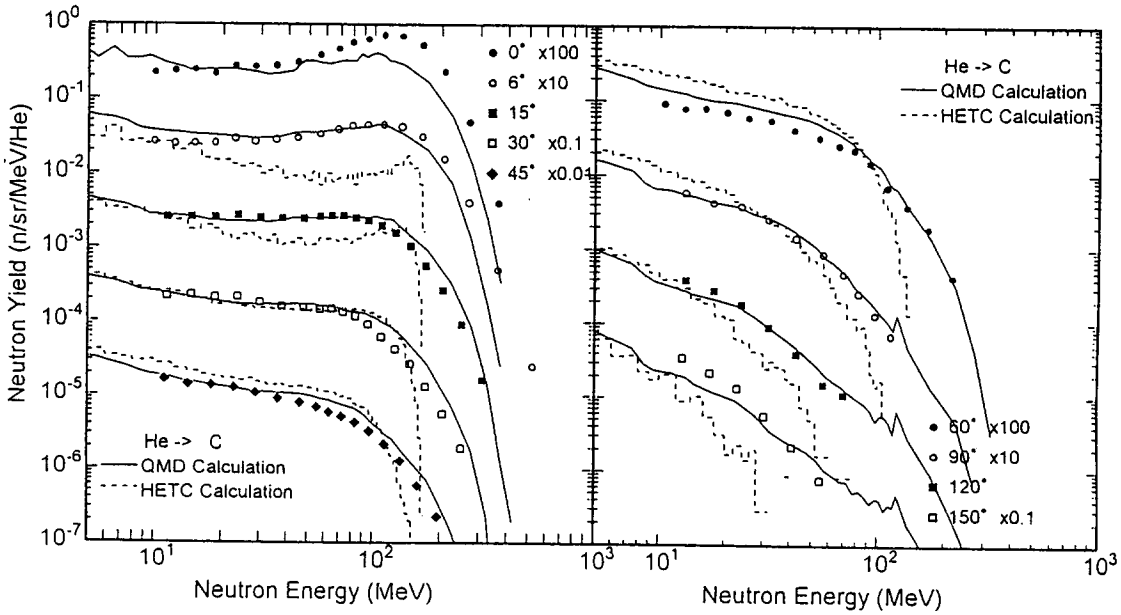

Figure 2.3.2 ***Double differential neutron yields of the carbon target calculated by QMD and HETC-KFA1 codes compared with the experimental data by 710-MeV alpha particles***

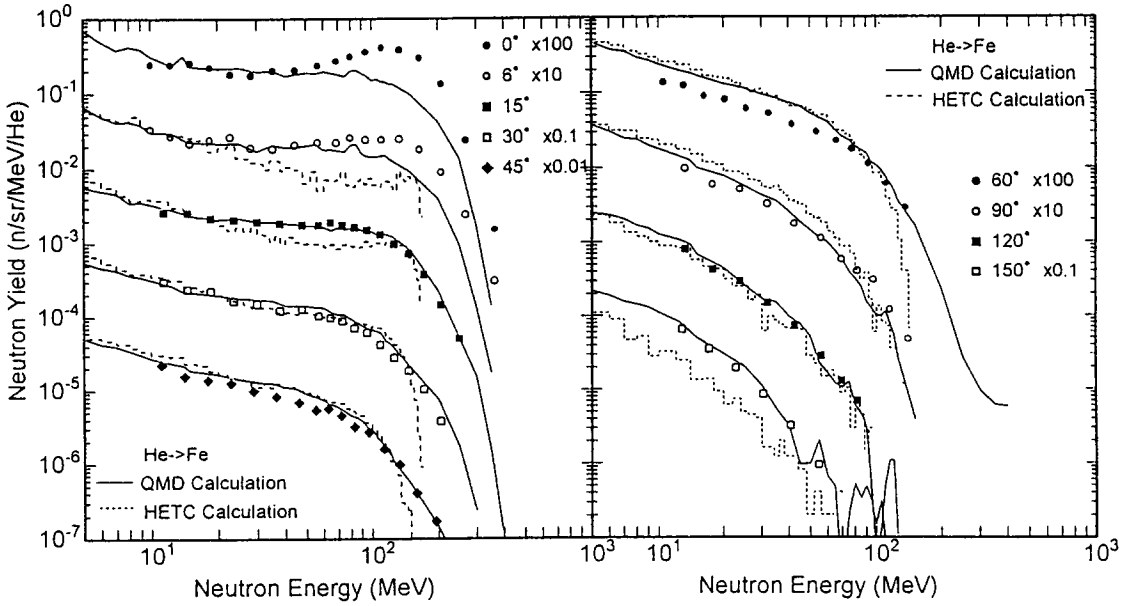

Figure 2.3.3 ***Double differential neutron yields of the iron target calculated by QMD and HETC-KFA1 codes compared with the experimental data by 710-MeV alpha particles***

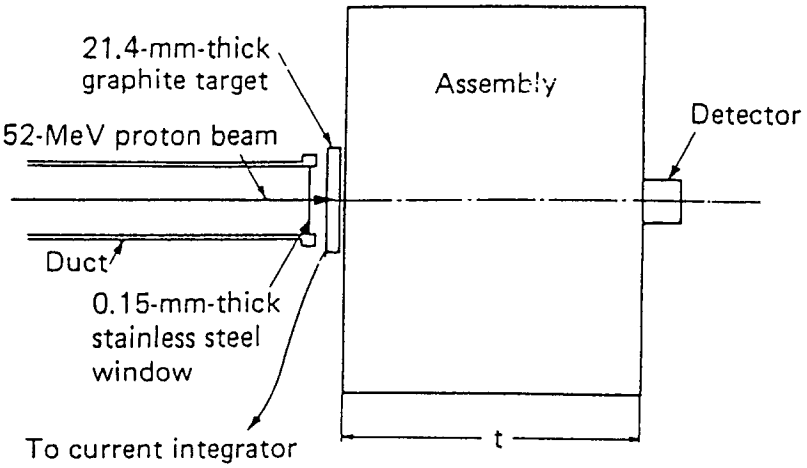

Figure 3.1.1 ***Experimental arrangement for the 52-MeV proton experiment***

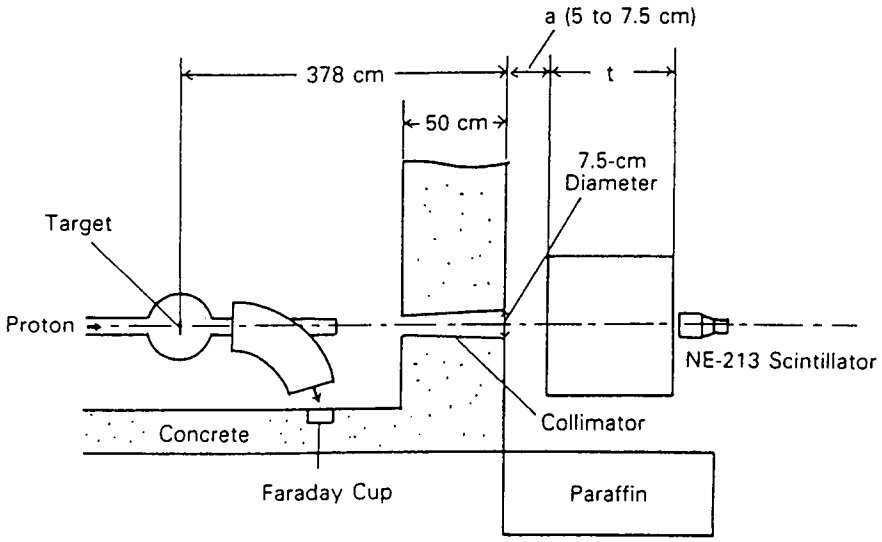

Figure 3.1.2 ***Experimental setup for the 65-MeV proton experiment***

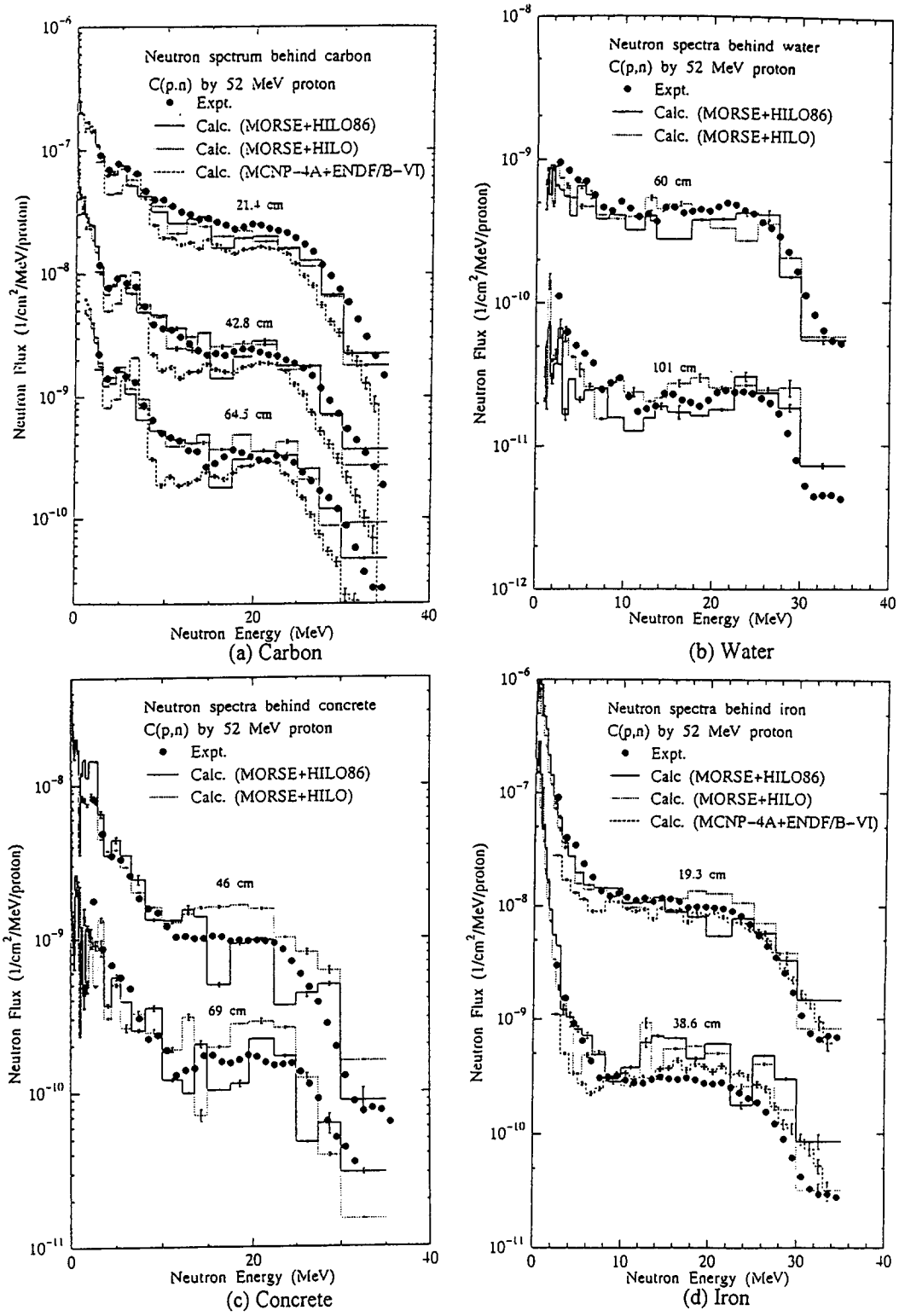

Figure 3.1.3
Comparison of transmitted neutron energy spectra through shields between measurements and calculations for the 52-MeV proton experiment

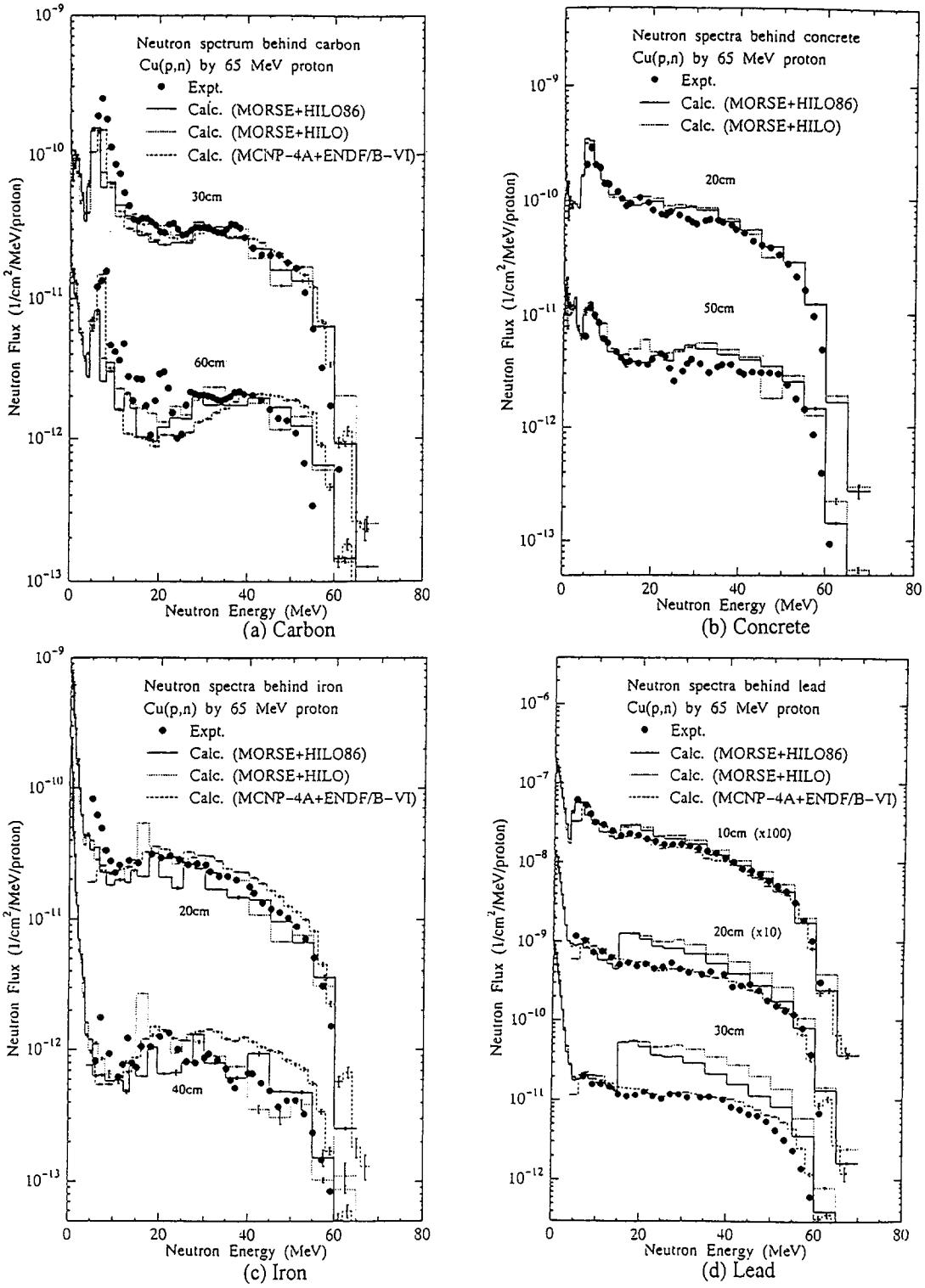

Figure 3.1.4
Comparison of transmitted neutron energy spectra through shields between measurements and calculations for the 65-MeV proton experiment

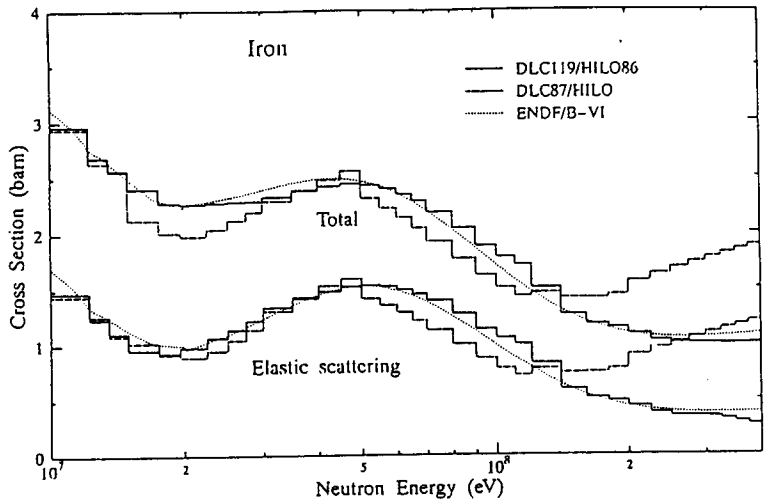

Figure 3.1.5
Comparison of total elastic cross-sections in the DLC87/HILO, DLC119/HILO86 and ENDF/B-VI high energy file

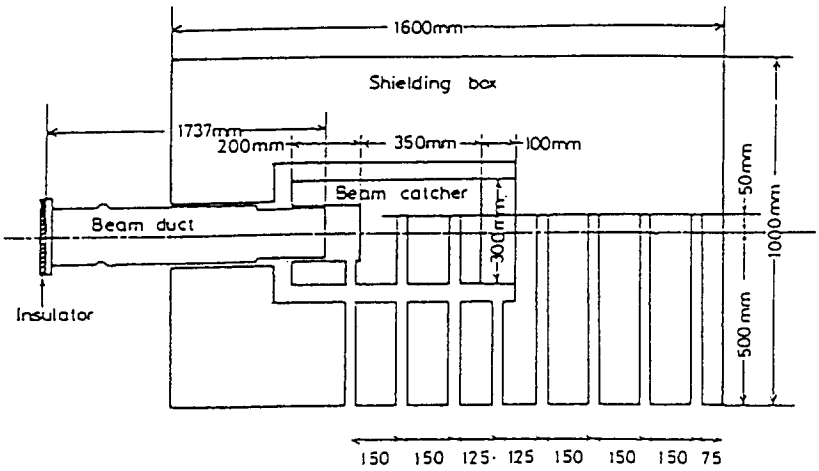

Figure 3.2.1
Cross-sectional plane view of beam stop [45].
Samples were packed in iron pipes and put into the holes which were bored in the beam stop.

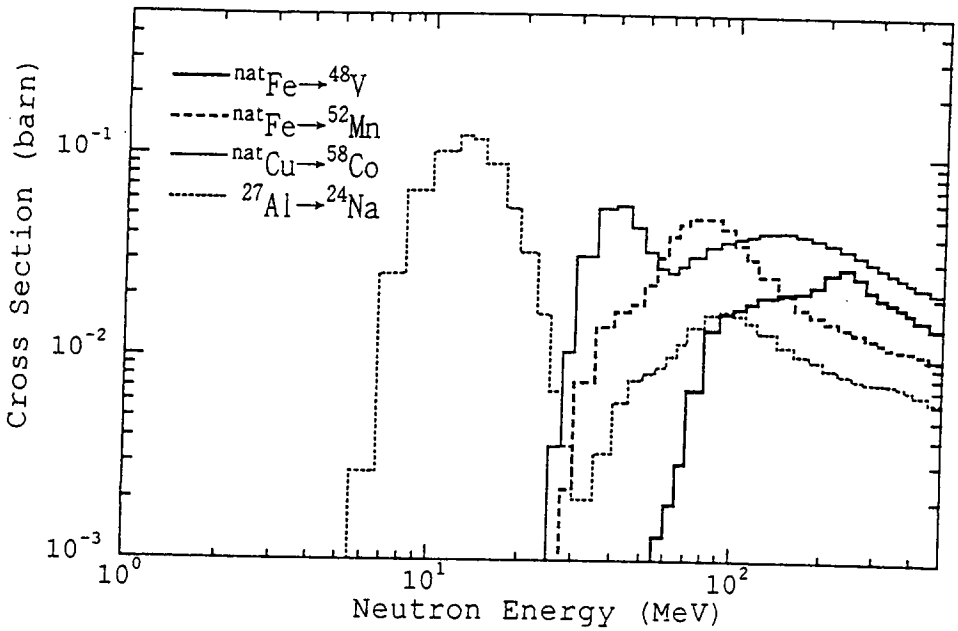

Figure 3.2.2
Calculated neutron cross-sections of
Fe-nat (n,x) V-48, Fe-nat (n,x) Mn-52, Cu-nat (n,x) Co-58, and Al-27 (n,x) Na-24.

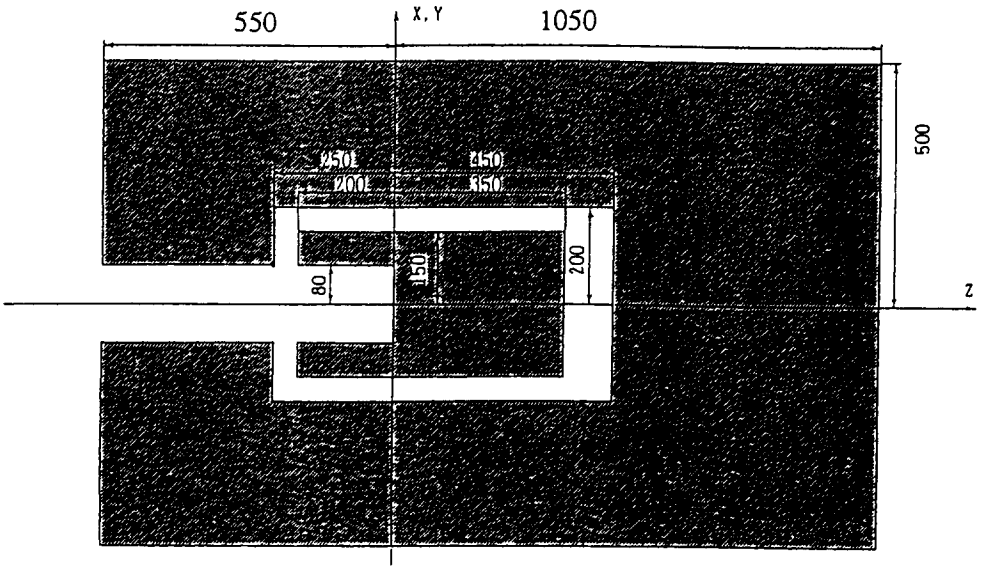

Figure 3.2.3
Geometrical model of the beam stop used in this calculation. The unit in the figure is shown in millimeter.

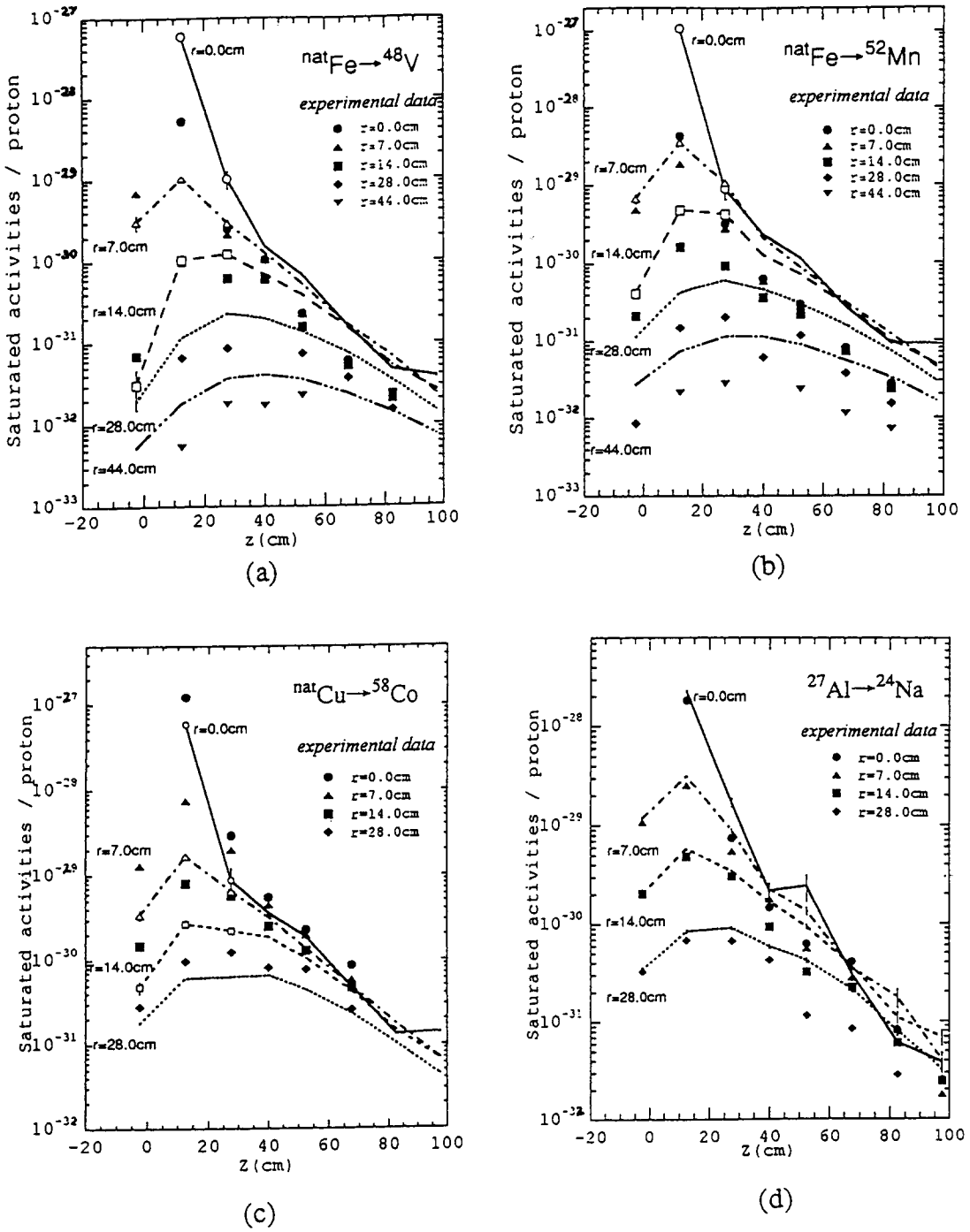

Figure 3.2.4

Calculated saturated activities of V-48 (a), Mn-52 (b), Co-58 (c) and Na-24 (d) in the beam catcher and the shielding box are shown respectively. Lines represent saturated activities calculated with HETC-3STEP and evaluated cross-section. Saturated activities in the beam catcher are calculated with only HETC-3STEP. These results are represented by O, Δ and . For Al-27 → Na-24 reaction, activities induced by high energy proton in the beam catcher were negligibly small.

APPROXIMATE DESCRIPTION OF DOSE ATTENUATION PROFILES OF INTERMEDIATE ENERGY NEUTRONS (I)

Yukio Sakamoto, Hiroshi Kotegawa, Yoshihiro Nakane, Hiroshi Nakashima
Japan Atomic Energy Research Institute
Tokai Research Establishment, Tokai, Ibaraki 319-11, Japan

Akira Hasegawa
Nuclear Power Engineering Corporation
Human Factor Center, Toranomon, Minato-ku, Tokyo 105, Japan

and
Shun-ichi Tanaka
Japan Atomic Energy Research Institute
Uchisaiwai-cho, Chiyoda-ku, Tokyo 100, Japan

ABSTRACT

A macroscopic multigroup cross section library for neutron energies up to 400 MeV, HILO86R was prepared for typical shielding materials. The library is a revision of the DLC-119/HILO86, in which the cross sections below 19.6 MeV have been replaced with group cross sections processed from the JENDL-3 microscopic cross sections and self-shielding factors were used for the production of effective cross sections. Neutron energy spectra and dose attenuation in ordinary concrete and iron have been compared among the results obtained by using HILO, HILO86 and HILO86R for different energy neutron sources. The self-shielding factors in iron cause significant changes of neutron spectra in the energy region below a few MeV and large difference in dose attenuation.

A comprehensive attenuation data of dose equivalent for point isotropic mono-energetic neutron sources up to 400 MeV in infinite shields of ordinary concrete and iron have been obtained by using the ANISN-JR code and HILO86R. The attenuation factors in buildup region were fitted to a 4th order polynomial exponent formula for the use of point kernel codes. Correction factors for the finite effect of shields were also calculated. Effective attenuation length for mono-energetic neutrons in deep penetration has been obtained. It was shown that the attenuation length was strongly dependent upon the penetration length and the Moyer's model using a single attenuation length brought large error in estimating dose behind thick shields for the intermediate neutrons up to 400 MeV.

A point-kernel integral code PKN-H has been developed for the calculations of neutron and neutron-induced-photon dose equivalents for neutron sources up to 400 MeV in ordinary concrete and iron shields of 3-dimensional geometry. If source neutron spectrum was known, dose equivalents behind thick shields in proton accelerators can be estimated easily.

1. Introduction

Multigroup cross section libraries have been widely used for shielding calculations of nuclear facilities with discrete ordinates codes and Monte Carlo codes. DLC58/HELLO [1], DLC87/HILO [2] and DLC119/HILO86 [3] for neutron energies higher than 20 MeV contain microscopic cross sections for each elements and nuclei. The calculations of neutron dose attenuation in iron for a ^{252}Cf neutron source by using ANISN-JR code [4] revealed serious discrepancy between HILO86 and JSD100/120 [5, 6] which was effective macroscopic cross sections prepared by using self-shielding factors. The HILO86R [7], the revision of HILO86, was developed for the calculations of the accurate neutron spectra and dose equivalents even for thick iron shield.

The attenuation data of dose equivalents for 55 neutron energy groups above 0.01 MeV up to 400 MeV have been obtained by using ANISN-JR and HILO86R [8]. The new attenuation factors were fitted to a polynomial exponent formula to represent the dose buildup near a source and the attenuation in deep penetration [8]. Additional correction factors for the finite effects of shields were calculated. The attenuation length [8], which is especially important for shielding calculations of high energy neutrons, has been obtained from the attenuation data and compared with conventional data.

A point-kernel integral code PKN-H [9] has been developed for the calculation of neutron and neutron-induced-photon dose equivalents for neutron sources up to 400 MeV in ordinary concrete and iron shields by using of the attenuation data. With this code, the dose equivalents for infinite and finite shields can be calculated easily. Moreover, the combinatorial geometry (CG) technique is used in the code to represent the source and shield geometries of 3-dimensional configuration. If source neutron spectrum was known, dose equivalents behind thick shields in proton accelerators will be estimated by PKN-H without difficulty .

2. HILO86R Neutron-Photon Multigroup Cross Section Library

HILO86R is a revision of HILO86 with 66 neutron groups for neutron energies up to 400 MeV and 22 photon groups for photon energies up to 20 MeV, and contains macroscopic multigroup cross sections for 10 typical materials; water, ordinary concrete, iron, air, graphite, polyethylene, heavy concrete, lead, aluminum and soil.

The cross section data above 19.6 MeV are the same as in HILO86. Neutron cross sections of 37 energy groups less than 19.6 MeV have been collapsed from 295-neutron and 104-photon group JSSTDL library [10] produced from JENDL-3 cross sections [11] by using of the self-shielding factors. Macroscopic effective cross sections for HILO86R were obtained as the products of infinite dilution cross sections and Bondarenko type self-shielding factors [12] for each material.

Photon production cross sections by neutrons have been not changed from those in the HILO86, while photon cross sections have been condensed from the JSSTDL library by using of a flat weighting spectrum.

Energy spectra and dose equivalent attenuation for point isotropic sources with neutron energies of 50 and 400 MeV in ordinary concrete and iron have been calculated with ANISN-JR by using of HILO, HILO86 and HILO86R. The conversion factors from fluence to dose equivalent were taken from ICRP Publication-51 [13].

Figures 1 and 2 show neutron energy spectra for 50 MeV neutron source at thickness of 100 and 200 cm in ordinary concrete, and show attenuation of neutron and photon dose equivalents.

Difference of neutron energy spectra between the results by using of HILO86 and HILO86R is small. The influence of the different cross section libraries to attenuation of dose equivalent is marginal for ordinary concrete.

Neutron energy spectra at thickness of 100 and 200 cm for 50 MeV neutron source in iron, and attenuation of dose equivalent are shown in Figs.3 and 4. Those for 400 MeV neutron source in iron are also shown in Figs.5 and 6. Difference of energy spectra in iron is remarkable in energy region less than about 10 MeV even for neutron source higher than 19.6 MeV, and increases significantly with penetration. The difference in attenuation of neutron and photon dose equivalents is very large for iron, and the influence of the different cross sections less than 19.6 MeV is significant even for 400 MeV neutron source.

3. Attenuation Data of Point Isotropic Neutron Sources

Attenuation factors of neutron and neutron-induced-photon dose equivalents for monoenergetic neutron sources from 0.01 MeV to 400 MeV in infinite ordinary concrete and iron were calculated by using of ANISN-JR and HILO86R. In Figs.7 and 8 are shown the examples of the attenuation of neutron and neutron-induced-photon dose equivalents for 1st group (375-400 MeV), 5th group (275-300 MeV), 9th group (180-200 MeV), 15th group (90-100 MeV), 22nd group (45-50 MeV) and 29th group (19.6-22.5 MeV) neutron sources in ordinary concrete and iron. These figures suggest that the attenuations, in general, become smaller with increasing neutron energy and approach an exponential decay in deep penetration. The slope of an exponential decay in iron is almost the same independent of source neutron energy.

For the point kernel code PKN-H, the attenuation data in dose buildup region were fitted to a polynomial exponent formula by the following equations,

$$H_j(r)=\frac{\exp(F_j(r))}{4\pi r^2} \quad , \qquad (3.1)$$

where

$$F_j(r)=\sum_{m=0}^{N} a^N{}_{mj} r^m \quad , \qquad (3,2)$$

j is an energy index and $a^N{}_{mj}$ is m-th coefficient of N-order polynomial for j-th source energy. According to the systematic survey for source neutron energy below 20 MeV [14], N=4 has been also chosen to intermediate energy neutrons. The parameter set $a^N{}_{mj}$ was determined by a least square fitting. The fitting error for neutron doses is very small except for thickness less than 5-10 cm and the maximum error is almost within 20 % for the combination of every source energy and shielding material. For neutron-induced-photon doses, the fitting error becomes fairly larger, especially in the region close to source because of steep increase of photons, but it doesn't increase monotonously with penetration depth.

The shields thicker than 8 m for concrete or 5 m for iron have been often employed in high energy accelerators, especially in proton accelerators. Thus, the feature of the attenuation was examined in deep penetration concerning attenuation data. Figures 9 and 10 represent two kind of attenuation length changing with the penetration, where solid lines show the attenuation length obtained by fitting the attenuation data to an exponential function divided by $4\pi r^2$ and broken lines show that obtained by a simple exponential function fitting. In concrete, the attenuation length

shown by broken line approaches more quickly to a constant value, while in iron the solid line converges faster to an asymptotic value. These results suggest that the extrapolation is better to be made based on the different fitting formula for ordinary concrete and iron, as follows:

$$H_j(r) \propto \exp(-\frac{r}{\lambda_0{}^j}) \qquad \text{for ordinary concrete,} \qquad (3.3)$$

$$H_j(r) \propto \frac{\exp(-\frac{r}{\lambda_0{}^j})}{4\pi r^2} \qquad \text{for iron,} \qquad (3.4)$$

where $\lambda_0{}^j$ is the attenuation length for energy group of source neutron j, determined from the attenuation in deeper penetration, where the attenuation length becomes almost constant.

The attenuation factors mentioned above have been calculated in infinite media. Therefore, the dose equivalent obtained using those data becomes overestimation comparing with that for finite ones, which are rather realistic shields. The correction factor is defined as the ratio of dose equivalent behind finite medium to dose equivalent in infinite one at the same penetration, and is calculated for finite thickness of ordinary concrete and iron. The reflection of neutrons in iron is significant, the correction factor attains to 0.23 at 400 cm radius for source neutron of 400 MeV.

4. Attenuation Length

The attenuation of dose equivalent for high energy source neutron has been represented as followed,

$$H(R)=\frac{H_0}{4\pi r^2}\exp(-\frac{r}{\lambda_{eff}}) \qquad (4,1)$$

where λ_{eff} is the effective attenuation length, and it has been shown that the value for ordinary concrete is independent upon the penetration in the range greater than 200 g/cm^2 thickness [15]. As seen in Fig.9, however, the attenuation length λ up to 400 MeV neutrons depends on the radius up to fairly deep penetration, and a limited value λ_0 of the attenuation length has been determined by Eq.(3.3) for ordinary concrete. Therefore, Eq.(4.1) has to be written using the attenuation length depending on the penetration distance as a following,

$$H(R)=\frac{H_0}{4\pi r^2}\exp(-\frac{r}{\lambda(r)}) \qquad (4,2)$$

where λ (r) is equivalent to the effective attenuation length at radius r. The inverse of λ (r) at distance r is defined as the differentiation of $-\ln\{r^2 H(r)\}$ vs r, and subsequently it is related to λ_0 for ordinary concrete as

$$\lambda(r)=\frac{\lambda_0}{1-2\frac{\lambda_0}{r}} \qquad (4,3)$$

The attenuation length λ (r) for ordinary concrete consists with the attenuation length λ_0 where the radius is enough large to neglect the $2\lambda_0/r$. The attenuation length at 300, 500, 1000 cm thickness and infinite thickness in ordinary concrete are compared in Fig.11. The figure presents clearly that the attenuation length in ordinary concrete doesn't become constant for neutron energy at least up to 400 MeV. Figure 11 shows also the effective attenuation length recommended by Thomas et al. [15], calculated values by Alsmiller et al. [16] and Wycoff et al. [17] and the

measured values by Gilbert et al. [18] Other calculated values agree almost with the present attenuation length at 500 cm radius calculated in spherical geometry. λ_0 reveals the attenuation length for infinite thick ordinary concrete.

In Fig.12, the attenuation length λ_0 in iron is shown with other data. The effects of self-shielding factor in resonance energy region below 1 MeV is serious for the dose attenuation in iron, because the dose equivalent is dominated by neutrons less than 1 MeV in deep penetration even for several hundreds MeV source neutrons [7] . The attenuation length in iron calculated with HILO86R cross section is constant from 1 MeV up to 400 MeV, and nearly equal to the evaluated value for 12 GeV proton incident at KEK [19] , although the value is larger than the measurements of Howe et al. [20] and the estimated value by Stevenson et al. [21]

5. A Point-Kernel Integral Code PKN-H

A point kernel integral code PKN-H [9] is developed for shielding calculations for intermediate energy neutrons up to 400 MeV using the attenuation data of neutron and neutron-induced-photon dose equivalents. Geometrical routine of this program is mainly based on combinatorial geometry (CG) package of QAD-CG program [22] . PKN-H code can calculate the dose equivalent for infinite thickness shields and finite thickness shields using the correction factors of finite effect. The dose equivalents for single-layer shield obtained by PKN-H code are in good agreement with those of ANISN-JR and MCNP.

In the PKN-H code, dose equivalents in multi-layer shields are also calculated by applying the point kernel for a single layer. When the first layer is a hydrogenous shield, the neutron dose with the PKN-H become a little underestimation, while the estimation of neutron-induced-photon dose equivalent is almost reasonable except for 400 MeV neutron source. When hydrogenous shield is arranged for the second layer, the PKN-H calculations overestimate largely.

For the shielding design calculations for proton accelerator facilities, the PKN-H code can be used in junction with source neutron spectra calculated by hadron cascade codes such as HETC [23] and NMTC [24] . Fig.13 shows the preliminary calculation result of a problem which is a copper target surrounded by ordinary concrete shield with 575cm-inner-radius and 900cm-thickness. The neutron yield spectrum from the target to perpendicular direction bombarded by 500 MeV protons was calculated by HETC code for 10cm-diameter and 10cm-long target. Evaluated value by Tesch formula [25] and ANISN calculation for a spherical geometry are also shown in Fig.13. The result by PKN-H code is almost similar with other data in whole thickness of ordinary concrete.

6. Summary

A neutron-photon macroscopic cross section library HILO86R for shielding calculations of intermediate energy neutron has been presented by revising the cross sections below 19.6 MeV in the HILO86. Comprehensive comparisons of neutron energy spectrum and attenuation of dose equivalent between the results obtained by using of HILO86R and other libraries, HILO86, HILO and JSD100/120, made clear the significant effect of self-shielding factors in resonance energy region.

The attenuation of dose equivalents for a point isotropic source in ordinary concrete and iron have been calculated for 55 neutron energy groups from 0.01 to 400 MeV by using of the revised

cross section library HILO86R. These attenuation data were fitted to a 4th order polynomial exponent formula having an exponential term for extrapolation. In the Moyer model for neutron shielding in high energy accelerators, the dose attenuation of neutron above 150 MeV is represented by exponential decay with an attenuation length independent of neutron energy. This special feature wasn't satisfied for source neutrons in the intermediate energy up to 400 MeV.

A point kernel integral code PKN-H has been developed for the easy calculations of the neutron and neutron-induced-photon dose equivalents up to 400 MeV neutron sources which have volume. For the shielding design calculations for proton accelerator facilities, the PKN-H code can be used in conjunction with source neutron spectra obtained by hadron cascade codes and measurements.

REFERENCES

1) R.G.Alsmiller,Jr. and J.Braish : "Neutron-Photon Multigroup Cross Sections for Neutron Energies < 60 MeV", ORNL/TM-6486 (1978).
2) R.G.Alsmiller,Jr. and J.Braish : "Neutron-Photon Multigroup Cross Sections for Neutron Energies < 400 MeV", ORNL/TM-7818 (1981).
3) R.G.Alsmiller,Jr., J.M.Barnes and J.D.Drischler : "Neutron-Photon Multigroup Cross Sections for Neutron Energies < 400 MeV (Revision 1)", ORNL/TM-9801 (1986).
4) K.Koyama et al. : "ANISN-JR, A One-Dimensional Discrete Ordinates Code for Neutron and Gamma-Ray Transport Calculations", JAERI-M 6954 (1977).
5) ORNL-RSIC Data Library Collection, DLC-51/JSD-100/120.
6) K.Koyama, Y.Okumura, K.Furuta and S.Miyasaka : "Multi-group Cross Section Sets for Shielding Materials -100 neutron groups and 20 gamma-ray groups in P_5 approximation", JAERI-M 6928 (1977) (In Japanese).
7) H.Kotegawa, Y.Nakane, A.Hasegawa and S.Tanaka : "Neutron-photon Multigroup Cross Sections for Neutron energies Up to 400 MeV : HILO86R - Revision of HILO86 Library -", JAERI-M 93-020 (1993).
8) H.Kotegawa, S.Tanaka, Y.Sakamoto, Y.Nakane and H.Nakashima : "Attenuation Data of Point Isotropic Neutron Sources up to 400 MeV in Water, Ordinary Concrete and Iron", JAERI-Data/Code 94-003 (1994).
9) H.Kotegawa, Y.Sakamoto and S.Tanaka : "PKN-H : A Point Kernel Shielding Code for Neutron Source Up to 400 MeV", JAERI-Data/Code 95-004 (1995).
10) A.Hasegawa : "Development of a Common Nuclear Group Constants Library System : JSSTDL-295n-104 γ Based on JENDL-3 Nuclear Data Library", Nuclear Data Science and Technology, pp.232, Springer-Verlag (1991).
11) K.Shibata, T.Nakagawa and T.Asami : "Japanese Evaluated Nuclear Data Library, Version-3 -JENDL-3-", JAERI-1319 (1990).
12) L.P.Abagyan et al. : "Group Constants for Nuclear Reactor Constants", Consultants Bureau, N.Y. (1964).
13) ICRP Publication-51 : "Data for Use in Protection Against External Radiation", (1987).
14) H.Kotegawa and S.Tanaka : "Attenuation Data of Point Isotropic Neutron Sources in the Shielding Materials of Water, Concrete and Iron", JAERI-M 90-174 (1990) , (in Japanese).
15) R.H.Thomas and G.R.Stevenson : "Ragiological Safety Aspect of the Operation of Proton Accelerator", Technical Reports Series No.283, IAEA, Vienna (1988).

16) R.G.Alsmiller,Jr. et al. : "Shielding Against Neutrons in the Energy Range 50 to 400 MeV", Nucl. Instrum. Methods, 72, P.213 (1969).
17) J.M.Wycoff and A.G.Chilton : "Dose due to Practical Neutron Energy Distributions Incident on Concrete Shielding Walls", Proc. 3rd Int. Conf. IRPA (W.S.Snyder ed.), Rep. CONF-730907-P1, p.694 (1973).
18) W.S.Gilbert et al. : "1966 CERN-LRL-RHEL Shielding Experiment at the CERN Proton Synchrotron", UCRL-17941 (1968).
19) S.Ban et al. : "Measurement of Traverse Attenuation Lengths for Paraffin, Heavy Concrete and Iron around an External Target for 12 GeV Protons", Nucl. Instrum. Methods, 174, p.271 (1980).
20) H.J.Howe,Jr. et al. : "On the Shielding of the External Proton Tunnel Area of Argonne's Zero Gradient Synchrotron", ANL-7273 (1966).
21) G.R.Stevenson et al. : "Determination of Traverse Shielding for Proton Accelerator Using the Moyer Model", Health Phys., 43, p.13 (1982).
22) V.R.Cain : "A User's Manual for QAD-CG, the Combinatorial Geometry Version of the QAD-P5A Point Kernel Shielding Code", Bechtel Computer Code - NE007 (1977).
23) K.C.Chandler and T.W.Armstrong : "HETC Monte Carlo High Energy Nucleon Meson Transport Code", RSIC CCC-178.
24) W.A.Coleman and T.W.Armstrong : "The Nucleon-Meson Transport Code NMTC", ORNL-4606 (1970), RSIC CCC-161.
25) K.Tesch : "A Simple Estimation of the Lateral Shielding for Proton Accelerators in the Energy Range 50 to 1000 MeV", Radiation Protection Dosimetry, 11, p.165 (1985).

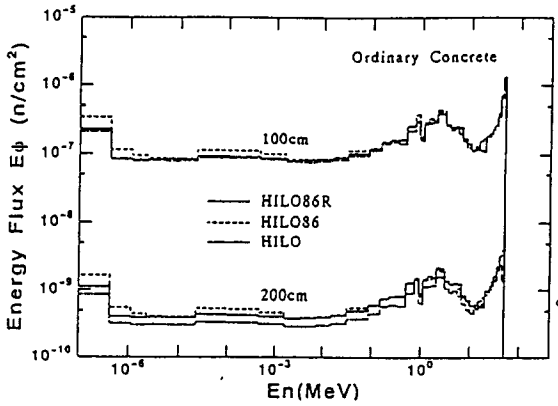

Figure 1

Energy spectra at thichnesses of 100 and 200 cm in ordinary concrete for 50 MeV neutron source

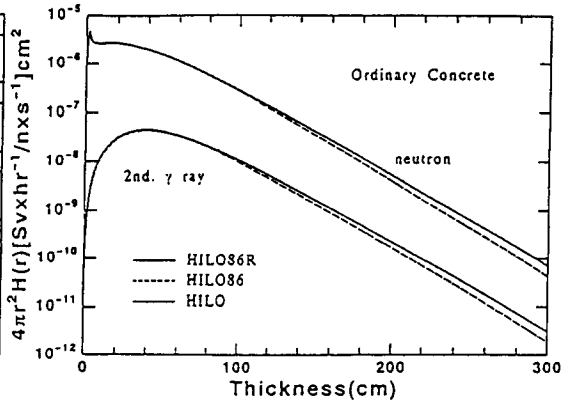

Figure 2

Attenuation of dose equivalent in ordinary concrete for 50 MeV neutron source

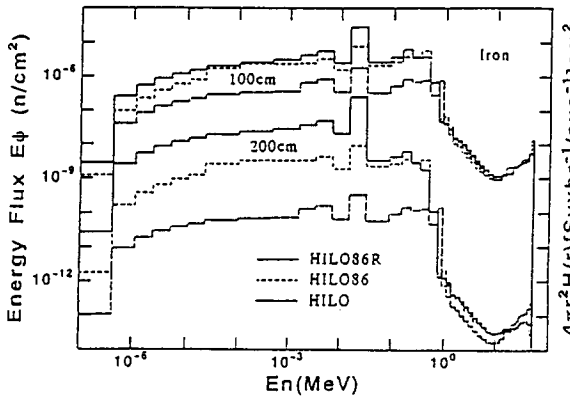

Figure 3

Energy spectra at thichnesses of 100 and 200 cm in iron for 50 MeV neutron source

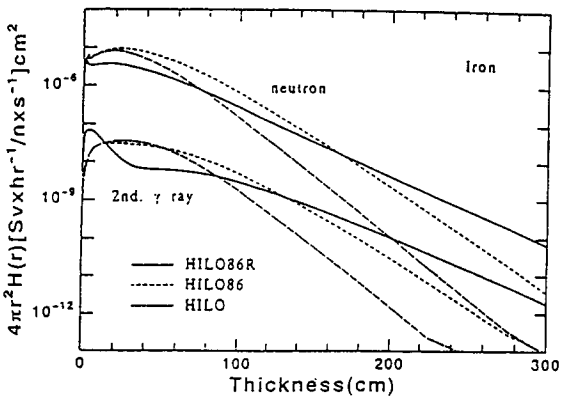

Figure 4

Attenuation of dose equivalent in iron for 50 MeV neutron source

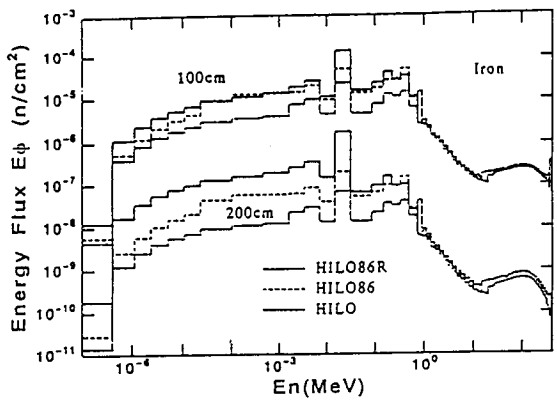

Figure 5
Energy spectra at thichnesses of 100 and 200 cm in iron for 400 MeV neutron source

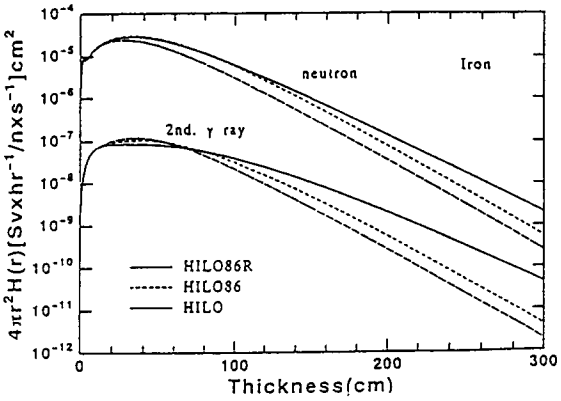

Figure 6
Attenuation of dose equivalent in iron for 400 MeV neutron source

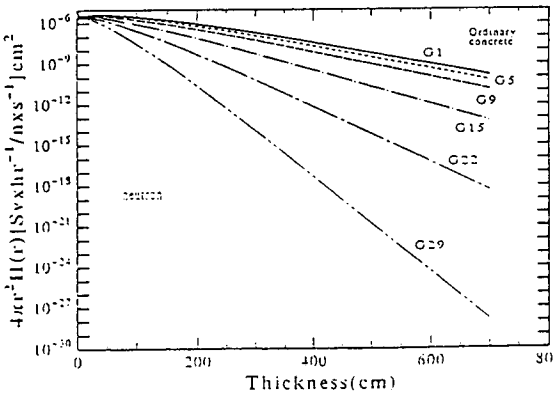

Figure 7
Neutron dose equivalent in ordinary concrete for monoenergetic neutron sources
G1: 375-400, G5: 275-300, G9: 180-200 MeV
G15: 90-100, G22: 45-50, G29: 19.6-22.5 MeV

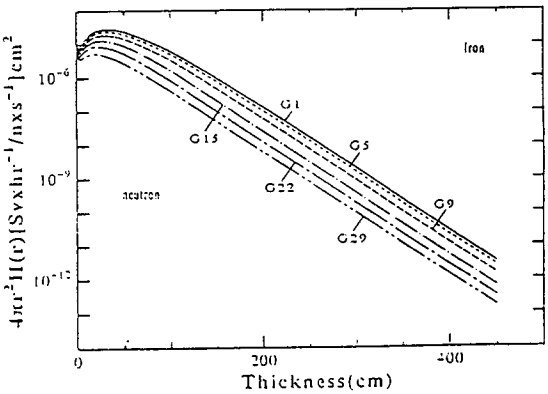

Figure 8
Neutron dose equivalent in iron for monoenergetic neutron sources
G1: 375-400, G5: 275-300, G9: 180-200 MeV
G15: 90-100, G22: 45-50, G29: 19.6-22.5 MeV

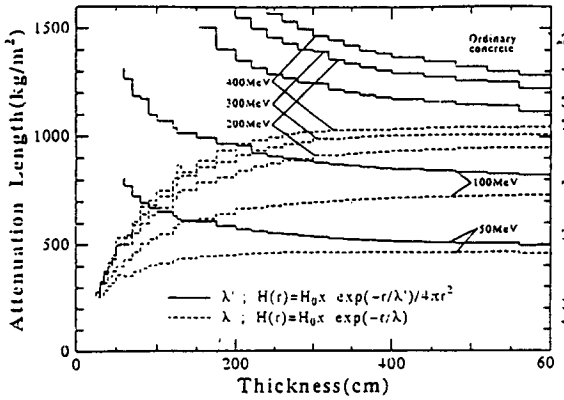

Figure 9

Attenuation length vs. thichness for different source energies in ordinary concrete

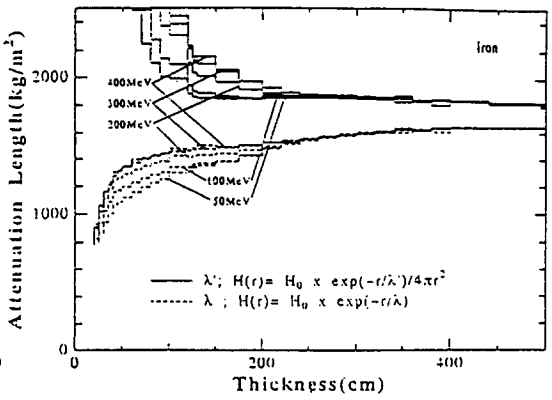

Figure 10

Attenuation length vs. thichness for different source energies in iron

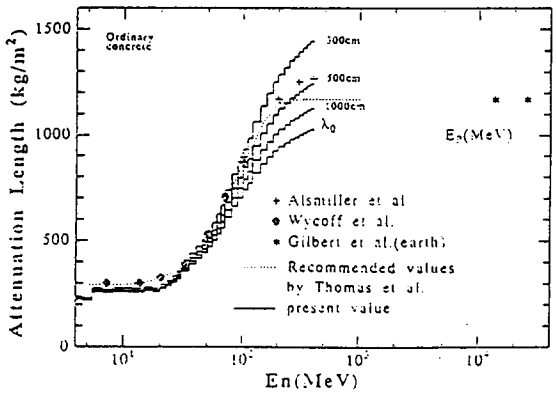

Figure 11

Energy dependence of attenuation length obtained at different thickness in ordinary concrete, in which other data are compared. Gilbert et al.'s data denotes for 14.6 and 26.4 GeV/c protons.

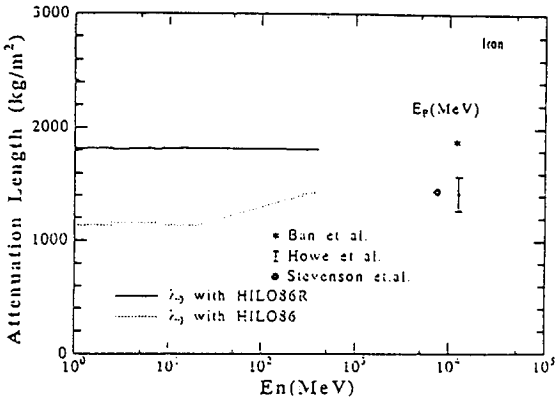

Figure 12

Energy dependence of attenuation length obtained in iron, in which other data are compared. Experimental data by Ban et al. and Howe et al., and evaluated data by Stevenson et al., were given for incident proton energy in MeV.

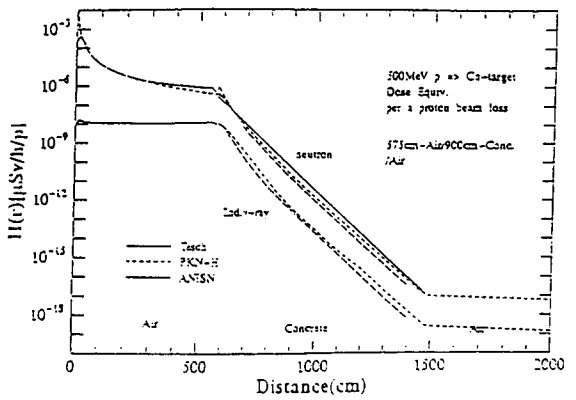

Figure 13

Test calculation of dose equivalent for p-Cu target bombarbed by 500 MeV protons

APPROXIMATE DESCRIPTION OF DOSE ATTENUATION PROFILES OF INTERMEDIATE ENERGY NEUTRONS (II)

Kazuo Shin
Department of Nuclear Engineering, Kyoto University,
Yoshida, Sakyo-ku, Kyoto 606-01, Japan

Hiroshi Kotegawa
Japan Atomic Energy Research Institute, Tokai Establishment
Tokai, Ibaraki 319-11, Japan

Yoshitomo Uwamino
The Institute of Physical and Chemical Research,
2-1 Hirosawa, Wako, Saitama 351-01, Japan

Syuiti Ban, Hideo Hirayama
National Laboratory for High Energy Physics,
Oho, Tukuba, Ibaraki 305, Japan

Susumu Tanaka
Japan Atomic Energy Research Institute, Takasaki Establishment,
1233 Watanuki, Takasaki, Gunma 370-12, Japan

Abstract

A new phenomenological method was developed for describing the dose equivalent profiles in shields of concrete, iron and double-layered shield of iron+concrete for monoenergy neutrons up to 400 MeV in a way analogous to the gamma-ray buildup factors. Neutron buildup factors were parameterized by empirical expressions. Systematics of the parameters in the expressions and removal cross sections which were used instead of the linear attenuation coeficients in gamma-ray cases, were examined regarding the neutron energy. Attenuation lengths for monoenergy neutrons at higher energies of 0.8 and 1.5 GeV were estimated. They were strong functions of the depth.

1 Introduction

Estimation of the neutron dose attenuation in thick shields is of importance for accelerator shielding. The estimations of neutron dose are usually made by simplified empirical formulae, like Moyer model. Unfortunately except for high energies, such formulae are still not well established, although many formulae were proposed for neutrons in the medium energy range.[1-9]

It was listed in agreed actions of the 1st specialists' meeting at Arlington, 1994, to examine the definition of attenuation length and source term for medium energy neutrons. Correspondingly, a working group was set up in Japan. The group met four times, and reviewed existing litertures on the empirical expression of neutron dose attenuation profiles in shields. The discussions were made frankly on present status of the neutron attenuation length, the limitation of the present neutron dose estimation formulae, possible alternative ways to describe the dose equivalent profiles, parameterization of the thick target differential neutron yields, and the practical shielding method which should be constructed in Japan.

It was agreed that, in the shielding design needed is a quick calculational method such as point kernel code, which incorporates simple estimation methods of dose attenuations for monoenergy neutrons, thick target differential neutron yields data, and a geometry routine which handles the 3-dimensional geometrical complexity. And hopefully it includes a routine that visualizes results of the calculation together with the geometry.

The problem was how well the neutron dose profiles in thick shields could be reproduced by a simple way in the point kernel method. It is known that the attenation length at higher energies in the medium energy range becomes larger than the high energy limit, which needs extended reexamination of the definition of the attenuation length, or even the way of describing the dose attenuation profiles. It was recognized that the neutron dose attenuation length below 400 MeV is a strong function of the depth.

Therefore, we decided to consider alternative methods of decribing the attenuation profiles rather than to modify the values of attenuation length. Since a double-layered shield of iron followed by concrete is often used in accelerator facilities rather than an iron monolayer, new methods should have a capability of describing the profile in the above double-layered shield as well as those in the concrete and iron monolayers.

From these considerations, we selected three methods to be examined as alternative methods for describing the neutron attenuation profiles; (1)one method that defines a buildup factor as a function of depth based on the removal cross section of neutrons at the source energy, (2)another one which describes fast neutron doses in the three group approximation by a single exponential formula in each energy group, and (3)the last method that describes the total dose

by a single exponential function with the attenuation length being a function of depth. The third method has been already incorporated in a point kernel code PKN[10], which has been developed in JAERI. The thick target differential neutron yields are newly included in the code through this work.

The energy range of the examination is tentatively limitted to below 400 MeV, where HILO86R data library[11] is available. Materials are restricted to concrete, iron and a double layer of iron followed by concrete. To test the attenuation length of monoenergy neutrons beyond 400 MeV, we also made HETC/KFA2[12] calculations at two energies of 0.8 and 1.5 GeV for thick concrete and iron shields.

The 3rd method, the outline of the PKN code and their results are reported separately[13] in this meeting. The 2nd method is still in the process of the parameter testing, and their results are not described here.

This report is organized as followed. In section 2, the results of the examination of the 1st method will be described. Section 3 is for the fast neutron dose attenuations above 400 MeV calculated by the HETC/KFA2. The last section is for summary.

2 Description of Dose Attenuation Profiles by Removal Cross Sections and Buildup Factors

2.1 Objectibves and Method of Dose Equivalent Calculation

The purpose of the work is to provide a new alternative method for the parameterization of neutron dose attenuation profiles in a way analogous to gamma-ray buildup factors. It should be emphasized that the introduction of the new method is to enable one to describe the profiles in the double-layered shield of iron+concrete with a combination of parameters of iron and concrete.

The calculations of the neutron dose equivalent were made by ANISN/HILO86R for a point isotropic source of unity intensity at energies 2, 10, 50, 100, 200, 300, 350, and 400 MeV. The 1-cm depth dose in ICRP-51[14] was used to convert the fluence to dose equivalent. Since the ANISN calculation needs less computing time, it is suited for this kind of a trial study which needs calculations for many cases. The material configurations of the calculations are listed in Table 1.

2.2 Results of the Calculation

2.2.1 Attenuation of Dose Equivalent and Neutron Fluxes

The attenuation of neutron dose equivalent is considered to be dominated by fast neutrons in concrete, but in iron the dominant component may be different, which may affect the dose profile in a double-layered shield of iron+concrete. To test this point, dose attenuation profiles in the materials are compared with corresponding ones of neutron fluences at various energies. An example for iron is showed in Fig.1 for a 400-MeV case, where the normalization is made at 100-cm depth. In concrete, neutron fluences except for the source energy decrease with the same slope, which quite well agrees with that of the dose equivalent. On the other hand, as is showed in Fig.1, the slopes of the curves are different in iron for neutrons at the source energy, fast neutrons above resonance energy and slow neutrons below the resonance. The dose attenuation is largely affected by the slow neutrons in iron.

The neutron dose equivalent at 50 MeV in concrete, iron and iron+concrete is showed in Fig.2. The slope of the dose attenuation curves is almost the same for both the iron and concrete. However, in the double-layered shield, the neutron dose equivalent attenuates very quickly just after the iron shield, then the slope approaches to that of concrete. For higher energies, the dose attenuation in iron is quicker than in concrete but the trend in the double-layered shield is the same.

2.2.2 Definition of Point Isotropic Buildup Factor and Removal Cross Section

Tentatively we decided the removal cross section of the source neutron to be,

$$\Sigma_r = \Sigma_t - \Sigma_{gg} \quad , \tag{1}$$

where Σ_t is the total cross section, and Σ_{gg} is the ingroup scattering cross section.

Then the pointisotropic buildup factor is defined as a function of depth by Eq.(2):

$$B(r) = \frac{D(r)}{\phi_0(r)\eta_0} \quad , \tag{2}$$

where the fluence of the source neutrons $\phi_0(r)$ is given by,

$$\phi_0(r) = \frac{1}{4\pi r^2} e^{-\Sigma_r r} \quad , \tag{3}$$

where r is the depth in the shield, $D(r)$ the neutron dose equivalent at the depth r and η_0 a neutron fluence to dose conversion factor at the source energy. In Fig. 3 results of $B(r)$ is plotted for the 50 MeV case, where the horizontal axis is the optical thickness; $x = \Sigma_r r$.

In the case of the double-layered shield, the source neutron fluence is given by;

$$\phi_0(r) = \frac{1}{4\pi r^2} e^{-\{\Sigma_1 r_1 + \Sigma_2 (r - r_1)\}} \quad , \tag{4}$$

where r_1 is the thickness of the 1st layer and Σ_i is the removal cross section of the i-th layer.

The buildup factors in concrete of both the monolayer and the double-layered shields come close to each other, but show a slight discrepancy. We considered that this discrepancy arose from an inaccuracy of the removal cross section given by Eq.(1). We considered that the removal cross section should be defined so that the buildup factors in concrete agree with each other. We adjusted the removal cross sections of both iron and concrete to realize the above agreement. The variation in the cross section caused by this process is generally less than 5%. However, for 10 MeV, the variation was $\sim$ 20% for concrete and $\sim$ 40% for iron. At energies higher than 200 MeV, no adjustment was needed.

Eamples of the obtained buildup factors are plotted in Figs.4 through 6 for 400, 50, and 10 MeV, respectively. From these figures, the followings are pointed out. The buildup factor of the double-layered shield of iron+concrete approaches to that of the monolayer concrete via the transient part whose slope is almost the same regardless of the 1st layer thickness. The slope of the transient part in the buildup factor of the double layer shield decreases with energy. At 10 MeV, the transient part extends over very wide region, and the buildup factor of the case of 150-cm iron 1st layer does not reach the concrete one even at 80 mfp thickness.

On the other hand, at 2 MeV, the slope of the transient part of the double layer buildup factor becomes almost parallel to that of concrete. We need to make up a different model at lower energies which correspond to evaporation neutrons. However, in general, the contribution by these low energy neutrons to dose equivalent behind thick shields is not large.

2.3 Parameterization of Buildup Factor

We use the following empirical formula to parameterize the obtained buildup factor.

$$B(x) = 1 + ag(1 - e^{-bx})e^{cx} \quad , \tag{5}$$

where

$$g = \begin{cases} 1 & \text{(concrete)} \\ x & \text{(iron)} \end{cases} \quad , \tag{6}$$

and a, b and c are empirical parameters to be determined by the least squares method.

Obtained parameter values are listed in Table 2. The parameter values in the table vary smoothly with the neutron energy, except for the parameter b of iron which decreases quickly

between 100 MeV and 200 MeV. However, it should be noted that the parameter b affects the buildup factor only at shallow locations.

The buildup factor in the double-layered shield of iron+concrete is given by,

$$B_{1+2}(x_1 + x_2) = B_2(x_1 + x_2) + \{B_1(x_1) - B_2(x_1)\} e^{-\alpha x_2} \quad , \tag{7}$$

and parameter values of α which best reproduces the buildup factor are given in Table 3. The α value decreases with decreasing the neutron energy.

Buildup factors reproduced by Eqs.(5) and (7) are showed by solid lines in Figs. 4 through 6. It is seen that the buildup factors of all the cases including the double-layered shields are very well reproduced by the empirical expresssions (5) and (7).

2.3.1 Systematic in Removal Cross Sections

The removal cross sections are plotted in Figs. 7 and 8 as well as other cross sections, for concrete and iron, respectively. In general, the removal cross section is in between the total and nonelastic cross sections. It approaches to the nonelastic cross section as the energy is increased. However, in concrete, the removal cross section is slightly larger than the nonelastic cross section even at 400 MeV, whereas that of iron is almost the same as the nonelastic cross section at 400 MeV. The elastic scattering in concrete may be still effective to attenuate source neutrons.

3 Attenuation of Higher Energy Neutrons

3.1 Objectives and Calculation Method

To estimate the dose attenuation profiles for monoenergy neutrons at energies higher than 400 MeV, and test the applicability of a single exponential function for describing the dose profiles in thick shields, the dose profiles were calculated for 8-m thick concrete and 5-m thick iron slabs. Calculations were made by HETC/KFA2[12] for neutrons above 15 MeV. The neutron energies were 387.5 MeV, 800 MeV and 1500 MeV.

Monoenergy neutrons with the above energies were injected normally to the slab shields. The shields were divided into 1-m thick slabs, and the calculation was made one by one for each slab from the upstream to the downstream, passing the results to the next calculation. In connecting the calculations, a certain thickness of the slab was overlapped to take into account the reflection effects in the calculation.

Neutron fluxes were estimated by the tracklength estimator at 25-cm intervals. The CPU time needed for each 1-m slab calculation is 30 minutes. The history number of the calculations were 100,000~200,000.

3.2 Neutron Attenuations in Slabs

Examples of calculated energy spectra in the concrete shield are showed in Fig. 9 for 1500-MeV neutrons. It should be noted that the vertical axis is written in lethagy unit. The followings are pointed out for this figure. The spectra get softer with the depth and a broad peak around 100 MeV grows gradually with the depth. On the other hand, the higher energy part above 300 MeV, where the nonelastic cross section is at a minimum value, decreases with the depth. The spectrum shape at the same depth is almost the same for the three energies except for the source energy region.

The neutron fluences($E_n \geq 15$ MeV) are converted to the dose equivalent using ICRP-51 1-cm depth dose, and obtained dose depth profiles are showed in Fig. 10 for all the calculated cases. The profiles have a peak at around 40-cm depth and then decrease following exponential-like curves. However, the dose profile is not expressed by a single exponential function with a constant attenuation length.

The slope of the curves is estimated as an attenuation length dividing the depth into 4 regions, i.e. 300-600, 600-1000, 1000-2000 and 2000-4000 g/cm^2. The results are showed in Fig. 11 as a function of the depth. It is known from the figure that the estimated attenuation length is a very strong function of the shield depth. It is not possible to define a single attenuation length. The estimated attenuation length increases with the neutron energy, although the increasing rate is not large.

4 Summary

1. Neutron buildup factor was defined in the analogous way to gamma-ray ccases.
2. Empirical expressions of the point isotropic neutron buildup factor were obtained for iron and concrete at energies from 10 MeV up to 400 MeV.
3. The buildup factor in double layer shields of iron followed by concrete was expressed by the combination of the buildup factors of iron and concrete.
4. The energy dependence of the empirical parameters of the expressions of buildup factor and removal cross sections are generally smooth functions of the neutron energy.

5. The removal cross section approaches to the nonelastic cross sections at higher energies.

6. The attenuation length for monoenergy neutrons up to 1.5 GeV is a strong function of the depth and a constant attenuation length is not defined.

7. The attenuation length for monoenergy neutrons above 400 MeV is an increasing function of energy.

References

1. S. Ban, H. Hirayama and K. Katoh,"Measurements of Secondary Neutron Fluxes around Beam Stop for 500 MeV Protons", Nucl. Instr. Methods 184, 409 (1981).

2. K. Tesch, "A Simple Estimation of the Lateral Shielding for Proton Accelerators in the Energy Range 50 to 1000 MeV", Rad. Protec. Dosim. 11, 165 (1984).

3. K. O'Brien and J. E. Mclaughlin, "The Propagation of the Neutron Component of the Nuclear Cascade at Energies Less Than 500 MeV: Theory and a Solution to the Accelerator Transverse Shielding Problem", Nulc. Instr. Methods 60, 129 (1968).

4. K. O'Brien, "Tables for the Determination of the Lateral Shielding Requirements of High Energy Electron and Proton Accelerator", IEEE Trans NS-16, 568 (1969).

5. T. Braid, R. F. Rapids, R. H. Siemssen and J. W. Tippie,"Calculations of Shielding for Large Cyclotrons", IEEE NS-18, 82 (1971).

6. K. Shin and Y. Ishii,"Buildup Factors for Medium Energy Neutrons up to 400 MeV", Rad. Protec. Dosim. 40, 185 (1992).

7. A. Fasso, A. Ferrari and G. R. Stevenson, "Forward Shielding for Intermediate-Energy Proton Accelerators", Proc. Spec. Meet. Shielding Aspects of Accelators, Targets and Radiation Facilities, Arlington, Texas 28-29 April 1994, pp.155-162.

8. A. Fasso, A. Ferrari and G. R. Stevenson, "Forward Shielding for Intermediate-Energy Proton Accelerators", Proc. Spec. Meet. Shielding Aspects of Accelators, Targets and Radiation Facilities, Arlington, Texas 28-29 April 1994, pp.155-162, OECD/NEA.

9. D. Filges, R. D. Neef, H. Schaal and B. Wolfertz,"Procedures and Data for Shielding Calculations of Spallation Target Stations and Accelerators in the Medium Energy Range", Proc. Spec. Meet. Shielding Aspects of Accelators, Targets and Radiation Facilities, Arlington, Texas 28-29 April 1994, pp.253-270, OECD/NEA.

10. H. Kotegawa, Y. Sakamoto and S. Tanaka, "PKN-H:A Point Kernel Shielding Code for Neutron Source up to 400 MeV", JAERI-DATA/Code 95-0004 (1995).

11. H. Kotegawa, Y. Nakane, A. Hasedawa and S. Tanaka, "Neutron-Photon Cross Sections for Neutron Energies up to 400 MeV:HILO86R - Revision of HILO86 Library-", JAER-M 93-020 (1993).

12. P. Cloth et al., "HERMES, A Monter Carlo Program System for Beam Materials Interaction Studies", Jul-2203, Kernforschungsanlag Julich GmbH (1988).

13. Y. Sakamoto et al.,"Approximating Description of Dose Attenuation Profiles of Intermediate Energy Neutrons(I)", submitted to this specialists' meeting.

14. ICRP Publication 51. Data for Use in Protection Against External Radiation, Annals of the ICRP 17(2/3) (1987).

Table 1 ***Geometries and energies calculations***

Shields	1st Layer Thickness(cm)	Neutron Energy(MeV)
Concrete	800	2,10,50,100,200,300,350,400
Iron	560	2,10,50,100,200,300,350,400
Iron+Concrete	100,200,300,600	50,100,200,400
Iron+Concrete	50,100,150	2,10

Table 2 ***Empirical parameters in expressions of buildup factors***

Material	Parameter	E_n(MeV)				
		10	50	100	200	400
Concrete	a	90.3	90.3	90.3	90.3	90.1
	b	5.08E-2	4.78E-2	3.63E-2	4.22E-2	4.65E-2
	c	3.49E-2	4.80E-3	-3.41E-2	1.32E-2	1.55E-1
Iron	a	1.31	6.68	13.7	24.7	40.5
	b	2.39	2.41	2.35	1.56	0.6
	c	0.718	0.503	0.32	0.217	0.281

Table 3 ***Values of parameter α***

E_n(MeV)	10	50	100	200	400
α	0.17	1.06	2.30	2.90	2.70

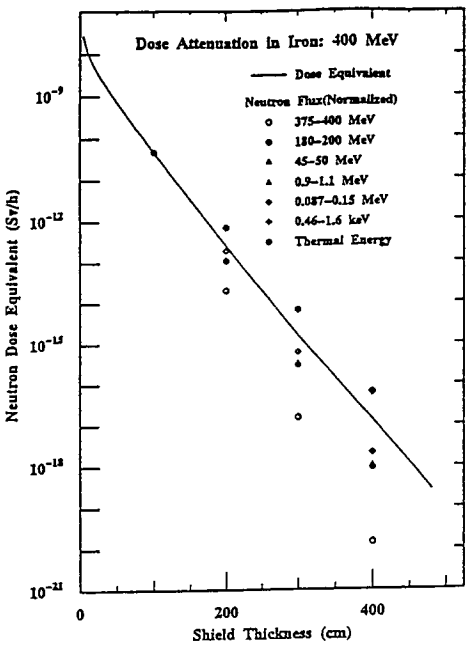

Figure 1 ***Neutron dose attenuation in iron at 400 MeV***

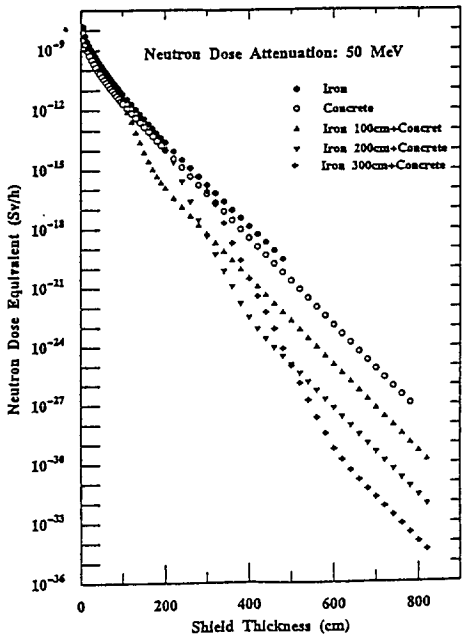

Figure 2 ***Neutron dose attenuation in iron, concrete and iron + concrete shields at 400 MeV***

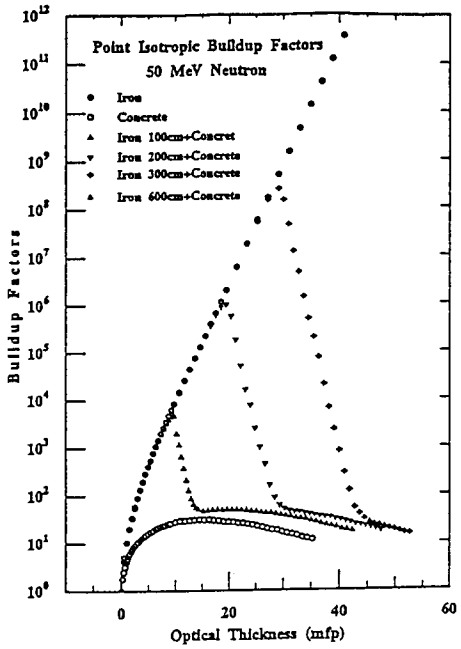

Figure 3 ***Point isotropic buildup factors of iron, concrete and iron + concrete shields at 50 MeV***

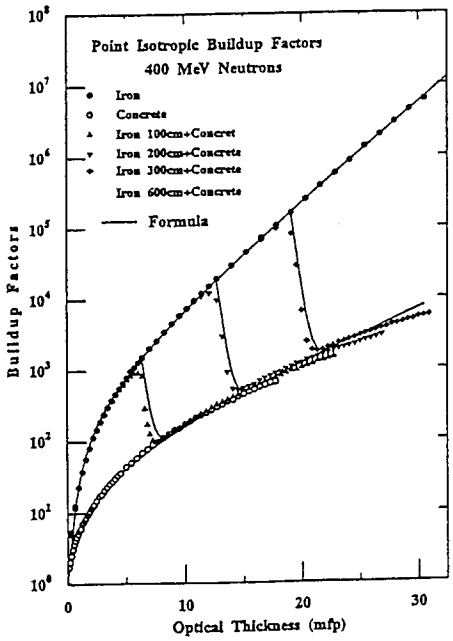

Figure 4 ***Point isotropic buildup factors of iron, concrete and iron + concrete shields at 400 MeV***

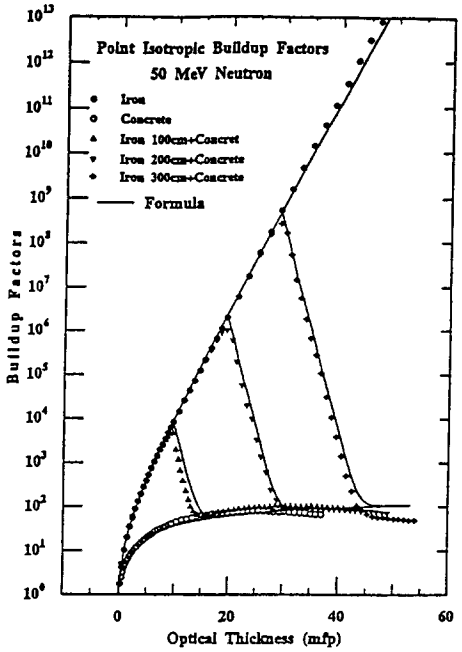

Figure 5 ***Point isotropic buildup factors of iron, concrete and iron + concrete shields at 50 MeV***

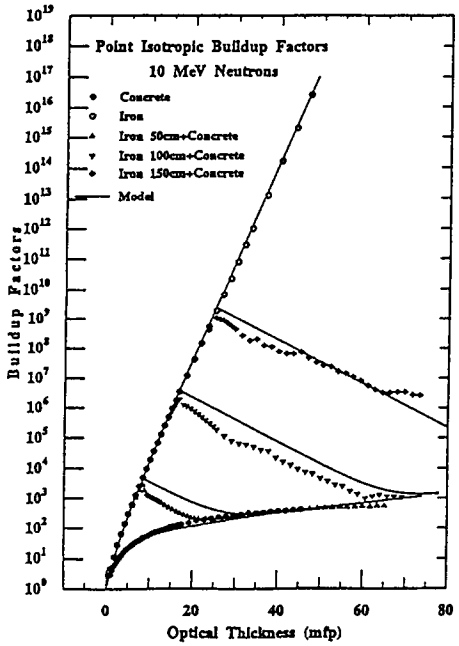

Figure 6 ***Point isotropic buildup factors of iron, concrete and iron + concrete shields at 10 MeV***

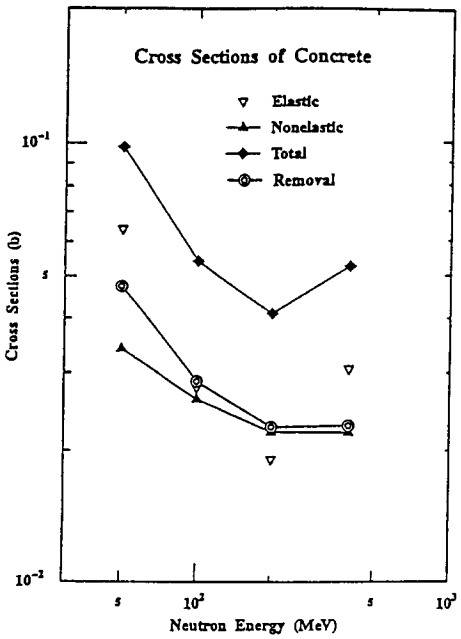

Figure 7 ***Energy dependence of removal, total, nonelactic and elastic cross-sections of concrete***

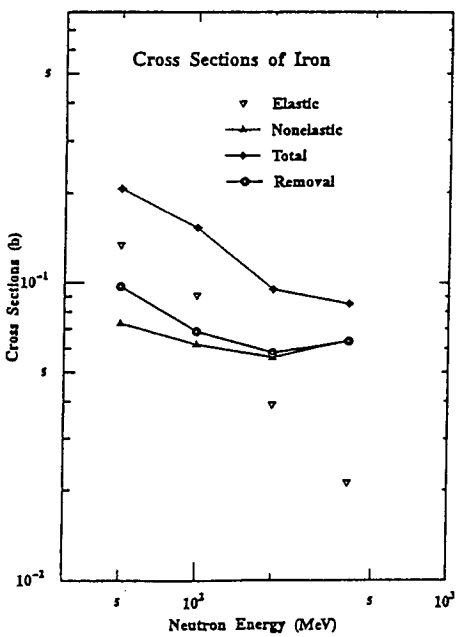

Figure 8 ***Energy dependence of removal, total, nonelactic and elastic cross-sections of iron***

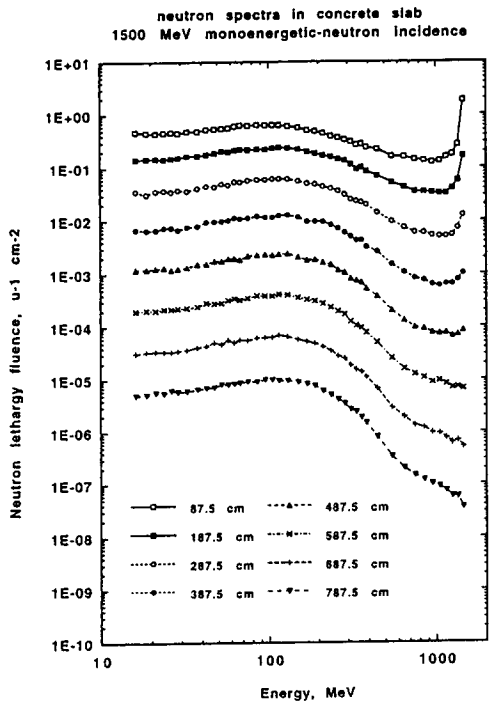

Figure 9 ***Neutron spectra in concrete slab for 1500 MeV source neutrons***

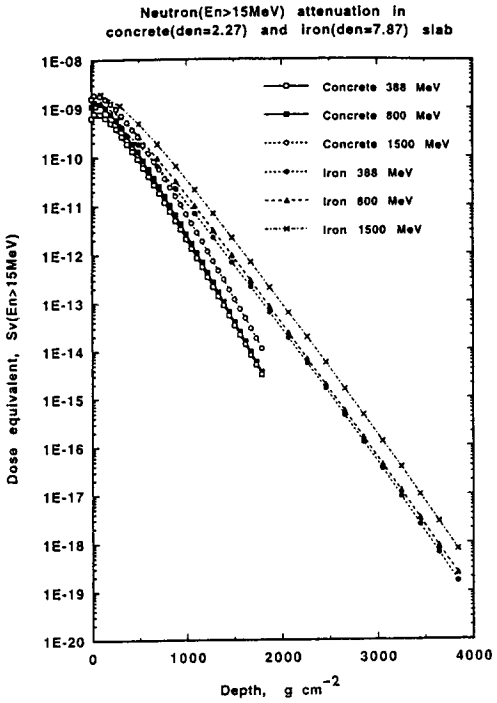

Figure 10 ***Attenuations of neutron dose equivalent ($E_n \geq 15$ MeV) in concrete and iron slabs***

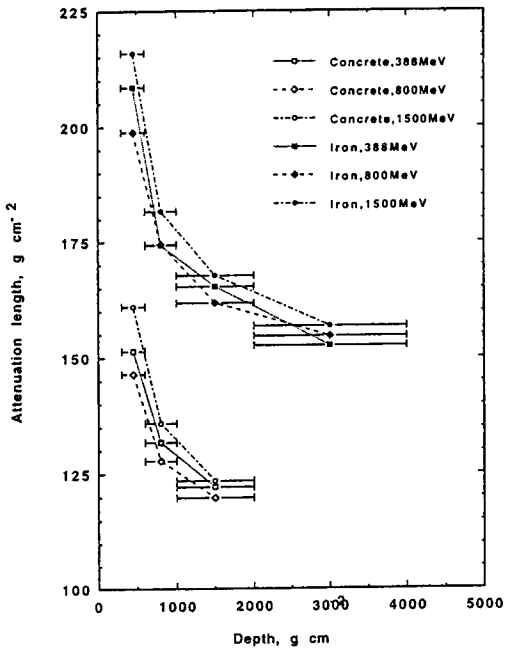

Figure 11 ***Attenuation lengths of neutron dose equivalent ($E_n \geq 15$ MeV) of iron and concrete***

MEASUREMENTS AND SIMULATIONS IN HIGH ENERGY NEUTRON FIELDS

C. Birattari [#], E. De Ponti [#], A. Esposito*, A. Ferrari [†],
M. Magugliani [#], M. Pelliccioni*, T. Rancati [#], M. Silari°

Abstract

The application of the FLUKA Monte Carlo code in the simulation of particle cascades in the shielding of the H6 beam in the SPS North Experimental Hall (CERN) has been tested against experimental results. The present paper demonstrates the validity of the code in predicting neutron spectra in very complex geometrical conditions with large attenuation factors involved. The same experimental data served as a confirmation of the behaviour of a modified Andersson-Braun rem counter with a response function extended up to hundreds of MeV (LINUS).

[#] **Universit a di Milano, Dipartimento di Fisica**, LASA,
Via Fratelli Cervi 201, 20090 Segrate, Italy.

* **Istituto Nazionale di Fisica Nucleare, Laboratori Nazionali di Frascati**,
00044 Frascati, Italy.

[†] **Istituto Nazionale di Fisica Nucleare, Sezione di Milano**,
Via Celoria 16,
20133 Milano, Italy.

° **Consiglio Nazionale delle Ricerche, Istituto Tecnologie Biomediche Avanzate**
Via Ampere 56, 20131 Milano, Italy.

1. Introduction

Three series of measurements in high energy stray radiation fields were performed at CERN in July 1993, May 1994 and April 1995. These measurements were carried out at the beam line H6 from the Super Proton Synchrotron (SPS), in the North Area of the Prevessin site, where a reference facility for high energy neutron dosimetry studies is available. Several European (and also from outside Europe) laboratories participated with dosimeters and spectrometers in these field investigations, organised within the framework of a CERN-CEC collaboration.

The INFN Milan and Frascati groups participated with the rem counters SNOOPY (a standard Andersson-Braun rem counter) and LINUS (a new rem counter) and with 5 polyethylene cylinders of different size having at their centre a BF_3 proportional counter. The bare BF_3 counter and the counter under a cadmium cover were also used.

These measurements were performed to test the response of the two rem counters in high energy neutron fields and to allow a comparison between field measurements and Monte Carlo simulations performed using the FLUKA code. The polyethylene cylinders were also used to get an experimental estimate of the neutron spectrum (each cylinder being capable of detecting neutrons belonging to different energy regions).

A description of the experimental conditions is given in section 2, while the Monte Carlo simulations are discussed in section 3. In particular, section 3.1 refers to the simulation of the response function of the detecting devices while section 3.2 deals with the simulation of the CERN test beam set up. The experimental data and the Monte Carlo results are compared and discussed in section 4.

2. Experimental setup

The beam consisted of 205 GeV/c positively charged particles (about 2/3 protons and 1/3 pions). This beam was shot at the centre of a cylindrical copper target (50-cm length, 7-cm diameter) which was located either under a 40-cm thick iron roof shield ("iron" position) or under a 80-cm thick concrete roof shield ("concrete" position). The arrangement of the shielding blocks around the target area is shown in Figures 1 and 2 where the measurement positions are also indicated. All the shields were made by concrete blocks ($240\times160\times80$ cm^3) except the roof above the iron position.

During the three experimental runs measurements were performed at a number of locations around the shieldings. These locations are divided into four groups according to the following classification:

- CONCRETE TOP,
- CONCRETE SIDE,
- IRON TOP and
- IRON SIDE (the last group refers to the condition with the target placed under the iron roof but measurements made behind a 160-cm concrete side wall).

Measurement positions are listed in Table 1. The beam monitoring was provided by CERN by means of a Precision Ionization Chamber (PIC) [1]. One count of this instrument was estimated with independent methods to correspond to 2.2×10^4 $\pm10\%$ (the error is systematic) primary particles incident on the target. All the data presented in this paper are normalised to one PIC count.

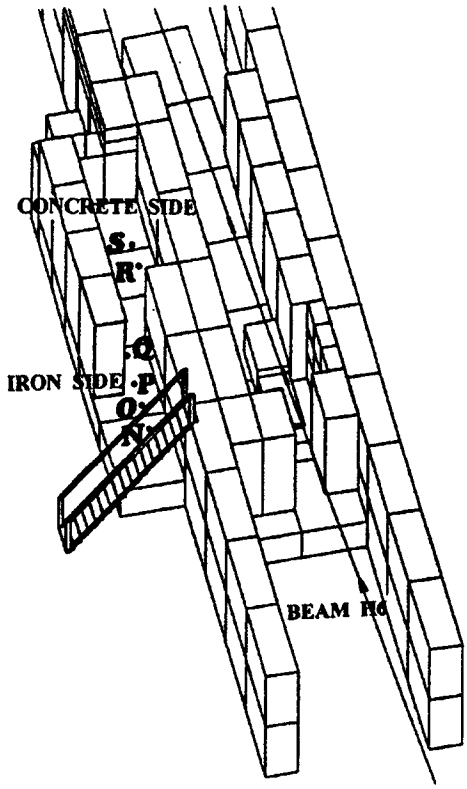

Figure 1 ***Axonometric view of the target area and lateral shielding. The top shieldings are removed.***

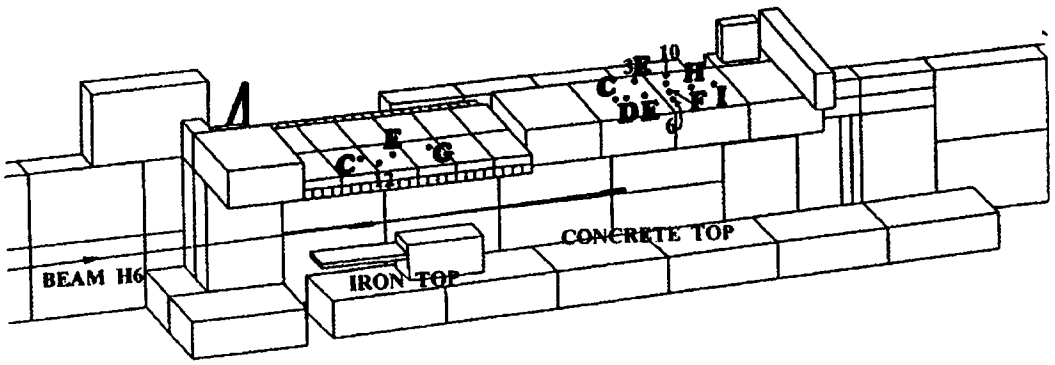

Figure 2 ***Axonometric side view of the target area, with the lateral shielding removed.***

Table 1 ***Measurements positions***

POSITION GROUP	SHORT NAME	DISTANCE TO SHIELDING	DOWNSTREAM DISTANCE FROM TARGET	POSITION WITH RESPECT TO THE BEAM DIRECTION
CONCRETE TOP	C	25 cm	0 cm	aligned
	D	25 cm	25 cm	aligned
	E	25 cm	75 cm	aligned
	3E	25 cm	75 cm	100 cm left
	F	25 cm	125 cm	aligned
	6	25 cm	125 cm	125 cm right
	10	25 cm	125 cm	125 cm left
	H	25 cm	175 cm	aligned
	I	25 cm	213 cm	aligned
IRON TOP	C	25 cm	0 cm	aligned
	E	25 cm	75 cm	aligned
	G	25 cm	150 cm	aligned
	12	25 cm	25 cm	25 cm right
POSITION GROUP	**SHORT NAME**	**DISTANCE TO SHIELDING**	**DOWNSTREAM DISTANCE FROM TARGET**	**HEIGHT WITH RESPECT TO BEAM**
CONCRETE SIDE	R	50 cm	-125 cm	0 cm
	S	50 cm	0 cm	0 cm
IRON SIDE	N	50 cm	0 cm	0 cm
	O	50 cm	100 cm	0 cm
	P	50 cm	200 cm	0 cm
	Q	50 cm	340 cm	0 cm

3. Monte Carlo simulations

Monte Carlo simulations were carried out with the last version of the FLUKA code (see [2,3,4,5,6,7] and references therein). The present version of the code has been developed in Milan and includes the capability of transporting also low energy neutrons ($E_n < 20$ MeV) using a multigroup cross-section library especially developed for FLUKA [8].

Calculations were performed using a three-step procedure:

- First, the detector response functions were calculated;
- Second, the neutron fluences at the measurement positions were computed; and,
- Third, the computed responses to monoenergetic neutron beams were folded with the scored fluences.

3.1 Calculation of the response functions

In order to compute the fluence response of the various devices each monitor was represented using the combinatorial geometry and the detector and the surrounding attenuator/moderator were reproduced

as accurately as possible. A track length estimator corresponding to the effective volume of the BF_3 counter was used for scoring. Its response function was the same as that of the B-10 (n,α) reaction.

Three kinds of response functions were considered: lateral and isotropic irradiation for energies below 20 MeV and lateral irradiation for energies above 20 MeV. By lateral irradiation we mean irradiation by a uniform and parallel radiation field (a situation which corresponds to the conditions under which the ambient dose equivalent is calculated). In isotropic irradiation an isotropic neutron fluence around the detectors was simulated. These two kinds of irradiations were chosen in order to allow the use either of a single response function or of an appropriate mix of both, according to the angular distribution of the neutrons striking the detector.

For LINUS and SNOOPY only the lateral response function was calculated because of their low sensitivity to low energy neutrons. In all the experimental conditions presented in this paper high and intermediate energy neutrons can be considered as striking the detectors laterally, while angular distributions become nearly isotropic for decreasing neutron energies (see also section 3.2): these low energy neutrons arise from a great number of interactions and do not record the direction of the primary particle from which they derive. For the same reason no isotropic response above 20 MeV was calculated. Looking carefully at the computed response functions one can see that the anisotropy of the response becomes smaller with increasing energy and vanishes above 10 MeV.

Below 20 MeV use was made of the multigroup cross-section data sets, with 72-neutron energy groups in the energy range from thermal to 20 MeV [8]. In this range the histogram representation of the response function curves presented in the following reflects the group structure of the cross-section data sets. Above 20 MeV lateral irradiation with monoenergetic neutrons was simulated. Sixteen energies (from 21 MeV up to 2 GeV) were considered. In the following the detectors are described and their computed response functions are presented. These response functions are also given numerically in the Annex, Tables 13-17.

All simulations were carried out on a DEC Alpha 3000/600 workstation running Open VMS 6.1. The average CPU time per primary particle depends on the device and the neutron energy considered:

- For LINUS (which is the most complex device) it is about 2×10^{-2} s (E<20 MeV), 2.5×10^{-2} s (E<25 MeV), and 8×10^{-2} s (E<2 GeV), and,

- For cylinder 2 it is about 3×10^{-3} s (E<20 MeV), 8×10^{-4} s (E<25 MeV), and 10^{-3} s (E<2 GeV).

The number of primary particles required to achieve statistical errors of few percent was about 10^7 for energies below 20 MeV (the 72 groups were handled at the same time) and about 10^4 – 10^5 (single energy) above 20 MeV.

3.1.1 The rem counters LINUS and SNOOPY

A rem counter consists of a detector with a high efficiency for thermal neutrons placed inside a moderator/attenuator structure such that the response function of the instrument reproduces as faithfully as possible the curve of the conversion coefficients from neutron fluence to ambient dose equivalent -H*(10) – over a wide energy range.

SNOOPY is a conventional Andersson-Braun rem counter [9]. It consists of a BF_3 proportional counter of 2.54-cm diameter and 5.08-cm nominal active length (95% B-10 enrichment, fill pressure 8.0×10^4 Pascal) surrounded by: an inner polyethylene moderator (1.9 cm thick), a boron doped synthetic rubber attenuator (7.6 cm outer diameter, 14 cm length and 0.6 cm thickness) and an outer polyethylene moderator (21.7 cm outer diameter, 23.9 cm length and 7 cm thickness). A number of holes are drilled in both the lateral and front surfaces of the boron plastic attenuator in order to allow some of the thermal neutrons to penetrate. The area of the holes covers about 20% of the boron attenuator total area. Figure 3 shows a longitudinal cross-section of the instrument as it was coded into the computer.

The SNOOPY response is considered acceptable for radiation protection purposes for neutron energies from thermal to 14 MeV. For energies above 14 MeV its response becomes inadequate: its sensitivity drops and the instrument underestimates the ambient dose equivalent [10].

LINUS (Long Interval NeUtron Survey-meter) is an extended range version of SNOOPY. A lead layer (1 cm thick) has been placed between the boron-doped synthetic rubber attenuator and the outer polyethylene moderator. Lead has no significant effect at energies below 10 MeV, while the fluence response is highly increased above 10 MeV (at 14 MeV its response is about 40% larger than that of SNOOPY and about 55% larger at 19 MeV) (for details see [10,11,12]). Figure 4 shows a longitudinal cross-section of the new rem counter as described in combinatorial geometry.

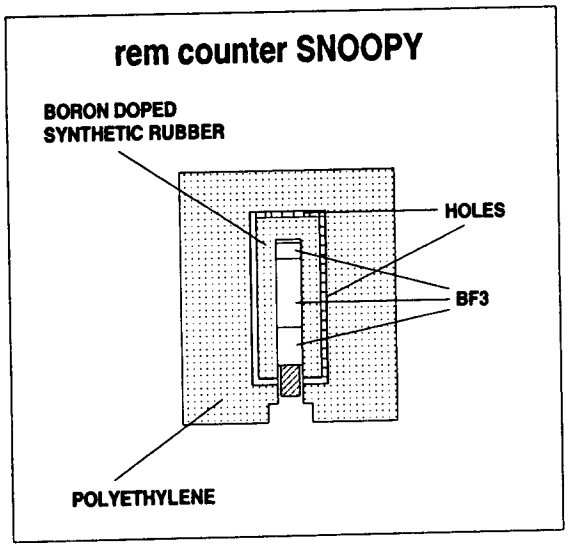

Figure 3 ***Rem counter SNOOPY. Longitudinal cross-section.***

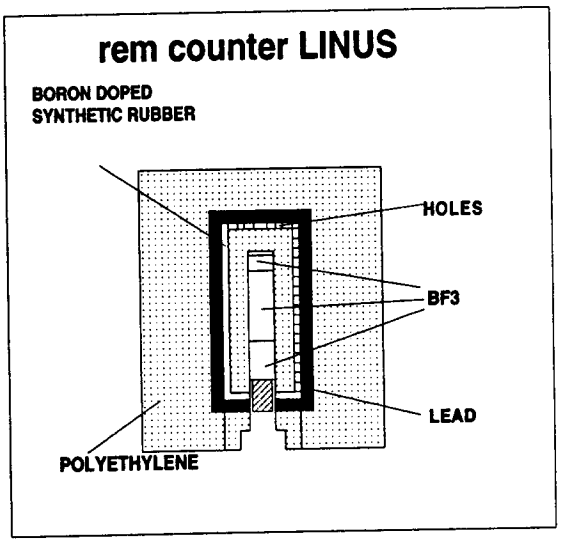

Figure 4 ***Rem counter LINUS. Longitudinal cross-section.***

The improved rem counter LINUS has already been tested in high energy stray radiation fields in two previous experiments at CERN 13,14] and has been calibrated with monoenergetic neutrons in the range from thermal to 19 MeV provided by the Physikalische-Technische Bundesanstalt (PTB) in Braunschweig (Germany) [12,14]. Measurements with nearly monoenergetic neutron fields at 39.5,

50, 60.7 and 70 MeV were also performed at the Paul Scherrer Institute (PSI) in Villigen (Switzerland) [14] (the energies are those of the protons hitting the beryllium target).

The computed response for the LINUS counter together with the H*(10) curve and the experimental values resulting from the PTB calibration are drawn in Figure 5. The dashed lines correspond to one (calculated) standard deviation statistical error. The energy scale on the horizontal axis has been split in correspondence to 10^5 eV in order to expand and better show the high energy region. When plotting the H*(10) curve we have chosen the conversion coefficients from neutron fluence to ambient dose equivalent proposed in [15,16]. The computed response for the SNOOPY counter is drawn in Figure 6. The curves in Figures 5 and 6 have been drawn according to a nominal sensitivity referred to a sensitive volume and a pressure of the filling gas of the BF^3 counter as given above.

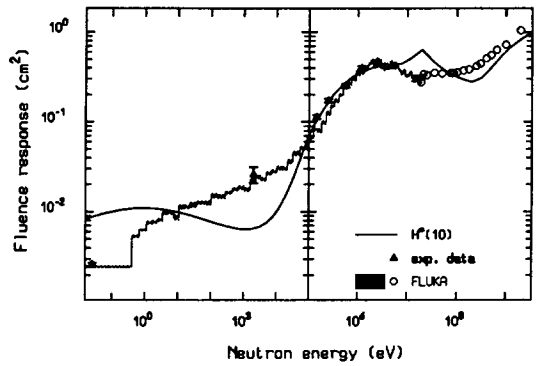

Figure 5 ***Rem counter LINUS. Fluence response***

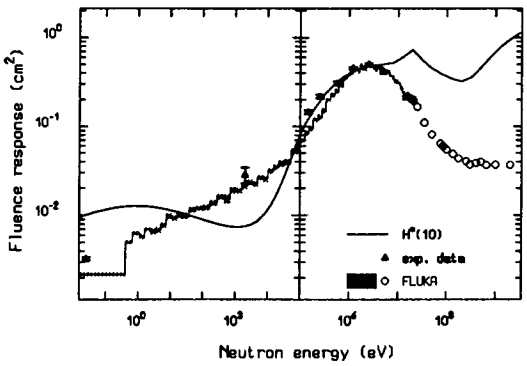

Figure 6 ***Rem counter SNOOPY. Fluence response***

As one can see the LINUS response function shows a marked increase at high energies (when compared with the SNOOPY response function) and no significant change in the other regions. There is also good agreement between the calculated response function and the experimental calibration points.

3.1.2 Polyethylene cylinders

The five high-density (0.96 g/cm^3) polyethylene cylinders are shown in Figure 7. Their diameters range from 7.8 cm to 22.8 cm. The thickness of the lateral polyethylene is: 2.55 cm (cylinder 1), 3.85 cm (cylinder 1B), 5.05 cm (cylinder 2), 7.55 cm (cylinder 3) and 10.5 cm (cylinder 4). The top and bottom thicknesses are the same but for cylinder 1B (5 cm).

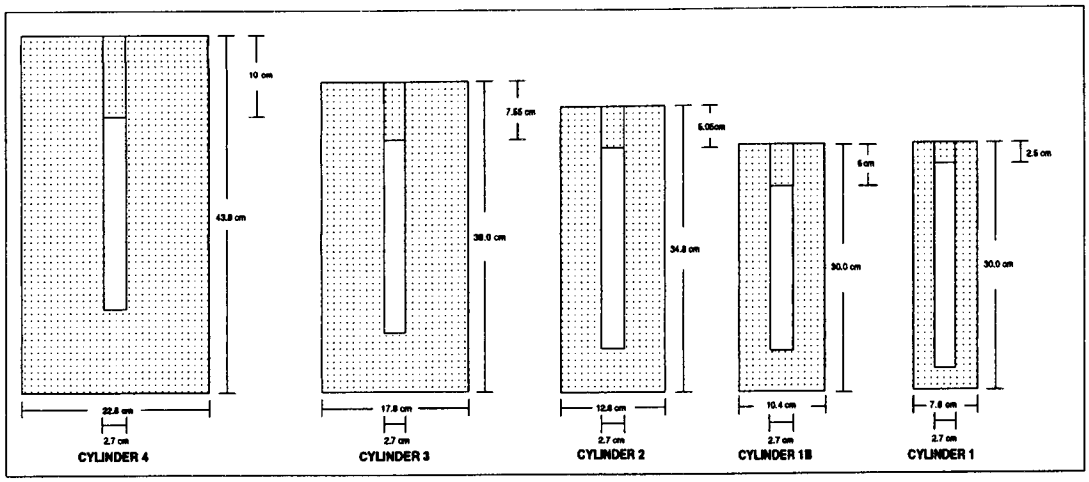

Figure 7 ***Polyethylene cylinders. Longitudinal cross-section***

Figures 8-12 show the response functions of the five cylinders. These detectors are especially sensitive to energies ranging from 10 eV (cylinder 1) up to 2 MeV (cylinder 4).

3.1.3 Bare BF_3 proportional counter

For the bare counter no fluence response was calculated: the curve of the B-10 (n,α) cross-section versus energy was adopted. This curve is shown in Figure 13. The maximum sensitivity is obviously reached at thermal energy.

3.1.4 BF_3 proportional counter under a cadmium cover

Also for the BF_3 proportional counter covered with a cadmium layer no fluence response was computed. The same response function of the bare counter was adopted for energies above 0.414 eV. For energies below 0.414 eV a zero response was assumed. In this energy range the cadmium cross-section is indeed very large.

3.2 Simulation of the CERN experimental set up

The CERN-CEC experimental area was modelled using the combinatorial geometry. Because of lack of information, the concrete composition was assumed to be a standard one, as reported in nuclear reactor guidelines. In particular Portland concrete was chosen with composition (weight fractions): 52.9% oxygen, 33.7% silicon, 4.4% calcium, 3.4% aluminium, 1.6% sodium, 1.4% iron, 1.3% potassium, 1% hydrogen, 0.2% magnesium and 0.1% carbon. The iron roof consisted of two layers with different average densities: upper-layer 7.2 g/cm^3, lower-layer 7.65 g/cm^3. These densities were determined by weighting a few blocks.

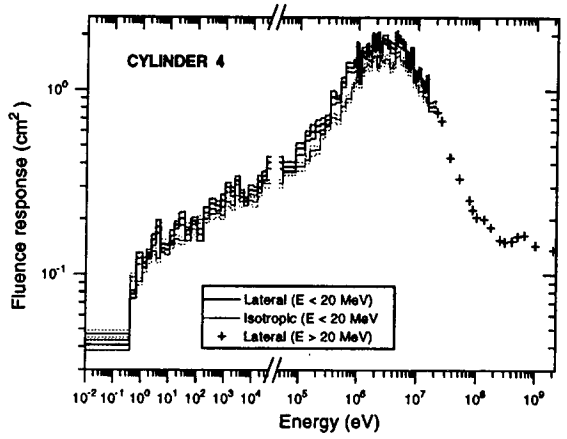

Figure 8: Cylinder 4. Fluence response.

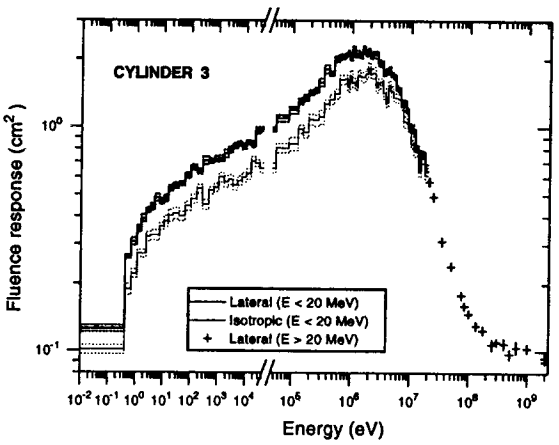

Figure 9: Cylinder 3. Fluence response.

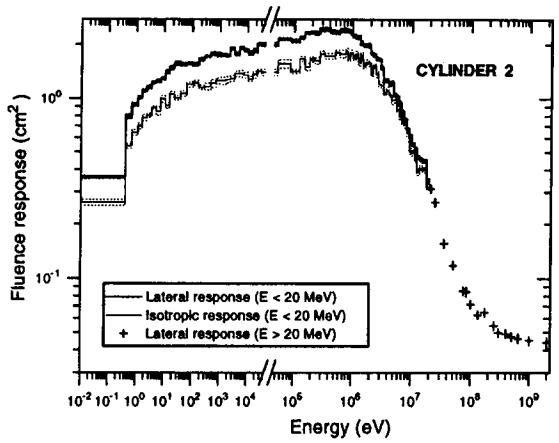

Figure 10: Cylinder 2. Fluence response.

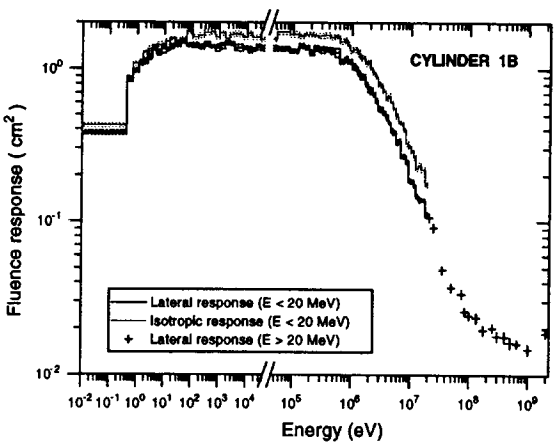

Figure 11: Cylinder 1B. Fluence response.

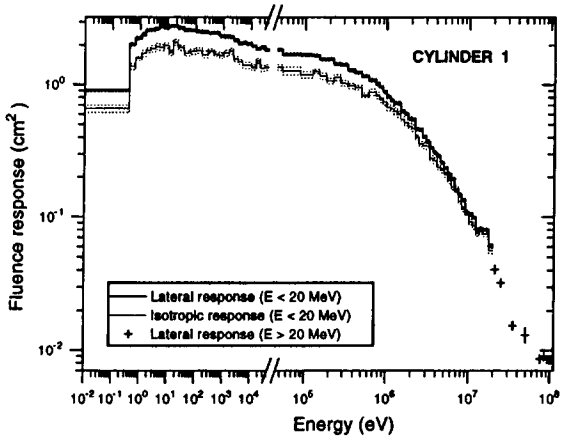

Figure 12: Cylinder 1. Fluence response.

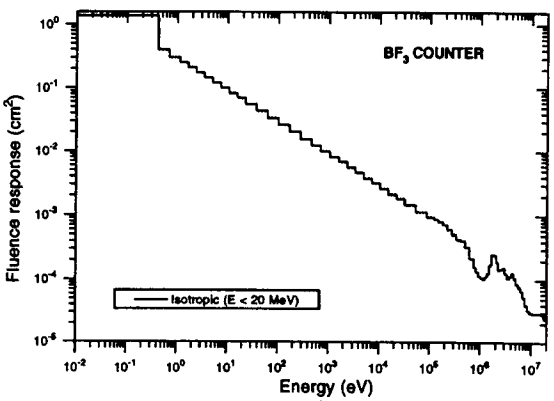

Figure 13: Bare counter. Fluence response.

According to the experimental conditions a beam consisting of 2/3 protons and 1/3 positive pions with a FWHM of 2.8 and 2.1 cm in the horizontal and vertical plane respectively was used in the simulations. All particle but electrons, positrons and photons were tracked through the geometry until they were absorbed or escaped from the system. Electromagnetic particles were discarded because of no interest for the present problem.

Two scoring spheres (24 cm and 40 cm diameter) were inserted in the geometry in each experimental measurement point. When this was not possible (because of overlapping with other regions) either the diameters were suitably reduced or only one sphere was considered. When two scoring regions were available the neutron fluence in the largest one was chosen because of better statistics. If a strong gradient was present the neutron fluence in the internal region was considered. The neutron fluences scored in some measurement positions are shown in Figures 14 and 15.

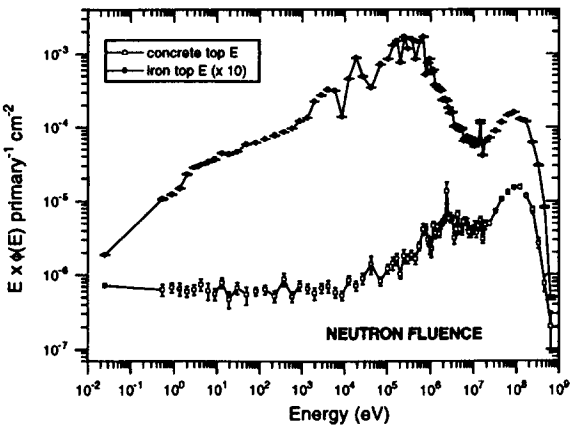

Figure 14 ***Concrete top (E) and iron top (E) positions. Neutron fluence as resulting from calculations.***

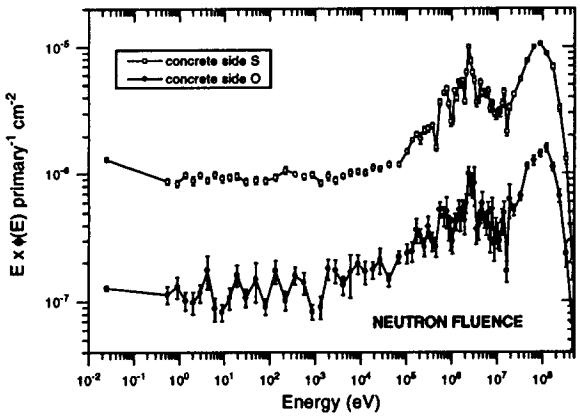

Figure 15 ***Concrete side (S) and iron side (O) positions. Neutron fluence as resulting from calculations.***

In order to better understand and reproduce the neutron fluence present at experimental locations the angular distribution of neutrons as a function of energy was also calculated. This information allowed us to determine (for each energy group and for each experimental position) a suitable figure r, to represent the degree of anisotropy of the neutron beam. This number is the fraction of neutron fluence which has to be folded with the detector isotropic response function, while the fraction $(1-r)$ is folded with the lateral response function. As already expected, r increases with decreasing neutron energies and it is ≈ 1 for the thermal group. For this reason for the two rem counters LINUS and SNOOPY only the lateral response function was considered (their sensitivity to thermal neutron is very low) and, on the other hand, for the bare proportional counter only the isotropic response function was used (it practically detects only thermal neutrons).

The number r has been determined as explained in the following. The Monte Carlo code has been used to calculate a double differential distribution of neutron fluence in energy and solid angle (angular distributions are intended as distributions in $\cos.\theta$, where θ is the angle between the particle trajectory and the normal to the shielding at the point of crossing). For each energy group 60 angular

trajectory and the normal to the shielding at the point of crossing). For each energy group 60 angular groups were considered. We chose to considered all neutrons crossing the shielding with 48°< q<180° (angular groups from 11 to 60) as belonging to the isotropic fluence (I). The neutrons belonging to the first ten angular groups were considered as contributing to the lateral fluence (L). The figure r has been calculated from the expression $r = \frac{I}{I+L}$. The choice of the groups contributing to isotropic and lateral response is somewhat arbitrary and the whole procedure could be improved.

In order to save computing time extensive use of variance reduction techniques was made. Importance biasing at boundaries and energy dependent weight windows were applied in order to favour particle streaming towards the detector locations and not to waste CPU time following particles with a little probability of giving a contribution. The typical CPU time was about 18 s per primary particle. About 10^4 particles were tracked in order to obtain adequate statistics.

3.3 Folding and simulation results

The previously computed response of the counting devices to monoenergetic neutrons were finally folded with the fluxes scored at the measurement positions and the estimated number of counts per PIC was obtained. The results are given in the next section (Tables 3-10) together with the experimental counts.

For the polyethylene cylinders three simulated results are given. They correspond to three different kinds of folding: lateral response only, isotropic response only and the mix deriving from considering the angular distribution of neutrons through the r number discussed above (Section 3.1).

4. Experimental results and discussion

4.1 Calibration factor

All results presented in this paper (both experimental and calculated) are given for a BF_3 proportional counter whose sensitive volume and gas fill pressure are the nominal ones (see Section 3.1.1). The actual efficiencies of the BF_3 counters used in the experimental measurements are usually different from the nominal one and they were found to be not stable with time. One of the BF_3 counters was therefore calibrated at PTB in 1991 (exposing it to monoenergetic neutrons and to a calibrated Am-Be source) inside the LINUS and SNOOPY rem counters [12,14]. From this calibration the actual efficiency of this BF_3 counter at the time of the calibration was known and the following time evolution was monitored exposing it to an Am-Be source in standard conditions at the Laboratorio Acceleratori Superconduttivit a Applicata (LASA) in Milan (see Section 4.2). Of course the same calibration provided an intercalibration of the LASA source, which is now our standard reference when calibrating the counters.

Therefore from 1991 on, efficiency fluctuations are controlled through routine tests performed at LASA. This allows to determine (for each BF_3 counter) a factor K which takes the difference between "nominal" and real efficiency into account ("nominal" refers to the efficiency of a BF_3 counter with sensitive volume, gas pressure and B-10 enrichment corresponding to those given in Section 3.1) and which is used to normalise all the experimental results presented in this paper. For the PTB calibrated

tube this K factor was 0.74 ± 0.03 in 1991, 0.75 ± 0.05 in July 1993, 0.78 ± 0.05 in May 1994 and 0.76 ± 0.05 in April 1995. The other BF_3 counters have different K factors.

The ambient dose equivalent calibration factor S was established using the PTB calibration points. It comes from the ratio between the rem counter fluence response and the fluence to ambient dose equivalent conversion coefficients. For an ideal rem counter S would be the same in the whole energy range considered. For LINUS and SNOOPY it slightly varies; we chose an average value: 1.044 cts/nSv ± 8.0% for the rem counter LINUS and 1.209 cts/nSv ± 9.5% for SNOOPY (the quoted errors give an indication of the variation of S with energy). These values refer to a counter whose sensitivity is the nominal one.

4.2 Time stability of the counter

Since it was not possible to control the stability of the proportional counters during the CERN measurements, tests were performed at LASA before and after each measurement period. During these tests the detectors were exposed to an Am-Be source. The source emission rate is 2.3×10^6 n/s (±4%) (the source was intercalibrated with a PTB Am-Be source as explained above). The source was placed 3 m above the concrete floor, all other walls being at much larger distances. The detectors sat on a plexiglas support, with their centre at 2 m from the source. The neutron fluence rate at the measurement location was 4.58 n/cm^2/s ±4%. The LASA measurement geometry is shown in Figure 16. Simulations of this experimental set up were also carried out.

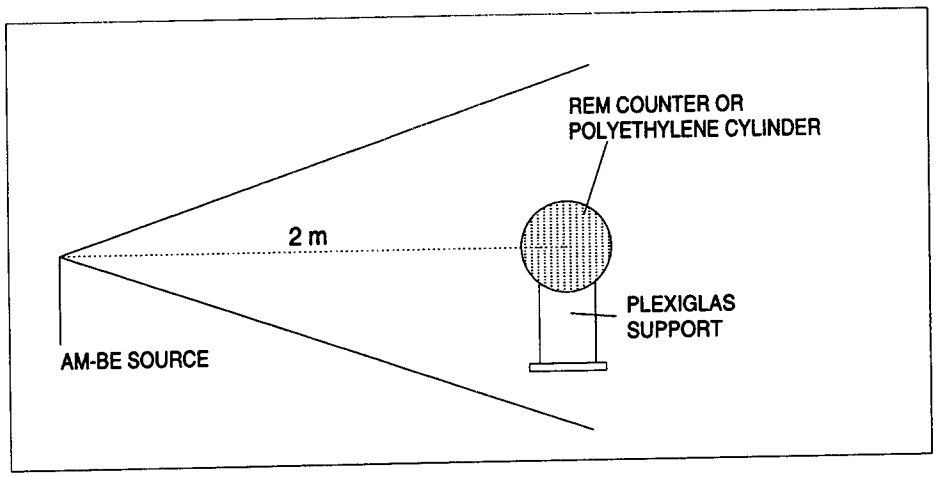

Figure 16 ***LASA geometry as described in the simulations***

Prior and following each experimental run the counters were exposed to the Am-Be source. This allowed to control that no significant change occurred and to establish a reference efficiency for the CERN period. For each counter the ratio between the LASA response and the response obtained with the calibrated tube in 1991 is assumed to be the ratio between the corresponding counting efficiencies. This ratio allows to refer to the PTB calibration efficiency and to normalise all results to a counter whose efficiency is the nominal one. Table 2 gives the LASA response (1995) together with the simulated response. The experimental results are reported to the nominal efficiency.

Table 2 ***LASA response. Experimental and computed results. Statistical errors only are shown***

DETECTOR	EXPERIMENTAL		FLUKA	
	cm^2	err%	cm^2	err%
LINUS	0.349	0.4	0.374	0.6
SNOOPY	0.354	0.3	0.398	0.5
CYLINDER 4	1.44	0.1	1.42	2.2
CYLINDER 3	1.54	0.1	1.51	1.9
CYLINDER 2	1.29	0.1	1.23	2.0
CYLINDER 1B	0.898	0.5	0.872	2.1
CYLINDER 1	0.387	0.2	0.414	2.5

4.3 Experimental results

The experimental and the computed results are presented in Tables 3-10. The quoted errors are only statistical and do not include systematic uncertainties in the beam monitoring (which are estimated to be 10%) and in the efficiency of the BF_3 counter (5%).

Experimental data were collected in different years. In general there is no great difference among them; in this case the 1995 results are reported. When important differences were found, the data obtained in other years are also presented. As one can see, the agreement between experimental and simulated counts is fairly good. It should be stressed that the problem is very complex and uncertainties are not negligible. The major differences between simulated and experimental counts were found for the bare counter (iron positions) and for the counter under the cadmium cover (1995 measurements). The bare counter is extremely sensitive to thermal neutrons. The presence of moderating materials modifies the thermal portion of the spectrum. As it is shown by the sequence of measurements presented in Table 9, the counts coming from the bare counter are quite dependent on the presence of other (polyethylene) detectors near it. When the measurement area was left free, the response of the counter dropped and it came closer to the computed one. This fact shows that the problem came from the experimental area overcrowding. For the concrete positions *a* significant uncertainty on the simulated counts for the bare counter is due to the unknown concrete composition. The actual intensity of the thermal neutron spectrum is strongly dependent on concrete composition and it has great importance for a device which practically detects only thermal neutrons.

On the other hand the counter under the cadmium cover is insensitive to thermal neutrons because of the high cadmium neutron cross-section at these energies. Here a problem rises when the cover is not tightly sealed: This allows some thermal neutrons to penetrate and be detected. Concrete positions are especially critical. Here a great number of thermal neutrons are present and a small aperture in the cadmium cover can cause a lot of them to be detected.

Table 3 ***LINUS and SNOOPY. CERN experimental and computed results. Statistical errors only are shown.***

POSITION	LINUS				SNOOPY			
	EXPERIMENTAL		FLUKA		EXPERIMENTAL		FLUKA	
	cts/PIC	err%	cts/PIC	err%	cts/PIC	err%	cts/PIC	err%
CONCRETE TOP								
C	0.268	0.62	0.281	2.4	0.156	0.78	0.153	2.4
E	0.364	0.36	0.391	2.8	0.200	0.59	0.201	3.1
F	0.362	0.35	0.367	3.1	0.209	0.52	0.201	3.8
I	0.319	0.56	0.367	2.2	0.174	0.78	0.184	2.1
6	0.359	0.54	0.400	2.3	0.199	0.72	0.200	2.2
10	0.379	0.54	0.401	1.9	0.214	0.69	0.202	1.9
CONCRETE SIDE								
R	0.154	0.29	0.141	2.3	0.113	0.16	0.094	2.2
S	0.316	0.45	0.299	2.1	0.214	0.56	0.182	1.9
IRON TOP								
C	1.78	0.30	1.52	1.9	1.83	0.75	1.49	1.9
E	2.12	0.11	1.87	2.0	2.16	0.27	1.79	2.1
G	1.65	0.65	1.60	2.2	1.69	0.68	1.50	2.1
IRON SIDE *								
N	0.0268	2.1	0.0259	3.6	-	-	-	-
O	0.0414	1.8	0.0398	3.0	0.0297	2.4	0.0216	3.8
P	0.0545	1.8	0.0543	3.1	-	-	-	-
Q	0.0865	1.2	0.0908	2.9	-	-	-	-
R	0.194	0.65	0.193	2.6	-	-	-	-
S	0.156	1.0	0.155	2.7	-	-	-	-

* 1993 measurements.

Table 4 ***CYLINDER 4. CERN experimental and computed results. Statistical errors only are shown***

POSITION	EXPERIMENTAL		FLUKA-ISOTROPIC		FLUKA-MIXTURE		FLUKA-LATERAL	
	cts/PIC	err%	cts/PIC	err%	cts/PIC	err%	cts/PIC	err%
CONCRETE TOP								
C	0.541	0.29	0.555	2.3	0.593	2.3	0.647	2.3
D	0.723	0.36	0.583	3.7	0.640	3.7	0.731	3.7
E	0.700	0.24	0.728	2.8	0.782	2.8	0.843	2.8
F	0.871	0.62	0.657	3.5	0.736	3.5	0.822	3.5
H	0.819	0.47	0.678	2.7	0.754	2.7	0.846	2.7
3E	0.568	0.50	0.459	3.1	0.509	3.1	0.541	3.1
CONCRETE SIDE								
R	0.331	0.31	0.352	2.1	0.380	2.21	0.414	2.1
S	0.709	0.49	0.674	1.9	0.721	1.9	0.790	1.9
IRON TOP								
C	6.84	0.15	6.04	1.9	6.83	1.9	7.53	1.9
E	7.53	0.15	7.08	2.1	8.03	2.1	8.83	2.1
12	7.41	0.29	5.37	2.1	7.55	2.1	6.51	2.1

Table 5 ***CYLINDER 3. CERN experimental and computed results. Statistical errors only are shown.***

POSITION	EXPERIMENTAL		FLUKA-ISOTROPIC		FLUKA-MIXTURE		FLUKA-LATERAL	
	cts/PIC	err%	cts/PIC	err%	cts/PIC	err%	cts/PIC	err%
CONCRETE TOP								
C	0.683	0.45	0.631	2.3	0.685	2.3	0.772	2.3
D	0.870	0.36	0.703	3.4	0.768	3.4	0.880	3.4
E	0.886	0.32	0.820	2.9	0.899	2.9	0.995	2.9
F	1.08	0.59	0.789	3.8	0.878	3.8	0.990	3.8
H	1.02	0.39	0.815	2.8	0.906	2.8	1.02	2.8
3E	0.691	0.43	0.549	3.1	0.609	3.1	0.687	3.1
CONCRETE SIDE								
R	0.484	0.38	0.453	2.1	0.497	2.1	0.570	2.1
S	0.972	0.07	0.831	1.9	0.908	1.9	1.04	1.9
IRON TOP								
C	13.6	0.11	10.9	1.9	12.8	1.9	14.7	1.9
E	14.9	0.11	12.4	2.1	14.6	2.1	16.7	2.1
12	13.2	0.23	10.4	2.1	12.4	2.1	14.2	2.1

Table 6 ***CYLINDER 2. CERN experimental and computed results. Statistical errors only are shown.***

POSITION	EXPERIMENTAL		FLUKA-ISOTROPIC		FLUKA-MIXTURE		FLUKA-LATERAL	
	cts/PIC	err%	cts/PIC	err%	cts/PIC	err%	cts/PIC	err%
CONCRETE TOP								
C	0.813	0.41	0.681	2.3	0.753	2.3	0.881	2.3
D	1.00	0.31	0.788	3.3	0.872	3.3	1.03	3.3
E	1.04	0.24	0.871	3.0	0.977	3.0	1.12	3.0
F	1.21	0.34	0.887	3.6	0.998	3.6	1.15	3.6
H	1.18	0.36	0.912	2.9	1.03	2.9	1.19	2.9
3E	0.801	0.47	0.612	3.0	0.688	3.0	0.794	3.0
CONCRETE SIDE								
R	0.655	0.24	0.580	2.0	0.642	2.0	0.769	2.0
S	1.22	0.14	1.01	1.7	1.12	1.7	1.33	1.7
IRON TOP								
C	20.2	0.03	16.6	1.9	19.7	1.9	22.8	1.9
E	22.0	0.11	18.6	2.1	22.1	2.1	25.5	2.1
12	18.4	0.15	16.2	2.1	19.3	2.1	22.3	2.1

Table 7 ***CYLINDER 1B. CERN experimental and computed results. Statistical errors only are shown.***

POSITION	EXPERIMENTAL		FLUKA-ISOTROPIC		FLUKA-MIXTURE		FLUKA-LATERAL	
	cts/PIC	err%	cts/PIC	err%	cts/PIC	err%	cts/PIC	err%
CONCRETE TOP								
C	0.798	0.34	0.645	2.4	0.601	2.4	0.528	2.4
E	1.01	0.18	0.811	2.9	0.747	2.9	0.663	2.9
CONCRETE SIDE								
R	0.686	0.23	0.615	1.9	0.579	1.9	0.518	1.9
S	1.26	0.37	1.03	1.8	0.970	1.8	0.858	1.8
IRON TOP								
C	20.7	0.06	17.2	2.0	15.6	2.0	14.0	2.0
E	22.3	0.10	19.1	2.1	17.3	2.1	15.6	2.1

Table 8 ***CYLINDER 1. CERN experimental and computed results. Statistical errors only are shown.***

POSITION	EXPERIMENTAL		FLUKA-ISOTROPIC		FLUKA-MIXTURE		FLUKA-LATERAL	
	cts/PIC	err%	cts/PIC	err%	cts/PIC	err%	cts/PIC	err%
CONCRETE TOP								
C	0.685	0.49	0.558	2.6	0.623	2.6	0.752	2.6
D	0.862	0.34	0.634	3.9	0.708	3.9	0.862	3.9
E	0.858	0.35	0.688	2.8	0.780	2.8	0.924	2.8
F	1.02	0.37	0.713	3.6	0.809	3.6	0.969	3.6
H	0.980	0.41	0.717	3.2	0.815	3.2	0.973	3.2
3E	0.679	0.60	0.472	3.0	0.536	3.0	0.641	3.0
CONCRETE SIDE								
R	0.781	0.21	0.597	1.9	0.656	1.9	0.811	1.9
S	1.14	0.23	0.970	1.8	1.09	1.8	1.32	1.8
IRON TOP								
C	14.0	0.07	12.9	1.9	15.1	1.9	17.4	1.9
E	17.4	0.07	14.2	2.1	16.5	2.1	19.1	2.1
12	15.3	0.20	11.6	2.1	13.3	2.1	15.2	2.1

Table 9 ***BARE COUNTER. CERN experimental and computed results. Statistical errors only are shown.*** *See comments in the text.*

POSITION	EXPERIMENTAL 1993		EXPERIMENTAL 1995		FLUKA-ISOTROPIC	
	cts/PIC	err%	cts/PIC	err%	cts/PIC	err%
CONCRETE TOP						
C	0.250	0.44	0.248	0.87	0.321	3.9
E	0.322	0.578	0.284	0.73	0..379	3.9
CONCRETE SIDE						
R	0.309	0.58	0.362	0.70	0.454	1.9
S	0.467	0.33	0.567	0.25	0.667	1.9
IRON TOP						
C	-	-	0.632*	0.54	0.138	4.0
	-	-	0.285***	0.84	0.138	4.0
E	0.243	0.76	0.581*	0.74	0.160	6.0
	-	-	0.490**	0.66	0.160	6.0
	-	-	0.286***	1.0	0.160	6.0

* with a poly counter at about 1 m and on a plexiglas support.

** on a plexiglas support.

*** scotch taped to a light box.

Table 10 ***COUNTER under a CADMIUM cover. CERN experimental and computed results. Statistical errors only are shown.*** *See comments in the text.*

POSITION	EXPERIMENTAL 1993		EXPERIMENTAL 1995		FLUKA-ISOTROPIC	
	cts/PIC	err%	cts/PIC	err%	cts/PIC	err%
CONCRETE TOP						
C	0.0112	3.0	0.0210	1.9	0.0106	4.7
E	0.0131	2.7	0.0305	1.7	0.0129	4.7
CONCRETE SIDE						
R	0.0108	3.2	0.0160	2.4	0.0109	2.5
S	0.0175	2.4	0.0324	2.4	0.0181	2.6
IRON TOP						
C	-	-	0.150	1.2	0.0596	2.3
	-	-	0.102*	1.0	0.0596	2.3
E	0.649	1.5	0.146	1.4	0.0655	3.1
	-	-	0.105*	1.0	0.0655	3.1

* five minutes later, after having better closed the cadmium cover.

During the 1993 measurements we had a dedicated proportional counter with a well sealed cadmium cover around it. In 1995 we preferred to use the same proportional counter in all the detecting devices (in order to minimise intercalibration errors); for this reason the cadmium cover had to be sealed by hand each time the counter was used with the cadmium layer. Despite our efforts the cover was clearly not well closed. This is why the two experimental data sets are so different and we believe that the 1993 results are more reliable.

FLUKA proved to be reliable in transporting hadrons in a complex geometry with large attenuation factors and over approximately 13 orders of magnitude in energy. The agreement between experimental and computed results is also an indication that not only the overall fluence but also the relative importance of the low and high energy components are well predicted by the FLUKA code. Each instrument is in fact mainly sensitive to different neutron energies.

4.4 H(10) measurements*

Once the reliability of the FLUKA code in providing meaningful predictions about the neutron spectra outside the beam shieldings has been proven, the simulated spectra have been used to derive for each rem counter (LINUS or SNOOPY) the simulated ambient dose equivalent reading, $H^*_{lin}(10)$ and $H^*_{sno}(10)$ according to the following expressions:

$$H^*_{lin}(10) = \frac{1}{S_{lin}} \times \int R(E)_{lin}\, \Phi(E)\, dE \qquad (1)$$

$$H^*_{sno}(10) = \frac{1}{S_{sno}} \times \int R(E)_{sno}\, \Phi(E)\, dE \qquad (2)$$

where $\Phi(E)$ is the computed neutron fluence at a given position, $R(E)_{lin}$ and $R(E)_{sno}$ are the computed rem counter fluence responses. S (see Section 4.1) is the ambient dose equivalent calibration factor: S_{lin} is 1.044 cts/nSv ± 8.0 % (LINUS) and S_{sno} is 1.209 cts/nSv ± 9.5 % (SNOOPY).

These results are then compared with the "true" value, H*(10), given by FLUKA in the same positions, computed according to:

$$H^*(10) = \int F(E)\, \Phi(E)\, dE \qquad (3)$$

where F(E) is the fluence to ambient dose equivalent conversion factor [15,16]. The results of such comparison are presented in Table 11.

The ratios $\frac{H^*_{lin}(10)}{H^*(10)}$ and $\frac{H^*_{sno}(10)}{H^*(10)}$ get rid of the differences between the computed and the measured counts and can be used to judge the ability of LINUS and SNOOPY to measure the ambient dose equivalent in such environment, provided the simulated spectrum is similar to the real one as supported by the good agreement for all counters.

These ratios show that the new rem counter can be used to monitor the ambient dose equivalent over the whole energy spectrum whereas SNOOPY underestimates H*(10) in all positions, except those

those above the iron roof where low energy neutrons are expected to dominate because of the peculiar behaviour of the iron cross-section.

Table 11 ***H*(10) as measured with LINUS and SNOOPY. Statistical errors only are shown.*** *See comments in the text.*

Pos	$H^*(10)$		LINUS					SNOOPY				
			$H^*_{lin}(10)$		$\overline{H^*_{lin}}(10)$		$\frac{H^*_{lin}(10)}{H^*(10)}$	$H^*_{sno}(10)$		$\overline{H^*_{sno}}(10)$		$\frac{H^*_{sno}(10)}{H^*(10)}$
	nSv/PIC	err%	nSv/PIC	err%	nSv/PIC	err%		nSv/PIC	err%	nSv/PIC	err%	
CONCRETE TOP												
C	0.282	2.4	0.269	2.4	0.257	0.62	0.95	0.127	2.4	0.129	0.78	0.45
E	0.387	2.6	0.374	2.6	0.349	0.36	0.97	0.166	2.6	0.165	0.59	0.43
F	0.365	3.1	0.351	3.1	0.347	0.35	0.96	0.166	3.1	0.173	0.52	0.45
I	0.354	2.2	0.351	2.2	0.306	0.56	0.99	0.152	2.2	0.144	0.78	0.43
6	0.391	2.2	0.383	2.2	0.348	0.54	0.98	0.156	2.2	0.165	0.72	0.42
10	0.394	1.9	0.384	1.9	0.368	0.54	0.97	0.166	1.9	0.177	0.69	0.42
CONCRETE SIDE												
R	0.145	2.2	0.135	2.2	0.148	0.29	0.93	0.077	2.2	0.093	0.16	0.53
S	0.303	2.1	0.286	2.1	0.303	0.45	0.94	0.151	2.1	0.177	0.56	0.50
IRON TOP												
C	1.60	1.9	1.46	1.9	1.70	0.30	0.91	1.23	1.9	1.51	0.75	0.77
E	1.94	2.2	1.79	2.2	2.03	0.11	0.92	1.48	2.2	1.79	0.27	0.76
G	1.65	2.1	1.53	2.1	1.58	0.65	0.93	1.24	2.1	1.40	0.68	0.75
IRON SIDE												
N	0.0258	4.0	0.0248	4.0	0.0257	2.1	0.96	-	-	-	-	-
O	0.0395	3.2	0.0381	3.2	0.0397	1.8	0.96	0.0179	3.2	0.0246	2.4	0.45
P	0.0510	4.0	0.0494	4.0	0.0522	1.8	0.97	-	-	-	-	-
Q	0.093	3.1	0.0870	3.1	0.0829	1.2	0.94	-	-	-	-	-
R	0.188	2.5	0.185	2.5	0.186	0.65	0.98	-	-	-	-	-
S	0.152	2.7	0.148	2.7	0.149	1.0	0.97	-	-	-	-	-

The ambient dose equivalent values computed from the experimental counts, $\overline{H^*_{lin}}(10)$ and $\overline{H^*_{sno}}(10)$, are also reported for completeness. They have been calculated from the expressions: equation

$$\overline{H^*_{lin}}(10) = \frac{1}{S_{lin}} \times CTS^{exp}_{lin} \tag{4}$$

$$\overline{H^*_{sno}}(10) = \frac{1}{S_{sno}} \times CTS^{exp}_{sno} \tag{5}$$

where CTS^{exp}_{lin} and CTS^{exp}_{sno} are the experimental counts.

5. Work in progress

Further work is now being carried out in order to develop an improved version of the rem counter LINUS. The efforts are going in two directions: study of different geometries in order to remove the dependence of the monitor response on the direction of irradiation [10,17], and the use of detectors other than BF_3 proportional counters whose operation was found to be not stable with time. During extensive tests at LASA BF_3 tubes showed deterioration of their response and recovery in

an unpredictable way after a number of hours of running period. These problems have also been reported in literature [18]. While for the purpose of the present work these efficiency drifts were monitored and accurately accounted for using calibrations at LASA, no such possibility does exist for routine practice.

For this reason we chose to investigate the use of He-3 proportional counters. These counters are fairly insensitive to radiations other than neutrons and may prove successful for use with LINUS. Moreover spherical He-3 proportional counters are commercially available and they can be used in a spherical version of LINUS. In fact a LINUS "sphere" and a SNOOPY "sphere" housing a spherical He-3 proportional counter (3.2 cm active diameter, fill pressure 2 ats) have been built; they have been tested during April 1995 run at CERN (their data analysis is still in progress). The geometry of the LINUS sphere is shown in Figure 17 and its computed response function is presented in Figure 18.

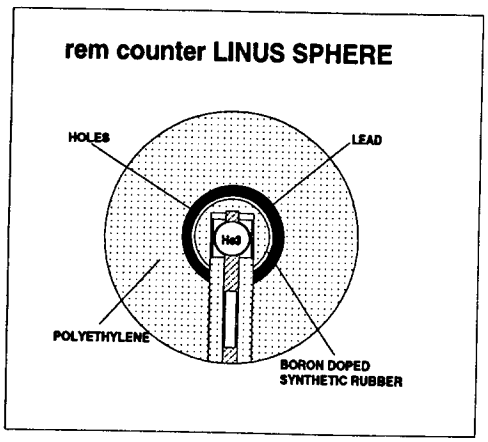

Figure 17 ***Rem counter LINUS sphere as coded into the computer.***

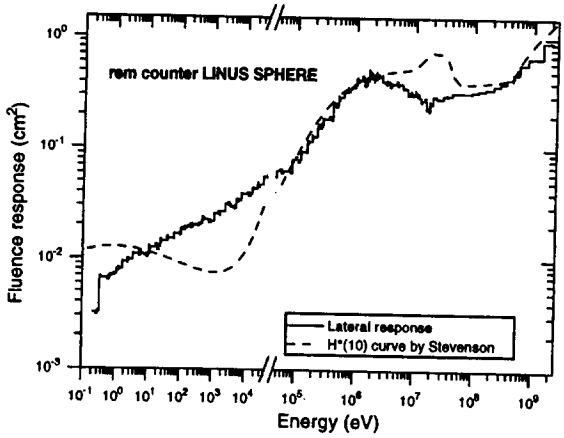

Figure 18 ***Rem counter LINUS sphere. Fluence response.***

These spherical rem counters have been exposed to the LASA Am-Be source and the results are given in Table 12. (The bonner sphere is a polyethylene sphere of 19 cm diameter). The experimental counts given in Table 12 are the "real" ones. The comparison between simulated and experimental results shows that the real efficiency is probably lower than the nominal one. A calibration at PTB is planned for the next months.

Table 12 ***Spherical rem counters. Experimental and computed results. Statistical errors are shown.***

DETECTOR	EXPERIMENTAL		FLUKA	
	cm^2	err%	cm^2	err%
LINUS SPHERE	0.503	2.3	0.552	1.7
SNOOPY SPHERE	0.466	3.1	0.560	1.7
BONNER SPHERE (r = 9.5 cm)	1.95	0.8	2.52	2.1

6. Conclusions

The reliability of the FLUKA code in the simulation of stray radiation fields around high energy hadron accelerators has been validated experimentally. The capability of the code in predicting neutron spectra in very complex geometrical conditions has been demonstrated.

The same experiment was used to confirm the behaviour of LINUS, a new rem counter with a response function greatly extended towards the highest energies. The present results confirm previous experimental evidence of the much increased response of this monitor with respect to conventional instruments when used in radiation fields where a substantial high energy neutron component is present.

Acknowledgements

We are greatly indebted to the CERN radiation protection group and in particular to the head of the group, M. Höefert, for providing us with the beam time and facilities for carrying out the experimental work. Many helpful discussions with A. Fassò and G.R. Stevenson are acknowledged. We are also grateful to G.C. Panini (ENEA, Bologna, Italy) for preparing the cross-section data library.

References

[1] R.C. Raffnsœ , "Instrumentation for Beam Experiments in North Hall", CERN Technical Memorandum TIS-RP-DC/TM/92-27 (1992).

[2] A. Fassò, A. Ferrari, J. Ranft, P.R. Sala, G.R. Stevenson and J.M. Zazula, Proc. of the Workshop on Simulating Accelerator Radiation Environment, Santa Fe, January 11-15, 1993, A. Palounek ed., Los Alamos LA-12835-C, (1994) 134.

[3] A. Ferrari, P.R. Sala, Proc. of the MC93 Int. Conf. on Monte Carlo Simulation in High-Energy and Nuclear Physics , Tallahassee, February 22-26, 1993, Ed. P. Dragovitsch, S.L. Linn, M. Burbank, World Scientific, Singapore, (1994) 277.

[4] A. Fassò, A. Ferrari, J. Ranft and P.R. Sala, Proc. of the 4th Int. Conf. on Calorimetry in High Energy Physics , La Biodola, Italy, September 21-26, 1993, Ed. A. Menzione and A. Scribano, World Scientific, Singapore, (1994) 493.

[5] A. Fassò, A. Ferrari, J. Ranft and P.R. Sala, Proc. of Specialists' Meeting on Shielding Aspects of Accelerators, Target and Irradiation Facilities, Arlington, Texas, April 28-29, 1994, OECD/NEA (1995) 287.

[6] A. Ferrari, P.R. Sala, G. Guaraldi and F. Padoani, Nucl. Instr. Meth. B71 (1992) 412.

[7] A. Fassò, A. Ferrari, J. Ranft, P.R. Sala, G.R. Stevenson and J.M. Zazula, Nucl. Instr. and Meth. A332 , (1993) 459.

[8] E. Cuccoli, A. Ferrari and G.C. Panini, "A Group Library from JEF-1.1 for Flux Calculations in the LHC Machine Detectors", JEF-DOC-340 (1991).

[9] I.O. Andersson and J. Braun, Proc. of the IAEA Symposium on Neutron Dosimetry, Vol. II, IAEA, Vienna, (1963) 87.

[10] C. Birattari, A. Ferrari, C. Nuccetelli, M. Pelliccioni, and M. Silari, Nucl. Instr. and Meth, A297 , (1990) 250.

[11] C. Birattari, A. Esposito, A. Ferrari, M. Pelliccioni, and M. Silari, Radiat. Prot. Dosim., 44, (1992) 193.

[12] C. Birattari, A. Esposito, A. Ferrari, M. Pelliccioni, and M. Silari, Nucl. Instr. and Meth., A324, (1993) 232.

[13] C. Birattari, E. De Ponti, A. Esposito, A. Ferrari, M. Pelliccioni, and M. Silari, Nucl. Instr. and Meth., A338 , (1994) 534.

[14] C. Birattari, E. De Ponti, A. Esposito, A. Ferrari, M. Pelliccioni, and M. Silari, Proc. of the 8th Int. Conf. on Radiation Shielding , Arlington, Texas, April 24-28, 1994, American Nuclear Society ed., Vol. 1, (1994) 254.

[15] A.V. Sannikov, E.N. Savitskaya, "Ambient Dose and Ambient Dose Equivalent Conversion Factors for High Energy Neutrons", Divisional report CERN/TIS-RP/93-14 , 1993.

[16] G.R. Stevenson, "Dose Equivalent per Star in Hadron Cascade Calculations", CERN Divisional Report TIS-RP/173 , 1986.

[17] M. Cosack and H. Lesiecki, ``Dependence of the Response of Eight Neutron Dose Equivalent Survey Meters with Regard to the Energy and Direction of Incident Neutrons", Report EUR-7448-EN , Commission of the European Communities, Luxemburg (1981) 407.

[18] T. Tomoda and S. Fukakusa, Nucl. Instr. and Meth. 224 , (1984) 557.

The computed response functions of the counting devices are given numerically in tables 13-17.

Table 13: computed fluence response ($E_n > 20$ MeV). Statistical errors are shown.

Energy (eV)	CYLINDER 1		CYLINDER 1B		CYLINDER 2		CYLINDER 3	
	cm^2	err%	cm^2	err%	cm^2	err%	cm^2	err%
$2.10 \cdot 10^7$	$4.06 \cdot 10^{-2}$	4.2	$1.06 \cdot 10^{-1}$	3.8	$3.14 \cdot 10^{-1}$	1.5	$5.73 \cdot 10^{-1}$	1.8
$2.50 \cdot 10^7$	$3.22 \cdot 10^{-2}$	3.7	$9.12 \cdot 10^{-2}$	2.7	$2.65 \cdot 10^{-1}$	1.7	$4.92 \cdot 10^{-1}$	1.8
$3.50 \cdot 10^7$	$1.55 \cdot 10^{-2}$	5.2	$4.87 \cdot 10^{-2}$	5.6	$1.56 \cdot 10^{-1}$	2.2	$3.10 \cdot 10^{-1}$	1.0
$5.00 \cdot 10^7$	$1.31 \cdot 10^{-2}$	8.1	$3.71 \cdot 10^{-2}$	4.7	$1.18 \cdot 10^{-1}$	3.8	$2.40 \cdot 10^{-1}$	3.6
$7.50 \cdot 10^7$	$8.60 \cdot 10^{-3}$	4.4	$3.37 \cdot 10^{-2}$	3.8	$8.53 \cdot 10^{-2}$	3.9	$1.79 \cdot 10^{-1}$	2.8
$8.50 \cdot 10^7$	$8.97 \cdot 10^{-3}$	5.1	$2.58 \cdot 10^{-2}$	4.8	$8.42 \cdot 10^{-2}$	5.9	$1.60 \cdot 10^{-1}$	2.8
$1.00 \cdot 10^8$	$8.43 \cdot 10^{-3}$	5.8	$2.41 \cdot 10^{-2}$	5.3	$7.15 \cdot 10^{-2}$	3.3	$1.47 \cdot 10^{-1}$	3.8
$1.35 \cdot 10^8$			$2.35 \cdot 10^{-2}$	6.6	$6.24 \cdot 10^{-2}$	4.6	$1.30 \cdot 10^{-1}$	3.1
$1.75 \cdot 10^8$			$1.95 \cdot 10^{-2}$	6.6	$6.45 \cdot 10^{-2}$	4.6	$1.24 \cdot 10^{-1}$	4.4
$2.50 \cdot 10^8$			$2.01 \cdot 10^{-2}$	4.9	$5.44 \cdot 10^{-2}$	5.1	$1.07 \cdot 10^{-1}$	5.6
$3.00 \cdot 10^8$			$1.78 \cdot 10^{-2}$	6.9	$4.97 \cdot 10^{-2}$	4.5	$1.10 \cdot 10^{-1}$	3.9
$4.00 \cdot 10^8$			$1.76 \cdot 10^{-2}$	7.5	$4.91 \cdot 10^{-2}$	4.1	$1.08 \cdot 10^{-1}$	5.1
$5.00 \cdot 10^8$			$1.62 \cdot 10^{-2}$	7.3	$4.74 \cdot 10^{-2}$	2.9	$9.70 \cdot 10^{-2}$	4.6
$6.50 \cdot 10^8$			$1.59 \cdot 10^{-2}$	5.6	$4.63 \cdot 10^{-2}$	5.3	$1.04 \cdot 10^{-1}$	6.3
$1.00 \cdot 10^9$			$1.47 \cdot 10^{-2}$	7.1	$4.51 \cdot 10^{-2}$	5.5	$1.03 \cdot 10^{-1}$	3.4
$2.00 \cdot 10^9$			$1.86 \cdot 10^{-2}$	4.9	$4.39 \cdot 10^{-2}$	6.8	$9.35 \cdot 10^{-2}$	5.8

Energy (eV)	CYLINDER 4		SNOOPY		LINUS	
	cm^2	err%	cm^2	err%	cm^2	err%
$2.10 \cdot 10^7$	$7.57 \cdot 10^{-1}$	1.2	$1.93 \cdot 10^{-1}$	1.1	$3.39 \cdot 10^{-1}$	1.1
$2.50 \cdot 10^7$	$6.79 \cdot 10^{-1}$	1.4	$1.66 \cdot 10^{-1}$	0.6	$3.29 \cdot 10^{-1}$	1.0
$3.50 \cdot 10^7$	$4.32 \cdot 10^{-1}$	2.4	$1.10 \cdot 10^{-1}$	1.1	$3.51 \cdot 10^{-1}$	0.9
$5.00 \cdot 10^7$	$3.31 \cdot 10^{-1}$	2.8	$8.11 \cdot 10^{-2}$	1.0	$3.43 \cdot 10^{-1}$	1.0
$7.50 \cdot 10^7$	$2.54 \cdot 10^{-1}$	3.0	$6.41 \cdot 10^{-2}$	1.4	$3.48 \cdot 10^{-1}$	1.2
$8.50 \cdot 10^7$	$2.25 \cdot 10^{-1}$	2.0	$5.98 \cdot 10^{-2}$	1.1	$3.48 \cdot 10^{-1}$	0.7
$1.00 \cdot 10^8$	$2.06 \cdot 10^{-1}$	3.9	$5.47 \cdot 10^{-2}$	1.1	$3.53 \cdot 10^{-1}$	1.3
$1.35 \cdot 10^8$	$2.00 \cdot 10^{-1}$	3.3	$4.89 \cdot 10^{-2}$	1.1	$3.72 \cdot 10^{-1}$	1.2
$1.75 \cdot 10^8$	$1.81 \cdot 10^{-1}$	3.0	$4.37 \cdot 10^{-2}$	1.0	$3.84 \cdot 10^{-1}$	1.1
$2.50 \cdot 10^8$	$1.54 \cdot 10^{-1}$	2.2	$4.07 \cdot 10^{-2}$	1.3	$4.19 \cdot 10^{-1}$	1.4
$3.00 \cdot 10^8$	$1.51 \cdot 10^{-1}$	4.1	$3.70 \cdot 10^{-2}$	2.3	$4.44 \cdot 10^{-1}$	0.5
$4.00 \cdot 10^8$	$1.52 \cdot 10^{-1}$	3.9	$3.87 \cdot 10^{-2}$	2.4	$5.08 \cdot 10^{-1}$	1.0
$5.00 \cdot 10^8$	$1.61 \cdot 10^{-1}$	2.4	$3.98 \cdot 10^{-2}$	1.6	$5.53 \cdot 10^{-1}$	1.0
$6.50 \cdot 10^8$	$1.63 \cdot 10^{-1}$	3.9	$3.66 \cdot 10^{-2}$	2.7	$6.35 \cdot 10^{-1}$	0.8
$1.00 \cdot 10^9$	$1.44 \cdot 10^{-1}$	3.1	$3.69 \cdot 10^{-2}$	1.9	$7.24 \cdot 10^{-1}$	1.1
$2.00 \cdot 10^9$	$1.36 \cdot 10^{-1}$	3.5	$3.68 \cdot 10^{-2}$	1.9	$1.04 \cdot 10^{0}$	0.4

Table 14: CYLINDER 1 computed fluence response ($E_n < 20$ MeV). Statistical errors are shown.

FLUKA group	Energy interval (eV)		CYLINDER 1			
			lateral response		isotropic response	
	E_{max}	E_{min}	cm^2	err%	cm^2	err%
1	$1.96 \cdot 10^7$	$1.75 \cdot 10^7$	$6.10 \cdot 10^{-2}$	2.2	$5.65 \cdot 10^{-2}$	5.0
2	$1.75 \cdot 10^7$	$1.49 \cdot 10^7$	$8.02 \cdot 10^{-2}$	1.8	$7.50 \cdot 10^{-2}$	5.1
3	$1.49 \cdot 10^7$	$1.35 \cdot 10^7$	$8.20 \cdot 10^{-2}$	2.2	$7.80 \cdot 10^{-2}$	4.4
4	$1.35 \cdot 10^7$	$1.22 \cdot 10^7$	$8.06 \cdot 10^{-2}$	2.0	$7.60 \cdot 10^{-2}$	5.7
5	$1.22 \cdot 10^7$	$1.11 \cdot 10^7$	$9.88 \cdot 10^{-2}$	2.0	$8.63 \cdot 10^{-2}$	5.7
6	$1.11 \cdot 10^7$	$9.99 \cdot 10^6$	$1.05 \cdot 10^{-1}$	2.0	$9.20 \cdot 10^{-2}$	4.5
7	$9.99 \cdot 10^6$	$9.05 \cdot 10^6$	$1.06 \cdot 10^{-1}$	2.0	$1.09 \cdot 10^{-1}$	3.6
8	$9.05 \cdot 10^6$	$8.19 \cdot 10^6$	$1.34 \cdot 10^{-1}$	1.9	$1.15 \cdot 10^{-1}$	4.5
9	$8.19 \cdot 10^6$	$7.41 \cdot 10^6$	$1.47 \cdot 10^{-1}$	2.2	$1.32 \cdot 10^{-1}$	4.5
10	$7.41 \cdot 10^6$	$6.70 \cdot 10^6$	$1.60 \cdot 10^{-1}$	1.8	$1.62 \cdot 10^{-1}$	5.4
11	$6.70 \cdot 10^6$	$6.07 \cdot 10^6$	$1.95 \cdot 10^{-1}$	1.8	$1.69 \cdot 10^{-1}$	5.1
12	$6.07 \cdot 10^6$	$5.49 \cdot 10^6$	$2.12 \cdot 10^{-1}$	2.2	$1.91 \cdot 10^{-1}$	5.1
13	$5.49 \cdot 10^6$	$4.97 \cdot 10^6$	$2.35 \cdot 10^{-1}$	1.8	$2.09 \cdot 10^{-1}$	4.3
14	$4.97 \cdot 10^6$	$4.49 \cdot 10^6$	$2.59 \cdot 10^{-1}$	1.9	$2.25 \cdot 10^{-1}$	4.1
15	$4.49 \cdot 10^6$	$4.07 \cdot 10^6$	$2.91 \cdot 10^{-1}$	2.1	$2.39 \cdot 10^{-1}$	4.2
16	$4.07 \cdot 10^6$	$3.68 \cdot 10^6$	$3.10 \cdot 10^{-1}$	2.0	$2.68 \cdot 10^{-1}$	5.9
17	$3.68 \cdot 10^6$	$3.33 \cdot 10^6$	$3.34 \cdot 10^{-1}$	1.8	$2.80 \cdot 10^{-1}$	4.3
18	$3.33 \cdot 10^6$	$3.01 \cdot 10^6$	$3.73 \cdot 10^{-1}$	2.2	$3.44 \cdot 10^{-1}$	5.4
19	$3.01 \cdot 10^6$	$2.73 \cdot 10^6$	$4.05 \cdot 10^{-1}$	1.8	$3.48 \cdot 10^{-1}$	4.9
20	$2.73 \cdot 10^6$	$2.47 \cdot 10^6$	$4.57 \cdot 10^{-1}$	2.2	$3.58 \cdot 10^{-1}$	4.8
21	$2.47 \cdot 10^6$	$2.23 \cdot 10^6$	$4.66 \cdot 10^{-1}$	1.9	$4.03 \cdot 10^{-1}$	3.9
22	$2.23 \cdot 10^6$	$2.02 \cdot 10^6$	$5.49 \cdot 10^{-1}$	1.9	$4.71 \cdot 10^{-1}$	5.5
23	$2.02 \cdot 10^6$	$1.83 \cdot 10^6$	$5.56 \cdot 10^{-1}$	2.2	$4.87 \cdot 10^{-1}$	4.8
24	$1.83 \cdot 10^6$	$1.65 \cdot 10^6$	$6.08 \cdot 10^{-1}$	2.0	$5.17 \cdot 10^{-1}$	5.0
25	$1.65 \cdot 10^6$	$1.49 \cdot 10^6$	$6.33 \cdot 10^{-1}$	2.0	$5.51 \cdot 10^{-1}$	4.1
26	$1.49 \cdot 10^6$	$1.35 \cdot 10^6$	$7.28 \cdot 10^{-1}$	2.0	$5.98 \cdot 10^{-1}$	5.0
27	$1.35 \cdot 10^6$	$1.22 \cdot 10^6$	$7.26 \cdot 10^{-1}$	1.8	$6.33 \cdot 10^{-1}$	5.9
28	$1.22 \cdot 10^6$	$1.11 \cdot 10^6$	$7.66 \cdot 10^{-1}$	1.9	$6.60 \cdot 10^{-1}$	4.6
29	$1.11 \cdot 10^6$	$1.00 \cdot 10^6$	$8.19 \cdot 10^{-1}$	1.9	$6.76 \cdot 10^{-1}$	5.3
30	$1.00 \cdot 10^6$	$9.07 \cdot 10^5$	$8.88 \cdot 10^{-1}$	1.8	$7.45 \cdot 10^{-1}$	6.0
31	$9.07 \cdot 10^5$	$8.21 \cdot 10^5$	$9.60 \cdot 10^{-1}$	1.8	$7.74 \cdot 10^{-1}$	4.2
32	$8.21 \cdot 10^5$	$7.43 \cdot 10^5$	$1.01 \cdot 10^0$	2.3	$8.33 \cdot 10^{-1}$	5.6
33	$7.43 \cdot 10^5$	$6.08 \cdot 10^5$	$1.08 \cdot 10^0$	2.3	$8.82 \cdot 10^{-1}$	5.5
34	$6.08 \cdot 10^5$	$4.98 \cdot 10^5$	$1.16 \cdot 10^0$	2.1	$8.34 \cdot 10^{-1}$	4.1
35	$4.98 \cdot 10^5$	$4.08 \cdot 10^5$	$1.25 \cdot 10^0$	2.0	$9.55 \cdot 10^{-1}$	4.6
36	$4.08 \cdot 10^5$	$3.34 \cdot 10^5$	$1.30 \cdot 10^0$	2.0	$9.85 \cdot 10^{-1}$	5.0
37	$3.34 \cdot 10^5$	$2.73 \cdot 10^5$	$1.42 \cdot 10^0$	1.8	$1.03 \cdot 10^0$	5.0
38	$2.73 \cdot 10^5$	$2.24 \cdot 10^5$	$1.45 \cdot 10^0$	1.9	$1.14 \cdot 10^0$	5.4
39	$2.24 \cdot 10^5$	$1.83 \cdot 10^5$	$1.57 \cdot 10^0$	2.0	$1.07 \cdot 10^0$	5.1
40	$1.83 \cdot 10^5$	$1.50 \cdot 10^5$	$1.57 \cdot 10^0$	1.6	$1.17 \cdot 10^0$	6.2
41	$1.50 \cdot 10^5$	$1.23 \cdot 10^5$	$1.67 \cdot 10^0$	1.8	$1.27 \cdot 10^0$	4.1
42	$1.23 \cdot 10^5$	$8.65 \cdot 10^4$	$1.70 \cdot 10^0$	2.2	$1.20 \cdot 10^0$	5.6
43	$8.65 \cdot 10^4$	$5.25 \cdot 10^4$	$1.71 \cdot 10^0$	1.8	$1.28 \cdot 10^0$	7.3
44	$5.25 \cdot 10^4$	$3.18 \cdot 10^4$	$1.86 \cdot 10^0$	1.9	$1.36 \cdot 10^0$	4.8
45	$3.18 \cdot 10^4$	$2.19 \cdot 10^4$	$1.94 \cdot 10^0$	2.1	$1.34 \cdot 10^0$	5.5
46	$2.19 \cdot 10^4$	$1.50 \cdot 10^4$	$1.88 \cdot 10^0$	1.7	$1.53 \cdot 10^0$	4.8
47	$1.50 \cdot 10^4$	$1.03 \cdot 10^4$	$1.98 \cdot 10^0$	1.6	$1.36 \cdot 10^0$	5.1
48	$1.03 \cdot 10^4$	$7.10 \cdot 10^3$	$2.06 \cdot 10^0$	1.9	$1.41 \cdot 10^0$	6.0
49	$7.10 \cdot 10^3$	$4.88 \cdot 10^3$	$2.10 \cdot 10^0$	2.2	$1.41 \cdot 10^0$	5.7
50	$4.88 \cdot 10^3$	$3.35 \cdot 10^3$	$2.07 \cdot 10^0$	1.9	$1.50 \cdot 10^0$	3.7
51	$3.35 \cdot 10^3$	$2.31 \cdot 10^3$	$2.18 \cdot 10^0$	1.9	$1.58 \cdot 10^0$	5.1
52	$2.31 \cdot 10^3$	$1.58 \cdot 10^3$	$2.31 \cdot 10^0$	2.0	$1.81 \cdot 10^0$	4.7
53	$1.58 \cdot 10^3$	$1.04 \cdot 10^3$	$2.32 \cdot 10^0$	2.1	$1.75 \cdot 10^0$	5.4
54	$1.04 \cdot 10^3$	$6.89 \cdot 10^2$	$2.33 \cdot 10^0$	2.2	$1.67 \cdot 10^0$	4.6
55	$6.89 \cdot 10^2$	$4.54 \cdot 10^2$	$2.47 \cdot 10^0$	2.0	$1.71 \cdot 10^0$	4.3
56	$4.54 \cdot 10^2$	$2.75 \cdot 10^2$	$2.45 \cdot 10^0$	1.6	$1.81 \cdot 10^0$	3.4
57	$2.75 \cdot 10^2$	$1.67 \cdot 10^2$	$2.50 \cdot 10^0$	2.0	$1.70 \cdot 10^0$	5.6
58	$1.67 \cdot 10^2$	$1.01 \cdot 10^2$	$2.53 \cdot 10^0$	2.2	$1.83 \cdot 10^0$	5.1
59	$1.01 \cdot 10^2$	$6.14 \cdot 10^1$	$2.58 \cdot 10^0$	2.1	$1.79 \cdot 10^0$	4.4
60	$6.14 \cdot 10^1$	$3.73 \cdot 10^1$	$2.60 \cdot 10^0$	2.1	$1.74 \cdot 10^0$	3.8
61	$3.73 \cdot 10^1$	$2.26 \cdot 10^1$	$2.69 \cdot 10^0$	2.0	$1.92 \cdot 10^0$	4.9
62	$2.26 \cdot 10^1$	$1.55 \cdot 10^1$	$2.79 \cdot 10^0$	1.9	$2.10 \cdot 10^0$	5.0
63	$1.55 \cdot 10^1$	$1.07 \cdot 10^1$	$2.78 \cdot 10^0$	1.9	$1.76 \cdot 10^0$	4.8
64	$1.07 \cdot 10^1$	$7.34 \cdot 10^0$	$2.71 \cdot 10^0$	1.9	$1.99 \cdot 10^0$	4.7
65	$7.34 \cdot 10^0$	$5.04 \cdot 10^0$	$2.78 \cdot 10^0$	2.0	$1.92 \cdot 10^0$	5.2
66	$5.04 \cdot 10^0$	$3.47 \cdot 10^0$	$2.67 \cdot 10^0$	1.8	$1.96 \cdot 10^0$	5.8
67	$3.47 \cdot 10^0$	$2.38 \cdot 10^0$	$2.61 \cdot 10^0$	1.9	$1.88 \cdot 10^0$	6.1
68	$2.38 \cdot 10^0$	$1.64 \cdot 10^0$	$2.60 \cdot 10^0$	1.8	$1.83 \cdot 10^0$	4.2
69	$1.64 \cdot 10^0$	$1.13 \cdot 10^0$	$2.40 \cdot 10^0$	2.3	$1.73 \cdot 10^0$	5.5
70	$1.13 \cdot 10^0$	$6.83 \cdot 10^{-1}$	$2.26 \cdot 10^0$	1.8	$1.59 \cdot 10^0$	3.5
71	$6.83 \cdot 10^{-1}$	$4.14 \cdot 10^{-1}$	$2.03 \cdot 10^0$	2.0	$1.38 \cdot 10^0$	5.2
72	$4.14 \cdot 10^{-1}$	$1.00 \cdot 10^{-2}$	$9.06 \cdot 10^{-1}$	1.8	$6.61 \cdot 10^{-1}$	6.2

Table 15: CYLINDER 1B and CYLINDER 2. computed fluence response ($E_n < 20$ MeV). Statistical errors are shown.

FLUKA group	CYLINDER 1B				CYLINDER 2			
	lateral response		isotropic response		lateral response		isotropic response	
	cm^2	err%	cm^2	err%	cm^2	err%	cm^2	err%
1	$1.11 \cdot 10^{-1}$	3.4	$1.75 \cdot 10^{-1}$	3.3	$3.50 \cdot 10^{-1}$	1.9	$3.22 \cdot 10^{-1}$	3.8
2	$1.39 \cdot 10^{-1}$	2.4	$2.19 \cdot 10^{-1}$	3.8	$4.47 \cdot 10^{-1}$	2.0	$3.99 \cdot 10^{-1}$	3.2
3	$1.39 \cdot 10^{-1}$	3.4	$2.34 \cdot 10^{-1}$	4.3	$4.56 \cdot 10^{-1}$	2.1	$4.12 \cdot 10^{-1}$	3.1
4	$1.47 \cdot 10^{-1}$	2.7	$2.23 \cdot 10^{-1}$	3.4	$4.71 \cdot 10^{-1}$	1.7	$3.90 \cdot 10^{-1}$	4.0
5	$1.72 \cdot 10^{-1}$	2.3	$2.64 \cdot 10^{-1}$	3.8	$5.30 \cdot 10^{-1}$	1.7	$4.59 \cdot 10^{-1}$	4.1
6	$1.83 \cdot 10^{-1}$	2.6	$2.89 \cdot 10^{-1}$	3.2	$5.57 \cdot 10^{-1}$	1.8	$4.97 \cdot 10^{-1}$	3.6
7	$1.87 \cdot 10^{-1}$	2.9	$3.10 \cdot 10^{-1}$	3.3	$6.18 \cdot 10^{-1}$	2.3	$5.08 \cdot 10^{-1}$	3.5
8	$2.45 \cdot 10^{-1}$	3.5	$3.25 \cdot 10^{-1}$	3.6	$6.70 \cdot 10^{-1}$	1.8	$6.37 \cdot 10^{-1}$	4.1
9	$2.67 \cdot 10^{-1}$	3.1	$3.99 \cdot 10^{-1}$	3.0	$7.65 \cdot 10^{-1}$	2.0	$7.15 \cdot 10^{-1}$	4.0
10	$2.67 \cdot 10^{-1}$	2.4	$4.38 \cdot 10^{-1}$	3.1	$8.50 \cdot 10^{-1}$	2.0	$7.38 \cdot 10^{-1}$	3.7
11	$3.39 \cdot 10^{-1}$	2.4	$4.50 \cdot 10^{-1}$	3.1	$9.43 \cdot 10^{-1}$	2.2	$7.94 \cdot 10^{-1}$	3.4
12	$3.29 \cdot 10^{-1}$	3.1	$4.90 \cdot 10^{-1}$	4.1	$1.02 \cdot 10^{0}$	2.2	$8.74 \cdot 10^{-1}$	3.9
13	$3.82 \cdot 10^{-1}$	4.0	$5.46 \cdot 10^{-1}$	3.0	$1.06 \cdot 10^{0}$	2.2	$9.89 \cdot 10^{-1}$	3.8
14	$3.95 \cdot 10^{-1}$	3.3	$6.11 \cdot 10^{-1}$	3.1	$1.24 \cdot 10^{0}$	1.9	$9.83 \cdot 10^{-1}$	5.2
15	$4.46 \cdot 10^{-1}$	2.0	$6.74 \cdot 10^{-1}$	3.4	$1.21 \cdot 10^{0}$	2.0	$1.06 \cdot 10^{0}$	2.6
16	$4.83 \cdot 10^{-1}$	3.7	$6.41 \cdot 10^{-1}$	3.1	$1.28 \cdot 10^{0}$	1.7	$1.12 \cdot 10^{0}$	4.8
17	$5.14 \cdot 10^{-1}$	3.1	$7.22 \cdot 10^{-1}$	3.2	$1.27 \cdot 10^{0}$	2.3	$1.07 \cdot 10^{0}$	2.2
18	$5.56 \cdot 10^{-1}$	1.4	$7.84 \cdot 10^{-1}$	2.8	$1.49 \cdot 10^{0}$	2.0	$1.19 \cdot 10^{0}$	4.2
19	$5.48 \cdot 10^{-1}$	3.8	$7.99 \cdot 10^{-1}$	3.5	$1.66 \cdot 10^{0}$	1.4	$1.21 \cdot 10^{0}$	3.7
20	$6.20 \cdot 10^{-1}$	4.2	$8.96 \cdot 10^{-1}$	3.1	$1.67 \cdot 10^{0}$	1.9	$1.38 \cdot 10^{0}$	4.5
21	$6.88 \cdot 10^{-1}$	3.0	$9.47 \cdot 10^{-1}$	3.7	$1.75 \cdot 10^{0}$	2.4	$1.53 \cdot 10^{0}$	2.6
22	$7.24 \cdot 10^{-1}$	4.6	$1.01 \cdot 10^{0}$	4.0	$1.79 \cdot 10^{0}$	2.0	$1.38 \cdot 10^{0}$	3.2
23	$7.41 \cdot 10^{-1}$	4.0	$1.13 \cdot 10^{0}$	2.6	$1.99 \cdot 10^{0}$	2.0	$1.58 \cdot 10^{0}$	3.1
24	$7.97 \cdot 10^{-1}$	2.9	$1.08 \cdot 10^{0}$	3.4	$1.98 \cdot 10^{0}$	1.9	$1.60 \cdot 10^{0}$	2.9
25	$8.94 \cdot 10^{-1}$	4.2	$1.18 \cdot 10^{0}$	3.3	$1.97 \cdot 10^{0}$	2.0	$1.53 \cdot 10^{0}$	3.4
26	$8.84 \cdot 10^{-1}$	3.3	$1.19 \cdot 10^{0}$	4.1	$2.04 \cdot 10^{0}$	2.2	$1.75 \cdot 10^{0}$	3.6
27	$9.47 \cdot 10^{-1}$	4.2	$1.27 \cdot 10^{0}$	4.4	$2.21 \cdot 10^{0}$	1.5	$1.60 \cdot 10^{0}$	4.1
28	$1.01 \cdot 10^{0}$	4.5	$1.34 \cdot 10^{0}$	3.5	$2.18 \cdot 10^{0}$	1.9	$1.77 \cdot 10^{0}$	4.1
29	$1.04 \cdot 10^{0}$	4.9	$1.34 \cdot 10^{0}$	3.2	$2.22 \cdot 10^{0}$	2.1	$1.69 \cdot 10^{0}$	3.1
30	$1.12 \cdot 10^{0}$	4.0	$1.32 \cdot 10^{0}$	3.5	$2.30 \cdot 10^{0}$	1.6	$1.80 \cdot 10^{0}$	3.7
31	$1.12 \cdot 10^{0}$	3.9	$1.44 \cdot 10^{0}$	3.8	$2.37 \cdot 10^{0}$	1.9	$1.68 \cdot 10^{0}$	3.2
32	$1.16 \cdot 10^{0}$	4.3	$1.55 \cdot 10^{0}$	3.4	$2.39 \cdot 10^{0}$	2.0	$1.84 \cdot 10^{0}$	4.0
33	$1.12 \cdot 10^{0}$	3.2	$1.51 \cdot 10^{0}$	3.9	$2.39 \cdot 10^{0}$	2.3	$1.78 \cdot 10^{0}$	4.8
34	$1.28 \cdot 10^{0}$	6.3	$1.63 \cdot 10^{0}$	3.2	$2.33 \cdot 10^{0}$	2.0	$1.81 \cdot 10^{0}$	3.4
35	$1.31 \cdot 10^{0}$	4.2	$1.61 \cdot 10^{0}$	3.7	$2.35 \cdot 10^{0}$	2.1	$1.73 \cdot 10^{0}$	3.2
36	$1.34 \cdot 10^{0}$	3.0	$1.66 \cdot 10^{0}$	3.5	$2.43 \cdot 10^{0}$	2.2	$1.73 \cdot 10^{0}$	3.7
37	$1.33 \cdot 10^{0}$	4.2	$1.64 \cdot 10^{0}$	3.5	$2.42 \cdot 10^{0}$	2.2	$1.78 \cdot 10^{0}$	3.6
38	$1.37 \cdot 10^{0}$	3.5	$1.65 \cdot 10^{0}$	3.3	$2.31 \cdot 10^{0}$	2.3	$1.63 \cdot 10^{0}$	4.0
39	$1.28 \cdot 10^{0}$	3.9	$1.68 \cdot 10^{0}$	2.9	$2.33 \cdot 10^{0}$	1.7	$1.66 \cdot 10^{0}$	3.0
40	$1.38 \cdot 10^{0}$	2.9	$1.68 \cdot 10^{0}$	3.1	$2.32 \cdot 10^{0}$	1.7	$1.51 \cdot 10^{0}$	4.8
41	$1.41 \cdot 10^{0}$	3.2	$1.63 \cdot 10^{0}$	3.7	$2.18 \cdot 10^{0}$	1.9	$1.67 \cdot 10^{0}$	3.1
42	$1.31 \cdot 10^{0}$	3.1	$1.68 \cdot 10^{0}$	4.5	$2.10 \cdot 10^{0}$	1.8	$1.43 \cdot 10^{0}$	2.5
43	$1.35 \cdot 10^{0}$	2.9	$1.74 \cdot 10^{0}$	4.0	$2.14 \cdot 10^{0}$	1.4	$1.57 \cdot 10^{0}$	4.8
44	$1.36 \cdot 10^{0}$	4.0	$1.55 \cdot 10^{0}$	3.5	$2.00 \cdot 10^{0}$	2.2	$1.41 \cdot 10^{0}$	4.0
45	$1.38 \cdot 10^{0}$	4.1	$1.60 \cdot 10^{0}$	3.9	$2.01 \cdot 10^{0}$	2.0	$1.43 \cdot 10^{0}$	3.1
46	$1.33 \cdot 10^{0}$	2.6	$1.59 \cdot 10^{0}$	3.2	$1.85 \cdot 10^{0}$	2.6	$1.37 \cdot 10^{0}$	4.1
47	$1.33 \cdot 10^{0}$	4.6	$1.70 \cdot 10^{0}$	3.4	$1.79 \cdot 10^{0}$	2.2	$1.29 \cdot 10^{0}$	3.2
48	$1.37 \cdot 10^{0}$	2.4	$1.59 \cdot 10^{0}$	3.1	$1.86 \cdot 10^{0}$	2.0	$1.36 \cdot 10^{0}$	3.9
49	$1.37 \cdot 10^{0}$	5.0	$1.66 \cdot 10^{0}$	3.9	$1.92 \cdot 10^{0}$	1.7	$1.38 \cdot 10^{0}$	4.7
50	$1.37 \cdot 10^{0}$	4.1	$1.69 \cdot 10^{0}$	3.9	$1.77 \cdot 10^{0}$	1.8	$1.38 \cdot 10^{0}$	3.8
51	$1.45 \cdot 10^{0}$	2.5	$1.66 \cdot 10^{0}$	3.9	$1.90 \cdot 10^{0}$	1.6	$1.30 \cdot 10^{0}$	4.2
52	$1.47 \cdot 10^{0}$	3.0	$1.57 \cdot 10^{0}$	4.4	$1.74 \cdot 10^{0}$	1.6	$1.28 \cdot 10^{0}$	4.1
53	$1.41 \cdot 10^{0}$	4.3	$1.70 \cdot 10^{0}$	3.6	$1.75 \cdot 10^{0}$	1.5	$1.26 \cdot 10^{0}$	5.1
54	$1.36 \cdot 10^{0}$	5.1	$1.60 \cdot 10^{0}$	3.4	$1.76 \cdot 10^{0}$	2.4	$1.26 \cdot 10^{0}$	4.0
55	$1.39 \cdot 10^{0}$	2.4	$1.73 \cdot 10^{0}$	2.8	$1.78 \cdot 10^{0}$	2.0	$1.22 \cdot 10^{0}$	5.0
56	$1.44 \cdot 10^{0}$	3.2	$1.71 \cdot 10^{0}$	3.9	$1.72 \cdot 10^{0}$	1.6	$1.17 \cdot 10^{0}$	4.3
57	$1.39 \cdot 10^{0}$	3.6	$1.64 \cdot 10^{0}$	3.4	$1.66 \cdot 10^{0}$	2.0	$1.16 \cdot 10^{0}$	2.8
58	$1.42 \cdot 10^{0}$	3.8	$1.60 \cdot 10^{0}$	3.6	$1.55 \cdot 10^{0}$	2.0	$1.23 \cdot 10^{0}$	2.9
59	$1.42 \cdot 10^{0}$	2.6	$1.74 \cdot 10^{0}$	2.9	$1.57 \cdot 10^{0}$	1.5	$1.20 \cdot 10^{0}$	3.5
60	$1.48 \cdot 10^{0}$	2.3	$1.56 \cdot 10^{0}$	3.4	$1.55 \cdot 10^{0}$	2.1	$1.07 \cdot 10^{0}$	3.8
61	$1.43 \cdot 10^{0}$	3.8	$1.52 \cdot 10^{0}$	3.4	$1.57 \cdot 10^{0}$	2.3	$1.01 \cdot 10^{0}$	3.1
62	$1.39 \cdot 10^{0}$	3.9	$1.57 \cdot 10^{0}$	2.8	$1.49 \cdot 10^{0}$	2.3	$1.06 \cdot 10^{0}$	4.1
63	$1.33 \cdot 10^{0}$	2.5	$1.49 \cdot 10^{0}$	4.9	$1.41 \cdot 10^{0}$	2.0	$9.15 \cdot 10^{-1}$	3.7
64	$1.35 \cdot 10^{0}$	6.7	$1.43 \cdot 10^{0}$	4.3	$1.30 \cdot 10^{0}$	1.9	$9.96 \cdot 10^{-1}$	4.4
65	$1.27 \cdot 10^{0}$	3.6	$1.43 \cdot 10^{0}$	3.6	$1.26 \cdot 10^{0}$	1.9	$8.50 \cdot 10^{-1}$	5.3
66	$1.36 \cdot 10^{0}$	3.5	$1.33 \cdot 10^{0}$	3.5	$1.23 \cdot 10^{0}$	1.7	$8.88 \cdot 10^{-1}$	2.6
67	$1.19 \cdot 10^{0}$	4.0	$1.34 \cdot 10^{0}$	3.7	$1.16 \cdot 10^{0}$	1.9	$8.04 \cdot 10^{-1}$	2.7
68	$1.12 \cdot 10^{0}$	4.8	$1.27 \cdot 10^{0}$	3.3	$1.12 \cdot 10^{0}$	1.7	$7.81 \cdot 10^{-1}$	4.2
69	$1.07 \cdot 10^{0}$	2.1	$1.11 \cdot 10^{0}$	3.8	$1.01 \cdot 10^{0}$	2.0	$7.01 \cdot 10^{-1}$	3.9
70	$9.75 \cdot 10^{-1}$	2.9	$1.08 \cdot 10^{0}$	3.1	$9.24 \cdot 10^{-1}$	2.0	$6.43 \cdot 10^{-1}$	3.9
71	$8.52 \cdot 10^{-1}$	4.0	$8.67 \cdot 10^{-1}$	3.8	$7.96 \cdot 10^{-1}$	2.6	$5.41 \cdot 10^{-1}$	3.1
72	$3.78 \cdot 10^{-1}$	3.3	$4.22 \cdot 10^{-1}$	3.0	$3.62 \cdot 10^{-1}$	1.4	$2.63 \cdot 10^{-1}$	3.9

Table 16: CYLINDER 3 and CYLINDER 4. computed fluence response ($E_n < 20$ MeV). Statistical errors are shown.

FLUKA group	CYLINDER 3				CYLINDER 4			
	lateral response		isotropic response		lateral response		isotropic response	
	cm^2	err%	cm^2	err%	cm^2	err%	cm^2	err%
1	$6.62 \cdot 10^{-1}$	3.2	$6.09 \cdot 10^{-1}$	3.7	$8.21 \cdot 10^{-1}$	6.4	$8.10 \cdot 10^{-1}$	5.1
2	$7.64 \cdot 10^{-1}$	2.8	$7.29 \cdot 10^{-1}$	4.8	$8.14 \cdot 10^{-1}$	5.5	$8.14 \cdot 10^{-1}$	5.0
3	$7.64 \cdot 10^{-1}$	3.4	$6.34 \cdot 10^{-1}$	4.6	$1.16 \cdot 10^{0}$	4.9	$8.69 \cdot 10^{-1}$	3.9
4	$8.04 \cdot 10^{-1}$	3.0	$7.90 \cdot 10^{-1}$	4.8	$1.03 \cdot 10^{0}$	5.5	$9.24 \cdot 10^{-1}$	6.4
5	$9.47 \cdot 10^{-1}$	3.3	$7.86 \cdot 10^{-1}$	5.6	$1.11 \cdot 10^{0}$	4.7	$9.89 \cdot 10^{-1}$	5.5
6	$9.95 \cdot 10^{-1}$	3.1	$8.42 \cdot 10^{-1}$	4.3	$1.27 \cdot 10^{0}$	5.2	$9.88 \cdot 10^{-1}$	5.3
7	$1.00 \cdot 10^{0}$	3.6	$9.95 \cdot 10^{-1}$	4.5	$1.19 \cdot 10^{0}$	5.5	$1.06 \cdot 10^{0}$	4.9
8	$1.19 \cdot 10^{0}$	3.1	$1.04 \cdot 10^{0}$	4.5	$1.23 \cdot 10^{0}$	5.0	$1.11 \cdot 10^{0}$	6.1
9	$1.30 \cdot 10^{0}$	2.5	$1.06 \cdot 10^{0}$	6.1	$1.65 \cdot 10^{0}$	4.6	$1.33 \cdot 10^{0}$	4.9
10	$1.30 \cdot 10^{0}$	3.3	$1.27 \cdot 10^{0}$	5.3	$1.44 \cdot 10^{0}$	6.4	$1.27 \cdot 10^{0}$	5.7
11	$1.46 \cdot 10^{0}$	2.8	$1.33 \cdot 10^{0}$	4.7	$1.55 \cdot 10^{0}$	6.1	$1.33 \cdot 10^{0}$	4.9
12	$1.50 \cdot 10^{0}$	2.7	$1.35 \cdot 10^{0}$	4.5	$1.75 \cdot 10^{0}$	5.2	$1.40 \cdot 10^{0}$	4.6
13	$1.68 \cdot 10^{0}$	2.9	$1.36 \cdot 10^{0}$	4.5	$1.81 \cdot 10^{0}$	5.5	$1.45 \cdot 10^{0}$	4.5
14	$1.72 \cdot 10^{0}$	2.7	$1.45 \cdot 10^{0}$	5.4	$1.86 \cdot 10^{0}$	6.9	$1.63 \cdot 10^{0}$	5.8
15	$1.80 \cdot 10^{0}$	3.3	$1.54 \cdot 10^{0}$	4.4	$1.97 \cdot 10^{0}$	7.2	$1.60 \cdot 10^{0}$	5.7
16	$1.78 \cdot 10^{0}$	3.0	$1.29 \cdot 10^{0}$	4.5	$1.69 \cdot 10^{0}$	6.4	$1.38 \cdot 10^{0}$	5.2
17	$1.74 \cdot 10^{0}$	2.6	$1.42 \cdot 10^{0}$	5.6	$1.71 \cdot 10^{0}$	7.4	$1.33 \cdot 10^{0}$	6.1
18	$1.92 \cdot 10^{0}$	3.0	$1.60 \cdot 10^{0}$	3.2	$1.78 \cdot 10^{0}$	5.5	$1.47 \cdot 10^{0}$	5.1
19	$1.93 \cdot 10^{0}$	2.9	$1.57 \cdot 10^{0}$	5.3	$1.89 \cdot 10^{0}$	6.1	$1.48 \cdot 10^{0}$	5.3
20	$2.10 \cdot 10^{0}$	3.7	$1.51 \cdot 10^{0}$	5.4	$1.92 \cdot 10^{0}$	4.3	$1.41 \cdot 10^{0}$	4.6
21	$2.10 \cdot 10^{0}$	3.4	$1.75 \cdot 10^{0}$	5.5	$1.63 \cdot 10^{0}$	7.7	$1.45 \cdot 10^{0}$	6.2
22	$2.07 \cdot 10^{0}$	2.8	$1.73 \cdot 10^{0}$	4.2	$1.92 \cdot 10^{0}$	8.4	$1.33 \cdot 10^{0}$	4.6
23	$2.19 \cdot 10^{0}$	3.0	$1.84 \cdot 10^{0}$	5.4	$1.73 \cdot 10^{0}$	5.8	$1.53 \cdot 10^{0}$	4.7
24	$2.13 \cdot 10^{0}$	2.8	$1.73 \cdot 10^{0}$	5.1	$1.95 \cdot 10^{0}$	5.6	$1.49 \cdot 10^{0}$	4.2
25	$2.25 \cdot 10^{0}$	2.7	$1.67 \cdot 10^{0}$	5.2	$1.59 \cdot 10^{0}$	9.2	$1.34 \cdot 10^{0}$	5.0
26	$2.09 \cdot 10^{0}$	3.1	$1.68 \cdot 10^{0}$	4.3	$1.69 \cdot 10^{0}$	6.9	$1.39 \cdot 10^{0}$	5.5
27	$2.13 \cdot 10^{0}$	3.1	$1.71 \cdot 10^{0}$	5.1	$1.60 \cdot 10^{0}$	7.6	$1.34 \cdot 10^{0}$	4.5
28	$2.12 \cdot 10^{0}$	3.9	$1.54 \cdot 10^{0}$	4.8	$1.63 \cdot 10^{0}$	4.8	$1.26 \cdot 10^{0}$	5.8
29	$2.23 \cdot 10^{0}$	3.0	$1.58 \cdot 10^{0}$	4.8	$1.22 \cdot 10^{0}$	4.6	$1.08 \cdot 10^{0}$	4.8
30	$2.04 \cdot 10^{0}$	2.9	$1.69 \cdot 10^{0}$	6.0	$1.74 \cdot 10^{0}$	4.8	$1.19 \cdot 10^{0}$	5.6
31	$2.16 \cdot 10^{0}$	2.6	$1.51 \cdot 10^{0}$	4.6	$1.36 \cdot 10^{0}$	8.0	$1.09 \cdot 10^{0}$	4.7
32	$2.09 \cdot 10^{0}$	2.3	$1.64 \cdot 10^{0}$	4.0	$1.33 \cdot 10^{0}$	6.1	$1.03 \cdot 10^{0}$	5.0
33	$2.06 \cdot 10^{0}$	3.1	$1.63 \cdot 10^{0}$	5.2	$1.34 \cdot 10^{0}$	5.8	$9.02 \cdot 10^{-1}$	5.0
34	$2.01 \cdot 10^{0}$	3.1	$1.41 \cdot 10^{0}$	5.0	$1.11 \cdot 10^{0}$	6.1	$8.15 \cdot 10^{-1}$	5.8
35	$1.74 \cdot 10^{0}$	2.7	$1.33 \cdot 10^{0}$	5.3	$8.96 \cdot 10^{-1}$	4.2	$6.92 \cdot 10^{-1}$	5.8
36	$1.81 \cdot 10^{0}$	3.9	$1.27 \cdot 10^{0}$	4.5	$9.12 \cdot 10^{-1}$	8.4	$7.07 \cdot 10^{-1}$	5.5
37	$1.58 \cdot 10^{0}$	4.0	$1.11 \cdot 10^{0}$	6.8	$6.89 \cdot 10^{-1}$	5.8	$6.37 \cdot 10^{-1}$	4.9
38	$1.46 \cdot 10^{0}$	2.6	$1.07 \cdot 10^{0}$	5.8	$6.56 \cdot 10^{-1}$	7.4	$5.76 \cdot 10^{-1}$	5.4
39	$1.43 \cdot 10^{0}$	2.7	$1.08 \cdot 10^{0}$	6.0	$6.40 \cdot 10^{-1}$	7.0	$4.74 \cdot 10^{-1}$	4.4
40	$1.35 \cdot 10^{0}$	3.3	$9.44 \cdot 10^{-1}$	5.3	$5.95 \cdot 10^{-1}$	8.6	$4.70 \cdot 10^{-1}$	6.0
41	$1.30 \cdot 10^{0}$	3.0	$9.80 \cdot 10^{-1}$	4.1	$5.66 \cdot 10^{-1}$	6.0	$4.19 \cdot 10^{-1}$	4.8
42	$1.19 \cdot 10^{0}$	3.7	$8.41 \cdot 10^{-1}$	6.6	$4.81 \cdot 10^{-1}$	7.1	$3.85 \cdot 10^{-1}$	5.3
43	$1.09 \cdot 10^{0}$	3.6	$8.06 \cdot 10^{-1}$	4.9	$3.82 \cdot 10^{-1}$	6.5	$3.65 \cdot 10^{-1}$	5.6
44	$9.74 \cdot 10^{-1}$	2.1	$6.57 \cdot 10^{-1}$	5.1	$4.05 \cdot 10^{-1}$	7.6	$3.11 \cdot 10^{-1}$	5.3
45	$9.63 \cdot 10^{-1}$	3.3	$6.91 \cdot 10^{-1}$	3.5	$3.43 \cdot 10^{-1}$	5.6	$3.11 \cdot 10^{-1}$	5.1
46	$8.37 \cdot 10^{-1}$	3.3	$7.04 \cdot 10^{-1}$	5.1	$3.20 \cdot 10^{-1}$	7.3	$2.77 \cdot 10^{-1}$	4.6
47	$8.53 \cdot 10^{-1}$	2.4	$6.19 \cdot 10^{-1}$	5.1	$2.85 \cdot 10^{-1}$	5.1	$2.47 \cdot 10^{-1}$	6.6
48	$8.19 \cdot 10^{-1}$	3.2	$5.97 \cdot 10^{-1}$	4.7	$2.88 \cdot 10^{-1}$	5.6	$2.52 \cdot 10^{-1}$	4.9
49	$8.41 \cdot 10^{-1}$	2.7	$5.78 \cdot 10^{-1}$	4.6	$2.50 \cdot 10^{-1}$	4.9	$2.63 \cdot 10^{-1}$	6.0
50	$8.24 \cdot 10^{-1}$	2.9	$5.53 \cdot 10^{-1}$	5.2	$2.76 \cdot 10^{-1}$	4.5	$2.48 \cdot 10^{-1}$	6.8
51	$7.92 \cdot 10^{-1}$	3.2	$5.84 \cdot 10^{-1}$	4.9	$3.24 \cdot 10^{-1}$	5.1	$2.68 \cdot 10^{-1}$	5.0
52	$7.62 \cdot 10^{-1}$	3.8	$5.72 \cdot 10^{-1}$	5.8	$2.81 \cdot 10^{-1}$	5.5	$2.37 \cdot 10^{-1}$	5.9
53	$7.23 \cdot 10^{-1}$	2.9	$5.98 \cdot 10^{-1}$	4.6	$2.96 \cdot 10^{-1}$	5.9	$2.47 \cdot 10^{-1}$	5.3
54	$7.20 \cdot 10^{-1}$	3.2	$5.38 \cdot 10^{-1}$	4.2	$2.52 \cdot 10^{-1}$	7.9	$2.10 \cdot 10^{-1}$	5.2
55	$7.05 \cdot 10^{-1}$	2.5	$5.21 \cdot 10^{-1}$	3.7	$2.35 \cdot 10^{-1}$	6.0	$2.14 \cdot 10^{-1}$	4.7
56	$7.09 \cdot 10^{-1}$	4.1	$4.52 \cdot 10^{-1}$	5.0	$2.41 \cdot 10^{-1}$	6.4	$2.12 \cdot 10^{-1}$	5.9
57	$6.34 \cdot 10^{-1}$	2.6	$5.32 \cdot 10^{-1}$	4.3	$2.16 \cdot 10^{-1}$	7.1	$2.00 \cdot 10^{-1}$	4.3
58	$6.61 \cdot 10^{-1}$	2.8	$4.78 \cdot 10^{-1}$	4.8	$1.64 \cdot 10^{-1}$	7.7	$1.99 \cdot 10^{-1}$	5.0
59	$6.08 \cdot 10^{-1}$	2.8	$4.45 \cdot 10^{-1}$	4.5	$1.95 \cdot 10^{-1}$	4.4	$1.75 \cdot 10^{-1}$	6.6
60	$5.60 \cdot 10^{-1}$	2.2	$4.01 \cdot 10^{-1}$	4.8	$1.63 \cdot 10^{-1}$	6.7	$1.80 \cdot 10^{-1}$	5.5
61	$5.49 \cdot 10^{-1}$	2.9	$4.13 \cdot 10^{-1}$	5.9	$2.01 \cdot 10^{-1}$	8.1	$1.52 \cdot 10^{-1}$	4.4
62	$5.34 \cdot 10^{-1}$	3.2	$4.04 \cdot 10^{-1}$	6.3	$1.86 \cdot 10^{-1}$	4.7	$1.55 \cdot 10^{-1}$	5.1
63	$4.81 \cdot 10^{-1}$	3.5	$3.81 \cdot 10^{-1}$	5.7	$1.61 \cdot 10^{-1}$	7.7	$1.45 \cdot 10^{-1}$	4.7
64	$4.67 \cdot 10^{-1}$	3.3	$3.61 \cdot 10^{-1}$	3.9	$1.36 \cdot 10^{-1}$	6.2	$1.46 \cdot 10^{-1}$	6.1
65	$4.85 \cdot 10^{-1}$	3.7	$3.29 \cdot 10^{-1}$	5.7	$1.38 \cdot 10^{-1}$	5.1	$1.47 \cdot 10^{-1}$	5.5
66	$4.42 \cdot 10^{-1}$	3.5	$3.29 \cdot 10^{-1}$	5.2	$1.82 \cdot 10^{-1}$	8.5	$1.21 \cdot 10^{-1}$	4.9
67	$4.27 \cdot 10^{-1}$	2.4	$3.24 \cdot 10^{-1}$	5.0	$1.54 \cdot 10^{-1}$	6.6	$1.33 \cdot 10^{-1}$	4.6
68	$3.92 \cdot 10^{-1}$	3.8	$2.72 \cdot 10^{-1}$	4.4	$1.30 \cdot 10^{-1}$	4.8	$1.20 \cdot 10^{-1}$	5.4
69	$3.52 \cdot 10^{-1}$	3.3	$2.73 \cdot 10^{-1}$	3.9	$1.15 \cdot 10^{-1}$	6.6	$1.09 \cdot 10^{-1}$	6.0
70	$3.08 \cdot 10^{-1}$	3.6	$2.22 \cdot 10^{-1}$	4.7	$1.22 \cdot 10^{-1}$	7.3	$9.10 \cdot 10^{-2}$	4.3
71	$2.64 \cdot 10^{-1}$	2.1	$1.89 \cdot 10^{-1}$	5.9	$7.78 \cdot 10^{-2}$	4.9	$9.62 \cdot 10^{-2}$	5.0
72	$1.26 \cdot 10^{-1}$	3.4	$1.01 \cdot 10^{-1}$	4.5	$4.09 \cdot 10^{-2}$	6.5	$4.71 \cdot 10^{-2}$	4.4

Table 17: LINUS and SNOOPY computed fluence response ($E_n < 20$ MeV). Statistical errors are shown.

FLUKA group	Energy interval (eV)		LINUS		SNOOPY	
			lateral response		lateral response	
	E_{max}	E_{min}	cm^2	err%	cm^2	err%
1	$1.96 \cdot 10^7$	$1.75 \cdot 10^7$	$2.73 \cdot 10^{-1}$	3.6	$2.01 \cdot 10^{-1}$	4.7
2	$1.75 \cdot 10^7$	$1.49 \cdot 10^7$	$2.99 \cdot 10^{-1}$	3.6	$2.34 \cdot 10^{-1}$	4.2
3	$1.49 \cdot 10^7$	$1.35 \cdot 10^7$	$3.24 \cdot 10^{-1}$	3.6	$2.27 \cdot 10^{-1}$	3.4
4	$1.35 \cdot 10^7$	$1.22 \cdot 10^7$	$3.18 \cdot 10^{-1}$	3.3	$2.37 \cdot 10^{-1}$	4.0
5	$1.22 \cdot 10^7$	$1.11 \cdot 10^7$	$3.55 \cdot 10^{-1}$	3.4	$2.69 \cdot 10^{-1}$	4.5
6	$1.11 \cdot 10^7$	$9.99 \cdot 10^6$	$3.31 \cdot 10^{-1}$	4.1	$3.02 \cdot 10^{-1}$	3.2
7	$9.99 \cdot 10^6$	$9.05 \cdot 10^6$	$3.25 \cdot 10^{-1}$	3.8	$3.19 \cdot 10^{-1}$	4.4
8	$9.05 \cdot 10^6$	$8.19 \cdot 10^6$	$3.71 \cdot 10^{-1}$	4.2	$3.23 \cdot 10^{-1}$	4.2
9	$8.19 \cdot 10^6$	$7.41 \cdot 10^6$	$3.49 \cdot 10^{-1}$	4.4	$3.56 \cdot 10^{-1}$	4.1
10	$7.41 \cdot 10^6$	$6.70 \cdot 10^6$	$3.70 \cdot 10^{-1}$	3.4	$3.65 \cdot 10^{-1}$	2.9
11	$6.70 \cdot 10^6$	$6.07 \cdot 10^6$	$4.20 \cdot 10^{-1}$	4.1	$4.11 \cdot 10^{-1}$	3.5
12	$6.07 \cdot 10^6$	$5.49 \cdot 10^6$	$4.48 \cdot 10^{-1}$	3.6	$4.14 \cdot 10^{-1}$	4.5
13	$5.49 \cdot 10^6$	$4.97 \cdot 10^6$	$4.45 \cdot 10^{-1}$	4.3	$4.26 \cdot 10^{-1}$	4.3
14	$4.97 \cdot 10^6$	$4.49 \cdot 10^6$	$4.63 \cdot 10^{-1}$	4.1	$4.46 \cdot 10^{-1}$	4.9
15	$4.49 \cdot 10^6$	$4.07 \cdot 10^6$	$4.00 \cdot 10^{-1}$	4.4	$4.60 \cdot 10^{-1}$	3.6
16	$4.07 \cdot 10^6$	$3.68 \cdot 10^6$	$4.38 \cdot 10^{-1}$	4.2	$4.66 \cdot 10^{-1}$	3.7
17	$3.68 \cdot 10^6$	$3.33 \cdot 10^6$	$3.86 \cdot 10^{-1}$	5.0	$4.29 \cdot 10^{-1}$	3.8
18	$3.33 \cdot 10^6$	$3.01 \cdot 10^6$	$4.25 \cdot 10^{-1}$	4.7	$4.63 \cdot 10^{-1}$	4.2
19	$3.01 \cdot 10^6$	$2.73 \cdot 10^6$	$4.48 \cdot 10^{-1}$	4.0	$4.79 \cdot 10^{-1}$	4.9
20	$2.73 \cdot 10^6$	$2.47 \cdot 10^6$	$4.56 \cdot 10^{-1}$	4.0	$4.99 \cdot 10^{-1}$	4.6
21	$2.47 \cdot 10^6$	$2.23 \cdot 10^6$	$4.34 \cdot 10^{-1}$	4.6	$5.10 \cdot 10^{-1}$	4.0
22	$2.23 \cdot 10^6$	$2.02 \cdot 10^6$	$4.35 \cdot 10^{-1}$	4.6	$4.48 \cdot 10^{-1}$	6.2
23	$2.02 \cdot 10^6$	$1.83 \cdot 10^6$	$4.80 \cdot 10^{-1}$	4.2	$4.47 \cdot 10^{-1}$	4.9
24	$1.83 \cdot 10^6$	$1.65 \cdot 10^6$	$4.48 \cdot 10^{-1}$	3.7	$4.89 \cdot 10^{-1}$	3.8
25	$1.65 \cdot 10^6$	$1.49 \cdot 10^6$	$4.15 \cdot 10^{-1}$	3.9	$4.14 \cdot 10^{-1}$	4.4
26	$1.49 \cdot 10^6$	$1.35 \cdot 10^6$	$3.80 \cdot 10^{-1}$	4.5	$4.52 \cdot 10^{-1}$	3.9
27	$1.35 \cdot 10^6$	$1.22 \cdot 10^6$	$3.55 \cdot 10^{-1}$	4.6	$4.29 \cdot 10^{-1}$	4.1
28	$1.22 \cdot 10^6$	$1.11 \cdot 10^6$	$3.84 \cdot 10^{-1}$	4.3	$4.04 \cdot 10^{-1}$	5.3
29	$1.11 \cdot 10^6$	$1.00 \cdot 10^6$	$3.40 \cdot 10^{-1}$	3.9	$3.96 \cdot 10^{-1}$	4.4
30	$1.00 \cdot 10^6$	$9.07 \cdot 10^5$	$3.64 \cdot 10^{-1}$	3.9	$3.79 \cdot 10^{-1}$	4.3
31	$9.07 \cdot 10^5$	$8.21 \cdot 10^5$	$2.95 \cdot 10^{-1}$	3.6	$3.52 \cdot 10^{-1}$	5.1
32	$8.21 \cdot 10^5$	$7.43 \cdot 10^5$	$3.07 \cdot 10^{-1}$	4.3	$3.42 \cdot 10^{-1}$	4.1
33	$7.43 \cdot 10^5$	$6.08 \cdot 10^5$	$2.69 \cdot 10^{-1}$	4.5	$2.91 \cdot 10^{-1}$	5.0
34	$6.08 \cdot 10^5$	$4.98 \cdot 10^5$	$2.43 \cdot 10^{-1}$	5.3	$2.51 \cdot 10^{-1}$	6.0
35	$4.98 \cdot 10^5$	$4.08 \cdot 10^5$	$1.99 \cdot 10^{-1}$	3.7	$2.26 \cdot 10^{-1}$	5.7
36	$4.08 \cdot 10^5$	$3.34 \cdot 10^5$	$1.72 \cdot 10^{-1}$	5.1	$1.98 \cdot 10^{-1}$	4.4
37	$3.34 \cdot 10^5$	$2.73 \cdot 10^5$	$1.50 \cdot 10^{-1}$	3.7	$1.52 \cdot 10^{-1}$	6.7
38	$2.73 \cdot 10^5$	$2.24 \cdot 10^5$	$1.25 \cdot 10^{-1}$	5.1	$1.28 \cdot 10^{-1}$	7.1
39	$2.24 \cdot 10^5$	$1.83 \cdot 10^5$	$9.84 \cdot 10^{-2}$	4.9	$1.19 \cdot 10^{-1}$	5.3
40	$1.83 \cdot 10^5$	$1.50 \cdot 10^5$	$8.00 \cdot 10^{-2}$	5.4	$9.55 \cdot 10^{-2}$	6.5
41	$1.50 \cdot 10^5$	$1.23 \cdot 10^5$	$8.34 \cdot 10^{-2}$	4.8	$8.50 \cdot 10^{-2}$	6.5
42	$1.23 \cdot 10^5$	$8.65 \cdot 10^4$	$6.69 \cdot 10^{-2}$	4.8	$6.89 \cdot 10^{-2}$	5.7
43	$8.65 \cdot 10^4$	$5.25 \cdot 10^4$	$5.08 \cdot 10^{-2}$	5.2	$5.28 \cdot 10^{-2}$	6.2
44	$5.25 \cdot 10^4$	$3.18 \cdot 10^4$	$4.47 \cdot 10^{-2}$	5.5	$3.94 \cdot 10^{-2}$	7.3
45	$3.18 \cdot 10^4$	$2.19 \cdot 10^4$	$3.62 \cdot 10^{-2}$	5.9	$3.81 \cdot 10^{-2}$	7.6
46	$2.19 \cdot 10^4$	$1.50 \cdot 10^4$	$3.02 \cdot 10^{-2}$	4.6	$3.47 \cdot 10^{-2}$	6.4
47	$1.50 \cdot 10^4$	$1.03 \cdot 10^4$	$3.05 \cdot 10^{-2}$	5.3	$3.14 \cdot 10^{-2}$	5.7
48	$1.03 \cdot 10^4$	$7.10 \cdot 10^3$	$2.81 \cdot 10^{-2}$	4.6	$2.56 \cdot 10^{-2}$	7.2
49	$7.10 \cdot 10^3$	$4.88 \cdot 10^3$	$2.67 \cdot 10^{-2}$	4.7	$2.65 \cdot 10^{-2}$	5.4
50	$4.88 \cdot 10^3$	$3.35 \cdot 10^3$	$2.28 \cdot 10^{-2}$	4.8	$2.25 \cdot 10^{-2}$	6.5
51	$3.35 \cdot 10^3$	$2.31 \cdot 10^3$	$2.43 \cdot 10^{-2}$	5.3	$2.32 \cdot 10^{-2}$	6.9
52	$2.31 \cdot 10^3$	$1.58 \cdot 10^3$	$2.20 \cdot 10^{-2}$	4.9	$2.12 \cdot 10^{-2}$	7.1
53	$1.58 \cdot 10^3$	$1.04 \cdot 10^3$	$1.75 \cdot 10^{-2}$	5.2	$1.88 \cdot 10^{-2}$	6.3
54	$1.04 \cdot 10^3$	$6.89 \cdot 10^2$	$1.84 \cdot 10^{-2}$	5.0	$1.89 \cdot 10^{-2}$	7.7
55	$6.89 \cdot 10^2$	$4.54 \cdot 10^2$	$1.76 \cdot 10^{-2}$	4.0	$1.53 \cdot 10^{-2}$	10.6
56	$4.54 \cdot 10^2$	$2.75 \cdot 10^2$	$1.61 \cdot 10^{-2}$	4.3	$1.60 \cdot 10^{-2}$	6.6
57	$2.75 \cdot 10^2$	$1.67 \cdot 10^2$	$1.47 \cdot 10^{-2}$	5.3	$1.37 \cdot 10^{-2}$	6.4
58	$1.67 \cdot 10^2$	$1.01 \cdot 10^2$	$1.50 \cdot 10^{-2}$	5.5	$1.22 \cdot 10^{-2}$	6.8
59	$1.01 \cdot 10^2$	$6.14 \cdot 10^1$	$1.25 \cdot 10^{-2}$	5.4	$1.19 \cdot 10^{-2}$	5.4
60	$6.14 \cdot 10^1$	$3.73 \cdot 10^1$	$1.26 \cdot 10^{-2}$	4.8	$1.15 \cdot 10^{-2}$	6.8
61	$3.73 \cdot 10^1$	$2.26 \cdot 10^1$	$1.19 \cdot 10^{-2}$	6.6	$9.87 \cdot 10^{-3}$	7.4
62	$2.26 \cdot 10^1$	$1.55 \cdot 10^1$	$1.12 \cdot 10^{-2}$	5.0	$1.00 \cdot 10^{-2}$	7.2
63	$1.55 \cdot 10^1$	$1.07 \cdot 10^1$	$1.13 \cdot 10^{-2}$	5.8	$9.35 \cdot 10^{-3}$	6.6
64	$1.07 \cdot 10^1$	$7.34 \cdot 10^0$	$8.69 \cdot 10^{-3}$	6.7	$9.77 \cdot 10^{-3}$	6.9
65	$7.34 \cdot 10^0$	$5.04 \cdot 10^0$	$9.83 \cdot 10^{-3}$	5.4	$7.77 \cdot 10^{-3}$	6.7
66	$5.04 \cdot 10^0$	$3.47 \cdot 10^0$	$9.68 \cdot 10^{-3}$	5.1	$6.85 \cdot 10^{-3}$	6.7
67	$3.47 \cdot 10^0$	$2.38 \cdot 10^0$	$8.14 \cdot 10^{-3}$	3.5	$6.63 \cdot 10^{-3}$	7.0
68	$2.38 \cdot 10^0$	$1.64 \cdot 10^0$	$7.74 \cdot 10^{-3}$	4.0	$7.01 \cdot 10^{-3}$	3.7
69	$1.64 \cdot 10^0$	$1.13 \cdot 10^0$	$7.62 \cdot 10^{-3}$	3.5	$5.80 \cdot 10^{-3}$	5.3
70	$1.13 \cdot 10^0$	$6.83 \cdot 10^{-1}$	$6.28 \cdot 10^{-3}$	2.5	$6.30 \cdot 10^{-3}$	4.4
71	$6.83 \cdot 10^{-1}$	$4.14 \cdot 10^{-1}$	$5.35 \cdot 10^{-3}$	2.9	$5.01 \cdot 10^{-3}$	4.1
72	$4.14 \cdot 10^{-1}$	$1.00 \cdot 10^{-2}$	$2.47 \cdot 10^{-3}$	2.7	$2.19 \cdot 10^{-3}$	3.7

SINBAD
SHIELDING INTEGRAL BENCHMARK ARCHIVE AND DATABASE

H. T. Hunter, D. T. Ingersoll, R. W. Roussin, and C. O. Slater
Oak Ridge National Laboratory, U.S.A.

I. Kodeli and E. Sartori
OECD/NEA

Abstract

SINBAD is a new electronic database [1] developed to store a variety of radiation shielding benchmark data so that users can easily retrieve and incorporate the data into their calculations. SINBAD is an excellent data source for users who require the quality assurance necessary in developing cross-section libraries [2] or radiation transport codes. The future needs of the scientific community are best served by the electronic database format of SINBAD and its user-friendly interface, combined with its data accuracy and integrity. It has been designed to be able to include data from nuclear reactor shielding, fusion blankets and accelerator shielding experiments.

1. Introduction

For several decades, radiation shielding has been studied in fission, fusion, accelerator, and radioactive nuclide systems, world-wide, and involving investments of hundreds of millions of dollars. The experimental benchmarks resulting from these studies have been instrumental in the design of power reactors and nuclear research facilities. The information supplied by the experimental benchmarks exists in many forms at various locations. Some benchmarks may not contain a single reference with complete information and must be assembled from other documents or through verbal communication with sources such as the experimentalists responsible for the benchmark work. As experimental benchmark facilities close and experimentalists leave the field, the need to preserve experimental benchmark results now becomes increasingly important. Consequently, experimental benchmarks need to be collected and stored in a complete and accurate fashion [3,4].

2. Benchmark information

The guidelines developed by the Benchmark Problems Group of the American Nuclear Society Standards Committee (ANS-6) on formats for benchmark problem description have been followed by SINBAD [5]. SINBAD data include benchmark information on (1) the experimental facility and the source; (2) the benchmark geometry and composition; and (3) the detection system, measured data; and an error analysis. A full reference section is included with the data. Relevant graphical information, such as experimental geometry or spectral data, is included. All information that is compiled for inclusion with SINBAD has been verified for accuracy and reviewed by two scientists.

3. Selection of benchmarks

A feasibility study has been successfully completed, using a sample of fission and fusion benchmarks with associated computations installed in SINBAD. Currently, an extended list of high-priority benchmarks will be incorporated into SINBAD. The benchmarks to be installed in SINBAD will be selected from those previously sanctioned by an accredited group or organisation and/or have been widely used, such as those from the Nuclear Energy Agency Nuclear Science Committee (NEA/NSC), the Cross-Section Evaluation Working Group (CSEWG), and the IAEA Consultants' Meetings on Fusion Benchmarks [6]. The accelerator shielding community agreed to contribute benchmark experiments data for intermediate and high energy accelerator shields such as those reported in ref.[7]. Several more relevant benchmarks will be added as they become available. The list of selected benchmarks follows:

NEANSC

1–* Winfrith Iron Benchmark Experiment (ASPIS)

2–* Ispra Iron Benchmark Experiment (EURACOS)

3–* Wuerenlingen Iron Benchmark Experiment (PROTEUS)

4–* Osaka Iron Benchmark Experiment (OKTAVIAN)

5–* Karlsruhe Iron Sphere Benchmark Experiment

---

* indicates benchmark is currently in SINBAD or is in the process of being added.

6–* Winfrith Water/Iron Benchmark Experiment (ASPIS)

7–* Winfrith Water Benchmark Experiment (ASPIS)

8–* Ispra Sodium Benchmark Experiment (EURACOS)

9–* Cadarache Sodium Benchmark Experiment (HARMONIE)

10–* Winfrith Graphite Benchmark Experiment (ASPIS)

CSEWG

11– SDT1 Iron Broomstick Benchmark Experiment (TSF-ORNL)

12– SDT2 Oxygen Broomstick Benchmark Experiment (TSF-ORNL)

13– SDT3 Nitrogen Broomstick Benchmark Experiment (TSF-ORNL)

14– SDT4 Sodium Broomstick Benchmark Experiment (TSF-ORNL)

15–* SDT11 Iron and Stainless Steel Experimental Benchmark (TSF-ORNL)

16–* SB5 Fusion Benchmarks for Attenuation in Iron, Borated Polyethylen e, and Lithiated Paraffin (ORNL)

17–* SB6 Fusion Reactor Duct Streaming Experiment (ORNL)

Other benchmarks

18– University of Illinois Iron Sphere Benchmark

19–* PCA-PV 'Blind Test' and Replica Benchmarks

20– Winfrith NESDIP2 and NESDIP3 Radial Shield and Cavity Experiments.

21– YAYOI Iron and Sodium Fast Reactor Shielding Benchmarks (University of Tokyo)

22– Thermal Reactor Duct Streaming (IRI/University of Budapest)

IAEA fusion benchmarks [6]

23-38– OKTAVIAN facility neutron and gamma-ray measurements on chromium, manganese, iron, tungsten, nickel, molybdenum, lithium, beryllium, lead, beryllium/lithium, lithium fluoride, and lithium fluoride/lead

39-42– IPPE facility, at Obninsk, neutron leakage measurements on iron, beryllium, lead, and lead/lithium

43-52–* FNS facility neutron and gamma-ray spectra measurements on iron, carbon, oxygen, tungsten, SS316, SS316L, beryllium, lead, and lithium dioxide

53,54– TUD facility neutron and gamma-ray leakage measurements on iron and lead

55–* FNG facility gamma dose measurements on SS316

56-59–* ORNL facility neutron and gamma-ray spectra measurements on iron, SS304, tungsten, and borated-polyethylene (same as 16 and 17 above)

60– KfK facility neutron spectrum measurements on beryllium

61– INEL facility total neutron leakage measurements on beryllium

62,63– SWINPC facility, at Chengdu, total neutron leakage measurements on beryllium and lead

64-66– BARC facility total neutron leakage measurements on beryllium, beryllium oxide, and lead

67,68– LLNL facility neutron spectra measurements on lithium-6 and lithium-7

Those experiments involving combinations of different materials and/or sources or configurations will be broken down, subdividing the experiment into unique additions to SINBAD. Therefore, the above numbering of the experiments to be included into SINBAD is not representative of the final number of separate entries.

4. Computations

The secondary function of SINBAD is the incorporation of accompanying analyses of the benchmarks to help reduce redundant computational work in the future and to supply a user complete information, such as (1) description of the computational procedure, (2) references to codes, (3) approximations and simplifications in modelling, (4) code input deck, (5) computational results, etc., as described in reference [6]. Given the possible number of calculations performed for any one of the above benchmarks, and the effort required to install the results, only published calculations will be added as time and space allow.

5. Database design

SINBAD stores the benchmark information in relational databases that have index keys on unique identification numbers called Shielding Benchmark Experiment codes (SBE) assigned to each benchmark. The index key serves as a means of finding information quickly within a database and as a relationship with other databases housing different parts of the benchmark data.

An abstract outlining each benchmark has been constructed to allow the user to easily peruse important benchmark characteristics before making a selection. The abstract contains ten specific areas of information:

1. Name of Experiment,
2. Purpose and Phenomena Tested,
3. Description of the Source and Experimental Configuration,
4. Measurement System and Uncertainties,
5. Description of Results and Analysis,

6. Special Features,
7. Author/Organiser/Compiler,
8. Availability,
9. References, and
10. Data and Format.

Each benchmark has additional categorical information, such as source type, source particle(s), measured particle(s), materials and thicknesses, date of experiment, and data type that further aids in a user selection. Currently, SINBAD uses three databases to store benchmark characteristics, search parameters, and search results.

The experimental benchmark data, which includes the source, geometry, material(s), detector(s), and measurement(s), are stored in separate files that contain formatted text with associated graphs, figures, and equations.

The experimental benchmark file is retrieved into SINBAD upon user selection, along with associated computation(s) that are also stored in separate files.

6. Database access and retrieval

The retrieval process in SINBAD may progress by one of two methods. If the user knows a benchmark in which he is interested, information on the benchmark may be obtained by a perusal of the alphabetised list of benchmark experiment names. Before one selects the bulk of a benchmark's information, one may preview the benchmark via the process information and the experimental abstract, mentioned above. Once a benchmark has been selected, the experimental and calculational data are retrieved directly or may be accessed later by reference to the benchmark's SBE code (See Figure 1).

If the user is not familiar with the available benchmark experiments, then SINBAD has an interactive, multiple-search capability, whereby the user may select the benchmark from a list of candidates generated by user supplied experimental characteristics. For example, a user may specify an interest in penetration of experiments involving a source of fission neutrons passing through a 50-cm-thick steel plate. Only the benchmarks' satisfying these requirements will be retrieved, creating a subset of benchmarks which will improve the user's chances of finding the best benchmark to satisfy his needs (See Figure 2).

Benchmark information may be viewed, printed, or saved to an ASCII file for a user to manipulate further into computer readable formats. Currently under investigation is a standard format for source and measured data files to reduce the user's need for file manipulation when the data are used with personal plotting or computation codes. Hypertext, Bookmarks, and Sticky Notes may be added at the user's discretion to further aid in finding and interpreting the benchmark information.

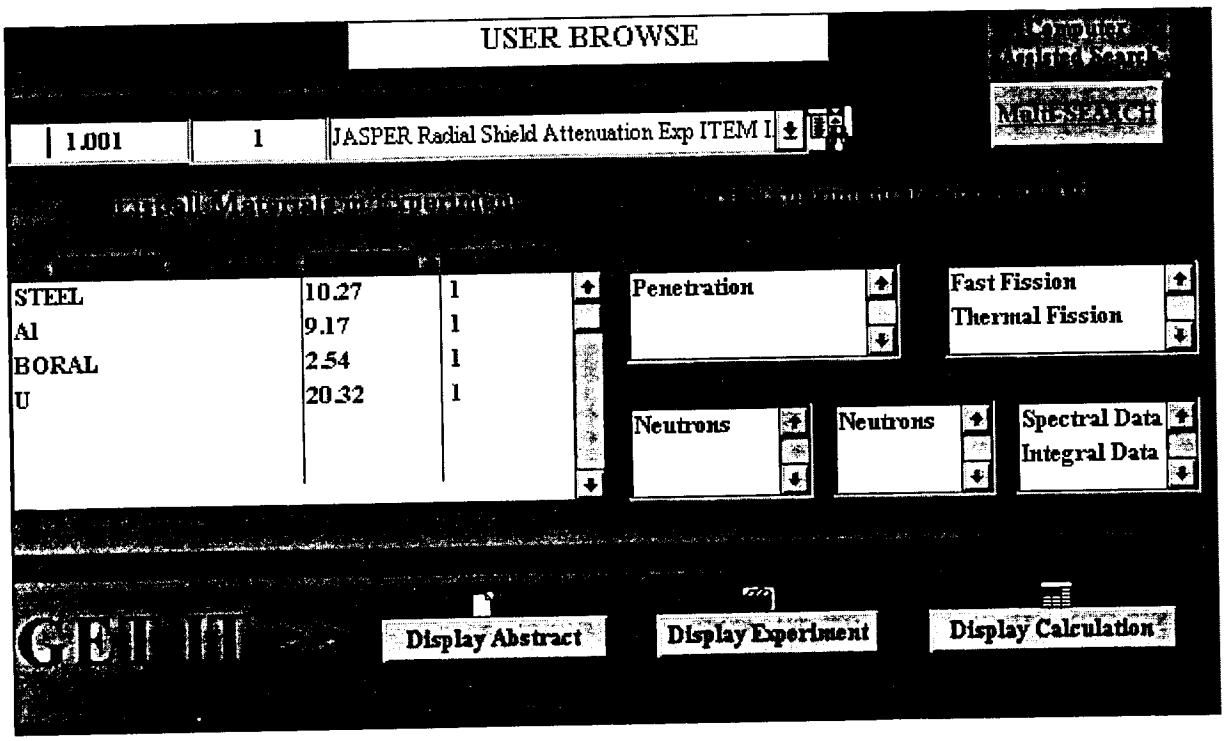

Figure 1 Sample SINBAD browse screen

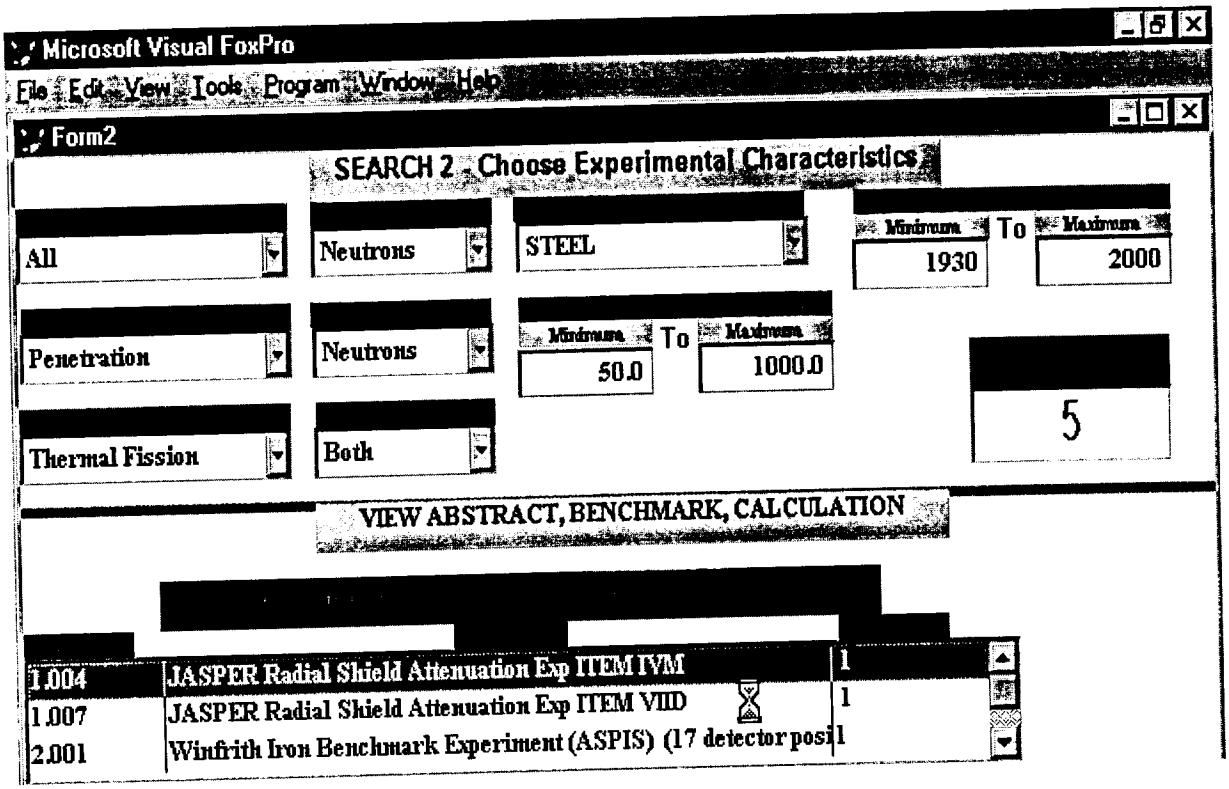

Figure 2 Sample SINBAD computer assisted search screen

7. Software requirements

The SINBAD database was written in Visual FoxPro 3.0 (Microsoft) for a Windows 3.1 (Microsoft) PC platform. SINBAD incorporates mouse control over selections on a 3-D-like windows display of drop-down lists and text boxes. Graphical data with accompanying text and tables of the experimental benchmark data are stored together within Envoy 1.1 (Novell), a self-opening document viewer compatible with Windows (Microsoft). The contents of the abstract, experiment, and/or associated calculations may be displayed to screen and/or printer from within SINBAD. Both the SINBAD program and the Envoy data files are run-time executable files (*.exe), eliminating the need for users to purchase additional software beyond Windows for the PC. Currently, SINBAD's programming has been completed, and 13 fission and fusion experimental benchmarks have been archived. Current work is proceeding to incorporate other types of benchmarks (accelerator, targets) as well as the many fission and fusion benchmarks recommended by CSEWG, NEANSC, and the IAEA.

8. Hardware requirements

A PC or compatible, with a 486 processor, 8 MB of RAM, 40 MB of free hard disk space, and a VGA colour monitor are necessary for adequate performance of SINBAD. A printer is recommended, but not necessary. The size and number of benchmarks will be the only limiting factor for PCs since hard disk space is used at the average rate of 1 MB/benchmark.

9. Future SINBAD upgrades

It is envisioned that SINBAD could eventually contain several hundred benchmark experiments, including computational benchmarks. The format and software presently used in SINBAD could be converted easily and used on the Internet, allowing greater access by potential users in the future.

10. Summary

The need for an electronic database system for shielding benchmarks to be used on an international level has been demonstrated. The objectives of the database are to:

(a) preserve the high quality and expensive results from phased-out experiments and lost expertise;
(b) compile complete and comprehensive benchmarks experiment data and description;
(c) provide a flexible data storage medium and a versatile, user friendly data access and retrieval process;
(d) provide an effective tool for quality assurance testing of data and methods;
(e) facilitate access, acquisition, and use of the benchmark data in the future; and
(f) provide a mechanism for feedback to data evaluators on the cross-section data inadequacies and improvements.

SINBAD has been structured with the software and hardware capabilities necessary to effectively store, access, and retrieve the data at the user's request and with the flexibility needed to expand to other areas of interest.

Acknowledgements

The authors wish to thank the Radiation Shielding Information Center and the Nuclear Analysis and Shielding sections of Computational Physics and Engineering Division at Oak Ridge National Laboratory for their continued support and encouragement, as well as the Organisation for Economic Co-operation and Development / Nuclear Energy Agency Nuclear Data Bank. This research is sponsored by the Office of Fusion Energy, U.S. Department of Energy, under contract number DE-AC05-96OR22464 with Lockheed Martin Energy Research Corp.

References

[1] H. T. Hunter et al., "SINBAD- A Shielding Integral Benchmark Archive and Database for PC's", Proceedings of the 8th International Conference on Radiation Shielding, Arlington, Texas, April 24-28, 1994, p 795, American Nuclear Society, La Grange Park, Illinois, 1994.

[2] American Nuclear Society Standards Committee, "Neutron and Gamma-Ray Cross Sections for Nuclear Radiation Protection Calculations for Nuclear Power Plants", ANSI/ANS-6.1.2, American Nuclear Society, La Grange Park, Illinois, 1989.

[3] P. Miller, et al., "International Conference on Radiation Shielding", NEACRP-A-884, September 12-16, 1988, Bournemouth, England, September 1988.

[4] A. K. McCracken, "The Establishment of a Shielding Experimental Benchmark at the NEA Data Bank", OECD/NEA NEACRP-A-1044, June 1990.

[5] G. L. Simmons, "Shielding Benchmark Problems", ORNL-RSIC-25 (ANS-SD-9), July 1974.

[6] S. Ganesan, "Preparation of Fusion Benchmarks in E lectronic Format for Nuclear Data Validation Studies", INDC(NDS)-298, International Atomic Energy Agency, Vienna, December 1993.

[7] H. Nakashima et al., "Benchmark Problems for Intermediate and High Energy Accelerator Shielding", JAERI 94-012 (Sept. 1994)

Session III

ENERGY RESPONSE FUNCTIONS – ACTIVATION, TRANSMUTATION, ISOTOPE PRODUCTION

CHAIR

Tony GABRIEL

CO-CHAIR

Kazuo SHIN

CALIBRATION OF A MODIFIED ANDERSSON-BRAUN REM COUNTER

S.Ban and T.Suzuki
National Laboratory for High Energy Physics, Tsukuba, Japan

J.Li, S.Liu and Y.Tang
Institute of High Energy Physics. Beijing, The People's republic of China

Y.Sakamoto
Japan Atomic Energy Research Institute, Tokai, Japan

Abstract

The energy response of four models of Andersson-Braun (A-B) rem counters were studied. Two models are the conventional A-B counters and the other two ones are the modified rem counters. The latter are added 1-cm-thick Pb layers to increase the energy response above 10 MeV. They were calibrated in different energy neutron fields, from thermal energy to 45 MeV. From 22 to 45 MeV, measurements were done using p-Li quasi-monoenergetic neutron source at TIARA and CYRIC. At 45 MeV, the sensitivity of the modified counters was two times larger than the conventional ones.

Introduction

The A-B counter is widely used to measure neutron doses. However, its efficiency decreases for neutron energy above 10 MeV. In the stray radiation fields around high energy accelerators, high energy neutrons (above 10 MeV) give a large contribution on the dose equivalent. Then the usual A-B counters underestimate the dose equivalent.

Some numerical calculations were carried out to modify the structure of the moderator and the attenuator [1]. And it was shown that the A-B rem counter increases its efficiency for high energy neutrons when a 1-cm-thick Pb layer is added around the boron plastic attenuator. The modified counter was tested in the stray radiation field of CERN SPS [2].

Radiation Protection Group in both KEK and IHEP are collaborating to develop the modified A-B counters [3]. Two types of A-B counters ware made in IHEP. One has the usual structure of the moderator-attenuator and the other was added the 1-cm-thick Pb layer. Two types of commercially manufactured A-B counters were also tested. One is the conventional counter (ALNOR type 2202D) and the other is the modified counter (Health Physics Instruments, type 6060). Four types of A-B counters were calibrated in several neutron fields as follows.

1. Thermal neutrons (0.025 eV) from graphite pile at Radiation dosimetry Division in JAERI;
2. 8 keV neutrons using Sc-45 (p,n) semi-monoenergetic source at Fast Neutron Laboratory in Tohoku University;
3. Cf-252 neutrons at CYRIC in Tohoku University;
4. 22.0 MeV and 32.5 MeV neutrons using p-Li quasi-monoenergetic source at CYRIC in Tohoku University;
5. 45.4 MeV neutrons using p-Li quasi-monoenergetic source at TIARA [4] in JAERI;
   Using these neutron sources, the modified A-B counters were studied to check the increase of the efficiency for neutron above 10 MeV, without decreasing the sensitivity below 8 keV [1].

Modified Andersson-Braun counter

Two types of the A-B counters were developed in IHEP. Detailed descriptions are shown elsewhere. The structure of the moderator-attenuator are shown in Figures 1 and 2. Both counters consist of a BF_3 proportional counter, an inner polyethylene moderator, a boron plastic attenuator and an outer polyethylene moderator. The modified A-B counter was added a 1-cm-thick Pb layer around the boron plastic.

Calibration of the counters

Four types of the counters were calibrated in different energy neutron fields, from thermal energy to 45 MeV [3]. All counters were laterally irradiated. Thermal neutron (0.025 eV) fields were placed beside graphite piles (150 × 164 × 16 cm). Dynamitron accelerator (4.5 MV) was used to produce 8 keV semi-monoenergetic neutrons using Sc-45 (p,n) reaction.

A high-energy response was calibrated using p-Li quasi-monoenergetic source and neutron spectra were determined with the TOF method [4]. Neutron spectra at 32.5 MeV and 45.4 MeV are shown in

Figures 3 and 4, which contain a continued spectra below the peaks. The contributions of the continued spectra were subtracted using measured sensitivities for lower energy neutrons.

The sensitivity of four counters are listed in Table 1 and shown in Figure 5 as a function of neutron energy. Because they are using different BF_3 counters, the sensitivity of the A-B counters are different. In Figure 5, they are normalised to have the same value at Cf-252 neutron energy, 2.5 MeV.

Conclusion

Pb layer increases the response above 10 MeV and do not affect the energy response of low energy region below 8 keV. At 45 MeV, the sensitivity of the modified counters was two times larger than the usual ones. The standard A-B counter has a little sensitivity up to 50 MeV. Though Pb improve the sensitivity in high energy region, 1-cm-thick Pb is not enough to fit the ICRP-51 curve.

References

[1] C.Birattari et al., "An Extended range Neutron Rem Counter", Nucl.Instrum.Methods A297,250-257 (1990).

[2] C.Birattari et al., "A Neutron Survey Meter with Sensitivity Extended up to 400 MeV", Radiat.Prot.Dosim.,44,193-197 (1992).

[3] J.Li et al., "Neutron Energy Response of a Modified Andersson-Braun Rem Counter", KEK Internal 95-8 (1995).

[4] S.tanaka and T.Nakamura, "Shielding Experiments and Analysis at 90 MV AVF Cyclotron Facility, TIARA", Shielding Aspects of Accelerators, Targets and Irradiation Facilities, OECD/NEA (1994).

Table 1. ***Absolute sensitivity of the A-B counters (cps per n cm^2 s^{-1})***

MODEL	MODIFIED (IHEP)	USUAL (IHEP)	MODIFIED (HPI)	USUAL (ALNOR)
0.025 eV	0.0063	0.0028	0.0061	0.0062
8 keV	0.095	0.056	0.10	0.11
2.5 MeV	0.42	0.27	0.29	0.48
22.0 MeV	0.34	0.18	0.23	0.30
32.5 MeV	0.28	0.13	0.18	0.24

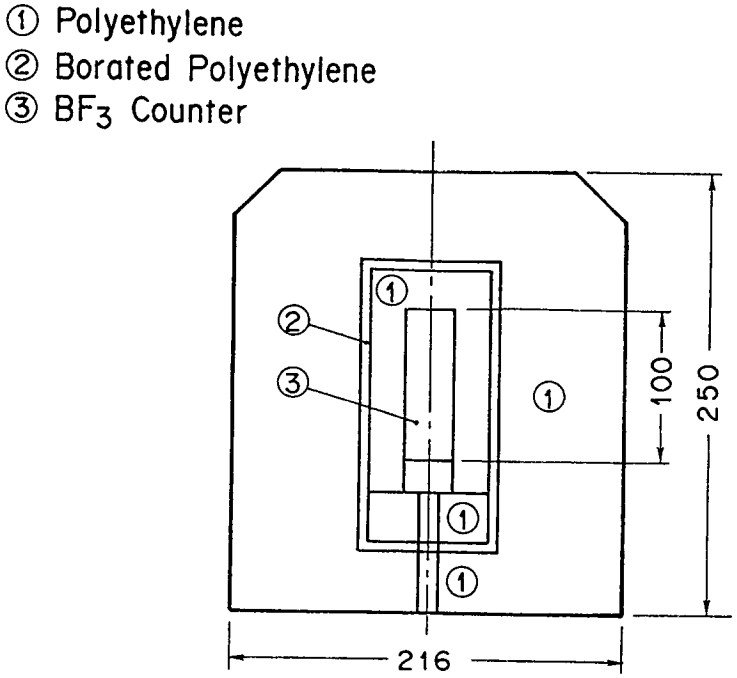

Figure 1 ***Construction of the standard A-B counter***

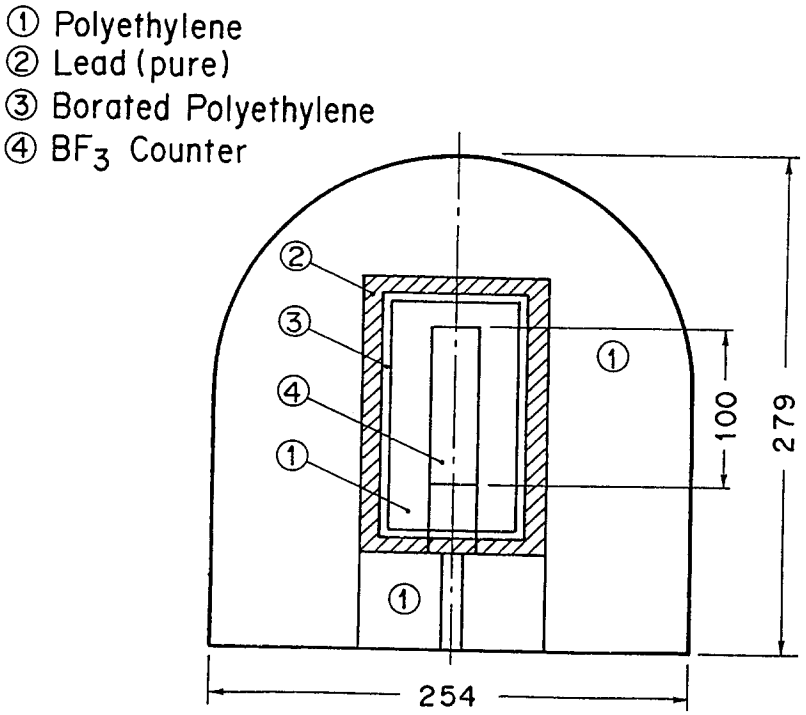

Figure 2 ***Contruction of the modified A-B counter***

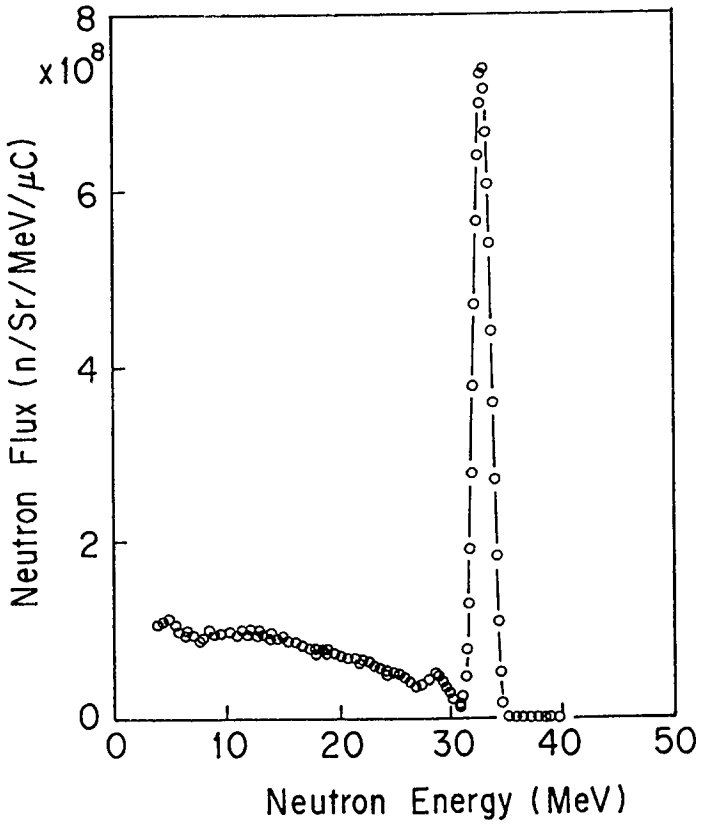

Figure 3 ***32.5-MeV neutron spectrum using p-Li reaction in CYRIC***

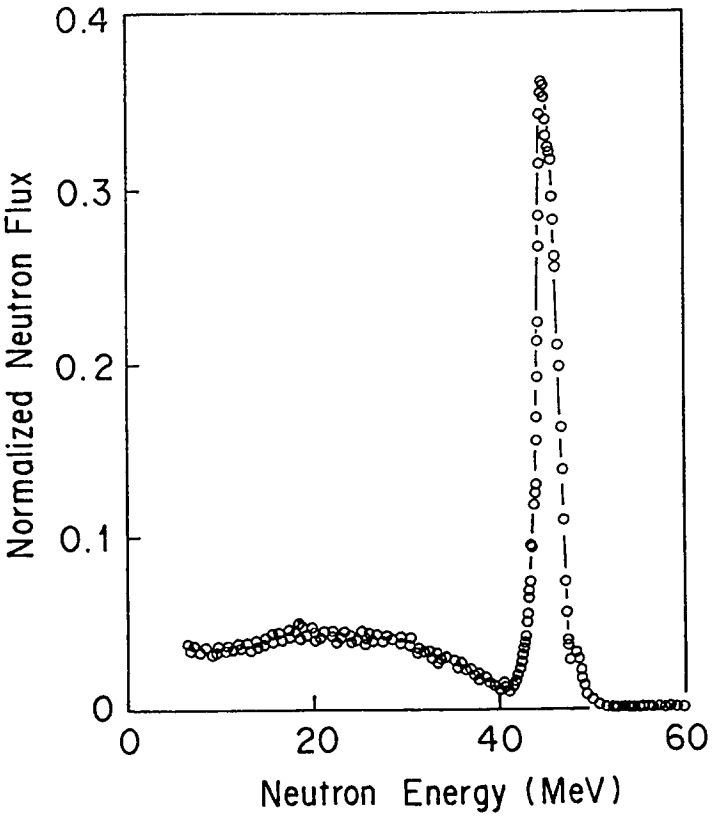

Figure 4 ***45.4-MeV neutron spectrum using p-Li reaction in TIARA*** [4]

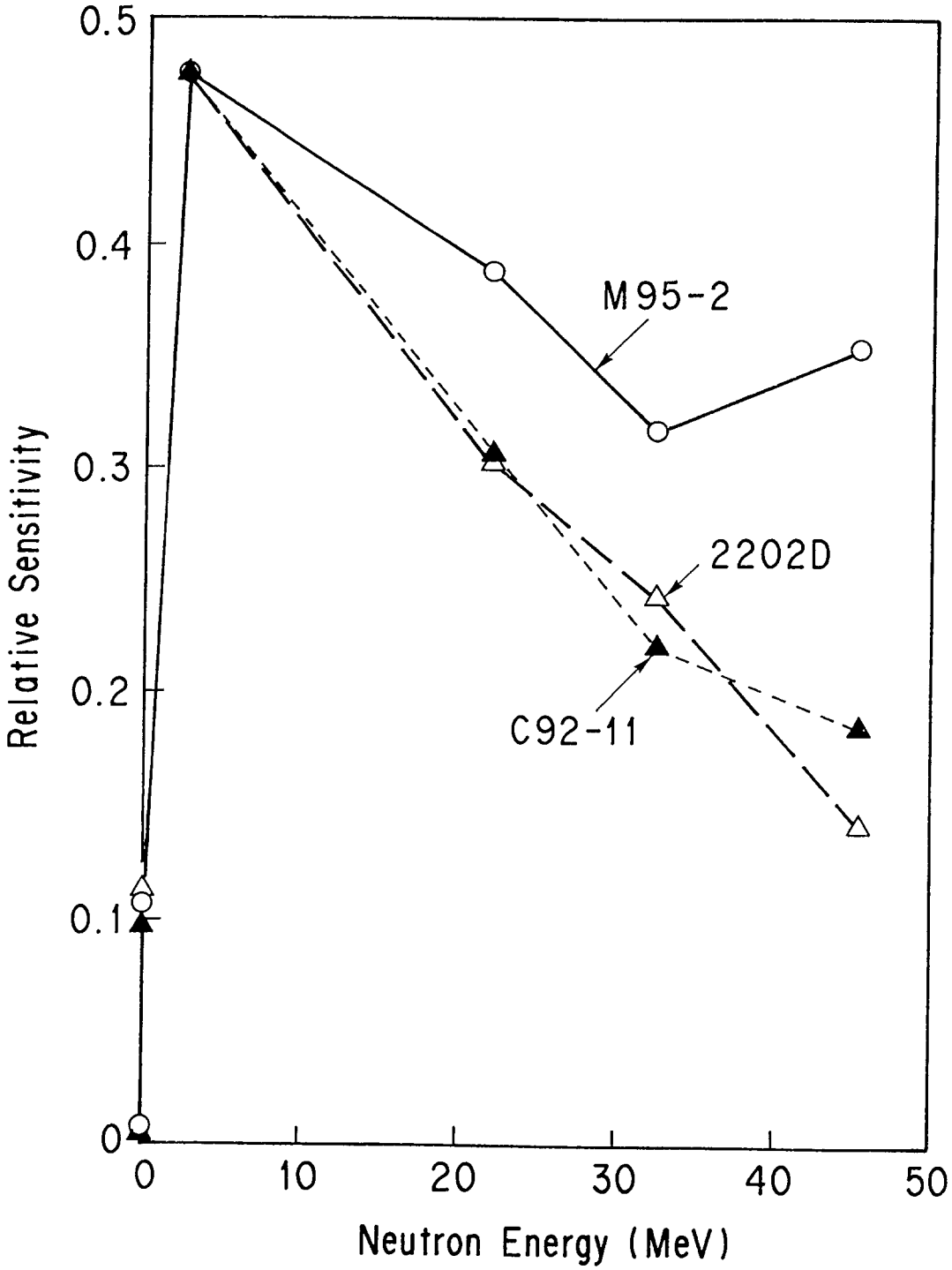

Figure 5 ***Sensitivity of the counters***

Normalised at Cf neutron energy
- *M95-2*: Modified (IHEP)
- *C92-11*: Usual (IHEP)
- *2202D*: Usual (ALNOR)

ACTIVATION CROSS-SECTION MEASUREMENTS USING QUASI-MONOENERGETIC NEUTRON FIELDS FROM 20 TO 150 MeV

T. Nakamura, E.Kim, A. Konno
CYRIC, Tohoku University, Japan

M. Imamura, N. Nakao,T. Shibata
INS, University of Tokyo, Japan

Y. Uwamino, N. Nakanishi
Institute of Physical and Chemical Research, Japan

Su. Tanaka, H. Nakashima, Sh. Tanaka
JAERI, Japan

M. Baba
Dept. of Nuclear Engineering, Tohoku University, Japan

1. Introduction

Interest to neutron reaction data is world-wide increasing from the viewpoints of intense neutron source of material study, nuclear transmutation of radioactive wastes, induced radioactivity and shielding design of high energy accelerators. Nevertheless, neutron reaction data in the energy range above 20 MeV are still very poor and no evaluated data file exists at present mainly due to very limited number of facilities having quasi -monoenergetic neutron fields available for neutron reaction cross-section and shielding experiments above 20 MeV.

The accelerator shielding research group has been doing as a co-operative project between JAERI and several universities. In this study, we developed the quasi -monoenergetic neutron fields using Li-7 (p,n) reaction at four AVF cyclotron facilities; 1) Institute for Nuclear Study, University of Tokyo (INS) for 20 to 40 MeV protons, 2) Cyclotron and Radioisotope Center, Tohoku University (CYRIC) for 20 to 40 MeV protons, 3) Takasaki Research Establishment, Japan Atomic Energy Research Institute (TIARA) for 40 to 90 MeV protons and 3) Institute of Physical and Chemical Research (RIKEN) for 80 to 150 MeV protons.

By using these neutron fields, we did the experiments on:

1. Response functions and efficiencies of neutron detectors,
2. Neutron production yield by charged particles,
3. Neutron-induced charged particle production cross-sections,
4. Neutron penetration and streaming through shielding materials,

5. Neutron activation and spallation cross-sections, and so on

These experimental results are quite valuable data in the intermediate neutron energy region, where there exists very poor data. Here, only the experiments on neutron activation and spallation cross-sections will be given in this report.

2. Establishment of quasi-monoenergetic neutron field

CYRIC neutron field

The CYRIC neutron field has the 45-m long neutron TOF facility coupled with the beam chopping system and the beam swinger system. The quasi -monoenergetic neutrons of 22.0 and 32.5 MeV having 1.7 and 1.4 MeV FWHM were obtained from 2 mm thick Li-7 target bombarded by 25 and 35 MeV protons, respectively, and the proton beam hit the target at 10°C through the swinger magnet and was fully stopped at the Faraday cup. The neutrons were extracted in the TOF facility through the 50-cm thick iron-polyethylene collimator of 30 cm × 20 cm aperture settled in the 280-cm thick concrete wall of 100 cm × 50 cm aperture. Figure 1 shows the cross-sectional view of the CYRIC neutron field. This neutron field was established as the neutron reference field for detector calibration by determining the absolute neutron fluence with the proton recoil counter telescope (PRT). The 22.0 and 32.5 MeV peak neutron fluences were 1.1×10^3 and 1.7×10^3 n cm^{-2} μC^{-1} at the collimator exit behind 8.6 m from the target. The neutron spectra measured with the TOF method using a 12.7-cm-diameter by 12.7-cm long BC501A detector are shown in Figure 2.

INS neutron field

The INS neutron field can be used only for neutron irradiation and the irradiation samples are placed 10 cm away from the Li target in the forward direction, in order to get high neutron fluence and to depress the contribution of room-scattered neutrons, since the irradiation room is small in space. The neutron spectra are the same as those in the CYRIC neutron field.

TIARA neutron field

The TIARA neutron field was established in the neutron beam line collimated into 10 -cm diameter. The 2- to 5-mm thick Li-7 target settled in the cyclotron room was bombarded by the proton beam of 20 to 90 MeV at 0°C and the protons passed through the target were bent down to the beam dump by a clearing magnet, and the neutrons produced at 0°C were extracted through the 220 -cm thick concrete wall. Figure 3 shows the cross-sectional view of the TIARA neutron field.

The absolute fluence of source neutrons was determined with PRT and the neutron fluence during the experiment was monitored simultaneously with the U-238 and Th-232 fission chambers fixed closely to the target. The FWHM of 40.5 and 64.5 MeV monoenergetic peak and the peak neutron yield have the respective values of 2.0 MeV and 2.1×10^4 n cm^{-2} μC^{-1}, 2.1 MeV and 3.2×10^4 n cm^{-2} μC^{-1}, at the collimator exit behind 4 m from the target, for 43 and 67 MeV proton incidence. The neutron spectra measured with the TOF method using BC501A and PRT are shown in Figure 4 for 43, 58, 67 and 87 MeV proton incidence.

RIKEN neutron field

The RIKEN neutron field is now being established at the E4 experimental room of the separate sector ring cyclotron. The proton beam having energies of 80, 90, 100,110,120,135, 150 and 210 MeV were injected on a 10-mm thick Li-7 target through the beam swinger. Protons passed through the target were cleared out by the magnet and absorbed in the spectrograph. Neutrons produced at 0°C were transported through the iron-concrete collimator of 20 cm by 20 cm aperture and 120 cm length. Figure 5 shows the experimental layout at this field.

The neutron spectra were measured with the TOF method using BC50lA and the absolute neutron fluence with the Li activation method using the Be-7 activity from the Li-7 (p,n) Be -7 reaction. Figure 6 shows the neutron spectra for 90, 100, 110 and 120 MeV proton incidence.

3. Neutron activation and spallation cross-sections

The neutron reaction cross-sections of C, Al, Co, Cu and Bi were measured by irradiating these samples by the p-Li quasi-monoenergetic neutrons at INS, TIARA and RIKEN. The gamma-ray activities of the irradiated samples were counted by using a Ge detector and the reaction rates of identified radioisotopes were obtained after correction of sum-coincidence effect.

By using the neutron energy spectrum $\Phi(E)$ and the reaction rate, A, the activation cross-section $\sigma(E)$ can be estimated as follows. The reaction rate, A is divided into two parts; one is induced by the peak energy neutrons and the other by the low energy continuum neutrons, as:

$$A = N \int_{Eth}^{E\,min} \sigma(E)\Phi(E)\,dE \quad + N\sigma(Ep)\Phi(Ep)$$

where *N* number of target atoms relating to the relevant reaction,
Eth threshold energy,
Emim lowest energy of monoenergetic peak neutrons,
s(Ep) cross-section at peak neutron energy,
F(Ep) monoenergetic peak neutron flux.

If the threshold energy *Eth* is higher than *Emin*, the first integration term must be zero. Otherwise, this term can be estimated by successive subtraction method using the neutron flux *F(E)* having lower peak energy. The *s(E)* values in lower energy region were cited from the evaluated data files, ENDF/B-VI(I), McLane et al.(2) and so on. Some examples of thus-obtained activation cross-sections are shown in Figures 7 and 8. Figure 7 gives the cross-section data of C-12(n,2n) reaction. Our results are much lower in the peak region around 40 MeV than the ENDF/B-VI high energy file data, but the agreement becomes better above about 60 MeV. Figure 8 gives the cross-section data of Bi-209(n,xn) reaction, compared with other experimental data and the ENDF/B-VI high energy file data. Our data are generally in good agreement with them, but some discrepancy can be found in high energy region.

References

[1] National Nuclear Data Center, Brookhaven National Laboratory, "Evaluated Nuclear Data File", ENDF/B-VI (1990).

[2] V. McLane, C.L. Dunford and P.F. Rose, "Neutron Cross Sections", Vol.2, Neutron Cross Section Curves, Academic Press Inc., New York (1988).

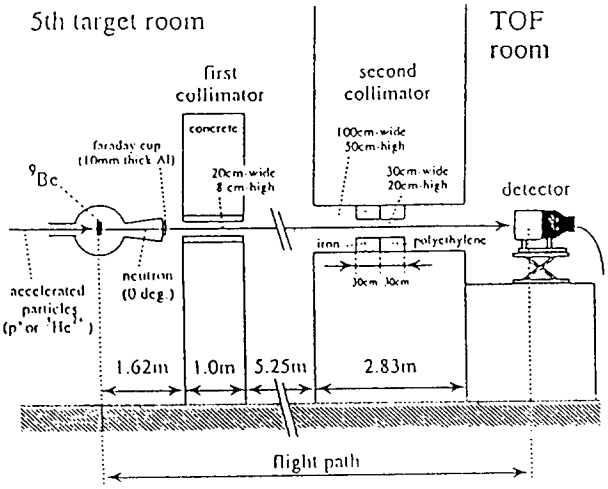

Figure 1 ***Cross-sectional view of CYRIC neutron field***

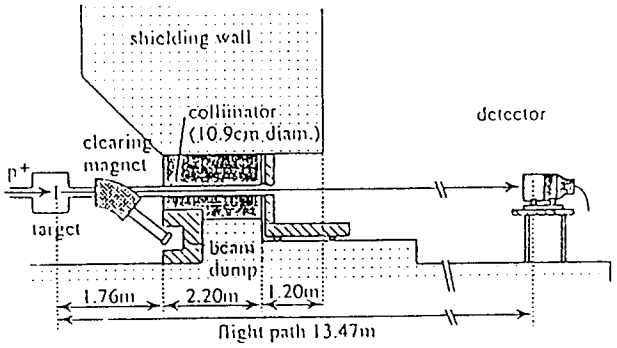

Figure 3 ***Cross-sectional view of TIARA neutron field***

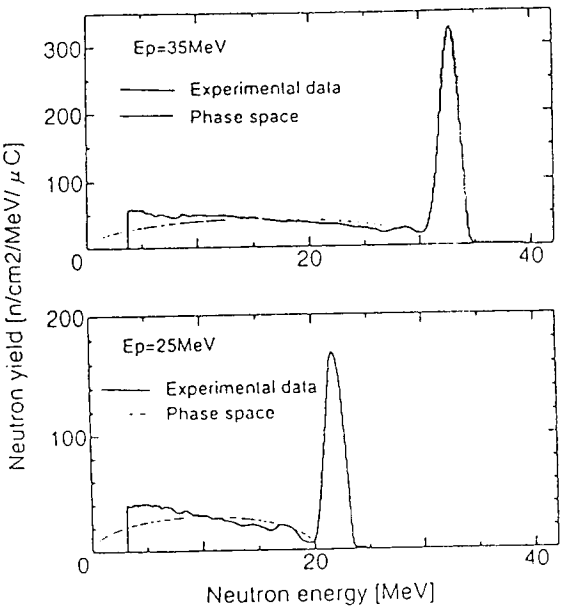

Figure 2 ***Neutron spectra of 25 and 35 MeV p-Li reaction at CYRIC***

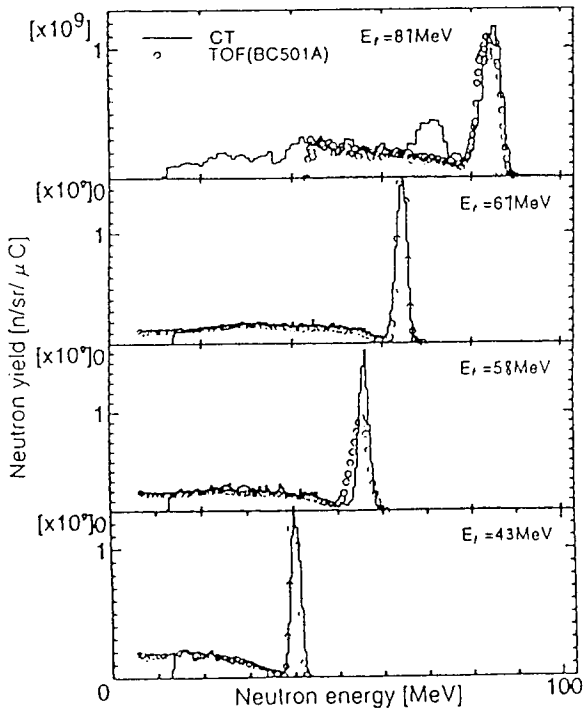

Figure 4 ***Neutron spectra of 43, 58, 67 and 87 MeV p-Li reaction at TIARA***

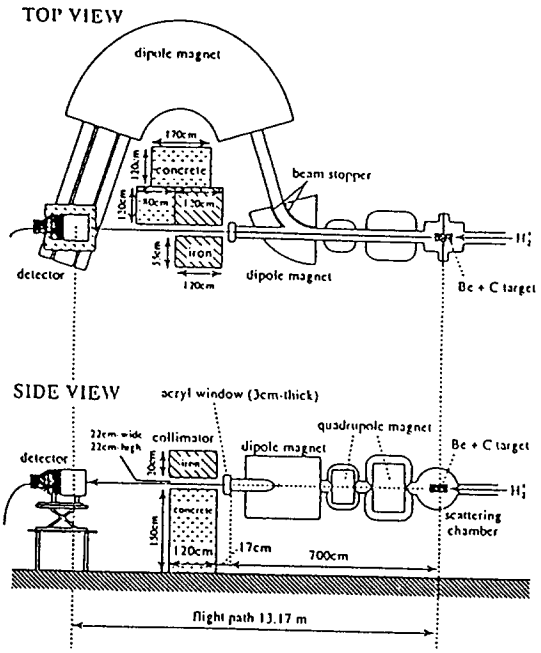

Figure 5 ***Cross-sectional view of RIKEN neutron field***

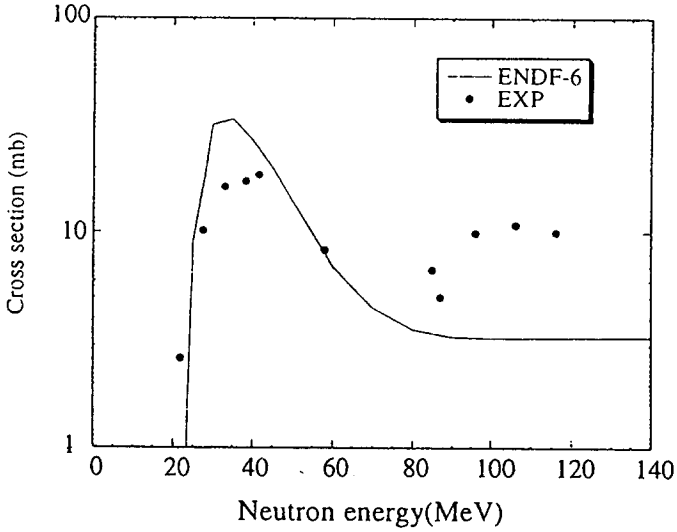

Figure 7 ***Cross-section data of C-12 (n,2n) reaction compared with ENDF/B-VI***

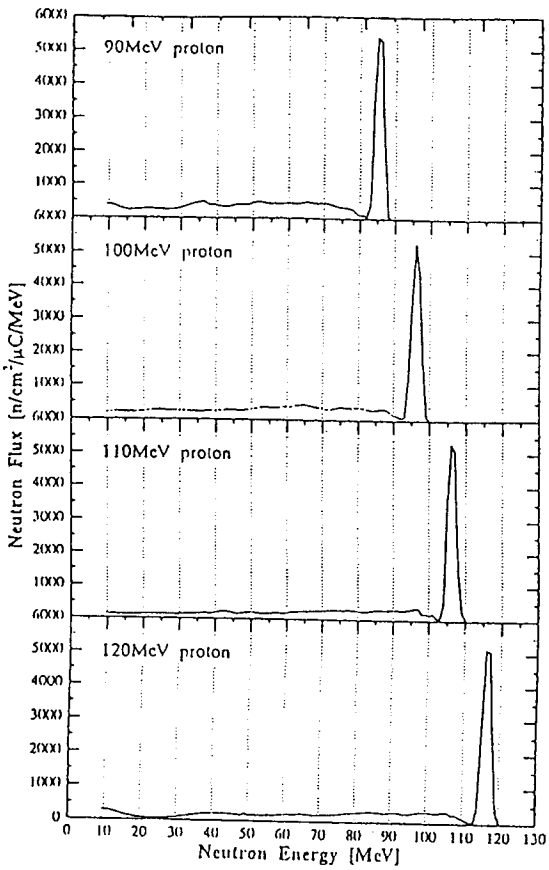

Figure 6 ***Neutron spectra of 90, 100, 110 and 120 MeV p-Li reaction at RIKEN***

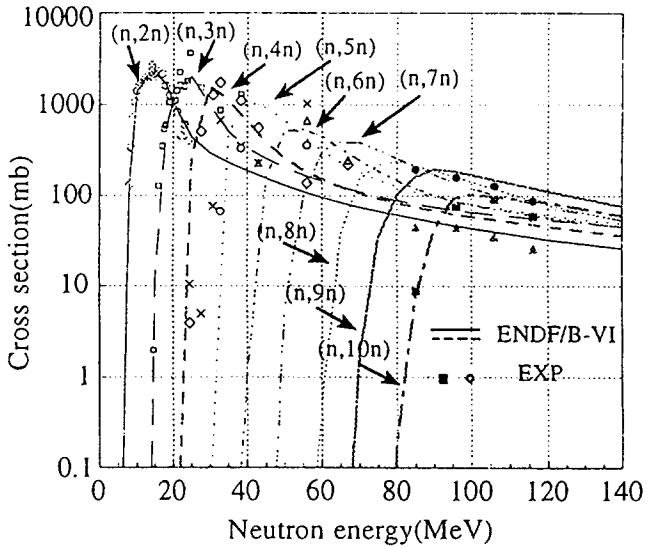

Figure 8 ***Cross-section data of Bi-209 (n,xn) reaction compared with ENDF/B-VI***

NEUTRON INDUCED ACTIVATION AND TRANSMUTATION HEAVY ION INDUCED ISOTOPE PRODUCTION WITH C, Ne, Ar, Kr AT 100A.MeV.

F. Clapier, N. Pauwels, J. Proust.
Institut de Physique Nucléaire, Orsay, France

Abstract

The radioactive ion beam facility SPIRAL, presently under construction, will be based on high intensity heavy ion beams (6 kW from He to Ar) at GANIL, France. The isobaric yields for Ar+C and Ar+W were studied. The first tests for the production of radioactive ion beams have been undertaken with the test bench on line separator SIRa. During the target and separator tests the secondary neutron fluxes and interactions with a series of materials were investigated.The experimental data collected and derived predictions are presented.

1. Introduction

The studies described hereafter are justified by the SPIRAL project which will upgrade GANIL beam intensities from 400W to 6kW expected to operate on line separators during hundreds of hours [1]. Both conception and operating conditions of the new facility will strongly depend on the radiation levels associated with the impinging ions on the devices and target materials. The radioisotopes produced in selected targets needed an inventory of yields and a study of the decay processes; the neutron fields related to different projectiles bombarding a light target for fragmentation were needed. The activation of the materials surrounding the target by the secondary neutrons was studied in order to simulate operational conditions properly extrapolated from the available intensities to the future beam power; it was expected that a better knowledge of the reaction mechanisms could possibly help to optimize the use of materials by taking into account radiation hazards, radiation and contamination levels, when designing beam transport devices, experimental instruments and shielding.

2. Target activation

The data available for short operation times for a small number of projectile and target sets did not suffice to predict radiation levels after given irradiation and decay times. The former experiments at CERN had been performed with ^{12}C and ^{18}O at 86A.MeV on Al, Fe and Ta (1a and 1c) [2]. We decided to use 95A.MeV ^{36}Ar as a heavier projectile bombarding C and W in order to investigate the respective influences of the projectile and target atomic mass numbers. Induced radioactivity has been monitored off-line of the GANIL facility, both by gamma-ray spectrometry and dose rate measurements with tissue-equivalent ionisation chambers; the beam doses were delivered in 1, 10 and 27 hours at 1.10^{11} particles per second. Ten percent of the energy was lost in W foils and the remaining in carbon (from 86 to 0 A.MeV) [3].

The measured isobaric yield distribution for Ar+C shows (Figure 1c) that the nuclide production is dominated by a projectile fragmentation process (Be and Na mainly, Sc) when decay time is greater than some hours; on the other hand, Ar+W reactions produce 106 identified radioisotopes ranging from ^{7}Be to ^{185}Os (Figure 1d), the decay lines haven been followed until 22 months after the experience. As the atomic mass of radioactive residue increases, several regions of interest can be interpreted as resulting from:

- Projectile-like fragments,
- Target fragments,
- Symmetric fission,
- Abrasion followed by evaporation,
- A questionable contribution of semi-peripheral reactions ($A \approx A_t - A_p$)
- A small number of products under the curve are probably created by secondary nucleons on impurities contained in the matter.

The dose rate dependence at 20cm from the C and W targets after 27h exposure to ^{36}Ar was monitored during 200h with a tissue-equivalent ionization chamber. Former experiments [2] with a carbon projectile have given evidence for a heavy ion interaction with targets behaving as

hadrons-induced spallation [4] according to the function expressing the dose rate at a distance of 1 meter from the target:

$$dD/dt = k.\phi.\log[(T_a+t)/ t],$$

where k = is determined in Sv/h/pps
f = ion flux causing the activation in pps
T_a = irradiation time
t = decay time, same units as T_a

When our results are compared with C +Fe (Figure 1c) and as shown in Figure 1b, the stochastic isotope prediction function can fit with a tungsten target and not with carbon because in the first case the target nucleus contains a great number of nucleons and th erefore a large variety of reactions are possible, whereas the small number of nucleons in carbon leads to a limited number of projectile -like contributors to the dose rate, explaining the discrepancy with a stochastic assumption. The assessment of the contamination hazard in units of Annual Limits on Intake has been described elsewhere [3].

3. Secondary neutrons

The neutron fluxes were determined in parallel with the on -line separation of exotic nuclei. The projectiles were ^{13}C, ^{78}Kr at 75A.MeV and ^{20}Ne, ^{36}Ar at 95A.MeV [5]. The production target consisted in a 25µm tantalum foil and a carbon thick target. The neutron activation detectors were based on the classical reactions $^{12}C(n,X)^{7}Be$, $^{27}Al(n,\alpha)^{24}Na$ and $^{27}Al(n,spall.)\ ^{22}Na$, thanks to 5-mm thick and 40-mm diameter disks displayed at 50cm from the position where the beam starts to interact. At forward angle the samples were displayed at two distances and separated by a 45mm copper cylinder for the purpose of charged particle discrimination when unfolding the data. The results are presented in Tables 1 and 2.

It appears that the in the direction of the beam the two flux components vary very little regardless of the neutron energy and ion considered. At a large angle the lower energy component dominates, as expected because of kinematics; both fast and higher energy neutrons fluxes decrease smoothly with the projectile size, this effect may be due to atomic stripped charge states and speed differences. The flux data will be useful for radiation damage studi es.

Table 1
Neutrons with energy greater than 30 MeV in $n.cm^{-2}.s^{-1}$ at 30 cm from interaction point, for 10^{12} incident ions per second

Projectile	C	Ne	Ar	Kr
Angle 3°	$1.4\ 10^{8}$	$1.7\ 10^{8}$	$2.4\ 10^{8}$	$1.2\ 10^{8}$
Angle 80°	$5.7\ 10^{5}$	$2.3\ 10^{5}$	$5.5\ 10^{5}$	$1.1\ 10^{5}$

Table 2
Neutrons in the energy range 6 < E MeV< 30 in n.cm^{-2}.s^{-1} at 30 cm from interaction point, for 10^{10} incident ions per second.

Projectile	C	Ne	Ar	Kr
Angle 3°	1.2 10^{8}	1.2 10^{8}	9.7 10^{7}	1.2 10^{8}
Angle 80°	5 10^{6}	2.8 10^{6}	4.1 10^{6}	2 10^{6}

4. Neutron induced activation

In order to assess the magnitude of induced radioactivity expected in realistic operating conditions, pieces of materials usually required for the construction of instruments built around a thick target, samples of industrial carbon, aluminum, copper, stainless steel, molybdenum, tantalum, tungsten and permanent magnets used for ECRIS ion sources were exposed in the experimental conditions cited at two to five angular positions. The induced radioactivity and its angular distribution was measured by off-line gamma ray spectrometry at time intervals depending on the appearance of nuclide filiations and decay of radionuclides occurring within months after irradiation. Identification of the reaction and decay processes made the extrapolation to higher exposure regime pertinent. For instance, unfolding of data at small decay times, down to minutes after exposures at 400W beams lead to a comprehensive description of n,xn activation path rather than a spallation mechanism in the case of tantalum. ^{171}Ta and its' daughter isotopes were followed, ^{169}Lu was identified also; therefore $^{181-x}$Ta isotopes are produced as far as x=13 [6].

Accordingly, the dose rate time dependencies due to a given material exposed to the secondary neutrons 50, 100 and 300 hours will be drastically related to the fast and slow regime radioactivity production mechanisms and the family decay lines toward stability opened in the case of a given matter. In some cases the material is quite sensitive to neutron capture inducing a radionuclide having a critical decay half-life on a basis of operation times. Different examples (Figures 2 and 3) show that the dose rate per unit mass of material (mSv/h.g at 10cm) may build up slowly but will not decrease after exposure such as in the cases of carbon (at a small specific rate), and tantalum stainless steel, specially at large angles. Quite differently, aluminum and copper will reach saturated levels of dose rate whatever the exposure time but decrease by 100 to 1000 fold within times comparable to the exposure duration [5]. Expectedly the dose rates generated by neutrons depend on the type, geometry and position of material and the corresponding level and time functions were investigated for simulation in the process of designing real devices before construction in terms of dose costs in decision making. A specific computer program has been derived from these experiments by the SPIRAL staff; it will also be used for the design of shields to protect equipments against beam loss induced burning at a limited dose cost when possible [7].

5. Neutron induced transmutation

The description and experimental data relevant to induced radiation levels were desired for radiation safety requirements. Beyond the scope of such a study, when analyzing the radioactivity produced in

given that charged particles are absorbed. The feature is quite clear when the probability of residues in terms of $\sigma.\phi_n$ (the n,xn cross-section multiplied by the neutron flux) are plotted versus the atomic mass number of Ta neutron deficient radionuclides (Figure 4a). The same behavior was observed in a recent thick target experience we performed at LNS facility (100A.MeV ^{3}He+Ta) in July 1995, with similar motivations.

6. Final remarks

As pointed out at previous meetings organized under the auspices of OECD/NEA [8, 9] and in JAERI reviews [10], there is a need for the measurement of the n,xn cross-sections and appropriate codes fitted to heavy ions making high energy neutron spectra determinations achievable, for instance with a ^{181}Ta activation detector (Figure 4b). The authors express their willing to collaborate with colleagues having the corresponding skills or engaged in the course of adapting a facility for the mentioned purpose: there is a lot of work before us as far as heavy ions are concerned.

References

[1] A.C.C. Villari et al., "Radioactive Ion Beam at SPIRAL", Nucl. Phys. A588 (1995) 267c-272c.

[2] J. W. N. Tuyn, R. Deltendre, C. Lamberet and G. Roubaud, "Radiation Measurement with the SC External ^{12}C Ion Beam", Report HS-RT/TM80-5, CERN, 1980.

[3] F. Clapier and al., "Activation of Thick Targets by Energetic Heavy Ions and the Resultant Radiation Levels", Radiat. Environ. Biophys. Vol. 34, n°4 Nov. 1995.

[4] A.H. Sullivan, "A Guide to Radiation and Radioactivity Levels near High Energy Particle Accelerators", Nuclear Technology Publishing (1992).

[5] F. Clapier, N. Pauwels, J. Proust, "Neutrons créés par ions louds et activation induite dans divers matériaux", IPNO - 95 -02 (1995).

[6] F. Clapier, N. Pauwels, J. Proust, "Spallation par neutrons: (n,13n) ?" Radioprotection Vol. 29 n°4 (1994).

[7] B. Rannou, "Calcul d'activation par ions et par neutrons. Application à l'ensemble cible-source NANOGAN II", GANIL/95/SPI/57 (1995).

[8] A.J. Koning, "Requirements for an Evaluated Nuclear Data File for Accelerator Based Transmutation", NEA/NSC/DOC/(93) 6 OCDE 1993, Paris.

[9] "Intermediate Energy Nuclear Data: Models and Codes", Proceedings of a Specialists' Meeting, 30 May-June 1994, AEN-OCDE, Paris (France).

[10] "Overview of Physics Aspects of Different Transmutation Concepts", NEA/NSC/DOC (94) 11, OECD NEA (1994).

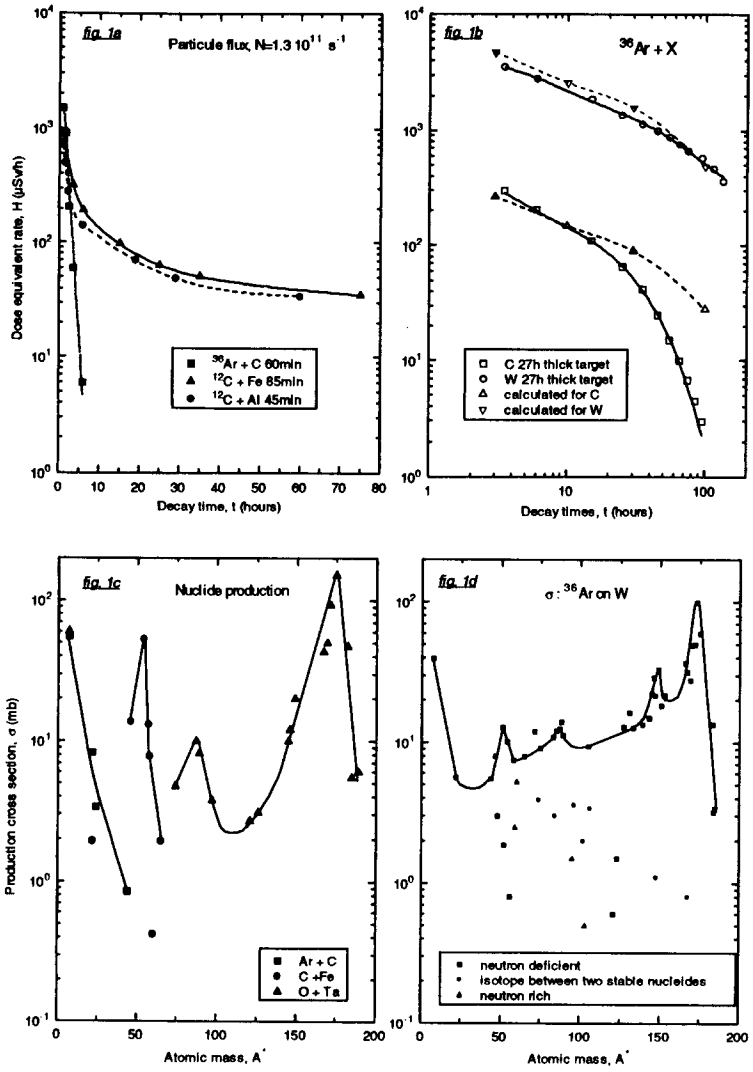

Figure 1 ***Dose rates and nuclide production with 86 to 95 A.MeV heavy ions***

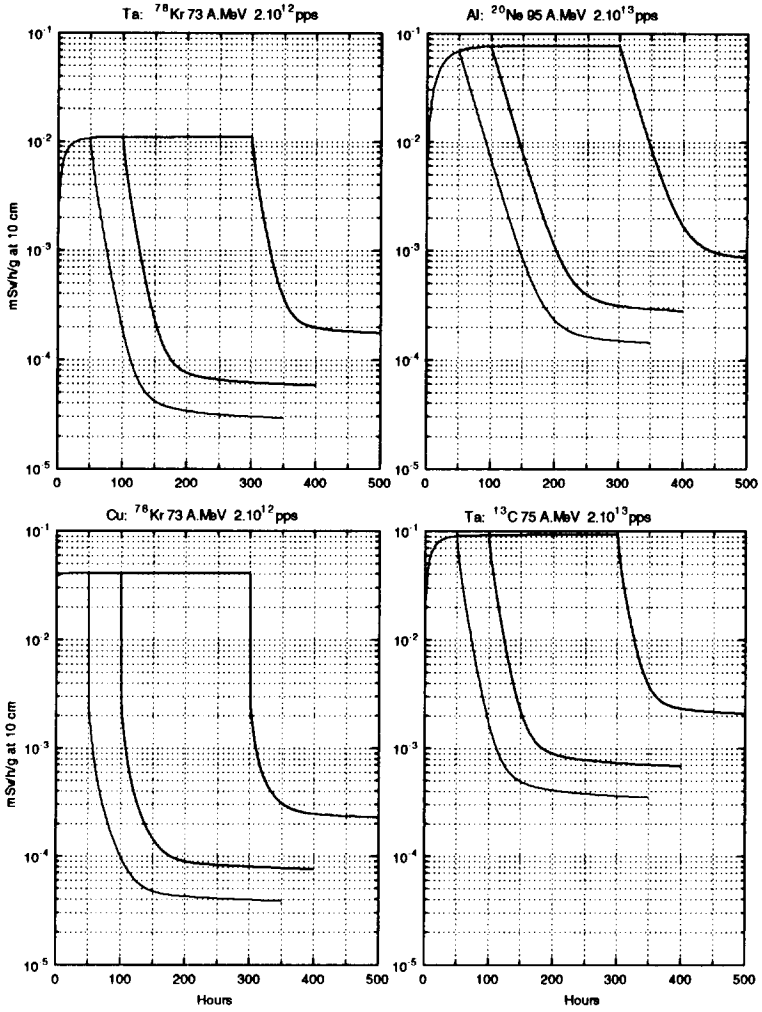

Figure 2 ***Dose rate predictions for neutron-induced activation of materials at 3° and 30 cm***

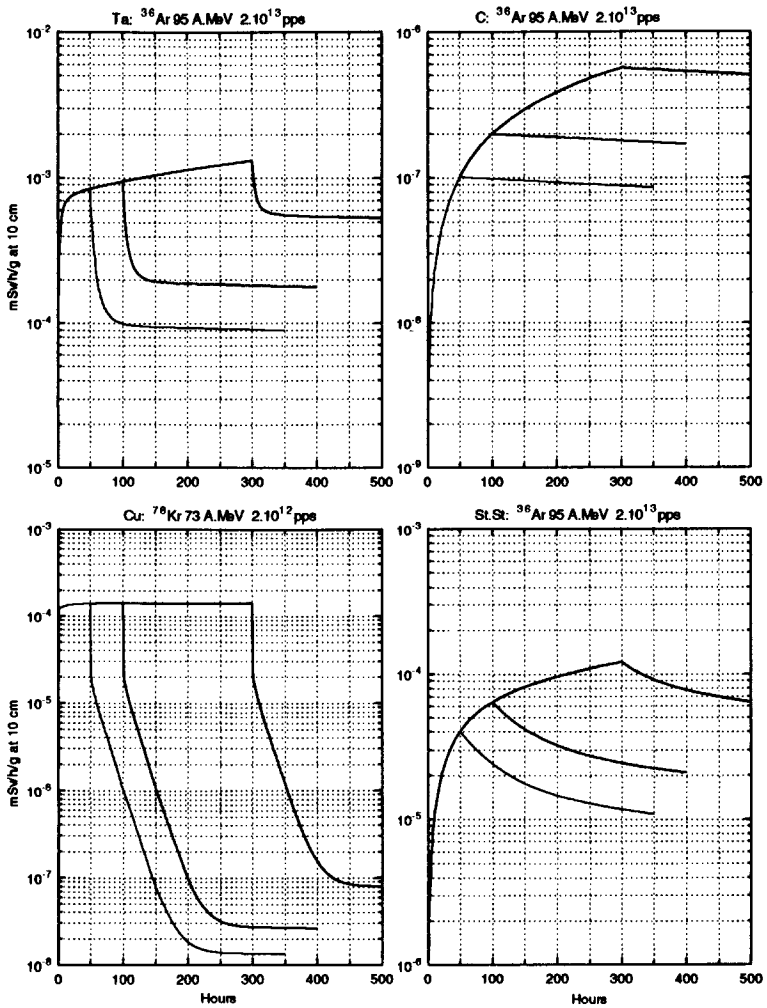

Figure 3 ***Dose rate predictions for neutron-induced activation of materials at 80° and 30 cm***

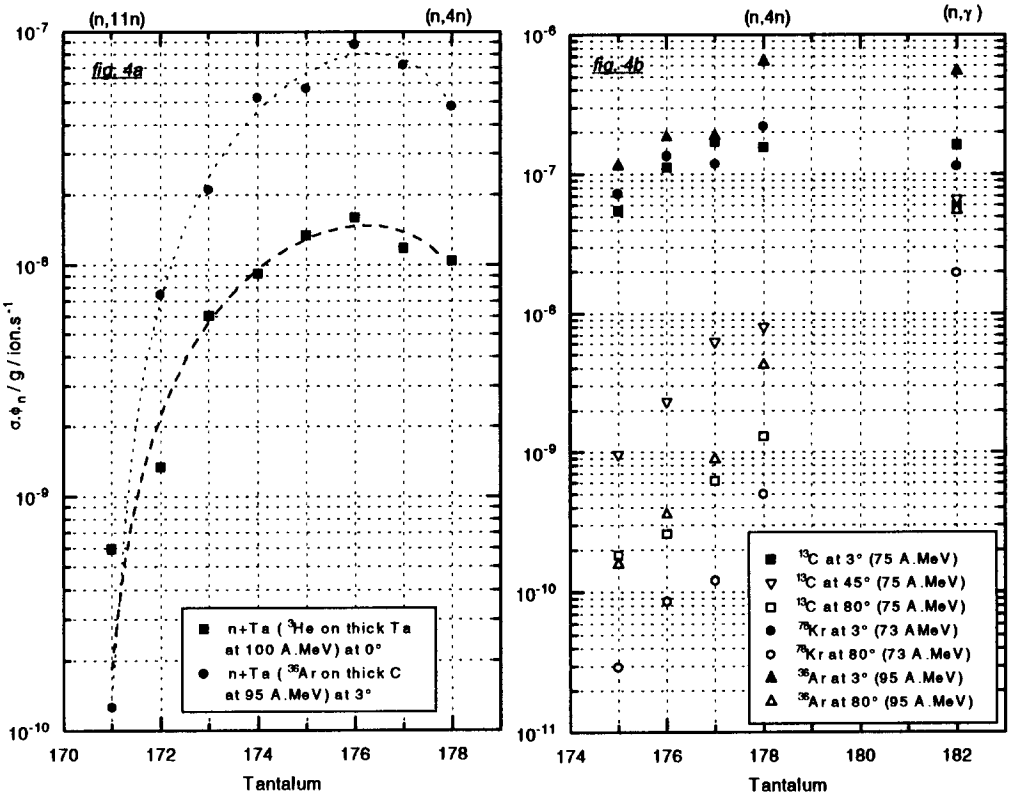

Figure 4 ***Probability of (n,xn) reactions on Tantalum 181 by secondary neutrons***

Session IV

HIGH ENERGY DOSIMETRY – CONVERSION FACTORS, ANTHROPOMORPHIC MODELS, ACCELERATORS

CHAIR

Graham STEVENSON

CO-CHAIR

Yukio SAKAMOTO

EVALUATION OF FLUENCE TO DOSE EQUIVALENT CONVERSION COEFFICIENTS FOR HIGH ENERGY NEUTRONS – CALCULATION OF EFFECTIVE DOSE EQUIVALENT AND EFFECTIVE DOSE

Satoshi Iwai[1], *Takashi Uehara*[1], *Osamu Sato*[2], *Nobuaki Yoshizawa*[2], *Shiori Furihata*[2], *Shunji Tagaki*[2], *Shun-ichi Tanaka*[3], *and Yukio Sakamoto*[4]

Abstract

In and around high energy accelerator facilities, neutron dose estimation is important for the radiation protection of workers. The contribution of high energy neutrons to the radiation exposure of astronauts cannot be also disregarded inside a spacecraft. Although the fluence-to-effective-dose-equivalent (or effective-dose) conversion coefficients for high energy neutrons are essential to the workers in high accelerator facilities and space crews, the coefficients above 180 MeV have not been calculated so far. This study shows the methodology for calculating the fluence-to-effective-dose-equivalent (or effective-dose) conversion coefficients for high energy radiations including neutrons. The conversion coefficients of high energy neutrons were calculated in the energy range from 20 MeV to 10 GeV for the Anterior-Posterior and Posterior-Anterior geometries, by use of the method developed in this study. The calculated results led to the findings that, for the same high energy neutron, large discrepancy could be found between the effective dose equivalent and the effective dose, which are the important quantities used in radiological protection for exposure.

[1] Mitsubishi Heavy Industries, Japan.
[2] Mitsubishi Research Institute, Japan.
[3] Japan Atomic Research Institute, Office of Planning, Japan.

[4] Japan Atomic Research Institute, Applied Radiation Laboratory Dept. of Reactor Engineering, Japan.

1. Introduction

Due to the increase of high energy accelerator facilities and space missions, high energy radiation protection has come to be an important issue. The neutron spectra around high energy accelerator facilities are estimated to distribute from thermal energy to 100 MeV or more [1]. Neutrons inside space shuttles are estimated to contribute maximally to 20% of astronauts' whole-body dose equivalents [2]. Inside a spacecraft, the neutron flux is assumed to spread from thermal energy to 1 GeV [2].

Although the neutron-fluence-to-effective-dose equivalent conversion coefficients have been given in the energy range from 2.5×10^{-2} eV to 14 MeV in the ICRP51 [3] (ICRP Publ. 5.1), the conversion coefficients of neutron effective dose equivalent (or effective dose) above 14 MeV are not shown in any document except those from 20 to 180 MeV by Nabelssi et al. [4,5].

Our work shows the methodology for calculating the conversion coefficients from high energy neutron fluence to effective dose equivalent (or effective dose). By use of this method, the conversion coefficients of high energy neutrons were calculated from 20 MeV to 10 GeV.

2. Methodology to estimate the conversion coefficients

2.1 Method of calculating effective dose and effective dose equivalent

The ICRP26 [6] introduced the averaged organ dose equivalent $\hat{H}_T$ expanded from the dose equivalent at a point in organ or tissue *T*. By use of $\hat{H}_T$ this publication defined the effective dose equivalent H_E which is the weighted sum of the dose equivalents of six specified organs and a remainder consisting of five organs at most:

$$H_E = \sum_T W_{T,26} \hat{H}_T \qquad (1)$$

where $W_{T,26}$ is the tissue weighting factor specified in the ICRP26.

In 1990, the ICRP60 [7] recommended new quantities used for radiological protection: equivalent dose H_T is defined as the average organ-absorbed-dose multiplied by a radiation weighting factor W_R; the ICRP recommended weighting factors in place of effective quality factor $\overline{Q}$ because of the uncertainties in the radio-biological information for the high LET part of the Q-L relationship specified in the ICRP60. Although the radiation weighting factors are presented in the ICRP60, the theoretical background on the derivation of the factors is not explained in this publication.

The effective dose *E* is defined as the weighted sum of the equivalent dose of twelve specified organs* and a remainder consisting of ten organs additionally specified in the ICRP60.

---

* The equivalent dose to the colon Hcolon is given as:

Hcolon = 0.57 H_{ULI} + 0.47 H_{LLI}

where H_{ULI} and H_{LLI} are the equivalent doses to the ULI (upper large intestine) and the LLI (lower large intestine), according to the ICRP67.

$$E = \sum_T W_{T,60} H_T \tag{2}$$

where $W_{T,60}$ is the appropriate tissue weighting factor shown in the ICRP60.

In 1993, the ICRU51 [8] redefined the effective dose equivalent H_E by use of the equation (3) according to the consistency to the ICRP26, ICRP60, and ICRP67 [9].

$$H_E = \sum_T W_{T,60} D_T Q_T = \sum_T W_{T,60} \hat{H}_T \tag{3}$$

where D_T and Q_T are the mean absorbed dose and the mean quality factor in a specified tissue (or organ) *T*, respectively. In equation (3) Q_T is defined as follows:

$$Q_T = \frac{1}{m_T D_T} \int_{m_T} \int_L Q(L) \bullet D(L)\, dL\, dm \tag{4}$$

where Q_T is the mass of the tissue or organ *T*, D(L) denotes an absorbed dose distribution in the tissue (or organ) *T* as a function of *L*, and Q(L) denotes the Q-L relationship of ICRP60. $\hat{H}_T$ is the averaged dose equivalent in the tissue (or organ) *T*. This paper employs the definition of equation (3) as the term of "effective dose equivalent, H_E".

2.2 Method of calculating the averaged dose equivalent

The ICRP recommends the radiation weighting factor in place of the effective quality factor derived from the Q-L relationship in the ICRP60, which is shown in Figure 1. According to the ICRP60, the radiation weighting factor has a stronger relation to the radiation type and energy before incidence to the body rather than to those distributed in the organ of interest.

For high energy radiations, the application of a radiation weighting factor is not appropriate for the calculation of the averaged dose equivalent $\hat{H}_T$ to the organ of interest, since this factor is more related to the external radiation type and energy incident to the body rather than to those within the organs where several kinds of secondary particle are mixed.

In this study, the averaged dose equivalent $\hat{H}_T$ has been calculated using averaged quality factors which have been prepared as a function of the energy of a charged particle as follows:

When a charged particle *R* enters an organ *T* with initial energy E_0 and leaves the organ with the energy E_1 where the energy is lost only by continuous slowing-down process as shown in Figure 2, the dose equivalent averaged in an organ *T* caused by charged particle *R*, $\hat{H}_{T,R}$, is given by:

$$\begin{aligned} \hat{H}_{T,R} &= \hat{Q}_R(E_0) \bullet D_0 - \hat{Q}_R(E_1) \bullet D_1 \\ &= \hat{Q}_R(E_0) \bullet E_0 / m_T - \hat{Q}_R(E_1) \bullet E_1 / m_T \end{aligned} \tag{5}$$

where $\hat{Q}_R(E)$ is the "averaged" quality factor [10] for a charged particle *R* having energy *E*, which is defined in Section 2.3, and m_T the mass of the organ *T*. D_0 and D_1 are the absorbed doses to the organ when the charged particles of energy E_0 and E_1 lose their whole kinetic energies in the organ. If the charged particle interacts to emit additional energetic particles and radiations in the organ, the energy E_1 in equation (5) is replaced by the energy of the charged particle immediately before the interaction, as shown in Figure 2. Subsequently, the averaged dose equivalent to the organ, which corresponds to the total equivalent dose H_T defined in ICRP60, is obtained by summing $\hat{H}_{T,R}$ along all charged particles' trucks in the organ of interest as follows:

$$\hat{H}_T = \sum_R \hat{H}_{T,R} \tag{6}$$

In case of the incidence of uncharged ionising particles such as neutrons and photons, the averaged dose equivalent $\hat{H}_T$ can be calculated by the sum of the $\hat{H}_{T,R}$ along the trucks of secondary charged particles generated by the interactions of the incident uncharged particles with the medium of the organ. This work treats high energy neutrons which have possibilities to produce secondary charged particles, photons, and mesons.

2.3 Averaged quality factor

The effective quality factor $\overline{Q}$ at a point of interest in an organ for charged particle is defined in the ICRU40 [11] as follows:

$$\overline{Q} = \frac{\int_0^\infty Q(L) \bullet D(L)dL}{\int_0^\infty D(L)dL} = \frac{1}{D}\int_0^\infty Q(L) \bullet D(L)dL \tag{7}$$

where D(L) denotes the absorbed dose spectrum with respect to unrestricted linear energy transfer *L* of a charged particle, and Q(L) is the quality factor specified in ICRP60. If a charged particle *R* with energy E_0 is plunged into an organ *T* having a mass of m_T and loses the whole energy by a continuous slowing down, the "averaged" quality factor [12] in the organ, which is a mean quality factor [8] when a charged particle with energy E_0 loses its whole energy in the organ , is obtained as follows:

$$\hat{Q}_R = \frac{1}{\left(\frac{E_0}{m_T}\right)} \int_0^{L_{0,R}} Q(L) \bullet D(L)dL \tag{8}$$

where $L_{0,R}$ is the maximum of unrestricted linear energy transfer of the charged particle *R* during the process of continuous slowing down from energy E_0 to 0. As the absorbed dose D(L) is equal to $(1/m_T)$ dE/dL, equation (8) is modified as follows:

$$\hat{Q}_R = \frac{1}{\left(\frac{E_0}{m_T}\right)} \int_0^{L_{0,R}} Q(L) \bullet \frac{dE}{m_T \bullet dL} dL \qquad (9)$$

Finally, the averaged quality factor for the charged particle *R* is represented as a function of its initial energy E_0,

$$\hat{Q}_R(E_0) = \frac{1}{(E_0)} \int_0^{E_0} Q(L_R(E))\, dE \qquad (10)$$

where $L_R(E)$ is an unrestricted energy transfer of the charged particle *R* with energy *E* in water.

When a human body is irradiated by high energy neutrons, various kinds of secondary particles are produced by nuclear reactions in the body. Energies of those particles are widely distributed. We calculated averaged quality factors corresponding to 186 charged particles up to Z = 26. All kinds of these particles are shown in Table 1. These 186 particles were selected from the spallation products of the nuclei in the materials used in the MIRD-5 mathematical human body phantom [13]. For charged pions and muons, the averaged quality factors were also calculated. Calculated energy ranges for all particles are 0.2 eV to 10 GeV.

In these calculations of the averaged quality factors, the restricted linear energy transfers *L* corresponding to energies of charged particles are evaluated by the way described below. The values of *L* of proton, charged pions and muons were calculated with the computer code SPAR [14]. For the other charged particles below 10 MeV /nucleon, *L* was calculated with the STOPPING code [15], and above that energy, with the SPAR code.

Calculated averaged quality factors of proton, charged pions, alpha particle, C-12, O-16, and Fe-56 are shown in Figure 3; averaged quality factors of some particles have two peaks. The shapes of the quality factors are attributed to the maximum *L* values of those particles exceeding 100 keV/micro-meter at which Q(L) has the maximum value in the Q-L relationship in the ICRP60.

Averaged quality factors of electrons and positrons are shown as follows.

The relationships between the unrestricted linear energy transfers *L* and the energies *E* of electrons and positrons in water are presented in the ICRU37 [16] over the energy from 10 keV to 1 GeV. The L-E relationship of positron agrees with that of electron within the discrepancy of 3% from 1 GeV to 10 GeV [17]. The averaged quality factor $\hat{Q}_R$ of electron and positron over the energy from 10 keV to 10 GeV is evaluated to be unity, by use of the E-L relationship in the ICRU37 and ICRU16, and the Q-L relationship in the ICRP60.

2.4 Anthropomorphic phantom

In this work, an adult hermaphroditic anthropomorphic phantom was applied to evaluate the effective dose equivalents and effective doses. Figure 4 shows the internal structure of this phantom. This phantom represents a modified version of Yamaguchi's data [18] based on the Cristy phantom [19] of MIRD-5 type [13].

Three modification points were applied to this phantom:

- *Addition of an oesophagus.* An oesophagus model was added to the phantom using the mathematical form reported by Lewis et al. [20].

- *Modification of stomach location.* Although a description is included in Yamaguchi's version, the stomach location was altered on the consideration reported by Lewis et al.

- *Size of breast models.* The height of this breast model is about half that of the Cristy phantom model because this phantom is hermaphroditic.

Internal organs are considered to be homogeneous in composition and density. Different densities and compositions are used for the lungs, skeleton and soft tissue. The composition description of the three tissues are limited to 17 elements (H, C, N, O, Na, Mg, P, S, Cl, K, Ca, Fe, Zn, Rb, Sr, Zr, and Pb). The densities of the lungs, skeleton, and soft tissue are 0.2958, 1.4682, and 0.9869 g/cm ^{3} respectively; these values are cited from the MIRD-5 report and not from Cristy's value. The density of Cristy's soft tissue is about 5% higher than that of the MIRD-5 phantom because the density of Cristy's soft tissue is assumed to be modified for the calculation of internal dosimetry; it is most important to keep the mass of organs and the distance between the organs in the human body for the internal dosimetry calculation. Therefore the density of Cristy's soft tissue is assumed to be increased so as to keep both parameters. The densities of MIRD-5 were adopted into this work because this phantom was employed to the external dosimetry.

2.5 Calculational method with Monte Carlo code

We used the HERMES [21] computer code system for nuclear interaction and transport calculation for incident particles and various kinds of particles produced in nuclear reactions between high energy particles and nuclei composing a human body. In HERMES, four Monte Carlo codes are implemented, namely HETC-KFA2 [22], MORSE-CG [23], EGS-4 [24] and NDEM [25].

The kinds of particles which are considered in the calculation of the dose equivalent from high energy neutrons with HERMES and the methods of calculation of dose equivalent for those particles are given in this section.

2.5.1 Charged particles

To calculate neutron-fluence-to-effective-dose equivalent conversion coefficients, we added a new estimator into HETC-KFA2 for the dose equivalent calculation with the averaged quality factors described in Section 2.3.

The mean absorbed dose and the averaged dose equivalent from protons, charged pions and muons, which include those produced in spallation reactions, are calculated with HETC-KFA2. The energy losses of these particles are treated in the continuous slowing-down approximation along the particle trucks. The averaged dose equivalents are calculated with the averaged quality factors described in Section 2.3.

The mean absorbed dose and the averaged dose equivalent from heavy ions, which are evaporated particles and spallation fragments, are also calculated with HETC-KFA2. Because of the short ranges of these particles, their kinetic energies are deposited locally. The averaged dose equivalents are calculated in the same way as the other charged particles described above.

Electrons and positrons are produced through the neutral pion decay. The productions of neutral pions are calculated with HETC-KFA2. Transportation and energy deposition of electrons and positrons are calculated with EGS-4. For electrons and positrons, averaged dose equivalents are equal to mean absorbed doses because the averaged quality factors of unity are applied at all energies of the particles.

2.5.2 Neutrons

For neutrons above 15 MeV, nuclear reactions and transportation are calculated with HETC-KFA2.

The mean absorbed dose D_T and the averaged dose equivalent $\hat{H}_T$ in the tissue (or organ) *T*, from neutrons with energy E_n below 15 MeV, are given by:

$$D_T = \int k_{f,T}(E_n)\, \varnothing_T(E_n) dE_n \tag{11}$$

$$\hat{H}_T = \int \hat{Q}_n k_{f,T}(E_n)\, \varnothing_T(E_n) dE_n \tag{12}$$

where $k_{f,T}$: kerma factors in *T*
$\hat{Q}_n k_{f,T}$: kerma factors in *T* multiplied by averaged quality factors of charged particles
$\varnothing_T$: neutron fluence in *T*

$k_{f,T}$ and $\hat{Q}_n k_{f,T}$ are given by:

$$k_{f,T}(E_n) = \sum_i a_i \sum_j \sum_r k_{f,i}(E_n, E_j^r) \tag{13}$$

$$\hat{Q}_n k_{f,T}(E_n) = \sum_i a_i \sum_j \sum_r \hat{Q}_n(E_j^r)\, k_{f,i}(E_n, E_j^r) \tag{14}$$

where a_i : the weight fraction of element in *T*
$k_{f,i}(E_n, E_j^r)$: kerma factor [26] of charged particle j with energy E_j^r from nuclear reaction r between neutron s with energy E_n and element I.
$\hat{Q}_n(E_j^r)$: averaged quality factors of charged particle j with energy E_j^r

The fluence of neutrons below 15 MeV in *T* is calculated with MORSE-CG and the multigroup neutron cross-section library based on the evaluated nuclear data library JENDL-3 [27].

2.5.3 Photons

In this study, two types of photons are considered.

The first-type photons are produced from the transition of the residual excited nucleus from spallation reactions. Productions of these photons are calculated with NDEM. For these photons, transportation and absorbed doses are calculated with EGS-4.

The second-type photons are produced from inelastic scattering of neutrons below 15 MeV. The fluence of these photons is calculated with MORSE-CG. The absorbed doses are obtained from calculated fluence and kerma factors [26]. The averaged dose equivalents are equal to the mean absorbed doses because the averaged quality factors of unity are applied to all photons as to electrons and positrons.

3. Results

We calculated the neutron-fluence-to-effective-dose-equivalent conversion coefficients for 14 kinds of monoenergetic neutrons of 20, 30, 50, 80, 100, 180, 200, 400, 700, 1000, 1500, 3000, 5000, and 10000 MeV, for anterior-posterior (AP) and posterior-anterior (PA) irradiation geometries. For simplicity, this calculation was performed in a vacuum boundary condition.

The calculated results for effective dose equivalents for neutrons are shown in Figure 5, using the HERMES code system with the data of averaged quality factor $\hat{Q}$ database described in Section 2.3. The effective dose equivalents calculated by Nabelssi et al. [5] are also shown in this figure from 30 MeV to 180 MeV for verification. For reference, effective doses were also calculated using the HERMES code system with the data of the radiation weighting factor W_R in equation (5).

$$W_R = 5 + 17 \exp\left[(\ln 2E)^2 / 6\right] \tag{15}$$

which is the approximate formula of neutron radiation weighting factor in ICRP60, where E is the neutron energy in MeV. The results calculated for the effective dose are shown in Figure 6 with effective doses by Nabelssi et al. from 30 MeV to 180 MeV.

Although the effective doses of our result show good agreement with those by Nabelssi et al., the effective dose equivalents are rather small than those by Nabelssi et al. We estimate that the main reason is ascribed to the difference in the quality factors employed in both studies from the following facts:

1. Good agreements are observed in both kinds of effective doses calculated with the same radiation weighting factors of neutrons expressed in equation (5);

2. Although Nabelssi et al. assigned the constant value of 20 to the quality factors of charged particles ($Z \geq 3$) for the calculation of the effective dose equivalents, our study applied the averaged quality factors shown in Figure 3, which are smaller than 20 in most of the energy range below 180 MeV.

Figure 7 shows the effective dose and the effective dose equivalent for the unit fluence of neutrons from 20 MeV to 10 GeV. The following results have been proven from Figure 7:

1. The effective dose equivalents for the AP and PA geometries agree well within Monte Carlo errors;

2. The effective doses for the AP and PA geometries have a good agreement within the Monte Carlo errors;

3. The effective doses are maximally twice higher than the effective dose equivalent. Discrepancies between both values are enlarged with the increase in neutron energy.

We assumed that the discrepancy between the effective dose equivalent and the effective dose may be ascribed to the difference between the radiation weighting factor W_R and the quality factors based on the Q-L relationship in the ICRP60. We have investigated the following factors of neutron from 20 MeV to 10 GeV so as to resolve the problem:

1. Radiation weighting factor W_R,

2. Ratio H_E/D_E for the AP and PA geometries, $\overline{Q_E}$, [28,29]

where H_E is the effective dose equivalent, and

D_E $\sum_T W_T \bullet D_T$

W_T : tissue weighting factor of ICRP60

D_T : mean absorbed dose in *T*

Figure 8 shows the radiation weighting factor W_R and the quality factors $\overline{Q_E}$ for the AP and PA geometries from 20 MeV to 10 GeV.

This result proves that the W_R values always show higher values than the $\overline{Q_E}$ values. The maximum discrepancy is approximately doubled at 10 GeV, and the discrepancy is enlarged with the increase in the neutron energy. These results indicate that the discrepancy between the effective dose is dominantly ascribed to the difference in the applications of the radiation weighting factors and quality factors based on the Q-L relationship in the ICRP60.

4. Summary and future subjects

The neutron-fluence-to-effective-dose-equivalent (effective-dose) conversion coefficients for the AP and PA geometries were calculated from 20 MeV to 10 GeV needed for radiation protection from high energy neutrons. The calculated values were verified under the comparison with the data by Nabelssi et al. below 180 MeV. This result proves that the effective doses show maximally twice higher values than the effective dose equivalents for neutrons from 20 MeV to 10 GeV. This discrepancy was proven to be ascribed to the difference in the radiation weighting factor and the quality factors in the ICRP60.

For photons over all the energy range, the effective dose equivalent agrees completely with the effective dose for all irradiation geometries because of the complete agreement of the quality factor and the radiation weighting factor for photons [10]. But the siginificant discrepancy can be recognised for the same energy neutrons between the two quantities (effective dose eqiuvalent and effective dose) used for radiological protection. This result may cause some confusion in the radiological protection of neutron.

There remain some subjects which require future study:

- In this study, a vacuum boundary condition was applied to the calculations in order to eliminate the complexity but the effect of air around the phantom should be treated for greater reality;

- Discussions on the operational quantities for high energy neutrons should be performed;

- Quantitative evaluations are required for the comparison between radiation weighting factors and quality factors for other particles.

References

[1] S. Ban, "Dosimetry around High Energy Accelerators", Proc. of the Workshop on Dosimetry for External Radiations, Jan 19 -20, 1995, pp l22-127, JAERI-Cont. 95-007 (1995) (in Japanese).

[2] J.E. Keith, G.D. Badhwar, and D.J. Lindstorm, "Neutron Spectrum and Dose-Equivalent in Shuttle Fights during Solar Maximum", Nucl. Tracks Radiat. Meas. 20 (1992) 41.

[3] ICRP Publication 51, "Data for Use in Protection Against External Radiation", Annals of the ICRP 17 (2/3) (1987).

[4] B.K. Nabelssi and N.E. Hertel, "Ambient Dose Equivalents, Effective Dose Equivalents, and Effective Doses for Neutrons from 10 to 20 MeV", Radiat. Prot, Dosim. 48 (1993) 153.

[5] B.K. Nabelssi and N.E. Hertel, "Effective Dose Equivalents and Effective Doses for Neutrons from 30 to 180 MeV", Radiat. Prot. Dosim. 48 (1993) 227.

[6] ICRP Publication 26, "Recommendations of the ICRP", Annals of the ICRP1 (3) (1977), Reprinted (with additions) in 1987, Superseded by ICRP Publication 60.

[7] ICRP Publication 60. 1990 Recommendations of the International Commission on Radiological Protection. Annals of the ICRP21(1-3)(1991).

[8] ICRU Report 51, "Quantities and Units in Radiation Protection Dosimetry", International Commission on Radiation Units and Measurements (1993)..

[9] ICRP Publication 67, "Age-dependent Doses to Members of the Public from Intake of Radionuclides: Part 2, Ingestion Dose Coefficients", Annals of the ICRP23 (3/4) (1993).

[10] O. Sato, S. Iwai, S. Tanaka, T. Uehara, Y. Sakamoto, N. Yoshizawa, and S. Furihata, "Calculations of Equivalent Dose and Effective Dose Conversion Coefficients for Photons from l MeV to 10 GeV", Radiat. Prot. Dosim. (in printing).

[11] ICRU Report 40, "The Quality Factor in Radiation Protection, International Commission on Radiation Units and Measurements" (1986).

[12] V.T. Golovachik, V.N. Kustarjov, E.N. Savitskaya, and A.V. Sannikov, "Absorbed Dose and Dose Equivalent Depth Distributions for Protons with Energies from 2 to 600 MeV", Radiat. Prot. Dosim. 28 (1989) 189.

[13] W.S. Synder, M.R. Ford, and G.G. Warner, "Estimates of Specific Absorbed Fractions for Photon Sources Uniformly Distributed in Various Organs of Heterogeneous Phantom", NM/MIRD Pamphlet No.5 (revised) J. Nucl. Med. 19 Supplement: 5 -67(1987).

[14] T.W. Armstrong and K.C. Chandler, "SPAR: A FORTRAN Program for Computing Stopping Powers and Ranges for Muons, Charged Pions, Protons, and Heavy Ions", ORNL-4869(1973).

[15] J.F. Ziegler, J.P. Biersack and U. Littmark, "The Stopping and Range of Ions in Solids", Volume 1 of the Stopping and Ranges of Ions in Matter, Pergamon Press, Oxford (1985).

[16] ICRU Report 37, "Stopping Power for Electrons and Positrons, International Commission on Radiation Units and Measurements" (1984).

[17] ICRU Report 16, "Linear Energy Transfer, International Commission on Radiation Units and Measurements" (1970).

[18] Y. Yamaguchi, "DEEP Code to Calculate Dose Equivalents in Human Pha ntom for External Photon Exposure by Monte Carlo", JAERI-M- 90-235 (1990).

[19] M. Cristy and K.F. Eckerman, "Specific Absorbed Fractions of Energy at Various Ages from Internal Photon Sources ORNL/TM-8381/V1-V7 (1987).

[20] C.A. Lewis and R.E. Ellis, "Additions to the Synder Mathematical Phantom", Phys. Med. Biol. 24 (1979) 1019.

[21] P. Cloth, D. Filges, R.D. Neef, G. Sterzenbach, Ch. Ruel, T.W. Armstrong, B.L. Colbom, B. Anders, and H. Bruckman, "HERMES A Monte Carlo Program System for Beam-Materials Interaction Studies", KFA-IRE-E AN 12/88 (1988).

[22] P. Cloth, D. Filges, G. Sterzenbach, T.W. Armstrong and B.L. Colborn, "The KFA -Version of the High-Energy Transport Code HETC and the Generalized Evaluation Code SIMPLE", RSIC Computer Code Collection, CCC-196 (1983).

[23] M.B. Emmett, "The MORSE Monte Carlo Radiation Rough Draft, LANL Group X-6, May (1985).

[24] W.R. Nelson, H. Hirayama, D.W.O. Rogers, "The EGS4 Cocle System", SLAC-265 (1985).

[25] R.E. Prael, "User's Guide to the HETC Code System", Rough Draft, LANL Group X-6, May (1985).

[26] K. Maki, H. Kawasaki, K. Kosako and Y. Seki, "Nuclear Heating Constant KERMA Library", JAERI-M 91-073 (1991).

[27] K. Shibata, T. Nakagawa and T. Asami, "Japanese Evaluated Nuclear Data Library, Version -3; JENDL-3", JAERI-1319 (1990).

[28] G. Leuthold and H. Schraube, "Critical Analysis of the ICRP60 Proposals for Neutron Radiation and a Possible Solution", Radiat. Prot. Dosim. 54 (1994) 217.

[29] W.G. Alberts and R.A. Hollnagel, "Radiation Weighting Factor and Quality Factor for Neutrons", Radiat. Prot. Dosim. 46 (1993) 291.

Table 1 ***List of nuclides of which the effective quality factors were calculated***

Atomic Number	Elemental Symbol	Mass Number A											Number of Nuclides
1	H	1	2	3									3
2	He	3	4	5	6								4
3	Li	6	7	8									3
4	Be	7	8	9	10	11							5
5	B	8	9	10	11	12							5
6	C	10	11	12	13	14							5
7	N	13	14	15	16	17							5
8	O	14	15	16	17	18	19	20					7
9	F	17	18	19	20	21	22						6
10	Ne	18	19	20	21	22	23	24					7
11	Na	21	22	23	24	25							5
12	Mg	23	24	25	26	27	28						6
13	Al	24	25	26	27	28	29	30					7
14	Si	26	27	28	29	30	31	32					7
15	P	29	30	31	32	33	34	35					7
16	S	30	31	32	33	34	35	36	37	38			9
17	Cl	33	34	35	36	37	38	39	40				8
18	Ar	35	36	37	38	39	40	41	42	43	44		10
19	K	37	38	39	40	41	42	43	44	45	46	47	11
20	Ca	40	41	42	43	44	45	46	47	48	49	50	11
21	Sc	42	43	44	45	46	47	48	49	50	51		10
22	Ti	44	45	46	47	48	49	50	51	52			9
23	V	47	48	49	50	51	52	53	54				8
24	Cr	48	49	50	51	52	53	54	55	56			9
25	Mn	50	51	52	53	54	55	56	57	58			9
26	Fe	52	53	54	55	56	57	58	59	60	61		10
												Total	186

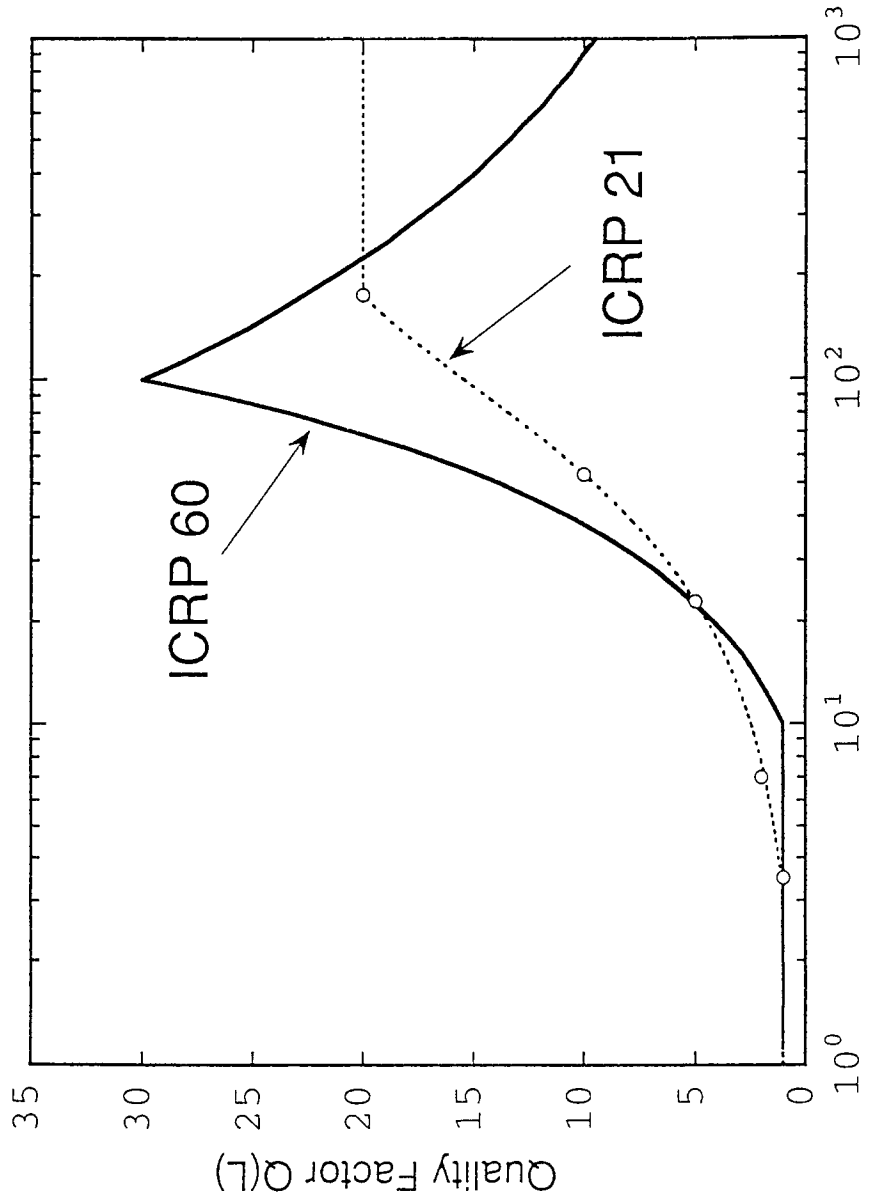

Figure 1 ***Q-L relationships specified in ICRP60 and ICRP 21***

(a)

$$\hat{H}_{T,R} = \hat{Q}_R(E_0)\frac{E_0}{m_T} - \hat{Q}_R(E_1)\frac{E_1}{m_T}$$

(b)

$$\hat{H}_{T,R} = \hat{Q}_R(E_0)\frac{E_0}{m_T} - \hat{Q}_R(E_1)\frac{E_1}{m_T}$$

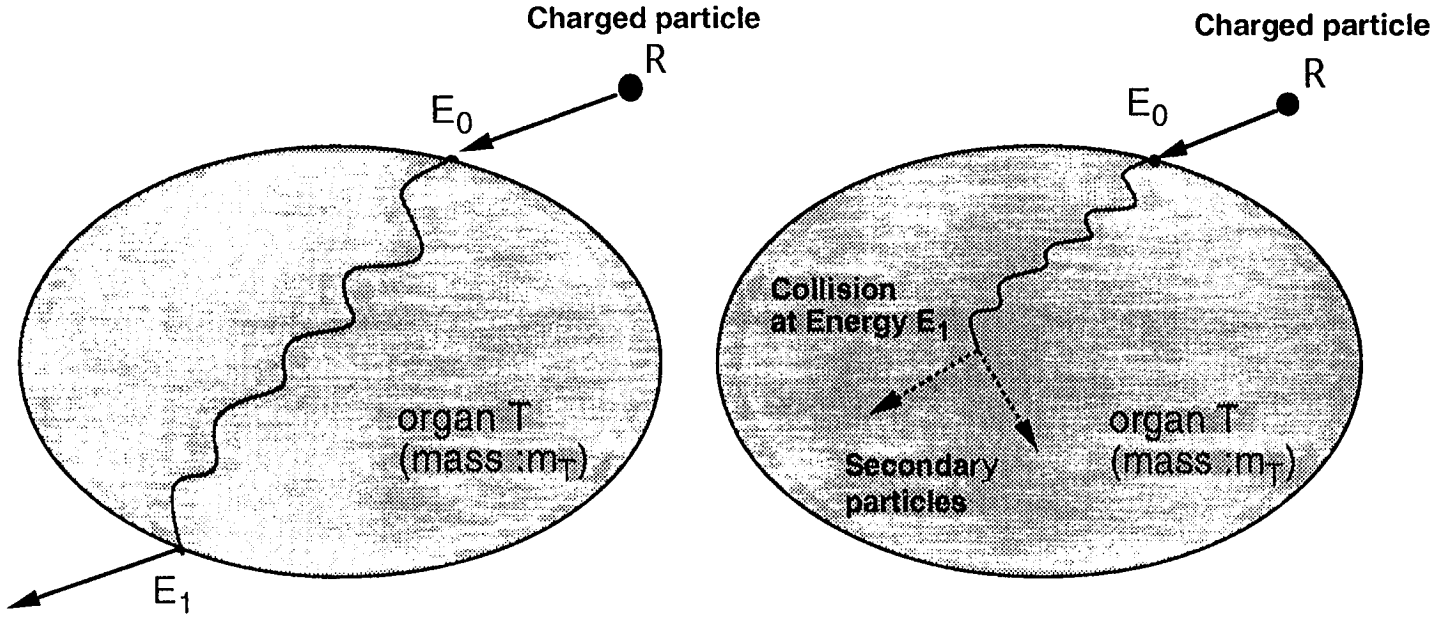

Figure 2 ***Averaged dose equivalent of organ T from the charged particle R with initial energy E_0***

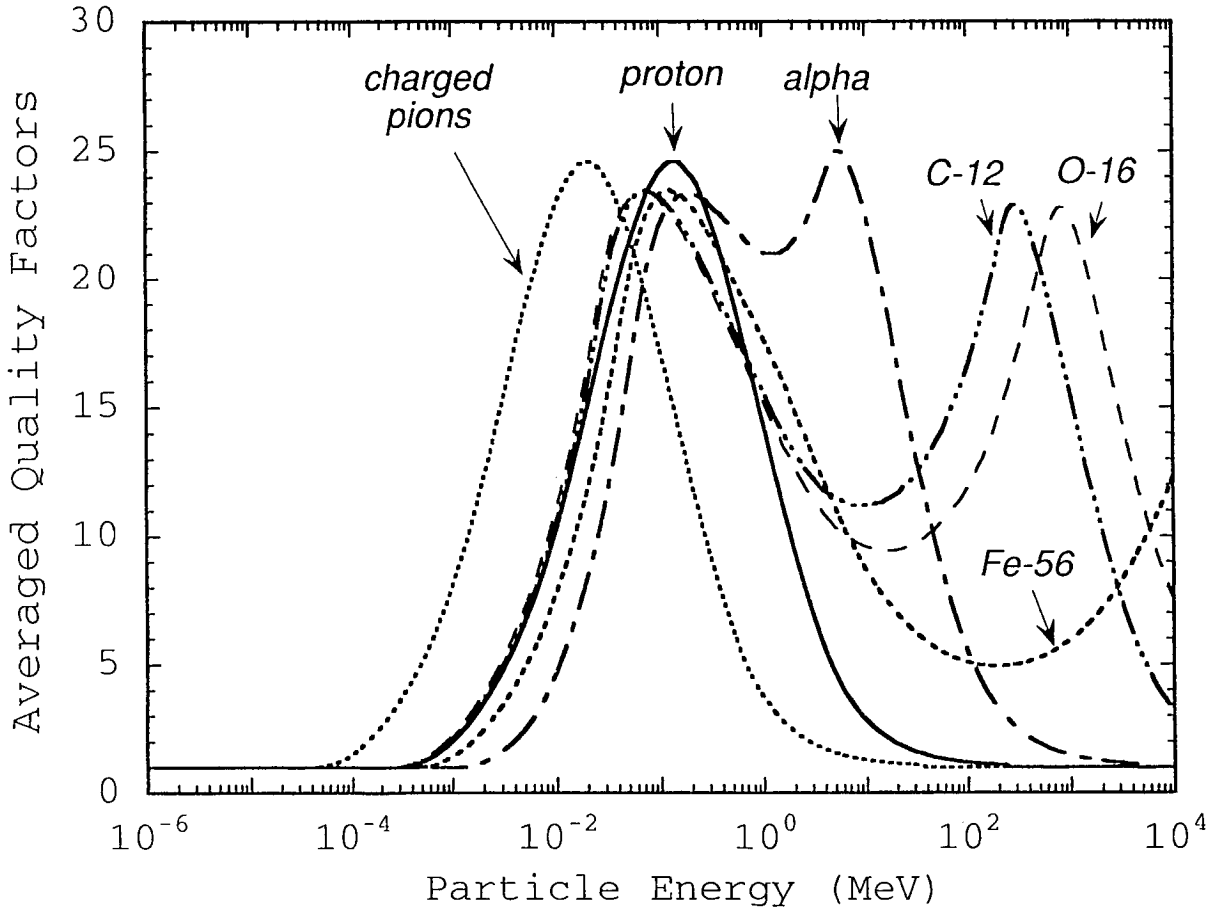

Figure 3 ***Averaged quality factors for charged particles calculated with the Q-L relationship as specified in ICRP60***

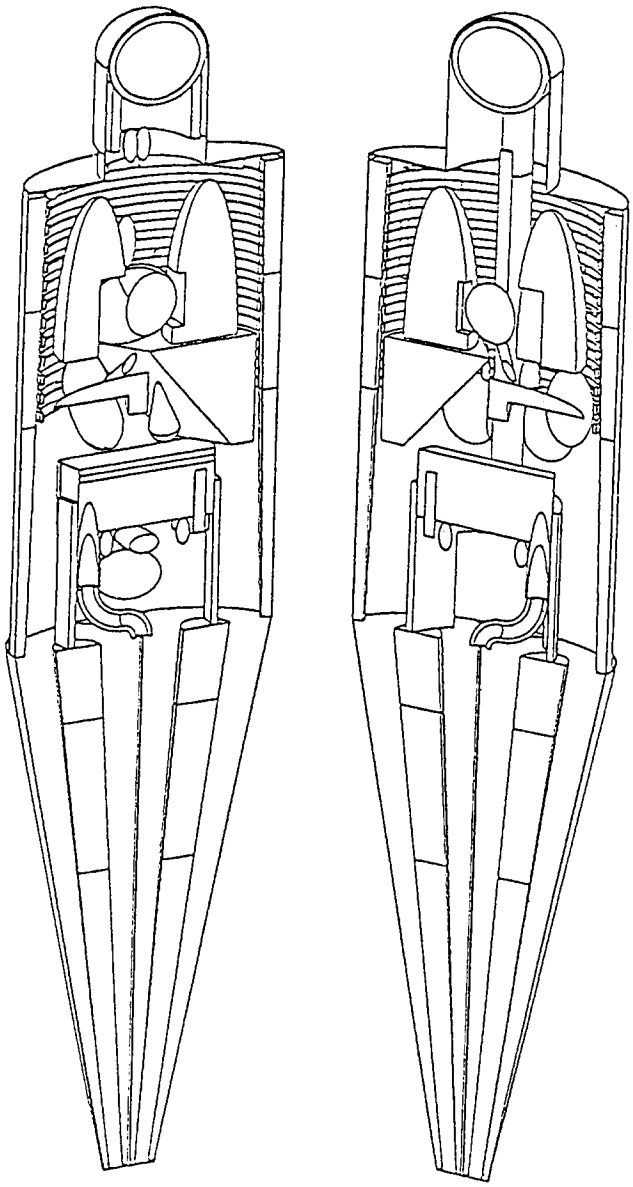

Figure 4
Internal structure of the adult hermaphroditic anthropomorphic phantom of MIRD-5 type in this study

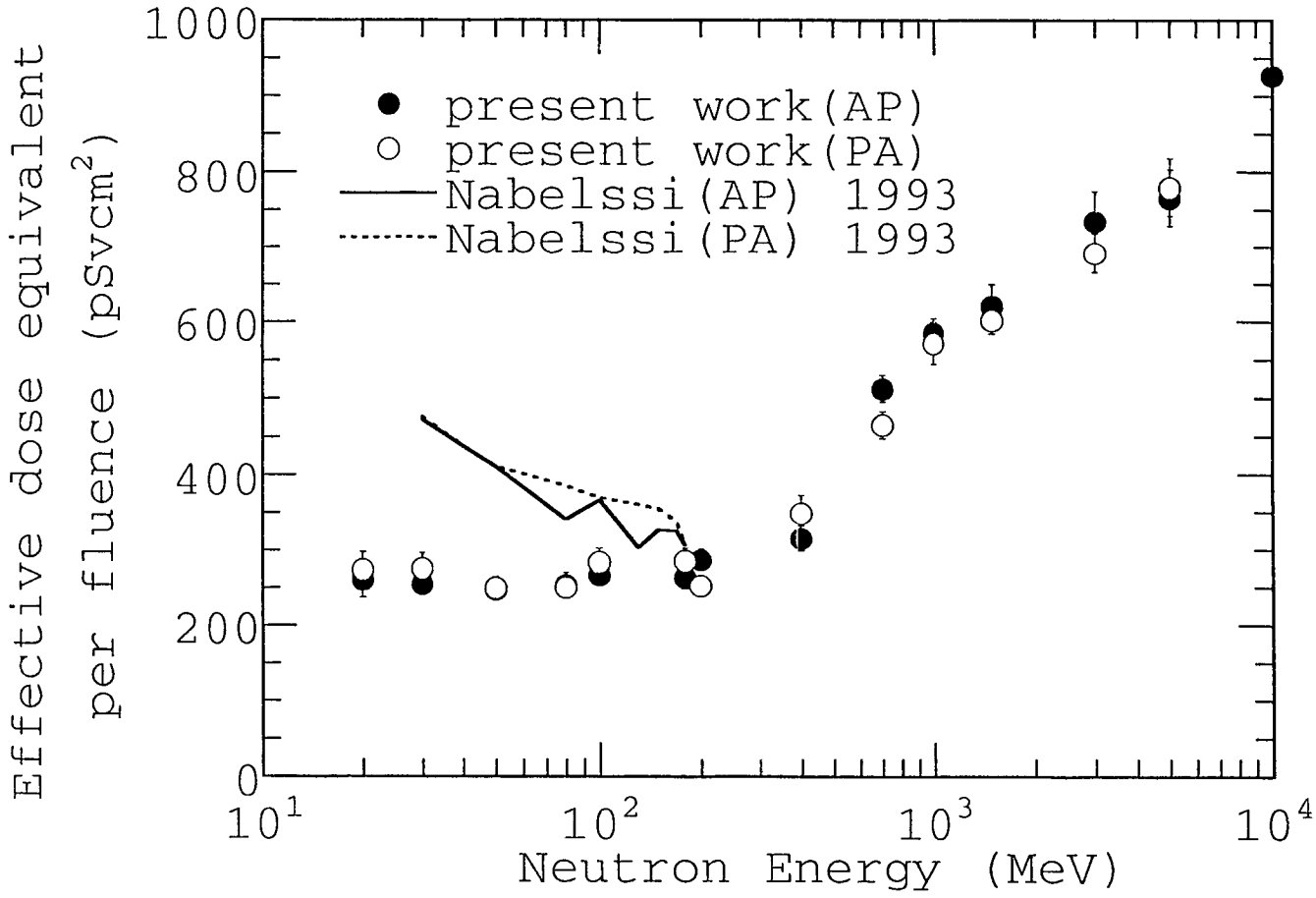

Figure 5

Effective dose equivalent per unit neutron fluence, calculated by use of averaged quality factors based on the Q-L relationship as specified in ICRP60

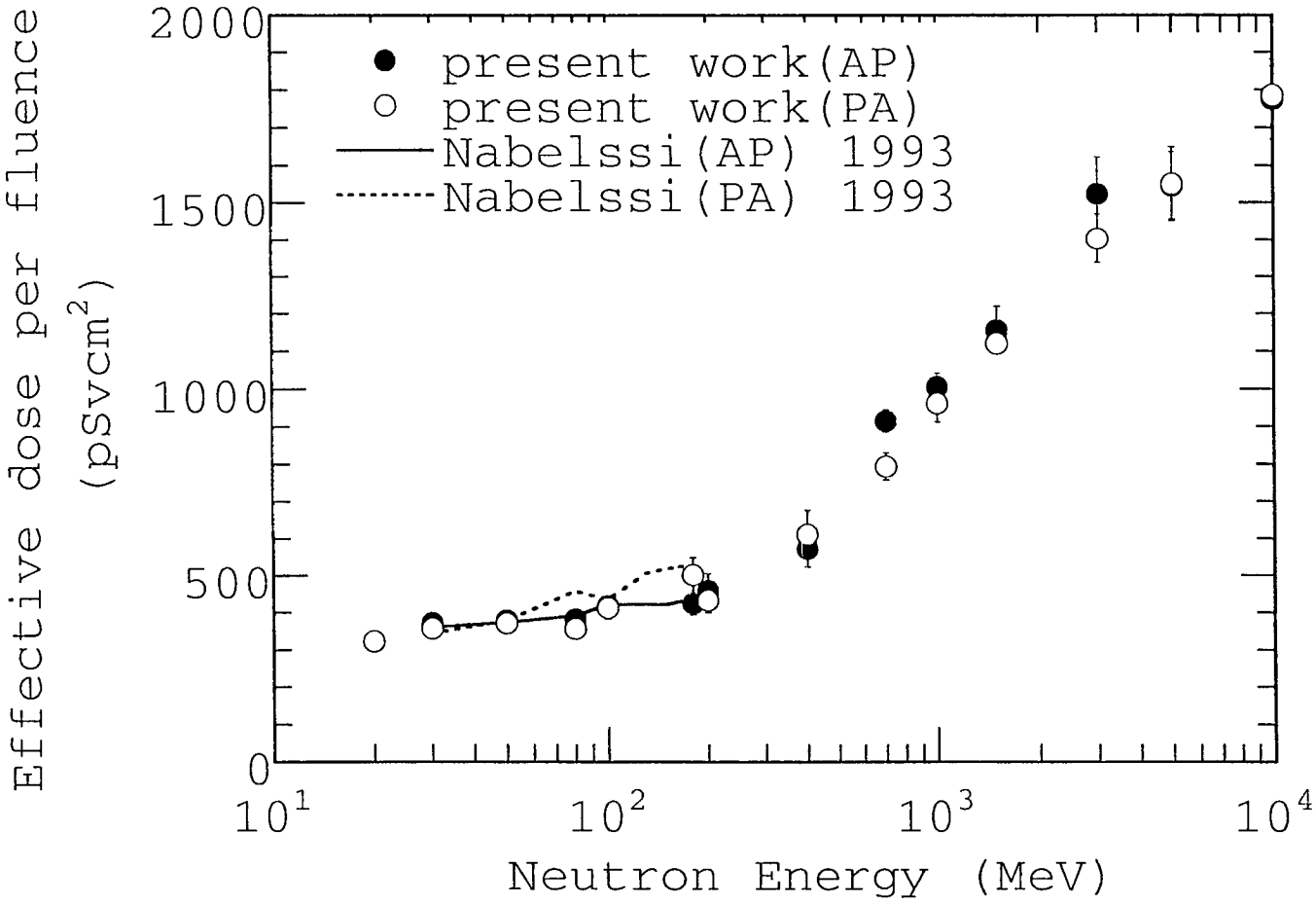

Figure 6

Effective dose per unit neutron fluence, calculated by use of averaged quality factors based on the Q-L relationship as specified in ICRP60

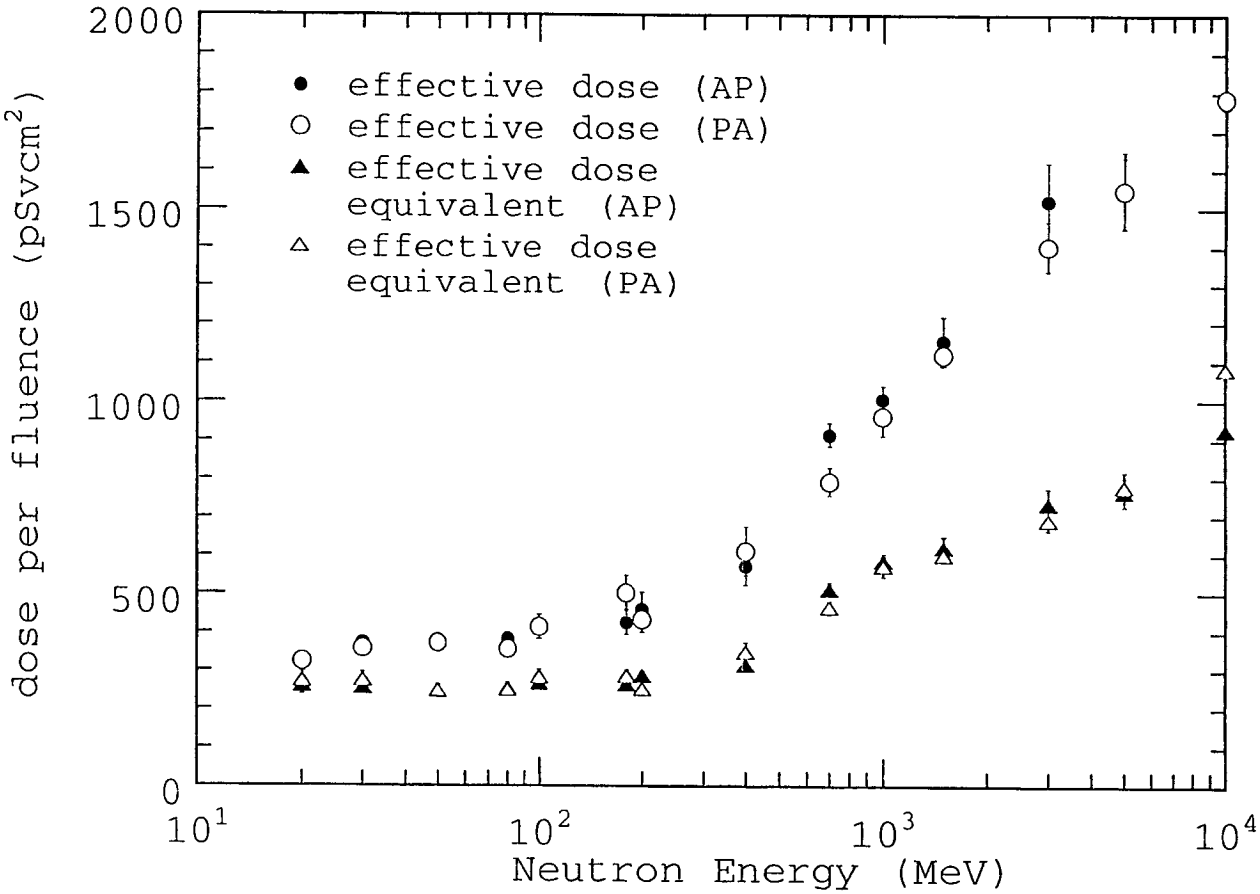

Figure 7 ***Comparison of the following dose equivalents for parallel beam high energetic neutrons***
(1) effective dose (● AP, ○ PA), (2) effective dose equivalents (▲ AP, △ PA)

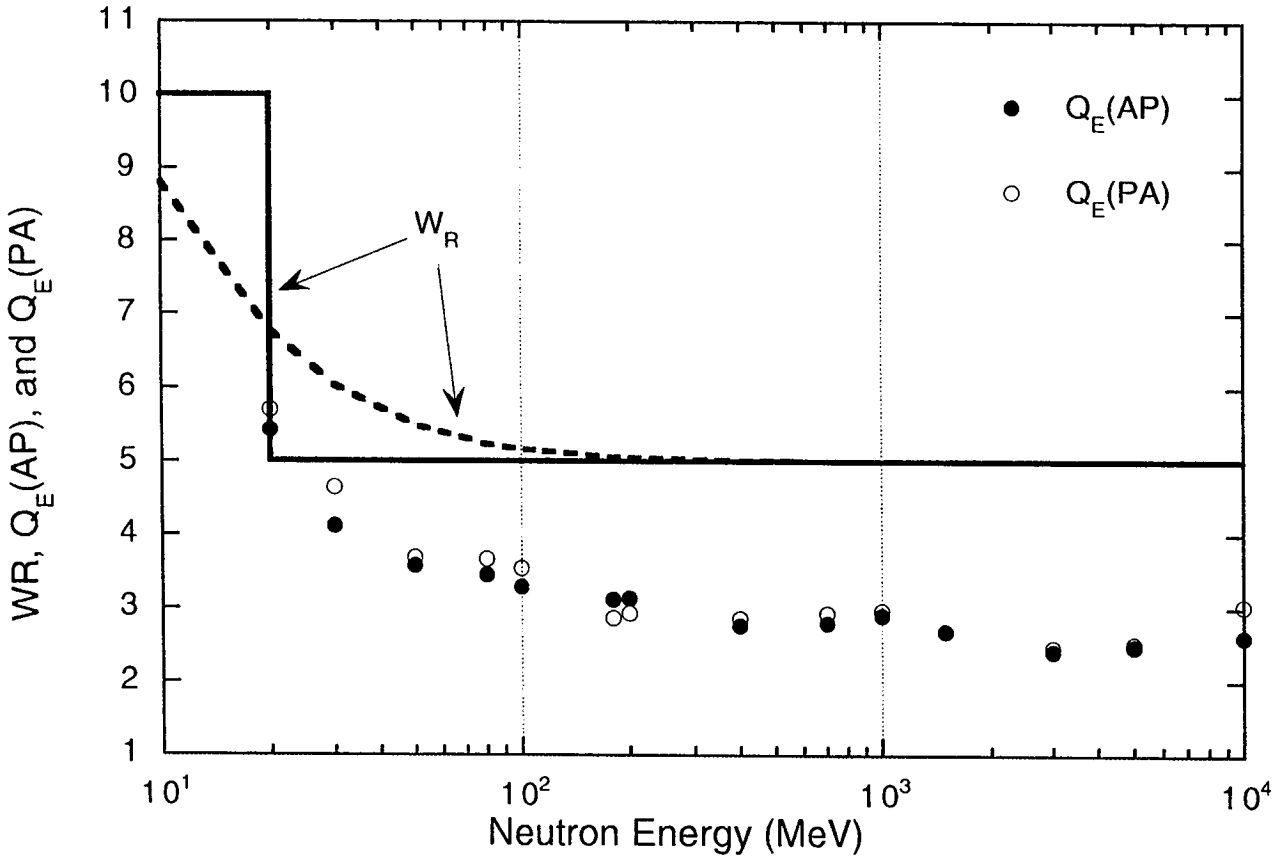

Figure 8

Quality factor Q_E for H_E and radiation weighting factor W_R for neutrons as a function of incident energy

($Q_E = H_E / \Sigma W_T D_T$, where D_T denotes the mean absorbed dose in T, and W_T means the tissue weighting factor)

RESULTS OF INQUIRY ON ANTHROPOMORPHIC COMPUTATIONAL MODELS

Enrico Sartori
OECD/NEA

Background

During the specialists' meeting on *Shielding Aspects of Accelerators, Targets, and Irradiation Facilities*, held from 28-29 April 1994 in Arlington, Texas, one of the recommendations and agreed actions concerned standardisation of anthropomorphic phantoms [1].

Here is the specific agreed action: *"Collect and make available anthropomorphic phantom geometries including material compositions as used in Monte Carlo radiation transport codes"*. This wish was expressed on several occasions by other groups as well.

The Chairman D. R. White of the ICRU Report No.48 [2] Committee has pointed out that there is confusion in using 'phantoms' and 'computational models'. That committee had decided that the term *'phantom'* would apply to solid objects made up of tissue substitutes. The specific action described here concerns *'anthropomorphic computational models*. As a first step to standardisation we use this terminology as of now.

An inquiry was sent out using a questionnaire prepared by G. F. Gualdrini, ENEA Bologna, with the objective first to identify the anthropomorphic computational models used today.

Several replies were received which are included in this compendium. James A. Spahn, jr, Senior Staff Scientist of the International Commission on Radiation Units and Measurement, Inc. (ICRU) has authorised us in the frame of this project to reproduce the tables describing the information assembled in their report N. 48 [2] in tables C.1 and C.2 and concerning anthropomorphic models.

We would like now to start a second phase in which the actual geometrical models and composition are collected. These models should be compared in two ways:

1. Geometry composition,

2. Effect of differences on dose calculations.

This technical point should be provided to standard committees like ICRU, ICRP, as a contribution in the process of standardisation.

A standardisation process should be started in the following with the concurrence of the specialists in this field.

It was pointed out, that geometry and composition are very important, but in a process of standardisation the aspect of standard particle interaction cross-sections, covering a wide range of energies required for the different applications should not be neglected. This aspect should be addressed at a further stage.

The result of this work will be available to the international community for their use in applications on computer readable medium or accessible on the World Wide Web.

FORM

INQUIRY ON AVAILABLE

ANTHROPOMORPHIC COMPUTATIONAL MODELS

(send to sartori@nea.fr or fax to: +33 (1) 4524 1110)

YOUR ADDRESS:

PHONE AND FAX:

MODEL (NAME): (e.g. GSF MALE and FEMALE, ADAM and EVA)

TYPE: (Mathematical or Tomographic)

AGE: (e.g. Adult, New-born, 1, 5, 10 etc. years)

POPULATION GROUP: (European, Japanese etc.)

APPLICATION FIELD: Radiation Protection
Diagnosis
Therapy

.....

COMPUTER PROGRAM for which
the geometry package has been implemented: (e.g. MCNP, MORSE etc.)

DESCRIPTION:

.....

PHYSICAL DIMENSIONS:

	Baby	*Child*	*Adult*
Age	8 weeks	7 years	30 years
Mass (kg)	4.2	21.7	70
Height (cm)	57	115	172
Trunk+Arms (cm) (lateral diameter)	21.8	33.1	40
Trunk (cm) (antero-posterior diameter)	12.2	17.6	20

BODY TISSUES:

	Mass Density (kg m-3)
Soft Tissues	987-1050
Lung	296
Cortical Bone	1765
Bone Marrow	1006
etc.	

SIMPLIFIED MIXTURES: (bone-soft tissue etc.)

REFERENCES:

.....

Availability of the phantom for wider distribution to users *YES* *NO*

Tables with

ANTHROPOMORPHIC COMPUTATIONAL MODELS

Satoshi IWAI

NAME: **Satoshi IWAI**

ADDRESS: Mitsubishi Atomic Power Ind., Inc.
Omiya Technical Institute
1-297, Kitabukuro, Omiya, Saitama, 330 JAPAN

PHONE: 81 48 642 4404

FAX: 81 48 645 0189

MODEL: A modified version of the Yamaguchi's data [1] based on the Cristy phantom [2]

TYPE: Mathematical phantom

AGE: Adult

POPULATION: Caucasian (MIRD-5 [3] type adult)

APPLICATION FIELD: Radiation protection, Radiation shielding

COMPUTER PROGRAM: MARS [5] geometry package with the addition of the new three bodies general ellipsoid, and truncated right elliptical cone. [1]

Description

This phantom represents a modified version of the Yamaguchi's data [1] based on the Cristy phantom [2] of MIRD-V type. [3]

Three modification points were applied to this phantom:

1. Addition of an oesophagus. An oesophagus model was added to the phantom using the mathematical form reported by Lewis et al. [4]

2. Modification of stomach location. Although a description is included in the Yamaguchi's version, the stomach location was altered on the consideration reported by Lewis et al. [4]

3. Size of breasts' models. The height of this breast model is about half of the Cristy phantom model, because this phantom is hermaphroditic for shielding to the A.P. irradiation geometry. Internal organs are considered to be homogeneous in composition and density.

Different densities and compositions are used for the lungs, skeleton, and soft tissue. The composition description of the three tissues are limited to 17 elements (H, C, N, O, Na, Mg, P, S, Cl, K, Ca, Fe, Zn, Rb, Sr, and Pb). The densities of the lungs, skeleton, and soft tissue are 0.2958, 1.4682, and 0.9869 g/cm**3 respectively; these values are cited from the MIRD-5 report, [3] not from the Cristy's value. [2] The density of the Cristy's soft tissue is about 5% higher than that of MIRD-5 phantom, because the density of the Cristy's soft tissue is assumed to be modified for the calculation of internal dosimetry; it is most important to keep the mass of organs and the distance between the organs in the human body for the internal dosimetry calculation. Therefore the density of the Cristy's soft tissue is assumed to be increased to as to keep the two parameters. The densities of MIRD-5 were adopted into this work, because this phantom was employed to the external dosimetry.

Physical dimensions

Age	**ADULT**
Mass (*kg*)	about **70**
Height (*cm*)	**174**
Trunk+Arms (*cm*) – *Lateral diameter*	**40**
Trunk (*cm*) – *Antero-posterior diameter*	**20**
Leg length (*cm*)	**80**

Body tissues

	Mass Density (g/cm^3)
Soft Tissues	**0.9869**
Lungs	**0.2958**
Skeleton – Mineral bone+bone marrows	**1.4682**

Availability of the Phantom for wider distribution to users: Yes

NAME:	**Vladimir MARES**
ADDRESS:	GSF - Forschungszentrum fuer Umwelt und Gesundheit, GmbH Neuherberg Postfach 11 29 85758 Oberschleissheim Germany
PHONE:	+49-89-3187-2652
FAX:	+49-89-3187-3323
E-MAIL:	mares@cony.gsf.de

MODEL:	ADAM and EVA
TYPE:	Mathematical
AGE:	Adult
POPULATION:	European
APPLICATION FIELD:	Radiation Protection
COMPUTER PROGRAM:	MCNP

Description

Skin and oesophagus included.

Physical dimensions

	Baby	Child	Adult	*ADAM*	*EVA*
Age				**adult**	**adult**
Mass (*kg*)				**70.44**	**59.15**
Height (*cm*)				**170**	**160**
Trunk+Arms (*cm*) – *lateral diameter*				**40**	**38**
Trunk (*cm*) – *antero-posterior diameter*				**25**	**19**

Body tissues

	Mass Density (kg m^3)
Soft Tissues	987
Lung	296
Bone	1486
Skin	1105

Simplified Mixtures (bone-soft tissue etc.)

Availability of the phantom for wider distribution to users: I am not responsible to answer it but I suppose YES.

NAME: **Frank W. SCHULTZ**

ADDRESS: TNO-ME, Radiological Service,
Center for Radiological Protection and Dosimetry
c/o P.O.Box 5815
NL-2280 HV Rijswijk
The Netherlands

PHONE: +31 15 842750
FAX: +31 15 843998

MODEL: GSF Male (ADAM) and Female (EVA)
TYPE: Mathematical
AGE: Adult
POPULATION: Group: European
APPLICATION FIELD: Radiation protection, Diagnostic radiology
(Calculation of organ and tissue doses, using Monte Carlo methods)
COMPUTER PROGRAM: MCNP

Description

These are mathematical models of an adult male and an adult female. The heights and masses of the whole body, as well as the masses of internal organs, are based on the ICRP Reference Man data (ICRP Report 23, 1975)

Physical dimensions

	ADAM	*EVA*
Mass (*kg*)	**70.4**	**59.2**
Height (*cm*)	**170**	**160**
Width (Trunk+Arms; *cm*)	**40.0**	**37.6**
Thickness (Trunk; *cm*)	**20.0**	**18.8**

Body tissues

	mass density ($g.cm^3$)
Skeletal tissue	**1.486**
Skin tissue	**1.105**
Soft tissue	**0.987**
Lung tissue	**0.296**

skeletal tissue includes bone, marrow and cartilage

Availability for Distribution to Users: Yes

NAME: **S. HONGO, H. TAKESHITA, H. YAMAGUCHI, S. IWAI** (MAPI), **K. IWAI** (Nihon University)

ADDRESS: National Institute of Radiological Sciences, 9-1 Anagawa 4-chome, Inage-ku, Chiba-shi, JAPAN 263
PHONE: +81 43 251 2111
FAX: +81 43 290 1112
E-MAIL: s_hongo@nirs.go.jp

MODEL: Modified phantoms based on Cristy phantoms [1]
TYPE: Mathematical phantoms and their tomographic expressions
AGE: N.B., 1, 5, 10, 15, Adult (Male and Female)
POPULATION: Japanese
PACKAGE: Japanese_par (all parameters in terms of the Cristy's phantom)

Description

Study to build mathematical phantoms for Japanese public has been carried out by using the ORNL mathematical phantoms [1].

Japanese data on physics are compiled with measured and evaluated values [2].

This study used only its measured values of organ mass and external measures of body, and set the values for the ages, *NEW BORN (N.B), 1-, 5-, 10-, 15-YEAR OLD*, and *ADULT*, by weighting populations of age categories. These values, as shown in Table 1, are the target values which we tried to establish in the phantoms. The processes to find proper parameters that define geometry of an organ based on these mass data were trial and errors.

The final results are shown in Table 2. They are realised mass values in the phantoms.

The values in the parenthesis of Table 1 are the standard deviations of the measured and age categorised processes, and those in Table 2 are the ratios of the realised to measured values. In the tables, *HEIGHT* and *SITHEIGHT* are in unit *cm*, *BODY* in *kg* and others in *gram*. We assume the same atomic compositions of tissues and bone as the Cristy's.

Physical dimensions

Table 1
Mass of organs based on measured values

JAPANESE MALE

ORGAN	N.B	1	5	10	15	ADULT
ADRENAL	4.3 ()	4.4 (40)	5.9 (54)	9.0 (51)	11.8 (30)	14.5 (43)
BRAIN	717.1 ()	1187.1 (15)	1388.5 (13)	1480.2 (12)	1465.4 (09)	1424.9 (08)
HEART	39.2 ()	61.6 (23)	105.2 (28)	174.1 (31)	276.7 (10)	354.1 (21)
KIDNEY	47.3 ()	78.3 (45)	123.5 (55)	180.0 (32)	258.2 (24)	313.6 (34)
LIVER	262.1 ()	414.1 (30)	593.7 (29)	869.8 (22)	1235.0 (17)	1497.4 (23)
LUNG	127.1 ()	215.1 (43)	292.0 (41)	504.8 (14)	1022.6 (21)	1146.3 (45)
TESTS	2.8 ()	3.0 (160)	3.3 (40)	6.8 (86)	28.9 (46)	35.7 (42)
PANCREAS	12.1 ()	33.6 (74)	40.6 (35)	64.5 (35)	101.7 (26)	129.4 (28)
SPLEEN	22.4 ()	44.6 (70)	56.0 (58)	80.1 (29)	120.4 (30)	118.6 (43)
THYMUS	23.7 ()	22.1 (74)	25.3 (38)	41.5 (43)	34.9 (33)	28.8 (55)
THYROID	2.2 ()	3.0 (53)	4.2 (35)	6.4 (33)	15.8 (28)	18.8 (33)
HEIGHT	67.2 ()	84.7 (05)	110.3 (04)	138.9 (05)	165.7 (04)	166.1 (04)
SITHEIGHT	43.8 ()	50.9 (06)	62.1 (04)	75.4 (05)	88.7 (04)	88.0 (04)
BODY	8.1 ()	12.0 (13)	19.2 (14)	34.6 (22)	55.8 (16)	62.5 (14)

JAPANESE FEMALE

ORGAN	N.B	1	5	10	15	ADULT
ADRENAL	4.5 ()	4.2 (37)	6.2 (50)	7.4 (43)	11.0 (34)	12.8 (41)
BRAIN	636.4 ()	1002.5 (28)	1226.8 (18)	1300.7 (14)	1320.7 (06)	1288.4 (08)
HEART	29.9 ()	59.4 (26)	95.7 (33)	162.4 (18)	219.0 (26)	296.2 (22)
KIDNEY	47.6 ()	67.4 (43)	96.7 (34)	182.9 (16)	249.9 (27)	264.3 (37)
LIVER	234.3 ()	356.8 (34)	499.7 (30)	868.3 (20)	1082.2 (26)	1280.7 (26)
LUNG	112.8 ()	200.7 (36)	287.2 (46)	435.3 (39)	675.8 (26)	854.8 (43)
PANCREAS	17.3 ()	23.4 (28)	37.4 (22)	58.8 (23)	86.1 (21)	108.6 (27)
SPLEEN	19.0 ()	31.0 (34)	57.0 (38)	76.8 (31)	92.7 (45)	106.5 (44)
THYMUS	21.9 ()	21.8 (47)	16.1 (61)	26.8 (25)	27.7 (72)	23.4 (44)
THYROID	2.4 ()	3.5 (106)	5.1 (24)	8.9 (36)	13.5 (20)	16.4 (36)
HEIGHT	65.9 ()	83.8 (06)	109.4 (05)	139.5 (05)	156.4 (03)	152.5 (04)
SITHEIGHT	43.0 ()	50.2 (08)	61.8 (04)	75.4 (05)	88.7 (04)	82.2 (04)
BODY	7.8 ()	11.3 (13)	18.8 (15)	34.3 (20)	49.5 (13)	51.8 (15)

Table 2

Mass of organs realised in phantoms

JAPANESE MALE

ORGAN	1	5	10	15	ADULT
ADRENAL	2.8 (0.65)	4.4 (0.75)	7.6 (0.84)	12.6 (1.07)	14.5 (1.13)
BRAIN	884.0 (0.74)	1260.0 (0.91)	1360.0 (0.92)	1410.0 (0.96)	1420.0 (1.00)
HEART	55.2 (0.90)	85.7 (0.81)	147.2 (0.85)	245.0 (0.89)	319.0 (0.90)
KIDNEY	52.2 (0.67)	81.1 (0.66)	139.3 (0.77)	231.8 (0.90)	301.9 (0.96)
LIVER	333.6 (0.81)	518.2. (0.87)	889.9 (1.02)	1480.9 (1.20)	1928.3 (1.29)
LUNG	174.7 (0.81)	271.3 (0.93)	465.9 (0.92)	775.3 (0.76)	1009.6 (0.88)
PANCREAS	16.5 (0.49)	25.6 (0.63)	43.9 (0.68)	73.1 (0.72)	95.2 (0.74)
SPLEEN	32.0 (0.72)	49.7 (0.89)	85.3 (1.06)	141.9 (1.18)	184.7 (1.56)
TESTS	6.8 (2.28)	10.6 (3.21)	18.2 (2.68)	30.3 (1.05)	39.5 (1.11)
THYMUS	3.7 (0.17)	5.7 (0.22)	9.7 (0.23)	16.2 (0.46)	21.1 (0.73)
THYROID	3.6 (1.21)	5.6 (1.34)	9.6 (1.51)	16.0 (1.02)	20.9 (1.11)
HEIGHT	84.7 (1.00)	110.3 (1.00)	138.9 (1.00)	165.7 (1.00)	166.1 (1.00)
SITHEIGHT	50.9 (1.00)	62.1 (1.00)	75.4 (1.00)	88.7 (1.00)	88.0 (1.00)
BODY	12.0 (1.00)	19.2 (1.00)	34.6 (1.00)	55.8 (1.00)	62.5 (1.00)

JAPANESE FEMALE

ORGAN	1	5	10	15	ADULT
ADRENAL	2.6 (0.62)	4.2 (0.68)	7.5 (1.02)	12.5 (1.14)	12.7 (0.99)
BRAIN	884.0 (0.88)	1260.0 (1.03)	1360.0 (1.05)	1410.0 (1.07)	1420.0 (1.10)
HEART	50.6 (0.85)	81.3 (0.85)	146.0 (0.90)	242.2 (1.11)	245.7 (0.83)
KIDNEY	47.8 (0.71)	76.9 (0.80)	138.1 (0.76)	229.2 (0.92)	232.5 (0.88)
LIVER	305.6 (0.86)	491.2 (0.98)	882.3 (1.02)	1463.8 (1.35)	1485.1 (1.16)
LUNG	160.0 (0.80)	257.2 (0.90)	461.9 (1.06)	766.4 (1.13)	777.5 (0.91)
PANCREAS	15.1 (0.64)	24.3 (0.65)	43.6 (0.74)	72.3 (0.84)	73.3 (0.68)
SPLEEN	29.3 (0.94)	47.1 (0.83)	84.5 (1.10)	140.3 (1.51)	142.3 (1.34)
THYMUS	3.3 (0.15)	5.4 (0.33)	9.7 (0.36)	16.0 (0.58)	16.3 (0.69)
THYROID	3.3 (0.95)	5.3 (1.04)	9.6 (1.07)	15.9 (1.18)	16.1 (0.98)
HEIGHT	83.8 (1.00)	109.4 (1.00)	139.5 (1.00)	156.4 (1.00)	152.5 (1.00)
SITHEIGHT	50.2 (1.00)	61.8 (1.00)	75.4 (1.00)	88.7 (1.00)	82.2 (1.00)
BODY	11.3 (1.00)	18.8 (1.00)	34.3 (1.00)	49.5 (1.00)	51.8 (1.00)

NAME: **Maria ZANKL**

ADDRESS: GSF - Forschungszentrum für Umwelt und Gesundheit
Institut fuer Strahlenschutz
Neuherberg, Postfach 1129
D - 85758 Oberschleissheim

PHONE: +49 89 3187-2792
FAX: +49 89 3187-3373
E-MAIL: zankl@gsf.de

MATHEMATICAL ADULT

MODEL: GSF male and female, ADAM and EVA
TYPE: mathematical
AGE: adult
POPULATION: European or European Ancestry (ICRP23 Reference Man)
APPLICATION FIELD: Radiation protection, diagnosis, (with restrictions also therapy)
COMPUTER PROGRAM:

a) "home-made"
actually derived from the ALGAM code written by Warner and Craig, Oak Ridge National Laboratory (1968);

b) EGS4
by Dr. Keith Wise
Australian Radiation Laboratory
Dept. of Health, Housing, Local Government and Community Services
Lower Plenty Road
Yallambie
Victoria 3085

Description

Mathematical models of an adult male and an adult female. Heights and masses of whole bodies as well as masses of internal organs based on ICRP Reference Man data (ICRP Publication 23, 1975)

Physical dimensions

	ADAM	*EVA*
Mass (*kg*)	**69.9**	**58.8**
Height (*cm*)	**170**	**160**
Trunk+Arms (*cm*) – *lat.diam.*	**40.0**	**37.6**
Trunk (*cm*) – *a.p. diameter*	**20.0**	**18.8**

Body tissues

	Mass Density (kg m^3)
Soft tissue	**987**
Lung	**296**
Skeleton	**1486**
Red bone marrow	**987**
Skin	**1105**

The skeleton is a homogeneous mixture of osseous tissue, marrow, cartilage and certain peri-articular tissue.

Availability of the phantoms for wider distribution to users: Yes

TOMOGRAPHIC PAEDIATRIC MODELS

MODEL:	GSF BABY and CHILD
TYPE:	Tomographic
AGE:	8 weeks (Baby) and 7 years (Child)
POPULATION:	European
APPLICATION FIELD:	Radiation protection, diagnosis, (with restrictions also therapy)
COMPUTER PROGRAM:	"home-made" (see above)

Description

Tomographic models of an eight week old baby and a seven year old child, obtained from whole body computed tomographic (CT) scans. Size and mass of model can be adjusted by changing size of volume elements.

Physical dimensions

	Baby	*Child*
Age	**8 weeks**	**7 years**
Mass (*kg*)	**4.2**	**21.7**
Height (*cm*)	**57.0**	**115**
Trunk+Arms (*cm*) – *lat.diam.*	**21.8**	**33.1**
Trunk (*cm*) – *a.p. diameter*	**12.2**	**17.6**

Body tissues

	Mass density (kg m^3)
Soft tissue	**987 – 1050**
Lung	**296**
Cortical bone	**1765**
Red bone marrow (BABY)	**1027**
Red bone marrow (CHILD)	**1006**
Skin	**1105**

Availability of the phantoms for wider distribution to users: No

George ZUBAL

NAME: **George ZUBAL** PhD

ADDRESS: Dept. of Diagnostic Radiology
Yale School of Medicine
333 Cedar Street
New Haven, CT 06510

PHONE: (203) 785-4911
FAX: (203) 737-4273
E-MAIL: Zubal@BioMed.Med.Yale.Edu
Zubal@Venus.YCC.Yale.Edu

MODEL: Male
TYPE: Tomographic = voxel-based
AGE: Adult
POPULATION GROUP: European
APPLICATION FIELD: Diagnosis
COMPUTER PROGRAM: ALGAMP (original MIRD S-factor program, now converted to diagnosis)

Physical dimensions

	Baby	*Child*	*Adult*
Age	**8 weeks**	**7 years**	**30 years**
Mass(*kg*)	**4.2**	**21.7**	**70**
Height (*cm*)	**57**	**115**	**170**
Trunk+Arms (*cm*) – *Lateral diameter*	**21.8**	**33.1**	**48**
Trunk (*cm*) – *Antero-posterior diameter*	**12.2**	**17.6**	**22**

Body tissues

	Mass Density (kg m^3)
Soft Tissues	**987-1050**
Lung	**296**
Cortical Bone	**1765**
Bone Marrow	**1006**

Simplified Mixtures (bone-soft tissue etc.)

Availability of the phantom for wider distribution to users: YES

Table 3

Specifications of selected computational models – Digitised mathematical model [1]

Description

This is a conversion of the mathematical model of Snyder et al. (1969) into a model consisting of cubic volume elements with organ identification symbols. it represents a hermaphrodite adult. Height and mass of the whole body, as well as the masses of the internal organs, are based on the ICRP Reference Man data (ICRP, 1975).

Physical Dimensions

Height	**173** cm
Trunk + arm – *Lateral diameter*	**40.0** cm
Trunk – *Antero-posterior diameter*	**20.0** cm

Applications

This model is the basis for more realistic models based on medical images obtained by CT or MRI for absorbed dose calculations, especially in radiotherapy, using Monte Carlo methods.

[1] H. Yamaguchi et al., 1985.
Contact Address: National Institute of Radiological Sciences, Division of Physics, 4-9-1, Anagawa, Chiba, 260 Japan.

Table 4

Specifications of selected computational models –
GSFa adult male and female mathematical models (Adam and Eva) [2]

Description

These are mathematical models of an adult male and an adult female. The heights and masses of the whole bodies, as well as the masses of the internal organs, are based on the ICRP Reference Man data (ICRP, 1975).

a. GSF - Forschungszentrum für Umwelt und Gesundheit, Germany

Physical Dimensions

	ADAM	*EVA*
Mass (*kg*)	**69.9**	**58.8**
Height (*cm*)	**170**	**160**
Trunk + arms (*cm*) – *Lateral diameter*	**40.0**	**37.6**
Trunk (*cm*) – *Antero-posterior diameter*	**20.0**	**18.8**

Body Tissues

	Mass Density (kg/m^3)
Soft tissue	**978**
Lung	**296**
Whole skeleton b	**1486**
Skin	**1105**

b. include osseous tissue, marrow, cartilage and certain peri-articular tissue

Applications

For the calculation of organ and tissue doses from external photon irradiation in x ray diagnosis, radiotherapy, occupational and environmental exposures, using Monte Carlo methods.

[2] R. Kramer et al., 1982b.
Contact Address: GSF – Forschungszentrum für Umwelt und Gesundheit, Ingolstädter Landstrasse 1, D-8042 Neuherberg, Germany.

Table 5

Specifications of selected computational models –GSFa paediatric tomographic models (Baby and Child) [3]

Description

These tomographic models of an eight week old baby and a seven year old child have been obtained from whole body computed tomography (CT) scans. Size and mass of each model can be adjusted by changing size of volume elements (voxels).

a. GSF - Forschungszentrum für Umwelt und Gesundheit, Germany

Physical Dimensions

	Baby	*Child*
Age	**8 weeks**	**7 years**
Mass (*kg*)	**4.2**	**21.7**
Height (*cm*)	**57.0**	**115**
Trunk + arms (*cm*) – *Lateral diameter*	**21.8**	**33.1**
Trunk (*cm*) – *Antero-posterior diameter*	**12.2**	**17.6**

All dimensions may be varied

Body Tissues

	Mass Density (kg/m^3)
Soft tissue	**987-1050**
Lung	**296**
Cortical bone	**1765**
Bone marrow (Baby)	**1027**
Bone marrow (Child)	**1006**
Skin	**1105**

Applications

For the calculation of organ and tissue doses and absorbed-dose distributions from external photon irradiation in x-ray diagnosis, radiotherapy, occupational and environmental exposures, using Monte Carlo methods.

[3] G. Williams et al. 1986b; Zankl et al., 1988; Veit et al., 1989.
Contact Address: GSF - Forschungszentrum für Umwelt und Gesundheit, Ingolstädter Landstrasse 1, D-8042 Neuherberg, Germany.

Table 6

Specifications of selected computational models – ICRU spherical reference mathematical model [4]

Description

This mathematical model describes a sphere of 30 cm diameter.

Physical Dimensions

Mass (*kg*)	**14.14**
Diameter (a) (*cm*)	**30**

Tissues

Average soft tissue having elemental composition (%, by mass):

H	**10.1**
C	**11.1**
N	**2.6**
O	**76.2**

Mass Density: 1000 kg/m^3

Applications

Reference computational model used in radiation protection for the definition of operation al quantities for dose equivalent.

[4] ICRU Reports 33 (ICRU, 1980) and 39 (ICRU, 1985a).
Contact Address: International Commission on Radiation Units and Measurements, 7910 Woodmont Avenue, Bethesda, Maryland 20814, U.S.A.

Table 7

Specifications of selected computational models – JAERIa Japanese pregnant woman mathematical model [5]

Description

Mathematical model of a pregnant Japanese woman at various stages of pregnancy. The model is based on the model of Snyder et al. (1969), but with reduced size and modified abdomen.

a. Japanese Atomic Energy Research Institute

Physical Dimensions

	Female body		
Height (*cm*)	**155**		
Mass (*kg*)	**51.0**		
	Embryo or foetus		
Gestation (*month*)	**1-2**	**6**	**9**
Length (*cm*)	**8.6**	**21.0**	**31.6**
Mass (*kg*)	**0.048**	**0.600**	**2.400**

Applications

For the calculation of absorbed doses to the embryo or foetus from exposure to a radioactive plume accidentally released from a nuclear reactor, using Monte Carlo methods.

[5] M. Kai, 1985.
Contact Address: Japan Atomic Energy Research Institute,
Department of Environmental Safety Research,
Tokai-mura, Naka-gun, Ibaraki-ken, 319-11 Japan.

Table 8

Specifications of selected computational models – JAERI mathematical model (VADMAP) [6]

Description

Mathematical model based on the formulae from Cristy (1980), but with individually variable external and internal dimensions as well as individually variable tissue mass densities.

a. Japan Atomic Energy Research Institute

Physical Dimensions

Variable from new-born to adult.

Body Tissues

	Mass Density (mg/m^3)
Soft tissue	variable
Lung	variable
Whole skeleton b	variable

b. includes osseous tissue, marrow, cartilage and certain peri-aticular tissue

Applications

For the calculation of specific absorbed fractions from monoenergetic photons for selected source and target organ combinations, using the Monte Carlo code VADMAP.

[6] H. Yamaguchi et al., 1987.
Contact Address: Japan Atomic Energy Research Institute,
Department of Environmental Safety Research,
Tokai-mura, Naka-gun, Ibaraki-ken, 319-11 Japan.

Table 9

Specifications of selected computational models – MIRDa-5 adult mathematical model [7]

Description

The model represents a hermaphrodite adult. Height and mass of the whole body, as well as the masses of the internal organs, are based on the ICRP Reference Man data (ICRP, 1975).

a. Medical Internal Radiation Dose Committee

Physical Dimensions

Mass	**70** kg
Height	**174** cm
Trunk + arms – *Lateral diameter*	**40.0** cm
Trunk – *Antero-Posterior diameter*	**20.0** cm

Body Tissues

	Mass Density (kg/m^3)
Soft tissue	**1000**
Lung	**300**
Whole skeleton b	**1500**

b. includes osseous tissue, marrow, cartilage and certain peri-articular tissue

Applications

For the calculation of specific absorbed fractions from monoenergetic photons for selected source and target organ combinations, using Monte Carlo methods.

[7] W.S. Snyder et al., 1969, 1978.
Contact Address: Oak Ridge National Laboratory, Health Physics Division, Oak Ridge, Tennessee 37830, U.S.A.

Table 10

Specifications of selected computational models – ORNLa paediatric and adult mathematical models [8]

Description

The model represents a hermaphrodite adult. The total body mass and height are based on anatomical data from several Japanese studies.

a. Oak Ridge National Laboratory, U.S.A.

Physical Dimensions

Mass	**55.0** kg
Height	**160** cm
Trunk + arms – *Lateral diameter*	**34.5** cm
Trunk – *Antero-posterior diameter*	**19.6** cm

Body Tissues

	Mass Density (kg/m^3)
Soft tissue	**1040**
Lung	**296**
Whole skeleton b	**1400**

b. includes osseous tissue, marrow, cartilage and certain peri-articular tissue

Applications

For the calculation of the absorbed dose received by survivors of the 1945 bombings of Hiroshima and Nagasaki and for the calculation of organ and issue doses from diagnostic and therapeutic radiation practices in Japan

[8] G.D. Kerr et al., 1976; Cristy, 1985.

Contact Address: Japan Atomic Energy Research Institute,
Department of Environmental Safety Research,
Tokai-mura, Naka-gun, Ibaraki-ken, 319-11 Japan.

Table 11

Specifications of selected computational models – ORNLa paediatric and adult mathematical models [9]

Description

This group of mathematical models represent an adult and children of various ages. The dimensions of the body regions are determined from anthropological data. The organ volumes are based on the ICRP Reference Mandate (ICRP, 1975).

a. Oak Ridge National Laboratory, U.S.A.

Physical Dimensions

Age (*years*)	**New-born**	**1**	**5**
Mass (*kg*)	**3.60**	**9.72**	**19.8**
Height (*cm*)	**51.5**	**75.0**	**109.0**
Trunk + arms (*cm*) – *Lateral diameter*	**12.7**	**17.6**	**22.9**
Trunk (*cm*) – *Antero-posterior diameter*	**9.8**	**13.0**	**15.0**
Age (years)	**10**	**15b**	**Adult (male)**
Mass (kg)	**33.2**	**56.8**	**73.7**
Height (cm)	**139**	**164**	**174**
Trunk + arms (*cm*) – *Lateral diameter*	**27.8**	**34.5**	**40.0**
Trunk (*cm*) – *Antero-posterior diameter*	**16.8**	**19.6**	**20.0**

b. also represents adult female

Body Tissues

	Mass Density (kg/m^3)
Soft tissue	**1040**
Lung	**296**
Whole skeleton	
New-born	**1220**
All others	**1400**

c. includes osseous tissue, marrow, cartilage and certain peri-articular tissue

Applications

The models are used for the calculation of specific absorbed fractions from monoenergetic photons for selected source and target organ combinations, using Monte Carlo Methods.

[9] M. Chisty, 1980; Cristy and Eckerman, 1987a.
Contact Address: Oak Ridge National Laboratory, Health and Safety Research Division
Oak Ridge, Tennessee 37831-6383, USA.

Table 12

Specifications of selected computational models – SAICa adult contour mathematical model [10]

Description

The model represents a North American adult male. The geometry and physical dimensions are based on a commercial anthropomorphic phantom. The model is represented as a three-dimensional array of volume elements.

a. Science Applications International Corporation

Physical Dimensions

Mass	**74** kg
Height	**174** cm
Chest – *Lateral*	**32.8** cm
Chest width – *Antero-posterior*	**20.8** cm

Applications

For the calculation of fluence and absorbed dose in target organs or other regions of interest from external neutron and gamma radiation.

[10] D.C. Kaul et al., 1987.
Contact Address: Science Applications International Corporation,
10260 Campus Point Drive, MS33, San Diego, CA 92121, U.S.A.

Table 13

Specifications of selected computational models – SAICa adult mathematical model [11]

Description

The model represents a North American adult male. The total body mass and height are based on a commercial anthropomorphic phantom. Arms and legs are adjustable to the sitting or kneeling position.

a. Science Applications International Corporation

Physical Dimensions

Mass	**73.6** kg
Height	**174** cm
Trunk + arms – *Lateral diameter*	**34.4** cm
Trunk – *Antero-posterior diameter*	**20** cm

Body Tissues

	Mass Density (mg/m^3)
Soft tissues	**1040**
Lung	**296**
Whole skeleton b	**1400**

b. includes osseous tissue, marrow, and cartilage

Applications

For the calculation of fluence and absorbed dose in target organs or other regions of interest from external neutron and gamma radiation.

[11] D.C. Kaul et al., 1987.
Contact Address: Science Applications International Corporation,
10260 Campus Point Drive, MS33, San Diego, CA 92121, U.S.A.

Table 14

Specifications of selected computational models – SAICa Japanese paediatric and adult mathematical model [12]

Description

The model represents an hermaphrodite Japanese adult and children of various ages. The models are based on anatomical data from several studies of Japanese populations. Arms and legs are adjustable to the sitting or kneeling positions.

a. Science Applications International Corporation

Physical Dimensions

Age (*years*)	**<3**	**3 - 12**	**Adult**
Mass *kg*	**9.7**	**19.8**	**55.0**
Height (*cm*)	**74.3**	**108.4**	**163.9**
Chest width (*cm*) – *Lateral*	**15.0**	**19.5**	**29.3**
Chest width (*cm*) – *Antero-posterior*	**12.7**	**14.7**	**19.2**

Body Tissues

	Mass Density (mg/m^3)
Soft tissues	**1040**
Lung	**296**
Whole skeleton b	**1400**

b. includes osseous tissue, marrow, and cartilage

Applications

The models were used for the calculation of neutron and gamma ray fluences and absorbed doses in fifteen organs of survivors of the 1945 bombings of Hiroshima and Nagasaki. They are also used for the calculation of organ and tissue doses from diagnostic and therapeutic practices in Japan.

[12] D.C. Kaul et al., 1987.
Contact Address: Science Applications International Corporation,
10260 Campus Point Drive, MS33, San Diego, CA 92121, U.S.A.

References

Satoshi IWAI

[1] Y. Yamaguchi, "DEEP Code to Calculated Dose Equivalents in Human Phantom for External Photon Exposure by Monte Carlo", JAERI-M 90-235 (1990).

[2] M. Christy and K.F. Eckeman, "Specific Absorbed Fraction of Energy at Various Ages from Internal Photon Sources", ORNL/TM-8381/V1-V7 (1987).

[3] W.S. Snyder, M.R. Ford, and G.G. Warner, "Estimates of Specific Absorbed Fractions for Photon Sources Uniformly Distributed in Various Organs of Heterogeneous Phantom" NM/MIRD Pamphlet No. 5 (revised), J. Nucl. Med., 19, Supplement: 5-67 (1987).

[4] C.A. Lewis and R.E. Ellis, "Additions to the Snyder Mathematical Phantom", Phys. Med. Biol. Vol. 24, No. 5 (1979) 1019-1024.

[5] J.T. West and M.B. Emmett, "MARS: A Multiple Array System Using Combinatorial Geometry", NUREG/CR-0200, volume 3, section M9, ORNL/NUREG/CSD-2/V3/R2 (1984).

[6] S. Iwai, T. Uehara, O. Sato, N. Yoshizawa, S. Furihata, S. Tanaka, and Y. Sakamoto, "Evaluation of Effective Dose Irradiated by High Energy Radiation", Proc. of Specialists' Meeting on Shielding Aspects of Accelerators, and Irradiation Facilities, 28-29 Apr. 1994, Arlington, Texas, U.S.A. (OECD/NEA/NSC)

Vladimir MARES

R.Kramer, M.Zankl, G.Williams and G.Drexler, "The Calculation of Dose from External Photon Exposures Using Reference Human Phantoms and Monte Carlo Methods", GSF-Report S-885 (1982).

M.Zankl, N.Petoussi and G.Drexler, "Effective Dose and Effective Dose Equivalent The Impact of the New ICRP Definition for External Photon Irradiation", Health Phys. 62(5) 395-399 (1992).

G.Leuthold, V.Mares and H.Schraube, "Computed Organ Dose Equivalents for Neutrons ...", GSF-Report, in preparation.

Frank W. SCHULTZ

R. Kramer, M. Zankl, G. Williams, and G. Drexler, "The Calculation of Dose from External Photon Exposures using Reference Human Phantoms and Monte Carlo Methods; Part I: The Male (ADAM) and Female (EVA) Adult Mathematical Phantoms", GSF Bericht S-885 (M•nchen: Institut für Strahlenschutz, Gesellschaft für Strahlen- und Umweltforschung mbH) (1986).

S. HONGO, H. TAKESHITA, H. YAMAGUCHI, S. IWAI, K. IWAI

[1] M. Cristy and K. F. Ekerman, "Specific Absorbed Fractions of Energy at Various Ages from Internal Photon Sources", Oak Ridge National Laboratory, ORNL/TM-8381/V1 (1987).

[2] G. Tanaka, "Anatomical Data, Safety Analysis Report", Volume 1, NIRS-M-85,(1992).

Maria ZANKL

R. Kramer, M. Zankl, G. Williams, G. Drexler, "The Calculation of Dose from External Photon Exposures using Reference Human Phantoms and Monte Carlo Methods, Part I: The Male (ADAM) and Female (EVA) Adult Mathematical Phantoms. GSF-Bericht S-885 (GSF – Forschungszentrum für Umwelt und Gesundheit, Neuherberg) (1982).

M. Zankl, R. Veit, G. Williams, K. Schneider, H. Fendel, N. Petoussi, G. Drexler, "The Construction of Computer Tomographic Phantoms and Their Application in Radiology and Radiation Protection", Radiat. Environ. Biophys. 27, 153-164 (1988).

R. Veit, M. Zankl, N. Petoussi, E. Mannweiler, G. Williams, G. Drexler, "Voxel Anthropomorphic Models, Part I: Construction Technique and Description of Models of an Eight-week-old Baby and a Seven-year-old Child", GSF-Bericht 3/89 (GSF – Forschungszentrum für Umwelt und Gesundheit, Neuherberg) (1989).

George ZUBAL

I.G. Zubal et. al.,"Computerized 3D Segmented Human Anatomy", Med Phys 21 (2), p.299-302, February 1994.

Comparative Table ***Anthropomorphic Computational Models***

ORIGIN	MODEL	TYPE	POPULATION	APPLICATION	CODE	AVAILABILITY
Gualdrini, ENEA	Yamaguchi Cristy	Adult	European (Caucasian)	RP RS	MARS	YES
Mares, GSF	Adam & Eva	Adult	European	RP	MCNP	YES
Schultz, TNO-ME	Adam & Eva	Adult	European	RP DG	MCNP	YES
Hongo et al., NIRS	Modified Cristy	New Born 1, 5, 10, 15 yr Adult	Japanese	RP		YES
Zankl, GSF	Adam & Eva	Adult	European	RP DG	ALGAM EGS4	YES
Zankl, GSF	Baby & Child	0.15, 7 yr	European	RP DG		NO
Zubal, Yale	Tomographic voxel-based	0.15, 7 yr Adult	European	DG	ALGAMP	
Yamaguchi, NIRS	Modified Snyder	Adult				
Kramer, GSF	Adam & Eva	Adult	European	RP DG	MC	
Zankl, GSF	Baby & Child	0.15, 7 yr	European	RP		
Rai, JAERI	Pregnant Woman	Adult	Japanese	RP	MC	
Yamaguchi, NIRS		from New Born to Adult	Japanese	RP	VADMAP MC	
Snyder, ORNL		Adult	European	RP	MC	
JAERI	Hermaphrodite	Adult	Japanese	RP DG		
ORNL	Paediatric	New Born 1, 5, 10, 15 yr Adult	European	RP	MC	
KAUL, SAIC	N.-American Adult	Adult	European	RP		3 MODELS

RP = Radiation Protection DG = Diagnosis RS = Radiation Shielding

Session V

MODELLING CODES AND DATA – RECENT RELEASES, COMPILATIONS, DEVELOPMENT REQUIRED, SHARING

CHAIR

Robert ROUSSIN

CO-CHAIR

Hideo HIRAYAMA

STATUS REPORT ON THE COLLECTION OF COMPUTER CODES AND DATA FOR ACCELERATOR SHIELD MODELLING

Robert W. Roussin
ORNL/RSIC, U.S.A.

Enrico Sartori and *Pedro Vaz*
OECD/NEA

Abstract

During the Specialists' Meeting on Shielding Aspects of Accelerators, Targets and Irradiation Facilities held in Arlington, Texas, on 28-29 April 1994, it was felt that the NEA-DB[1] and RSIC[2] can provide beneficial services to the accelerator shielding specialists by packaging and disseminating modern frozen versions of the transport and auxiliary codes and data libraries in common use. At the same time it was recommended that these two Centers try to obtain new or updated versions of a number of computer codes, some performing low-energy neutron transport, others modelling hadronic and electromagnetic cascades or implementing intermediate energy nuclear models. This note summarizes the progress made since then in collecting new computer codes and data libraries. An exhaustive survey is also presented in the form of tables displaying the computer codes available from the two Centers in the areas previously mentioned. These tables supersede the ones presented in the Arlington Specialists' Meeting[3].

---

1 Data Bank of the Nuclear Energy Agency of the Organisation for Economic Co-operation and Development (O.E.C.D), in Paris , FRANCE.

2 Radiation Shielding Information Centre at the Oak Ridge National Laboratory (O.R.N.L.), in Oak Ridge, Tennessee, U.S.A.

3 Proceedings of the Specialists' Meeting on Shielding Aspects of Accelerators, Targets and Irradiation Facilities, held in Arlington, Texas (U.S.A.) on 28-29 April 1994, published as an OECD document ISBN 92-64-14327-0.

1. Introduction

RSIC and the NEA DB collect, test and distribute computer programs and data in the field of nuclear applications. This activity is coordinated with other similar centers in the United States (ESTSC, NNDC), Japan (RIST) and outside the OECD area through an arrangement with the IAEA.

This information is shared worldwide for the benefit of scientists and engineers working on the safe and economic use of nuclear technology. Among the fields RSIC is specialised, technology for radiation transport holds an eminent place; the NEA DB covers instead a wider range of topics with less specific expertise. The two centers share to a large extent the same programs through a long standing cooperative arrangement.

Major emphasis has been given in the past to nuclear energy applications. In order to respond to needs expressed by new communities of users, covering other aspects of nuclear technology, special efforts were made to acquire programs and data in their fields of interest. Shielding aspects of accelerators and targets has in fact received attention over the last several years. It is the intention of both centers to devote additional effort so that state-of-the-art technology in this field is shared among the specialists.

2. Radiation Shielding Information Center (RSIC)

RSIC is embedded in the Computational, Physics and Engineering Division of the directorate for Computing, Robotics and Education (CRE) at ORNL. That Division is noted for its role as a leader in the development of radiation transport technology throughout the years. It is very beneficial for RSIC to be located with such an organisation so that staff members have close proximity to these major developments and the transfer of such technology is enhanced by a climate of close cooperation.

In practice, RSIC is an information analysis center following the concepts suggested by Alvin Weinberg in 1963 [1]. It is staffed by scientists, engineers, computer specialists, and support personnel. While being physically located at ORNL, it is embedded in the national research and development of its sponsors and interacts dynamically with contributors and users.

It was founded in 1962 by the U.S. Atomic Energy Commission to provide support for its reactor research programmes. Over the years the scope of RSIC has broadened to include radiation transport from nuclear weapons, radioisotopes, accelerators, fusion reactors, nuclear waste. Current sponsors include the U.S. Department of Energy (Nuclear Energy, Fusion, Defense Programs, Environmental), and the Defense Nuclear Agency.

3. The NEA Data Bank (NEA DB)

The NEA Data Bank is part of the OECD Nuclear Energy Agency, financed by 19 of the 25 OECD countries (Austria, Belgium, Denmark, Finland, France, Germany, Greece, Italy, Japan, Republic of Korea, Mexico, The Netherlands, Norway, Portugal, Spain, Sweden, Switzerland, Turkey, United Kingdom). A cooperative arrangement is in force, covering the exchange of computer programs and data between these countries, Canada and USA. Exchange with other countries is ruled by an arrangement with the International Atomic Energy Agency.

The work programme is approved yearly by the Nuclear Science Committee, one of the NEA Committees (others cover Nuclear Safety, Development, Waste Management).

The staff consists of physicists, engineers, computing experts and is international. In order to stay in close contact with the scientific community and engineers in the member countries, modern communication systems are extensively used.

The Computer Program and Data Services were set up in 1964 following the same objectives and standards established at the centers in the USA.

The primary objective as stated in the original statute was "to improve the communication between the originators of computer programs and data, and the using scientist and engineers so that the most efficient and economic use in the field of atomic energy may be made of the numerous large and expensive computers ..." . Evolution in the last thirty years has not changed this objective except that today "expensive computers" should read rather "expensive to develop computer codes".

References

[1] R.W.Roussin and E.Sartori, "Sharing of Computer Codes and Data for Accelerator Shield Modelling", Proceedings of the Specialists' Meeting on *Shielding Aspects of Accelerators, Targets and Irradiation Facilities*, Arlington, Texas, U.S.A., on 28-29 April 1994, published as OECD document ISBN 92-64-14327-0

Table 1 ***List of programs and data in alphabetical order***

Programs marked (*) or (**) in the following table, represent additions to the corresponding table of [1]

(*) Programs available

(**) Programs known but not available

Name	*Identification*	*Function*
ACTIV-87(*)	IAEA1275	Library with fast neutron activation x-sections
AIRSCAT	CCC-0341	dose rate from gamma air scattering, single scat. approx.
ALBEDO	NEA 1353	gamma, neutron attenuation in air ducts
ALDOSE(*)	CCC-0577	Calculates of absorbed dose and dose equivalent rates as function of depth in water irradiated by alpha source
ALICE91	PSR-0146	precompound/compound nuclear decay model
ALPHN(*)	CCC-0612	Calculates the (alpha,n) production rate in a mixture receiving alpha particles from emitting actinides
AMALTHEE	NEA 0675	emission spectra for n, p, d, h3, he3, alpha reaction
ANISN	CCC-0254	1-D Sn, n, gamma transport in slab, cylinder, sphere
ASOP	CCC-0126	1-D Sn shield calculation
ASTAR(*)	IAEA1282	Calculates stopping power and range for alphas
ASTROS	CCC-0073	primary/secondary proton dose in sphere/slab tissue
AUJP	IAEA0906	optical potential parameters search by chi**2 method
BALTORO	NEA 0675	n, gamma transport perturbation from MORSE,ANISN calculation
BERMUDA	NEA 0949	1-D,2-D,3-D n. gamma transport for shielding
BETA-2B	CCC-0117	MC time-dep bremsstrahlung, electron transport
BREESE	PSR-0143	distribution function for MORSE from albedo data
BREMRAD	CCC-0031	external/internal bremsstrahlung
BRHGAM	CCC-0350	MC absorbed dose from x-rays in phantom
CADE	NEA 1020	multiple particle emission xsec by Weisskopf-Ewing
CALOR89	CCC-0610	MC system for design, analysis of calorimeter system
CALOR93		MC system for design, analysis of calorimeter system
CAMERA	CCC-0240	radiation transport and computerized man model
CARP-82	PSR-0131	currents for BREESE from DOT flux
CASCADE	CCC-0176	high energy electron-photon transport in matter
CASIM	NESC0742	MC high energy cascades in complex shields
CEM95(*)	IAEA1247	MC calculation of nucl. reations (Cascade Exciton Model)
CENDL(*)	IAEA1256	Chinese Evaluated Nuclear Data Library, namely the Optical Model Parameters for 6 types of projectiles (neutron, proton, deuteron, triton, He3 and He4)
CEPXS/ONELD	CCC-0544	1-D coupled electron photon multigroup transport
CFUP1	IAEA1266	n, charged-particle reaction of fissile nuclei E<33 MeV
CHARGE-2/C	CCC-0070	electron, p, heavy particle flux/dose behind shield
CHUCK	USCD1021	n, charged particle xsec, coupled channel model
CMUP2	IAEA1265	reaction xsec for n ,p, d, t, he3, he4, E<50 MeV
COLLI-PTB	NEA 1126	MC n fluence spectra for 3-D collimator system
COMNUC3B	PSR-0302	compound nucleus interaction in n reactions
COVFILES(*)	DLC-0091	Library of neutron x-sections covariance data, useful to estimate radiation damage or heating
DANTSYS(*)	CCC-0547	1-D, 2-D, 3-D Sn neutron, photon transport
DASH	CCC-0366	void tracing Sn - MC coupling with fluxes from DOT
DCTDOS	CCC-0520	n,gamma penetration in composite duct system
DDCS(*)	IAEA1290	Calculation of neutron, proton, deuteron, triton, He3, and alpha induced reations of medium heavy nuclei in the energy range up to 50 MeV
DISDOS	CCC-0170	dose from external photons in phantom

Name	*Identification*	*Function*
DOMINO	PSR-0064	coupling of Sn DOT with MC MORSE
DORT	CCC-0543	1-D 2-D Sn n, photon transport with deep penetration
DOSDAT-2	DLC-0079	gamma, electron dose factors data lib. for body organs
DOSEDAT-DOE	DLC-0144	doserate factors for external photon, electron exposure
DOT	CCC-0276	2-D Sn n, photon transport with deep penetration
DROSG-87(*)	IAEA1234	Library of Legendre coefficients for neutron reactions
DUST	CCC-0453	albedo MC simulation of n streaming inducts
DWBA82	NEA 1209	Distorted Wave Born Approximation nuclear model
DWUCK-4	NESC9872	Distorted Wave Born Approximation nuclear model
E-DEP-1	CCC-0275	heavy ion energy deposition
EADL(*)	USCD1192	Library of atomic subshell and relaxation data
ECIS-95(*)	NEA 0850	Schroedinger/Dirac nuclear model with experimental fit
ECPL-86(*)	DLC-0106	evaluated charged particle cross-sections
EDMULT	NEA 0969	electron depth dose in multilayer slab absorbers
EEDL(*)	USCD1193	Electron interaction x-section from 10 eV to 100 GeV
EGS4	CCC-0331	MC electron photon shower simulation
ELBA	CCC-0119	bremsstrahlung dose from electron flux on Al shield
ELPHIC-PC	IAEA1223	statistical model MC simulation of heavy ion reaction
ELPHO	CCC-0301	MC muon, electron, positron generation from pions
ELTRAN	CCC-0155	MC 1-D electron transport
EMPIRE-MSC	IAEA1169	multistep compound nucleus/pre-equilibrium xsec
ENLOSS	PSR-0047	energy loss of charged particles
EPDL-VI/MOD(*)	USCD1187	Photon interaction x-sections library(10 eV to 100 GeV)
EPICSHOW(*)	IAEA1285	Interactive Viewing of the Electron-Photon Interaction Code (EPIC) system databases (10 eV < E < 1 GeV)
ERINNI	NEA 0815	multiple cascades emission spectra by optical model
ESTAR(*)	IAEA1282	Calculates stopping power and range for electrons
ETRAN	CCC-0107	MC electron, gamma transport with secondary radiation
EVA(*)		Codes performing the nuclear evaporation processes (working on the output from ISABEL)
EVALPLOT(*)	IAEA0852	Plots x-sections in ENDF/B format, angular and energy distributions
EVAP_F(**)		Modified version of the Dresner evaporation code (run in HETC@PSI)
EXIFONGAMMA	IAEA1211	n, alpha, proton, gamma emission spectra model
FALSTF	CCC-0351	n, gamma flux detector response outside cyl shields
FEM-RZ	NEA 0566	2-D multigroup n transport in r-z geometry
FGR-DOSE(*)	DLC-0167	Library of dose coefficients for intake and exposure to radionuclides
FLEP	DLC-0022	neutron, proton nonelastic xsec and spectra E<400MeV
FLUKA	CCC-0207	MC high energy extranuclear hadron cascades
FLUNEV-DESY		
FOTELP	CCC-0581	MC photons, electrons and positron transport
FRITIOF(**)		Hadronic cascades in high-energy Heavy Ion Collisions (used to be availble from the CERN Program Library)
FSMN	IAEA1264	fission spectra by compound-nucleus optical model
G33-GP	CCC-0494	multigroup gamma scattering using gp buildup-factor
GAMMONE	NEA 0268	MC gamma penetration from various geometrical sources
GEANT-CERN		
GGG-GP	CCC-0564	Multigroup gamma-ray scattering - build-up factors
GNASH-FKK(*)	PSR-0125	multi-step direct and compound and Hauser Feshbach models
GNASH-LANL	PSR-0125	pre-equilibrium/statistical xsec, emission spectra
GRACE-1	NESC0045	multigroup gamma attenuation, dose in slab

Name	*Identification*	*Function*
GRAPE	NEA 1043	precompound/compound nuclear reaction models
HELLO	DLC-0058	47 n, 21 gamma group coupled xsec from VITAMIN-C library
HERMES-KFA	NEA 1265	MC high-energy radiation transport
HETC NMTC	CCC-0178	MC high energy nucleon meson cascade transport
HETC-KFA	CCC-0496	MC high energy nucleon-meson cascades
HETC95(**)		MC high energy nucleon-meson cascades and transport
HFTT	IAEA0954	n xsec by compound-nucleus evaporation model
HIC-1	CCC-0249	MC heavy ion reactions at E>50 MeV/nucleon
HIJET(**)		Hadronic cascades in high-energy Heavy Ion Collisions (used to be availble from the CERN Program Library)
HILO86	DLC-0119	66 N, 22 gamma grp XSEC lib. for ANISN, ORNL,DORT,MORSE-CGA
HOMO(*)	IAEA1253	Program for mixing/converting libraries in ANISN format
HUGO-VI	DLC-0146	photon interaction evaluated data library ENDF-6 format
IDC	CCC-0384	ICRP dosimetric calculational system
IHEAS-BENCH(*)	NEA 1468	High energy accelerator shielding benchmarks
IMPACTS(*)	ESTS0005	Radiological assessment code
ISABEL(*)	NEA 1413	Intranuclear cascade model allowing hydrogen and helium ions and antiprotons as projectiles (run in LAHET)
ISAJET(**)		Hadronic cascades in high-energy Heavy Ion Collisions (used to be availble from the CERN Program Library)
ISO-PC(*)	CCC-0636	Kernel integration code system for general purpose isotope shielding
ITS-3.0	CCC-0467	MC tiger system of coupled electron photon transport
JENKINS		photon, neutron dose in electron accelerator
K009	CCC-0062	Charged particle penetration - phantom
KAPSIES		quantum mechanical multi-step direct model
LA100	DLC-0168	Evaluated data library for n, p up to 100 MeV, ENDF-6 fmt
LAHET		MC nucleon, pion, muons, tritons, He-3, alpha transport
LAHIMAC	DLC-0128	neutron, gamma xsec - response fuctions, E<800MeV
LEP	DLC-0001	results from intra-nuclear cascade and evaporation
LIMES	NEA 1337	Intermediate mass fragments in heavy ion nuclear reactions
LPPC	CCC-0051	proton penetration, slab
LPSC	CCC-0064	p, n flux, spectra behind slab shield from p irradiation
LRSPC	CCC-0050	range and stopping power calculator for ions
MAGIK	CCC-0359	MC for computing induced residual activation dose rates
MAGNA	NEA 0163	dose rates from gamma source in slab or cyl shell shields
MARLOWE	PSR-0137	atomic displacement cascades in solids
MARMER	NEA 1307	point-kernel shielding, ORIGEN-S nuclide inventories
MATXS10(*)	DLC-0176	Library with 30n-12gamma energy groups for particle transport codes and high energy calculations
MATXS11(*)	DLC-0177	Library with 80n-24gamma energy groups for particle transport codes and high energy calculations
MCNP-4A	CCC-0200	MC 3-D time-dep coupled n, photon, electron transport
MCNPDAT(*)	DLC-0105	X-section data library for the MCNP-4A transport code
MCNPDAT6(*)	DLC-0181	X-section data library from ENDF/B-VI for MCNP-4A
MECC-7	CCC-0156	medium energy intra-nuclear cascade model
MENSLIB	DLC-0084	neutron 60 group xsec, E<60MeV
MERCURE-4	NEA 0351	MC 3-D gamma heating/gamma dose rate, fast flux
MEVDP	CCC-0157	radiation transport in computerized anatomical man
MICAP	PSR-0261	MC ionization chamber responses
MORSE-CGA	CCC-0474	MC n, gamma multigroup transport
MUONLM(*)	NEA 1475	Calorimeter Interaction of Muons

Name	*Identification*	*Function*
MUP-2	IAEA0907	fast n reaction xsec of medium-heavy nuclei
MUTIL(*)	NEA-1451	Calculates the asymmetry factor of the Mott scattering of electrons and positrons by point nuclei
NDEM(**)		Generates a gamma-ray source from the deexcitation of residual nuclei, assuming all particle decay modes have been exhausted (part of the HERMES system)
NESKA	NEA 1422	electron, positron scattering from point nuclei
NFCLIST(*)	ESTS0352	Radionuclide decay data tabulations (240 radionuclides)
NJOY-94(*)	PSR-0171	n, p, photon evaluated data processing system
NMTC/JAERI	NEA 0974	MC high-energy p, n, pion reactions
NUCDECAY(*)	DLC-0172	Nuclear decay data for radiation dosimetry calculations
NUCLEUS		Nuclear spallation simulation and primary products
PACE2(**)		Codes performing the nuclear evaporation processes (working on the output from ISABEL)
PALLAS-2DY	NEA 0702	2-D n ,gamma transport for fixed source
PCROSS	IAEA1220	pre-equilibrium emission spectra in neutron reaction
PEGAS	IAEA1261	unified model of particle and gamma emission reactions
PELSHIE	IAEA0855	dose rates from gamma source, point-kernel method
PEQAG-2	IAEA1185	pre-equilibrium model nucleon, gamma spectra, xsec
PEREGRINE(**)		Used to model dose to humans from radiation therapy.
PHOTX	DLC-0136	photon interaction xsec library for 100 elements
PICA	CCC-0160	MC calculation of nuclear cascade reactions caused by the collision of photons (30<E<400 Mev) with nuclei
PIPE	NEA 0416	1-D gamma transport for slab, spherical shields
PLACID	CCC-0381	MC gamma streaming in cylindrical duct shields
PNESD	IAEA1235	elastic xsec of 3 MeV to 1000 MeV p on natural isotopes
POTAUS	IAEA1249	H thru U ion ranges, stopping power for various materials
PREANG	NEA 0809	nuclear model particle spectra, angular distribution
PRECO-D2	PSR-0226	pre-equilibrium, direct reaction double differential xsec
PREM	NEA 0888	nucleon emission pre-equilibrium energy spectra, xsec
PSTAR(*)	IAEA1282	Calculates stopping power and range for protons
PTRAN	CCC-0618	MC proton transport for 50 to 250 MeV
PUTZ	CCC-0595	point-kernel 3-d gamma shielding
QMD		intra-nuclear cascade and classical molecular dynamics
RADCOMPT(*)	PSR-0348	Sample analysis for alpha and beta dual channel detect.
RADDECAY	DLC-0134	decay data library for radiological assessment
RADHEAT-V3	NEA 0467	transport, heat,radiation damage xsec in reactor, shield
RAID	CCC-0083	gamma, n scattering into cylindrical or multibend duct
REAC	CCC-0443	activation and transmutation
REAC-2	NESC9554	nuclide activation, transmutation
REAC3		high energy nuclide activation model
REBEL-3	IAEA0846	MC radiation dose to human organs
RECOIL/B	DLC-0055	heavy charged particle recoil spectra lib. for rad. damage
REMIT(*)	ESTS0579	Rad. Exposure Monitoring and Inf. Transmittal system
REPC	PSR-0195	dose from protons in tissue
RESRAD(*)	CCC-0552	Calculation of residual radioactive material guidelines, site specific radiation doses and risks
SAM-CE	CCC-0187	MC time-dep 3-d n ,gamma transport in complex geometry
SAMSY	IAEA0837	n, gamma dose rates, heat source for multilayer shields
SAND-II(*)	PSR-0345	Determines neutron energy spectra by an analysis of multiple experimental activation detector data
SANDYL	CCC-0361	MC 3-d time-dep gamma electron cascade transport
SCAP-82	CCC-0418	scattering, albedo, point-kernel anal. in complex geometry

Name	*Identification*	*Function*
SCINFUL(*)	PSR-0267	MC to compute the response of scintillation neutron detector (incident neutron energies from 0.1 to 75 MeV)
SEECAL(*)	CCC-0620	Computes age-dependent effective energies for 54 and 32 target regions in the human body (825 radionuclides)
SFERXS	NEA 1239	photon absorption, coherent,incoherent xsec for shielding
SHIELD(**)	IAEA1287	Universal code for exclusive simulation of hadron cascades in complex macroscopic targets. Transport of nucleons, pions, kaons, antinucleons and muons in the energy range up to 100 GeV is taken into account. Electromagnetic cascades are simulated by means of the EGS4 code, intranuclear cascades follow the model CASCAD, hadron-nucleus and nucleus-nucleus intranuclear interactions generated according to the QGSM based quark-gluon string model, Fermi break-up, multi-fragmentations and evaporation/fission according to the extended nuclear deexcitation model DEEX.
SIGMA-A(*)	DLC-0139	Photon interaction and absorption data 1 KeV-100 MeV
SITHA(**)	IAEA1179	SImulation Transport HAdron, used to calculate hadron transport in matter blocks of complex geometry. The nucleon and charged pions transport are carried out for the energy interval 10 MeV to 10 GeV and neutron transport for energies less than 20 MeV.
SKYPORT	DLC-0093	importance of n, photon skyshine dose from accelerators
SNLRML(*)	DLC-0178	Dosimetry library compendium
SNL/SAND-II(*)	PSR-0345	Enhanced version of SAND-II
SOURCE(**)		Description of the proton transmission and generation of n source. Based on the Moving Source Model formalism and Bethe stopping theory with relativistic corrections for protons, allows the estimation of the proton range and the changes of the proton current and the neutron production versus the depth.
SPACETRAN	CCC-0120	radiation leakage from cylinder with ANISN flux
SPAR	CCC-0228	stopping power and ranges from muons, pions, protons, ions
SPARES	CCC-0148	space radiation environment and shielding evaluation
SPCHAIN(**)		Calculates accumulation and decay of nuclides by taking the half-life and the decay chain of each nuclide into account.
SPECTER-ANL	PSR-0263	n damage for material irradiation
STAC-8		transmitted, absorbed power/spectrum - synchrotron radiation
STAPRE-H	IAEA0971	evaporation, pre-equilibrium model reaction xsec
STARCODES	PSR-0330	stopping power, ranges for electrons, protons, alpha
STOPOW	IAEA0970	stopping power of fast ions in matter
STRAGL	CCC-0201	energy loss straggling of heavy charged particles
SWIMS(*)	ESTS0682	Calculates the angular dispersion of ion beams that undergo small-angle incoherent multiple scattering by gaseous or solid media
TART95(*)		3D MC transport program for neutrons and photons
TEST(*)	IAEA1252	Program for sorting/listing/deleting ANISN libraries
TNG1	PSR-0298	N multi-step statistical model
TORT	CCC-0543	3-D Sn n, photon transport with deep penetration
TPASGAM(*)	DLC-0088	Library with gamma-ray decay data for 1438 radionuclides
TRANSX(*)	PSR-0317	Code system to produce neutron, photon transport tables for discrete ordinates and diffusion codes
TRAPP	CCC-0205	proton and alpha transport, reaction products neglected
TRIPOLI-2	NEA 0874	MC time-dep 3-D N, gamma transport
TRIPOS	CCC-0537	MC ion transport
TWODANT-SYS	CCC-0547	1-D,2-D multigroup Sn n, photon transport
UNGER	DLC-0164	effective dose equivalent data for selected isotopes

Name	*Identification*	*Function*
UNIFY	IAEA1177	fast n xsec, spectrum calculation for structural materials
VEGAS(**)		Intranuclear cascade code (from which ISABEL is derived)
VIRGIN(*)	IAEA0932	Calculates uncollided neutron flux and neutron reactions due to transmission of a neutron beam through any thickness of material
VITAMIN-E(*)	DLC-0113	X-section data library with 174n-38gamma energy groups
XCOM	USCD1156	photon cross sections from 1 keV to 100 GeV

CCC-,PSR-,DLC- : original packaging by RSIC
NESC : original packaging by NESC (now ESTSC)
USCD : originated in US/Canada, packaged by NEA DB
NEA, IAEA : original packaging by NEA DB
<blank> : acquisition sought
xsec : cross section
lib. : library

Table 2

Evaluated and processed data (cross sections, dose conversion, ranges, stopping powers)

Programs marked (*) or (**) in the following table, represent additions to the corresponding table of ref. [1]

(*) Programs available

(**) Programs known but not available

Name	*Identification*	*Function*
ACTIV-87(*)	IAEA1275	Library with fast neutron activation x-sections
CENDL(*)	IAEA1256	Chinese Evaluated Nuclear Data Library, namely the Optical Model Parameters for 6 types of projectiles (neutron, proton, deuteron, triton, He3 and He4)
COVFILES(*)	DLC-0091	Library of neutron x-sections covariance data, useful to estimate radiation damage or heating
DROSG-87(*)	IAEA1234	Library of Legendre coefficients for neutron reactions
DOSDAT-2	DLC-0079	gamma, electron dose factors data lib. for body organs
DOSEDAT-DOE	DLC-0144	doserate factors for external photon, electron exposure
EADL(*)	USCD1192	Library of atomic subshell and relaxation data
ECPL-86(*)	DLC-0106	evaluated charged particle cross-sections
EEDL(*)	USCD1193	Electron interaction x-section from 10 eV to 100 GeV
EPDL-VI/MOD(*)	USCD1187	Photon interaction x-sections library(10 eV to 100 GeV)
FGR-DOSE(*)	DLC-0167	Library of dose coefficients for intake and exposure to radionuclides
FLEP	DLC-0022	neutron, proton nonelastic xsec and spectra E<400MeV
HILO86	DLC-0119	66 N, 22 gamma grp XSEC lib. for ANISN-ORNL, DORT, MORSE-CGA
HELLO	DLC-0058	47 n, 21 gamma group coupled xsec from VITAMIN-C library
HUGO-VI	DLC-0146	photon interaction evaluated data library ENDF-6 format
IDC	CCC-0384	ICRP dosimetric calculational system
IHEAS-BENCH(*)	NEA 1468	High energy accelerator shielding benchmarks
LA100	DLC-0168	evaluated data library for n, p up to 100 MeV, ENDF-6 fmt
LAHIMACK	DLC-0128	Multigroup neutron and gamma x-sections up to 800 MeV
LEP	DLC-0001	results from intra-nuclear cascade and evaporation
LRSPC	CCC-0050	range and stopping power calculator
MATXS10(*)	DLC-0176	Library with 30n-12gamma energy groups for particle transport codes and high energy calculations
MATXS11(*)	DLC-0177	idem
MCNPDAT(*)	DLC-0105	X-section data library for the MCNP-4A transport code
MCNPDAT6(*)	DLC-0181	X-section data library from ENDF/B-VI for MCNP-4A
MENSLIB	DLC-0084	neutron 60 group xsec, E<60MeV
NFCLIST(*)	ESTS0352	Radionuclide decay data tabulations (240 radionuclides)
NUCDECAY(*)	DLC-0172	Nuclear decay data for radiation dosimetry calculations
PHOTX	DLC-0136	photon interaction xsec library for 100 elements
PNESD	IAEA1235	elastic xsec of 3 MeV to 1000 MeV p on natural isotopes
RADDECAY	DLC-0134	decay data library for radiological assessment
RECOIL/B	DLC-0055	heavy charged particle recoil spectra lib. for rad. damage
SFERXS	NEA 1239	photon absorption, coherent,incoherent xsec for shielding
SIGMA-A(*)	DLC-0139	Photon interaction and absorption data 1 KeV-100 MeV
SKYPORT	DLC-0093	importance of n, photon skyshine dose from accelerators
SNLRML(*)	DLC-0178	Dosimetry library compendium
SPAR	CCC-0228	stopping power and ranges from muons, pions, protons, ions
STAC-8		transmitted, absorbed power/spectrum - synchrotron radiat
STARCODES	PSR-0330	stopping power, ranges for electrons, protons, alpha
STOPOW	IAEA0970	stopping power of fast ions in matter

Name	*Identification*	*Function*
TPASGAM(*)	DLC-0088	Library with gamma-ray decay data for 1438 radionuclides
UNGER	DLC-0164	effective dose equivalent data for selected isotopes
VITAMIN-E(*)	DLC-0113	X-section data library with 174n-38gamma energy groups
XCOM	USCD1156	photon cross sections from 1 keV to 100 GeV

CCC-,PSR-,DLC-	: original packaging by RSIC
NESC	: original packaging by NESC (now ESTSC)
USCD	: originated in US/Canada, packaged by NEA DB
NEA, IAEA	: original packaging by NEA DB
<blank>	: acquisition sought
xsec	: cross section
lib.	: library

Table 3 ***Cross-sections - Spectra from nuclear models (for E>20 MeV)***

Programs marked (*) or (**) in the following table, represent additions to the corresponding table of ref. [1]
(*) Programs available
(**) Programs known but not available

Name	*Identification*	*Function*
ALICE91	PSR-0146	precompound/compound nuclear decay model
AMALTHEE	NEA 0675	emission spectra for n, p, d, h3, he3, alpha reaction
ASOP	CCC-0126	1-D Sn shield calculation
AUJP	IAEA0906	optical potential parameters search by chi**2 method
CADE	NEA 1020	multiple particle emission xsec by Weisskopf-Ewing
CEM95(*)	IAEA1247	MC calculation of nucl. reations (Cascade Exciton Model)
CFUP1	IAEA1266	n, charged-particle reaction of fissile nuclei E<33 MeV
CHUCK	USCD1021	n, charged particle xsec, coupled channel model
CMUP2	IAEA1265	reaction xsec for n ,p, d, t, he3, he4, E<50 MeV
COMNUC3B	PSR-0302	compound nucleus interaction in n reactions
DWBA82	NEA 1209	Distorted Wave Born Approximation nuclear model
DWUCK-4	NESC9872	Distorted Wave Born Approximation nuclear model
ECIS-95(*)	NEA 0850	Schroedinger/Dirac nuclear model with experimental fit
ELPHIC-PC	IAEA1223	statistical model MC simulation of heavy ion reaction
EMPIRE-MSC	IAEA1169	multistep compound nucleus/pre-equilibrium xsec
ERINNI	NEA 0815	multiple cascades emission spectra by optical model
EVA(*)		Codes performing the nuclear evaporation processes (working on the output from ISABEL)
EVAP_F(**)		Modified version of the Dresdner evaporation code (run in HETC@PSI)
EXIFONGAMMA	IAEA1211	n, alpha, proton, gamma emission spectra model
FRITIOF(**)		MC high-energy heavy ion collisions
GNASH-FKK(*)	PSR-0125	multi-step direct and compound and Hauser Feshbach models
GNASH-LANL	PSR-0125	pre-equilibrium/statistical xsec, emission spectra
GRAPE	NEA 1043	precompound/compound nuclear reaction models
HETC NMTC	CCC-0178	MC high energy nucleon meson cascade transport
HETC-KFA	CCC-0496	MC high energy nucleon-meson cascades
HETC95(**)		MC high energy nucleon-meson cascades and transport
HFTT	IAEA0954	n xsec by compound-nucleus evaporation model
HIJET(**)		MC high-energy heavy ion collisions
ISABEL(*)	NEA 1413	Intranuclear cascade model allowing hydrogen and helium ions and antiprotons as projectiles (run in LAHET)
ISAJET(**)		MC high-energy heavy ion collisions
KAPSIES		quantum mechanical multi-step direct model
LIMES	NEA 1337	Intermediate mass fragments in heavy ion nuclear reactions
MARLOWE	PSR-0137	atomic displacement cascades in solids
MECC-7	CCC-0156	medium energy intra-nuclear cascade model
MUP-2	IAEA0907	fast n reaction xsec of medium-heavy nuclei
MUTIL(*)	NEA 1451	Calculates the asymmetry factor of the Mott scattering of electrons and positrons by point nuclei
NDEM(**)		Generates a gamma-ray source from the deexcitation of residual nuclei, assuming all particle decay modes have been exhausted (part of the HERMES system)

Name	*Identification*	*Function*
NJOY-94(*)	PSR-0171	n, p, photon evaluated data processing system
NMTC/JAERI	NEA 0974	MC high-energy p, n, pion reactions
NUCLEUS		Nuclear spallation simulation and primary products
PACE2(**)		Codes performing the nuclear evaporation processes (working on the output from ISABEL)
PCROSS	IAEA1220	pre-equilibrium emission spectra in neutron reaction
PEGAS	IAEA1261	unified model of particle and gamma emission reactions
PELSHIE	IAEA0855	dose rates from gamma source, point-kernel method
PEQAG-2	IAEA1185	pre-equilibrium model nucleon, gamma spectra, xsec
PREANG	NEA 0809	nuclear model particle spectra, angular distribution
PRECO-D2	PSR-0226	pre-equilibrium, direct reaction double differential xsec
PREM	NEA 0888	nucleon emission pre-equilibrium energy spectra, xsec
QMD		intra-nuclear cascade and classical molecular dynamics
REAC	CCC-0443	activation and transmutation
REAC-2	NESC9554	nuclide activation, transmutation
REAC3		high energy activation model
STAPRE-H	IAEA0971	evaporation, pre-equilibrium model reaction xsec
TNG1	PSR-0298	N multi-step statistical model
UNIFY	IAEA1177	fast n xsec, spectrum calculation for structural materials
VEGAS(**)		Intranuclear cascade code (from which ISABEL is derived)

CCC-,PSR-,DLC-	: original packaging by RSIC
NESC	: original packaging by NESC (now ESTSC)
USCD	: originated in US/Canada, packaged by NEA DB
NEA, IAEA	: original packaging by NEA DB
<blank>	: acquisition sought
xsec	: cross section
lib.	: library

Table 4 ***Monte Carlo (MC) and deterministic radiation transport***

Programs marked (*) or (**) in the following table, represent additions to the corresponding table of ref. [1]
(*) Programs available
(**) Programs known but not available

Name	*Identification*	*Function*
Neutron/photon		
ALBEDO	NEA 1353	gamma, neutron attenuation in air ducts
ANISN	CCC-0254	1-D Sn, n, gamma transport in slab, cylinder, sphere
ASOP	CCC-0126	1-D Sn shield calculation
BALTORO	NEA 0675	n, gamma transport perturbation from MORSE, ANISN calculation
BERMUDA	NEA 0949	1-D,2-D,3-D n. gamma transport for shielding
BREESE	PSR-0143	distribution function for MORSE from albedo data
CARP-82	PSR-0131	currents for BREESE from DOT flux
COLLI-PTB	NEA 1126	MC n fluence spectra for 3-D collimator system
DANTSYS(*)	CCC-0547	1-D, 2-D, 3-D Sn neutron, photon transport
DASH	CCC-0366	void tracing Sn - MC COUPLING with fluxes from DOT
DCTDOS	CCC-0520	n, gamma penetration in composite duct system
DORT	CCC-0543	1-D 2-D Sn n, photon transport with deep penetration
DOMINO	PSR-0064	coupling of Sn DOT with MC MORSE
DOT	CCC-0276	2-D Sn n, photon transport with deep penetration
DUST	CCC-0453	albedo MC simulation of n streaming inducts
FALSTF	CCC-0351	n, gamma flux detector response outside cyl shields
FEM-RZ	NEA 0566	FEM 2-D multigroup n transport in r-z geometry
GEANT-CERN		MC hadron shower simulation
MAGIK	CCC-0359	MC induced residual activation dose rates
MCNP	CCC-0200	MC 3-D time-dep coupled n, photon, electron transport
MICAP(*)	PSR-0261	MC to determine the response of gas filled cavity ionization chamber, plastic scintilator or calorimeter in a mixed neutron and photon environment
MORSE-CGA	CCC-0474	MC n, gamma multigroup transport
PALLAS-2DY	NEA 0702	2-D n ,gamma transport for fixed source
RADHEAT-V3	NEA 0467	transport, heat,radiation damage xsec in reactor, shield
RAID	CCC-0083	gamma, n scattering into cylindrical or multibend duct
SAMSY	IAEA0837	n, gamma dose rates, heat source for multilayer shields
SAM-CE	CCC-0187	MC time-dep 3-d n ,gamma transport in complex geometry
SAND-II(*)	PSR-0345	Determines neutron energy spectra by an analysis of multiple experimental activation detector data
SCINFUL(*)	PSR-0267	MC to compute the response of scintillation neutron detector (incident neutron energies from 0.1 to 75 MeV)
SCAP-82	CCC-0418	scattering, albedo, point-kernel anal. in complex geometry
SNL/SAND-II(*)	PSR-0345	Enhanced version of SAND-II
SPACETRAN	CCC-0120	radiation leakage from cylinder with ANISN flux
SPECTER-ANL	PSR-0263	n damage for material irradiation
TART95(*)		3D MC transport program for neutrons and photons
TORT	CCC-0543	3-D Sn n, photon transport with deep penetration
TRANSX(*)	PSR-0317	Code system to produce neutron, photon transport tables for discrete ordinates and diffusion codes
TRIPOLI-2	NEA 0874	MC time-dep 3-D n, gamma transport
TWODANT-SYS	CCC-0547	1-D,2-D multigroup Sn n, photon transport
VIRGIN(*)	IAEA0932	Calculates uncollided neutron flux and neutron reactions due to transmission of a neutron beam through any thickness of material

Name	*Identification*	*Function*
Photon		
AIRSCAT	CCC-0341	dose rate from gamma air scattering, single scat. approx.
GAMMONE	NEA 0268	MC gamma penetration from various geometrical sources
MERCURE-4	NEA 0351	MC 3-D gamma heating/gamma dose rate, fast flux
PLACID	CCC-0381	MC gamma streaming in cylindrical duct shields
BRHGAM	CCC-0350	MC absorbed dose from x-rays in phantom
BREMRAD	CCC-0031	external/internal bremsstrahlung
G33-GP	CCC-0494	multigroup gamma scattering using gp buildup-factor
ISO-PC(*)	CCC-0636	Kernel integration code system for general purpose isotope shielding
MAGNA	NEA 0163	dose rates from gamma source in slab or cyl shell shields
MARMER	NEA 1307	point-kernel shielding, ORIGEN-S nuclide inventories
PELSHIE	IAEA0855	dose rates from gamma source, point-kernel method
PIPE	NEA 0416	1-D gamma transport for slab, spherical shields
PUTZ	CCC-0595	point-kernel 3-d gamma shielding
STAC-8		transmitted, absorbed power/spectrum - synchrotron radiat
Electron/photon		
BETA-2B	CCC-0117	MC time-dep bremsstrahlung, electron transport
CASCADE	CCC-0176	high energy electron-photon transport in matter
CEPXS ONELD	CCC-0544	1-D coupled electron photon multigroup transport
DOSDAT-2	DLC-0079	gamma, electron dose factors data lib. for body organs
EDMULT	NEA 0969	electron depth dose in multilayer slab absorbers
EGS4	CCC-0331	MC electron photon shower simulation
ELBA	CCC-0119	bremsstrahlung dose from electron flux on Al shield
EPICSHOW(*)	IAEA1285	Interactive Viewing of the Electron-Photon Interaction Code (EPIC) system databases (10 eV < E < 1 GeV)
ESTAR(*)	IAEA1282	Calculates stopping power and range for electrons
ETRAN	CCC-0107	MC electron, gamma transport with secondary radiation
ELTRAN	CCC-0155	MC 1-D electron transport
FOTELP	CCC-0581	MC photons, electrons and positron transport
ITS-3.0	CCC-0467	MC tiger system of coupled electron photon transport
MCNP-4A	CCC-0200	MC 3-D time-dep coupled n, photon, electron transport
SANDYL	CCC-0361	MC 3-D time-dep gamma electron cascade transport
Protons		
ASTROS	CCC-0073	primary/secondary proton dose in sphere/slab tissue
LPPC	CCC-0051	proton penetration, slab
PSTAR(*)	IAEA1282	Calculates stopping power and range for protons
PTRAN	CCC-0618	MC proton transport for 50 to 250 MeV
SOURCE(**)		Description of the proton transmission and generation of n source. Based on the Moving Source Model formalism and Bethe stopping theory with relativistic corrections for protons, allows the estimation of the proton range and the changes of the proton current and the neutron production versus the depth.
TRAPP	CCC-0205	proton and alpha transport, reaction products neglected

Name	*Identification*	*Function*
Alphas		
ALDOSE(*)	CCC-0577	Calculates of absorbed dose and dose equivalent rates as function of depth in water irradiated by alpha source
ALPHN(*)	CCC-0612	Calculates the (alpha,n) production rate in a mixture receiving alpha particles from emitting actinides
ASTAR(*)	IAEA1282	Calculates stopping power and range for alphas
RADCOMPT(*)	PSR-0348	Sample analysis for alpha and beta dual channel detectores
Nucleons/hadrons/cascades		
CALOR89	CCC-0610	MC system for design, analysis of calorimeter system
CALOR93		MC system for design, analysis of calorimeter system
CASIM	NESC0742	MC high energy cascades in complex shields
FLUKA	CCC-0207	MC high energy extranuclear hadron cascades
GEANT-CERN		MC hadron shower simulation
HERMES-KFA	NEA 1265	MC high-energy radiation transport
HETC NMTC	CCC-0178	MC high energy nucleon meson cascade transport
HETC-KFA	CCC-0496	MC high energy nucleon-meson cascade transport
LAHET		MC nucleon, pion, muons, tritons, He-3, alpha transport
LPSC	CCC-0064	p, n flux, spectra behind slab shield from p irradiation
NMTC/JAERI	NEA 0974	MC high-energy p, n, pion reactions
SITHA(**)	IAEA1179	SImulation Transport HAdron, used to calculate hadron transport in matter blocks of complex geometry. The nucleon and charged pions transport are carried out for the energy interval 10 MeV to 10 GeV and neutron transport for energies less than 20 MeV.
SHIELD(**)	IAEA1287	Universal code for exclusive simulation of hadron cascades in complex macroscopic targets. Transport of nucleons, pions, kaons, antinucleons and muons in the energy range up to 100 GeV is taken into account. Electromagnetic cascades are simulated by means of the EGS4 code, intranuclear cascades follow the model CASCAD, hadron-nucleus & nucleus-nucleusintranuclear interactions generated according to the QGSM based quark-gluon string model, Fermi break-up, multi-fragmentations and evaporation/fission according to the extended nuclear deexcitation model DEEX.
Heavy-ions		
E-DEP-1	CCC-0275	heavy ion energy deposition
ELPHIC-PC	IAEA1223	statistical model MC simulation of heavy ion reaction
HIC-1	CCC-0249	MC heavy ion reactions at E>50 MeV/nucleon
STRAGL	CCC-0201	energy loss straggling of heavy charged particles
SWIMS(*)	ESTS0682	Calculates the angular dispersion of ion beams that undergo small-angle incoherent multiple scattering by gaseous or solid media
TRIPOS	CCC-0537	MC ion transport
Muons		
MUONLM(*)	NEA 1475	Calorimeter Interaction of Muons

Name	*Identification*	*Function*
Others/cascades		
CHARGE-2/C	CCC-0070	electron, p, heavy particle flux/dose behind shield
DDCS(*)	IAEA1290	Calculation of neutron, proton, deuteron, triton, He3, and alpha induced reations of medium heavy nuclei in the energy range up to 50 MeV
ELPHO	CCC-0301	MC muon, electron, positron generation from pions
IMPACTS-BRC(*)	ESTS0005	Radiological assessment code
JENKINS		photon, neutron dose in electron accelerator
PICA	CCC-0160	MC calculation of nuclear cascade reactions caused by the collision of photons (30 < E < 400 Mev) with nuclei
SPARES	CCC-0148	space radiation environment and shielding evaluation
Anthropomorphic phantom modelling		
BRHGAM	CCC-0350	MC absorbed dose from x-rays in phantom
CAMERA	CCC-0240	radiation transport and computerized man model
DISDOS	CCC-0170	dose from external photons in phantom
K009	CCC-0062	Charged particle penetration - phantom
MEVDP	CCC-0157	radiation transport in computerized anatomical man
PEREGRINE(**)		Used to model dose to humans from radiation therapy.
REBEL-3	IAEA0846	MC radiation dose to human organs
REPC	PSR-0195	dose from protons in tissue
SEECAL(*)	CCC-0620	Computes age-dependent effective energies for 54 and 32 target regions in the human body (825 radionuclides)

CCC-,PSR-,DLC-	: original packaging by RSIC
NESC	: original packaging by NESC (now ESTSC)
USCD	: originated in US/Canada, packaged by NEA DB
NEA, IAEA	: original packaging by NEA DB
<blank>	: acquisition sought
xsec	: cross section
lib.	: library

APPENDICES

RESULTS OF INQUIRY ON ANTHROPOMORPHIC COMPUTATIONAL MODELS

Enrico Sartori
OECD/NEA

Background

During the specialists' meeting on *Shielding Aspects of Accelerators, Targets, and Irradiation Facilities*, held from 28-29 April 1994 in Arlington, Texas, one of the recommendations and agreed actions concerned standardisation of anthropomorphic phantoms [1].

Here is the specific agreed action: "*Collect and make available anthropomorphic phantom geometries including material compositions as used in Monte Carlo radiation transport codes*". This wish was expressed on several occasions by other groups as well.

The Chairman D. R. White of the ICRU Report No.48 [2] Committee has pointed out that there is confusion in using 'phantoms' and 'computational models'. That committee had decided that the term *'phantom'* would apply to solid objects made up of tissue substitutes. The specific action described here concerns *'anthropomorphic computational models*. As a first step to standardisation we use this terminology as of now.

An inquiry was sent out using a questionnaire prepared by G. F. Gualdrini, ENEA Bologna, with the objective first to identify the anthropomorphic computational models used today.

Several replies were received which are included in this compendium. James A. Spahn, jr, Senior Staff Scientist of the International Commission on Radiation Units and Measurement, Inc. (ICRU) has authorised us in the frame of this project to reproduce the tables describing the information assembled in their report N. 48 [2] in tables C.1 and C.2 and concerning anthropomorphic models.

We would like now to start a second phase in which the actual geometrical models and composition are collected. These models should be compared in two ways:

1. Geometry composition,

2. Effect of differences on dose calculations.

This technical point should be provided to standard committees like ICRU, ICRP, as a contribution in the process of standardisation.

A standardisation process should be started in the following with the concurrence of the specialists in this field.

It was pointed out, that geometry and composition are very important, but in a process of standardisation the aspect of standard particle interaction cross-sections, covering a wide range of energies required for the different applications should not be neglected. This aspect should be addressed at a further stage.

The result of this work will be available to the international community for their use in applications on computer readable medium or accessible on the World Wide Web.

FORM

INQUIRY ON AVAILABLE

ANTHROPOMORPHIC COMPUTATIONAL MODELS

(send to sartori@nea.fr or fax to: +33 (1) 4524 1110)

YOUR ADDRESS:

PHONE AND FAX:

MODEL (*NAME*): (e.g. GSF MALE and FEMALE, ADAM and EVA)

TYPE: (Mathematical or Tomographic)

AGE: (e.g. Adult, New-born, 1, 5, 10 etc. years)

POPULATION GROUP: (European, Japanese etc.)

APPLICATION FIELD: Radiation Protection
Diagnosis
Therapy

.....

COMPUTER PROGRAM for which
the geometry package has been implemented: (e.g. MCNP, MORSE etc.)

DESCRIPTION:

.....

PHYSICAL DIMENSIONS:

	Baby	*Child*	*Adult*
Age	8 weeks	7 years	30 years
Mass (kg)	4.2	21.7	70
Height (cm)	57	115	172
Trunk+Arms (cm) (lateral diameter)	21.8	33.1	40
Trunk (cm) (antero-posterior diameter)	12.2	17.6	20

BODY TISSUES:

	Mass Density (kg m-3)
Soft Tissues	987-1050
Lung	296
Cortical Bone	1765
Bone Marrow	1006

etc.

SIMPLIFIED MIXTURES: (bone-soft tissue etc.)

REFERENCES:

.....

Availability of the phantom for wider distribution to users *YES* *NO*

Tables with

ANTHROPOMORPHIC COMPUTATIONAL MODELS

Satoshi IWAI

NAME: **Satoshi IWAI**

ADDRESS: Mitsubishi Atomic Power Ind., Inc.
Omiya Technical Institute
1-297, Kitabukuro, Omiya, Saitama, 330 JAPAN
PHONE: 81 48 642 4404
FAX: 81 48 645 0189

MODEL: A modified version of the Yamaguchi's data [1] based on the Cristy phantom [2]
TYPE: Mathematical phantom
AGE: Adult
POPULATION: Caucasian (MIRD-5 [3] type adult)
APPLICATION FIELD: Radiation protection, Radiation shielding
COMPUTER PROGRAM: MARS [5] geometry package with the addition of the new three bodies general ellipsoid, and truncated right elliptical cone. [1]

Description

This phantom represents a modified version of the Yamaguchi's data [1] based on the Cristy phantom [2] of MIRD-V type. [3]

Three modification points were applied to this phantom:

1. Addition of an oesophagus. An oesophagus model was added to the phantom using the mathematical form reported by Lewis et al. [4]

2. Modification of stomach location. Although a description is included in the Yamaguchi's version, the stomach location was altered on the consideration reported by Lewis et al. [4]

3. Size of breasts' models. The height of this breast model is about half of the Cristy phantom model, because this phantom is hermaphroditic for shielding to the A.P. irradiation geometry. Internal organs are considered to be homogeneous in composition and density.

Different densities and compositions are used for the lungs, skeleton, and soft tissue. The composition description of the three tissues are limited to 17 elements (H, C, N, O, Na, Mg, P, S, Cl, K, Ca, Fe, Zn, Rb, Sr, and Pb). The densities of the lungs, skeleton, and soft tissue are 0.2958, 1.4682, and 0.9869 g/cm**3 respectively; these values are cited from the MIRD-5 report, [3] not from the Cristy's value. [2] The density of the Cristy's soft tissue is about 5% higher than that of MIRD-5 phantom, because the density of the Cristy's soft tissue is assumed to be modified for the calculation of internal dosimetry; it is most important to keep the mass of organs and the distance between the organs in the human body for the internal dosimetry calculation. Therefore the density of the Cristy's soft tissue is assumed to be increased to as to keep the two parameters. The densities of MIRD-5 were adopted into this work, because this phantom was employed to the external dosimetry.

Physical dimensions

Age	**ADULT**
Mass (*kg*)	about **70**
Height (*cm*)	**174**
Trunk+Arms (*cm*) – *Lateral diameter*	**40**
Trunk (*cm*) – *Antero-posterior diameter*	**20**
Leg length (*cm*)	**80**

Body tissues

	Mass Density (g/cm^3)
Soft Tissues	**0.9869**
Lungs	**0.2958**
Skeleton – Mineral bone+bone marrows	**1.4682**

Availability of the Phantom for wider distribution to users: Yes

Vladimir MARES

NAME:	**Vladimir MARES**
ADDRESS:	GSF - Forschungszentrum fuer Umwelt und Gesundheit, GmbH Neuherberg Postfach 11 29 85758 Oberschleissheim Germany
PHONE:	+49-89-3187-2652
FAX:	+49-89-3187-3323
E-MAIL:	mares@cony.gsf.de

MODEL:	ADAM and EVA
TYPE:	Mathematical
AGE:	Adult
POPULATION:	European
APPLICATION FIELD:	Radiation Protection
COMPUTER PROGRAM:	MCNP

Description

Skin and oesophagus included.

Physical dimensions

	Baby	Child	Adult	*ADAM*	*EVA*
Age				**adult**	**adult**
Mass (*kg*)				**70.44**	**59.15**
Height (*cm*)				**170**	**160**
Trunk+Arms (*cm*) – *lateral diameter*				**40**	**38**
Trunk (*cm*) – *antero-posterior diameter*				**25**	**19**

Body tissues

	Mass Density (kg m^3)
Soft Tissues	987
Lung	296
Bone	1486
Skin	1105

Simplified Mixtures (bone-soft tissue etc.)

Availability of the phantom for wider distribution to users: I am not responsible to answer it but I suppose YES.

NAME: **Frank W. SCHULTZ**

ADDRESS: TNO-ME, Radiological Service,
Center for Radiological Protection and Dosimetry
c/o P.O.Box 5815
NL-2280 HV Rijswijk
The Netherlands

PHONE: +31 15 842750
FAX: +31 15 843998

MODEL: GSF Male (ADAM) and Female (EVA)
TYPE: Mathematical
AGE: Adult
POPULATION: Group: European
APPLICATION FIELD: Radiation protection, Diagnostic radiology
(Calculation of organ and tissue doses, using Monte Carlo methods)
COMPUTER PROGRAM: MCNP

Description

These are mathematical models of an adult male and an adult female. The heights and masses of the whole body, as well as the masses of internal organs, are based on the ICRP Reference Man data (ICRP Report 23, 1975)

Physical dimensions

	ADAM	*EVA*
Mass (*kg*)	**70.4**	**59.2**
Height (*cm*)	**170**	**160**
Width (Trunk+Arms; *cm*)	**40.0**	**37.6**
Thickness (Trunk; *cm*)	**20.0**	**18.8**

Body tissues

	mass density ($g.cm^3$)
Skeletal tissue	**1.486**
Skin tissue	**1.105**
Soft tissue	**0.987**
Lung tissue	**0.296**

skeletal tissue includes bone, marrow and cartilage

Availability for Distribution to Users: Yes

NAME: **S. HONGO, H. TAKESHITA, H. YAMAGUCHI, S. IWAI** (MAPI),
K. IWAI (Nihon University)

ADDRESS: National Institute of Radiological Sciences, 9-1 Anagawa 4-chome,
Inage-ku, Chiba-shi, JAPAN 263
PHONE: +81 43 251 2111
FAX: +81 43 290 1112
E-MAIL: s_hongo@nirs.go.jp

MODEL: Modified phantoms based on Cristy phantoms [1]
TYPE: Mathematical phantoms and their tomographic expressions
AGE: N.B., 1, 5, 10, 15, Adult (Male and Female)
POPULATION: Japanese
PACKAGE: Japanese_par (all parameters in terms of the Cristy's phantom)

Description

Study to build mathematical phantoms for Japanese public has been carried out by using the ORNL mathematical phantoms [1].

Japanese data on physics are compiled with measured and evaluated values [2].

This study used only its measured values of organ mass and external measures of body, and set the values for the ages, *NEW BORN (N.B), 1-*, *5-*, *10-*, *15-YEAR OLD*, and *ADULT*, by weighting populations of age categories. These values, as shown in Table 1, are the target values which we tried to establish in the phantoms. The processes to find proper parameters that define geometry of an organ based on these mass data were trial and errors.

The final results are shown in Table 2. They are realised mass values in the phantoms.

The values in the parenthesis of Table 1 are the standard deviations of the measured and age categorised processes, and those in Table 2 are the ratios of the realised to measured values. In the tables, *HEIGHT* and *SITHEIGHT* are in unit *cm*, *BODY* in *kg* and others in *gram*. We assume the same atomic compositions of tissues and bone as the Cristy's.

Physical dimensions

Table 1
Mass of organs based on measured values

JAPANESE MALE

ORGAN	N.B	1	5	10	15	ADULT
ADRENAL	4.3 ()	4.4 (40)	5.9 (54)	9.0 (51)	11.8 (30)	14.5 (43)
BRAIN	717.1 ()	1187.1 (15)	1388.5 (13)	1480.2 (12)	1465.4 (09)	1424.9 (08)
HEART	39.2 ()	61.6 (23)	105.2 (28)	174.1 (31)	276.7 (10)	354.1 (21)
KIDNEY	47.3 ()	78.3 (45)	123.5 (55)	180.0 (32)	258.2 (24)	313.6 (34)
LIVER	262.1 ()	414.1 (30)	593.7 (29)	869.8 (22)	1235.0 (17)	1497.4 (23)
LUNG	127.1 ()	215.1 (43)	292.0 (41)	504.8 (14)	1022.6 (21)	1146.3 (45)
TESTS	2.8 ()	3.0 (160)	3.3 (40)	6.8 (86)	28.9 (46)	35.7 (42)
PANCREAS	12.1 ()	33.6 (74)	40.6 (35)	64.5 (35)	101.7 (26)	129.4 (28)
SPLEEN	22.4 ()	44.6 (70)	56.0 (58)	80.1 (29)	120.4 (30)	118.6 (43)
THYMUS	23.7 ()	22.1 (74)	25.3 (38)	41.5 (43)	34.9 (33)	28.8 (55)
THYROID	2.2 ()	3.0 (53)	4.2 (35)	6.4 (33)	15.8 (28)	18.8 (33)
HEIGHT	67.2 ()	84.7 (05)	110.3 (04)	138.9 (05)	165.7 (04)	166.1 (04)
SITHEIGHT	43.8 ()	50.9 (06)	62.1 (04)	75.4 (05)	88.7 (04)	88.0 (04)
BODY	8.1 ()	12.0 (13)	19.2 (14)	34.6 (22)	55.8 (16)	62.5 (14)

JAPANESE FEMALE

ORGAN	N.B	1	5	10	15	ADULT
ADRENAL	4.5 ()	4.2 (37)	6.2 (50)	7.4 (43)	11.0 (34)	12.8 (41)
BRAIN	636.4 ()	1002.5 (28)	1226.8 (18)	1300.7 (14)	1320.7 (06)	1288.4 (08)
HEART	29.9 ()	59.4 (26)	95.7 (33)	162.4 (18)	219.0 (26)	296.2 (22)
KIDNEY	47.6 ()	67.4 (43)	96.7 (34)	182.9 (16)	249.9 (27)	264.3 (37)
LIVER	234.3 ()	356.8 (34)	499.7 (30)	868.3 (20)	1082.2 (26)	1280.7 (26)
LUNG	112.8 ()	200.7 (36)	287.2 (46)	435.3 (39)	675.8 (26)	854.8 (43)
PANCREAS	17.3 ()	23.4 (28)	37.4 (22)	58.8 (23)	86.1 (21)	108.6 (27)
SPLEEN	19.0 ()	31.0 (34)	57.0 (38)	76.8 (31)	92.7 (45)	106.5 (44)
THYMUS	21.9 ()	21.8 (47)	16.1 (61)	26.8 (25)	27.7 (72)	23.4 (44)
THYROID	2.4 ()	3.5 (106)	5.1 (24)	8.9 (36)	13.5 (20)	16.4 (36)
HEIGHT	65.9 ()	83.8 (06)	109.4 (05)	139.5 (05)	156.4 (03)	152.5 (04)
SITHEIGHT	43.0 ()	50.2 (08)	61.8 (04)	75.4 (05)	88.7 (04)	82.2 (04)

BODY	7.8 ()	11.3 (13)	18.8 (15)	34.3 (20)	49.5 (13)	51.8 (15)

Table 2
Mass of organs realised in phantoms

JAPANESE MALE

ORGAN	1	5	10	15	ADULT
ADRENAL	2.8 (0.65)	4.4 (0.75)	7.6 (0.84)	12.6 (1.07)	14.5 (1.13)
BRAIN	884.0 (0.74)	1260.0 (0.91)	1360.0 (0.92)	1410.0 (0.96)	1420.0 (1.00)
HEART	55.2 (0.90)	85.7 (0.81)	147.2 (0.85)	245.0 (0.89)	319.0 (0.90)
KIDNEY	52.2 (0.67)	81.1 (0.66)	139.3 (0.77)	231.8 (0.90)	301.9 (0.96)
LIVER	333.6 (0.81)	518.2. (0.87)	889.9 (1.02)	1480.9 (1.20)	1928.3 (1.29)
LUNG	174.7 (0.81)	271.3 (0.93)	465.9 (0.92)	775.3 (0.76)	1009.6 (0.88)
PANCREAS	16.5 (0.49)	25.6 (0.63)	43.9 (0.68)	73.1 (0.72)	95.2 (0.74)
SPLEEN	32.0 (0.72)	49.7 (0.89)	85.3 (1.06)	141.9 (1.18)	184.7 (1.56)
TESTS	6.8 (2.28)	10.6 (3.21)	18.2 (2.68)	30.3 (1.05)	39.5 (1.11)
THYMUS	3.7 (0.17)	5.7 (0.22)	9.7 (0.23)	16.2 (0.46)	21.1 (0.73)
THYROID	3.6 (1.21)	5.6 (1.34)	9.6 (1.51)	16.0 (1.02)	20.9 (1.11)
HEIGHT	84.7 (1.00)	110.3 (1.00)	138.9 (1.00)	165.7 (1.00)	166.1 (1.00)
SITHEIGHT	50.9 (1.00)	62.1 (1.00)	75.4 (1.00)	88.7 (1.00)	88.0 (1.00)
BODY	12.0 (1.00)	19.2 (1.00)	34.6 (1.00)	55.8 (1.00)	62.5 (1.00)

JAPANESE FEMALE

ORGAN	1	5	10	15	ADULT
ADRENAL	2.6 (0.62)	4.2 (0.68)	7.5 (1.02)	12.5 (1.14)	12.7 (0.99)
BRAIN	884.0 (0.88)	1260.0 (1.03)	1360.0 (1.05)	1410.0 (1.07)	1420.0 (1.10)
HEART	50.6 (0.85)	81.3 (0.85)	146.0 (0.90)	242.2 (1.11)	245.7 (0.83)
KIDNEY	47.8 (0.71)	76.9 (0.80)	138.1 (0.76)	229.2 (0.92)	232.5 (0.88)
LIVER	305.6 (0.86)	491.2 (0.98)	882.3 (1.02)	1463.8 (1.35)	1485.1 (1.16)
LUNG	160.0 (0.80)	257.2 (0.90)	461.9 (1.06)	766.4 (1.13)	777.5 (0.91)
PANCREAS	15.1 (0.64)	24.3 (0.65)	43.6 (0.74)	72.3 (0.84)	73.3 (0.68)
SPLEEN	29.3 (0.94)	47.1 (0.83)	84.5 (1.10)	140.3 (1.51)	142.3 (1.34)
THYMUS	3.3 (0.15)	5.4 (0.33)	9.7 (0.36)	16.0 (0.58)	16.3 (0.69)
THYROID	3.3 (0.95)	5.3 (1.04)	9.6 (1.07)	15.9 (1.18)	16.1 (0.98)
HEIGHT	83.8 (1.00)	109.4 (1.00)	139.5 (1.00)	156.4 (1.00)	152.5 (1.00)
SITHEIGHT	50.2 (1.00)	61.8 (1.00)	75.4 (1.00)	88.7 (1.00)	82.2 (1.00)
BODY	11.3 (1.00)	18.8 (1.00)	34.3 (1.00)	49.5 (1.00)	51.8 (1.00)

Maria ZANKL

NAME: **Maria ZANKL**

ADDRESS: GSF - Forschungszentrum für Umwelt und Gesundheit
Institut fuer Strahlenschutz
Neuherberg, Postfach 1129
D - 85758 Oberschleissheim
PHONE: +49 89 3187-2792
FAX: +49 89 3187-3373
E-MAIL: zankl@gsf.de

MATHEMATICAL ADULT

MODEL: GSF male and female, ADAM and EVA
TYPE: mathematical
AGE: adult
POPULATION: European or European Ancestry (ICRP23 Reference Man)
APPLICATION FIELD: Radiation protection, diagnosis, (with restrictions also therapy)
COMPUTER PROGRAM:

a) "home-made"
actually derived from the ALGAM code written by Warner and Craig, Oak Ridge National Laboratory (1968);

b) EGS4
by Dr. Keith Wise
Australian Radiation Laboratory
Dept. of Health, Housing, Local Government and Community Services
Lower Plenty Road
Yallambie
Victoria 3085

Description

Mathematical models of an adult male and an adult female. Heights and masses of whole bodies as well as masses of internal organs based on ICRP Reference Man data (ICRP Publication 23, 1975)

Physical dimensions

	ADAM	*EVA*
Mass (*kg*)	**69.9**	**58.8**
Height (*cm*)	**170**	**160**
Trunk+Arms (*cm*) – *lat.diam.*	**40.0**	**37.6**

Trunk (*cm*) – *a.p. diameter*	**20.0**	**18.8**

Body tissues

	Mass Density (kg m^3)
Soft tissue	**987**
Lung	**296**
Skeleton	**1486**
Red bone marrow	**987**
Skin	**1105**

The skeleton is a homogeneous mixture of osseous tissue, marrow, cartilage and certain peri-articular tissue.

Availability of the phantoms for wider distribution to users: Yes

TOMOGRAPHIC PAEDIATRIC MODELS

MODEL:	GSF BABY and CHILD
TYPE:	Tomographic
AGE:	8 weeks (Baby) and 7 years (Child)
POPULATION:	European
APPLICATION FIELD:	Radiation protection, diagnosis, (with restrictions also therapy)
COMPUTER PROGRAM:	"home-made" (see above)

Description

Tomographic models of an eight week old baby and a seven year old child, obtained from whole body computed tomographic (CT) scans. Size and mass of model can be adjusted by changing size of volume elements.

Physical dimensions

	Baby	*Child*
Age	**8 weeks**	**7 years**
Mass (*kg*)	**4.2**	**21.7**
Height (*cm*)	**57.0**	**115**
Trunk+Arms (*cm*) – *lat.diam.*	**21.8**	**33.1**
Trunk (*cm*) – *a.p. diameter*	**12.2**	**17.6**

Body tissues

	Mass density (kg m^3)
Soft tissue	**987 – 1050**
Lung	**296**
Cortical bone	**1765**
Red bone marrow (BABY)	**1027**
Red bone marrow (CHILD)	**1006**
Skin	**1105**

Availability of the phantoms for wider distribution to users: No

George ZUBAL

NAME: **George ZUBAL** PhD

ADDRESS: Dept. of Diagnostic Radiology
Yale School of Medicine
333 Cedar Street
New Haven, CT 06510
PHONE: (203) 785-4911
FAX: (203) 737-4273
E-MAIL: Zubal@BioMed.Med.Yale.Edu
Zubal@Venus.YCC.Yale.Edu

MODEL: Male
TYPE: Tomographic = voxel-based
AGE: Adult
POPULATION GROUP: European
APPLICATION FIELD: Diagnosis
COMPUTER PROGRAM: ALGAMP (original MIRD S-factor program, now converted to diagnosis)

Physical dimensions

	Baby	*Child*	*Adult*
Age	**8 weeks**	**7 years**	**30 years**
Mass(*kg*)	**4.2**	**21.7**	**70**
Height (*cm*)	**57**	**115**	**170**
Trunk+Arms (*cm*) – *Lateral diameter*	**21.8**	**33.1**	**48**
Trunk (*cm*) – *Antero-posterior diameter*	**12.2**	**17.6**	**22**

Body tissues

	Mass Density (kg m^3)
Soft Tissues	**987-1050**
Lung	**296**
Cortical Bone	**1765**
Bone Marrow	**1006**

Simplified Mixtures (bone-soft tissue etc.)

Availability of the phantom for wider distribution to users: YES

Table 3

Specifications of selected computational models – Digitised mathematical model [1]

Description

This is a conversion of the mathematical model of Snyder et al. (1969) into a model consisting of cubic volume elements with organ identification symbols. it represents a hermaphrodite adult. Height and mass of the whole body, as well as the masses of the internal organs, are based on the ICRP Reference Man data (ICRP, 1975).

Physical Dimensions

Height	**173** cm
Trunk + arm – *Lateral diameter*	**40.0** cm
Trunk – *Antero-posterior diameter*	**20.0** cm

Applications

This model is the basis for more realistic models based on medical images obtained by CT or MRI for absorbed dose calculations, especially in radiotherapy, using Monte Carlo methods.

[1] H. Yamaguchi et al., 1985.
Contact Address: National Institute of Radiological Sciences, Division of Physics, 4-9-1, Anagawa, Chiba, 260 Japan.

Table 4
Specifications of selected computational models –
GSFa adult male and female mathematical models (Adam and Eva)[2]

Description

These are mathematical models of an adult male and an adult female. The heights and masses of the whole bodies, as well as the masses of the internal organs, are based on the ICRP Reference Man data (ICRP, 1975).

a. GSF - Forschungszentrum für Umwelt und Gesundheit, Germany

Physical Dimensions

	ADAM	*EVA*
Mass (*kg*)	**69.9**	**58.8**
Height (*cm*)	**170**	**160**
Trunk + arms (*cm*) – *Lateral diameter*	**40.0**	**37.6**
Trunk (*cm*) – *Antero-posterior diameter*	**20.0**	**18.8**

Body Tissues

	Mass Density (kg/m^3)
Soft tissue	**978**
Lung	**296**
Whole skeleton b	**1486**
Skin	**1105**

b. include osseous tissue, marrow, cartilage and certain peri-articular tissue

Applications

For the calculation of organ and tissue doses from external photon irradiation in x ray diagnosis, radiotherapy, occupational and environmental exposures, using Monte Carlo methods.

[2] R. Kramer et al., 1982b.
Contact Address: GSF – Forschungszentrum für Umwelt und Gesundheit, Ingolstädter Landstrasse 1, D-8042 Neuherberg, Germany.

Table 5

Specifications of selected computational models –GSFa paediatric tomographic models (Baby and Child)[3]

Description

These tomographic models of an eight week old baby and a seven year old child have been obtained from whole body computed tomography (CT) scans. Size and mass of each model can be adjusted by changing size of volume elements (voxels).

a. GSF - Forschungszentrum für Umwelt und Gesundheit, Germany

Physical Dimensions

	Baby	*Child*
Age	**8 weeks**	**7 years**
Mass (*kg*)	**4.2**	**21.7**
Height (*cm*)	**57.0**	**115**
Trunk + arms (*cm*) – *Lateral diameter*	**21.8**	**33.1**
Trunk (*cm*) – *Antero-posterior diameter*	**12.2**	**17.6**

All dimensions may be varied

Body Tissues

	Mass Density (kg/m^3)
Soft tissue	**987-1050**
Lung	**296**
Cortical bone	**1765**
Bone marrow (Baby)	**1027**
Bone marrow (Child)	**1006**
Skin	**1105**

Applications

For the calculation of organ and tissue doses and absorbed-dose distributions from external photon irradiation in x-ray diagnosis, radiotherapy, occupational and environmental exposures, using Monte Carlo methods.

[3] G. Williams et al. 1986b; Zankl et al., 1988; Veit et al., 1989.
Contact Address: GSF - Forschungszentrum für Umwelt und Gesundheit, Ingolstädter Landstrasse 1, D-8042 Neuherberg, Germany.

Table 6

Specifications of selected computational models – ICRU spherical reference mathematical model[4]

Description

This mathematical model describes a sphere of 30 cm diameter.

Physical Dimensions

Mass (*kg*)	**14.14**
Diameter (a) (*cm*)	**30**

Tissues

Average soft tissue having elemental composition (%, by mass):

H	**10.1**
C	**11.1**
N	**2.6**
O	**76.2**

Mass Density: 1000 kg/m^3

Applications

Reference computational model used in radiation protection for the definition of operation al quantities for dose equivalent.

[4] ICRU Reports 33 (ICRU, 1980) and 39 (ICRU, 1985a).
Contact Address: International Commission on Radiation Units and Measurements, 7910 Woodmont Avenue, Bethesda, Maryland 20814, U.S.A.

Table 7

Specifications of selected computational models – JAERIa Japanese pregnant woman mathematical model [5]

Description

Mathematical model of a pregnant Japanese woman at various stages of pregnancy. The model is based on the model of Snyder et al. (1969), but with reduced size and modified abdomen.

a. Japanese Atomic Energy Research Institute

Physical Dimensions

Female body

Height (*cm*)	**155**
Mass (*kg*)	**51.0**

Embryo or foetus

Gestation (*month*)	**1-2**	**6**	**9**
Length (*cm*)	**8.6**	**21.0**	**31.6**
Mass (*kg*)	**0.048**	**0.600**	**2.400**

Applications

For the calculation of absorbed doses to the embryo or foetus from exposure to a radioactive plume accidentally released from a nuclear reactor, using Monte Carlo methods.

[5] M. Kai, 1985.
Contact Address: Japan Atomic Energy Research Institute,
Department of Environmental Safety Research,
Tokai-mura, Naka-gun, Ibaraki-ken, 319-11 Japan.

Table 8

Specifications of selected computational models – JAERI mathematical model (VADMAP)[6]

Description

Mathematical model based on the formulae from Cristy (1980), but with individually variable external and internal dimensions as well as individually variable tissue mass densities.

a. Japan Atomic Energy Research Institute

Physical Dimensions

Variable from new-born to adult.

Body Tissues

	Mass Density (mg/m^3)
Soft tissue	variable
Lung	variable
Whole skeleton b	variable

b. includes osseous tissue, marrow, cartilage and certain peri-aticular tissue

Applications

For the calculation of specific absorbed fractions from monoenergetic photons for selected source and target organ combinations, using the Monte Carlo code VADMAP.

[6] H. Yamaguchi et al., 1987.
Contact Address: Japan Atomic Energy Research Institute,
Department of Environmental Safety Research,
Tokai-mura, Naka-gun, Ibaraki-ken, 319-11 Japan.

Table 9

Specifications of selected computational models – MIRDa-5 adult mathematical model[7]

Description

The model represents a hermaphrodite adult. Height and mass of the whole body, as well as the masses of the internal organs, are based on the ICRP Reference Man data (ICRP, 1975).

a. Medical Internal Radiation Dose Committee

Physical Dimensions

Mass	**70** kg
Height	**174** cm
Trunk + arms – *Lateral diameter*	**40.0** cm
Trunk – *Antero-Posterior diameter*	**20.0** cm

Body Tissues

	Mass Density (kg/m^3)
Soft tissue	**1000**
Lung	**300**
Whole skeleton b	**1500**

b. includes osseous tissue, marrow, cartilage and certain peri-articular tissue

Applications

For the calculation of specific absorbed fractions from monoenergetic photons for selected source and target organ combinations, using Monte Carlo methods.

[7] W.S. Snyder et al., 1969, 1978.
Contact Address: Oak Ridge National Laboratory, Health Physics Division, Oak Ridge, Tennessee 37830, U.S.A.

Table 10

Specifications of selected computational models – ORNLa paediatric and adult mathematical models[8]

Description

The model represents a hermaphrodite adult. The total body mass and height are based on anatomical data from several Japanese studies.

a. Oak Ridge National Laboratory, U.S.A.

Physical Dimensions

Mass	**55.0** kg
Height	**160** cm
Trunk + arms – *Lateral diameter*	**34.5** cm
Trunk – *Antero-posterior diameter*	**19.6** cm

Body Tissues

	Mass Density (kg/m^3)
Soft tissue	**1040**
Lung	**296**
Whole skeleton b	**1400**

b. includes osseous tissue, marrow, cartilage and certain peri-articular tissue

Applications

For the calculation of the absorbed dose received by survivors of the 1945 bombings of Hiroshima and Nagasaki and for the calculation of organ and issue doses from diagnostic and therapeutic radiation practices in Japan

[8] G.D. Kerr et al., 1976; Cristy, 1985.

Contact Address: Japan Atomic Energy Research Institute,
Department of Environmental Safety Research,
Tokai-mura, Naka-gun, Ibaraki-ken, 319-11 Japan.

Table 11

Specifications of selected computational models – ORNLa paediatric and adult mathematical models[9]

Description

This group of mathematical models represent an adult and children of various ages. The dimensions of the body regions are determined from anthropological data. The organ volumes are based on the ICRP Reference Mandate (ICRP, 1975).

a. Oak Ridge National Laboratory, U.S.A.

Physical Dimensions

Age (*years*)	**New-born**	**1**	**5**
Mass (*kg*)	**3.60**	**9.72**	**19.8**
Height (*cm*)	**51.5**	**75.0**	**109.0**
Trunk + arms (*cm*) – *Lateral diameter*	**12.7**	**17.6**	**22.9**
Trunk (*cm*) – *Antero-posterior diameter*	**9.8**	**13.0**	**15.0**
Age (years)	**10**	**15b**	**Adult (male)**
Mass (kg)	**33.2**	**56.8**	**73.7**
Height (cm)	**139**	**164**	**174**
Trunk + arms (*cm*) – *Lateral diameter*	**27.8**	**34.5**	**40.0**
Trunk (*cm*) – *Antero-posterior diameter*	**16.8**	**19.6**	**20.0**

b. also represents adult female

Body Tissues

	Mass Density (kg/m^3)
Soft tissue	**1040**
Lung	**296**
Whole skeleton	
New-born	**1220**
All others	**1400**

c. includes osseous tissue, marrow, cartilage and certain peri-articular tissue

Applications

The models are used for the calculation of specific absorbed fractions from monoenergetic photons for selected source and target organ combinations, using Monte Carlo Methods.

[9] M. Chisty, 1980; Cristy and Eckerman, 1987a.
Contact Address: Oak Ridge National Laboratory, Health and Safety Research Division
Oak Ridge, Tennessee 37831-6383, USA.

Table 12

Specifications of selected computational models – SAICa adult contour mathematical model[10]

Description

The model represents a North American adult male. The geometry and physical dimensions are based on a commercial anthropomorphic phantom. The model is represented as a three-dimensional array of volume elements.

a. Science Applications International Corporation

Physical Dimensions

Mass	**74** kg
Height	**174** cm
Chest – *Lateral*	**32.8** cm
Chest width – *Antero-posterior*	**20.8** cm

Applications

For the calculation of fluence and absorbed dose in target organs or other regions of interest from external neutron and gamma radiation.

[10] D.C. Kaul et al., 1987.
Contact Address: Science Applications International Corporation,
10260 Campus Point Drive, MS33, San Diego , CA 92121, U.S.A.

Table 13

Specifications of selected computational models – SAICa adult mathematical model[11]

Description

The model represents a North American adult male. The total body mass and height are based on a commercial anthropomorphic phantom. Arms and legs are adjustable to the sitting or kneeling position.

a. Science Applications International Corporation

Physical Dimensions

Mass	**73.6** kg
Height	**174** cm
Trunk + arms – *Lateral diameter*	**34.4** cm
Trunk – *Antero-posterior diameter*	**20** cm

Body Tissues

	Mass Density (mg/m^3)
Soft tissues	**1040**
Lung	**296**
Whole skeleton b	**1400**

b. includes osseous tissue, marrow, and cartilage

Applications

For the calculation of fluence and absorbed dose in target organs or other regions of interest from external neutron and gamma radiation.

[11] D.C. Kaul et al., 1987.
Contact Address: Science Applications International Corporation,
10260 Campus Point Drive, MS33, San Diego, CA 92121, U.S.A.

Table 14

Specifications of selected computational models – SAICa Japanese paediatric and adult mathematical model [12]

Description

The model represents an hermaphrodite Japanese adult and children of various ages. The models are based on anatomical data from several studies of Japanese populations. Arms and legs are adjustable to the sitting or kneeling positions.

a. Science Applications International Corporation

Physical Dimensions

Age (*years*)	**<3**	**3 - 12**	**Adult**
Mass *kg*	**9.7**	**19.8**	**55.0**
Height (*cm*)	**74.3**	**108.4**	**163.9**
Chest width (*cm*) – *Lateral*	**15.0**	**19.5**	**29.3**
Chest width (*cm*) – *Antero-posterior*	**12.7**	**14.7**	**19.**2

Body Tissues

	Mass Density (mg/m^3)
Soft tissues	**1040**
Lung	**296**
Whole skeleton b	**1400**

b. includes osseous tissue, marrow, and cartilage

Applications

The models were used for the calculation of neutron and gamma ray fluences and absorbed doses in fifteen organs of survivors of the 1945 bombings of Hiroshima and Nagasaki. They are also used for the calculation of organ and tissue doses from diagnostic and therapeutic practices in Japan.

[12] D.C. Kaul et al., 1987.
Contact Address: Science Applications International Corporation,
10260 Campus Point Drive, MS33, San Diego, CA 92121, U.S.A.

References

Satoshi IWAI

[1] Y. Yamaguchi, "DEEP Code to Calculated Dose Equivalents in Human Phantom for External Photon Exposure by Monte Carlo", JAERI-M 90-235 (1990).

[2] M. Christy and K.F. Eckeman, "Specific Absorbed Fraction of Energy at Various Ages from Internal Photon Sources", ORNL/TM-8381/V1-V7 (1987).

[3] W.S. Snyder, M.R. Ford, and G.G. Warner, "Estimates of Specific Absorbed Fractions for Photon Sources Uniformly Distributed in Various Organs of Heterogeneous Phantom" NM/MIRD Pamphlet No. 5 (revised), J. Nucl. Med., 19, Supplement: 5-67 (1987).

[4] C.A. Lewis and R.E. Ellis, "Additions to the Snyder Mathematical Phantom", Phys. Med. Biol. Vol. 24, No. 5 (1979) 1019-1024.

[5] J.T. West and M.B. Emmett, "MARS: A Multiple Array System Using Combinatorial Geometry", NUREG/CR-0200, volume 3, section M9, ORNL/NUREG/CSD-2/V3/R2 (1984).

[6] S. Iwai, T. Uehara, O. Sato, N. Yoshizawa, S. Furihata, S. Tanaka, and Y. Sakamoto, "Evaluation of Effective Dose Irradiated by High Energy Radiation", Proc. of Specialists' Meeting on Shielding Aspects of Accelerators, and Irradiation Facilities, 28-29 Apr. 1994, Arlington, Texas, U.S.A. (OECD/NEA/NSC)

Vladimir MARES

R.Kramer, M.Zankl, G.Williams and G.Drexler, "The Calculation of Dose from External Photon Exposures Using Reference Human Phantoms and Monte Carlo Methods", GSF-Report S-885 (1982).

M.Zankl, N.Petoussi and G.Drexler, "Effective Dose and Effective Dose Equivalent The Impact of the New ICRP Definition for External Photon Irradiation", Health Phys. 62(5) 395-399 (1992).

G.Leuthold, V.Mares and H.Schraube, "Computed Organ Dose Equivalents for Neutrons ...", GSF-Report, in preparation.

Frank W. SCHULTZ

R. Kramer, M. Zankl, G. Williams, and G. Drexler, "The Calculation of Dose from External Photon Exposures using Reference Human Phantoms and Monte Carlo Methods; Part I: The Male (ADAM)

and Female (EVA) Adult Mathematical Phantoms", GSF Bericht S-885 (M nchen: Institut für Strahlenschutz, Gesellschaft für Strahlen- und Umweltforschung mbH) (1986).

[1] M. Cristy and K. F. Ekerman, "Specific Absorbed Fractions of Energy at Various Ages from Internal Photon Sources", Oak Ridge National Laboratory, ORNL/TM-8381/V1 (1987).

[2] G. Tanaka, "Anatomical Data, Safety Analysis Report", Volume 1, NIRS -M-85,(1992).

Maria ZANKL

R. Kramer, M. Zankl, G. Williams, G. Drexler, "The Calculation of Dose from External Photon Exposures using Reference Human Phantoms and Monte Carlo Methods, Part I: The Male (ADAM) and Female (EVA) Adult Mathematical Phantoms. GSF-Bericht S-885 (GSF – Forschungszentrum für Umwelt und Gesundheit, Neuherberg) (1982).

M. Zankl, R. Veit, G. Williams, K. Schneider, H. Fendel, N. Petoussi, G. Drexler, "The Construction of Computer Tomographic Phantoms and Their Application in Radiology and Radiation Protection", Radiat. Environ. Biophys. 27, 153-164 (1988).

R. Veit, M. Zankl, N. Petoussi, E. Mannweiler, G. Williams, G. Drexler, "Voxel Anthropomorphic Models, Part I: Construction Technique and Description of Models of an Eight-week-old Baby and a Seven-year-old Child", GSF-Bericht 3/89 (GSF – Forschungszentrum für Umwelt und Gesundheit, Neuherberg) (1989).

George ZUBAL

I.G. Zubal et. al.,"Computerized 3D Segmented Human Anatomy", Med Phys 21 (2), p.299 -302, February 1994.

Session V

MODELLING CODES AND DATA – RECENT RELEASES, COMPILATIONS, DEVELOPMENT REQUIRED, SHARING

CHAIR

Robert ROUSSIN

CO-CHAIR

Hideo HIRAYAMA

STATUS REPORT ON THE COLLECTION OF COMPUTER CODES AND DATA FOR ACCELERATOR SHIELD MODELLING

Robert W. Roussin
ORNL/RSIC, U.S.A.

Enrico Sartori and *Pedro Vaz*
OECD/NEA

Abstract

During the Specialists' Meeting on Shielding Aspects of Accelerators, Targets and Irradiation Facilities held in Arlington, Texas, on 28-29 April 1994, it was felt that the NEA-DB [1] and RSIC[2] can provide beneficial services to the accelerator shielding specialists by packaging and disseminating modern frozen versions of the transport and auxiliary codes and data libraries in common use. At the same time it was recommended that these two Centers try to obtain new or updated versions of a number of computer codes, some performing low-energy neutron transport, others modelling hadronic and electromagnetic cascades or implementing intermediate energy nuclear models. This note summarizes the progress made since then in collecting new computer codes and data libraries. An exhaustive survey is also presented in the form of tables displaying the computer codes available from the two Centers in the areas previously mentioned. These tables supersede the ones presented in the Arlington Specialists' Meeting [3].

---

1 Data Bank of the Nuclear Energy Agency of the Organisation for Economic Co-operation and Development (O.E.C.D), in Paris , FRANCE.

2 Radiation Shielding Information Centre at the Oak Ridge National Laboratory (O.R.N.L.), in Oak Ridge, Tennessee, U.S.A.

3 Proceedings of the Specialists' Meeting on Shielding Aspects of Accelerators, Targets and Irradiation Facilities, held in Arlington, Texas (U.S.A.) on 28-29 April 1994, published as an OECD document ISBN 92-64-14327-0.

1. Introduction

RSIC and the NEA DB collect, test and distribute computer programs and data in the field of nuclear applications. This activity is coordinated with other similar centers in the United States (ESTSC, NNDC), Japan (RIST) and outside the OECD area through an arrangement with the IAEA.

This information is shared worldwide for the benefit of scientists and engineers working on the safe and economic use of nuclear technology. Among the fields RSIC is specialised, technology for radiation transport holds an eminent place; the NEA DB covers instead a wider range of topics with less specific expertise. The two centers share to a large extent the same programs through a long standing cooperative arrangement.

Major emphasis has been given in the past to nuclear energy applications. In order to respond to needs expressed by new communities of users, covering other aspects of nuclear technology, special efforts were made to acquire programs and data in their fields of interest. Shielding aspects of accelerators and targets has in fact received attention over the last several years. It is the intention of both centers to devote additional effort so that state-of-the-art technology in this field is shared among the specialists.

2. Radiation Shielding Information Center (RSIC)

RSIC is embedded in the Computational, Physics and Engineering Division of the directorate for Computing, Robotics and Education (CRE) at ORNL. That Division is noted for its role as a leader in the development of radiation transport technology throughout the years. It is very beneficial for RSIC to be located with such an organisation so that staff members have close proximity to these major developments and the transfer of such technology is enhanced by a climate of close cooperation.

In practice, RSIC is an information analysis center following the concepts suggested by Alvin Weinberg in 1963 [1]. It is staffed by scientists, engineers, computer specialists, and support personnel. While being physically located at ORNL, it is embedded in the national research and development of its sponsors and interacts dynamically with contributors and users.

It was founded in 1962 by the U.S. Atomic Energy Commission to provide support for its reactor research programmes. Over the years the scope of RSIC has broadened to include radiation transport from nuclear weapons, radioisotopes, accelerators, fusion reactors, nuclear waste. Current sponsors include the U.S. Department of Energy (Nuclear Energy, Fusion, Defense Programs, Environmental), and the Defense Nuclear Agency.

3. The NEA Data Bank (NEA DB)

The NEA Data Bank is part of the OECD Nuclear Energy Agency, financed by 19 of the 25 OECD countries (Austria, Belgium, Denmark, Finland, France, Germany, Greece, Italy, Japan, Republic of Korea, Mexico, The Netherlands, Norway, Portugal, Spain, Sweden, Switzerland, Turkey, United Kingdom). A cooperative arrangement is in force, covering the exchange of computer programs and data between these countries, Canada and USA. Exchange with other countries is ruled by an arrangement with the International Atomic Energy Agency.

The work programme is approved yearly by the Nuclear Science Committee, one of the NEA Committees (others cover Nuclear Safety, Development, Waste Management).

The staff consists of physicists, engineers, computing experts and is international. In order to stay in close contact with the scientific community and engineers in the member countries, modern communication systems are extensively used.

The Computer Program and Data Services were set up in 1964 following the same objectives and standards established at the centers in the USA.

The primary objective as stated in the original statute was "to improve the communication between the originators of computer programs and data, and the using scientist and engineers so that the most efficient and economic use in the field of atomic energy may be made of the numerous large and expensive computers ..." . Evolution in the last thirty years has not changed this objective except that today "expensive computers" should read rather "expensive to develop computer codes".

References

[1] R.W.Roussin and E.Sartori, “Sharing of Computer Codes and Data for Accelerator Shield Modelling”, Proceedings of the Specialists’ Meeting on *Shielding Aspects of Accelerators, Targets and Irradiation Facilities*, Arlington, Texas, U.S.A., on 28-29 April 1994, published as OECD document ISBN 92-64-14327-0

Table 1 ***List of programs and data in alphabetical order***

Programs marked (*) or (**) in the following table, represent additions to the corresponding table of [1]

(*) Programs available

(**) Programs known but not available

Name	***Identification***	***Function***
ACTIV-87(*)	IAEA1275	Library with fast neutron activation x-sections
AIRSCAT	CCC-0341	dose rate from gamma air scattering, single scat. approx.
ALBEDO	NEA 1353	gamma, neutron attenuation in air ducts
ALDOSE(*)	CCC-0577	Calculates of absorbed dose and dose equivalent rates as function of depth in water irradiated by alpha source
ALICE91	PSR-0146	precompound/compound nuclear decay model
ALPHN(*)	CCC-0612	Calculates the (alpha, n) production rate in a mixture receiving alpha particles from emitting actinides
AMALTHEE	NEA 0675	emission spectra for n, p, d, h3, he3, alpha reaction
ANISN	CCC-0254	1-D Sn, n, gamma transport in slab, cylinder, sphere
ASOP	CCC-0126	1-D Sn shield calculation
ASTAR(*)	IAEA1282	Calculates stopping power and range for alphas
ASTROS	CCC-0073	primary/secondary proton dose in sphere/slab tissue
AUJP	IAEA0906	optical potential parameters search by chi**2 method
BALTORO	NEA 0675	n, gamma transport perturbation from MORSE,ANISN calculation
BERMUDA	NEA 0949	1-D,2-D,3-D n. gamma transport for shielding
BETA-2B	CCC-0117	MC time-dep bremsstrahlung, electron transport
BREESE	PSR-0143	distribution function for MORSE from albedo data
BREMRAD	CCC-0031	external/internal bremsstrahlung
BRHGAM	CCC-0350	MC absorbed dose from x-rays in phantom
CADE	NEA 1020	multiple particle emission xsec by Weisskopf-Ewing
CALOR89	CCC-0610	MC system for design, analysis of calorimeter system
CALOR93		MC system for design, analysis of calorimet er system
CAMERA	CCC-0240	radiation transport and computerized man model
CARP-82	PSR-0131	currents for BREESE from DOT flux
CASCADE	CCC-0176	high energy electron-photon transport in matter
CASIM	NESC0742	MC high energy cascades in complex shields
CEM95(*)	IAEA1247	MC calculation of nucl. reations (Cascade Exciton Model)
CENDL(*)	IAEA1256	Chinese Evaluated Nuclear Data Library, namely the Optical Model Parameters for 6 types of projectiles (neutron, proton, deuteron, triton, He3 and He4)
CEPXS/ONELD	CCC-0544	1-D coupled electron photon multigroup transport
CFUP1	IAEA1266	n, charged-particle reaction of fissile nuclei E<33 MeV
CHARGE-2/C	CCC-0070	electron, p, heavy particle flux/dose behind shield
CHUCK	USCD1021	n, charged particle xsec, coupled channel model
CMUP2	IAEA1265	reaction xsec for n ,p, d, t, he3, he4, E<50 MeV
COLLI-PTB	NEA 1126	MC n fluence spectra for 3-D collimator system
COMNUC3B	PSR-0302	compound nucleus interaction in n reactions
COVFILES(*)	DLC-0091	Library of neutron x-sections covariance data, useful to estimate radiation damage or heating
DANTSYS(*)	CCC-0547	1-D, 2-D, 3-D Sn neutron, photon transport
DASH	CCC-0366	void tracing Sn - MC coupling with fluxes from DOT
DCTDOS	CCC-0520	n,gamma penetration in composite duct system

DDCS(*)	IAEA1290	Calculation of neutron, proton, deuteron, triton, He3, and alpha induced reations of medium heavy nuclei in the energy range up to 50 MeV
DISDOS	CCC-0170	dose from external photons in phantom

Name	*Identification*	*Function*
DOMINO	PSR-0064	coupling of Sn DOT with MC MORSE
DORT	CCC-0543	1-D 2-D Sn n, photon transport with deep penetration
DOSDAT-2	DLC-0079	gamma, electron dose factors data lib. for body organs
DOSEDAT-DOE	DLC-0144	doserate factors for external photon, electron exposure
DOT	CCC-0276	2-D Sn n, photon transport with deep penetration
DROSG-87(*)	IAEA1234	Library of Legendre coefficients for neutron reactions
DUST	CCC-0453	albedo MC simulation of n streaming inducts
DWBA82	NEA 1209	Distorted Wave Born Approximation nuclear model
DWUCK-4	NESC9872	Distorted Wave Born Approximation nuclear model
E-DEP-1	CCC-0275	heavy ion energy deposition
EADL(*)	USCD1192	Library of atomic subshell and relaxation data
ECIS-95(*)	NEA 0850	Schroedinger/Dirac nuclear model with experimental fit
ECPL-86(*)	DLC-0106	evaluated charged particle cross-sections
EDMULT	NEA 0969	electron depth dose in multilayer slab absorbers
EEDL(*)	USCD1193	Electron interaction x-section from 10 eV to 100 GeV
EGS4	CCC-0331	MC electron photon shower simulation
ELBA	CCC-0119	bremsstrahlung do se from electron flux on Al shield
ELPHIC-PC	IAEA1223	statistical model MC simulation of heavy ion reaction
ELPHO	CCC-0301	MC muon, electron, positron generation from pions
ELTRAN	CCC-0155	MC 1-D electron transport
EMPIRE-MSC	IAEA1169	multistep compound nucleus/pre-equilibrium xsec
ENLOSS	PSR-0047	energy loss of charged particles
EPDL-VI/MOD(*)	USCD1187	Photon interaction x-sections library(10 eV to 100 GeV)
EPICSHOW(*)	IAEA1285	Interactive Viewing of the Electron-Photon Interaction Code (EPIC) system databases (10 eV < E < 1 GeV)
ERINNI	NEA 0815	multiple cascades emission spectra by optical model
ESTAR(*)	IAEA1282	Calculates stopping power and range for electrons
ETRAN	CCC-0107	MC electron, gamma transport with secondary radiation
EVA(*)		Codes performing the nuclear evaporation processes (working on the output from ISABEL)
EVALPLOT(*)	IAEA0852	Plots x-sections in ENDF/B format, angular and energy distributions
EVAP_F(**)		Modified version of the Dresner evaporation code (run in HETC@PSI)
EXIFONGAMMA	IAEA1211	n, alpha, proton, gamma emission spectra model
FALSTF	CCC-0351	n, gamma flux detector response outside cyl shields
FEM-RZ	NEA 0566	2-D multigroup n transport in r-z geometry
FGR-DOSE(*)	DLC-0167	Library of dose coefficients for intake and exposure to radionuclides
FLEP	DLC-0022	neutron, proton nonelastic xsec and spectra E<400MeV
FLUKA	CCC-0207	MC high energy extranuclear hadron cascades
FLUNEV-DESY		
FOTELP	CCC-0581	MC photons, electrons and positron transport
FRITIOF(**)		Hadronic cascades in high-e nergy Heavy Ion Collisions (used to be availble from the CERN Program Library)
FSMN	IAEA1264	fission spectra by compound-nucleus optical model
G33-GP	CCC-0494	multigroup gamma scattering using gp buildup-factor
GAMMONE	NEA 0268	MC gamma penetration from various geometrical sources
GEANT-CERN		
GGG-GP	CCC-0564	Multigroup gamma-ray scattering - build-up factors
GNASH-FKK(*)	PSR-0125	multi-step direct and compound and Hauser Feshbach models
GNASH-LANL	PSR-0125	pre-equilibrium/statistical xsec, emission spectra

GRACE-1	NESC0045	multigroup gamma attenuation, dose in slab

Name	*Identification*	*Function*
GRAPE	NEA 1043	precompound/compound nuclear reaction models
HELLO	DLC-0058	47 n, 21 gamma group coupled xsec from VITAMIN-C library
HERMES-KFA	NEA 1265	MC high-energy radiation transport
HETC NMTC	CCC-0178	MC high energy nucleon meson cascade transport
HETC-KFA	CCC-0496	MC high energy nucleon-meson cascades
HETC95(**)		MC high energy nucleon-meson cascades and transport
HFTT	IAEA0954	n xsec by compound-nucleus evaporation model
HIC-1	CCC-0249	MC heavy ion reactions at E>50 MeV/nucleon
HIJET(**)		Hadronic cascades in high-energy Heavy Ion Collisions (used to be availble from the CERN Program Library)
HILO86	DLC-0119	66 N, 22 gamma grp XSEC lib. for ANISN, ORNL,DORT,MORSE-CGA
HOMO(*)	IAEA1253	Program for mixing/converting libraries in ANISN format
HUGO-VI	DLC-0146	photon interaction evaluated data library ENDF-6 format
IDC	CCC-0384	ICRP dosimetric calculational system
IHEAS-BENCH(*)	NEA 1468	High energy accelerator shi elding benchmarks
IMPACTS(*)	ESTS0005	Radiological assessment code
ISABEL(*)	NEA 1413	Intranuclear cascade model allowing hydrogen and helium ions and antiprotons as projectiles (run in LAHET)
ISAJET(**)		Hadronic cascades in high-energy Heavy Ion Collisions (used to be availble from the CERN Program Library)
ISO-PC(*)	CCC-0636	Kernel integration code system for general purpose isotope shielding
ITS-3.0	CCC-0467	MC tiger system of coupled electron photon transport
JENKINS		photon, neutron dose in electron accelerator
K009	CCC-0062	Charged particle penetration - phantom
KAPSIES		quantum mechanical multi-step direct model
LA100	DLC-0168	Evaluated data library for n, p up to 100 MeV, ENDF-6 fmt
LAHET		MC nucleon, pion, muons, tritons, He-3, alpha transport
LAHIMAC	DLC-0128	neutron, gamma xsec - response fuctions, E<800MeV
LEP	DLC-0001	results from intra-nuclear cascade and evaporation
LIMES	NEA 1337	Intermediate mass fragments in heavy ion nuclear reactions
LPPC	CCC-0051	proton penetration, slab
LPSC	CCC-0064	p, n flux, spectra behind slab shield from p irradiation
LRSPC	CCC-0050	range and stopping power calculator for ions
MAGIK	CCC-0359	MC for computing induced residual activation dose rates
MAGNA	NEA 0163	dose rates from gamma source in slab or cyl shell shields
MARLOWE	PSR-0137	atomic displacement cascades in solids
MARMER	NEA 1307	point-kernel shielding, ORIGEN-S nuclide inventories
MATXS10(*)	DLC-0176	Library with 30n-12gamma energy groups for particle transport codes and high energy calculations
MATXS11(*)	DLC-0177	Library with 80n-24gamma energy groups for particle transport codes and high energy calculations
MCNP-4A	CCC-0200	MC 3-D time-dep coupled n, photon, electron transport
MCNPDAT(*)	DLC-0105	X-section data library for the MCNP-4A transport code
MCNPDAT6(*)	DLC-0181	X-section data library from ENDF/B-VI for MCNP-4A
MECC-7	CCC-0156	medium energy intra-nuclear cascade model
MENSLIB	DLC-0084	neutron 60 group xsec, E<60MeV
MERCURE-4	NEA 0351	MC 3-D gamma heating/gamma dose rate, fast flux
MEVDP	CCC-0157	radiation transport in computerized anatomical man
MICAP	PSR-0261	MC ionization chamber responses
MORSE-CGA	CCC-0474	MC n, gamma multigroup transport

MUONLM(*)	NEA 1475	Calorimeter Interaction of Muons

Name	*Identification*	*Function*
MUP-2	IAEA0907	fast n reaction xsec of medium-heavy nuclei
MUTIL(*)	NEA-1451	Calculates the asymmetry factor of the Mott scattering of electrons and positrons by point nuclei
NDEM(**)		Generates a gamma-ray source from the deexcitation of residual nuclei, assuming all particle decay modes have been exhausted (part of the HERMES system)
NESKA	NEA 1422	electron, positron scattering from point nuclei
NFCLIST(*)	ESTS0352	Radionuclide decay data tabulations (240 radionuclides)
NJOY-94(*)	PSR-0171	n, p, photon evaluated data processing system
NMTC/JAERI	NEA 0974	MC high-energy p, n, pion reactions
NUCDECAY(*)	DLC-0172	Nuclear decay data for radiation dosimetry calculations
NUCLEUS		Nuclear spallation simulation and primary products
PACE2(**)		Codes performing the nuclear evaporation pro cesses (working on the output from ISABEL)
PALLAS-2DY	NEA 0702	2-D n ,gamma transport for fixed source
PCROSS	IAEA1220	pre-equilibrium emission spectra in neutron reaction
PEGAS	IAEA1261	unified model of particle and gamma emission reactions
PELSHIE	IAEA0855	dose rates from gamma source, point-kernel method
PEQAG-2	IAEA1185	pre-equilibrium model nucleon, gamma spectra, xsec
PEREGRINE(**)		Used to model dose to humans from radiation therapy.
PHOTX	DLC-0136	photon interaction xsec library for 100 elements
PICA	CCC-0160	MC calculation of nuclear cascade reactions caused by the collision of photons (30<E<400 Mev) with nuclei
PIPE	NEA 0416	1-D gamma transport for slab, spherical shields
PLACID	CCC-0381	MC gamma streaming in cylindrical duct shields
PNESD	IAEA1235	elastic xsec of 3 MeV to 1000 MeV p on natural isotopes
POTAUS	IAEA1249	H thru U ion ranges, stopping power for various materials
PREANG	NEA 0809	nuclear model particle spectra, angular distribution
PRECO-D2	PSR-0226	pre-equilibrium, direct reaction dou ble differential xsec
PREM	NEA 0888	nucleon emission pre-equilibrium energy spectra, xsec
PSTAR(*)	IAEA1282	Calculates stopping power and range for protons
PTRAN	CCC-0618	MC proton transport for 50 to 250 MeV
PUTZ	CCC-0595	point-kernel 3-d gamma shielding
QMD		intra-nuclear cascade and classical molecular dynamics
RADCOMPT(*)	PSR-0348	Sample analysis for alpha and beta dual channel detect.
RADDECAY	DLC-0134	decay data library for radiological assessment
RADHEAT-V3	NEA 0467	transport, heat,radiation damage x sec in reactor, shield
RAID	CCC-0083	gamma, n scattering into cylindrical or multibend duct
REAC	CCC-0443	activation and transmutation
REAC-2	NESC9554	nuclide activation, transmutation
REAC3		high energy nuclide activation model
REBEL-3	IAEA0846	MC radiation dose to human organs
RECOIL/B	DLC-0055	heavy charged particle recoil spectra lib. for rad. damage
REMIT(*)	ESTS0579	Rad. Exposure Monitoring and Inf. Transmittal system
REPC	PSR-0195	dose from protons in tissue
RESRAD(*)	CCC-0552	Calculation of residual radioactive material guidelines, site specific radiation doses and risks
SAM-CE	CCC-0187	MC time-dep 3-d n ,gamma transport in complex geometry
SAMSY	IAEA0837	n, gamma dose rates, heat source for multilayer shields
SAND-II(*)	PSR-0345	Determines neutron energy spectra by an analysis of multiple experimental activation detector data
SANDYL	CCC-0361	MC 3-d time-dep gamma electron cascade transport

SCAP-82	CCC-0418	scattering, albedo, point-kernel anal. in complex geometry

Name	*Identification*	*Function*
SCINFUL(*)	PSR-0267	MC to compute the response of scintillation neutron detector (incident neutron energies from 0.1 to 75 MeV)
SEECAL(*)	CCC-0620	Computes age-dependent effective energies for 54 and 32 target regions in the human body (825 radionuclides)
SFERXS	NEA 1239	photon absorption, coherent,incoherent xsec for shielding
SHIELD(**)	IAEA1287	Universal code for exclusive simulation of hadron cascades in complex macroscopic targets. Transport of nucleons, pions, kaons, antinucleons and muons in the energy range up to 100 GeV is taken into account. Electromagnetic cascades are simulated by means of the EGS4 code, intranuclear cascades follow the model CASCAD, hadron-nucleus and nucleus-nucleus intranuclear interactions generated according to the QGSM based quark-gluon string model, Fermi break-up, multi-fragmentations and evaporation/fission according to the extended nuclear deexcitation model DEEX.
SIGMA-A(*)	DLC-0139	Photon interaction and absorption data 1 KeV-100 MeV
SITHA(**)	IAEA1179	SImulation Transport HAdron, used to calculate hadron transport in matter blocks of complex geometry. The nucleon and charged pions transport are carried out for the energy interval 10 MeV to 10 GeV and neutron transport for energies less than 20 MeV.
SKYPORT	DLC-0093	importance of n, photon skyshine dose from accelerators
SNLRML(*)	DLC-0178	Dosimetry library compendium
SNL/SAND-II(*)	PSR-0345	Enhanced version of SAND-II
SOURCE(**)		Description of the proton transmission and generation of n source. Based on the Moving Source Model formalism and Bethe stopping theory with relativistic corrections for protons, allows the estimation of the proton range and the changes of the proton current and the neutron production versus the depth.
SPACETRAN	CCC-0120	radiation leakage from cylinder with ANISN flux
SPAR	CCC-0228	stopping power and ranges from muons, pions, protons, ions
SPARES	CCC-0148	space radiation environment and shielding evaluation
SPCHAIN(**)		Calculates accumulation and decay of nuclides by taking the half-life and the decay chain of each nuclide into account.
SPECTER-ANL	PSR-0263	n damage for material irradiation
STAC-8		transmitted, absorbed power/spectrum - synchrotron radiation
STAPRE-H	IAEA0971	evaporation, pre-equilibrium model reaction xsec
STARCODES	PSR-0330	stopping power, ranges for electrons, protons, alpha
STOPOW	IAEA0970	stopping power of fast ions in matter
STRAGL	CCC-0201	energy loss straggling of heavy charged particles
SWIMS(*)	ESTS0682	Calculates the angular dispersion of ion beams that undergo small-angle incoherent multiple scattering by gaseous or solid media
TART95(*)		3D MC transport program for neutrons and photons
TEST(*)	IAEA1252	Program for sorting/listing/deleting ANISN libraries
TNG1	PSR-0298	N multi-step statistical model
TORT	CCC-0543	3-D Sn n, photon transport with deep penetration
TPASGAM(*)	DLC-0088	Library with gamma-ray decay data for 1438 radionuclides
TRANSX(*)	PSR-0317	Code system to produce neutron, photon transport tables for discrete ordinates and diffusion codes
TRAPP	CCC-0205	proton and alpha transport, reaction products neglected
TRIPOLI-2	NEA 0874	MC time-dep 3-D N, gamma transport
TRIPOS	CCC-0537	MC ion transport

TWODANT-SYS	CCC-0547	1-D,2-D multigroup Sn n, photon transport
UNGER	DLC-0164	effective dose equivalent data for selected isotopes

Name	*Identification*	*Function*
UNIFY	IAEA1177	fast n xsec, spectrum calculation for structural materials
VEGAS(**)		Intranuclear cascade code (from which ISABEL is derived)
VIRGIN(*)	IAEA0932	Calculates uncollided neutron flux and neutron reacti ons due to transmission of a neutron beam through any thickness of material
VITAMIN-E(*)	DLC-0113	X-section data library with 174n-38gamma energy groups
XCOM	USCD1156	photon cross sections from 1 keV to 100 GeV

CCC-,PSR-,DLC- : original packaging by RSIC
NESC : original packaging by NESC (now ESTSC)
USCD : originated in US/Canada, packaged by NEA DB
NEA, IAEA : original packaging by NEA DB
<blank> : acquisition sought
xsec : cross section
lib. : library

Table 2

Evaluated and processed data (cross sections, dose conversion, ranges, stopping powers)

Programs marked (*) or (**) in the following table, represent additions to the corresponding table of ref. [1]

(*) Programs available

(**) Programs known but not available

Name	*Identification*	*Function*
ACTIV-87(*)	IAEA1275	Library with fast neutron activation x-sections
CENDL(*)	IAEA1256	Chinese Evaluated Nuclear Data Library, namely the Optical Model Parameters for 6 types of projectiles (neutron, proton, deuteron, triton, He3 and He4)
COVFILES(*)	DLC-0091	Library of neutron x-sections covariance data, useful to estimate radiation damage or heating
DROSG-87(*)	IAEA1234	Library of Legendre coefficients for neutron reactions
DOSDAT-2	DLC-0079	gamma, electron dose factors data lib. for body organs
DOSEDAT-DOE	DLC-0144	doserate factors for external photon, electron exposure
EADL(*)	USCD1192	Library of atomic subshell and relaxation data
ECPL-86(*)	DLC-0106	evaluated charged particle cross-sections
EEDL(*)	USCD1193	Electron interaction x-section from 10 eV to 100 GeV
EPDL-VI/MOD(*)	USCD1187	Photon interaction x-sections library(10 eV to 100 GeV)
FGR-DOSE(*)	DLC-0167	Library of dose coefficients for intake and exposure to radionuclides
FLEP	DLC-0022	neutron, proton nonelastic xsec and spectra E<400MeV
HILO86	DLC-0119	66 N, 22 gamma grp XSEC lib. for ANISN-ORNL, DORT, MORSE-CGA
HELLO	DLC-0058	47 n, 21 gamma group coupled xsec from VITAMIN-C library
HUGO-VI	DLC-0146	photon interaction evaluated data library ENDF-6 format
IDC	CCC-0384	ICRP dosimetric calculational system
IHEAS-BENCH(*)	NEA 1468	High energy accelerator shielding benchmarks
LA100	DLC-0168	evaluated data library for n, p up to 100 MeV, ENDF-6 fmt
LAHIMACK	DLC-0128	Multigroup neutron and gamma x-sections up to 800 MeV
LEP	DLC-0001	results from intra-nuclear cascade and evaporation
LRSPC	CCC-0050	range and stopping power calculator
MATXS10(*)	DLC-0176	Library with 30n-12gamma energy groups for particle transport codes and high energy calculations
MATXS11(*)	DLC-0177	idem
MCNPDAT(*)	DLC-0105	X-section data library for the MCNP-4A transport code
MCNPDAT6(*)	DLC-0181	X-section data library from ENDF/B-VI for MCNP-4A
MENSLIB	DLC-0084	neutron 60 group xsec, E<60MeV
NFCLIST(*)	ESTS0352	Radionuclide decay data tabulations (240 radionuclides)
NUCDECAY(*)	DLC-0172	Nuclear decay data for radiation dosimetry calculations
PHOTX	DLC-0136	photon interaction xsec library for 100 elements
PNESD	IAEA1235	elastic xsec of 3 MeV to 1000 MeV p on natural isotopes
RADDECAY	DLC-0134	decay data library for radiological assessment
RECOIL/B	DLC-0055	heavy charged particle recoil spectra lib. for rad. damage
SFERXS	NEA 1239	photon absorption, coherent,incoherent xsec for shielding
SIGMA-A(*)	DLC-0139	Photon interaction and absorption data 1 KeV-100 MeV
SKYPORT	DLC-0093	importance of n, photon skyshine dose from accelerators
SNLRML(*)	DLC-0178	Dosimetry library compendium
SPAR	CCC-0228	stopping power and ranges from muons, pions, protons, ions
STAC-8		transmitted, absorbed power/spectrum - synchrotron radiat
STARCODES	PSR-0330	stopping power, ranges for electrons, protons, alpha

STOPOW	IAEA0970	stopping power of fast ions in matter

Name	*Identification*	*Function*
TPASGAM(*)	DLC-0088	Library with gamma-ray decay data for 1438 radionuclides
UNGER	DLC-0164	effective dose equivalent data for selected isotopes
VITAMIN-E(*)	DLC-0113	X-section data library with 174n-38gamma energy groups
XCOM	USCD1156	photon cross sections from 1 keV to 100 GeV

CCC-,PSR-,DLC-	: original packaging by RSIC
NESC	: original packaging by NESC (now ESTSC)
USCD	: originated in US/Canada, packaged by NEA DB
NEA, IAEA	: original packaging by NEA DB
<blank>	: acquisition sought
xsec	: cross section
lib.	: library

Table 3 ***Cross-sections - Spectra from nuclear models (for E>20 MeV)***

Programs marked (*) or (**) in the following table, represent additions to the corresponding table of ref. [1]
(*) Programs available
(**) Programs known but not available

Name	***Identification***	***Function***
ALICE91	PSR-0146	precompound/compound nuclear decay model
AMALTHEE	NEA 0675	emission spectra for n, p, d, h3, he3, alpha reaction
ASOP	CCC-0126	1-D Sn shield calculation
AUJP	IAEA0906	optical potential parameters search by chi**2 method
CADE	NEA 1020	multiple particle emission xsec by Weisskopf-Ewing
CEM95(*)	IAEA1247	MC calculation of nucl. reations (Cascade Exciton Model)
CFUP1	IAEA1266	n, charged-particle reaction of fissile nuclei E<33 MeV
CHUCK	USCD1021	n, charged particle xsec, coupled channel model
CMUP2	IAEA1265	reaction xsec for n ,p, d, t, he3, he4, E<50 MeV
COMNUC3B	PSR-0302	compound nucleus interaction in n reactions
DWBA82	NEA 1209	Distorted Wave Born Approximation nuclear model
DWUCK-4	NESC9872	Distorted Wave Born Approximation nuclear model
ECIS-95(*)	NEA 0850	Schroedinger/Dirac nuclear model with experimental fit
ELPHIC-PC	IAEA1223	statistical model MC simulation of heavy ion reaction
EMPIRE-MSC	IAEA1169	multistep compound nucleus/pre-equilibrium xsec
ERINNI	NEA 0815	multiple cascades emission spectra by optical model
EVA(*)		Codes performing the nuclear evaporation processes (working on the output from ISABEL)
EVAP_F(**)		Modified version of the Dresdner evaporation code (run in HETC@PSI)
EXIFONGAMMA	IAEA1211	n, alpha, proton, gamma emission spectra model
FRITIOF(**)		MC high-energy heavy ion collisions
GNASH-FKK(*)	PSR-0125	multi-step direct and compound and Hauser Feshbach models
GNASH-LANL	PSR-0125	pre-equilibrium/statistical xsec, emission spectra
GRAPE	NEA 1043	precompound/compound nuclear reaction models
HETC NMTC	CCC-0178	MC high energy nucleon meson casca de transport
HETC-KFA	CCC-0496	MC high energy nucleon-meson cascades
HETC95(**)		MC high energy nucleon-meson cascades and transport
HFTT	IAEA0954	n xsec by compound-nucleus evaporation model
HIJET(**)		MC high-energy heavy ion collisions
ISABEL(*)	NEA 1413	Intranuclear cascade model allowing hydrogen and helium ions and antiprotons as projectiles (run in LAHET)
ISAJET(**)		MC high-energy heavy ion collisions
KAPSIES		quantum mechanical multi-step direct model
LIMES	NEA 1337	Intermediate mass fragments in heavy ion nuclear reactions
MARLOWE	PSR-0137	atomic displacement cascades in solids
MECC-7	CCC-0156	medium energy intra-nuclear cascade model
MUP-2	IAEA0907	fast n reaction xsec of medium-heavy nuclei
MUTIL(*)	NEA 1451	Calculates the asymmetry factor of the Mott scattering of electrons and positrons by point nuclei
NDEM(**)		Generates a gamma-ray source from the deexcitation of residual nuclei, assuming all particle decay modes have been exhausted (part of the HERMES system)

Name	*Identification*	*Function*
NJOY-94(*)	PSR-0171	n, p, photon evaluated data processing system
NMTC/JAERI	NEA 0974	MC high-energy p, n, pion reactions
NUCLEUS		Nuclear spallation simulation and primary products
PACE2(**)		Codes performing the nuclear evaporation processes (working on the output from ISABEL)
PCROSS	IAEA1220	pre-equilibrium emission spectra in neutron reaction
PEGAS	IAEA1261	unified model of particle and gamma emission reactions
PELSHIE	IAEA0855	dose rates from gamma source, point-kernel method
PEQAG-2	IAEA1185	pre-equilibrium model nucleon, gamma spectra, xsec
PREANG	NEA 0809	nuclear model particle spectra, angular distribution
PRECO-D2	PSR-0226	pre-equilibrium, direct reaction double differential xsec
PREM	NEA 0888	nucleon emission pre-equilibrium energy spectra, xsec
QMD		intra-nuclear cascade and classical molecular dynamics
REAC	CCC-0443	activation and transmutation
REAC-2	NESC9554	nuclide activation, transmutation
REAC3		high energy activation model
STAPRE-H	IAEA0971	evaporation, pre-equilibrium model reactio n xsec
TNG1	PSR-0298	N multi-step statistical model
UNIFY	IAEA1177	fast n xsec, spectrum calculation for structural materials
VEGAS(**)		Intranuclear cascade code (from which ISABEL is derived)

CCC-,PSR-,DLC-	: original packaging by RSIC
NESC	: original packaging by NESC (now ESTSC)
USCD	: originated in US/Canada, packaged by NEA DB
NEA, IAEA	: original packaging by NEA DB
<blank>	: acquisition sought
xsec	: cross section
lib.	: library

Table 4 ***Monte Carlo (MC) and deterministic radiation transport***

Programs marked (*) or (**) in the following table, represent additions to the corresponding table of ref. [1]
(*) Programs available
(**) Programs known but not available

Name	***Identification***	***Function***
Neutron/photon		
ALBEDO	NEA 1353	gamma, neutron attenuation in air ducts
ANISN	CCC-0254	1-D Sn, n, gamma transport in slab, cylinder, sphere
ASOP	CCC-0126	1-D Sn shield calculation
BALTORO	NEA 0675	n, gamma transport perturbation from MORSE, ANISN calculation
BERMUDA	NEA 0949	1-D,2-D,3-D n. gamma tran sport for shielding
BREESE	PSR-0143	distribution function for MORSE from albedo data
CARP-82	PSR-0131	currents for BREESE from DOT flux
COLLI-PTB	NEA 1126	MC n fluence spectra for 3-D collimator system
DANTSYS(*)	CCC-0547	1-D, 2-D, 3-D Sn neutron, photon transport
DASH	CCC-0366	void tracing Sn - MC COUPLING with fluxes from DOT
DCTDOS	CCC-0520	n, gamma penetration in composite duct system
DORT	CCC-0543	1-D 2-D Sn n, photon transport with deep penetration
DOMINO	PSR-0064	coupling of Sn DOT with MC MORSE
DOT	CCC-0276	2-D Sn n, photon transport with deep penetration
DUST	CCC-0453	albedo MC simulation of n streaming inducts
FALSTF	CCC-0351	n, gamma flux detector response outside cyl shields
FEM-RZ	NEA 0566	FEM 2-D multigroup n transport in r-z geometry
GEANT-CERN		MC hadron shower simulation
MAGIK	CCC-0359	MC induced residual activation dose rates
MCNP	CCC-0200	MC 3-D time-dep coupled n, photon, electron transport
MICAP(*)	PSR-0261	MC to determine the response of gas filled cavity ionization chamber, plastic scintilator or calorimeter in a mixed neutron and photon environment
MORSE-CGA	CCC-0474	MC n, gamma multigroup transport
PALLAS-2DY	NEA 0702	2-D n ,gamma transport for fixed source
RADHEAT-V3	NEA 0467	transport, heat,radiation damage xsec in reactor, shield
RAID	CCC-0083	gamma, n scattering into cylindrical or multibend duct
SAMSY	IAEA0837	n, gamma dose rates, heat source for multilayer shields
SAM-CE	CCC-0187	MC time-dep 3-d n ,gamma transport in complex geometry
SAND-II(*)	PSR-0345	Determines neutron energy spectra by an analysis of multiple experimental activation detector data
SCINFUL(*)	PSR-0267	MC to compute the response of scintillation neutron detector (incident neutron energies from 0.1 to 75 MeV)
SCAP-82	CCC-0418	scattering, albedo, point-kernel anal. in complex geometry
SNL/SAND-II(*)	PSR-0345	Enhanced version of SAND-II
SPACETRAN	CCC-0120	radiation leakage from cylinder with ANISN flux
SPECTER-ANL	PSR-0263	n damage for material irradiation
TART95(*)		3D MC transport program for neutrons and ph otons
TORT	CCC-0543	3-D Sn n, photon transport with deep penetration
TRANSX(*)	PSR-0317	Code system to produce neutron, photon transport tables for discrete ordinates and diffusion codes
TRIPOLI-2	NEA 0874	MC time-dep 3-D n, gamma transport
TWODANT-SYS	CCC-0547	1-D,2-D multigroup Sn n, photon transport

VIRGIN(*)	IAEA0932	Calculates uncollided neutron flux and neutron reactions due to transmission of a neutron beam through any thickness of material

Name	*Identification*	*Function*
Photon		
AIRSCAT	CCC-0341	dose rate from gamma air scattering, single scat. approx.
GAMMONE	NEA 0268	MC gamma penetration from various geometrical sources
MERCURE-4	NEA 0351	MC 3-D gamma heating/gamma dose rate, fast flux
PLACID	CCC-0381	MC gamma streaming in cylindrical duct shields
BRHGAM	CCC-0350	MC absorbed dose from x-rays in phantom
BREMRAD	CCC-0031	external/internal bremsstrahlung
G33-GP	CCC-0494	multigroup gamma scattering using gp buildup-factor
ISO-PC(*)	CCC-0636	Kernel integration code system for general purpose isotope shielding
MAGNA	NEA 0163	dose rates from gamma source in slab or cyl shell shields
MARMER	NEA 1307	point-kernel shielding, ORIGEN-S nuclide inventories
PELSHIE	IAEA0855	dose rates from gamma source, point-kernel method
PIPE	NEA 0416	1-D gamma transport for slab, spherical shields
PUTZ	CCC-0595	point-kernel 3-d gamma shielding
STAC-8		transmitted, absorbed power/spectrum - synchrotron radiat
Electron/photon		
BETA-2B	CCC-0117	MC time-dep bremsstrahlung, electron transport
CASCADE	CCC-0176	high energy electron-photon transport in matter
CEPXS ONELD	CCC-0544	1-D coupled electron photon multigroup transport
DOSDAT-2	DLC-0079	gamma, electron dose factors data lib. for body organs
EDMULT	NEA 0969	electron depth dose in multilayer slab absorbers
EGS4	CCC-0331	MC electron photon shower simulation
ELBA	CCC-0119	bremsstrahlung dose from electron flux on Al shield
EPICSHOW(*)	IAEA1285	Interactive Viewing of the Electron-Photon Interaction Code (EPIC) system databases (10 eV < E < 1 GeV)
ESTAR(*)	IAEA1282	Calculates stopping power and range for electrons
ETRAN	CCC-0107	MC electron, gamma transport with secondary radiation
ELTRAN	CCC-0155	MC 1-D electron transport
FOTELP	CCC-0581	MC photons, electrons and positron transport
ITS-3.0	CCC-0467	MC tiger system of coupled electron photon transport
MCNP-4A	CCC-0200	MC 3-D time-dep coupled n, photon, electron transport
SANDYL	CCC-0361	MC 3-D time-dep gamma electron cascade transport
Protons		
ASTROS	CCC-0073	primary/secondary proton dose in sphere/slab tissue
LPPC	CCC-0051	proton penetration, slab
PSTAR(*)	IAEA1282	Calculates stopping power and range for protons
PTRAN	CCC-0618	MC proton transport for 50 to 250 MeV
SOURCE(**)		Description of the proton transmission and generation of n source. Based on the Moving Source Model formalism and Bethe stopping theory with relativistic corrections for protons, allows the estimation of the proton range and the changes of the proton current and the neutron production versus the depth.
TRAPP	CCC-0205	proton and alpha transport, reaction products neglected

Name	*Identification*	*Function*
Alphas		
ALDOSE(*)	CCC-0577	Calculates of absorbed dose and dose equivalent rates as function of depth in water irradiated by alpha source
ALPHN(*)	CCC-0612	Calculates the (alpha,n) production rate in a mixture receiving alpha particles from emitting actinides
ASTAR(*)	IAEA1282	Calculates stopping power and range for alphas
RADCOMPT(*)	PSR-0348	Sample analysis for alpha and beta dual channel detectores
Nucleons/hadrons/cascades		
CALOR89	CCC-0610	MC system for design, analysis of calorimeter system
CALOR93		MC system for design, analysis of calorimeter system
CASIM	NESC0742	MC high energy cascades in complex shields
FLUKA	CCC-0207	MC high energy extranuclear hadron cascades
GEANT-CERN		MC hadron shower simulation
HERMES-KFA	NEA 1265	MC high-energy radiation transport
HETC NMTC	CCC-0178	MC high energy nucleon meson cascade transport
HETC-KFA	CCC-0496	MC high energy nucleon-meson cascade transport
LAHET		MC nucleon, pion, muons, tritons, He-3, alpha transpor t
LPSC	CCC-0064	p, n flux, spectra behind slab shield from p irradiation
NMTC/JAERI	NEA 0974	MC high-energy p, n, pion reactions
SITHA(**)	IAEA1179	SImulation Transport HAdron, used to calculate hadron transport in matter blocks of complex geometry. The nucleon and charged pions transport are carried out for the energy interval 10 MeV to 10 GeV and neutron transport for energies less than 20 MeV.
SHIELD(**)	IAEA1287	Universal code for exclusive simulation of hadron cascades in complex macroscopic targets. Transport of nucleons, pions, kaons, antinucleons and muons in the energy range up to 100 GeV is taken into account. Electromagnetic cascades are simulated by means of the EGS4 code, intranuclear cascades follow the model CASCAD, hadron-nucleus & nucleus-nucleusintranuclear interactions generated according to the QGSM based quark-gluon string model, Fermi break-up, multi-fragmentations and evaporation/fission according to the extended nuclear deexcitation model DEEX.
Heavy-ions		
E-DEP-1	CCC-0275	heavy ion energy deposition
ELPHIC-PC	IAEA1223	statistical model MC simulation of heavy ion reaction
HIC-1	CCC-0249	MC heavy ion reactions at E>50 MeV/nucleon
STRAGL	CCC-0201	energy loss straggling of heavy charged particles
SWIMS(*)	ESTS0682	Calculates the angular dispersion of ion beams that undergo small-angle incoherent multiple scattering by gaseous or solid media
TRIPOS	CCC-0537	MC ion transport
Muons		
MUONLM(*)	NEA 1475	Calorimeter Interaction of Muons

Name	*Identification*	*Function*
Others/cascades		
CHARGE-2/C	CCC-0070	electron, p, heavy particle flux/dose behind shield
DDCS(*)	IAEA1290	Calculation of neutron, proton, deuteron, triton, He3, and alpha induced reations of medium heavy nuclei in the energy range up to 50 MeV
ELPHO	CCC-0301	MC muon, electron, positron generation from pions
IMPACTS-BRC(*)	ESTS0005	Radiological assessment code
JENKINS		photon, neutron dose in electron accelerator
PICA	CCC-0160	MC calculation of nuclear cascade reactions caused by the collision of photons (30 < E < 400 Mev) with nuclei
SPARES	CCC-0148	space radiation environment and shielding evaluation
Anthropomorphic phantom modelling		
BRHGAM	CCC-0350	MC absorbed dose from x-rays in phantom
CAMERA	CCC-0240	radiation transport and computerized man model
DISDOS	CCC-0170	dose from external photons in phantom
K009	CCC-0062	Charged particle penetration - phantom
MEVDP	CCC-0157	radiation transport in computerized anatomical man
PEREGRINE(**)		Used to model dose to humans from radiation therapy.
REBEL-3	IAEA0846	MC radiation dose to human organs
REPC	PSR-0195	dose from protons in tissue
SEECAL(*)	CCC-0620	Computes age-dependent effective energies for 54 and 32 target regions in the human body (825 radionuclides)

CCC-,PSR-,DLC- : original packaging by RSIC
NESC : original packaging by NESC (now ESTSC)
USCD : originated in US/Canada, packaged by NEA DB
NEA, IAEA : original packaging by NEA DB
<blank> : acquisition sought
xsec : cross section
lib. : library

Appendix A

Agenda

GENERAL INTRODUCTION
Scope and objectives of the meeting, announcements, introduction of participants

CHAIR: Takashi Nakamura
CO-CHAIR: Alfredo Ferrari

SESSION I: BASIC PHYSICS DATA – DOUBLE-DIFFERENTIAL CROSS-SECTIONS, YIELDS

Speaker / Title

Enrico Sartori for *P. Vaz*
Review of existing or planned proton accelrators and neutron beams
in the intermediate energy range

H. Hirayama
Review of actions in Japan after SATIF-I

K. Hayashi
Survey of thick target neutron yield data and accelerator shielding experiments

J. Ranft
Hadronic photon-hadron and photon-photon interactions at high energies

P. Degtyarenko
Applications of the photonuclear fragmentation model to radiation protection problems

P.K. Job and T. Gabriel
The photoneutron yield predictions by PICA and comparison with measurements

E. Sartori
1994 compilation of charged particle interaction data *– oral presentation only*

CHAIR: **Herbert Dinter**
CO-CHAIR: **Laurie Waters**

SESSION II: SHIELDING – EXPERIMENTAL BENCHMARKS, SOURCE TERMS AND ATTENUATION LENGTHS, EMPIRICAL METHODS, SHIELDING POLICY

Speaker / Title

P. Tabarelli de Fatis
Double differential distributions, attenuation lengths and source terms for proton accelerator shielding

H. Nakashima and N. Yoshizawa
Accelerator shielding benchmark experiment analyses

Y. Sakamoto
Approximate description of dose attenuation profiles of intermediate energy neutrons – I

K. Shin
Approximate description of dose attenuation profiles of intermediate energy neutrons – II

A. Ferrari,
Measurements and simulations in high energy neutron fields

R. Nelson
Shielding calculations for LANSCE upgrade *– oral presentation only*

R.W. Roussin
SINBAD, Shielding Integral Benchmark Archive and Database

CHAIR: **Tony Gabriel**
CO-CHAIR: **Kazuo Shin**

SESSION III: ENERGY RESPONSE FUNCTIONS – ACTIVATION, TRANSMUTATION, ISOTOPE PRODUCTION

Speaker / Title

S. Ban
Calibration of a modified Andersson-Braun rem counter

T. Nakamura
Activation cross-section measurements using quasi-monoenergetic neutron field from 20 to 150 MeV

F. Clapier
Neutron induced activation and transmutation, heavy ion induced isotope production with C, Ne, Ar, Kr at 100 A.MeV

CHAIR: **Graham Stevenson**
CO-CHAIR: **Yukio Sakamoto**

SESSION IV: **HIGH ENERGY DOSIMETRY – CONVERSION FACTORS, ANTHROPOMORPHIC MODELS, ACCELERATORS**

Speaker / Title

S. Iwai
Evaluation of fluence to dose equivalent conversion coefficients for high energy neutrons – calculation of effective dose equivalent and effective dose

E. Sartori
Results of inquiry on anthropomorphic computational models

N. Ipe
Narrow beam dosimetry at accelerator facilities – *oral presentation only*

CHAIR: **Robert Roussin**
CO-CHAIR: **Hideo Hirayama**

SESSION V: **MODELLING CODES AND DATA – RECENT RELEASES, COMPILATIONS, DEVELOPMENT REQUIRED, SHARING**

Speaker / Title

L. Waters
Current status and applications of the LAHET code system – *oral presentation only*

N. Mokhov
Recent applications using MARS13 (95) code – *oral presentation only*

T. Gabriel
Current improvement in HETC95 – *oral presentation only*

R.W. Roussin
Status report on the collection of computer codes and data for accelerator shield modelling

CHAIR: **Nisy Ipe**
CO-CHAIR: **Alberto Fassò**

SESSION VI: **DISCUSSION, RECOMMENDATIONS, FUTURE ACTIONS AND INTERNATINAL CO-OPERATION – GENERAL DISCUSSION**

Appendix B

List of participants

CANADA

MORITZ, Lutz E.
TRIUMF
Canada's National Meson Research Facility
404 Wesbrook Mall
VANCOUVER, BC V6T 2A3

Tel: +1 (604) 222 1047
Fax: +1 (604) 222 1074
Net: moritz@erich.triumf.ca

FINLAND

AARNIO, Pertti A.
Helsinki University of Technology
Rakentajanaukio 2C
FIN-02150 ESPOO

Tel: +358 (0) 451 3191
Fax: +358 (0) 451 3195
Net: aarnio@hut.fi

FRANCE

BOTH, Jean-Pierre
C.E. Saclay
DRN/DMT/SERMA/LEPP
Bât. 470
F-91191 GIF/YVETTE Cedex

Tel: +33 (1) 6908 8478
Fax: +33 (1) 6908 4572
Net: bot@soleil.serma.cea.fr

CLAPIER, François
Ingénieur de Radioprotection
CNRS-IN2P3
Institut Physique Nucléaire
SPR
91406 ORSAY

Tel: +33 (1) 6941 7170
Fax: +33 (1) 6941 6470
Net: clapier@ipncls.in2p3.fr

CUENDET, Pascal
C.E. Saclay
DRN/DMT/SERMA
Bât 470
91191 GIF-SUR-YVETTE Cedex

Tel: +33 (1) 6908 6358
Fax: +33 (1) 6908 4572
Net: strb@soleil.serma.cea.fr

FRANCK, Jean-Claude
LURE
Université Paris-Sud
Bâtiment 201
F- 91405 ORSAY Cedex

Tel: +33 (1) 6446 8201
Fax: +33 (1) 6907 1499

PAUWELS, Nicolas
CNRS-IN2P3
Institut Physique Nucléaire
SPR
91406 ORSAY

Tel: +33 (1) 6941 7170
Fax: +33 (1) 6941 6470
Net: pauwels@ipncls.in2p3.fr

RANFT, Johannes
B.P. 110
LAPP
F-74941 ANNECY-LE-VIEUX

Tel: +33 5009 1680
Net: ran@cernvm.cern.ch

Now at Physics Department
University of Santiago de Campostela
Galicia, SPAIN

GERMANY

DINTER, Herbert
Deutsches Elektronen - Synchrotron DESY
Notkestr. 85
D-22603 HAMBURG

Tel: +49 (40) 89 98 3446
Fax: +49 (40) 89 98 3282
Net: D03DIN@dsyibm.desy.de

FESTAG, Johannes Georg
c/o Gesellschaft für Schwerionenforschung mbH
Planckstrasse 1
D-64291 DARMSTADT

Tel: +49 (6159) 71 2400
Fax: +49 (6159) 71 2109
Net: bt12@ddagsi3.gsi.de

MARES, Vladimir
GSF-
Forschungszentrum für Umwelt und Gesundheit
GmbH Neuherberg
Postfach 1129
D-85758 OBERSCHLEISSHEIM

Tel: +49 (89) 3187 2652
Fax: +49 (89) 3187 3323
Net: mares@gsf.de

ROESLER, Stefan
Dept. of Physics
University of Siegen
SIEGEN D-57068

Tel: +49 (271) 740 4533
Fax: +49 (271) 740 2330
Net: sroesler@cernvm.cern.ch

TESCH, Klaus
Deutsches Elektronen - Synchrotron DESY
Notkestr. 85

Tel: +49 (40) 89 98 3402
Fax: +49 (40) 89 98 3282

D-22603 HAMBURG Net: d03tes@dsyibm.desy.de

ITALY

BURN, Kenneth W.
ENEA-ERG-FISS-FIRE
ENEA
Via Martiri di Monte Sole 4
I-40129 BOLOGNA
Tel: +39 (51) 6098 486
Fax: +39 (51) 6098 629
Net: burn@rin365.arcoveggio.enea.it

FERRARI, Alfredo
I.N.F.N., Dipartimento di
Fisica dell'Universita e INFN
Via Celoria 16
I-20133 MILANO
Tel: +39 (2) 2392 310
Fax: +39 (2) 2392 624
Net: ferrari@almif2.mi.infn.it

MENAPACE, Enzo
E.N.E.A.
Applied Physics Division
Via Don G. Fiammelli 2
I-40128 BOLOGNA
Tel: +39 (51) 60 98 239
Fax: +39 (51) 60 98 359
Net: menapace@eborsk1.bologna.enea.it

PELLICCIONI, Maurizio
INFN
Laboratori Nazionali di Frascati
Casella Postale 13
I-00044 FRASCATI
Tel: +39 (6) 940 32246
Fax: +39 (6) 940 32364
Net: pelliccm@vaxlnf.lnf.infn.it

TABARELLI DE FATIS, Paola
Fondazione TERA
Istituto Europeo di Oncologia
via Ripamonti 435
I-20140 MILANO
Net: ptabarelli@vaxmi.mi.infn.it

JAPAN

BAN, Syuichi
KEK, National Laboratory for High Energy Physics
1-1 Oho
Tsukuba-shi, IBARAKI-KEN 305
Tel: +81 (298) 64 5494
Fax: +81 (298) 64 1993
Net: ban@kekrc3.kek.jp

HAYASHI, Katsumi
Hitachi Engineering Company
3-2-1 Saiwai-cho
Hitachi-shi
IBARAKI-KEN 317
Tel: +81 (294) 24 1111 X 286
Fax: +81 (294) 23 6748
Net: i90084@sinet.ad.jp

HIRAYAMA, Hideo
KEK, National Laboratory for High Energy Physics
1-1 Oho
Tel: +81 (298) 64 5493
Fax: +81 (298) 64 1993

Tsukuba-shi, IBARAKI-KEN 305 Net: hirayama@kekrc3.kek.jp

IWAI, Satoshi
Nuclear Application Techn. G.
Mitsubishi Heavy Industries
1-297 Kitabukuro-cho
Omiya-shi
SAITAMA-KEN 330

Tel: +81 (48) 642 4404
Fax: +81 (48) 645 0189

NAKAMURA, Takashi
Cyclotron and Radioisotope Centre
Tohoku University
Aramaki, Aoba, Aoba-ku
SENDAI 980-77

Tel: +81 (22) 217 7805
Fax: +81 (22) 217 7809
Net: nakamura@risun1.cyric.tohoku.ac.jp

NAKASHIMA, Hiroshi
Applied Radiation Laboratory
JAERI
Tokai Research Establishment
Tokai-Mura
IBARAKI-KEN 319-11

Tel: +81 (29) 282 5356
Fax: +81 (29) 282 5663
Net: nakasima@shield2.tokai.jaeri.go.jp

SAKAMOTO, Yukio
Applied Radiation Laboratory
Dept. Reactor Engineering
JAERI
Tokai-mura, Naka-gun
IBARAKI-KEN 319-11

Tel: +81 (29) 282 5355
Fax: +81 (29) 282 5663
Net: sakamoto@Shield2.tokai.jaeri.go.jp

SHIN, Kazuo
Dept. of Nuclear Engineering
Kyoto University
Yoshida
Sakyo-ku
KYOTO 606-01

Tel: +81 (75) 753 5825
Fax: +81 (75) 753 5845

YOSHIZAWA, Nobuaki
Mitsubishi Research Institute
3-6, Otemachi 2-chome
Chiyoda-ku
TOKYO 100

Tel: +81 (3) 3277 0772
Fax: +81 (3) 3277 3480
Net: yoshizaw@mri.co.jp

SWEDEN

STALNACKE, Carl-Goeran
The Svedberg Laboratory
Uppsala University
Thunbergsv 5
Box 553

Tel: +46 (18) 1838 83
Fax: +46 (18) 1838 33
Net: stalnacke@tsl.uu.se

S-75 121 Uppsala

SWITZERLAND

ARKUSZEWSKI, Jacek J.
Paul Scherrer Institute
OBUA/22
CH-5232 VILLIGEN PSI

Tel: +41 (56) 310 20 83
Fax: +41 (56) 310 44 12
Net: Arkuszewski@psi.ch

UNITED STATES OF AMERICA

COKINOS, Dimitri
Brookhaven National Lab.
Building 475B
UPTON, N.Y. 11973

Tel: +1 (516) 282 2146
Fax: +1 (516) 282 2613
Net: cokinos@bnl.gov

DEGTYARENKO, Pavel
CEBAF, MS 12A1
12000, Jefferson Ave.,
NEWPORT NEWS, VA 23606

Fax: +1 (804) 249 7363
Net: pavel@cebaf.gov

DONAHUE, Richard J.
Lawrence Berkeley Laboratory
University of California
1, Cyclotron Rd
BERKELEY, CA 94720

Tel: +1 (510) 486 5597
Fax: +1 (510) 486 6608
Net: RJDonahue@lbl.gov

GABRIEL, Tony A.
Oak Ridge National Laboratory
P. O. Box 2008
OAK RIDGE, TN 37831-6364

Tel: +1 (615) 574 6082
Fax: +1 (615) 574 9619
Net: tag@ornl.gov

IPE, Nisy E.
SLAC
MS-48
P.O. BOX 4349
STANFORD, CA 94309

Tel: +1 (415) 926 4324
Fax: +1 (415) 926 3569
Net: ipe@slac.stanford.edu

JOB, P.K.
Advanced Photon Source
Argonne National Laboratory
9700 South Cass Avenue
ARGONNE, IL 60439

Tel: +1 (708) 252 6573
Net: pkj@aps.anl.gov

MOKHOV, Nikolai
FERMILAB
MS 345
P.O. Box 500
BATAVIA, IL 60510

Tel: +1 (708) 840 4409
Fax: +1 (708) 840 4552
Net: mokhov@fnalv.fnal.gov

NELSON, Ronald O.
LANL-LANSCE
MS H805
Los Alamos National Laboratory
LOS ALAMOS, NM 87545

Tel: +1 (505) 665 0394
Net: ron@lanl.gov

ROKNI, Sayed H.
Radiation Physics Department
SLAC
P.O.Box 4349
STANFORD, CA 94309

Tel: +1 (415) 926 3544
Fax: +1 (415) 926 3569
Net: Rokni@slac.stanford.edu

ROUSSIN, Robert W.
Director, Engineering Physics
Information Center
Oak Ridge National Laboratory
Post Office Box 2008
OAK RIDGE, TN 37831-6362

Tel: +1 (423) 574 6176
Fax: +1 (423) 574 6182
Net: rwr@ornl.gov

WATERS, Laurie S.
Radiation Transport Group XTM
MS B226
Los Alamos National Laboratory
LOS ALAMOS, NM 87545

Tel: +1 (505) 665 4127
Net: lsw@lanl.gov

INTERNATIONAL ORGANISATIONS

CARMINATI, Federico
CERN
Division DD
CH-1211 GENEVE 23
SWITZERLAND

Tel: +41 (22) 767 49 59
Fax: +41 (22) 767 55 55
Net: federico_carminati@eet.cern.ch

CHABRATOVA, Galina
CERN
CH-1211 GENEVE 23
SWITZERLAND

Tel: +41 (22) 767 3852
Net: gshabrat@vxcern.cern.ch

FASSO', Alberto
CERN
CH-1211 GENEVE 23
SWITZERLAND

Tel: +41 (22) 767 3937
Fax: +41 (22) 767 5700
Net: fasso@afsmail.cern.ch

Now at SLAC, MS-48
P.O.Box 4349
STANFORD, CA 94309

Net: fasso@slac.stanford.edu

ROLLET, Sofia
CERN
CH-1211 GENEVE 23
SWITZERLAND

Tel: +41 (22) 767 5081
Fax: +41 (22) 767 9080
Net: srollet@dxcern.cern.ch

STEVENSON, Graham Roger
CERN
CH-1211 GENEVE 23
SWITZERLAND

Tel: +41 (22) 767 4623
Fax: +41 (22) 783 05 52
Net: GRS@cernvm.cern.ch

ZAZULA, Jan M.
CERN
Div SL/BT (TA)
CH-1211 GENEVE 23
SWITZERLAND

Tel: +41 (22) 767 5372
Fax: +41 (22) 767 8480
Net: zazula@cernvm.cern.ch

SARTORI, Enrico
OECD/NEA
Data Bank
Le Seine-Saint Germain
12 boulevard des Iles
F-92130 ISSY-LES-MOULINEAUX
FRANCE

Tel: +33 (1) 4524 1072
Fax: +33 (1) 4524 1110
Net: sartori@nea.fr

Appendix C

Index